2 (mix) -P

APOLLO LASER RANGING RETRO-REFLECTOR EXPERIMENT

(S078)

Final Report

Contract NAS 9-7809

February 1971

Prepared by

C. O. Alley, Principal Investigator

UNIVERSITY OF MARYLAND
DEPARTMENT OF PHYSICS AND ASTRONOMY
COLLEGE PARK, MARYLAND

APOLLO LASER RANGING RETRO-REFLECTOR EXPERIMENT

(S078)

Final Report

Contract NAS 9-7809

February 1971

Prepared by

C. O. Alley, Principal Investigator

UNIVERSITY OF MARYLAND

Department of Physics and Astronomy

College Park, Maryland

TABLE OF CONTENTS

Appendixes (cont.)

FOREWORD

As a major part of the Apollo Lunar Laser Ranging Experiment it was essential to design and guide the construction of corner reflector arrays which would give satisfactory optical performance at all times during the extreme thermal conditions encountered on the moon's surface. The responsibility for this work was carried by the University of Maryland as the institution of the Principal Investigator, C. O. Alley. Other key personnel at Maryland who made major contributions were participating scientists D. G. Currie, Ren-Fang Chang, S. K. Poultney, and Project Engineer H. Kriemelmeyer. Among the group of co-investigators, J. E. Faller of Wesleyan University contributed importantly to early design concepts and thermal analyses and participated in the supervision of contractors. The other co-investigators were: P. L. Bender (National Bureau of Standards and University of Colorado), R. H. Dicke (Princeton University), W. M. Kaula (University of California at Los Angeles), G. J. F. MacDonald (Council on Environmental Quality), J. D. Mulholland (Jet Propulsion Laboratory), H. H. Plotkin (Goddard Space Flight Center) and D. T. Wilkinson (Princeton University).

We wish to acknowledge the excellent work of the major industrial contractors who have participated in this program. These include the Perkin-Elmer Company, the Arthur D. Little Company, and the Bendix Aerospace Corporation. Specific individuals and contributions are discussed in the report and the appendixes.

The active support of many individuals of the National Aeronautics and Space Administration has been essential to the successful completion of this work. We wish to thank particularly Dr. Harvey Hall, scientific

adviser to the Manned Space Flight Experiments Board, Dr. Urner Liddel, Mr. Richard Green and Mr. Edward Davin of the Lunar Exploration Office, Mr. A. J. Calio and Mr. Ausley Carraway of the Science and Applications Directorate of the Manned Spacecraft Center, and in more recent times, Mr. Richard Johnston of the Apollo Spacecraft Office.

I. SUMMARY

This report describes the accomplishments of the University of Maryland, as the principal investigator institution, and its subcontractors in the research and development that has produced the successful Apollo Laser Ranging Retro-Reflectors (LR^3s). The place of this activity in the overall development of the Apollo Lunar Laser Ranging Experiment is also briefly presented. The performance of the LR^3's in the lunar environment can only be assessed through the ground instrumentation part of the experiment for which the University of Maryland also carried a major initial design and development responsibility.

The performance of the Apollo 11 and Apollo 14 LR^3's is entirely satisfactory and seems to be in accordance with the design parameters within the limits of the ability to measure their reflectivity (within a factor of 2 or 3). There has as yet been no NASA support to develop the instrumentation to measure the atmospheric seeing so as to provide a more accurate monitoring of the reflectivity. One cannot rule out a possible degradation of reflector performance produced by dust and debris generated during the lift-off of the LM ascent stage.

There is some preliminary information that the Apollo 14 LR^3 may have been degraded during lift-off since it was possible to get laser pulse returns from it both before and after this event. There is not yet sufficient information from a series of ranging operation to say this with assurance, however.

There is no evidence that the reflectivity of the Apollo 11 LR^3 is decreasing with time within the present limits of our ability to measure it.

Following the Introduction, the report is divided into sections on Optical Design, Thermal and Mechanical Design, Testing of Optical Performance in Simulated Lunar Environment, and Performance on the Moon. The detailed discussion of these topics is contained in published papers, technical reports, and contractor reports which are included with this final report as appendixes.

II. INTRODUCTION

A. Background

To place the work performed under the present contract in proper context a brief history of the development of the Lunar Laser Ranging Experiment will be given.

The concept of placing optical corner reflectors on earth satellites was discussed shortly after the first Russian Sputnik among members of the gravitational research group of Professor R. H. Dicke at Princeton University. A paper showing the feasibility of observing such satellites in near earth orbit with searchlight illumination was written for the group by Hoffman, Krotkov, and Dicke.[1] When the Soviet Union succeeded in impacting a rocket on the moon there were discussions within the above group of the possibilities of providing an optical reference spot on the moon. This possibility took on more reality in 1960 and 1961 with the experimental realization of the laser and, in particular, the development of the technique of "Q-switching" to provide very short bursts of highly collimated light. The development of the technique of laser ranging to corner reflector equipped artificial satellites was undertaken by H. H. Plotkin and the Optical Systems Branch of the Goddard Space Flight Center.[2]

In 1962 plans were made in several places to actually detect laser pulses bounced off the surface of the moon.[3] Successful detection was achieved by groups in the U.S.[4] and in the USSR[5]. In the summer of 1964 the development of space engineering and the planning for lunar missions had reached such a stage that a paper was written pointing out the

desirability of placing a suitably designed optical corner reflector on the moon.[6]

In the fall of 1964 discussions were held by some of the authors of this paper with Mr. Benjamin Milwitzky, director of the Surveyor program, and with other NASA officials in an effort to have NASA develop suitable reflectors for lunar emplacement by the Surveyors.

In the spring of 1965, it was suggested by Mr. Milwitzky that the best way to proceed would be to submit a proposal from a group outside NASA willing to accept responsibility for the development of a lunar laser beam reflector. At a meeting of the NASA Physics Committee in May, 1965 this approach was endorsed by Dr. Homer Newell, Associate Administrator for Space Science and Applications, Dr. John Naugle, the Deputy Associate Administrator for Space Science, and by Dr. Urner Liddel, Secretary of the Physics Committee and Chairman of the Lunar and Planetology Subcommittee. The author of this report agreed to accept responsibility as principal investigator and with the active help of the co-investigators listed in the Foreword and Prof. Dirk Brouwer of Yale University, later deceased, a detailed proposal was developed during the summer and fall of 1965 on the scientific importance of precise point to point earth-moon distance measurements. Specific experimental approaches for both the lunar and ground instrumentation were also given. This proposal was submitted from the University of Maryland in December, 1965.[7]

Following reviews by the Lunar and Planetology and by the Astronomy subcommittees, a grant of $60,000 was established at the University of Maryland in July, 1966. This was used to test the optical performance of solid fused silica corner reflectors in a simulated lunar environment

as had been proposed. The test facilities of the Goddard Space Flight Center were used and the assistance of the Perkin-Elmer Company was obtained in support of the experimental activity. The main features of the proposed design were confirmed in October, 1966 but significant problems were exposed.[8] These are discussed in later sections.

In January, 1967, a second supplement to the original proposal was prepared, updating the entire discussion of the total experiment. A brief first supplement had been prepared in the summer of 1966. There was further review of the proposal by NASA scientific subcommittees, with a resulting assignment to Category I.

During the spring of 1967 when an increment of $40,000 was provided for experiment definition, small study contracts were established with industry. The Arthur D. Little Company was asked to provide engineering assistance in the thermal-mechanical problem of mounting the corner reflectors so as to keep the temperature gradients suitably small during sunlit conditions. The Bendix Aerospace Corporation was asked to examine the problems of integrating the reflector package into the Apollo Lunar Surface Experiments Package (ALSEP). The results of these studies were used to prepare the NASA 1346 Form: Experiment Proposal for Manned Space Flight. The Manned Spaceflight Experiments Board approved the experiment in June, 1967 for the earliest possible Apollo moon landing.

B. Major Contractual Activities

Interaction with personnel at the Manned Spacecraft Center began in May, 1967 in anticipation of favorable action by the MSFEB. Discussions continued during the summer and fall of 1967. Subsequent highlights are shown in the following tables.

Late 1967	Request for proposal received from Manned Spacecraft Center.
Dec. 1967	Proposal in response to RFP submitted.
Feb. 1967	Contract negotiation.
May 17, 1968	Contract awarded.
Sept. - Oct. 1968	Final decision made by NASA to complete hardware for Apollo 11 emplacement as part of Early Apollo Scientific Experiments Package.
July 20, 1969	Laser Ranging Retro-Reflector placed on moon by Astronauts Neil Armstrong and Edwin Aldrin. The LR^3 is the only remaining operational experiment from Apollo 11.
Feb. 5, 1971	LR^3 placed on moon by Apollo 14 Astronauts A. Sheppard and E. Mitchell. Successful range measurments before and after lift-off.

Principal University of Maryland Subcontracts:

Arthur D. Little			
Aug. 6, 1968	P.O. 210900	$71,313	Analysis of Thermal Control Designs for Retro-Reflector Array
Dec. 18, 1969	P.O. 240495	95,000	Thermal-Optical Analysis and Testing
Perkin Elmer Company			
Oct. 14, 1968	P.O. 217032	30,500	Procurement of 95 blocks of Amersil Supra Sil 1. Perform index of refraction and homogeneity tests of samples of Dynasil
Nov. 14, 1968	P.O. 218344	35,075	Procurement of 66 each, 41 mm cubes of Supra Sil 1 and 120 test retro-reflectors
Feb. 14, 1969	P.O. 218350	295,930	Fabrication of 330 retro-reflectors 120 flight optical " " 100 test optical " " 110 residual retro-ref. (flight quality)
Nov. 11, 1969	P.O. 238410	85,760	Completion of fabrication of 80 flight quality retro-reflectors
Nov. 11, 1969	P.O. 238411	26,520	Manufacture 20 flight quality retro-reflectors from residual material
Wesleyan University			
Nov. 18, 1968	P.O. 218996	27,144	Support of Co-investigator J. E. Faller

Arthur D. Little, Inc. was placed under contract to us to provide engineering studies of the performance of a retro-reflector in the lunar environment, and to propose designs which would allow continuous use of a reflector placed on the lunar surface. This effort resulted in the general design of the array tray used in Apollo 11 and Apollo 14 and planned for Apollo 15. Specific design was accomplished under a program with Bendix Aerospace and under our continuing technical supervision.[9] The ADL subcontract under this contract was formally established August 16, 1968, but a large amount of work preceded this date.

The Perkin Elmer Company was selected for the manufacture of flight quality retro-reflectors. They had, over the several prior years, provided technical information and assisted us in preliminary tests and analysis. They had confidence in their own ability to produce optical retro-reflectors of the required accuracy within the short period of time available because of a proprietary manufacturing process developed partly in anticipation of this program. The University of Maryland staff worked in complete open exposure to Perkin Elmer and their problems. We continually monitored their progress and advised on their problems. All goals were met, and the large number of Apollo 11 flight reflectors were delivered in adequate time, of higher than specified quality, and under budget. In order to expedite actions in the face of slow official NASA decisions, it was necessary to award the series of subcontracts to Perkin Elmer as listed above. In some cases, earlier commitment was made but late formal MSC approval delayed a firm award until the date given.

An earnest compliment must be paid to the management and technical staffs of both the Perkin Elmer Company and Arthur D. Little, Inc. Once

a commitment was made to get the LRRR ready for the Apollo 11 flight, the stringent time schedule end date was readily apparent. Both companies were responsive and began vigorous work based upon the assurances of the University of Maryland that contractural coverage would be forthcoming from MSC. Had this not been the case, several critical months would have been lost, and with that the ability to complete the LRRR for Apollo 11 would have been sacrificed.

The total cost of the above subcontracts, and including support for Professor Faller at Wesleyan University, was about $655,000. These have been processed without a markup or loading of any type. This action has saved the government the standard industrial loadings (18% G&A, 7% profit) of about $163,000. Further, the University of Maryland has contributed significantly to the stability and successful conclusion of this program by allowing deficit financing at its liability during times of funding gaps. At times this liability exceeded $50,000. All deficit costs have been properly recovered.

Certain personnel have been made available to this program in proportion of time much greater than that directly charged. Additionally, non-governmental facilities have been utilized during the application of this program at no cost to NASA. This benefit exceeded a total of $45,000 during this period of performance.

C. Major Scientific and Technical Activities

These have consisted of theoretical and experimental studies of the optical properties of totally internally reflecting corner reflectors; of the effects of fabrication errors and temperature gradients on these

properties; and of methods of mounting the solid fused silica corner reflectors to provide passive control of temperature gradients during the periods when the reflector array is sunlit. The work has been a continuation of that described in section II A above.

New and firm knowledge has been developed in these areas which has allowed the setting of realistic specifications of corner reflector properties for procurement, and a basis for selection and guidance of the fabrication contractors. This knowledge has also been essential to the guidance of the engineering design work on the mounting of individual corners and the construction of the entire array. It also provides a basis for assessment of the performance of the LR^3 in the lunar environment.

More detail about these activities is given in the remaining sections of this report.

It should be noted that the overall lunar ranging experiment was conceived from the outset as a unified combination of both the lunar and ground instrumentation. Work in the latter area continued at Maryland under support from NASA Headquarters and was essential in specifying the optical performance required of the LR^3 for use by our own group as well as by other groups.

III. OPTICAL DESIGN

In the summer of 1965 a number of possible design concepts were examined by several of the investigators in cooperation with members of the research and engineering groups of the Perkin Elmer Company. The principal investigator had received the full and enthusiastic cooperation of the Perkin Elmer Director of Research, John Atwood, who brought in Paul Forman of the optical operations division and Harold Hemstreet of the space engineering division. The complete technical information on optical properties of materials and fabrication techniques known to Perkin Elmer was made available to us. A number of specific approaches were developed by both Perkin Elmer and the investigator group. These were considered and the most promising design consisting of small solid fused silica reflectors was selected to be explicitly proposed to NASA. This was written up in an appendix to our original proposal by J. E. Faller who also made an important initial thermal analysis based on optical data on volume absorption of sunlight supplied by Perkin Elmer. This suggested that small solid reflectors would not be appreciably distorted optically in direct sunlight.

An analytical study of the detailed diffraction patterns of corner reflectors was begun also in the summer of 1965 by R. F. Chang, D. G. Currie, M. F. Pittman and C. O. Alley. This considered the case of total internal reflection which had never been carefully analyzed in the scientific literature. This proved invaluable when the test program conducted during the summer of 1966 demonstrated that one could not use metallized back surfaces due to their high absorption of sunlight and resulting

distortion of the optical diffraction pattern. This work, which was extended during the course of this contract, appears here in Appendix 1. It will appear as a paper in the Journal of the Optical Society of America in April, 1971.

Other studies of reflector properties conducted under this contract are assembled in the appendixes. These are:

Appendix 2 Effects of Multiple Reflections on the Far Field Diffraction Pattern of a Corner Reflector, R. F. Chang

Appendix 3 Numerical Ray Trace Analysis for Diffraction Central Irradiance of a Retroreflector for Off-Axis Incidence of Light, R. F. Chang

Appendix 4 The Possible Failure of Total Reflection in an Uncoated Solid Retroreflector - R. F. Chang

Appendix 5 Test Report on the Optical Quality of Three 1-1/2" Retro-Reflectors, R. F. Chang and W. J. Scott

Appendix 6 Experimental Studies on the Central Irradiance of Diffraction Pattern of Retro-Reflectors for Off-Axis Incidence of Light, R. F. Chang and W. J. Scott

Appendix 7 Effects of Small Angular Errors in Retro-reflectors on the Far Field Diffraction Pattern, R. F. Chang

All of these studies are available separately as Technical Reports and the material will be published in several papers. No summary will be given here since each appendix contains an abstract to which the interested reader is referred.

Attention is called to the discovery of the extreme sensitivity of the central irradiance to the angle between the electric vector and the corner edge for corners with small angular errors discussed in Appendixes 6 and 7. However, since the effect is sinusoidal in this angle, and since the lunar corners are arranged randomly (modulo 120°)

the effect will average out over the 100 corner reflectors in the Apollo 11 and 14 packages.

There has been full confirmation in the laboratory of the theoretical analyses. However, due to slow funding of the program as discussed in section II B above, much of the explicit design of the lunar package for Apollo 11 was based on the analytical work. Because of the need to proceed rapidly with the development of the Apollo 11 hardware due to the late decision to fly the LR^3, it was not possible to take advantage of all of the knowledge available. For example, the rapid off-axis fall off of recessed circular corner reflectors as calculated in Appendix 3, showed the desirability of increasing the flare of the retainer ring to allow for unvignetted use of the reflectors out to the most frequent libration angle. The stringent fabrication schedule did not allow this to be done. However, the sockets for the Apollo 14 and 15 had the flare increased to 7.5° as contrasted with the flare of 1.5° for Apollo 11.

The vastly improved off-axis performance for triangular front face reflectors was also known but because of the more difficult mounting and thermal control problems this geometry was not used.

It is of interest to contrast our approach to the optical design of the LR^3 with that of the French, since a French made array of 14 corner reflectors was attached to the Soviet Lunokhod on Luna 17. They designed their reflector to perform only during lunar night. Consequently the difficult thermal problems of assuring performance during sunlit periods were not addressed. They were thus able to use metallized back surfaces, with the accompanying increase in central irradiance of about a factor of 4 over

the uncoated case, to make the reflectors somewhat larger and with triangular front faces, and to mount them without recessing. This produces an on-axis performance about 2 1/2 times greater than our design and an off-axis performance several times greater as can be seen from Figures 19 and 20 in Appendix 3. However the sacrifice of range data during lunar days is a major scientific loss.

The central irradiance in the far field from a corner reflector is proportional to the square of its area, or to the fourth power of its diameter as shown in Appendix 1 and Appendix 3. Therefore a small increase in size can have a large effect. Due to the intermittent funding of the development of the LR^3 experiment as discussed in section II above it was not possible to design and test mountings to explore the use of larger corner reflectors while still keeping the temperature gradients sufficiently small to allow adequate optical performance during lunar day. The design sent to the moon was based on the corner size which had been experimentally tested and shown to perform adequately under on-axis simulated solar radiation. It seems likely that suitable mountings for larger reflectors could be developed.

IV. THERMAL-MECHANICAL DESIGN

The major problem that had to be solved in order to allow nearly diffraction limited performance of the reflector array at all times in the lunar environment was the following. The tests done in the summer of 1966 showed that one could not use a metal coating on the back planes of the solid reflectors because of thermally induced distortions as discussed in section III above. It was therefore necessary to use total internal reflection. However for off-axis angles of incidence beyond a certain value (which depends on the azimuth angle of the corner reflector - see Appendix 4) total internal reflection fails. The solar radiation can then be transmitted through the reflector and will be deposited behind the fused silica reflectors. This energy must be reradiated from the array structure without producing temperature gradients of more than a few degrees across the corner reflectors. Otherwise, even with the low temperature coefficient of expansion of fused silica, unacceptable optical distortions will result. The scientific results from the experiment depend on there being no systematic gaps in the range data associated with the phase of the moon, since an analysis is made of the range time series for various frequency components in the earth-moon system.

The need to solve this problem of mounting if one were to continue to use small solid reflectors, which had been shown to work for sun angles near normal incidence, became clear in the fall of 1966. Because of the outstanding reputation of the engineering physics division at Arthur D. Little, Inc., under Peter Glaser, for coupled thermal-mechanical design accomplishments in space instrumentation, we selected

them to provide engineering help in solving the problem. The successful outcome of the design effort is demonstrated by the performance of the LR^3's on the moon. The studies done at A. D. Little, Inc. under our guidance that led to this result are assembled in Appendix 8 and will not be summarized here.

Some material on the successful final design is given in the Apollo 11 Science Report which is reproduced in Appendix 10. The approach was to lightly mount the reflectors between teflon rings acting on tapered tabs projecting from the reflectors, each corner being recessed by about one-half of its 3.8 cm diameter in a cylindrical cavity in an aluminum block. In providing the actual lunar hardware, A. D. Little, Inc. was under contract to the Bendix Aerospace Company, and reference is made to the report, Laser Ranging Retro-Reflector Array for the Early Apollo Scientific Experiments Package made by A. D. Little to Bendix, June 30, 1969, for details on the fabrication.

V. OPTICAL TESTING OF RETRO-REFLECTORS IN A SIMULATED LUNAR ENVIRONMENT

Although the University of Maryland group and the co-investigators strongly recommended that an active experimental optical testing program accompany the thermal-mechanical mounting design studies, this was not allowed by NASA in time to influence the design of the Apollo 11 LR[3]. However such studies were authorized in the fall of 1969 and a subcontract was established with A. D. Little, Inc. The experimental techniques were based on those developed by us in the initial test program during the summer of 1966 and much equipment was lent to A. D. Little.

The purpose of undertaking a new test program was to examine the performance of the actual mounting used on the moon (a flare of 6° was adopted) to substantiate the analytical methods used to predict the optical performance (see Appendix 8) during the failure of total internal reflection. Although the real test of the design has been its successful performance in the actual lunar environment, no provision has been made as yet for monitoring the reflectivity to better than a factor of 2 or 3 using the ground ranging equipment. (To do better will require the measurement of the atmospheric "seeing" and other parameters not needed for time of flight measurements.) Thus careful simulated laboratory measurements are important in checking on the design methods to aid in optimization of future designs and to allow a better assessment of performance when the "seeing" and other parameters are measured. Such measurements could provide information on long term degradation of the reflectors in the lunar environment.

The results of the test program and the description of the instrumentation and procedures are presented in Appendix 9. The general conclusion is that of reasonable agreement with the analysis although there are some disturbing discrepancies between predicted and measured temperatures and between predicted and measured central irradiances in the total internal reflection breakthrough region of off-axis angles. The situation is further complicated by the polarization effects in corners with small errors discussed in Appendix 5. For the details, the reader is referred to the report from A. D. Little in Appendix 9.

VI. PERFORMANCE ON THE MOON

This topic requires a discussion of the ground station instrumentation and of the scientific aims of the experiment. Such a discussion was given in the Apollo 11 Preliminary Science Report which is included in this report as Appendix 10. Also included is the report to the Apollo 11 Lunar Science Conference in January 1970 (later published in Science) on Apollo 11 and the report to the Second Apollo Lunar Science Conference in January 1971 as Appendix 12. These show that the Apollo 11 LR^3 is performing in agreement with its design within our present ability to measure and that the scientific aims of the experiment are being realized.

The Apollo 14 LR^3 which was deployed on February 5, 1971 is also performing well. In this case it was possible to obtain reflected signals at the McDonald Observatory before the lift-off of the LM from the lunar surface. (In the case of Apollo 11, the moon was low in the sky at the time of deployment for the continental U. S. and there was no subsequent opportunity for ranging before lift-off. A strenuous effort was made to acquire the LR^3 from the Mt. Haleakala Observatory of the University of Michigan in Hawaii but this was not successful.) This early acquisition of the Apollo 14 LR^3 has provided a calibration point as to possible degradation by dust or debris during lift-off, and information on such possible degradation of the Apollo 11 LR^3 since the predicted optical performance of the two LR^3's is similar. Let us quote from the monthly report of Eric Silverberg, Project Scientist for the ranging operations of the Lunar Laser Ranging Experiment Team at the McDonald Observatory:

Apollo 14 Acquisition: The minute that the 107" telescope cleared the obstruction created by its piers, (5:45 PM) we began to range on the Apollo 14 site. About 600 shots and 75 minutes later we had acquired about 25 photoelectrons and had the situation well in hand. (The acquition could have been made considerably sooner but a slip-up in crater identification by the project scientist caused the reticle to be drawn about 2 arc seconds out of position.) During the last 100 shots we had 17 returns. Since we were defocussed to about 4 arc seconds at the time and the corner reflector was supposedly 9 degrees off axis, that represents a better return than we have ever had on the Apollo 11 corner. About 3 hours later we repeated that performance, getting 26 returns in 150 shots with the same system parameters. Even though I can probably only say with great surety that the beam divergence was greater than 3 but less than 5 arc seconds, there is no escaping the fact that on Feb. 5 the A. 14 corner had a better performance than ever observed for the A. 11 corner.

Since Feb. 6 when the lunar module lifted off, we have had about 8 acquisitions on that LR^3. None of these are of the quality seen on February 5th. I would be willing to say that this is indicative of some dust coverage but for some extenuating circumstances. February 5th was an exceptionally good night. Even though we diverged the beam, the person guiding had a considerable advantage over his usual fare. Secondly, we have now switched to the upstairs guider. The latter has resulted in spotty performance to date. It will take at least another month to determine the state of the Apollo 14 corner.

Although the case for degradation is not yet established, it is perhaps appropriate to review the arguments for a protective cover on the LR^3, to be removed by a thermally activated switch during the first lunar night after lift-off. Such a cover was strongly urged by the principal investigator and the co-investigators for Apollo 11 and a satisfactory design was demonstrated by A. D. Little, Inc. It consisted of a piece of light sailcloth spring loaded at the sides with flat springs which would roll up like a window shade when a thermal switch

relying on differential expansion was released during the lunar night. The development of this concept for flight was not approved by NASA on the grounds that the risk of its not working were greater than the risks of degradation. If the degradation of the Apollo 14 LR^3 is confirmed by continuing measurements, the case for a protective cover on future LR^3's will need to be examined. Factors of 2 or 3 in optical performance are significant for the development of small ground stations.

REFERENCES

1. W. F. Hoffman, R. Krotkov, and R. H. Dicke, Institute of Radio Engineering Transactions on Military Electronics 4, 28 (1960). The authors served as a committee for the whole group: C. O. Alley, J. Brault, D. Brill, R. H. Dicke, J. E. Faller, W. F. Hoffman, L. Jordan, R. Krotkov, S. Liebes, R. Moore, J. Peebles, J. Stoner, and K. Turner.

2. H. H. Plotkin, Quantum Electronics 3, Vol 2, p 1319, Columbia University Press, New York, 1964.

3. These included the group of Peter Franken at the University of Michigan, the group of Smullin at MIT, the group of Basov at the Lebedev Physical Institute in Moscow, and the group of Alley at the University of Rochester in cooperation with the University of Toronto Observatory.

4. L. D. Smullin and G. Fiocco, Proc. IRE 50, 1703, 1962.

5. A. Z. Grasyuk, V. S. Zuev, Yu. L. Kokurin, P. G. Kryukov, V. V. Kurbasov, V. F. Lobanov, V. M. Mozhzherin, A. N. Sukhanovskii, N. S. Chernykh, and K. K. Chuvaev, Soviet Physics Doklady 9, 162 (1964).

6. C. O. Alley, P. L. Bender, R. H. Dicke, J. E. Faller, P. H. Franken, H. H. Plotkin, and D. T. Wilkinson, Journal of Geophysics Research 70, 2267 (1965).

7. C. O. Alley, et al, Laser Ranging to Optical Retro-Reflectors on the Moon, University of Maryland Proposal to NASA, Dec. 13, 1965 (Revised Feb. 11, 1966).

8. C. O. Alley, R. F. Chang, D. G. Currie, J. E. Faller, et al, Confirmation of Predicted Performance of Solid Fused Silica Optical Corner Reflectors in Simulated Lunar Environment, University of Maryland Progress Report to NASA, October 10, 1966.

9. Laser Ranging Retro-Reflector Array for the Early Apollo Scientific Experiments Package. Final Report to the Bendix Aerospace Systems Division, from Arthur D. Little, Inc., June 30, 1969.

APPENDIX 1

The Far Field Diffraction Pattern for Corner Reflectors with Complex Reflection Coefficients

R. F. Chang, D. G. Currie, C. O. Alley and M. Pittman

THE FAR FIELD DIFFRACTION PATTERN FOR CORNER REFLECTORS WITH COMPLEX REFLECTION COEFFICIENTS*

R. F. Chang, D. G. Currie, and C. O. Alley

Department of Physics and Astronomy
University of Maryland
College Park, Maryland

and

M. E. Pittman

Department of Physics
Louisiana State University
New Orleans, Louisiana

Technical Report 70-104

April 1970

* This work was supported by NASA Grants NGR 21-002-199 and NAS 9-7809, and The University of Maryland Computer Science Center under NASA Grant NsG-398. Grant NsG-398.

ABSTRACT

The far field diffraction pattern of a geometrically perfect corner reflector is examined analytically for normally incident monochromatic light. The states of polarization and the complex amplitudes of the emerging light are expressed through transformation matrices in terms of those of the original incident light for each sextant of the face in a single coordinate system. The analytic expression of the total diffraction pattern is obtained for a circular face. This expression consists of three component functions in addition to the basic Airy function. The coefficient of each function is expressed in terms of complex coefficients of reflectance of the reflecting surface. Some numerical results for different reflecting surfaces, including total internal reflection, are presented. The iso-intensity contours of the diffraction pattern evaluated from the analytical expressions for an uncoated solid corner reflector are also presented along with the photographs of the pattern.

INDEX HEADINGS: Diffraction, Corner Reflector.
Total Internal Reflection.
Polarization Effects.

I. INTRODUCTION

It is known that a monochomatic plane wave of light falling normally upon a flat circular mirror produces in the far field, upon reflection, the well-known Airy diffraction pattern. When the flat mirror is replaced by a corner reflector of the same circular aperture the far field pattern is no longer the Airy pattern. We will consider, in this report, the far field diffraction pattern of a corner reflector with special emphasis on the effects of the relative phase shifts between orthogonal polarizations caused by total internal reflection. Mahan[1] has reported a similar comprehensive study on the polarization effects from a roof prism.

E. R. Peck[2] has studied the resultant state of polarization of the reflected light when a pencil of light falls upon one sector of a corner reflector. M. M. Rao[3], following the method of Peck, has made a numerical study of the state of polarization for a corner reflector constructed of a particular type of glass. The eigen states of polarization predicted by Peck have been experimentally verified by Rabinowitz, et al[4]. A study, in terms of geometric optics, of the effects of angular errors in the prism on the return image has been made by P. R. Yoder, Jr.[5], and also by R. C. Spencer[6]. However, our present discussion shall assume that the corner is geometrically perfect; i.e. there are no angular erros in the corner reflector.

In the following we consider the far field pattern produced by combining the beams of different polarization which emerge from the six sectors of the corner reflector. The polarization and amplitude of each of these six beams is determined by the optical properties of the reflection surface. The reflection surface can be one of many forms, such as air to metal, glass to metal and glass to air for the case of an open corner, a solid corner with metal coating, and an uncoated solid corner,

respectively. In general, this pattern has more structure and angular divergence than the pattern which would be obtained if the corner reflector acted in the same manner as a flat mirror of the same diameter.

In more detail, each ray which "composes" the incident plane wave falling on a corner reflector is followed through the corner reflector in the manner of Peck, and the phase and amplitude of the ray emerging from the face of the corner reflector are determined. We thus neglect diffraction effects which occur inside the corner reflector. The phase shift and amplitude are determined by the optical properties of the rear surface; i.e., the glass-metal, glass-air, or air-metal interface. Each of these rear interfaces causes a relative phase shift between the components polarized parallel and perpendicular to the plane of incidence. An interface with a metal component also introduces a change in the amplitude of the light wave. Our results will be compared to those for a "perfect" metal coating at the rear interface by which we mean an interface with the ideal properties of no change in amplitude and a relative change of phase between the parallel and perpendicular components of polarization of $-\pi$. (A material with infinite conductivity at optical frequencies would satisfy this criterion of "perfection.")

The amplitude and phase or, equivalently, the complex amplitudes thus determined have different values on the different sextants. In this computation, it has been assumed that the incident plane wave is perpendicular to the front face. Tilting the corner reflector by an angle ϕ would have two effects: (1) an overall change in the apparent shape of the front face (or the aperture) which would expand one axis of the resultant diffraction pattern, and (2) a change in the angles of refraction at the rear interface, which would involve the change of relative phase shifts with angle. The latter effect is second order in the angle

ϕ and thus small for small angles. For a larger angle, the analytic expression of the complex amplitude of the emerging beam cannot be obtained simply. We have, utilizing a computer, adopted the ray trace technique and we will report the results separately.

The face of the corner reflector is assumed to be circular. Scalar diffraction theory is used to determine the far field pattern which results from all sextants with different complex amplitudes. The diffraction is calculated first for an arbitrary complex amplitude for each sector, and later the complex amplitudes are given the values which would result from a particular rear interface. The Fresnel reflection from the front face has been neglected at present as we may assume an anti-reflection coating on the front face of a corner reflector. The presence of the Fresnel reflection at the front face causes multiple reflections which interfere with the original retro beam. We will present a detailed discussion of this aspect separately.

The properties of specific interfaces are considered in Section V, and the diffraction patterns for silver, aluminum and total internal reflection are discussed. The metals have diffraction patterns rather similar to that of a "perfect" metal, and total internal reflection produces marked diffraction effects. The iso-intensity contours, which are evaluated from the analytic expressions, of the diffraction pattern for an uncoated solid corner reflector are presented along with the photographs of the pattern.

The analysis was undertaken to provide a thorough understanding of the diffraction pattern of corner reflectors in connection with the design and testing of the Apollo 11 Laser Ranging Retro-Reflector. This uses total internal reflection to allow near diffraction limited operation in the lunar thermal environment.[7]

II. POLARIZATION AND INTENSITY EFFECTS OF A CORNER REFLECTOR ON A PENCIL OF LIGHT

The front face of a corner reflector is divided into six equal sections, when viewed from the front, by the projections of the three real back edges and their images. We define a coordinate system in the face of the corner reflector by a pair of mutually orthogonal unit vectors $\hat{i}$ and $\hat{j}$ with the $\hat{j}$-axis coincident with the projection of one of the real back edges in the face as shown in Fig. 1. The six sections are labeled by numbers 1 through 6. A beam of light entering the corner reflector through one of the sections always emerges from the opposite section.

If we consider a pencil of light which enters axially into the sextant labeled by 4 then the unit vectors $\hat{i}$ and $\hat{j}$ are perpendicular and parallel respectively to this plane of incidence. We assume here the light to be monochromatic and of single polarization. The amplitude of the light entering the 4th sextant can then be represented by $\underset{\sim}{u}$ which has two complex components u_1 and u_2 in the directions $\hat{i}$ and $\hat{j}$. This light beam, after being reflected consecutively from three back surfaces, emerges from the sextant labeled by 1 with amplitude $\underset{\sim}{v}$ which is different from $\underset{\sim}{u}$. By tracing the light through each reflection, it has been found[1] that $\underset{\sim}{u}$ and $\underset{\sim}{v}$ can be related by a 2 x 2 matrix $\underset{\sim}{C}$, such that $v_i = \sum_{j=1}^{2} C_{ij} u_j$, $i = 1,2$ or $\underset{\sim}{v} = \underset{\sim}{\underset{\sim}{C}}\,\underset{\sim}{u}$.

The matrix $\underset{\sim}{C}$ has the form

$$C_{11} = \frac{1}{8} r_s \left[(r_s + r_p)^2 + 4 r_p (r_s - r_p) \right] \tag{1a}$$

$$C_{12} = \frac{\sqrt{3}}{8} r_p (r_s + r_p)^2 \tag{1b}$$

$$C_{21} = \frac{\sqrt{3}}{8} r_s (r_s + r_p)^2 \tag{1c}$$

$$C_{22} = \frac{1}{8} r_p \left[4r_s (r_s - r_p) - (r_s + r_p)^2\right]. \tag{1d}$$

where r_s and r_p are complex coefficients of reflectance which may be written as $r_s = \rho_s \exp(i\delta_s)$ and $r_p = \rho_p \exp(i\delta_p)$. For lossless reflection ρ_s and ρ_p have unit magnitude. In general, however, the magnitudes of ρ_s and ρ_p are less than unity, representing the losses in reflection. This is the matrix for light emerging from the first sextant and the matrix in Eq. (1) could be labeled $\underset{\sim}{C}^1$. In general, the transformation matrix or the relation between incident intensity and polarization is different for each sextant, so we have

$$\underset{\sim}{v}^n = \underset{\sim}{C}^n \underset{\sim}{u}$$

where n = 1, 2, 3, 4, 5, and 6. The superscript n of the complex amplitude $\underset{\sim}{v}^n$ and the matrix $\underset{\sim}{C}^n$ is associated with the light emerging from the nth sextant. The matrix in Eq. (1), now identified as $\underset{\sim}{C}^1$ can be re-expressed in terms of Pauli's spin matrices, for the convenience of the following calculation, in the form

$$\underset{\sim}{C}^1 = \xi \underset{\sim}{1} + \sqrt{3/2}\ \eta \underset{\sim}{\sigma}_x + \zeta \underset{\sim}{\sigma}_y + \sqrt{1/2}\ \eta \underset{\sim}{\sigma}_z$$

where

$$\underset{\sim}{1} \equiv \begin{pmatrix} 1 & 0 \\ 0 & 1 \end{pmatrix}, \quad \underset{\sim}{\sigma}_x \equiv \begin{pmatrix} 0 & 1 \\ 1 & 0 \end{pmatrix}, \quad \underset{\sim}{\sigma}_y \equiv \begin{pmatrix} 0 & -i \\ i & 0 \end{pmatrix}, \quad \underset{\sim}{\sigma}_z \equiv \begin{pmatrix} 1 & 0 \\ 0 & -1 \end{pmatrix}$$

and

$$\xi \equiv \frac{1}{16} (r_s - r_p) \left[3(r_s + r_p)^2 - 2(r_s - r_p)^2\right], \tag{2a}$$

$$\eta \equiv \frac{\sqrt{2}}{16} (r_s + r_p)^3, \tag{2b}$$

$$\zeta \equiv -i \frac{\sqrt{3}}{16} (r_s + r_p)^2 (r_s - r_p). \tag{2c}$$

The 3rd and the 5th sextants transform into the first sextant if we rotate the coordinates by $\pm 120°$, therefore one can obtain the matrices $\underset{\sim}{C}^3$ and $\underset{\sim}{C}^5$ through the rotation of the coordinate system. Such a rotation may be accomplished by $\underset{\sim}{R}^{-1}\ \underset{\sim}{C}\ \underset{\sim}{R}$, where $\underset{\sim}{R} = -\frac{1}{2}(\underset{\sim}{1} - \sqrt{3}\ i\ \underset{\sim}{\sigma}_y)$ for $+120°$ and $\underset{\sim}{R} = -\frac{1}{2}(\underset{\sim}{1} + \sqrt{3}\ i\ \underset{\sim}{\sigma}_y)$ for $-120°$, yielding

$$\underset{\sim}{C}^3 = \xi\underset{\sim}{1} - \sqrt{3/2}\eta\underset{\sim}{\sigma}_x + \zeta\underset{\sim}{\sigma}_y + \sqrt{1/2}\eta\underset{\sim}{\sigma}_z ,$$

$$\underset{\sim}{C}^5 = \xi\underset{\sim}{1} + \zeta\underset{\sim}{\sigma}_y - \sqrt{2}\eta\underset{\sim}{\sigma}_z .$$

Matrices $\underset{\sim}{C}^2$, $\underset{\sim}{C}^4$, and $\underset{\sim}{C}^6$ can be obtained by inverting $\underset{\sim}{C}^5$, $\underset{\sim}{C}^3$, and $\underset{\sim}{C}^1$ respectively with σ_z because they are mirror image pairs and we obtain

$$\underset{\sim}{C}^n = \underset{\sim}{\sigma}_z\underset{\sim}{C}^{7-n}\underset{\sim}{\sigma}_z, \quad n = 2,\ 4,\ \text{and}\ 6 .$$

This equation, because of the anticommutation relation of σ's, results in simply changing of signs of the coefficients of σ_x and σ_y components. Consequently we can write $\underset{\sim}{C}^n$ in a general form as

$$\underset{\sim}{C}^n = \xi\underset{\sim}{1} + f_n\sqrt{3/2}\eta\underset{\sim}{\sigma}_x + g_n\zeta\underset{\sim}{\sigma}_y + h_n\sqrt{1/2}\eta\underset{\sim}{\sigma}_z \tag{3}$$

The coefficients f_n, g_n and h_n are tabulated in Table I for all sextants.

As indicated by the form of the transformation matrices $\underset{\sim}{C}^n$ the polarization and amplitude of the entering light is in general not preserved. One can, however, use projection operators to decompose the emerging beam into two polarization components along directions other than $\hat{i}$ and $\hat{j}$. In particular we will consider one component parallel to the incident polarization and the other perpendicular to it. Assume the

incident light to be linearly polarized with the direction of the electric field at an angle θ to the $\hat{i}$-axis so it has the form $\underset{\sim}{u} = u_o \begin{pmatrix} \cos\theta \\ \sin\theta \end{pmatrix}$ where u_o is the amplitude of the field. The eigenvectors of these projection operators are,

$$v_p = \begin{pmatrix} \cos\ \theta \\ \sin\ \theta \end{pmatrix} \text{ and } v_s = \begin{pmatrix} \sin\ \theta \\ -\cos\ \theta \end{pmatrix}$$

respectively for the components parallel and perpendicular to the incident polarization. Thus the normalized complex amplitudes of the emerging light from nth sextant for these two components are,

$$\gamma_p^n \equiv \underset{\sim p}{v^\dagger}\ \underset{\sim}{C^n}\ \underset{\sim}{u}/(\underset{\sim}{u}^\dagger \underset{\sim}{u})^{\frac{1}{2}}$$

$$= \xi + f_n \sqrt{3/2}\eta\ \sin(2\theta) + h_n \sqrt{1/2}\eta\ \cos\ (2\theta) \qquad (4a)$$

$$\gamma_s^n \equiv \underset{\sim s}{v}\ \underset{\sim}{C^n}\ \underset{\sim}{u}/(\underset{\sim}{u}^\dagger \underset{\sim}{u})^{\frac{1}{2}}$$

$$= -g_n i\zeta + h_n \sqrt{1/2}\eta\ \sin\ (2\theta) - f_n \sqrt{3/2}\eta\ \cos\ (2\theta) \qquad (4b)$$

It is now clear that the polarization and intensity of the emerging light are different from one sextant to the other and are also determined by the magnitudes and relative phase of γ_p^n and γ_s^n .

III. DIFFRACTION PATTERN FOR A SIX-SECTORED CIRCLE WITH ARBITRARY PHASES AND AMPLITUDES

For a single polarization the integral governing Fraunhofer diffraction for circular aperture of radius a is given, in polar coordinates, by[8]

$$U(P) = B \int_o^a \int_o^{2\pi} e^{-ik\rho w \cos(\phi-\psi)} \rho d\rho d\phi \qquad (5)$$

where U(P) is the amplitude at the far field point P, and (ρ,ϕ) is the polar coordinate at the aperture whereas (w,ψ) is the polar coordinate of the point P, and $k \equiv 2\pi/\lambda$. However, w is the sine of the angle between the direction of the light beam and the direction of point P. The constant B is the complex amplitude of the light in the aperture.

Now consider a circular aperture of radius a with imaginary lines dividing the aperture into six sextants. Suppose the linearly polarized light emerging from the aperture has different phases and amplitudes at different sextants but with uniform phase and amplitude over a given sextant. Then the diffraction integral should become

$$U(P) = \sum_{n=1}^{6} B_n \int_o^a \int_{(n-1)\pi/3}^{n\pi/3} e^{-ik\rho w \cos(\phi-\psi)} \rho d\rho d\phi \ , \qquad (6)$$

where B_n describes the phase and the amplitude of the light emerging from the n-th sextant. The polar angles ψ and ϕ are both measured counterclockwise from j-axis when we are facing the emerging beam.

In order to consider the problem of the corner reflector we may assume the aperture to be a certain reflector and the emerging beam to be the reflection of the incident beam impinging normally on the reflector.

Since our interest is in the distribution of the energy, we can normalize the amplitude such that in the case of a circular "perfect" mirror

the central intensity $I_o \equiv |U(0,0)|^2$ is unity. This yields

$$A(P) = \frac{1}{\pi a^2} \sum_{n=1}^{6} \gamma^n \int_0^a \int_{(n-1)\pi/3}^{n\pi/3} e^{-ik\rho w \cos(\phi-\psi)} \rho d\rho d\phi \tag{7}$$

where A(P) is the normalized complex amplitude of the diffraction and γ^n is the normalized complex amplitude of the n-th sextant.

To evaluate the integral in Eq. (7), we use the formulas[9]

$$\cos(z \cos\theta) = J_o(z) + 2 \sum_{k=1}^{\infty} (-)^k J_{2k}(z) \cos(2k\theta),$$

$$\sin(z \cos\theta) = 2 \sum_{k=0}^{\infty} (-)^k J_{2k+1}(z) \cos[(2k+1)\theta],$$

where $J_{2k}(z)$ are the Bessel functions, to separate the radial and angular parts in the integral.[10] After evaluating the angular part, we obtain

$$A(P) = \frac{1}{\pi x^2} \sum_{n=1}^{6} \gamma^n \int_o^x y\, dy \{\frac{\pi}{3} J_o(y) + 4 \sum_{\ell=1}^{\infty} \frac{(-i)^\ell}{\ell} J_\ell(y) \sin\frac{\ell\pi}{6} \cos[\ell(\frac{n\pi}{3} - \psi - \frac{\pi}{6})]\} \tag{8}$$

where $x \equiv kaw$, $y \equiv k\rho w$.

It is known that

$$\int_o^x y\, J_o(y)\, dy = xJ_1(x), \tag{9}$$

and the second integral which involves higher orders of the Bessel functions

can be expressed in terms of the Bessel functions or in a power series of x. In either case the series converges rather quickly, and has the form.[9]

$$\int_0^x y\, J_\ell(y)\, dy = 2\ell x \sum_{m=0}^{\infty} \frac{(\ell + 2m + 1)}{(\ell + 2m + 2)(\ell + 2m)}\, J_{\ell + 2m + 1}(x) \tag{10}$$

or

$$\int_0^x y J_\ell(y)\, dy = 4\left(\frac{x}{2}\right)^{\ell+2} \sum_{m=0}^{\infty} \frac{(-x^2/4)^m}{(\ell + 2m + 2)(m!)(\ell + m)!} \tag{11}$$

Since the integral is well-determined, we can, for short, define a new function $F_\ell(x)$ for $\ell \geq 1$ as:

$$F_\ell(x) \equiv \frac{1}{\ell x^2} \int_0^x y\, J_\ell(y)\, dy\ . \tag{12}$$

Then Eq. (8) can be rewritten as:

$$A(P) = \frac{2J_1(x)}{x} \sum_{n=1}^{6} \frac{\gamma^n}{6} + \frac{4}{\pi} \sum_{\ell=1}^{\infty} (-i)^\ell F_\ell(x) \sin\frac{\ell\pi}{6} \sum_{n=1}^{6} \gamma^n \cos\left[\ell\left(\frac{n\pi}{3} - \psi - \frac{\pi}{6}\right)\right]. \tag{13}$$

In the case of a "perfect" mirror, all γ^n's are equal to unity (omitting the common phase). Then $\sum_{n=1}^{6} \gamma^n/6 = 1$ plus the indentity

$$\sin\frac{\ell\pi}{6} \sum_{n=1}^{6} \cos\left[\ell\left(\frac{n\pi}{3} - \alpha\right)\right] \equiv 0$$

for all ℓ and α, reduces Eq.(13) to the well-known diffraction pattern resulting from a circular aperture,

$$A(P) = \frac{2J_1(kaw)}{kaw}\ .$$

This discussion has been for a single polarization. In general, (and for the corner reflector in particular) the polarization from each of the sextants may not be the same. Since beams of orthogonal polarization do not interfere, we may calculate the diffraction pattern due to each polarization, calculate the intensities due to each polarization, and then add the intensities. Although this may be done for a resolution into any pair of orthogonal polarization states, we will find it convenient to consider orthogonal linear polarizations.

IV. DIFFRACTION PATTERNS AS A FUNCTION OF THE REFLECTING SURFACE

In Section II we have derived the expressions of the normalized complex amplitudes for two orthogonal polarization states resulting from an incident linearly polarized plane wave with uniform intensity. The coefficients ξ, η and ζ, first defined in Eq. (2) are indeed determined by the properties of the reflecting surfaces; and the reflecting surfaces may be, as far as the corner reflector is concerned, glass-metal, glass-air or air-metal interface.

Since the light in orthogonal polarization states do not interfere, we will treat each of the outgoing polarizations separately. First we substitute the value of γ_p^n and γ_s^n obtained from Eq. (4) into Eq. (13) and then sum over n from 1 to 6. After somewhat lengthy algebraic calculations we obtain the expression of the normalized amplitude for both polarizations

$$A_p(x,\psi,\theta) = \xi G_0(x) + \eta G_1(x,\psi;\theta) \tag{14}$$

$$A_s(x,\psi;\theta) = \zeta G_2(x,\psi) + \eta G_3(x,\psi;\theta), \tag{15}$$

where

$$G_0(x) = \frac{2J_1(x)}{x} \tag{16}$$

$$G_1(x,\psi;\theta) \equiv \frac{(6)^{\frac{3}{2}}}{\pi} \sum_{\ell=1}^{2} \sum_{m=0}^{\infty} (-)^{m+1} F_{2\ell+6m}(x) \cos[(2\ell+6m)\psi + (-)^{\ell} 2\theta] \tag{17}$$

$$G_2(x,\psi) \equiv \frac{24}{\pi} \sum_{m=0}^{\infty} (-)^{m+1} F_{3+6m}(x) \sin(3+6m)\psi \tag{18}$$

$$G_3(x,\psi;\theta) \equiv \frac{(6)^{\frac{3}{2}}}{\pi} \sum_{\ell=1}^{2} \sum_{m=0}^{\infty} (-)^{m+\ell-1} F_{2\ell+6m}(x) \sin[(2\ell+6m)\psi + (-)^{\ell} 2\theta]. \tag{19}$$

It is interesting to note that the basic diffraction pattern of a corner reflector depends solely on four functions regardless of the property of the

surface. The difference in the properties of the reflecting surfaces affects only the strengths and the relative phases of these four functions.

Now we consider the energy which lies within a given angular radius from the center of the beam. Let $L(w_o)$ denote the fraction of the total energy which lies within an angular radius w_o. Then we obtain [11]

$$L(w_o) = \frac{\pi a^2}{\lambda^2} \int_0^{2\pi} \int_0^{w_o} I(w,\psi;\theta)\, w\, dw\, d\psi \tag{20}$$

where $\lambda = 2\pi/k$ is the wavelength of the light. The intensity is given by

$$I(w,\psi;\theta) = |A_p(x,\psi;\theta)|^2 + |A_s(x,\psi;\theta)|^2 \tag{21}$$

where $x = kaw$ as before. Using Eqs. (14) and (15), we get

$$I(w,\psi;\theta) = |\xi|^2 G_o^2(x) + (\xi\eta^* + \xi^*\eta) G_o(x) G_1(x,\psi;\theta) + |\eta|^2 G_1^2(x,\psi;\theta)$$
$$+ |\zeta|^2 G_2^2(x,\psi) + (\zeta\eta^* + \zeta^*\eta) G_2(x,\psi) G_3(x,\psi;\theta) + |\eta|^2 G_3^2(x,\psi;\theta). \tag{22}$$

Noting that the cross terms in $I(w,\psi;\theta)$ vanish after the angular integration over ψ, we may evaluate the angular part for each term and obtain

$$L(w_o) = 2|\xi|^2 \int_0^x \frac{J_1^2(x)}{x}\, dx + \frac{108}{\pi^2} |\eta|^2 \sum_{\ell=1}^{2} \sum_{m=0}^{\infty} \int_0^{x_o} F_{2\ell+6m}^2(x)\, x\, dx$$
$$+ \frac{144}{\pi^2} |\zeta|^2 \sum_{m=0}^{\infty} \int_0^{x_o} F_{3+6m}^2(x)\, x\, dx. \tag{23}$$

The energy within the first zero of the Airy pattern is given by $L(w_o)$ when $x_o = 3.83$ (or $w_o = 3.83/ka$) where the first zero of the Airy pattern occurs. Evaluating Eq. (23) numerically with that argument we obtain

$$L(w_o) = 0.840\, |\xi|^2 + 0.415\, |\eta|^2 + 0.056\, |\zeta|^2. \tag{24}$$

If we also consider the effect of absorption by the back surfaces we can denote the ratio of the total output energy to the total input energy by R and we have

$$R \equiv \frac{1}{6} \sum_{n=1}^{6} \underset{\sim}{u}^{\dagger} \underset{\sim}{C}^{n\dagger} \underset{\sim}{C}^{n} \underset{\sim}{u} / (\underset{\sim}{u}^{\dagger} \underset{\sim}{u})$$

$$= |\xi|^2 + 2|\eta|^2 + |\zeta|^2 . \qquad (25)$$

As a simple illustration, let us consider the values of the coefficients ξ, η and ζ when the reflecting surface of a corner reflector acts as a "perfect" mirror. This ideal condition can be sufficiently described physically by the condition that the electric field which is parallel to the mirror surface vanishes, but the electric field which is perpendicular to the mirror surface remains unchanged. Then, it follows that $\rho_p = \rho_s = 1$ and $\delta_p = 0$, $\delta_s = \pi$ or in other words $r_p + r_s = 0$ and $r_p - r_s = 2$.

Substituting these values into Eq. (2), we obtain

$$\xi = 1 \text{ and } \eta = \xi = 0.$$

This result reduces Eqs. (14) and (15) to what we expect from a circular aperture, that is

$$A_p(x, \psi; \theta) = \frac{2J_1(x)}{x} \text{ and } A_s(x, \psi; \theta) = 0 .$$

Thus a corner reflector whose back surfaces act as a "perfect" mirror has the same diffraction pattern as a "perfect" flat circular mirror.

V. EXPECTED PATTERNS FROM CORNER REFLECTORS COATED WITH ALUMINUM. SILVER, UNCOATED, AND OPEN CORNER REFLECTORS

Since the diffraction pattern of a corner reflector is a linear combination of the four G-functions, we need only evaluate the coefficients ξ, η and ζ of different reflecting surfaces. We assume the wavelength of the light to be 6943 Å which is the value for a ruby laser. We have considered the cases of (1) an open corner reflector using the silver or the aluminum as the reflecting surfaces, (2) a solid corner reflector coated with the silver or the aluminum, and (3) an uncoated solid corner reflector. In all cases the index of refraction of the solid corner is assumed to be 1.45. The complex index of refraction of the metals was taken from Schulz and Tangherlini[12].

We have found that $|\eta|^2$ and $|\zeta|^2$ for the cases (1) and (2) are negligibly small (less than 1% of $|\xi|^2$). The energy ratios R are 95% and 70% for silver and aluminum, respectively, in case (1) and 92% and 61% in case (2).

For an uncoated solid corner $|\eta|^2$ and $|\zeta|^2$ are comparable with $|\xi|^2$. Although the energy ratio R is 100% in this case, the energy within the first zero of Airy pattern is about 36%.

The diffraction pattern for the case of (1) or (2) is approximately an Airy pattern. The diffraction pattern of an uncoated corner reflector is, however, quite different. We have evaluated the analytic expressions in Eqs. (14), (15) and (22) for $\Theta = 0°$ and plotted the iso-intensity contours at different intensities in Figs. 2, 3 and 4. The total pattern as well

as the two components of the mutually orthogonal polarization states are shown separately.

The contours show certain symmetries, such as $I_p(x,\psi;0) = I_p(x,-\psi;0) = I_p(x, \pi-\psi;0)$, $I_s(x,\psi;0) = I_s(x,-\psi;0)$ for two orthogonal polarizations, and $I(x,\psi;0) = I(x,-\psi;0)$ for the over all pattern. These symmetries are quite obvious in Eqs. (16), (17), (18) and (19).

The photographs of the diffraction pattern are shown in Figs. 5, 6, and 7 for comparison with the plots. The corner reflector has an aperture of one inch in diameter. The entrance face, contrary to the assumption in this report, did not have an anti-reflection coating. However, one notices a striking resemblance between the photographs and the plots.

VI. CONCLUSION AND THE COMMENT

In this study of the far field diffraction pattern of a corner reflector, we considered, among other things, mainly the energy concentration at the central region.

The purpose of this particular consideration was to investigate the possibility of ranging to the moon with an optical radar system on the ground and the corner reflectors on the moon[13]. Thus quantitative information on the concentration of the returning signal was the primary interest.

The diffraction pattern from a circular aperture illuminated uniformly by a plane wave contains about 84% of its energy within the angular radius of $1.22\ \lambda/d$, where d is the diameter of the aperture. The diffraction pattern from a corner reflector utilizing total internal reflection contains slightly less than half of the energy from a circular aperture within that angular radius. The central irradiance is, for the case of a corner reflector, about one-fourth of that from a circular aperture. It is because the polarization effect manifests itself to a greater extent in the total internal reflection. There is little tendency that the field at points far away from the central region would be cancelled as it would be in the case of circular apertures. The consequence is a greater spread of energy. Coating the back surfaces of the corner reflector with metals would generally improve the performance in the sense that more energy would tend to concentrate in the central region. But the absorption of the light by the metal would reduce the returning intensity. The light entering a corner reflector has to be reflected three times before emerging, thus the desirability of high reflectance at the reflecting interface is greatly increased.

The particular geometry of the corner reflector predetermines the basic structure of its diffraction pattern as a combination of four functions. The different optical constants of the different reflecting interfaces provide merely the different coefficients for each of these four functions, namely ξ, η, and ζ.

Higher values of η and ζ would cause a wider spread of optical energy because the functions of which η and ζ are the coefficients consist of Bessel functions of higher order divided by their argument. A Bessel function reaches its largest value when the argument is roughly equal to its order; therefore, under the condition that $|\xi| \approx |\eta| \approx |\zeta|$ the diffraction field does not become small compared to the field strength at the central direction except when the angular direction is some distance away from the central direction. It is necessary that $|\eta| << |\xi|$ and $|\zeta| << |\xi|$ in order to reduce the spread of energy by diffraction.

A corner reflector whose back surfaces are coated with metal such as silver or aluminum satisfies the condition that $|\eta|$ and $|\zeta|$ are much smaller than $|\xi|$. Although it appears that such a corner reflector behaves roughly as an ideal reflector, its application to the optimization of return signal for the lunar ranging experiment is not straight forward. The extreme temperature gradients and the direct exposure to solar radiation in the actual lunar environment make the optimization of return signal a problem of a different nature which will not be discussed in this report.

FOOTNOTES

1. A. I. Mahan, J. Opt. Soc. Am., 35, 623 (1945); also A. I. Mahan and E. E. Price, J. Opt. Soc. Am., 40, 664 (1950).

2. E. R. Peck, J. Opt. Soc. Am., 52, 253 (1962).

3. M. M. Rao, Thesis, Department of Optics, University of Rochester, Rochester, New York, 1963.

4. P. Rabinowitz, S. F. Jacobs, T. Shultz, and G. Gould, J. Opt. Soc. Am., 52, 452 (1962).

5. P. R. Yoder, Jr., J. Opt. Soc. Am., 48, 496 (1958).

6. R. C. Spender, Report 433, Radiation Laboratory, M.I.T. (1944).

7. C. O. Alley, R. F. Chang, D. G. Currie, J. V. Mullendore, S. K. Poultney, J. D. Rayner, E. C. Silverberg, C. A. Steggerda, H. H. Plotkin, W. Williams, B. Warner, H. Richardson, and B. W. Bopp, Science, 167, 368 (1970).

C. O. Alley, R. F. Chang, D. G. Currie, S. K. Poultney, P. L. Bender, R. H. Dicke, D. T. Wilkinson, J. E. Faller, W. M. Kaula, G. J. F. MacDonald, J. D. Mulholland, H. H. Plotkin, W. Carrion, and E. J. Wampler, Science, 167, 458 (1970).

C. O. Alley, P. L. Bender, R. F. Chang, D. G. Currie, R. H. Dicke, J. E. Faller, W. M. Kaula, G. J. F. MacDonald, J. D. Mulholland, H. H. Plotkin, S. K. Poultney, D. T. Wilkinson, Irvin Winer, Walter Carrion, Tom Johnson, Paul Spadin, Lloyd Robinson, E. Joseph Wampler, Donald Wieber, E. C. Silverberg, C. A. Steggerda, J. V. Mullendore, J. D. Rayner, W. Williams, Brian Warner, Harvey Richardson, and B. W. Bopp, Apollo 11 Preliminary Science Report, SP-214, 163 (1969).

J. E. Faller, Irving Winer, Walter Carrion, Thomas S. Johnson, Paul Spadin, Lloyd Robinson, E. J. Wampler, and Donald Wieber, Science, 166, 99 (1969).

8. M. Born and E. Wolf, Principles of Optics, 2nd revised edition, p. 395 (MacMillan Company, New York, 1964).

9. Abramowitz and Stegun, Handbook of Mathematical Functions, 1965 (Dover, New York).

10. A. I. Mahan, C. V. Bitterli, and S. M. Cannon, J. Opt. Soc. Am., 54, 721 (1964).

11. See Ref. 8, p. 398.

12. L. G. Schulz and F. R. Tangherlini, J. Opt. Soc. Am., 44, 362 (1954); and L. G. Schulz, J. Opt. Soc. Am., 44, 357 (1954).

13. C. O. Alley, P. L. Bender, R. H. Dicke, J. E. Faller, P. E. Franken, H. H. Plotkin, and D. A. Wilkinson, Journal of Geophysical Research, 70, 2267 (1965).

FIGURE CAPTIONS

Fig. 1 Front view of a corner reflector with a circular face is divided into six sections labeled by numbers 1 through 6. The projections of the real back edges and their images are indicated by the solid and dashed lines, respectively. The coordinate system is defined by the unit vectors $\hat{i}$ and $\hat{j}$.

Fig. 2 The iso-intensity contours of the total diffraction pattern are shown at three different intensities for $\theta = 0°$ in the polar coordinate. A quartz solid corner reflector (n=1.45) is assumed in the calculation. The contours at 50%, 10%, and 2% of the center intensity $I(0,\psi;0°)$ are shown by ————, ---------, and -·-·-·-· , respectively. The contour of the first zero of The Airy pattern is shown by the dotted line ..... for comparison.

Fig. 3 The iso-intensity contours of the diffraction pattern whose polarization is the same as that of the incident light.

Fig. 4 The iso-intensity contours of the orthogonal polarization. Notice that the 50% line is not present.

Fig. 5 The photograph of the total diffraction pattern from a quartz solid corner reflector without an anti-reflection coating.

FIGURE CAPTIONS

Fig. 6. The photograph of the component of the pattern having the original polarization.

Fig. 7 The photograph of the component of the pattern having the orthogonal polarization.

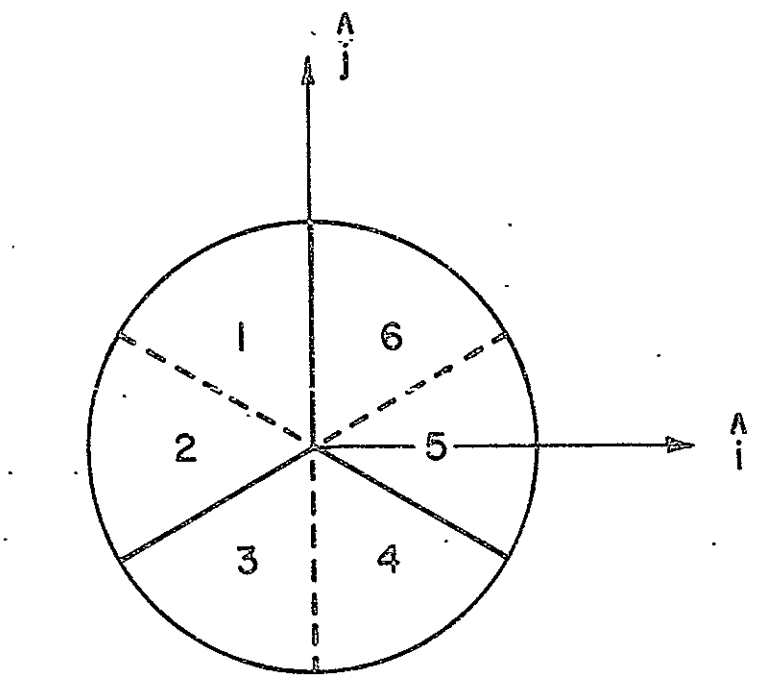

Figure 1

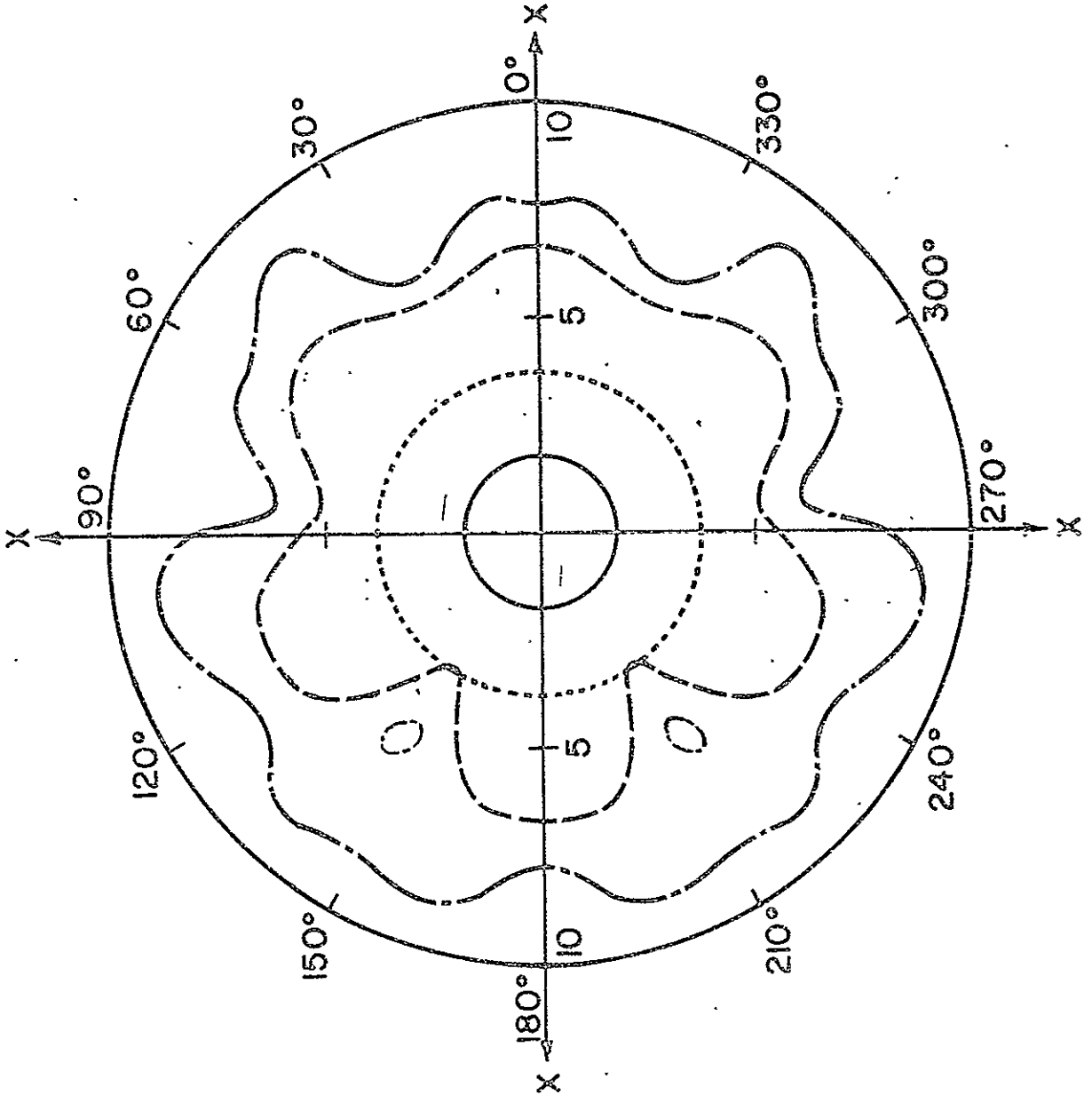

Figure 2

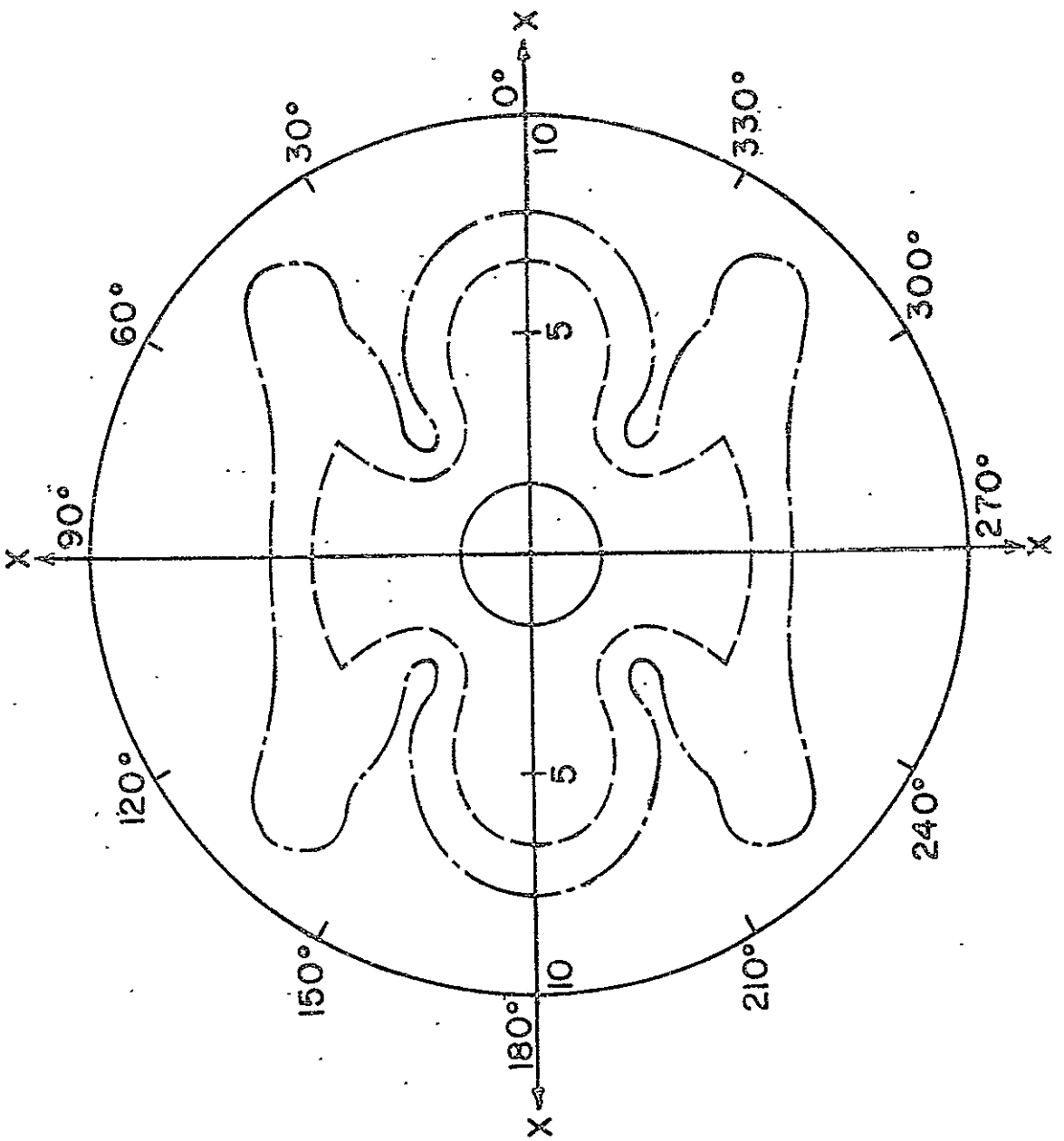

Figure 3

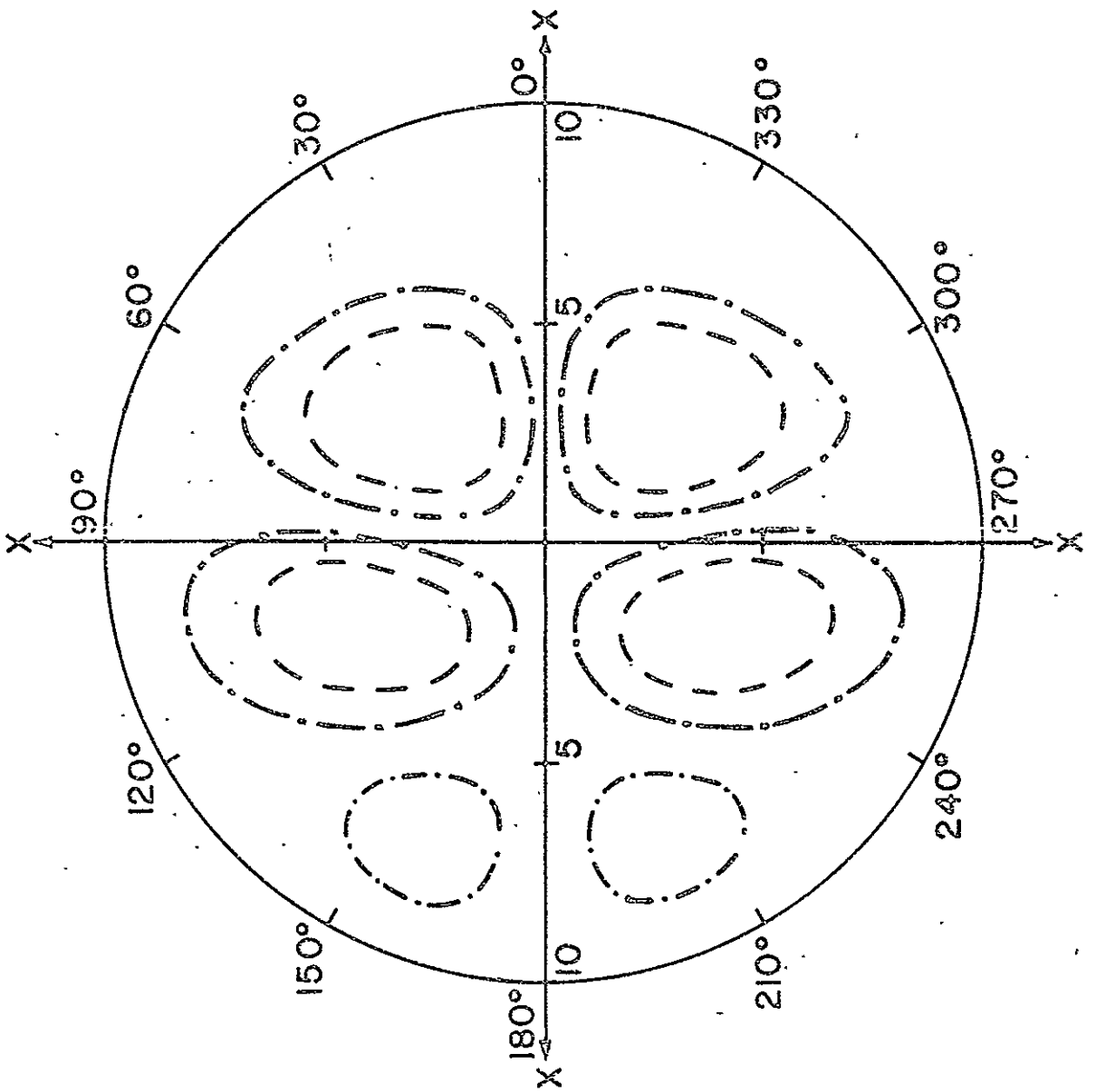

Figure 4

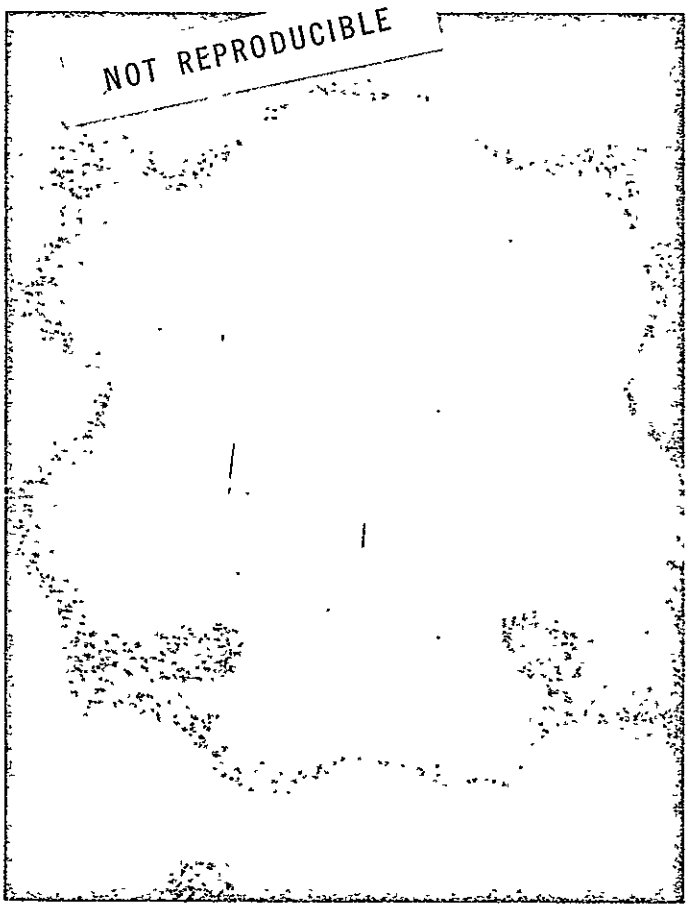

Figure 5

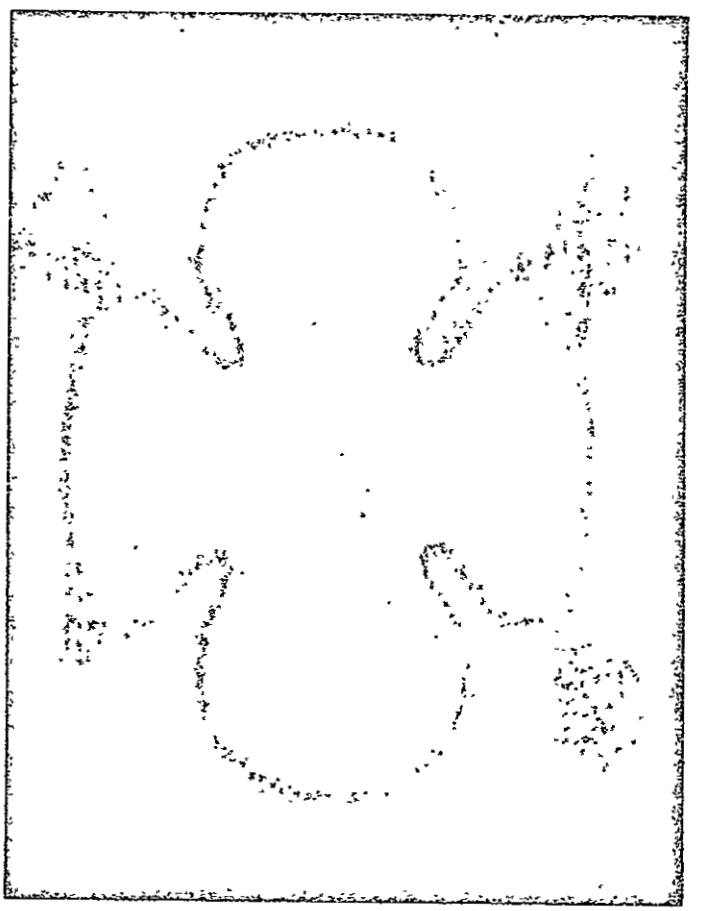

Figure 6

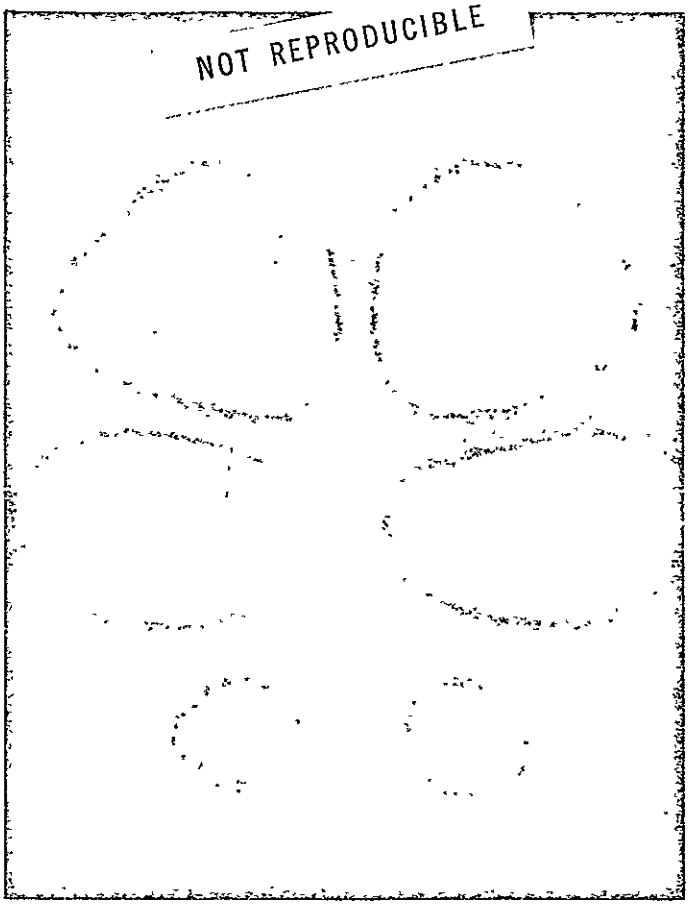

Figure 7

TABLE CAPTIONS

Table I: The Coefficients of the Transformation Matrices For the Six Sectors.

n	f_n	g_n	h_n
1	1	1	1
2	0	-1	-2
3	-1	1	1
4	1	-1	1
5	0	1	-2
6	-1	-1	1

TABLE I

ACKNOWLEDGMENT

The authors wish to acknowledge the assistance of George Hertzlinger in portions of the computer programming.

APPENDIX 2

Effects of Multiple Reflections on the Far Field Diffraction Pattern of a Corner Reflector

R. F. Chang

EFFECTS OF MULTIPLE REFLECTIONS ON THE FAR FIELD DIFFRACTION PATTERN OF A CORNER REFLECTOR

R. F. Chang

Technical Report 70-128

August 1969

University of Maryland
Department of Physics and Astronomy
College Park, Maryland
20742

This work was supported by NASA Contract NAS 9-7809.

ABSTRACT

We have studied the multiple reflections in a solid corner reflector. We have also calculated in detail the effects of multiple reflection on the far field diffraction pattern for the case of normal incidence of light. We have especially evaluated the central irradiance of the diffraction pattern as a function of the optical path difference between the primary and the secondary reflected beams. The variation of the central irradiance is also observed experimentally when the optical path difference is varied.

EFFECTS OF MULTIPLE REFLECTIONS ON THE FAR FIELD DIFFRACTION PATTERN OF A CORNER REFLECTOR

I. INTRODUCTION

We have reported the far field diffraction pattern of a corner reflector illuminated by a monochromatic plane polarized light.[1] In that report we assumed, in the case of a solid reflector, that the reflector[2] was coated with an antireflection film on its front face to eliminate the interference caused by the multiple reflections.

For a reflector without an antireflection coating on its entrance face the Fresnel reflection occurs every time the light hits the surface, either from the inside or from the outside of the reflector. Some amount of light is always reflected back into the reflector as it attempts to emerge from the reflector similar to what occurs where light is trapped in a glass plate between the parallel surfaces. The attenuation rate of the amplitude of the trapped light upon each Fresnel reflection is typically about 20%. All reflections should be taken into account to obtain an exact expression for the far field diffraction pattern.

We will discuss in the section II the geometry of multiple reflections in a reflector. In section III, we will present the mathematical equivalences of physical operations in the form of matrices and will then reduce the summation over all multiple reflections to a summation over a power series of a matrix. The analytical expression of the overall transformation matrix is

then presented in section IV and the resulting far field amplitude is discussed in section V along with a photograph of an oscilloscope trace showing the varying central irradiance of the far field diffraction pattern. Conclusions are given in section VI.

II. MULTIPLE REFLECTIONS IN A CORNER REFLECTOR

A ray of light entering a reflector emerges from the reflector after it has been reflected three times by the back surfaces. This emerging ray, however, is reflected partially by the front face, back into the reflector. After being reflected three more times by the back surfaces another emerging attempt is made and again partially reflected back into the reflector. This seemingly perpetuating reflection by the front face is what we call the multiple reflections in a reflector. An analogue to this is a ray of light passing through a piece of glass plate with two parallel surfaces.

The path of a ray in a reflector is three-dimensional in general. To illustrate its geometry in a simple fashion without losing its generality we chose a special cross section of a reflector where the path of a ray is in a plane. Such a cross section is shown in Fig. 1 where OX is one of the real back edges, OY is its image in the opposite surface and XY is the front face.

Consider a ray of light entering the reflector at a point denoted by A in Fig. 1. We have chosen a small incident angle for the ray in order to avoid overlapping of the rays in the illustration. The ray is partially reflected at A and the rest is transmitted into the reflector. The reflected light at A is denoted by F_1. The transmitted ray proceeds to points B, C, and exits at D. The emergent beam is denoted by R_1, which is a retro beam. The partially reflected ray at D proceeds to the points E, F, and exits at G. The emergent beam is denoted by F_2 which has the same direction as that

of F_1. A partial reflection will occur at the point G and the ray will proceed as before. Similarly we obtain R_2, and so on.

On examining the graph in Fig. 1, one notices that there are two distinct directions for the returning beams. One group of rays which consists of R_1, R_2, etc., is in the retro direction and we shall call this group R-rays. The other group of rays, which consists of F_1, F_2, etc., is in the reflected direction and we shall call this group F-rays. Here we have particularly pointed out the difference in the directions of the returning beams for the following reason.

In considering the effect of the multiple reflections on the far field we take into account only the beams which are in the retro direction. For all practical purposes, for instance, a slight misalignment of the incident ray of about 100 seconds of arc from the normal direction would throw the F-rays sufficiently far away from the R-rays. Thus we consider only the R-rays.

III. TRANSFORMATION MATRICES

When a plane wave of light enters normally a corner reflector the retro beam is shown[1,3] to be related to the incident beam by a transformation matrix. The front face is divided into six sections by the projection of the back edges and their images. Each section represents a unique sequence in which the entering beam hits the back surfaces. Therefore the transformation matrix is different for light entering different sections. If we denote the transformation matrix by $\underset{\sim}{C}^n$, where the subscript n=1 to 6 is the section identification, the incident light amplitude by $\underset{\sim}{u}=\begin{pmatrix} u \\ v \end{pmatrix}$ and the emerging beam by $\underset{\sim}{u}^n=\begin{pmatrix} u^n \\ v^n \end{pmatrix}$ then we have $\underset{\sim}{u}^n=\underset{\sim}{C}^n\underset{\sim}{u}$ when we ignore the front face reflection. The field components u and v, which are generally complex amplitudes, are taken in the directions perpendicular and parallel, respectively, to the projection of one of the real back edges in the front face. The matrix is given as[1]

$$\underset{\sim}{C}^n=\xi\underset{\sim}{1}+(\sqrt{3}/\sqrt{2})f_n\eta\underset{\sim}{\sigma}_x+g_n\zeta\underset{\sim}{\sigma}_y+(1/\sqrt{2})h_n\eta\underset{\sim}{\sigma}_z \qquad (1)$$

for n=1 to 6, with $f_1=g_1=h_1=g_3=h_3=f_4=h_4=g_5=h_6=1$, $f_2=f_5=0$, $g_2=f_3=g_4=f_6=g_6=-1$ and $h_2=h_5=-2$. The constants are given as

$$\xi=(r_s-r_p)[3(r_s+r_p)^2-2(r_s-r_p)^2]/16, \qquad (2a)$$

$$\eta=\sqrt{2}(r_s+r_p)^3/16, \qquad (2b)$$

$$\zeta=-i\sqrt{3}(r_s+r_p)^2(r_s-r_p)/16, \qquad (2c)$$

where $i\equiv\sqrt{-1}$ is the imaginary number, r_p and r_s are the coefficients of reflectance of the back surfaces for the parallel (p) and perpendicular (s) components, respectively, in respect to the plane of incidence, the $\underset{\sim}{\sigma}$'s are Pauli's spin matrices and $\underset{\sim}{1}$ is the unit matrix[4]. The matrix $\underset{\sim}{C}^n$ is in fact an equivalent matrix of the physical operation that a ray of light goes through a reflector except that a common phase factor of optical path, $\exp(i\phi)$, is omitted.

In order to sum up, in the case of multiple reflections, all the beams in the retro direction we shall represent every physical operation on the

ray of light in a reflector by an equivalent matrix. For the transmission of light at the entrance face into a reflector we have[5,6] $\underset{\sim}{T}_I=(\frac{2}{n_g+1})\underset{\sim}{1}$ where n_g is the index of refraction of the glass of which the reflector is made. The Fresnel reflection inside the reflector is represented by[7] $\underset{\sim}{R}=[(n_g-1)/(n_g+1)]\underset{\sim}{1}$. The transmission of light from inside the reflector to the air is represented by $\underset{\sim}{T}_E=[2n_g/(n_g+1)]\underset{\sim}{1}$. Then the first retro beam is given by $R_1^n=\exp(i\phi)(\underset{\sim}{T}_E\underset{\sim}{C}^n\underset{\sim}{T}_I)\underset{\sim}{u}$, as the consequence of the physical operations that the light first enters the reflector, then goes through the reflector and then leaves the reflector. If we refer back to Fig. 1, $\underset{\sim}{T}_I$ and $\underset{\sim}{T}_E$ occur at points A and D, respectively, while $\exp(i\phi)\underset{\sim}{C}^n$ describes the overall effects of the path ABCD.

Similarly, the second retro beam is given by[8] $R_2^n=\exp(i3\phi)(\underset{\sim}{T}_E\underset{\sim}{C}^n\underset{\sim}{R}\underset{\sim}{C}^{n+3}\underset{\sim}{R}\underset{\sim}{C}^n\underset{\sim}{T}_I)\underset{\sim}{u}$. Here $\underset{\sim}{T}_I$ and the first $\exp(i\phi)\underset{\sim}{C}^n$ are just as in R_1^n, the first $\underset{\sim}{R}$ occurs at D, $\exp(i\phi)\underset{\sim}{C}^{n+3}$ describes the effects of the path DEFG, the second $\underset{\sim}{R}$ occurs at G, another $\exp(i\phi)\underset{\sim}{C}^n$ describes the effects of the path GHIJ, and finally $\underset{\sim}{T}_E$ occurs at J. We shall mention, in order to avoid misleading the reader with the figure, that for normal incidence of the ray, the point A coincides with G, D with J and therefore three seemingly different paths are in fact the same one.

We can generate the remaining retro beams in the fashion of the second retro beam. Noticing that the matrices $\underset{\sim}{T}_I$, $\underset{\sim}{T}_E$, and $\underset{\sim}{R}$ are represented by the unit matrix which commutes with all other matrices, and that the m-th retro beam equals the (m-1)-th retro beam operated on by $(\underset{\sim}{C}^n\underset{\sim}{R}\underset{\sim}{C}^{n+3}\underset{\sim}{R})$, we can write the total sum of all retro beams as

$$R_T^n = \exp(i\phi)[4n_g/(n_g+1)^2]\sum_{\mu=0}^{\infty}\exp(i2\mu\phi)[(n_g-1)/(n_g+1)]^{2\mu}(\underset{\sim}{D}^n)^\mu\underset{\sim}{C}^n\underset{\sim}{u} \tag{3}$$

where $\underset{\sim}{D}^n\equiv\underset{\sim}{C}^n\underset{\sim}{C}^{n+3}$. The power series converges and we can use the formula as in the case of a scalar that $\sum_{\mu=0}^{\infty}x^\mu=(1-x)^{-1}$ for $|x|<1$ and obtain

$$R_T^n = \exp(i\phi)[4n_g/(n_g+1)^2](1-\alpha\underset{\sim}{D}^n)^{-1}\underset{\sim}{C}^n\underset{\sim}{u} \equiv \underset{\sim}{E}^n\underset{\sim}{u}, \tag{4}$$

where $\alpha \equiv \exp(i2\phi)[(n_g-1)/(n_g+1)]^2$.

The overall transformation matrix $\underset{\sim}{E}^n$ can be expressed explicitly in terms of Pauli's spin matrices and unit matrix as in the case of $\underset{\sim}{C}^n$. The detailed calculation and the final expressions are presented in the next section.

IV. ANALYTICAL EXPRESSIONS

The task of expressing $\underset{\sim}{E}^n$ in terms of Pauli's spin matrices and the unity matrix involves: a) finding the matrices $\underset{\sim}{D}^n$, which are the product of $\underset{\sim}{C}^n$ and $\underset{\sim}{C}^{n+3}$, b) finding the inverse of $(1-\alpha\underset{\sim}{D}^n)$, and c) finding the product of $(1-\alpha\underset{\sim}{D})^{-1}$ and $\underset{\sim}{C}^n$. Since each matrix is expressed in terms of Pauli's spin matrices, the multiplication of two such matrices can be evaluated by using the following properties of Pauli's spin matrices: $\sigma_x^2 = \underset{\sim}{\sigma}_y^2 = \underset{\sim}{\sigma}_z^2 = 1$, $\underset{\sim}{\sigma}_x\underset{\sim}{\sigma}_y + \underset{\sim}{\sigma}_y\underset{\sim}{\sigma}_x = 0$ and $\underset{\sim}{\sigma}_x\underset{\sim}{\sigma}_y = i\underset{\sim}{\sigma}_z$. Using these operational properties, we obtain $\underset{\sim}{D}^n = d_1^n \underset{\sim}{1} + d_2^n\underset{\sim}{\sigma}_x + d_3^n \underset{\sim}{\sigma}_y + d_4^n\underset{\sim}{\sigma}_z$ where

$$d_1^n = \xi^2 + 2\eta^2 - \xi^2, \qquad (5a)$$

$$d_2^n = \sqrt{2}\,\eta(\sqrt{3}\, f_n\, \xi + i\, g_n\, h_n\, \zeta), \qquad (5b)$$

$$d_3^n = 0, \qquad (5c)$$

$$d_4^n = \sqrt{2}\,\eta\,(h_n\,\xi - i\sqrt{3}\, f_n\, g_n\,\zeta). \qquad (5d)$$

Using similar algebraic procedure, we obtain

$$(1 - \alpha\underset{\sim}{D}^n)^{-1} = \frac{1}{Q}\,[(1 - \alpha d_1^n)\,\underset{\sim}{1} + \alpha d_2^n\,\underset{\sim}{\sigma}_x + \alpha d_4^n\,\underset{\sim}{\sigma}_z] \qquad (6)$$

where $Q = 1 - 2\alpha\ (\xi^2 + 2\eta^2 - \zeta^2) + \alpha^2(\xi^2 - 2\eta^2 - \zeta^2)^2$. Finally, multiplying $(1 - \alpha\underset{\sim}{D}^n)^{-1}$ with $\underset{\sim}{C}^n$, we obtain the expression of the total transformation matrix $\underset{\sim}{E}^n$:

$$\underset{\sim}{E}^n = \beta[\xi'\,\underset{\sim}{1} + (\sqrt{3}/\sqrt{2})\, f_n\eta'\underset{\sim}{\sigma}_x + g_n\zeta'\underset{\sim}{\sigma}_y + (1/2)\, h_n\eta'\underset{\sim}{\sigma}_z] \qquad (7)$$

where

$$\beta \equiv 4n_g\, \exp(i\phi)/[(n_g + 1)^2],$$

$$\xi' \equiv \xi[1-\alpha\ (\xi^2 - 2\eta^2 - \zeta^2)]/Q,$$

$$\eta' \equiv \eta[1 + \alpha\ (\xi^2 - 2\eta^2 - \zeta^2)]/Q,$$

$$\zeta' \equiv \zeta\ [1 - \alpha\ (\xi^2 - 2\eta^2 - \zeta^2)]/Q.$$

V. THE DIFFRACTION PATTERN

In our previous report[1], we have presented the far field of a reflector when plane polarized monochromatic light is used. In that report we ignored the effects of the multiple reflections from the front face. In fact, we took only the matrix C^n into account in obtaining the analytical expressions of the far field. To take into account the effects of multiple reflections all we have to do is to carry out the same calculation as before but use E^n in the calculation instead of C^n. However, comparing E^n to C^n we notice that the only differences between them are that ξ, η, and ζ are replaced by ξ', η', and ζ', and a reduction in the amplitude by the factor of β. Therefore, we come to the conclusion that the far field pattern with the multiple reflection effects can be readily written as

$$U_p(x,\psi;\theta) = \beta\{\xi'[2J_1(x)/x] + \eta'\frac{6\sqrt{6}}{\pi}\sum_{\ell=1}^{2}\sum_{m=o}^{\infty}\frac{(-)^{m+1}}{(2\ell+6m)}(1/x)^2 \times [\int_o^x yJ_{2\ell+6m}(y)dy]\cos[(2\ell+6m)\psi + (-)^{\ell}2\theta]\} \quad (8a)$$

$$U_s(x,\psi;\theta) = \beta\{\zeta'\frac{24}{\pi}\sum_{m=o}^{\infty}\frac{(-)^m}{(3+6m)}(\frac{1}{x})^2[\int_o^x yJ_{3+6m}(y)dy]\sin[(3+6m)\psi] + \eta'\frac{6\sqrt{6}}{\pi}\sum_{\ell=1}^{2}\sum_{m=o}^{\infty}\frac{(-)^{m+\ell-1}}{(2\ell+6m)}(\frac{1}{x})^2[\int_o^x yJ_{2\ell+6m}(y)dy]\sin[(2\ell+6m)\psi + (-)^{\ell}2\theta]\} \quad (8b)$$

where the subscript p denotes the component whose polarization is parallel to that of incident light whereas s denotes the orthogonal polarization component. The observation point is expressed by the polar coordinates x and ψ. The radial coordinate x is $(\frac{2\pi}{\lambda})aw$ where λ is the wavelength of the light, a is the radius of the circular aperture and w is the sine of the angle between the direction of the field point and the retro direction. The angle θ is the angle between the direction of the polarization of the incident light relative to the orientation of the reflector.

Although we can express the analytical form of the far field, the real difficulty in evaluating the expressions lies in the fact that the optical path is too uncertain to determine the phase factor, $\exp(i2\phi)$, in α. For example, for a reflector with an optical path of about 10 cm, it requires that the physical dimension as well as the index of refraction is known within one part in a million to determine the phase angle within thirty degrees. Such a requirement is impractical. However, $|\alpha|$ is on the order of 0.04, the effects of the phase factor, $\exp(i2\phi)$, on ξ', η', and ζ' are relatively small. As an example, we have calculated Ω_1 and Ω_2, which are defined as

$$\Omega_1 \equiv \xi'/\xi = \zeta'/\zeta = [1-\alpha(\xi^2 - 2\eta^2 - \zeta^2)]/Q \equiv W_1 \exp(i\Phi_1)$$

$$\Omega_2 \equiv \eta'/\eta = [1 + \alpha(\xi^2 - 2\eta^2 - \zeta^2)]/Q \equiv W_2 \exp(i\Phi_2)$$

in terms of the angle ϕ for the case of a reflector made of fused silica ($n_g = 1.4571$ at $\lambda = 6328$ Å).

The absolute values, W_1 and W_2, and the phase angles, Φ_1 and Φ_2, are plotted in Fig. 2. As we see in the figure that the effects of ϕ on ξ', η' and ζ' are indeed small, especially on η'. Therefore, the effects on the total diffraction pattern is small as well. However, we shall point out that it is not negligible. For example, the central irradiance of the diffraction pattern is directly proportional to $|\xi'|^2$. It means that the central irradiance varies approximately ±10% when ϕ varies from 0 to π.

To observe this effect experimentally, we have to vary the optical path within the reflector while we simultaneously monitor the central irradiance of the diffraction pattern with a photo-detector. One way to vary the optical path is to vary the temperature of the reflector. Because of the long thermal time constant of the reflector it is impractical to use this method. Another method is to rotate a reflector in the vicinity of the normal

direction, typically within a couple of degrees. Although the previous calculation does not apply to a non-normal (off axis) incident beam, it is still a good approximation within a small angle of rotation. This is so because the off axis effect is a second order effect in the vicinity of the normal direction.

A photograph of a scope trace of the output from a photo detector is shown in Fig. 3. The full trace covers about ±3° from the normal direction of incidence. The base line is indicated by a straight line on the upper portion of the photograph. Notice the intensity modulation in the vicinity of the normal direction. The modulation is about ±5%. The discrepency from the analytical prediction of ±10% can be explained by the fact that the wave front of all beams other than the direct return was degraded by the front face which is not "perfectly" flat. A flatness figure of about $\lambda/10$, that is the manufacture's specification of the reflector used, would decrease the modulation by approximately one-half.

VI. CONCLUSIONS

We have found that the effects of multiple reflections do not alter the basic structure of the pattern. As previously reported[1], the diffraction pattern is still determined by the four functions which we call G-functions. The optical parameters such as the index of refraction of the material of which the reflector is made and the optical constant of the back reflecting surfaces, (e.g. aluminized or silvered), only appear in the coefficients of these basic four functions. The multiple reflections only alter the way these parameters enter the coefficients. Although it is small, the effect of the multiple reflections still cause approximately 10% uncertainty in the central irradiance of the diffraction pattern.

1. R. F. Chang, D. G. Currie, C. O. Alley, and M. E. Pittman, to be published in J. Opt. Soc. Am. April (1971); University of Maryland, Department of Physics and Astronomy, Technical Report 70-104 (1970).
2. We will use "reflector" in this as an abbreviation of "corner reflector".
3. E. R. Peck, J. Opt. Soc. Am. 52, 253 (1862).
4. For detailed discussion see ref. 1.
5. Born & Wolf, Principles of Optics, 2nd revised edition (Macmillan Co., New York), 1964, p. 40.
6. Note that no physical distinction can be made for p- or s- component for normal incidence.
7. Note that the coordinates are not chosen the same way as in ref. 5.
8. The superscript of the transformation matrix is associated with the sextant from which the light emerges. The light entering the n-th sextant would emerge from the opposite sextant which is (n+3)-th sextant in the modulo of 6.

FIGURE CAPTIONS

1. A beam of light is traced through a corner reflector to illustrate the multiple reflections which occur at the front surface. A special cross section of the corner is so chosen that the ray lies in a plane. The directions of the light are indicated by the arrows.

2. The absolute values as well as the phase angles of Ω_1 and Ω_2 are plotted as functions of the optical path in a reflector. The optical path is expressed by the phase angle ϕ.

3. The modulation on the central irradiance of the diffraction pattern is traced on an oscilloscope screen when a corner reflector is rotated $\pm 3°$ from normal direction. A photomultiplier is used as a detector whose output is negative in polarity. The straight line on the upper part of the photograph is the base line. The signal trace is broadened slightly because of the shot noise in the weak light signal.

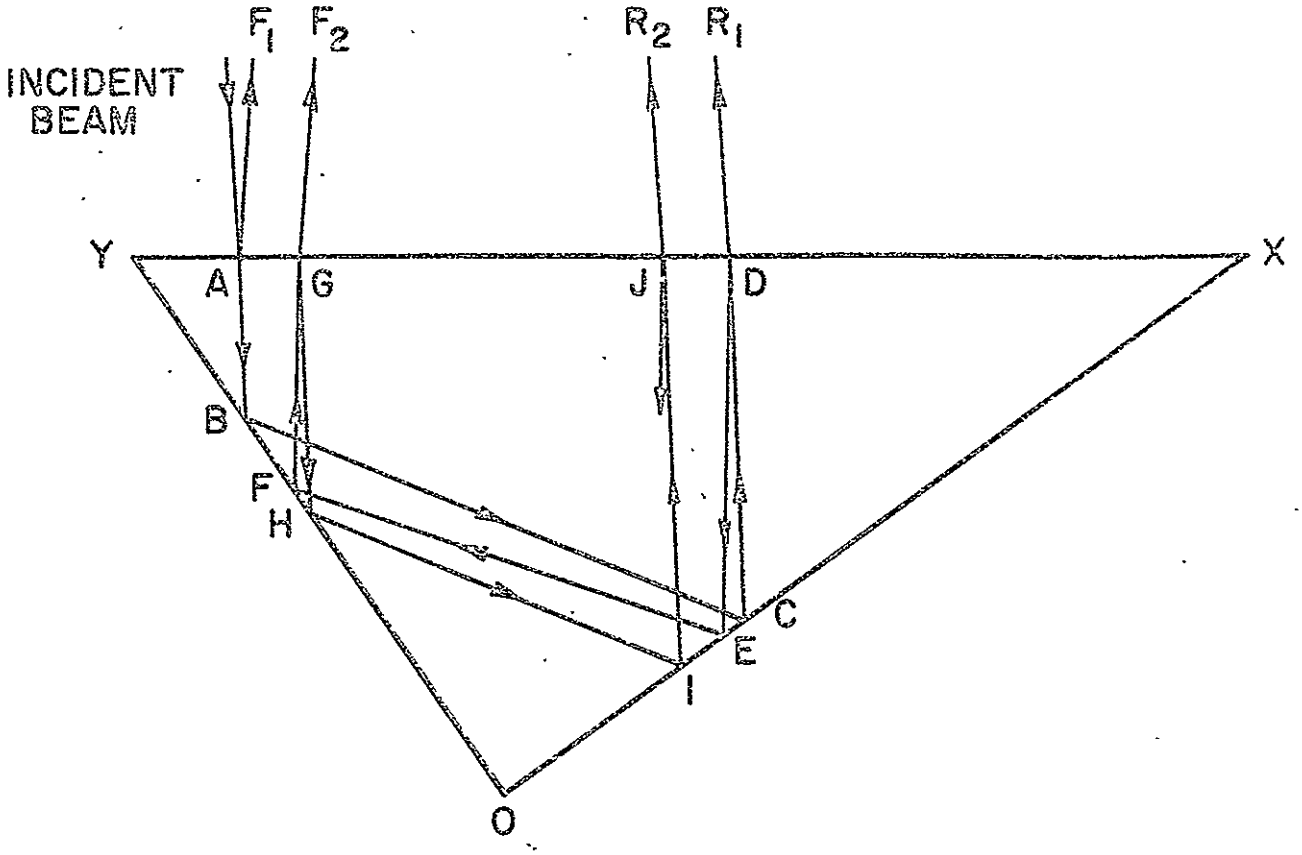

Fig. 1

A beam of light is traced through a corner reflector to illustrate the multiple reflections which occur at the front surface. A special cross section of the corner is so chosen that the ray lies in a plane. The directions of the light is indicated by the arrows.

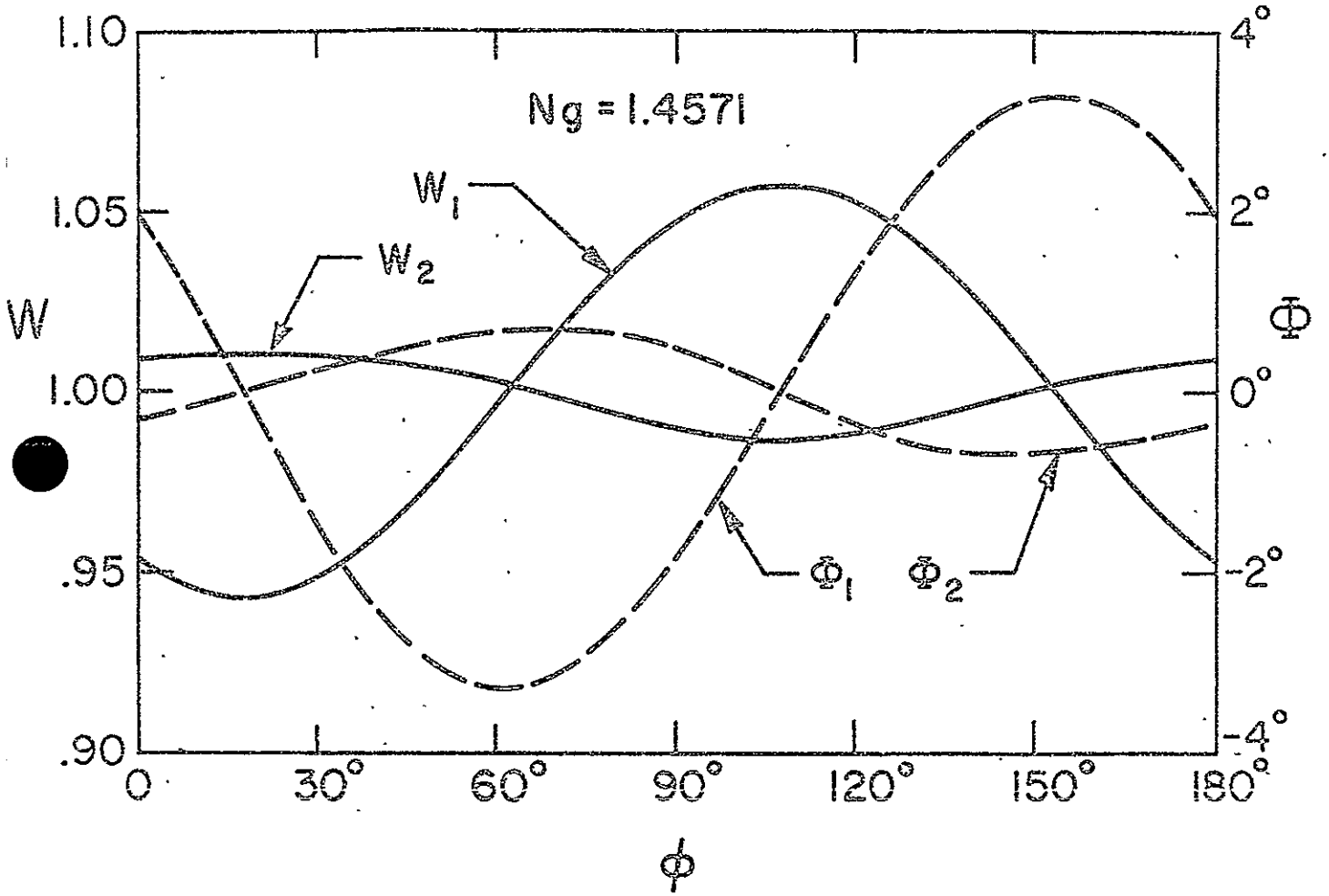

Fig. 2

The absolute values as well as the phase angles of Ω_1 and Ω_2 are plotted as functions of the optical path in a reflector. The optical path is expressed by the phase angle ϕ.

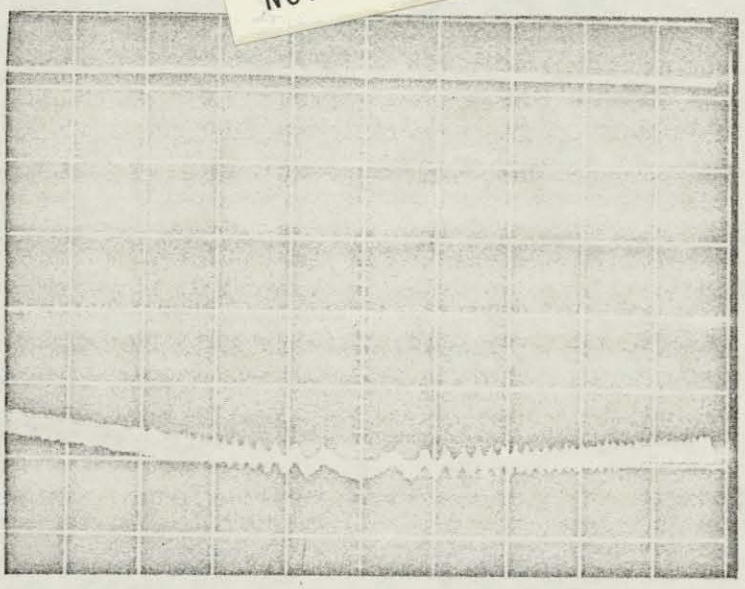

Fig. 3

The modulation on the central irradiance of the diffraction pattern is traced on an oscilloscope screen when a corner reflector is rotated $\pm 3^{o}$ from normal direction. A photomultiplier is used as a detector whose output is negative in polarity. The straight line on the upper part of the photograph is the base line. The signal trace is broadened slightly because of the shot noise in the weak light signal.

APPENDIX 3

Numerical Ray Trace Analysis for Diffraction Central Irradiance of a Retroreflector for Off-Axis Incidence of Light

R. F. Chang

NUMERICAL RAY TRACE ANALYSIS FOR DIFFRACTION CENTRAL IRRADIANCE OF A RETROREFLECTOR FOR OFF-AXIS INCIDENCE OF LIGHT*

R. F. Chang

Technical Report 70-129
February 1970

Department of Physics and Astronomy
University of Maryland
College Park, Maryland

*This work was supported by NASA Contract NAS 9-7809.

ABSTRACT

We have developed a ray tracing technique designed to provide the amplitudes of light reflected by a retroreflector for arbitrary direction of incidence. The area of the sub-apertures is also calculated. A computer is needed for the ray-trace as well as for the area calculation. Combining the amplitudes with the areas, we obtain the central irradiance of the diffraction pattern of a retroreflector. The emphasis of the report is on the method used in obtaining the results.

NUMERICAL RAY TRACE ANALYSIS FOR DIFFRACTION CENTRAL IRRADIANCE OF A RETROREFLECTOR FOR OFF-AXIS INCIDENCE OF LIGHT.

I. INTRODUCTION.

In connection with the design and testing of the Apollo 11 Laser Ranging Retroreflector[1-3], analysis was undertaken to provide a thorough understanding of the diffraction pattern of retroreflectors. Because of the libration effect, the laser beam which is transmitted from the earth must assume different angles of incidence on different days. We were able to analyze thoroughly for various reflecting surfaces and express the diffraction pattern in an analytical form for normal incidence of light because of the symmetry in the geometry[4]. However, for off-axis incidence of light the symmetry disappears. The lack of symmetry imposes difficulties in analysis. As as alternative, a numerical ray tracing method was developed starting the summer of 1968 to aid in pracical design questions.

The far field diffraction pattern of light is essentially a two-dimensional Fourier transform of the complex amplitude of light at the aperture. If the complex amplitude of light is known over the entire aperture the diffraction pattern can be obtained either by analytical or by numerical methods. The latter is more convenient for an aperture of irregular shape.

In this report we will present the ray trace technique for obtaining the complex amplitude of light reflected by a retroreflector for off-axis angles of incidence with the emphasis on technique. We consider

mainly the case of a solid retroreflector, made of fused silica or glass, utilizing total internal reflection. The retroreflector is assumed to be geometrically and optically perfect. We also present the analysis on the effective aperture of a retroreflector for off-axis angles of incidence.

II. GENERAL DESCRIPTIONS OF A RETROREFLECTOR.

A solid retroreflector can be most easily represented by the portion of a glass cube sliced off by a plane determined by the diagonals of three planes forming a corner as shown in Figure 1(a). In this case the triangle ABC is the front face of the retroreflector. The shape of the front face may be an inscribed circle as shown in Figure 1(b) instead of a triangle.

We define the normal direction of incidence to be the direction which is perpendicular to the front face; and the axis of symmetry of a retroreflector is the line which passes through the vertex of the corner in the direction of normal incidence.

The entrance aperture of light is the front face whereas the exit aperture is the image of the front face produced by the retroreflector itself. These two apertures do not coincide in general and the effective aperture depends not only on the shape of the front face but also on the angle of incidence of light.

A unique direction of incidence relative to the retroreflector can be defined by two angles. The first one is the angle of incidence θ and

the other is the azimuth angle ϕ. Since the incident light is assumed to be collimated we can define the plane of incidence to be the plane which is parallel to the direction of incidence and contains the axis of symmetry of the retroreflector in the plane. A reference plane is defined by the axis of symmetry and one of the back edges of the retroreflector. Each of the three back edges can be used because of the threefold symmetry in the geometry. The angle of incidence, θ, is the angle between the axis of symmetry and the light ray in the plane of incidence; the azimuth angle, ϕ, is the angle between the plane of incidence and the reference plane. The definitions of both θ and ϕ are illustrated graphically in Figure 2. The azimuth angle ϕ is confined to between 0° and 120° because of the threefold symmetry around the axis of symmetry.

III. RAY TRACE.

The direction of an incident ray is defined by θ and ϕ as discussed previously. However, after the ray enters a retroreflector the angle of incidence becomes θ_i because of the refraction at the front face; the angle of incidence before and after the refraction is related by Snell's law, $\sin \theta = N \sin \theta_i$, where N is the index of refraction of the glass. In order to trace the ray through a retroreflector the direction of incidence needs to be expressed in terms of more fundamental quantities, such as direction cosines, rather than θ and ϕ. We choose to define a

rectangular coordinate system by the three back edges of a retroreflector and designate OA, OB, and OC as x-, y-, and z-axis, respectively. Then we can express the unit vector of the axis of symmetry of the retroreflector in the outward direction as $\hat{a} = (\hat{x} + \hat{y} + \hat{z})/\sqrt{3}$, where $\hat{x}$, $\hat{y}$, and $\hat{z}$ are the unit vectors along the x-, y-, and z-axis, respectively. In order to obtain the expressions of the direction cosines in terms of θ_i and ϕ, we choose the following approach.

Assuming the direction cosines of the unit vector $\hat{k}$ in the direction of the incident ray within the retroreflector is $(-\ell, -m, -n)$, where ℓ, m, and n are non-negative numbers, we can relate the angle of incidence to the direction cosines by the scaler product

$$\cos \theta_i = (-\hat{k}) \cdot (\hat{a}) = \frac{1}{\sqrt{3}} (\ell + m + n). \tag{1}$$

The unit vector of the normal of the plane of incidence is given by $\hat{n}_p = \hat{k} \times \hat{a}/|\hat{k} \times \hat{a}|$ whereas the unit vector of the normal of the reference plane is given by $\hat{n}_r = \hat{a} \times \hat{x}/|\hat{a} \times \hat{x}|$. Then the azimuth angle can be related to the direction cosines by the scaler product $n_p \cdot n_r$ and we have

$$\cos \phi = (2\ell - m - n)/(\sqrt{6} \sin \theta_i). \tag{2}$$

Rewriting Eq. (1) and Eq. (2), we have, along with the constraint on the direction cosines,

$$2\ell - m - n = \sqrt{6} \sin \theta_i \cos \phi, \tag{3}$$

$$\ell + m + n = \sqrt{3} \cos \theta_i, \tag{4}$$

$$\ell^2 + m^2 + n^2 = 1. \tag{5}$$

Solving these three equations we obtain

$$\ell = \frac{1}{\sqrt{3}} (\cos \theta_i + \sqrt{2} \sin \theta_i \cos \phi) \tag{6}$$

$$m = \frac{1}{\sqrt{6}} (\sqrt{2} \cos \theta_i - \sin \theta_i \cos \phi + \sqrt{3} \sin \theta_i \sin \phi) \tag{7}$$

$$n = \frac{1}{\sqrt{6}} (\sqrt{2} \cos \theta_i - \sin \theta_i \cos \phi - \sqrt{3} \sin \theta_i \sin \phi). \tag{8}$$

Since our convention on ϕ requires that $m \geq n$ when $\phi \geq o$ we have chosen the solutions accordingly.

Now we assume that the incident light is polarized. The state of polarization of light is expressed in terms of two mutually orthogonal linear polarizations p- and s-components in the plane of incidence. The unit vectors of the polarization satisfy the relation that $\hat{k} = \hat{p} \times \hat{s}$, where $\hat{p}$ and $\hat{s}$ are the unit vectors in p and s directions, respectively. Furthermore, we can choose $\hat{s}$ in the same direction as $\hat{n}_p$ since $\hat{n}_p$ is the normal of the plane of incidence; then we have

$$\hat{s} = \sqrt{\frac{2}{3}} \left[(-\sqrt{2} \sin \phi)\, \hat{x} + \sin (\phi + 60°)\, \hat{y} + \sin (\phi - 60°)\hat{z}\right]. \tag{9}$$

It follows that $\hat{p} = \hat{s} \times \hat{k}$ and we have

$$\hat{p} = \frac{\cos \theta_i}{\sqrt{3}} \{(\tan \theta_i - \sqrt{2} \cos \phi)\, \hat{x} + [\tan \theta_i + \sqrt{2} \cos (\phi + 60°)]\hat{y} + [\tan \theta_i + \sqrt{2} \cos (\phi - 60°)]\hat{z}\}. \tag{10}$$

Now suppose that the complex amplitude of the incident light before entering the retroreflector is expressed by

$$\vec{A}_o = A_{op}\, \hat{p}_o + A_{os}\, \hat{s}_o\,, \tag{11}$$

where $\hat{p}_o$ and $\hat{s}_o$ are the unit polarization vectors prior to entering the retroreflector, then after entering the retroreflector the amplitude is[5]

$$\vec{A} = A_p\, \hat{p} + A_s\, \hat{s} \tag{12}$$

where

$$A_p = \frac{2 \cos \theta}{N \cos \theta + \cos \theta_i}\, A_{op},$$

$$A_s = \frac{2 \cos \theta}{\cos \theta + N \cos \theta_i}\, A_{os}.$$

The ray, after having entered a retroreflector, will be reflected consecutively by the three back surfaces before emerging from the retroreflector. There are six different sequences of the surfaces by which the ray is reflected. The choice depends upon the entering point on the front face and upon the direction of the incidence. These six different sequences are represented by the fact that the effective aperture is divided into six subapertures.

The front view, shown in Figure 3, of a retroreflector shows the effective aperture is the common area shared by ABC and its image A'B'C'; the edges OA, OB, and OC along with their images divide the aperture into six subapertures which can be labeled by the numbers 1 through 6. We can also label the planes OBC, OCA, and OAB whose normals are in the direction of $\hat{x}$, $\hat{y}$, and $\hat{z}$ as I, II, and III, respectively.

A ray that enters the retroreflector through subaperture 4 will emerge from the retroreflector through subaperture 1 after having been reflected consecutively by plane I, II, and III. The sequence can be written symbolically as 4(I) → II → 1(III). Similarly, the rest of the sequences can be written as 5(II) → I → 2(III), 6(II) → III → 3(I), 1(III) → II → 4(I), 2(III) → I → 5(II), and 3(I) → III → 6(II).

At every plane of reflection the process of reflection is the same in general. The state of light is characterized by the propagation vector ($\hat{k}$), the polarization vectors ($\hat{p}$ and $\hat{s}$) and the amplitude components A_p and A_s. All one has to do is to relate the state of light after the reflection to the state before the reflection.

Let us name the unit vector of the normal of the reflecting surface to be $\hat{v}$, the unit vectors of the directions of propagation before and after the reflection to be $\hat{k}_1$ and $\hat{k}_2$ respectively, the polarization vectors of the incident light to be $\hat{p}$ and $\hat{s}$, and the polarization vectors in the plane of incidence before and after the reflection to be $\hat{p}_1$, $\hat{s}_1$, and $\hat{p}_2$, $\hat{s}_2$, respectively, as shown in Figure 4. The amplitude of the incident light is expressed in the form of Eq.(12), then, because the reflection coefficients are different for p- and s-poliarization components with respect to the plane of incidence, we rewrite the light amplitude in terms of the polarization components appropriate to the plane of incidence as

$$\vec{A} = B_p \hat{p}_1 + B_s \hat{s}_1 \tag{13}$$

where

$$B_p = A_p (\hat{p} \cdot \hat{p}_1) + A_s (\hat{s} \cdot \hat{p}_1)$$
$$B_s = A_p (\hat{p} \cdot \hat{s}_1) + A_s (\hat{s} \cdot \hat{s}_1).$$

The unit vectors $\hat{p}_1$, $\hat{s}_1$, $\hat{p}_2$, $\hat{s}_2$, and $\hat{k}_2$ are expressed in terms of the known vectors $\hat{v}$ and $\hat{k}_1$:

$$\hat{p}_1 = [-(\hat{v} \cdot \hat{k}_1) \hat{k}_1 + \hat{v}]/|\hat{v} \times \hat{k}_1|,$$
$$\hat{s}_1 = (\hat{k}_1 \times \hat{v})/|\hat{k}_1 \times \hat{v}|,$$
$$\hat{p}_2 = \{(\hat{v} \cdot \hat{k}_1) \hat{k}_1 + [1-2 (\hat{v} \cdot \hat{k}_1)^2] \hat{v}\}/|\hat{v} \times \hat{k}_1|,$$
$$\hat{s}_2 = \hat{s}_1$$
$$\hat{k}_2 = \hat{k}_1 - 2 (\hat{v} \cdot \hat{k}_1)\hat{v}.$$

After the reflection, the amplitudes are given as

$$\vec{A}' = R_p B_p \hat{p}_2 + R_s B_s \hat{s}_2$$

where R_p and R_s are the reflection coefficients for p- and s-components.

When we assume internal total reflection, we have[5]

$$R_p = \frac{\cos\alpha - i N\sqrt{N^2 \sin^2\alpha - 1}}{\cos\alpha + i N\sqrt{N^2 \sin^2\alpha - 1}}$$

$$R_s = \frac{N\cos\alpha - i\sqrt{N^2 \sin^2\alpha - 1}}{N\cos\alpha + i\sqrt{N^2 \sin^2\alpha - 1}},$$

where i is the imaginary number $\sqrt{-1}$ and $\cos\alpha = -\hat{k}_1 \circ \hat{v}$. But when internal total reflection fails we have[5]

$$R_p = \tan(\alpha - \alpha')/\tan(\alpha + \alpha')$$

$$R_s = -\sin(\alpha - \alpha')/\sin(\alpha + \alpha')$$

where $\alpha' = \sin^{-1}(N \sin\alpha)$. Now $\vec{A}'$ becomes the new incident light for the next surface and the whole procedure may repeat again.

In a retroreflector, the procedure repeats three times because there are three back surfaces. The polarization components after the third reflection are again rearranged into $\hat{p}_3$ and $\hat{s}_3$ where $\hat{p}_3 = \hat{p}$ and $\hat{s}_3 = -\hat{s}$ prior to the emergence of light from the retroreflector. If we write the amplitude prior to the emergence to be $\vec{A}_3 = C_p \hat{p}_3 + C_s \hat{s}_3$, then the amplitude after the emergence is $\vec{A}_f = A_{fp} \hat{p}_f + A_{fs} \hat{s}_f$ where $\hat{p}_f = \hat{p}_o$, $\hat{s}_f = -\hat{s}_o$,

$$A_{fp} = \frac{2 N \cos\theta_i}{\cos\theta_i + N\cos\theta} C_p,$$

$$A_{fs} = \frac{2 N \cos\theta_i}{N\cos\theta_i + \cos\theta} C_s.$$

The complete process of reflections which transforms $\vec{A}_o$ to $\vec{A}_f$ can be repeated six times for six different sequences of reflection. In this way we obtain the final state of light emerging from each subaperture.

IV. SUBAPERTURES.

The diffraction integral for multiple-aperture configuration can be written as

$$U(p,q) = \sum_j C_j \iint_j \exp\,[\,-ik\,(px + qy)\,]\,dxdy,$$

where $U(p,q)$ is the amplitude at the diffraction field point (p,q), x and y are the coordinates in the aperture plane, k is the wave number of the light, and C_j is the amplitude of the light field in the j-th aperture. The light field at the center ($p = q = o$) of the diffraction pattern becomes

$$U(o,o) = \sum_j C_j \iint_j dxdy = \sum_j C_j A_j,$$

where A_j is the area of the j-th subaperture. Because we are only concerned with the central irradiance of the diffraction pattern in our application we will consider only the calculation of the area of each subaperture.

The shape of the subaperture depends on the shape of the front face of the retroreflector. We will present the retroreflector whose front face is an inscribed circle to the triangle. Other geometrical shapes are certainly permissible. The general approach employed here can be applied to all shapes of the front face.

The formation of the subapertures can be explained in the following way. The retroreflector and its image constitute a cylinder which is shown in Figure 5. By inspection, it is clear that the process of reflection of a ray by a retroreflector is equivalent to the process whereby a ray passes through a cylinder and emerges from the other end. The effective aperture is the intersection, along the direction of the

ray, of the front face and its image, as shown in Figure 6(a). The effective aperture is divided into six subapertures by the projections, along the direction of the ray on the effective aperture, of the back edges and their images as illustrated in Figure 6(b) for $\phi = 15°$, $\theta = 20°$. These dividing lines are the lines which connect the vertices of the triangular face to their corresponding vertices of the image. The inscribed circle becomes elliptical because of the $\cos\theta$ effect.

If we ignore the $\cos\theta$ effect for now because we can always take care of that effect later, then we will be dealing with a circle and the chords in the circle. Basically a subaperture is the intersection of two overlapping segments of a circle.

Let us denote the distances to two intersectiong chords from the center of the circle to be ℓ_1 and ℓ_2, as shown in Figure 7, and the angle between ℓ_1 and ℓ_2 to be $\ell_1\hat{}\ell_2$, then the area A can be expressed as a function of ℓ_1, ℓ_2 and $\ell_1\hat{}\ell_2$. If we present the formula in a normalized form so that the area of the circle is unity, then we have

$$A\,(L_1, L_2, \ell_1\hat{}\ell_2) = \frac{1}{\pi}\{\frac{1}{2}\, f\, g \sin \ell_1\hat{}\ell_2 + \sin^{-1}(\frac{h}{2}) - (\frac{h}{2})\sqrt{[1-(h/2)^2]}\} \quad (14a)$$

where $L_1 = \ell_1/R$ (14b)

$L_2 = \ell_2/R$ (14c)

$f = \sqrt{(1-L_1^2)} - (L_2 - L_1 \cos \ell_1\hat{}\ell_2)/\sin \ell_1\hat{}\ell_2$ (14d)

$g = \sqrt{(1-L_2^2)} - (L_1 - L_2 \cos \ell_1\hat{}\ell_2)/\sin \ell_1\hat{}\ell_2$ (14e)

$h = \sqrt{(f^2 + g^2 + 2fg \cos \ell_1\hat{}\ell_2)}$, (14f)

and R is the radius of the circle.

The typical geometrical configurations of subapertures are shown in Figure 8 and Figure 9 for the case of $\psi>\phi$ and $\psi<\phi$, respectively. The definition of ψ is self-evident in the figures. It is necessary to separate these two cases because in the case of $\psi>\phi$ we can evaluate the area of the subaperture 1 and 6 but not 2 by using the formula Eq.(14); whereas in the case of $\psi<\phi$ we can evaluate the area of the subapertures 1 and 2 but not 6. Since the area of the subapertures opposite of each other is the same, we evaluate only the area of three subapertures.

In order to evaluate the area of the third subaperture, we evaluate the total area of the effective aperture, divide this area by two, and then subtract the area of the other two subapertures. If we designate the displacement of the center of the image from that of the front face by d, then, after normalizing the area of the total effective aperture to unity at $\theta = 0°$, the area of one-half of the effective aperture is

$$A_h = \frac{1}{\pi}[\cos^{-1}(2\delta) - 2\delta\sqrt{(1-4\delta^2}], \tag{15}$$

where $\delta \equiv d/D$. The displacement d is expressed as a function of the angle of incidence as

$$d = \frac{\sin\theta}{\sqrt{[2(N^2-\sin^2\theta)]}} D. \tag{16}$$

We can also express the appropriate parameters which are suitable for Eq.(14) indirectly as a function of δ and ϕ and we have

$$L_1 = 2 \sin \psi_1, \tag{17a}$$

$$L_2 = 2 \sin \psi_2, \tag{17b}$$

$$L_3 = 2 \sin \psi_3, \tag{17c}$$

$$\ell_1 \hat{} \ell_3 = 2\pi/3 - \psi_1 + \psi_3, \tag{18a}$$

$$\ell_2 \hat{} \ell_3 = \pi/3 + \psi_2 + \psi_3, \tag{18b}$$

$$\ell_1 \hat{} \ell_2 = \pi/3 - \psi_1 - \psi_2, \tag{18c}$$

where

$$\psi_1 = \tan^{-1} \left(\frac{\delta \sin \phi}{1 - \delta \cos \phi}\right), \tag{18d}$$

$$\psi_2 = \tan^{-1} \left(\frac{1 + 2 \delta \cos \phi}{\sqrt{3} - 2 \delta \sin \phi}\right) - \pi/6, \tag{18e}$$

$$\psi_3 = \tan^{-1} \left(\frac{1 + 2 \delta \cos \phi}{\sqrt{3} + 2 \delta \sin \phi}\right) - \pi/6. \tag{18f}$$

Applying Eq.(17) and Eq.(18) to Eq.(14), we have symbolically the area of the n-th subaperture, A_n, where n = 1 to 6, as in the following:

If $\psi > \phi$, we have

$$A_1 = A_4 = A\ (L_1, L_3, \ell_1 \hat{} \ell_3), \tag{19a}$$

$$A_3 = A_6 = A\ (L_2, L_3, \ell_2 \hat{} \ell_3) - A_1, \tag{19b}$$

$$A_2 = A_5 = A_h - A\ (L_2, L_3, \ell_2 \hat{} \ell_3), \tag{19c}$$

and if $\psi < \phi$, we have

$$A_1 = A_4 = A\ (L_1, L_3, \ell_1 \hat{} \ell_3), \tag{19d}$$

$$A_2 = A_5 = A\ (L_1, L_2, \ell_1 \hat{} \ell_2) - A_1, \tag{19e}$$

$$A_3 = A_6 = A_h - A\ (L_1, L_2, \ell_1 \hat{} \ell_2). \tag{19f}$$

The formulae above were derived with an implicit assumption that ϕ is less than 60°. However, there is no need to modify the formulae for $\phi > 60°$ but only to relabel the indices. It can be shown that

$$A_n\ (\phi = 60° + \beta) = A_{n+3}\ (\phi = 60° + \beta) = A_{6-n}\ (\phi = 60° - \beta) \tag{20}$$

for n = 1, 2 and 3.

V. EFFECTS OF RECESSED MOUNTING.

The purpose of recessed mounting of a retroreflector is to protect the retroreflector partially from the sunlight in the lunar environment and to reduce the thermal gradients in the retroreflectors.

The recessed mounting of a retroreflector also reduces the effective aperture for off-axis incidence of light, because the effective aperture is now determined by the opening of the cavity and its image. Modifications are necessary in the formulation of the area of subapertures. The new parameter is the distance between the center of the opening of the cavity and its displaced image when viewed along the direction of light as shown in Figure 10. If we denote the displacement by t, then

$$t = d + D' \tan \theta \tag{21}$$

where D' is twice the depth of the depression. The half area for effective aperture in Eq.(15) is modified to be

$$A_h = \frac{1}{\pi} [\cos^{-1} (2\tau) - 2\tau \sqrt{1 - 4\tau^2}] \tag{22}$$

where $\tau \equiv t/D$.

The geometrical configuration of subaperture for the case of the recessed mounting is shown in Figure 11. A new set of angles, ψ_1', ψ_2' and ψ_3' are also created.

The equations derived in the previous section are still valid except Eq.(17) which is modified to be

$$L_1 = 2\sqrt{1 + \varepsilon^2 + 2\varepsilon \cos \phi} \sin (\psi_1 + \psi_1') \tag{23a}$$

$$L_2 = 2\sqrt{1 + \varepsilon^2 - 2\varepsilon \cos (\pi/3 + \phi)} \sin (\psi_2 + \psi_2') \tag{23b}$$

$$L_3 = 2\sqrt{1 + \varepsilon^2 - 2\varepsilon \cos (\pi/3 - \phi)} \sin (\psi_3 + \psi_3') \tag{23c}$$

where

$$\psi_1' = \cos^{-1}\left[\frac{1 + \varepsilon \cos\phi}{\sqrt{1 + \varepsilon^2 + 2\varepsilon \cos\phi}}\right],$$

$$\psi_2' = \cos^{-1}\left[\frac{1 - \varepsilon \cos(\pi/3 + \phi)}{\sqrt{1 + \varepsilon^2 - 2\varepsilon \cos(\pi/3 + \phi)}}\right],$$

$$\psi_3' = \cos^{-1}\left[\frac{1 - \varepsilon \cos(\pi/3 - \phi)}{\sqrt{1 + \varepsilon^2 - 2\varepsilon \cos(\pi/3 - \phi)}}\right],$$

and $\varepsilon = D' \tan\theta/D$.

Notice that when the depth of the depression becomes zero, Eq.(23) reduces to Eq.(17) as expected.

VI. COMPUTER PROGRAMS.

There are three programs and two plot routines written in Fortran IV. The first one, called COR15D, is the program designed to yield the complex amplitudes of the six subapertures for all ϕ and θ. The second one, called AREANA, has two tasks. The first task is to evaluate the areas of the subapertures. The second task is to yield the central irradiance of the diffraction pattern by summing over the products of the areas of the subapertures with the corresponding complex amplitudes. It also takes care of the cosθ effect. The third program, called AREANB, evaluates the area of subapertures for the case of recessed mounting.

The first plot routine, called PLOTND, plots the central irradiance versus ϕ with θ as a parameter, whereas the other one, called LR3INT, plots the central irradiance versus θ with ϕ as a parameter. All programs are presented in the Appendix.

VII. RESULTS.

The results are shown in Figure 12 to Figure 19. We assumed an index of refraction of 1.4554 which is the index of fused silica at 6943Å. Various polarizations are assumed for the incident light.

The results for a depth of depression of 0.5, which is measured by taking the ratio of the depth to the diameter, are presented along with those of the non-recessed mounting. Depths of depression of 0.3 and 0.4 are also considered for $\phi = 0°$ and $60°$; these results are compared with others.

As an extra comparison, the results from a retroreflector with a full triangular face are also presented for $\phi = 0°$ and $60°$ in Figure 20.

VIII. CONCLUSION AND DISCUSSION.

We have developed a computer program that is capable of calculating the central irradiance of the diffraction pattern of retroreflectors for all ϕ and θ. This program can be expanded to evaluate the detailed diffraction pattern instead of only the central irradiance.

The detailed diffraction pattern can be evaluated either numerically (fast Fourier transform) or analytically. The task is a large project in itself. We do not plan to undertake the task until a specific need arises.

REFERENCES

1. C. O. Alley, P. L. Bender, R. F. Chang, D. G. Currie, R. H. Dicke, J. E. Faller, W. M. Kaula, G. J. F. MacDonald, J. D. Mulholland, H. H. Plotkin, S. K. Poultney, D. T. Wilkinson, I. Winer, W. Carrion, T. Johnson, P. Spadin, L. Robinson, E. J. Wampler, D. Wieber, E. C. Silverberg, C. A. Steggerda, J. V. Mullendore, J. D. Rayner, W. Williams, B. Warner, H. Richardson, and B. W. Bopp, "Laser Ranging Retro-Reflector", Apollo 11 Preliminary Science Report (NASA Special Publication SP-214, 1969).
2. C. O. Alley, R. F. Chang, D. G. Currie, J. V. Mullendore, S. K. Poultney, J. D. Rayner, E. C. Silverberg, C. A. Steggerda, H. H. Plotkin, W. Williams, B. Warner, H. Richardson, B. W. Bopp, Science 167, 368 (1970); also J. E. Faller, I. Winer, W. Carrion, Thomas S. Johnson, Paul Spadin, Lloyd Robinson, E. J. Wampler, and Donald Wieber, Science 166, 99 (1969).
3. C. O. Alley, R. F. Chang, D. G. Currie, S. K. Poultney, P. L. Bender, R. H. Dicke, D. T. Wilkinson, J. E. Faller, W. M. Kaula, G. J. F. MacDonald, J. D. Mulholland, H. H. Plotkin, W. Carrion, and E. J. Wampler, Science 167, 458 (1970).
4. C. O. Alley, R. F. Chang, D. G. Currie, and M. E. Pittman, to be published in J. Opt. Soc. Am. April (1971); University of Maryland, Department of Physics and Astronomy, Technical Report 70-104 (1970).
5. M. Born and E. Wolf, Principles of Optics, 2nd revised edition (MacMillan Co., New York, 1964), pp. 40, 48.

FIGURE CAPTIONS

Figure

1. Representative views of a retroreflector.
2. Illustration of the angle of incidence θ and the azimuth angle ϕ.
3. The effective aperture and the subapertures of a retroreflector for normal incidence of light.
4. Unit vectors involved in the reflection of a ray by a plane.
5. Three-dimensional illustration of ray-trace in a retroreflector.
6. The effective aperture and the subapertures of a retroreflector for off-axis incidence of light.
7. A subaperture in its basic form.
8. A typical geometrical configuration of subapertures for $\psi > \phi$.
9. A typical geometrical configuration of subapertures for $\psi < \phi$.
10. The effect of the recessed mounting of a retroreflector on the effective aperture.
11. A typical geometrical configuration of subapertures of a retroreflector mounted in a cavity.
12. Normalized central irradiance plotted versus azimuth angle for various angles of incidence of light which is linearly polarized in p- direction.
13. The same as Figure 12 except the polarization of light is in s-direction.
14. The same as Figure 12 except the polarization of light is circular.
15. The same as Figure 12 except the retroreflector is mounted in a cavity. The depth of the depression is one-half of the diameter of the front face.
16. The same as Figure 15 except the polarization of light is in s-direction.
17. The same as Figure 15 except the polarization of light is circular.
18. Normalized central irradiance is plotted versus θ for $\phi = 0°$. The depth of the depression is expressed in the unit of the diameter of the front fact.

Figure

19. The same as Figure 18 except $\phi = 60°$.

20. Normalized central irradiance from a retroreflector with full triangular face is plotted versus θ for $\phi = 0°$ and $60°$. The internal total reflection fails at $\theta = 16.6°$ for $\phi = 0°$.

APPENDIX

```
$EXECUTE        IBJOB
$ID   CHANG*205/05/157*3M*099P*6000C*BS                                    21
$IBJOB          GO,MAP
$IBFTC COR15D  LIST,NODECK
       COMMON XN(3),XKK(3),PP(3),SS(3)
       COMMON BBP,BBS
       COMPLEX BBP,BBS,CP,CS,AP,AS,BP,BS
       REAL JPHI
       DIMENSION XK(3),P(3),S(3)
    11 FORMAT(10H1AZIMUTH =,F6.1,2X,7HDEGREES)
    13 FORMAT (1H ,I2,5X,2E14.5,5X,2E14.5)
    14 FORMAT(F5.1,F3.0,I1,4E17.9)
    15 FORMAT(1H ,1X,1HI,20X,2HCP,31X,2HCS)
    21 FORMAT(8H0THETA =,F7.2,7HDEGREES)
       YIN=1.4554
       SQ2=SQRT(2.)
       SQ3=SQRT(3.)
       PI=3.141593
       THIRTY=PI/6.
       RAC=PI/180.
       DO 40 IS=1,2
       AP=(1.,0.)
       AS=(0.,1.)
       PIS=IS-1
       SIS=2-IS
       AP=AP*PIS
       AS=AS*SIS
       DO 10 IPHI=1,17
       JPHI=(IPHI-1)*75
       JPHI=JPHI/10.
       PHI=JPHI
       PHI=PHI*RAC
       WRITE(6,11) JPHI
       COP=COS(PHI)
       SIP=SIN(PHI)
       PTD=PHI-THIRTY
       PTS=PHI+THIRTY
       COSD=COS(PTD)
       SIND=SIN(PTD)
       COSS=COS(PTS)
       SINS=SIN(PTS)
       DO 20 MAN=1,41,2
       DAN=MAN-1
       RAN=DAN*RAC
       WRITE(6,21) DAN
       WRITE (6,15)
       COEX=COS(RAN)
       SIEX=SIN(RAN)
       SIIN=SIEX/YIN
       COIN=SQRT(1.-SIIN*SIIN)
       FITO =YIN*COIN/COEX
       IF(MAN-1) 30,31,30
    30 TINP=2.*COEX/(YIN*COEX+COIN)
       TOUP=TINP*FITO
       TINS=2.*COEX/(COEX+YIN*COIN)
       TOUS=TINS*FITO
       GO TO 35
    31 TINP=2./(1.+YIN)
       TINS=TINP
       TOUP=TINP*YIN
```

```
 35 CONTINUE
    CODR3=COTN/SQ3
    SIDR3=SITN/SQ3
    ROTOT=SQ2/SQ3
    XK(1)=-(CODR3+SIDR3*COP*SQ2)
    XK(2)=-(CODR3+SIDR3*SIND*SQ2)
    XK(3)=-(CODR3-SIDR3*SINS*SQ2)
    P(1)=SIDR3-SQ2*CODR3*COP
    P(2)=SIDR3-SQ2*CODR3*SIND
    P(3)=SIDR3+SQ2*CODR3*SINS
    S(1)=-ROTOT*SIP
    S(2)=ROTOT*COSD
    S(3)=-ROTOT*COSS
    BP=AP*TINP
    BS=AS*TINS
    IG=0
200 DO 210 L=1,3
    XKK(L)=XK(L)
    PP(L)=P(L)
    SS(L)=S(L)
210 CONTINUE
    BBP=BP
    BBS=BS
    IG=IG+1
    GO TO (250,300,350,400,450,500,550),IG
250 CONTINUE
    XN(1)=1.
    XN(2)=0.
    XN(3)=0.
    CALL RFF
    XN(2)=1.
    CALL RFF
    XN(3)=1.
    CALL RFF
    GO TO 700
300 CONTINUE
    XN(2)=1.
    CALL RFF
    XN(1)=1.
    CALL RFF
    XN(3)=1.
    CALL RFF
    GO TO 700
350 CONTINUE
    XN(2)=1.
    CALL RFF
    XN(3)=1.
    CALL RFF
    XN(1)=1.
    CALL RFF
    GO TO 700
400 CONTINUE
    XN(3)=1.
    CALL RFF
    XN(2)=1.
    CALL RFF
    XN(1)=1.
    CALL RFF
    GO TO 700
450 CONTINUE
    XN(3)=1.
```

```
      CALL REF
      XN(1)=1.
      CALL REF
      XN(2)=1.
      CALL REF
      GO TO 700
  500 CONTINUE
      XN(1)=1.
      CALL REF
      XN(3)=1.
      CALL REF
      XN(2)=1.
      CALL REF
      GO TO 700
  700 CONTINUE
      QC=PP(1)*P(1)+PP(2)*P(2)+PP(3)*P(3)
      QS=SS(1)*P(1)+SS(2)*P(2)+SS(3)*P(3)
      CP=(BBP*QC+BBS*QS)*TOUP
      CS=(BBS*QC-BBP*QS)*TOUS
      WRITE(6,13) IG,CP,CS
      WRITE (7,14) JPHI,DAN,IG,CP,CS
      GO TO 200
  550 CONTINUE
   20 CONTINUE
   10 CONTINUE
   40 CONTINUE
      STOP
      END
$IBFTC REFLE   NODECK
      SUBROUTINE REF
      COMMON XN(3),XKK(3),PP(3),SS(3)
      COMMON BBP,BBS
      COMPLEX BBP,BBS,CP,CS,DEP,NOP,DFS,NOS
      DIMENSION PN(3),SN(3)
      YIN=1.4554
      ZIN=1./YIN
      ZIN2=ZIN*ZIN
      COAL=0.
      DO 600 L=1,3
      COAL=COAL+XN(L)*XKK(L)
  600 CONTINUE
      COAL=-COAL
      SIAL=SQRT(1.-COAL*COAL)
      DO 601 L=1,3
      PN(L)=(COAL*XKK(L)+XN(L))/SIAL
  601 CONTINUE
      SN(1)=(XKK(2)*XN(3)-XKK(3)*XN(2))/SIAL
      SN(2)=(XKK(3)*XN(1)-XKK(1)*XN(3))/SIAL
      SN(3)=(XKK(1)*XN(2)-XKK(2)*XN(1))/SIAL
      QC=PN(1)*PP(1)+PN(2)*PP(2)+PN(3)*PP(3)
      QS=PN(1)*SS(1)+PN(2)*SS(2)+PN(3)*SS(3)
      CP=BBP*QC+BBS*QS
      CS=BBS*QC-BBP*QS
      IF(SIAL-ZIN) 602,602,607
  602 CONTINUE
      ALPHA=ARCOS(COAL)
      BATA=ARSIN(SIAL*YIN)
      STH=ALPHA+BATA
      DTH=ALPHA-BATA
      RP=TAN(DTH)/TAN(STH)
```

```
      BBP=RP*CP
      BBS=RS*CS
      GO TO 603
  607 COM=SQRT(SIAL*SIAL-ZIN2)
      ZINC=ZIN2*COAL
      DEP=CMPLX(ZINC,COM)
      DES=CMPLX(COAL,COM)
      NOS=CONJG(DES)
      NOP=CONJG(DEP)
      BBP=CP*NOP/DEP
      BBS=CS*NOS/DES
  603 CONTINUE
      DO 609 L=1,3
      N=XN(L)
      IF (N-0) 610,610,611
  611 XKK(L)=-XKK(L)
  610 SS(L)=SN(L)
      PP(L)=(XN(L)-COAL*XKK(L))/SIAL
      XN(L)=0.
  609 CONTINUE
      RETURN
      END
```

```
$EXECUTE        IBJOB
$ID   CHANG*205/05/157*3M*500P*999C*B$
$IBJOB          GO,MAP
$IBFTC ARFANA  LIST,NODECK
      COMPLEX CP(6),CS(6),AP,AS
      REAL JPHI
      DIMENSION AR(6)
   12 FORMAT(10H1AZIMUTH =,F6.1,2X,7HDEGREES)
   13 FORMAT(1H ,F4.1,2E20.9,4E14.5,3F10.5)
   14 FORMAT(F5.1,F3.0,I1,4E17.9)
   15 FORMAT(4F20.9)
   16 FORMAT(1H ,36HDAN,TENN,TEN,AP,AS,AR(1),AR(2),AR(3))
   17 FORMAT(1H ,45X,F5.1,F4.0,I2,4E17.9)
      YINS=1.4554**2
      SQ2=SQRT(2.)
      SQ3=SQRT(3.)
      PI=3.141593
      RAC=PI/180.
      THIRTY=PI/6.
      SIXTY=PI/3.
  -10 DO 20 L=1,6
      READ(5,14) JPHI,DAN,IG,CP(L),CS(L)
   20 CONTINUE
      IF(61.-JPHI) 30,31,31
   30 PHI=120.-JPHI
      GO TO 32
   31 PHI=JPHI
   32 CONTINUE
      RAN=DAN*RAC
      PHI=PHI*RAC
      SINAN=SIN(RAN)
      COSAN=COS(RAN)
      D=SINAN/(SQ2*SQRT(YINS-SINAN**2))
      DD=2.*D
      AHALF=(ARCOS(DD)-DD*SQRT(1.-DD*DD))/PI
      DCOP=COS(PHI)*D
      DSIP=SIN(PHI)*D
      A=.5+DCOP
      B=SQ3*.5-DSIP
      C=B+2.*DSIP
      AOB=A/B
      AOC=A/C
      UNIQ=DSIP/(1.-DCOP)
      PSI=ATAN(AOB)
      PSI1=ATAN(UNIQ)
      PSI2=PSI-THIRTY
      PSI3=ATAN(AOC)-THIRTY
      EL1=2.*SIN(PSI1)
      EL2=2.*SIN(PSI2)
      EL3=2.*SIN(PSI3)
      ANG1=SIXTY+PSI1-PSI3
      ANG23=PI-ANG1
      AR(1)=AREA(EL1,EL3,ANG23)
      IF(PSI-PHI) 100,100,110
  110 ANG2=SIXTY+PSI2+PSI3
      AREA13=AREA(EL2,EL3,ANG2)
      AR(2)=AHALF-AREA13
      AR(3)=AREA13-AR(1)
      GO TO 120
  100 ANG3=SIXTY-PSI1-PSI2
      AREA12=AREA(EL1,EL2,ANG3)
```

```
      AR(2)=AREA12-AR(1)
      AR(3)=AHALF-AREA12
  120 CONTINUE
      IF(61.-JPHI) 40,41,41
   40 CONTINUE
      AR(5)=AR(1)
      AR(4)=AR(2)
      AR(6)=AR(3)
      AR(1)=AR(4)
      AR(2)=AR(5)
      GO TO 131
   41 CONTINUE
      DO 130 L=1,3
      M=3+L
      AR(M)=AR(L)
  130 CONTINUE
  131 CONTINUE
      AP=(0.,0.)
      AS=(0.,0.)
      DO 140 L=1,6
      AP=AP+CP(L)*AR(L)*COSAN
      AS=AS+CS(L)*AR(L)*COSAN
  140 CONTINUE
      TEN=CABS(AP)**2+CABS(AS)**2
      IF(DAN-0.5) 160,150,150
  160 CEN=TEN
      WRITE (6,12) JPHI
      WRITE(6,16)
  150 TENN=TEN/CEN
      WRITE(6,13) DAN,TENN,TEN,AP,AS,AR(1),AR(2),AR(3)
      WRITE(7,15) JPHI,DAN,TENN,TEN
      GO TO 10
      STOP
      END
$IBFTC SUBA     NODECK
      FUNCTION AREA(X,Y,ANG)
      PI=3.141593
      CAN=COS(ANG)
      SAN=SIN(ANG)
      C=SQRT(1.-X*X)-(Y-X*CAN)/SAN
      D=SQRT(1.-Y*Y)-(X-Y*CAN)/SAN
      E=SQRT(C*C+D*D+2.*D*C*CAN)/2.
      AREA=(C*D*SAN/2.+ARSIN(E)-E*SQRT(1.-E*E))/PI
      RETURN
      END
```

```
$EXECUTF        IBJOB
$ID   CHANG*205/05/157*3M*500P*999C*B$
$IBJOB          GO,MAP
$IBFTC AREANB  LIST,NODECK
      COMPLEX CP(6),CS(6),AP,AS
      REAL JPHI
      DIMENSION AR(6)
   12 FORMAT(10H1AZIMUTH =,F6.1,2X,7HDEGREES)
   13 FORMAT(1H ,F4.1,2E20.9,4E14.5,3F10.5)
   14 FORMAT(F5.1,F3.0,I1,4E17.9)
   15 FORMAT(4F20.9)
   16 FORMAT(1H ,36HDAN,TENN,TEN,AP,AS,AR(1),AR(2),AR(3))
   17 FORMAT(1H ,45X,F5.1,F4.0,I2,4F17.9)
      YINS=1.4554**2
      SQ2=SQRT(2.)
      SQ3=SQRT(3.)
      PI=3.141593
      RAC=PI/180.
      THIRTY=PI/6.
      SIXTY=PI/3.
   10 DO 20 L=1,6
      READ(5,14) JPHI,DAN,TG,CP(L),CS(L)
   20 CONTINUE
      IF(61.-JPHI) 30,31,31
   30 PHI=120.-JPHI
      GO TO 32
   31 PHI=JPHI
   32 CONTINUE
      RAN=DAN*RAC
      PHI=PHI*RAC
      SINAN=SIN(RAN)
      COSAN=COS(RAN)
      D=SINAN/(SQ2*SQRT(YINS-SINAN**2))
      EP=TAN(RAN)/2.
      DD=2.*(D+EP)
      IF(DD-1.) 5,5,10
    5 CONTINUE
      AHALF=(ARCOS(DD)-DD*SQRT(1.-DD*DD))/PI
      DCOP=COS(PHI)*D
      DSIP=SIN(PHI)*D
      A=.5+DCOP
      B=SQ3*.5-DSIP
      C=B+2.*DSIP
      AOB=A/B
      AOC=A/C
      UNIQ=DSIP/(1.-DCOP)
      PSI=ATAN(AOB)
      PSI1=ATAN(UNIQ)
      PSI2=PSI-THIRTY
      PSI3=ATAN(AOC)-THIRTY
      C1=SQRT(1.+EP*EP+2.*EP*COS(PHI))
      SPS=SIXTY+PHI
      C2=SQRT(1.+EP*EP-2.*EP*COS(SPS))
      SPD=SIXTY-PHI
      C3=SQRT(1.+EP*EP-2.*EP*COS(SPD))
      PPI1=(1.+EP*COS(PHI))/C1
      PPI1=ARCOS(PPI1)
      PPI2=(1.-EP*COS(SPS))/C2
      PPI2=ARCOS(PPI2)
      PPI3=(1.-EP*COS(SPD))/C3
      PPI3=ARCOS(PPI3)
```

```
      EL1=2.*C1*SIN(PSI1+PDI1)
      EL2=2.*C2*SIN(PSI2+PDI2)
      EL3=2.*C3*SIN(PSI3+PDI3)
      ANG1=SIXTY+PSI1-PSI3
      ANG23=PI-ANG1
      AR(1)=AREA(EL1,EL3,ANG23)
      IF(PSI-PHI) 100,100,110
  110 ANG2=SIXTY+PSI2+PSI3
      AREA13=AREA(EL2,EL3,ANG2)
      AR(2)=AHALF-AREA13
      AR(3)=AREA13-AR(1)
      GO TO 120
  100 ANG3=SIXTY-PSI1-PSI2
      AREA12=AREA(EL1,EL2,ANG3)
      AR(2)=AREA12-AR(1)
      AR(3)=AHALF-AREA12
  120 CONTINUE
      IF(61.-JPHI) 40,41,41
   40 CONTINUE
      AR(5)=AR(1)
      AR(4)=AR(2)
      AR(6)=AR(3)
      AR(1)=AR(4)
      AR(2)=AR(5)
      GO TO 131
   41 CONTINUE
      DO 130 L=1,3
      M=3+L
      AR(M)=AR(L)
  130 CONTINUE
  131 CONTINUE
      AP=(0.,0.)
      AS=(0.,0.)
      DO 140 L=1,6
      AP=AP+CP(L)*AR(L)*COSAN
      AS=AS+CS(L)*AR(L)*COSAN
  140 CONTINUE
      TEN=CABS(AP)**2+CABS(AS)**2
      IF(DAN-0.5) 160,150,150
  160 CEN=TEN
      WRITE (6,12) JPHI
      WRITE(6,16)
  150 TENN=TEN/CEN
      WRITE(6,13) DAN,TENN,TEN,AP,AS,AR(1),AR(2),AR(3)
      WRITE(7,15) JPHI,DAN,TENN,TEN
      GO TO 10
      STOP
      END
```

```
$EXECUTE        IBJOB
$ID   CHANG*2.5/05/157*3M*500P$
$* PLOT TAPE = B5
$* PLOT AFTER RUN
$* RELEASE AFTER PLOT
$PAUSE
$IBJOB          GO,MAP
$IBFTC PLOTND
      DIMENSION X(20),DAN(25),TENN(20,25),Y(20)
      DIMENSION D(1000)
   10 FORMAT(4E20.9)
      N=17
      M=10
      CALL PLOTS(D,1000)
      CALL PLOTC(0.,-11.,-3)
      CALL PLOTC(0.,.5,-3)
      X(N+1)=0.
      X(N+2)=20.
      Y(N+1)=0.
      Y(N+2)=0.1
      DO 104 K=1,2
      KK=28-7*K
      F=K-1
      F=F/2.
      DO 105 KP=1,2
      DO 100 I=1,N
      DO 101 J=1,KK
      READ (5,10) X(I),DAN(J),TENN(I,J),TEN
  101 CONTINUE
  100 CONTINUE
      DO 102 J=1,M
      THE=DAN(J)
      DO 103 I=1,N
      Y(I)=TENN(I,J)
  103 CONTINUE
      CALL LINE (X,Y,N,1,0,0)
      CALL WHERE(A,B)
      A=6.5
      CALL NUMBER(A,B,.1,THE,0.,1)
  102 CONTINUE
      CALL AXIS(0.,0.,22HAZIMUTH ANGLE(DEGREES),-22,6.,0.,X(N+1),X(N+2))
      CALL AXIS(0.,0.,9HINTENSITY,9,10.,90.,Y(N+1),Y(N+2))
      CALL AXIS(6.,0.,1H ,-1,10.,90.,Y(N+1),Y(N+2))
      GO TO (110,111),KP
  110 CALL SYMBOL(.5,9.5,.2,13HAP = 0,AS = 1,0.,13)
      GO TO 112
      CALL SYMBOL(.5,9.5,.2,13HAP = 1,AS = 1,0.,13)
  111 CALL SYMBOL(.5,9.5,.2,13HAP = 1,AS = 0,0.,13)
  112 CONTINUE
      CALL SYMBOL(3.5,9.5,.2,8HLOUVER =,0.,8)
      CALL WHERE(A,B)
      A=A+.3
      CALL NUMBER(A,9.5,.2,F,0.,1)
      CALL PLOTC(10.,0.,-3)
  105 CONTINUE
  104 CONTINUE
      CALL PLOTC(0,0,999)
      STOP
      END
```

```
$EXECUTE        IBJOB
$ID   CHANG*205/05/157*5M$
$* PLOT TAPE = 85
$* PLOT AFTER RUN
$* RELEASE AFTER PLOT
$PAUSE
$IBJOB          GO,MAP
$IBFTC LR3INT
      DIMENSION D(1000), X(100), Y(100)
   15 FORMAT(4F20.9)
      REAL JPHI
      L=17
C     L IS THE NO. OF JPHI.
      CALL PLOTS (D,1000)
      CALL PLOTC(0.,-11.,-3)
      CALL PLOTC(0.,2.,-3)
      DO 40 M=1,2
      N=21-7*(M-1)
      AM=M
      AM=(AM-1.)/2.
      XL=8.-4.*AM
      YL=XL+3.
      DO 20 J=1,2
C     J IS THE POLARIZATION INDEX. J=1 FOR (AP=0,AS=1),J=2 FOR (AP=1,AS=0)
      DO 30 II=1,L
      DO 10  I=1,N
      READ(5,15) JPHI,X(I),Y(I),TEN
   10 CONTINUE
      X(N+1)=0.
      X(N+2)=5.
      Y(N+1)=0.
      Y(N+2)=.2
      CALL AXIS (0.,0.,14HTHETA(DEGREES),-14,XL,0.,X(N+1),X(N+2))
      CALL AXIS (0.,0.,9HINTENSITY,9,5.,90.,Y(N+1),Y(N+2))
      CALL SYMBOL (1.5,7.,.25,20HPOLARIZATION AP/AS =,0.,20)
      CALL WHERE (A,B)
      A=A+.5
      IF(J.EQ.2) GO TO 50
      CALL SYMBOL (A,7.,.25,3H0/1,0.,3)
      GO TO 51
   50 CALL SYMBOL (A,7.,.25,3H1/0,0.,3)
   51 CONTINUE
      CALL SYMBOL (1.5,7.5,.25,9HAZIMUTH =,0.,9)
      CALL WHERE (A,B)
      A=A+0.3
      F=JPHI
      CALL NUMBER (A,7.5,.25,F,0.,1)
      CALL SYMBOL (1.5,6.5,.25,8HLOUVER =,0.,8)
      CALL WHERE (A,B)
      A=A+0.3
      CALL NUMBER (A,6.5,.25,AM,0.,1)
      CALL LINE (X,Y,N,1,0,0)
      CALL PLOTC(YL,0.,-3)
   30 CONTINUE
   20 CONTINUE
   40 CONTINUE
      CALL PLOTC(0,0,999)
      STOP
      END
```

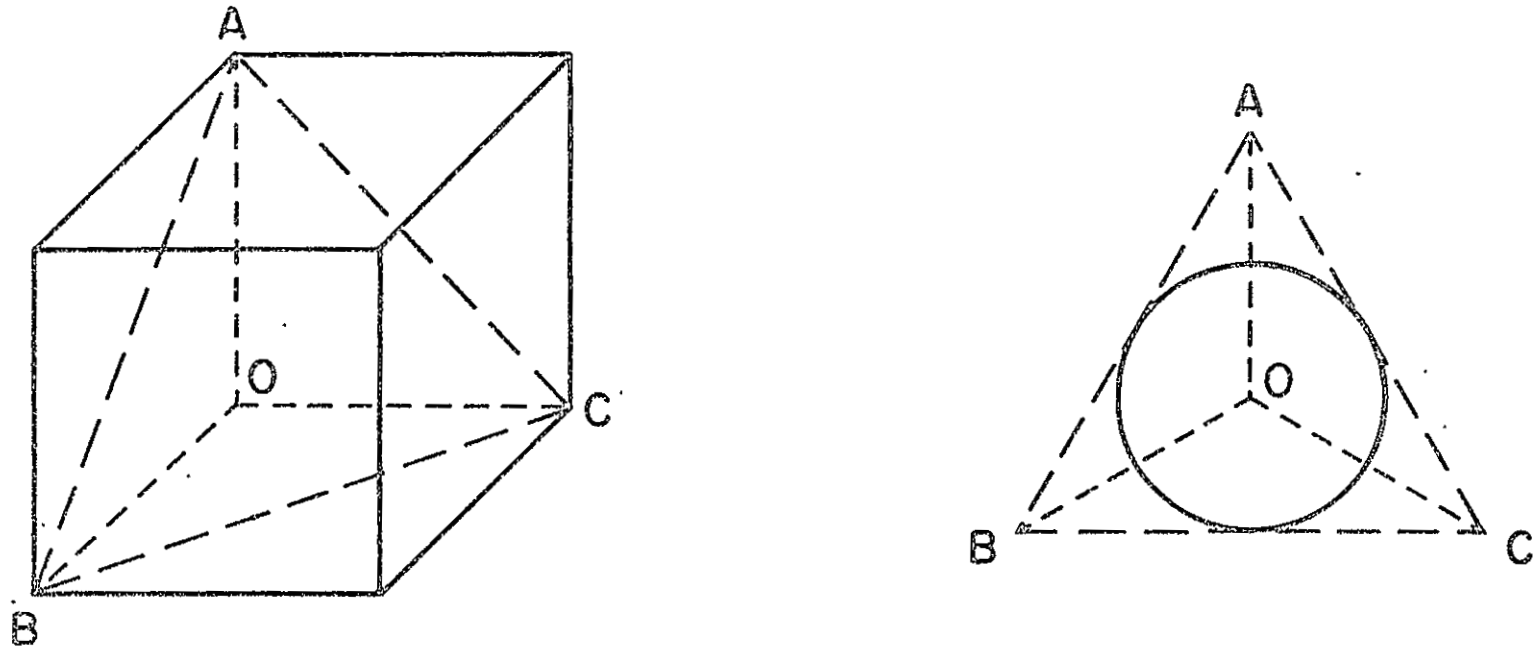

Fig. 1

Representative views of a retroreflector.

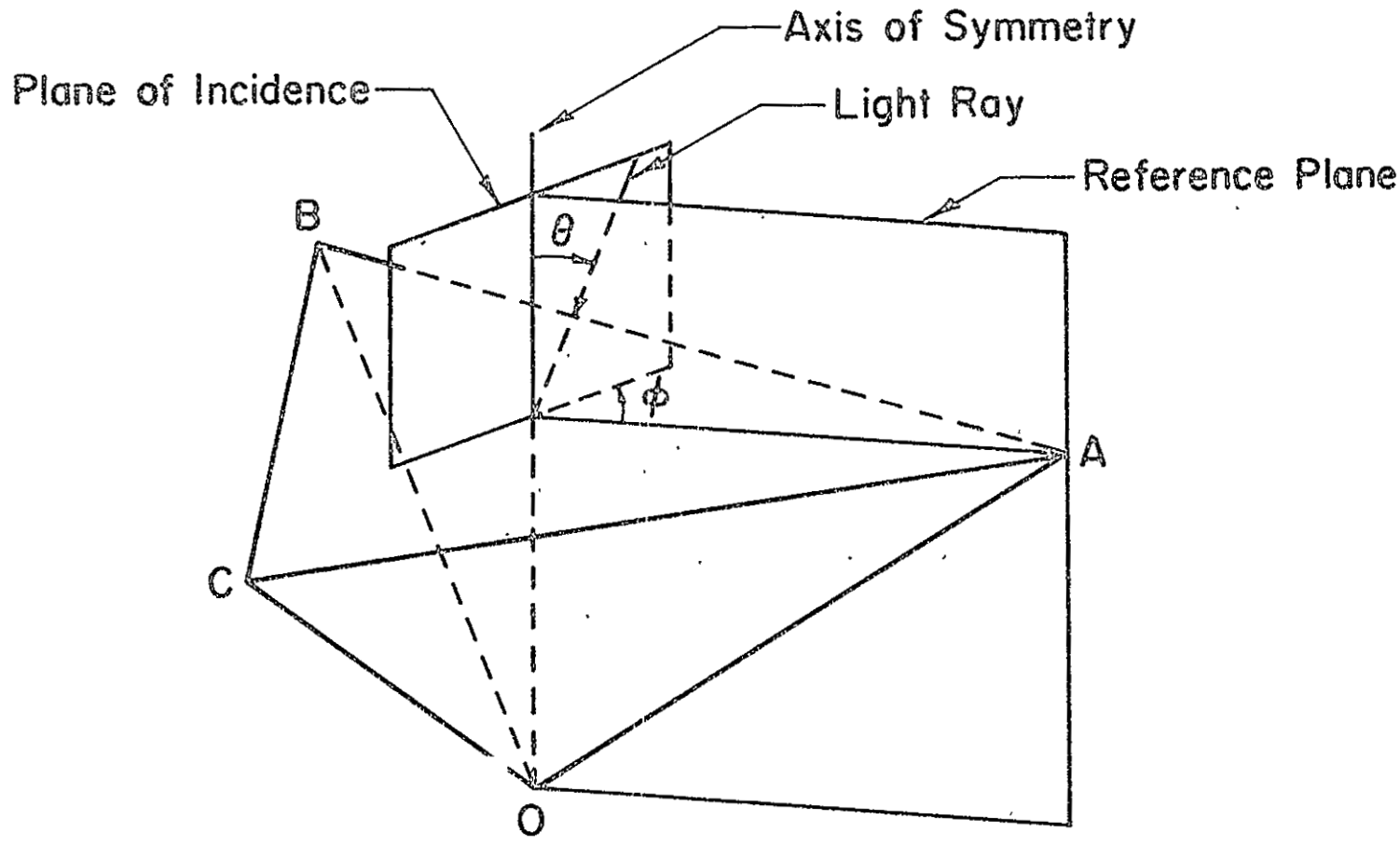

Fig. 2

Illustration of the angle of incidence θ and the azimuth angle ϕ.

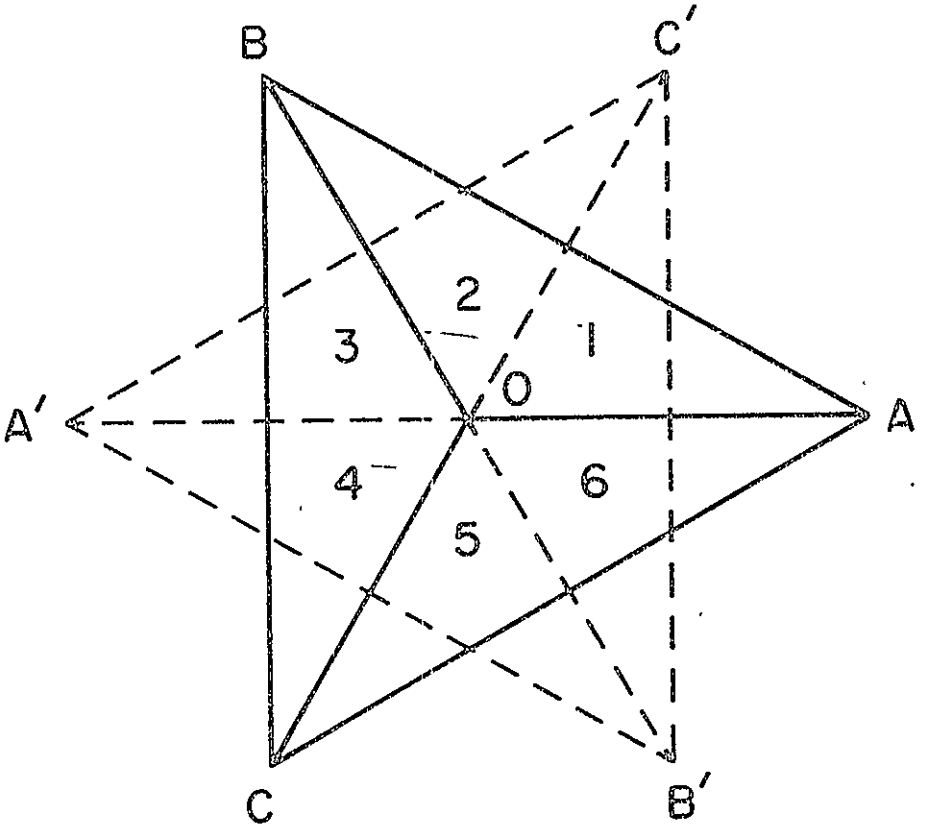

Fig. 3

The effective aperture and the subapertures of a retroreflector for normal incidence of light.

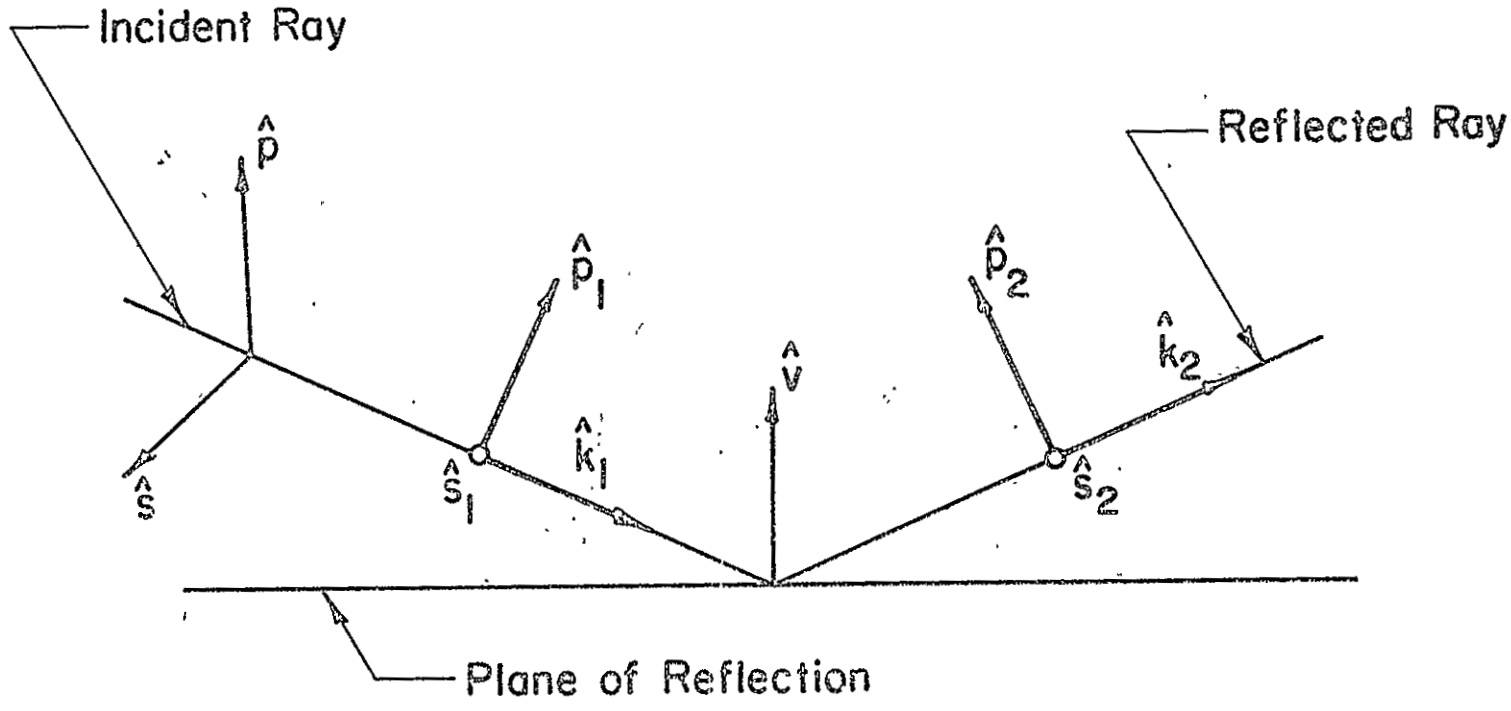

Fig. 4

Unit vectors involved in the reflection of a ray by a plane.

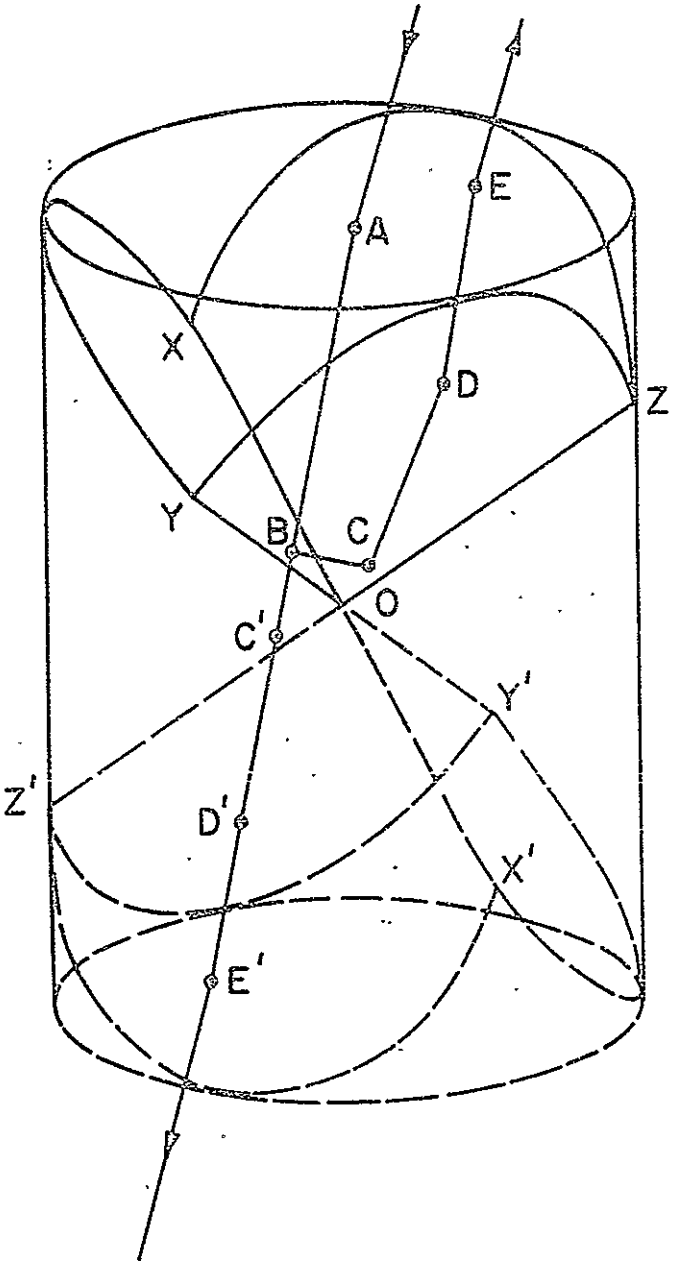

Fig. 5

Three-dimensional illustration of ray-trace in a retroreflector.

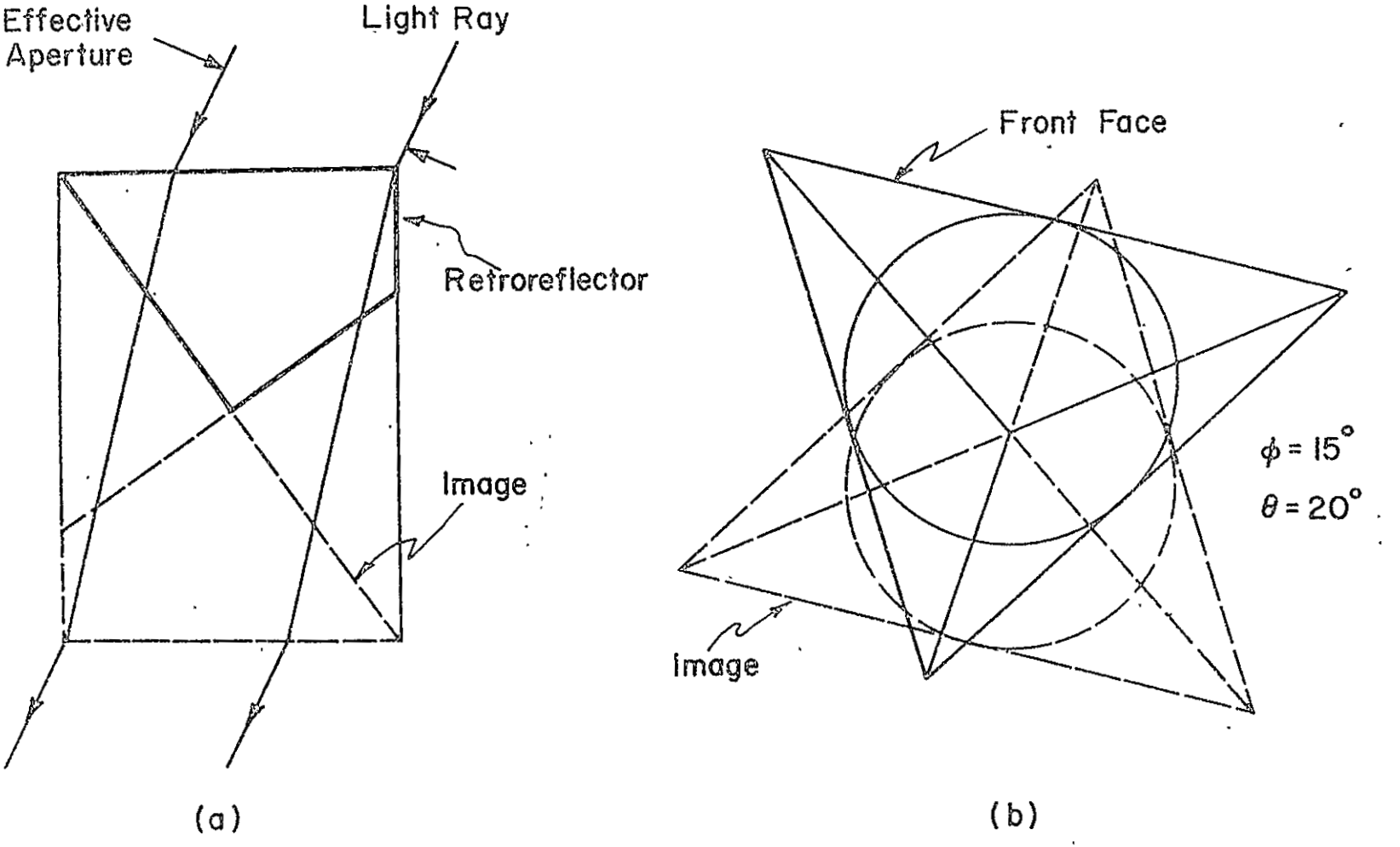

Fig. 6

The effective aperture and the subapertures of a retroreflector for off-axis incidence of light.

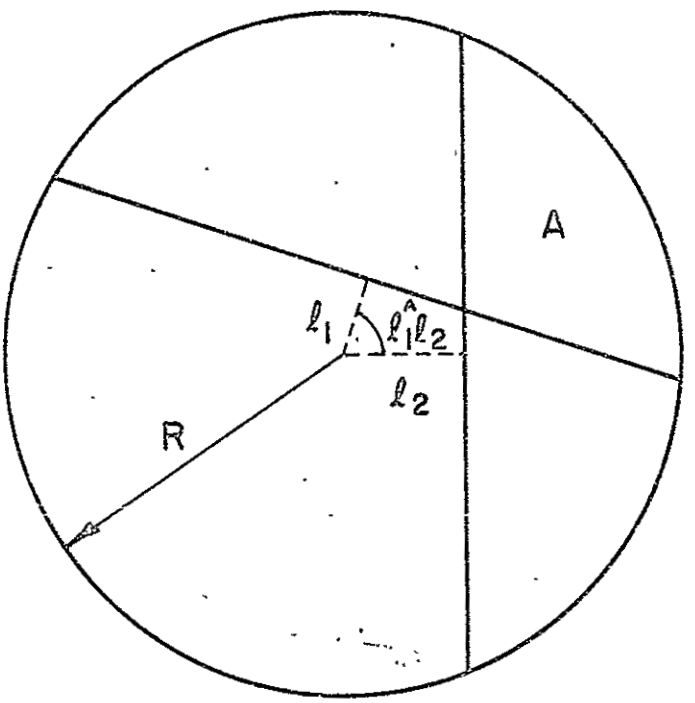

Fig. 7

A subaperture in its basic form.

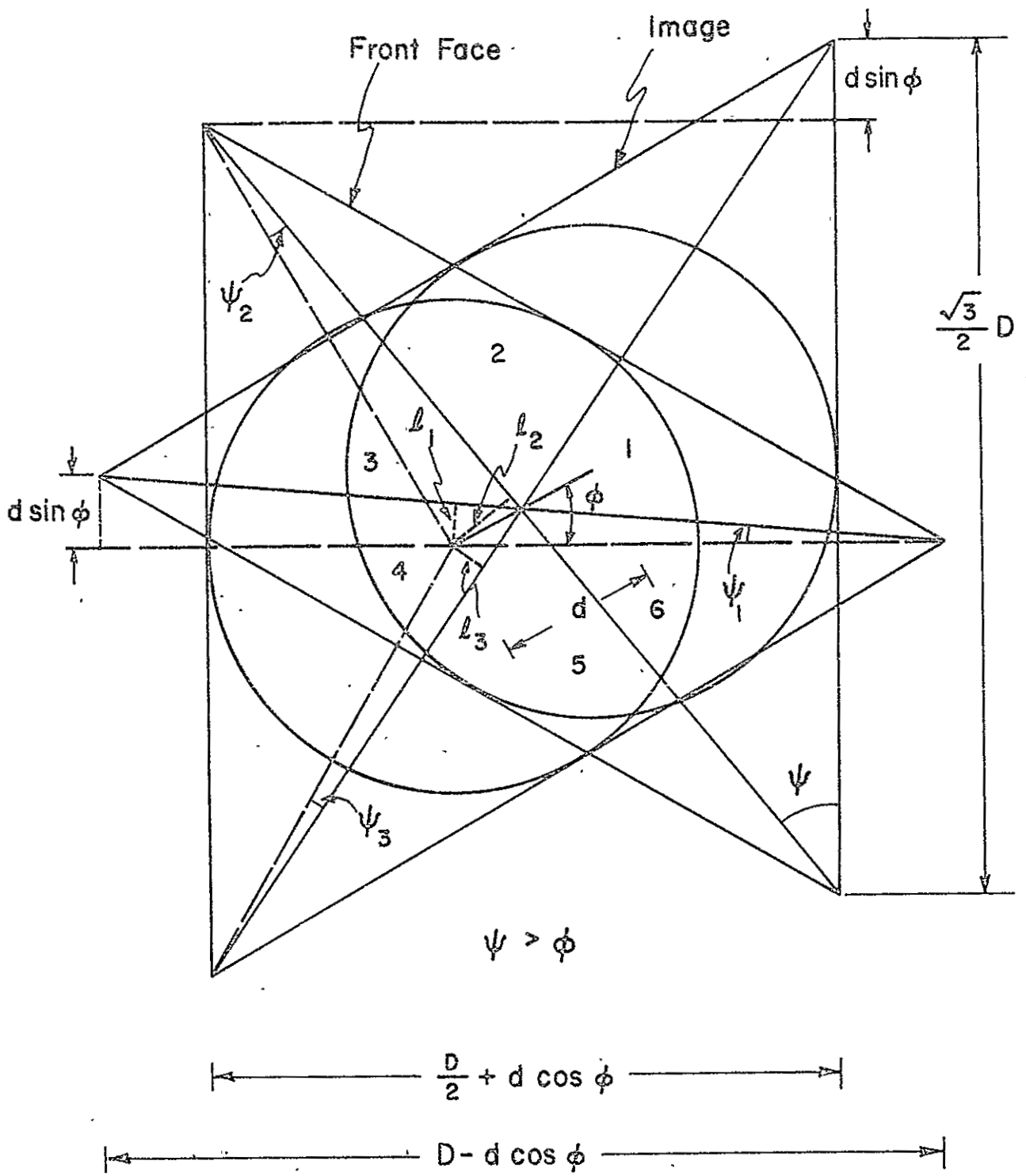

Fig. 8

A typical geometrical configuration of subapertures for $\psi > \phi$.

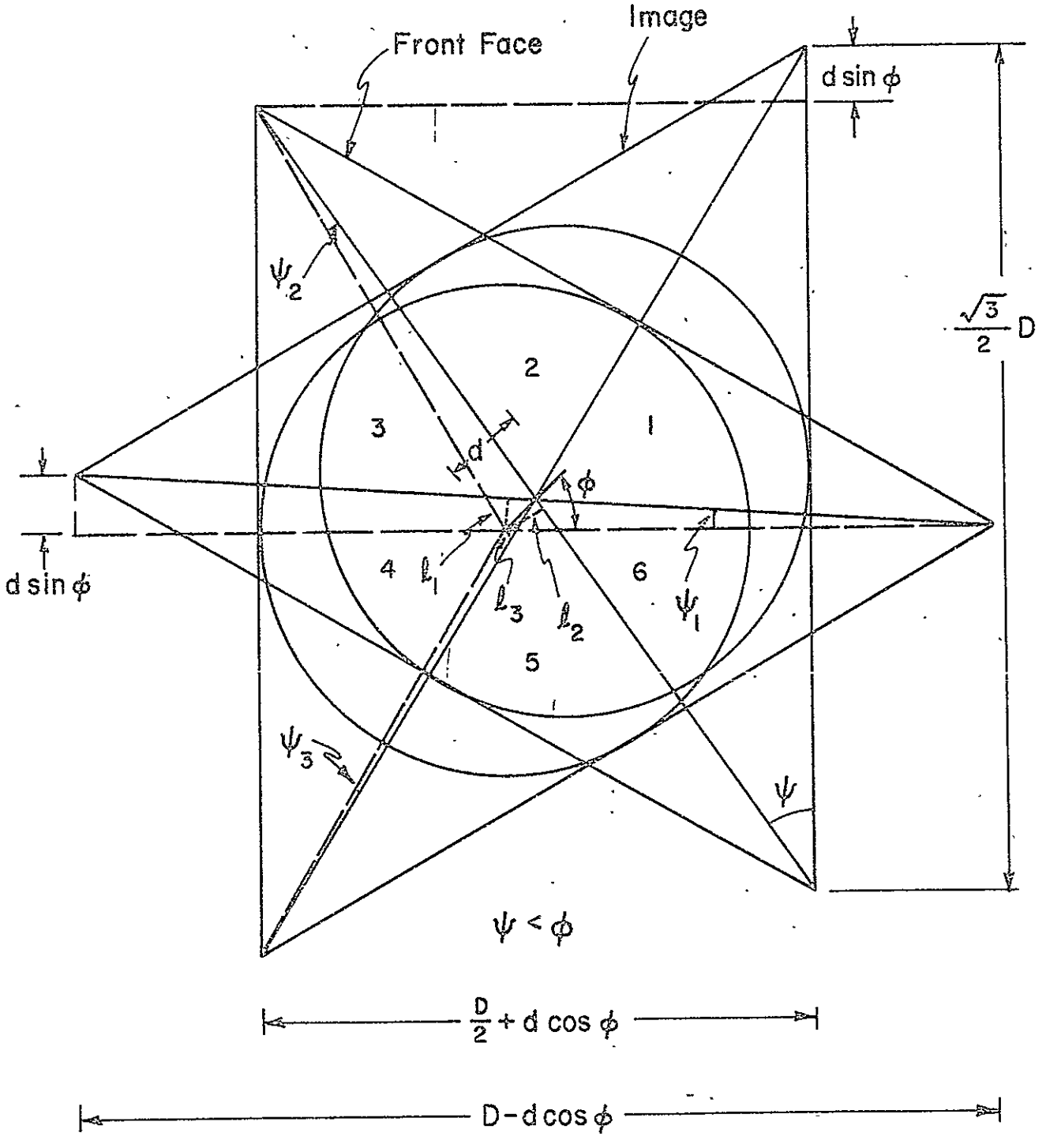

Fig. 9

A typical geometrical configuration of subapertures for $\psi<\phi$.

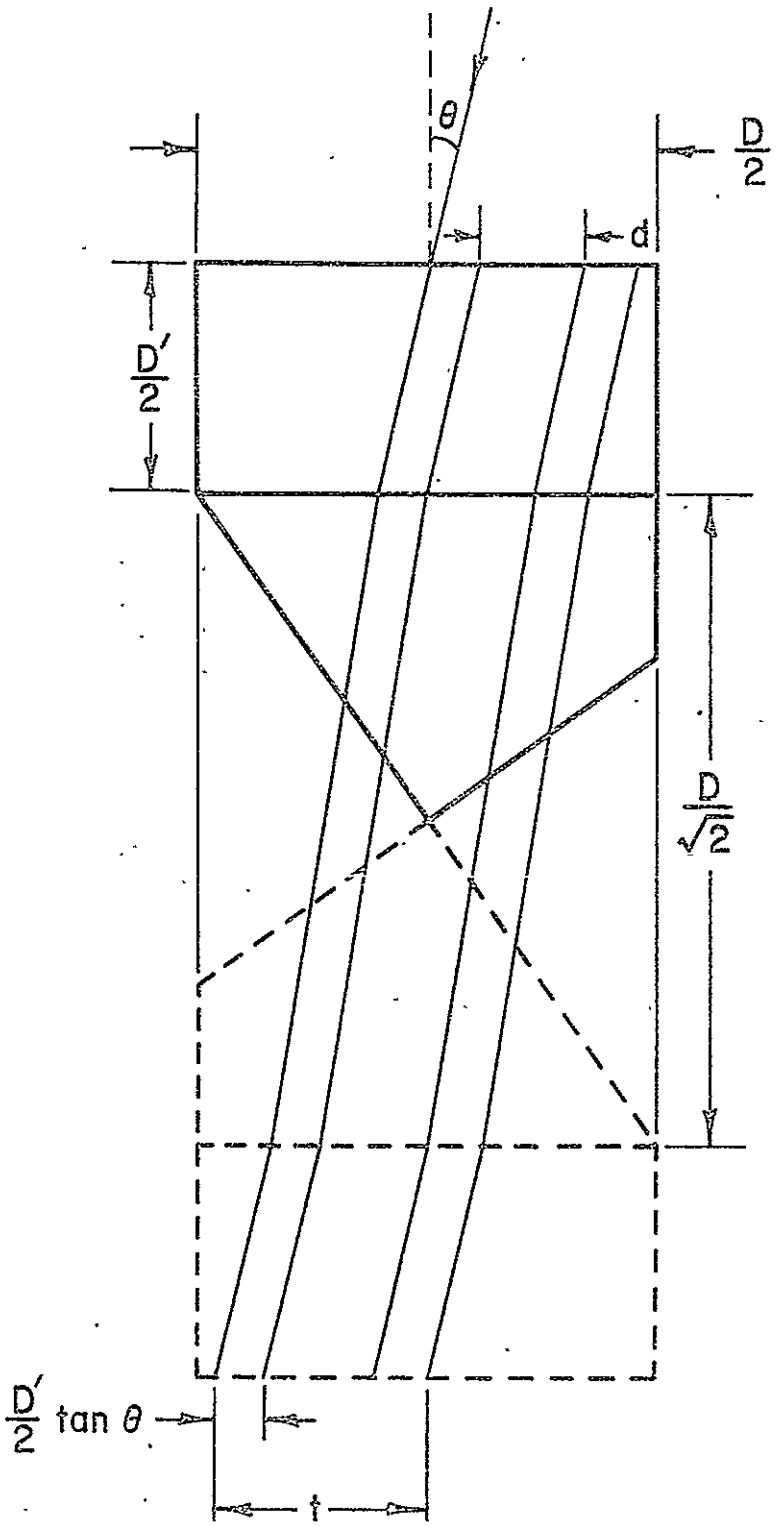

Fig. 10

The effect of the recessed mounting of a retroreflector on the effective aperture.

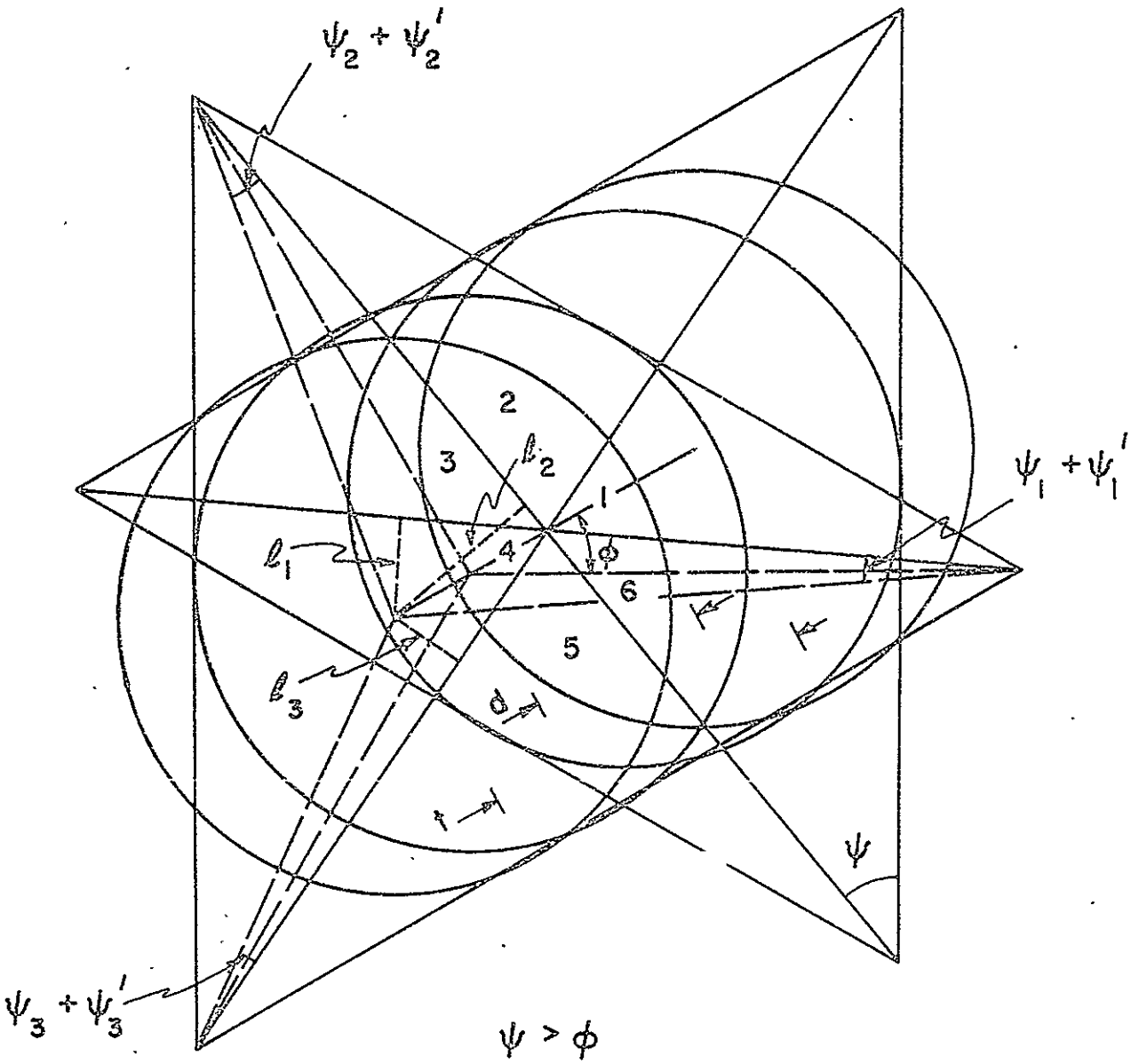

Fig. 11

A typical geometrical configuration of subapertures of a retroreflector mounted in a cavity.

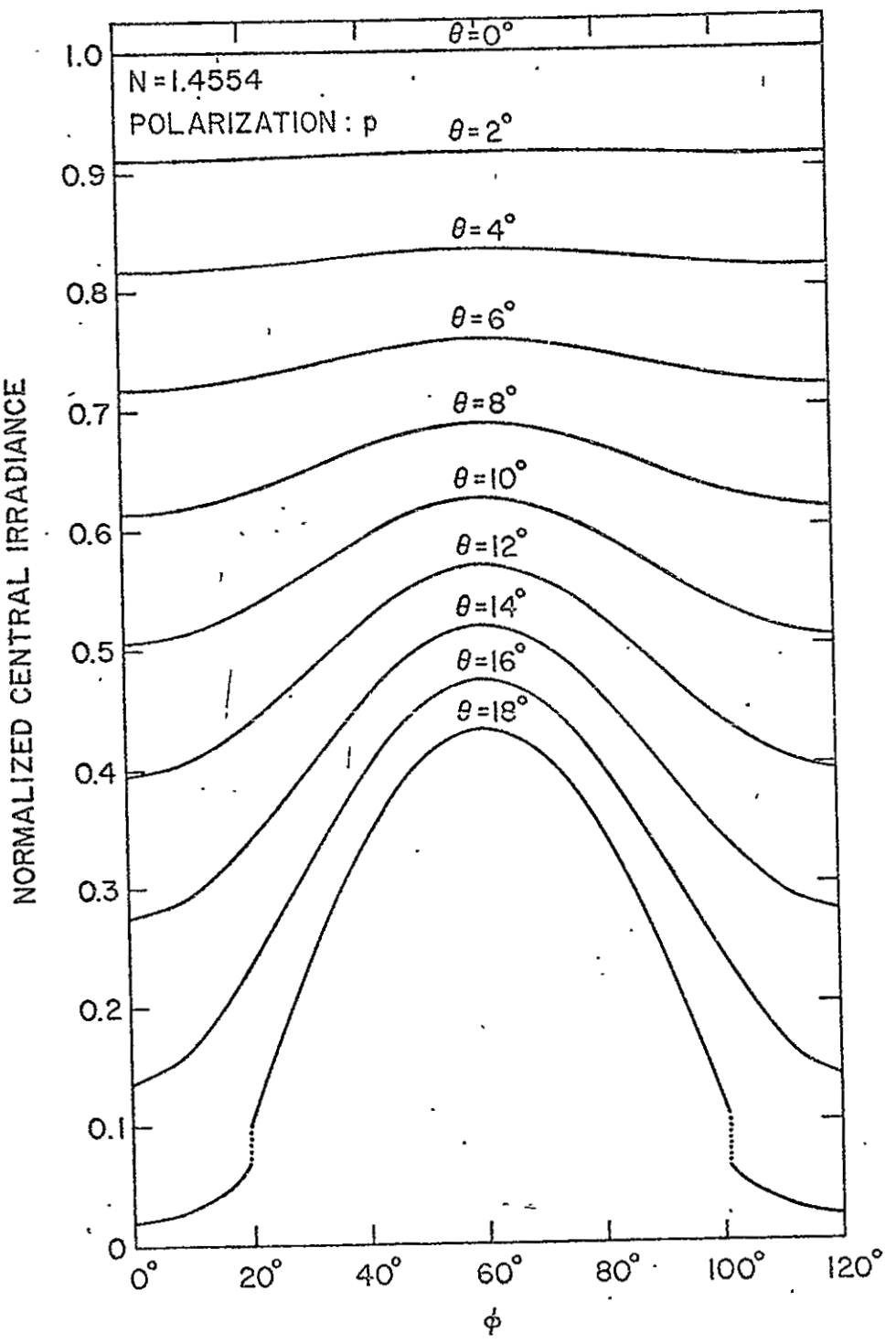

Fig. 12

Normalized central irradiance plotted versus azimuth angle for various angles of incidence of light which is linearly polarized in p- direction.

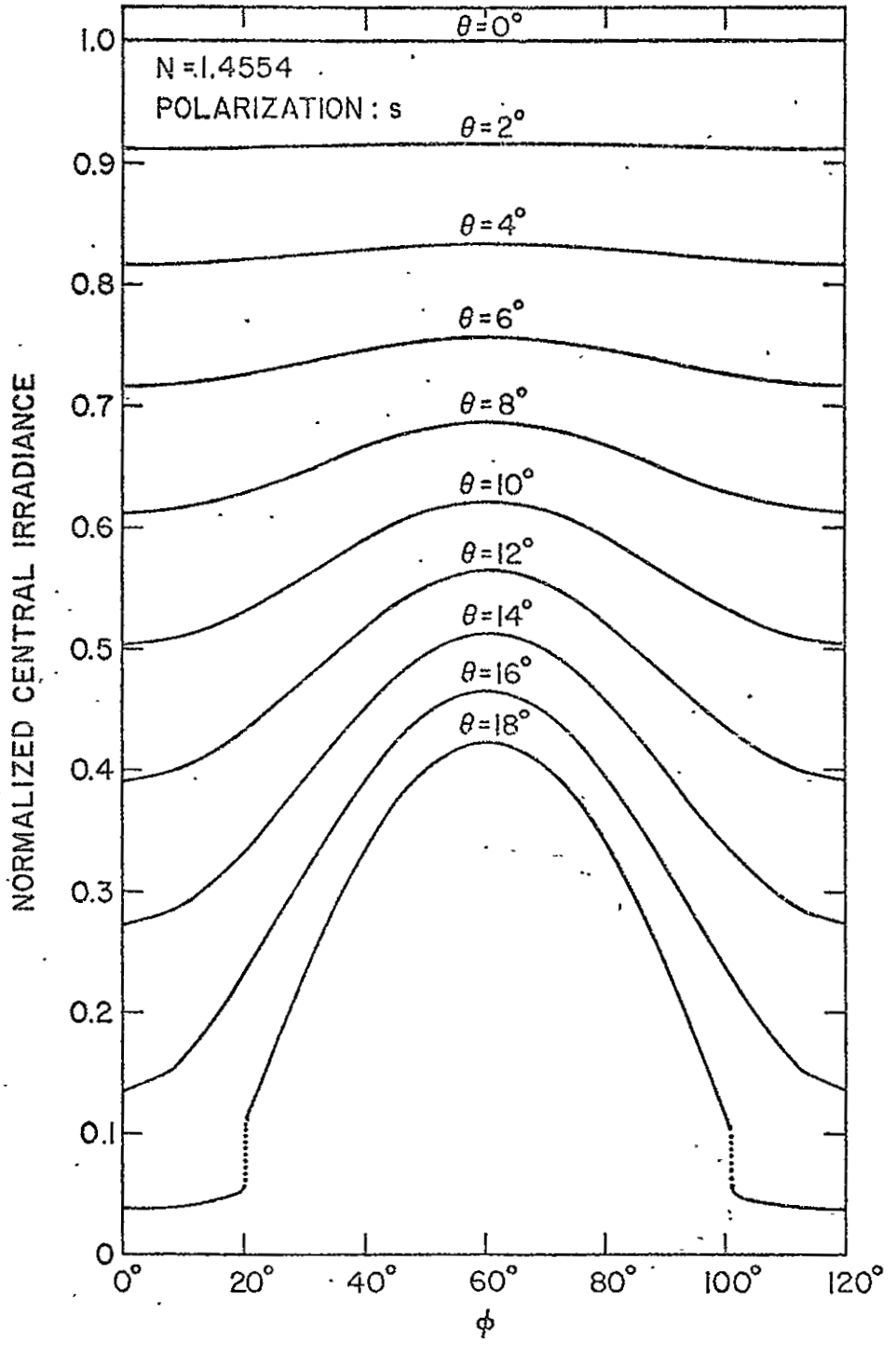

Fig. 13

The same as Figure 12 except the polarization of light is in s- direction.

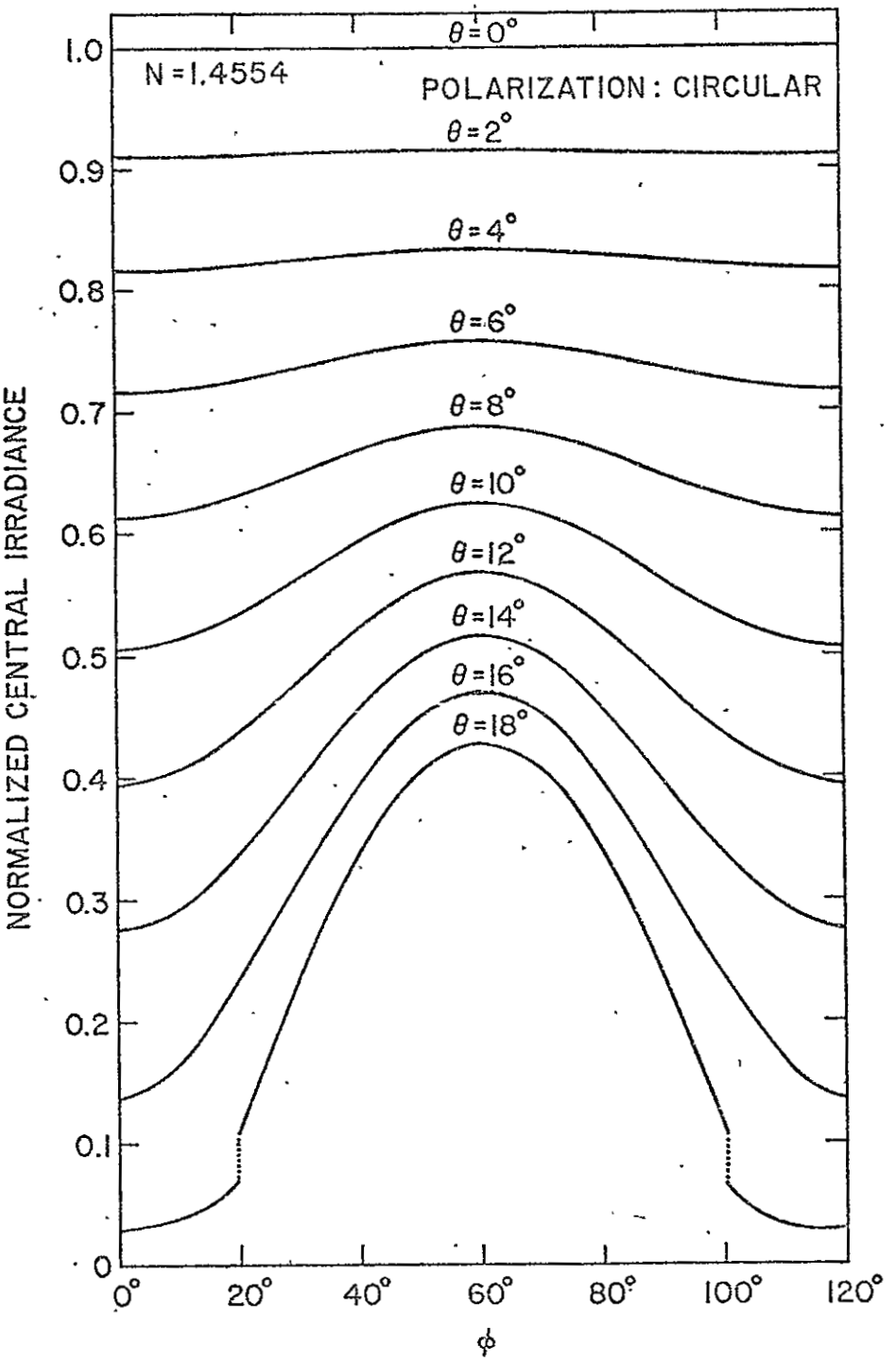

Fig. 14

The same as Figure 12 except the polarization of light is circular.

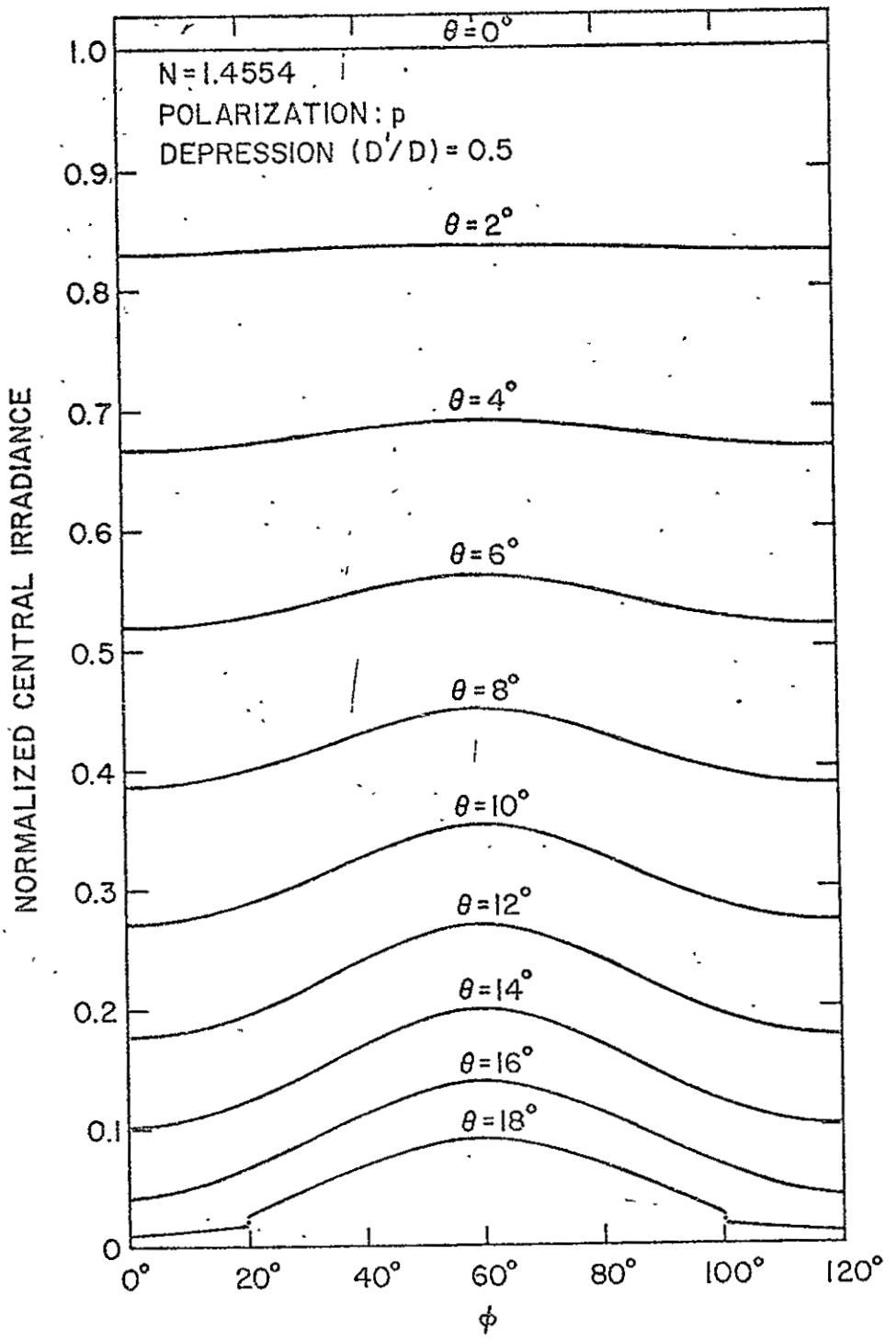

Fig. 15

The same as Figure 12 except the retroreflector is mounted in a cavity. The depth of the depression is one-half of the diameter of the front face.

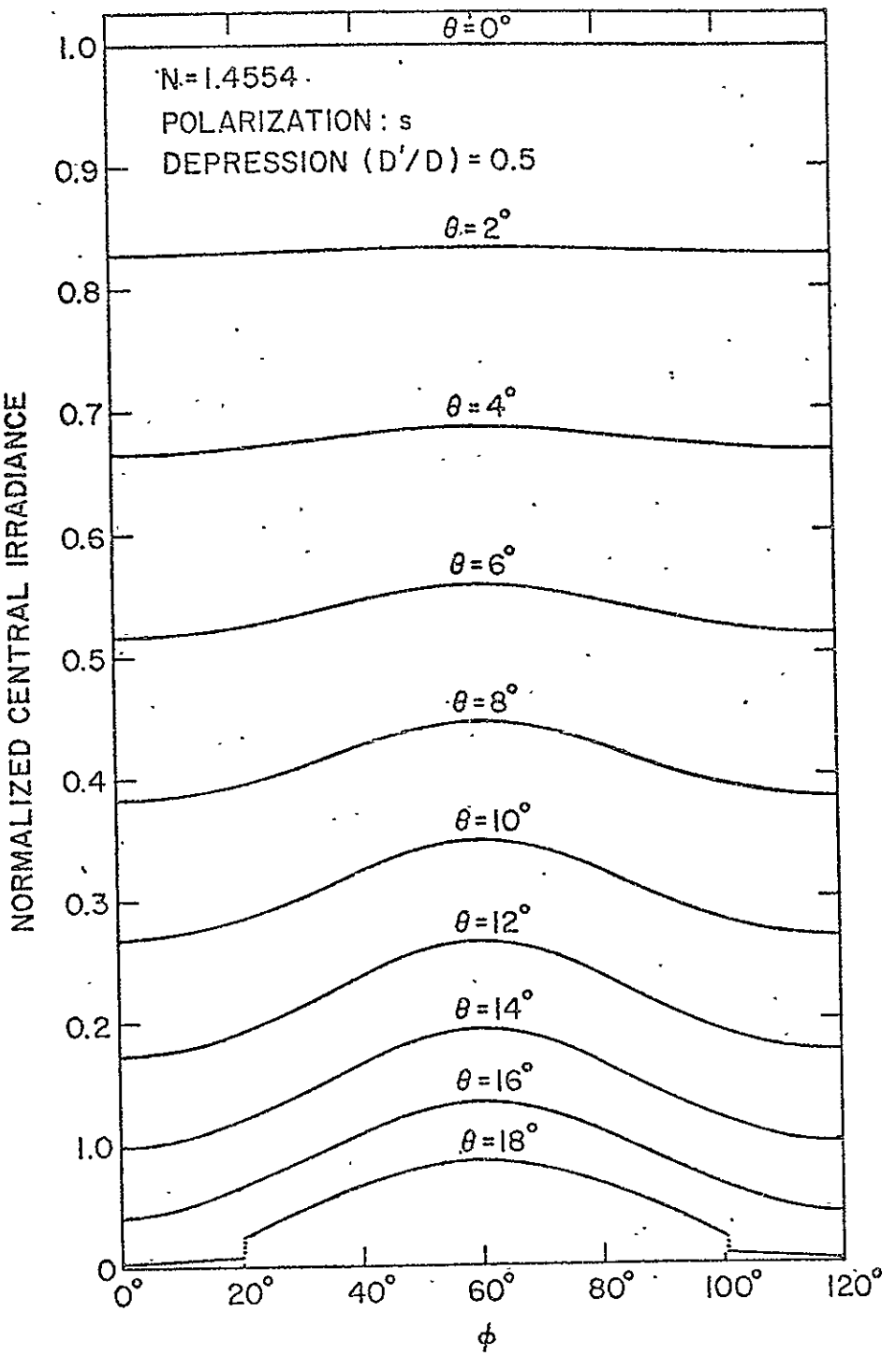

Fig. 16

The same as Figure 15 except the polarization of light is in s- direction.

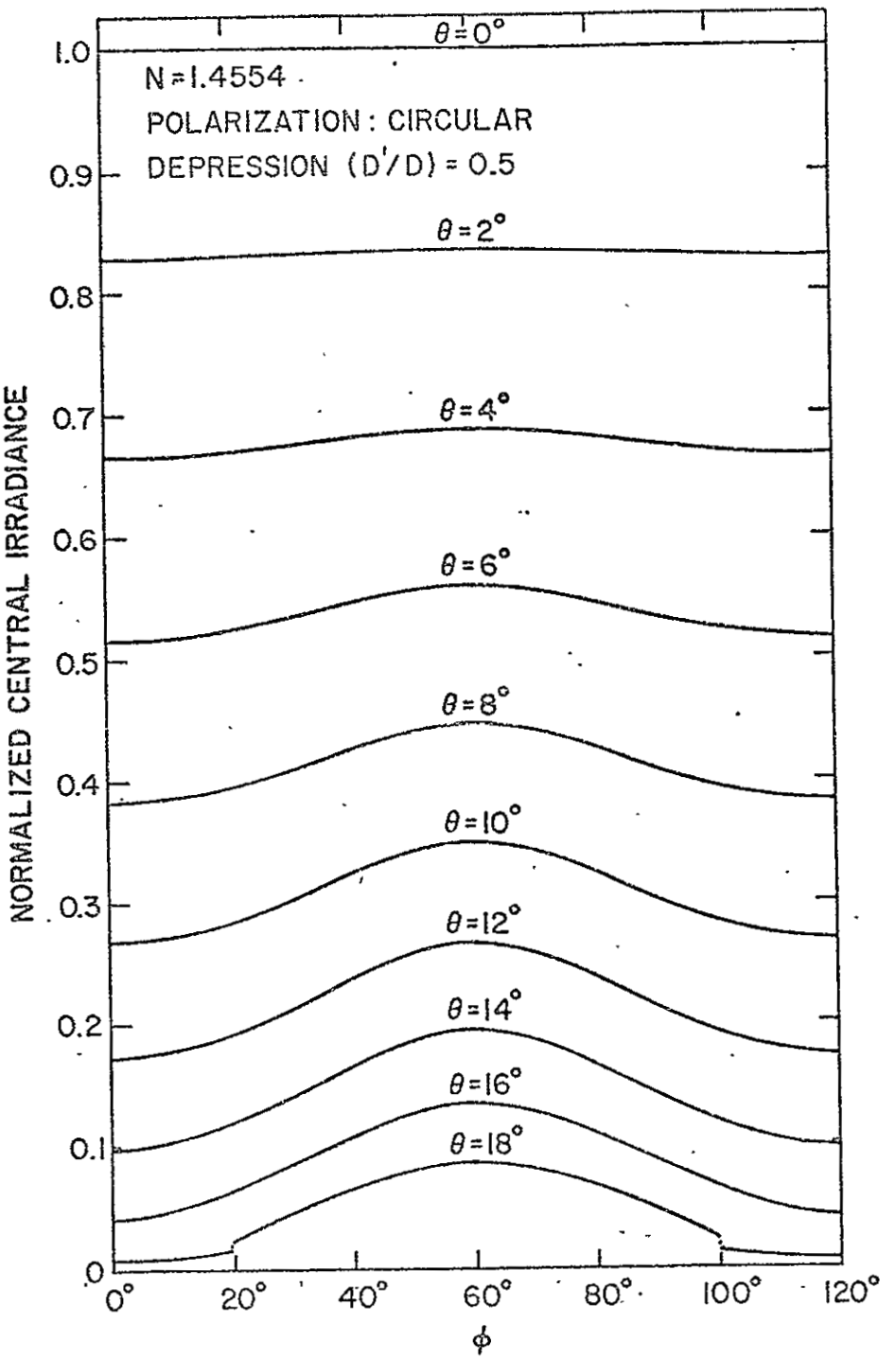

Fig. 17

The same as Figure 15 except the polarization of light is circular.

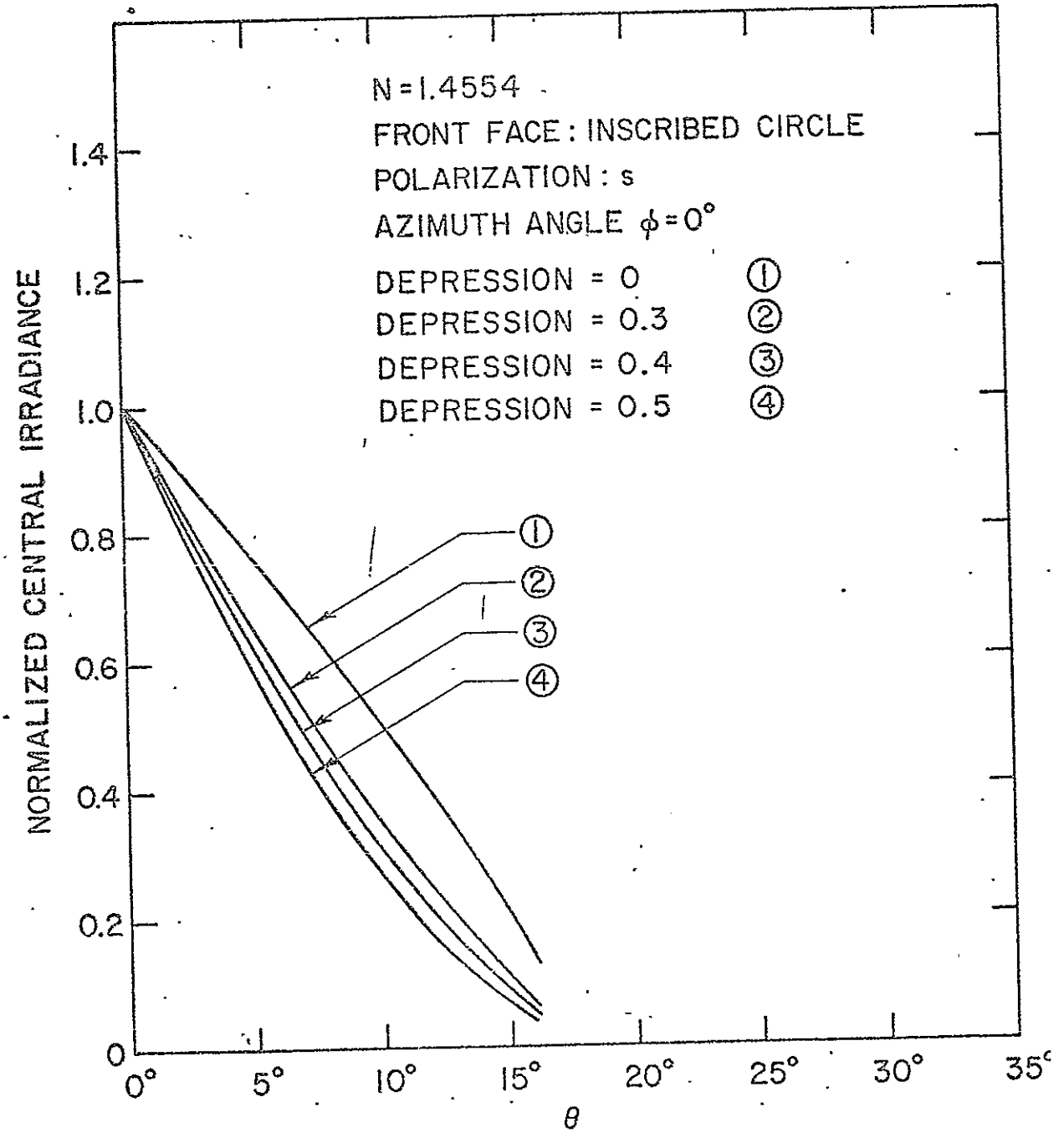

Fig. 18

Normalized central irradiance is plotted versus θ for φ = 0°. The depth of the depression is expressed in the unit of the diameter of the front face.

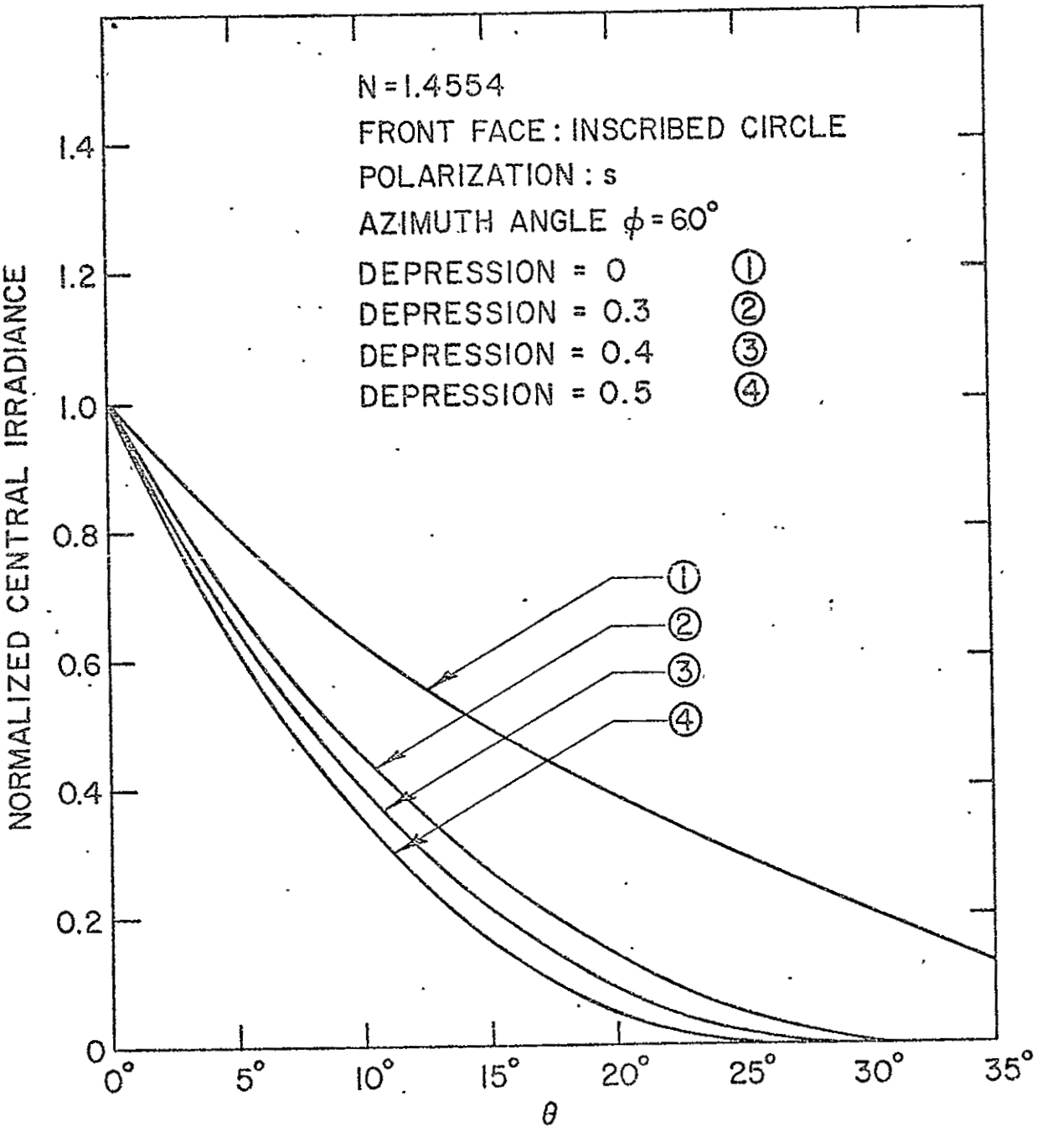

Fig. 19

The same as Figure 18 except ϕ = 60°.

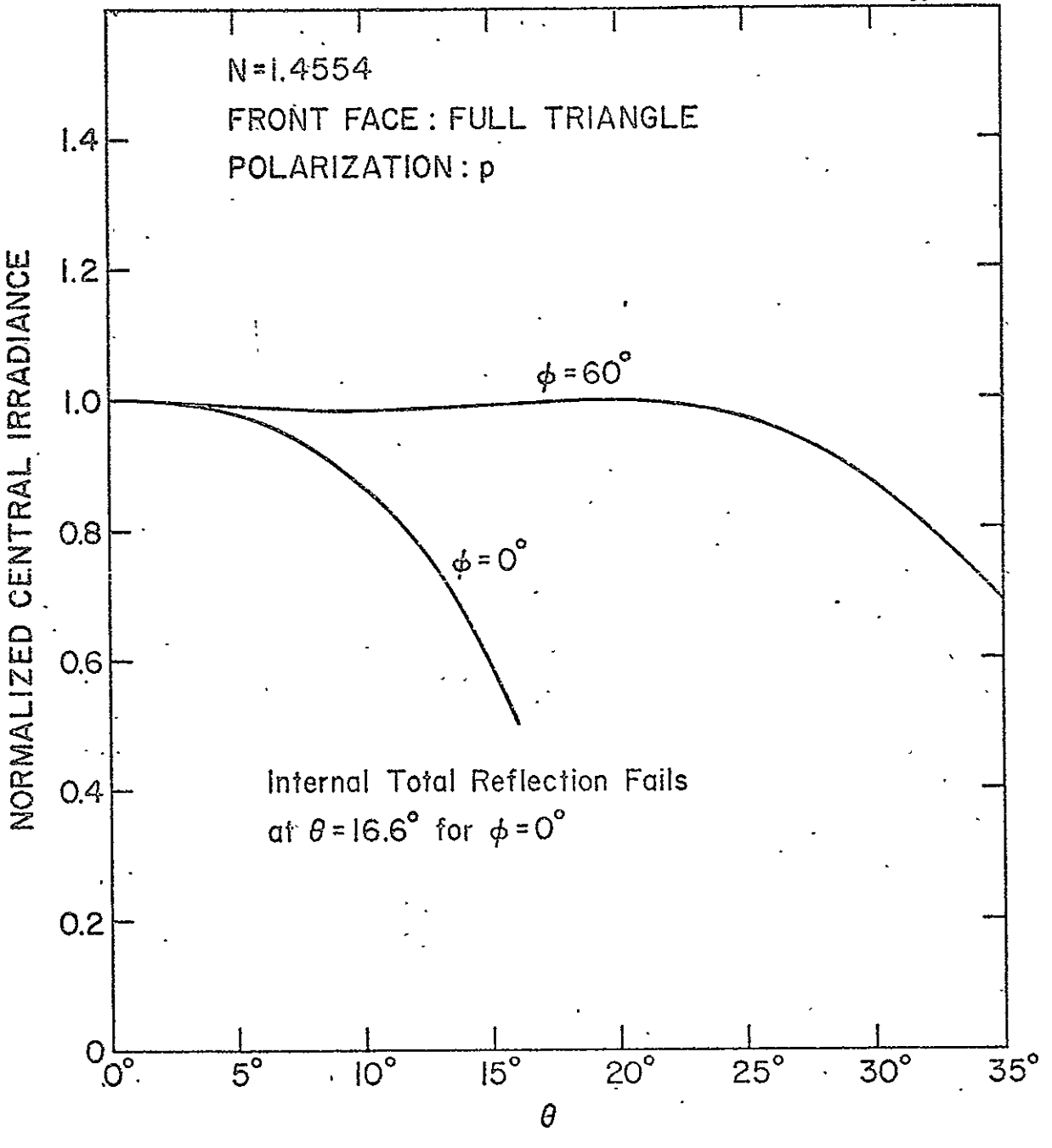

Fig. 20

Normalized central irradiance from a retroreflector with full triangular face is plotted versus θ for $\phi = 0°$ and $60°$. The internal total reflection fails at $\theta = 16.6°$ for $\phi = 0°$.

APPENDIX 4

The Possible Failure of Total Reflection in an Uncoated Solid Retroreflector

R. F. Chang

THE POSSIBLE FAILURE OF TOTAL REFLECTION IN AN UNCOATED SOLID RETROREFLECTOR*

R. F. Chang

Technical Report 70-130

June 1970

University of Maryland
Department of Physics and Astronomy
College Park, Maryland
20742

*This work was supported by NASA Contract NAS 9-7809.

ABSTRACT

A limit on the angle of incidence is imposed on a solid retroreflector with uncoated back surfaces because of the possible failure of total reflection. An expression is derived for the critical angle of incidence as a function of the index of refraction and the azimuth angle. The critical angle is the angle at which the total reflection initially fails.

The index of refraction must be greater than $\sqrt{3/2} = 1.23$ if we intend to utilize the total reflection in a retroreflector. On the other extreme, if the index of refraction is greater than $\sqrt{(3 + \sqrt{3})} = 2.18$ the retroreflector will retain its reflecting property at all angles of incidence.

THE POSSIBLE FAILURE OF TOTAL REFLECTION IN AN UNCOATED SOLID RETROREFLECTOR

I. INTRODUCTION.

In this report we will present the analysis on the conditions of the angle of incidence of a light ray when the internal total reflection fails in an uncoated solid retroreflector. When a retroreflector is used, especially for off-axis incidence of light, the failure of total reflection will limit the angle of incidence of light.

Intuitively, we know that the higher index of refraction of the glass would reduce the likelihood of the failure of the total reflection; consequently a larger angle of incidence is attained before the retroreflector loses its reflecting properties. Rityne has presented a figure of maximum permissible angle at which a retroreflector retains its reflecting properties[1]. However, he has not reported any details beyond that single figure.

We have studied the same subject independently, in connection with the LR^3 experiment [2-5]. We will discuss in detail how the failure occurs and how the index of refraction affects the largest permissible angle.

II. ANALYSIS.

A retroreflector can be basically represented by three mutually perpendicular reflecting planes. Let us consider a retroreflector as

shown in Figure 1(a); we can designate the back edges OA, OB, and OC as the x-, y-, and z-axis of a rectangular coordinate system.

The angles of incidence at the plane I, II, and III are $\cos^{-1}\ell$, $\cos^{-1}m$, and $\cos^{-1}n$, respectively, for the incident rays whose direction cosines are $(-\ell, -m, -n)$ within the glass. If the ray, which arrives at plane I fails internal total reflection, then,

$$\sin(\cos^{-1}\ell) = \sqrt{1-\ell^2} \leq \frac{1}{N}, \tag{1}$$

where N is the index of refraction of the glass. The angle of incidence at the plane I is always $\cos^{-1}\ell$, even though the ray has been reflected previously by other planes; the process of reflection only alters the sign of an appropriate component of the direction cosines because the normals of the planes are in x-, y-, and z-direction.

All rays satisfying the condition in Eq.(1) would lie in a cone whose half-angle is

$$\beta_c = \sin^{-1}\left(\frac{1}{N}\right), \tag{2}$$

around x-axis. Similar cones can be constructed around y- and z-axis. With the cone of failure defined as above, we can evaluate the largest angle of incidence allowed, which we will call critical angle of incidence from here on, outside the glass before the failure of internal total reflection occurs. The angle of incidence of the ray relative to a retroreflector is measured from the axis of symmetry. (A detailed definition of the angle of incidence can be found in reference 6.)

It has been shown that within the glass the x-component of the direction cosines is expressed in terms of the angle of incidence θ and the azimuth angle ϕ as[6]

$$\ell = \frac{1}{\sqrt{3}}(\cos\theta + \sqrt{2}\cos\phi\sin\theta). \tag{3}$$

Here we restrict the azimuth angle ϕ to be between -60° and 60°; because we can always reduce an azimuth angle into that region if we choose the cone of failure around an appropriate axis.

Combining Eq.(1), Eq.(3) and Snell's law,

$$\sin \theta_o = N \sin \theta, \tag{4}$$

we can solve for $\sin \theta_o$ and obtain

$$\sin \theta_o \geq \frac{1}{2\cos^2\phi+1} (\sqrt{6}\sqrt{N^2-1}\cos\phi \pm \sqrt{3-2N^2\sin^2\phi}). \tag{5}$$

The problem of dual sign in Eq.(5) can be resolved by considering the special case when $\phi = 0°$.

For the case of $\phi = 0°$, we can analyze the conditions on the angle of incidence directly as shown in Figure 1(b). Substituting $\cos^{-1}\ell$ with $\alpha-\theta$ in Eq.(1) we obtain

$$\frac{1}{\sqrt{3}} (\sqrt{2}\cos\theta - \sin\theta) \leq \frac{1}{N}, \tag{6}$$

since $\sin\alpha = \sqrt{\frac{2}{3}}$ and $\cos\alpha = \sqrt{\frac{1}{3}}$ in a retroreflector. Solving Eq.(6) for $\sin\theta_o$ we obtain

$$\sin \theta_o \geq \frac{1}{3} (\sqrt{6}\sqrt{N^2-1} - \sqrt{3}). \tag{7}$$

Comparing Eq.(7) with Eq.(5) when $\phi = 0°$, we come to the conclusion that the negative sign is the proper sign in Eq.(5) and we can express the critical angle of incidence as a function of ϕ and N:

$$\sin \theta_c = \frac{1}{2\cos^2\phi+1} (\sqrt{6}\sqrt{N^2-1}\cos\phi - \sqrt{3-2N^2\sin^2\phi}). \tag{8}$$

The limit on the angle of incidence of a retroreflector is imposed not only by the failure of the total reflection but also by the vanishing of the effective aperture. If we consider a retroreflector with a circular

face, especially when the circle is an inscribed circle to the triangular face, the angle at which the effective aperture vanishes is

$$\sin \theta_L = N/\sqrt{3}, \tag{9}$$

as shown in Figure 1(c). The smaller of the two angles, θ_L and θ_c, is the real limit to the angle of incidence.

III. DISCUSSION.

An examination of Eq.(2) reveals that $\beta_c < \pi/4$ if $N > \sqrt{2}$; physically speaking, the cones of failure do not intersect each other when $N > \sqrt{2}$ as shown in Figure 2(a). When $N = \sqrt{2}$, $\beta_c = \pi/4$ and the cones are tangent to each other as shown in Figure 2(b). When $N = \sqrt{3/2}$, $\beta_c = \cos^{-1}(1/3)$ and the cones are intersecting each other at the axis of symmetry of a retroreflector as the common line of intersection as shown in Figure 2(c).

In other words, the total reflection will not fail for all θ in a certain range of ϕ when $N > \sqrt{2}$ because there is a region in which the plane of incidence is between the cones of failure whereas the total reflection fails for all θ when $N < \sqrt{3/2}$ because there is no region which does not belong to at least one of the cones of failure.

Let us now consider Eq.(8) and Eq.(9) for the range of N when $\sqrt{3/2} \leq N \leq \sqrt{2}$. When $N = \sqrt{3/2}$ in Eq.(8) $\sin \theta_c = 0$ for all ϕ; this result is consistent with the early analysis on the cones of failure that the total reflection fails at all θ. The index of refraction must be greater than $\sqrt{3/2}$ if the retroreflector is to be used as a reflector with uncoated back surfaces.

In the range $\sqrt{3/2} \leq N \leq \sqrt{2}$, the expression under the radical sign in Eq.(8) is always non-negative therefore sin θ_c is always real, which is a fact supported by the geometrical analysis that the cones intersect each other.

A geometrical inspection on the cones of failure reveals that sin θ_c is a monotonic function of ϕ with its smallest value at $\phi = 0°$ and its largest at $\phi = 60°$. Now we shall prove that θ_c is always less than θ_L in the range $\sqrt{3/2} < N < \sqrt{2}$; the failure of total reflection occurs before the effective aperture vanishes and the limit on the angle of incidence is θ_c alone.

The largest θ_c is given by Eq.(8) as

$$\sin \theta_c \ (\phi = 60°) = \sqrt{2/3} \ (\sqrt{N^2-1} - \sqrt{2-N^2}). \qquad (10)$$

Comparing Eq.(10) with Eq.(9), we obtain

$$r \equiv \sin \theta_c(\phi=60°) \ / \ \sin \theta_L = \frac{\sqrt{2}}{N} \ (\sqrt{N^2-1} - \sqrt{2-N^2}). \qquad (11)$$

Since Eq.(11) indicates that $r = 1$ when $N = \sqrt{2}$ and $dr/dN > 0$, it is certainly true that $r < 1$ if $N < \sqrt{2}$. Consequently, $\theta_c < \theta_L$ for $\sqrt{3/2} < N < \sqrt{2}$ and $\theta_L = \theta_c$ at $\phi = 60°$ when $N = \sqrt{2}$.

The earlier geometrical analysis indicated that there should be a certain range in ϕ where no failure of total reflection can occur. The mathematical manifestation of the situation in Eq.(8) is that sin θ_c becomes complex because the expression under the radical sign becomes negative when $60° > \phi \geq \phi_o$ where $\phi_o = \sin^{-1}(\sqrt{3/2}/N)$.

Comparing sin θ_L with sin θ_c at $\phi = \phi_o$ for the case of $N > \sqrt{2}$, we find that θ_L is less than θ_c at $\phi = \phi_o$. The implication is that the angle θ_L becomes the limit even before ϕ reaches ϕ_o. The exact angle ϕ at which

$\theta_L = \theta_c$ can be evaluated by equating Eq.(8) to Eq.(9) and solving for ϕ.

If $N > \sqrt{3}$, Eq. (9) indicates that the effective aperture does not vanish; therefore the limit on the angle of incidence is imposed by the ultimate limit of 90° or θ_c.

The condition that a retroreflector retains its reflecting properties at all times is $N \geq \sqrt{3+\sqrt{3}}$. The condition is obtained from Eq.(8) by setting ϕ to 0° and $\sin \theta_c = 1$.

The critical angle θ_c combined with θ_L as the overall limit on the angle of incidence is plotted as a function of ϕ for various N in Figure 3. The region below the curve is the region in which a retroreflector retains its reflecting properties.

IV. CONCLUSIONS.

We have obtained the critical angle of incidence as a function of N and ϕ. The critical angle increases monotonically for increasing ϕ and N. The minimum value necessary for the index of refraction is $\sqrt{3/2}$ if a retroreflector with uncoated back surfaces is to retain its reflecting properties. The internal total reflection fails at all times when $N < \sqrt{3/2}$.

We also found that there was a range of ϕ where the internal reflection does not fail if $N > \sqrt{2}$; the limit on the angle of incidence is then the vanishing of the effective aperture. A retroreflector can be used even for the 90° angle of incidence for a certain range of ϕ if $N > \sqrt{3}$ and for all ϕ if $N > \sqrt{3+\sqrt{3}}$.

REFERENCES

1. N. E. Rityne, Soviet Journal of Optical Technology 1, 198 (1968).
2. C. O. Alley, P. L. Bender, R. F. Chang, D. G. Currie, R. H. Dicke, J. E. Faller, W. M. Kaula, G. J. F. MacDonald, J. D. Mulholland, H. H. Plotkin, S. K. Poultney, D. T. Wilkinson, I. Winer, W. Carrion, T. Johnson, P. Spadin, L. Robinson, E. J. Wampler, D. Wieber, E. C. Silverberg, C. A. Steggerda, J. V. Mullendore, J. D. Rayner, W. Williams, B. Warner, H. Richardson, and B. W. Bopp, "Laser Ranging Retro-Reflector," Apollo 11 Preliminary Science Report (NASA Special Publication SP-214, 1969).
3. C. O. Alley, R. F. Chang, D. G. Currie, J. V. Mullendore, S. K. Poultney, J. D. Ranyer, E. C. Silverberg, C. A. Steggerda, H. H. Plotkin, W. Williams, B. Warner, H. Richardson, B. W. Bopp, Science 167, 368 (1970).
4. C. O. Alley, R. F. Chang, D. G. Currie, S. K. Poultney, P. L. Bender, R. H. Dicke, D. T. Wilkinson, J. E. Faller, W. M. Kaula, G. J. F. MacDonald, J. D. Mulholland, H. H. Plotkin, W. Carrion, and E. J. Wampler, Science 167, 458 (1970).
5. J. E. Faller, I. Winer, W. Carrion, T. S. Johnson, P. Spadin, L. Robinson, E. J. Wampler, and D. Wieber, Science 166, 99 (1969).
6. R. F. Chang, University of Maryland, Department of Physics and Astronomy, Technical Report No. 70-129, 1970.

FIGURES

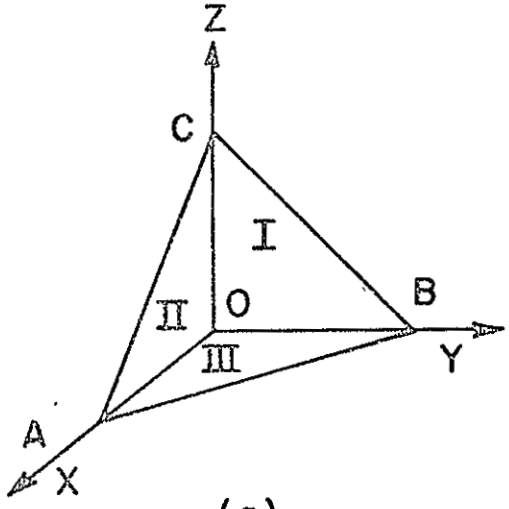

(a)

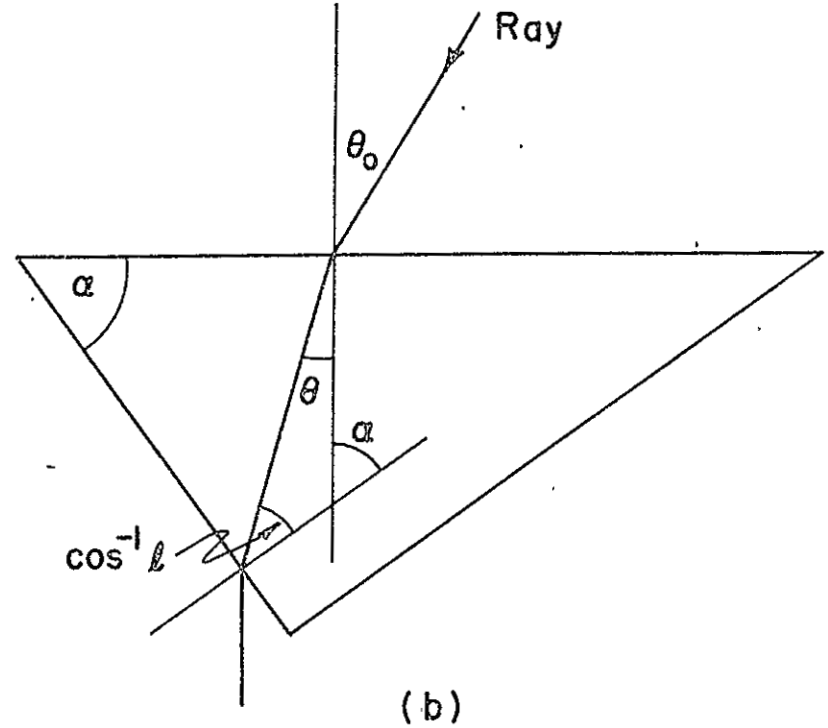

(b)

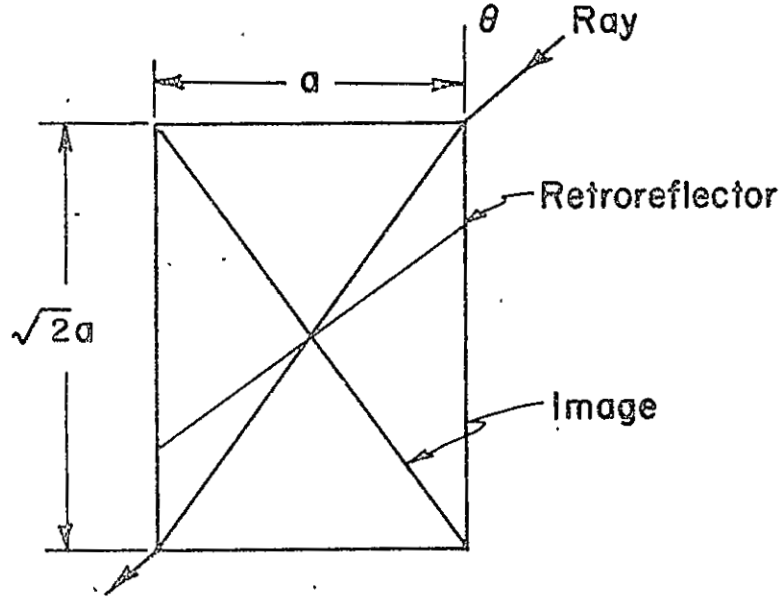

(c)

(a). A geometrical representation of a retroreflector.

(b). Cross-section of a retroreflector illustrating the failure of total reflection at some angle of incidence.

(c). Illustration showing the disappearance of the effective aperture.

Fig. 1

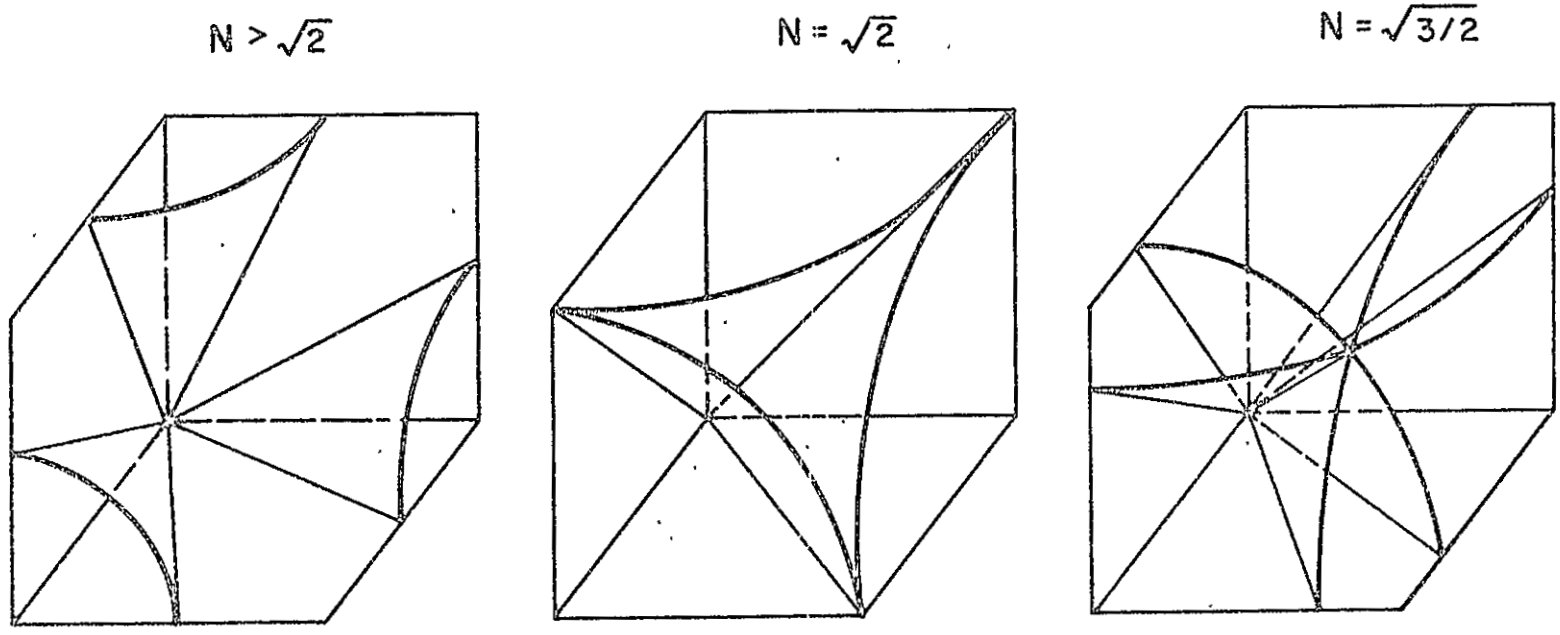

Fig. 2

The cones of failure for various values of the index of refraction.

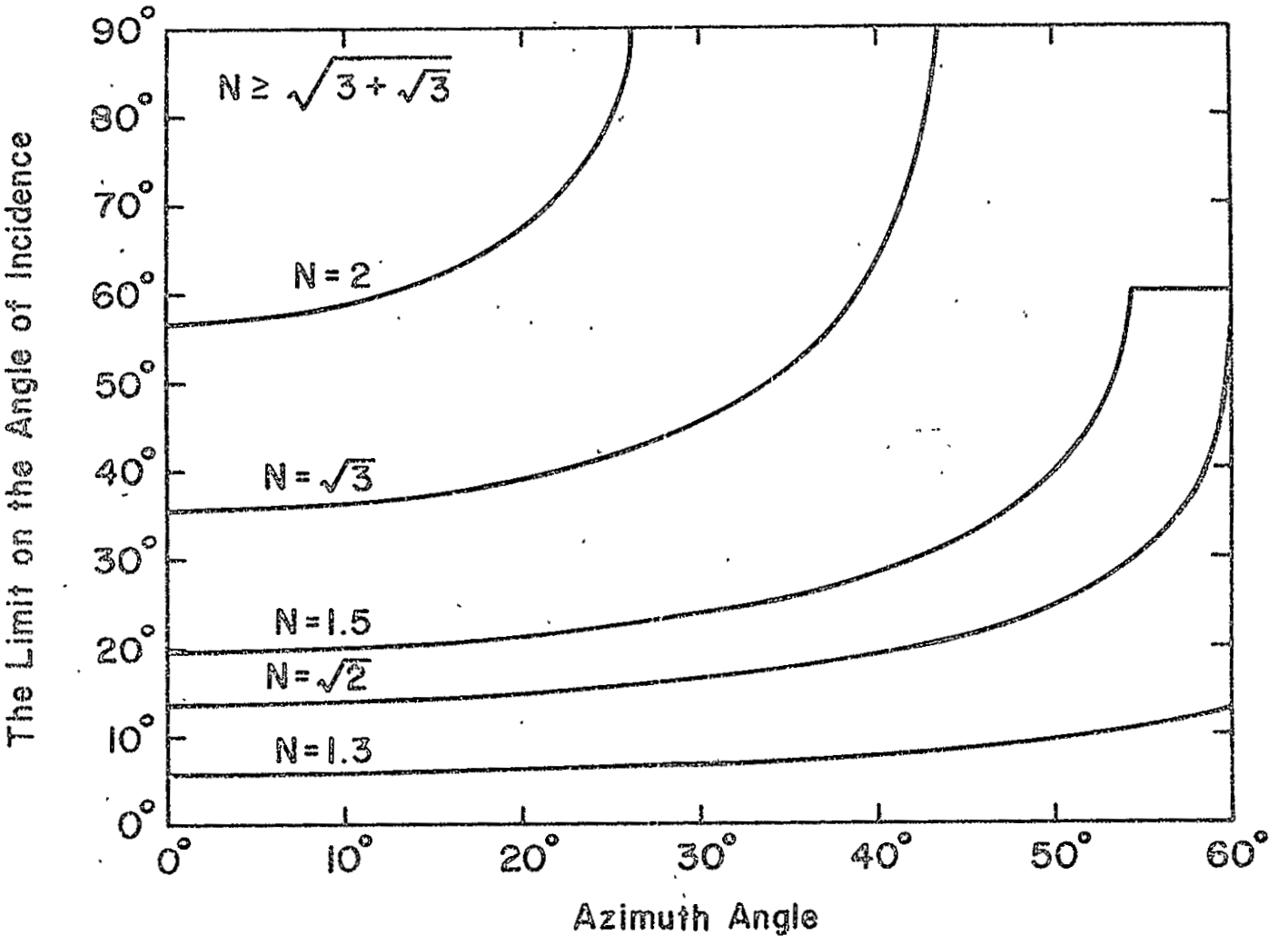

Fig. 3

The limit on the angle of incidence plotted as a function of azimuth angle for different values of the index of refraction.

APPENDIX 5

Test Report on the Optical Quality of Three 1-1/2" Retroreflectors

R. F. Chang

and

W. J. Scott

TEST REPORT ON THE OPTICAL QUALITY OF THREE 1-1/2" RETROREFLECTORS*

R. F. Chang and W. J. Scott†

Technical Report 70-132

June 1970

University of Maryland
Department of Physics and Astronomy
College Park, Maryland
20742

*This work was supported by NASA Contract NAS 9-7809 and National Science Foundation Grant GY-5461.

†On leave from Gettysburg College, Gettysburg, Pennsylvania.

ABSTRACT

Three aluminized 1-1/2" retroreflectors have been tested in the laboratory for their optical quality. The diffraction patterns from the retroreflectors are presented in comparison with the Airy pattern from a flat mirror. These retroreflectors are now in current use in the 107" telescope for the purpose of pointing the telescope precisely at the laser ranging retroreflector array on the moon.

TEST REPORT ON THE OPTICAL QUALITY OF THREE 1-1/2" RETROREFLECTORS

I. INTRODUCTION

After a successful deployment of a laser ranging retroreflector array on the Moon by the Apollo 11 astronauts, continuing measurements of the round-trip travel time of light are being made from the McDonald Observatory, University of Texas, at Mount Lock, Texas.[1-4] A short laser light pulse is transmitted through the 107" telescope pointed at the laser ranging retroreflector array on the Moon and the reflected light pulse from the array is collected by the same telescope. The transmitted laser beam is very narrow so that precise pointing of the telescope is essential.

Techniques for this purpose were developed during the Surveyor 7 laser-beam-pointing test.[5] Applying the techniques to the Apollo laser ranging experiment involves mounting retroreflectors on the secondary mirror-support structure of the telescope. These retroreflectors intercept a very small portion of the outgoing beam and return it back into the telescope in such a way that the light is brought to focus, superimposed on the image of the Moon at the spot to which the beam is being sent. The precise coincidence of the focused light spot and the location of the reflectors on the Moon assures a proper pointing of the telescope.

In practice, because of the diffraction effects in light, the size of the spot is not infinitely small when the light is brought to focus. The spot size is determined exactly by the theory of far field diffraction. In the process of reflection, the incident plane wave may be degraded by imperfections in the reflector. However, the degradation of the wave front becomes insignificant if it does not contribute appreciably to the divergence of the light beam. Since the accuracy of pointing depends on the smallness of the focused light spot it is essential that high quality retroreflectors be used.

It has been shown that even a retroreflector of perfect geometrical configuration may degrade the wave front of light significantly because of the polarization effects[6]. It is also found that when its back surfaces are coated with metals such as aluminum or silver the polarization effects are minimized to such an extent that the retroreflector acts almost like a flat mirror. But in practice unavoidable flaws exist. A laboratory test program was therefore initiated to determine the optical quality of a retroreflector.

Four retroreflectors were selected to be mounted in the 107" telescope at the McDonald Observatory. These retroreflectors were manufactured by the Perkin Elmer Corporation. They are made to the same specifications required for the retroreflectors deployed on the Moon. The reflectors are made of fused silica. Their front face is a circle of 1.5" diameter.

Three of these four are coated in the back with aluminum. The ID numbers are 190A, 191B, and 208A. The fourth one (ID number 181A) is being studied separately for extensive analysis.

In this report we will present only the studies for the case of normal incidence of light. The diffraction patterns of the returning light beam from the retroreflectors are compared to that from a flat mirror of the same aperture. We also present an abnormality of the central irradiance of the diffraction pattern which depends on the polarization orientation of the incident light beam.

We will start in section II with the description of the test procedures and results and follow that with a discussion in Section III. A brief conclusion is in Section IV.

II TEST PROCEDURES AND RESULTS

The test apparatus basically consists of a He-Ne laser, a spatial filter, a collimator, and a two-meter optical bench. The arrangement is shown in Fig. 1. The light beam from a 15 mW He-Ne laser passes initially through a spatial filter consisting of a 20X microscope objective and 12 μ pinhole. The widely diverging light after the spatial filter is collimated first to a beam of roughly one-half inch diameter. This beam then passes through a beam splitter and goes into a large collimator. The final collimated beam is 10 cm in diameter.

The first stage beam expansion is to serve the purpose of making the laser light intensity profile at the retroreflector as uniform as possible. It also enables us to reduce the area of the beam splitter in a collimated portion of the light beam to minimize possible wavefront distortion.

The returning beam from the retroreflector forms a diffraction pattern at the focal point of the large collimator lens and the pattern is enlarged by the focusing lens of the collimator. The pattern can be further enlarged with an additional lens system.

Photographs of the diffraction pattern of reflected light from each retroreflector were taken with the diffraction pattern focused on the camera film. The laser light was linearly polarized. Its direction was always made parallel to one of the projections of the rear edges on the front face of the retroreflector.

Because of the three-fold symmetry of a retroreflector we expect a repetition of the same pattern every time it is rotated 120°.

The photographs of the diffraction pattern are shown in Fig. 2 for 191B at all three orientations. Notice that the pattern rotates 120° counter-clockwise following the rotation of the retroreflector but does not repeat the same pattern at every 120° of rotation. Typical diffraction patterns produced by 190A and 208A are shown in Fig. 3 along with the Airy pattern from a flat mirror with 1.5" circular aperture.

The investigation on the central irradiance of the diffraction pattern from a retroreflector was prompted by the observation that the irradiance is a sensitive function of the relative orientation between the direction of the polarization of light and the direction of the projection of one particular back edge, which is arbitrarily chosen, on its front face. In other words, for fixed, linearly polarized incident light the central irradiance of the diffraction pattern varies when the retroreflector is rotated around a symmetric axis perpendicular to the front face. A large variation in central irradiance upon rotation has been observed in some uncoated retroreflectors[7]. Such a measurement was made on 191B retroreflector.

For this measurement, a photomultiplier tube and a pinhole were used in place of a camera. The diameter of the pinhole was less that 1/10 of the diameter of the Airy disc from a flat circular mirror of 1.5" diameter. The pinhole allows only the central

irradiance of the diffraction pattern to be measured by a photomultiplier tube.

The DC output from the photomultiplier tube was read with a digital voltmeter when the retroreflector was rotated in steps of 7.5° through one complete revolution. A photodiode was used simultaneously on the off-side of the beam splitter in the system to monitor the laser output intensity because it fluctuated a few percent over the experimental time. The readings were first corrected for monitor intensities and then the mean was normalized to 100.

Figure 4 shows the normalized central irradiance plotted against ϕ, the azimuth angle. The angle ϕ is measured clockwise from a reference direction to the arbitrary back edge projection mentioned above. This reference direction is taken from the direction of polarization, shown in the figure as a thick solid line.

III DISCUSSION

The diffraction patterns are expected to be virtually the same as the Airy pattern as indicated by analysis . The patterns show deviations from such expectations. Comparison between the pattern from a retroreflector and the Airy pattern indicates that the central lobe of the former is consistent with that of the latter in size. The apparent deviation seems to be the failure of the formation of the rings surrounding the Airy disc in the former case, especially the first ring. Either two sidelobes (190A) or four sidelobes (191B and 208A) are present instead of a ring.

The patterns produced by 191B and 208A are very similar to each other. A close inspection of the pattern produced by 190A indicates that the orientation of the sidelobes matches one pair of the sidelobes from 191B. However, it is not clear which pair from 191B matches the pair from 190A because Fig. 3(b) qualitatively matches either Fig. 2(a) or Fig. 2(c) as far as one pair of the sidelobes is concerned.

The cause of this deviation is unknown at present time. However, one may speculate that the flaw is fixed geometrically on the retroreflector because the pattern rotates with the reflector when it is rotated. Especially the fact that the pattern fails to repeat itself for every 120° rotation suggests that the flaw has broken the three-fold symmetry of the retroreflector.

The variation of the central irradiance, when the retroreflector (191B) was rotated, also indicated the lack of three-fold symmetry. The small variation can be easily differentiated from fluctuations in our system because of its repetition after 180° of rotation. The repetition is expected because the rotation corresponds to adding a phase angle of π to the incident light; this additional phase angle should have no effect on the intensity measurement. The contradiction of the early analysis[6] to the observed variation in the central irradiance is consistent with the observation on the diffraction pattern. From the comparison between the experiment and the analysis we have come to believe that the flaw is small enough to retain the over-all pattern but sufficiently sensitive to polarization to redistribute the energy within the pattern as manifested in the variation of central irradiance.

The similarity of the diffraction patterns from three different retroreflectors indicates that the flaw is the same kind in all of the retroreflectors. Possible sources of the flaw may be angular errors, departure from the surface flatness, and the inhomogeneities.

The retroreflectors are quoted to have the effective flatness of about $\lambda/17$ by the manufacturer. The figure is based on the computer analysis of the interferograms of the retroreflectors. Since the central irradiance is directly related to the flatness figure, in its first order approximation, by the equation

$$I = I_o \, (1 - \langle \delta^2 \rangle)$$

where $\langle\delta^2\rangle$ is the variance of the flatness in terms of phase angle, the variation on the central irradiance implies a different flatness figure for different orientations of the retroreflector. Unfortunately, comparisons of flatness figure for different orientations have not been made.

A study is still underway to understand the cause of this imperfection in a retroreflector. Further results will be reported later.

IV CONCLUSION

The optical quality of the retroreflectors under examination is slightly less than "diffraction limited." The statement is supported by the qualitative presentation of the diffraction pattern in Fig. 2 and Fig. 3. The origin of the flaw is unknown at this time but a study is being conducted on the subject.

ACKNOWLEDGMENT

We are grateful to Dr. D. G. Currie for his profitable suggestions and discussions.

REFERENCES

1. C. O. Alley, P. L. Bender, R. F. Chang, D. G. Currie, R. H. Dicke, J. E. Faller, W. M. Kaula, G. J. F. MacDonald, J. D. Mulholland, H. H. Plotkin, S. K. Poultney, D. T. Wilkinson, I. Winer, W. Carrion, T. Johnson, P. Spadin, L. Robinson, E. J. Wampler, D. Wieber, E. C. Silverberg, C. A. Steggerda, J. V. Mullendore, J. D. Rayner, W. Williams, B. Warner, H. Richardson, and B. W. Bopp, "Laser ranging retroreflector" in Apollo 11 Preliminary Science Report (NASA Special Publication SP-214, 1969).

2. C. O. Alley, R. F. Chang, D. G. Currie, J. Mullendore, S. K. Poultney, J. D. Rayner, E. C. Silverberg, C. A. Steggerda, H. H. Plotkin, W. Williams, B. Warner, H. Richardson, B. Bopp, Science 167, 368 (1970).

3. C. O. Alley, R. F. Chang, D. G. Currie, S. K. Poultney, P. L. Bender, R. H. Dicke, D. T. Wilkinson, J. E. Faller, W. M. Kaula, G. J. F. MacDonald, J. D. Mulholland, H. H. Plotkin, W. Carrion, and E. J. Wampler, Science 167, 458 (1970).

4. J. E. Faller, I. Winer, W. Carrion, T. S. Johnson, P. Spadin, L. Robinson, E. J. Wampler, and D. Wieber, Science 166, 99 (1969).

5. C. O. Alley and D. G. Currie, "Laser Beam Pointing Tests" in Surveyor Project Final Report, Part 2, Science Results (JPL NASA Tech. Report 32-1265, 1968).

6. C. O. Alley, R. F. Chang, D. G. Currie, and M. E. Pittman, to be published in J. Opt. Soc. Am., April (1971); University of Maryland, Department of Physics and Astronomy, Technical Report 70-104 (1970).

7. R. F. Chang and W. J. Scott, University of Maryland, Department of Physics and Astronomy Technical Report 70-131, (1970).

FIGURE CAPTIONS

Fig. 1 Experimental arrangement.

Fig. 2 Diffraction patterns from 191B at three orientations.

Fig. 3 (a) Diffraction pattern from 208A.
(b) Diffraction pattern from 190A.
(c) The Airy pattern from a flat mirror with 1.5" circular aperture.

Fig. 4 Normalized central irradiance of the diffraction pattern from 191B as function of the azimuth angle ϕ.

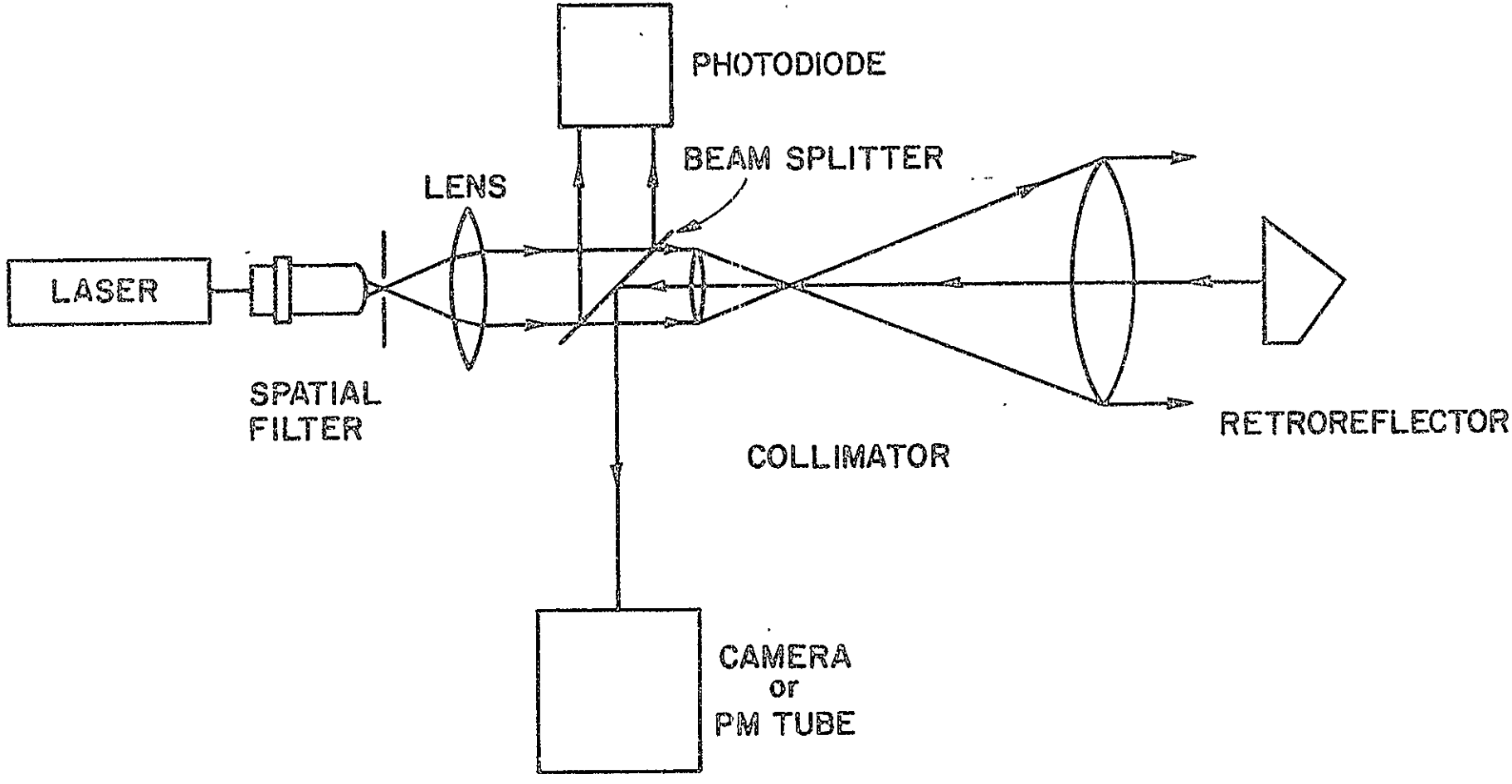

Fig. 1

Experimental arrangement.

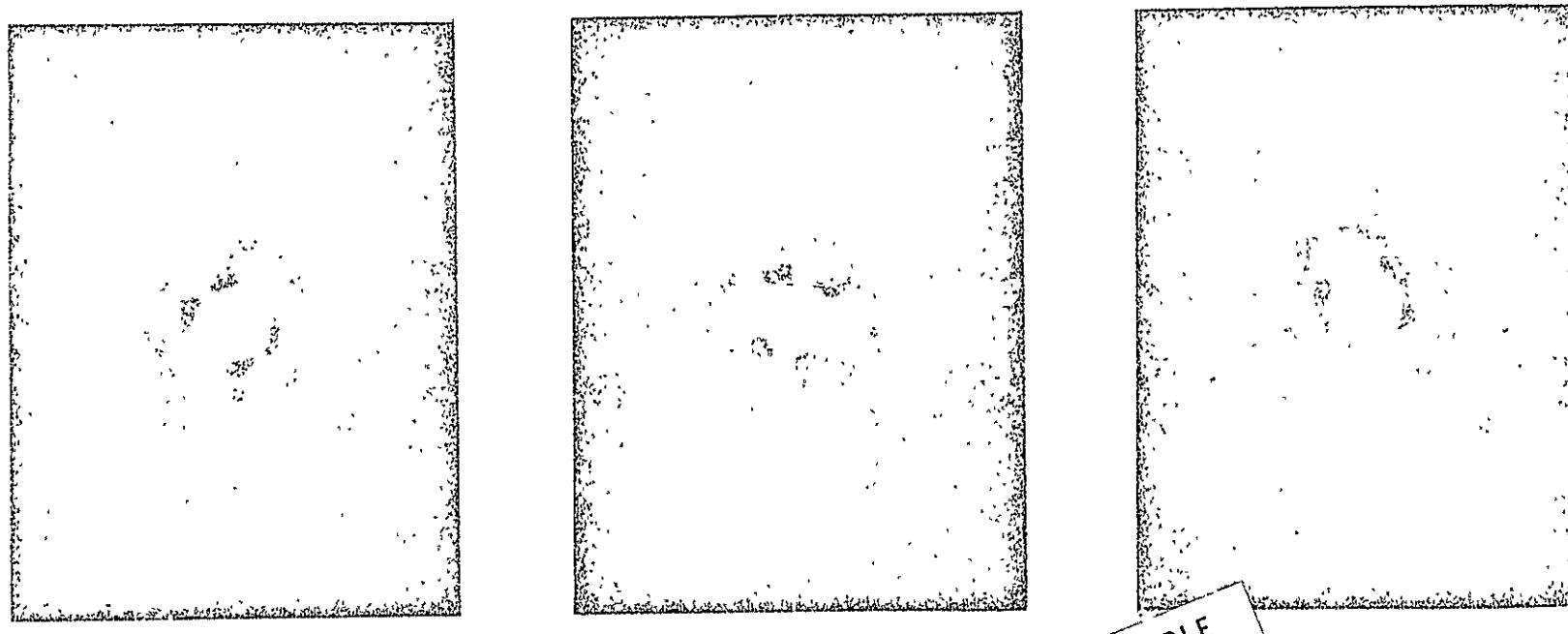

(a) (b) (c)

Fig. 2

Diffraction patterns from 191B at three orientations.

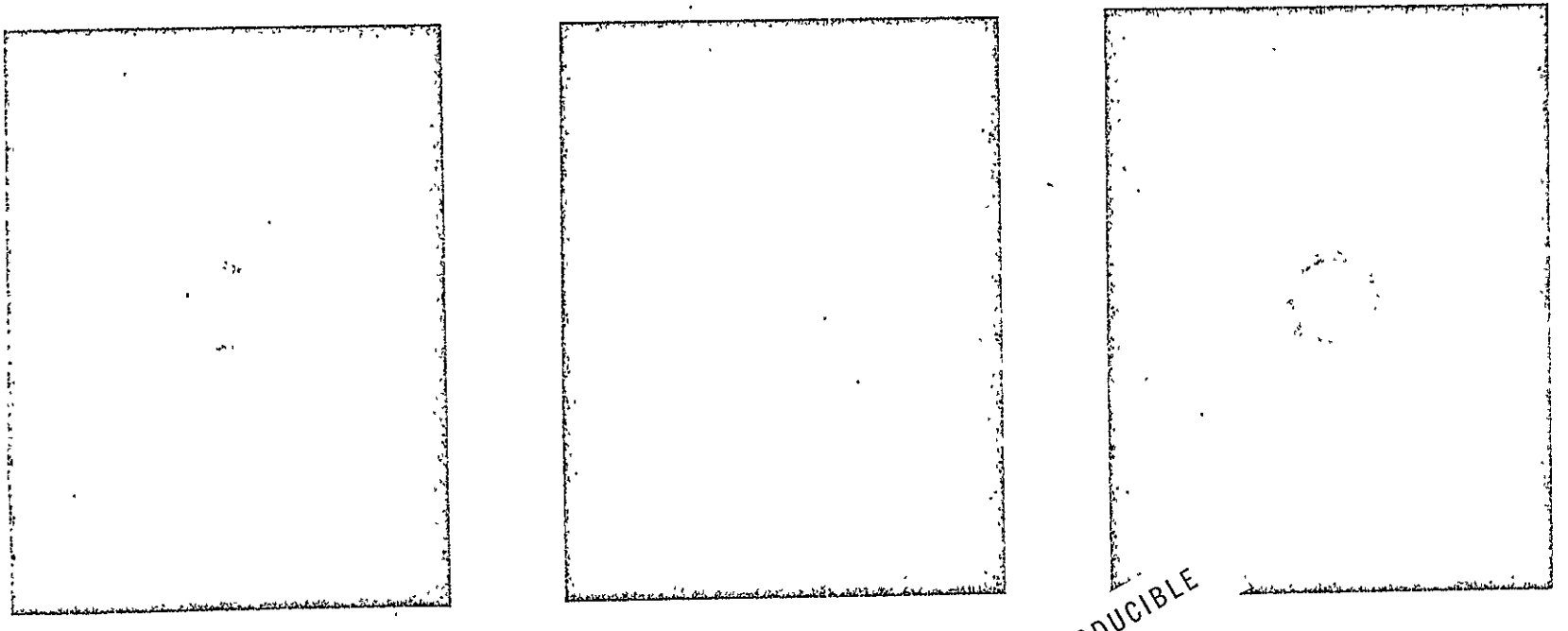

(a) (b) (c)

Fig. 3

(a) Diffraction pattern from 208A.
(b) Diffraction pattern from 190A.
(c) The Airy pattern from a flat mirror with 1.5" circular aperture.

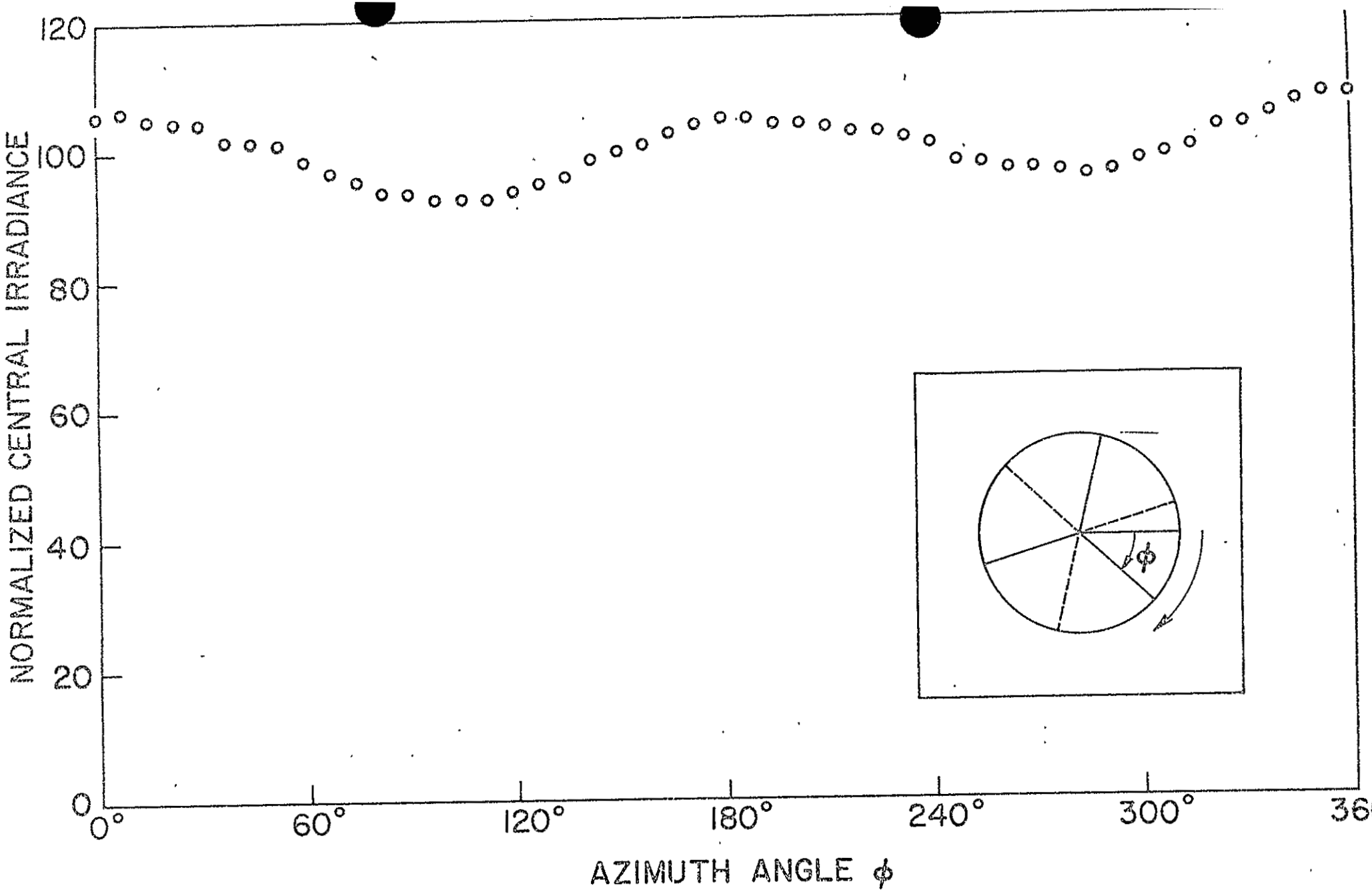

Fig. 4

Normalized central irradiance of the diffraction pattern from 191B as function of the azimuth angle ϕ.

APPENDIX 6

Experimental Studies on the Central Irradiance of Diffraction Pattern of Retro-Reflectors for Off-Axis Incidence of Light

R. F. Chiang

and

W. J. Scott

EXPERIMENTAL STUDIES ON THE CENTRAL IRRADIANCE OF DIFFRACTION PATTERN OF RETRO-REFLECTORS FOR OFF-AXIS INCIDENCE OF LIGHT*

R. F. Chang and W. J. Scott†

Technical Report 70-131

June 1970

UNIVERSITY OF MARYLAND
Department of Physics and Astronomy
College Park, Maryland
20742

*This work was supported by NASA Contract NAS 9-7809 and National Science Foundation Grant GY-5461.

†On leave from Gettysburg College, Gettysburg, Pennsylvania

ABSTRACT

Experimental measurements were made on the central irradiance of the diffraction pattern of a solid fused silica retro-reflector as a function of the incident angle θ at azimuth angles $\phi = 0°$ and $60°$.

We also observed a sinusoidal dependence of the central irradiance of the diffraction pattern on the polarization orientation of the incident light contrary to an early analysis that the central irradiance was independent of the polarization orientation. We believe, at this time, that the abnormality was caused by some flaws in the retro-reflector. Further study is underway to understand this phenomenon.

EXPERIMENTAL STUDIES ON THE CENTRAL IRRADIANCE OF DIFFRACTION PATTERN OF RETRO-REFLECTORS FOR OFF-AXIS INCIDENCE OF LIGHT

I. Introduction.

Comprehensive analyses concerning the far field diffraction pattern of reflected light from a retro-reflector have been made.[1,2] The analyses were undertaken to provide a thorough understanding of the diffraction pattern of retro-reflectors in connection with the design and testing of the Apollo 11 Laser Ranging Retro-Reflector.[3-6]

Because of the libration pattern of the earth viewed from the moon, the laser beam transmitted from the earth must assume different angles of incidence on different days. Therefore, one of the goals of the analyses was to obtain information as to how the central irradiance of the diffraction pattern varies for various angles of incidence. Such information is crucial in estimating the intensity of the returning signal of transmitted laser light.

Experimental work was undertaken along with analyses intended for comparison. We will present, in this report, the findings of the experimental measurements on two retro-reflectors. Their ID numbers are PE101B and BB30B. They are made of fused silica. The front face is a circle of 1.5" diameter. Both are uncoated.

II. Experimental Procedures.

The experimental apparatus basically consists of a He-Ne laser, a spatial filter, a collimator, and a two-meter optical bench. The

arrangement is shown in Figure 1. The light beam from a 15-mW He-Ne laser passes initially through a spatial filter consisting of a 20X microscope objective and 12μ pinhole. The highly diverging light after the spatial filter is collimated first to a beam of roughly one-half inch diameter. This beam passes through a beam splitter and goes into a large collimator. The final collimated beam is 10cm in diameter. A photodiode on the off-side of the beam splitter monitors the laser light intensity during the experiment.

The intensity profile across the laser beam is a Gaussian distribution. In order to obtain a uniform intensity at the reflector the laser beam is expanded twice so that only a small central portion of the Gaussian distribution is used. The variation in the intensity profile is reduced to a few percent. The first stage beam expansion also enables us to use a smaller area of the beam splitter in a collimated portion of the light beam to minimize possible wavefront distortion.

The returning beam from the retro-reflector forms a diffraction pattern at the focal point of the large collimator lens and this image is enlarged by the focusing lens of the collimator. The pattern can be further enlarged with an additional lens system.

A photomultiplier tube is used to measure the central irradiance of the diffraction pattern. A pinhole whose diameter is less than 1/10 of the diameter of the Airy disc of 1.5" aperture is used to mask the photomultiplier tube allowing only the central irradiance to be measured.

Two types of measurement were taken. The central irradiance was measured as a function of the angle of incidence θ at two azimuth angles, i.e.

ϕ= 0° and 60°. It was also measured as a function of ϕ at θ = 0° in steps of 7.5 degrees.

Simple sketches are shown in Figure 2 to illustrate the definitions of ϕ and θ. The azimuth angle ϕ is defined to be the angle between the plane of incidence PP' and the plane determined by the back edge AO and its image OA' as shown in Figure 2(a).

In the measurement of central irradiance as a function of θ, the polarization of incident light was chosen to be parallel to the plane of incidence. For normal incidence (θ = 0°), the plane of incidence was not defined. Therefore, the azimuth angle ϕ was better interpreted as the angle between the direction of the polarization of light and the projection of one of the back edges on the front face of the retro-reflector.

In the measurement of central irradiance as a function of θ, the angle θ is swept from one end (θ = 16°) to the other end (θ = 30°) on the opposite side in the plane of incidence. Because the same plane of incidence is shared by both ϕ = 0° and ϕ = 180° which is geometrically equivalent to 60°, we can obtain the data in one run for both with matched reading at θ = 0°.

III. Results and Discussions.

According to analyses, the central irradiance of the diffraction pattern is independent of the direction of the polarization of the incident light.[1,2] But in the process of the experiment we found that this was not the case. An unexpected polarization effect existed. Therefore, we

proceeded to measure the effect on the central irradiance as a function of ϕ. The results are shown in Figure 3. The solid dots are the data from PE101B whereas the open circles are the data from BB30B.

Three runs were taken on each retro-reflector. Each run consists of forty-nine readings for a complete revolution in steps on 7.5° including overlapping end points. Each reading was first corrected for the monitor reading and all readings of each run were adjusted so that the mean was 100. Then the mean and its standard deviation of the adjusted readings from three runs for a given ϕ was calculated. The error bars in the figure are the standard deviations of the means. When it is smaller than the dot size the error bar is not shown.

The variation in the central irradiance is large, especially so for BB30B. The ratio of the maximum and minimum is more than five. The cause of the variation is unknown at this time. It is suspected to be something very sensitive to polarization effects.

Notice that the variation does not repeat itself every 120° although in principle the retro-reflector has a threefold symmetry. It implies that the flaw has broken such a symmetry in the retro-reflector. However, it repeats itself after 180° of rotation. The repetition is expected because such a rotation corresponds to adding a phase angle of π to the incident light; this addtional phase angle should have no effect on the intensity measurement. In other words, twofold symmetry is manifested here because of such symmetry in the linearly polarized incident light.

One might speculate that the variation in the central irradiance could be caused by the tilt of the front face since we determine,

experimentally, the symmetric axis by the normal of the front face. A simple measurement on BB30B showed that the front face was only about 0.1° off from its proper direction. A deviation of 0.1° is too small to cause any significant variation in irradiance.

Another possible cause is the laminations in the fused silica. The effect of laminations on the diffraction pattern is yet to be investigated. A study is under way to understand the cause of the abnormal polarization effect. Further findings will be reported.

The measurement on the central irradiance as a function of the incident angle θ was complicated by the abnormal polarization effect, especially in the case of BB30B. The inconsistency in readings caused by lack of symmetry is demonstrated in Figure 4. Three sets of data are presumably identical because every back edge can be used as the reference for ϕ. All readings were corrected for fluctuations in the laser output, which was monitored by a photodiode.

In order to compare with analysis, the average values of readings taken at three supposedly identical orientations are used. The average values are normalized to unity at $\theta = 0°$. The result is shown in Figure 5 where the error bars are the standard deviations of the means. The large error bars are no surprise because of the large discrepancies in the readings at three different orientations as shown in Figure 4. The curve is the prediction of analysis.

A similar result is shown in Figure 6 for PE101B. Because the abnormal polarization effect is smaller in PE101B compared to BB30B, the discrepancy between readings of different orientations is also smaller as indicated by the error bars.

It is interesting to note that the average values in Figure 5 and Figure 6 agree with analysis to a great extent disregarding the large discrepancies between the readings taken at different orientations. It is possible that the averaging process canceled, to first order, the abnormal polarization effect. The close agreement between the data from PE101B and BB30B seems to suggest such a possiblity.

IV. Conclusions.

Both retro-reflectors under study exhibited an abnormal polarization effect which is manifested by the dependence of the central irradiance of the diffraction pattern on the orientation of the linear polarization of incident light at normal incidence. The origin of this effect is unknown at this time. A study is underway to understand such a phenomenon.

The central irradiance when measured as a function of the angle of incidence θ, the average of readings over three theoretically identical orientations is in agreement with analysis, though there are discrepancies in readings among the different orientations.

ACKNOWLEDGMENTS

We are grateful to Dr. C. O. Alley and Dr. D. G. Currie for their fruitful suggestions and discussions. We also wish to acknowledge the assistance of Burton Johnson and Rita Foster in the early phase of this work.

REFERENCES

1. C. O. Alley, R. F. Chang, D. G. Currie, and M. E. Pittman, to be published in J. Opt. Soc. Am. April (1971); University of Maryland, Department of Physics and Astronomy Technical Report 70-104 (1970).

2. R. F. Chang, University of Maryland, Department of Physics and Astronomy Technical Report 70-129 (1970).

3. C. O. Alley, P. L. Bender, R. F. Chang, D. G. Currie, R. H. Dicke, J. E. Faller, W. M. Kaula, G. J. F. MacDonald, J. D. Mulholland, H. H. Plotkin, S. K. Poultney, D. T. Wilkinson, I. Winer, W. Carrion, T. Johnson, P. Spadin, L. Robinson, E. J. Wampler, D. Wieber, E. C. Silverberg, C. A. Steggerda, J. V. Mullendore, J. D. Rayner, W. Williams, B. Warner, H. Richardson, and B. W. Bopp, Apollo 11 Preliminary Science Report, SP-214, 163 (1969).

4. C. O. Alley, R. F. Chang, D. G. Currie, J. V. Mullendore, S. K. Poultney, J. D. Rayner, E. C. Silverberg, C. A. Steggerda, H. H. Plotkin, W. Williams, B. Warner, H. Richardson, B. W. Bopp, Science 167, 368 (1970).

5. C. O. Alley, R. F. Chang, D. G. Currie, S. K. Poultney, P. L. Bender, R. H. Dicke, D. T. Wilkinson, J. E. Faller, W. M. Kaula, G. J. F. MacDonald, J. D. Mulholland, H. H. Plotkin, W. Carrion, and E. J. Wampler, Science 167, 458 (1970).

6. J. E. Faller, I. Winer, W. Carrion, T. S. Johnson, P. Spadin, L. Robinson, E. J. Wampler, and D. Wieber, Science 166, 99 (1969).

FIGURE CAPTIONS

Fig. 1 - Experimental arrangement.

Fig. 2 - Definitions of the angle of incidence θ and the azimuth angle ϕ.

Fig. 3 - The normalized central irradiance measured as a function of azimuth angle ϕ.

Fig. 4 - The central irradiance of diffraction pattern measured as a function of the angle of incidence θ for $\phi = 0°$ and 60° on BB30B at three supposedly identical orientations.

Fig. 5 - The normalized central irradiance of diffraction pattern measured as a function of the angle of incidence θ for $\phi = 0°$ and 60° on BB30B.

Fig. 6 - The normalized central irradiance of diffraction pattern measured as a function of the angle of incidence θ for $\phi = 0°$ and 60° on PE101B.

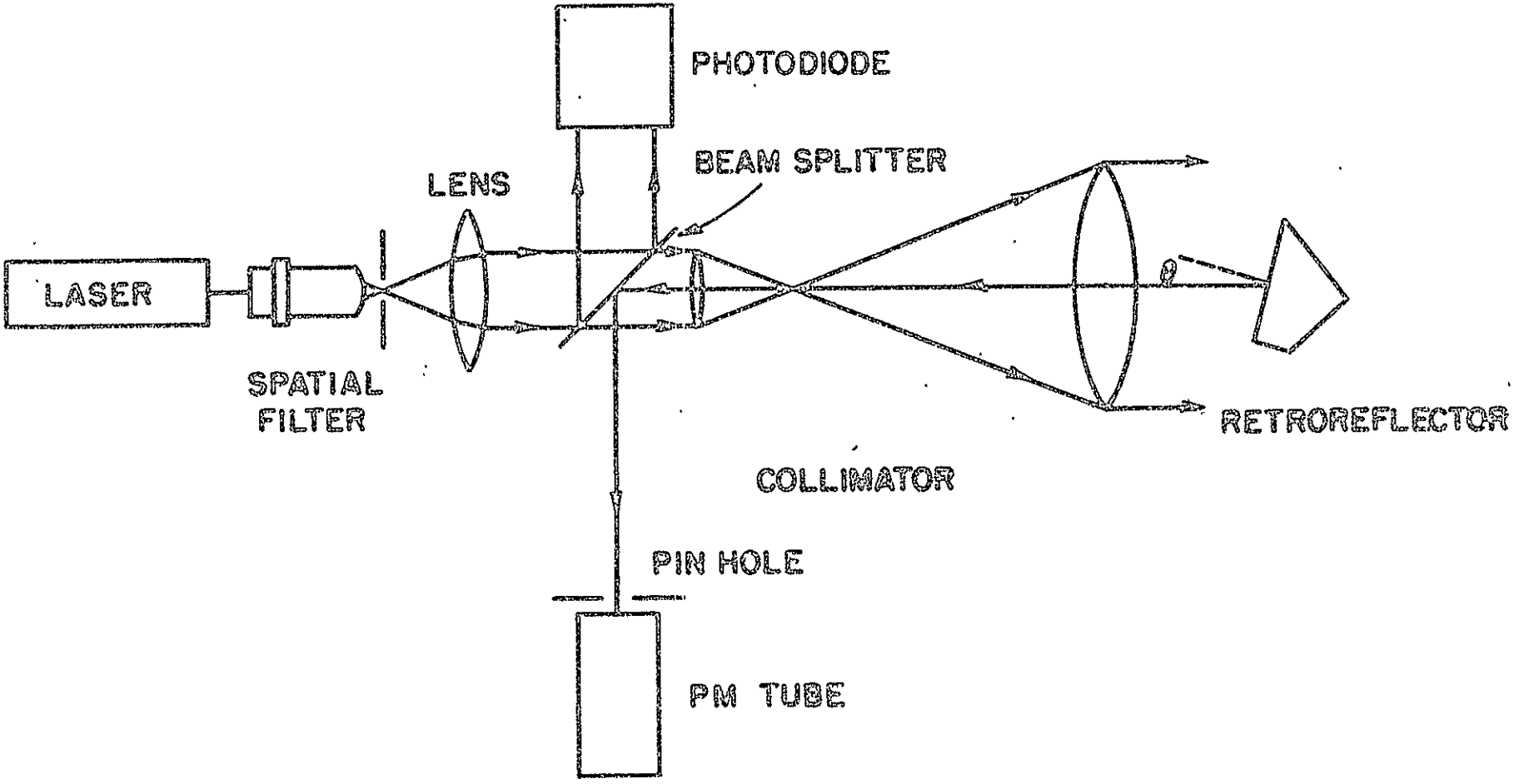

Fig. 1

Experimental arrangement.

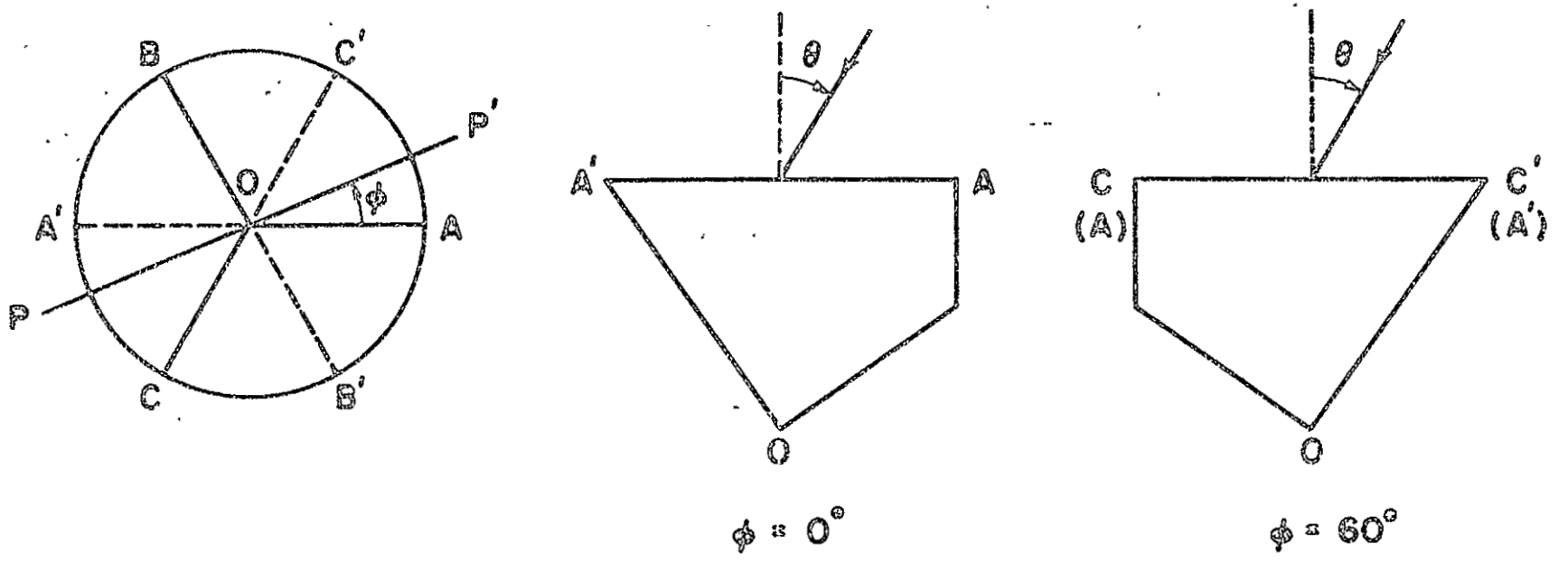

Fig. 2

Definitions of the angle of incidence θ and the azimuth angle φ.

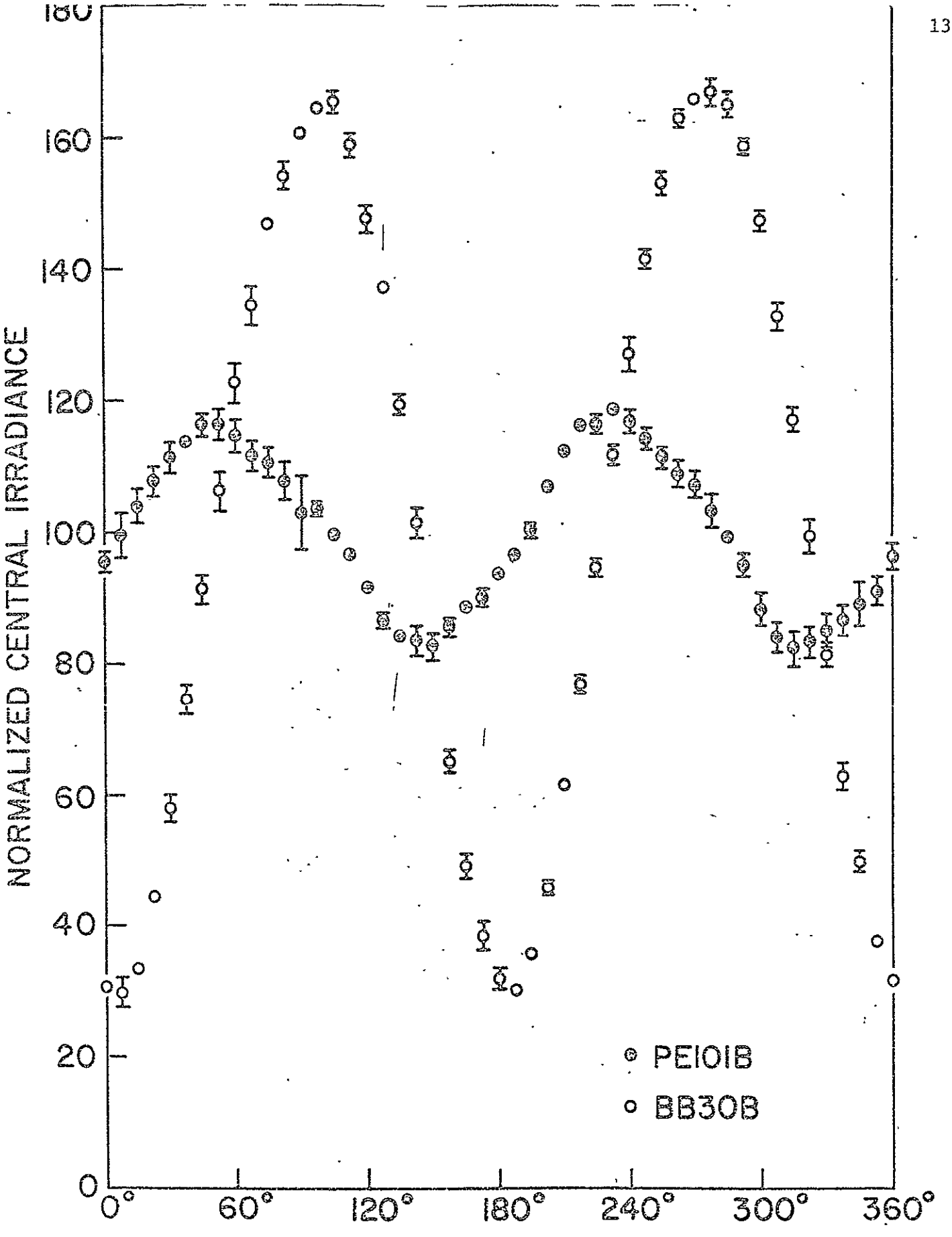

Fig. 3

The normalized central irradiance measured as a function of azimuth angle ϕ.

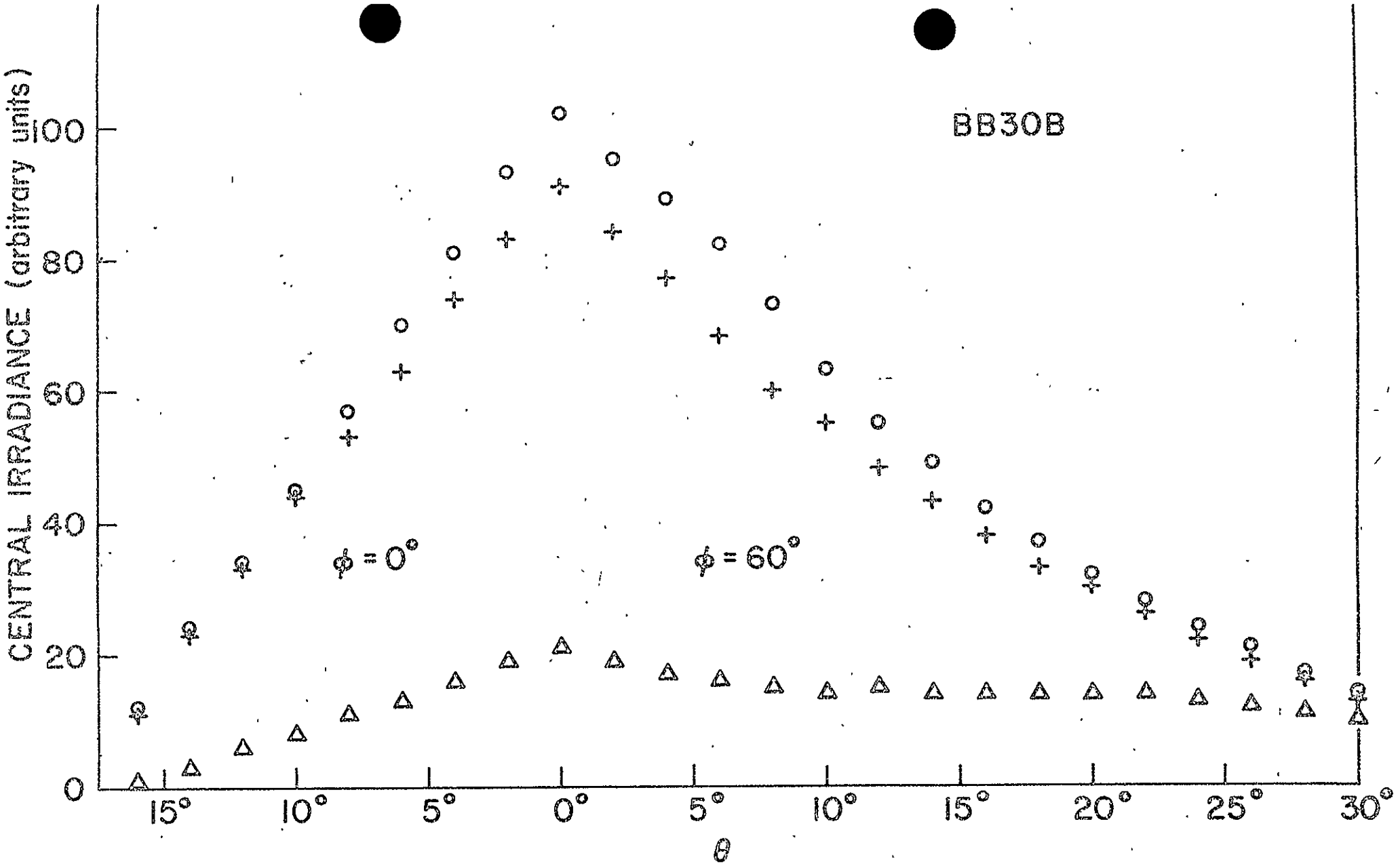

Fig. 4

The central irradiance of diffraction pattern measured as a function of the angle of incidence θ for $\phi = 0°$ and 60° on BB30B at three supposedly identical orientations.

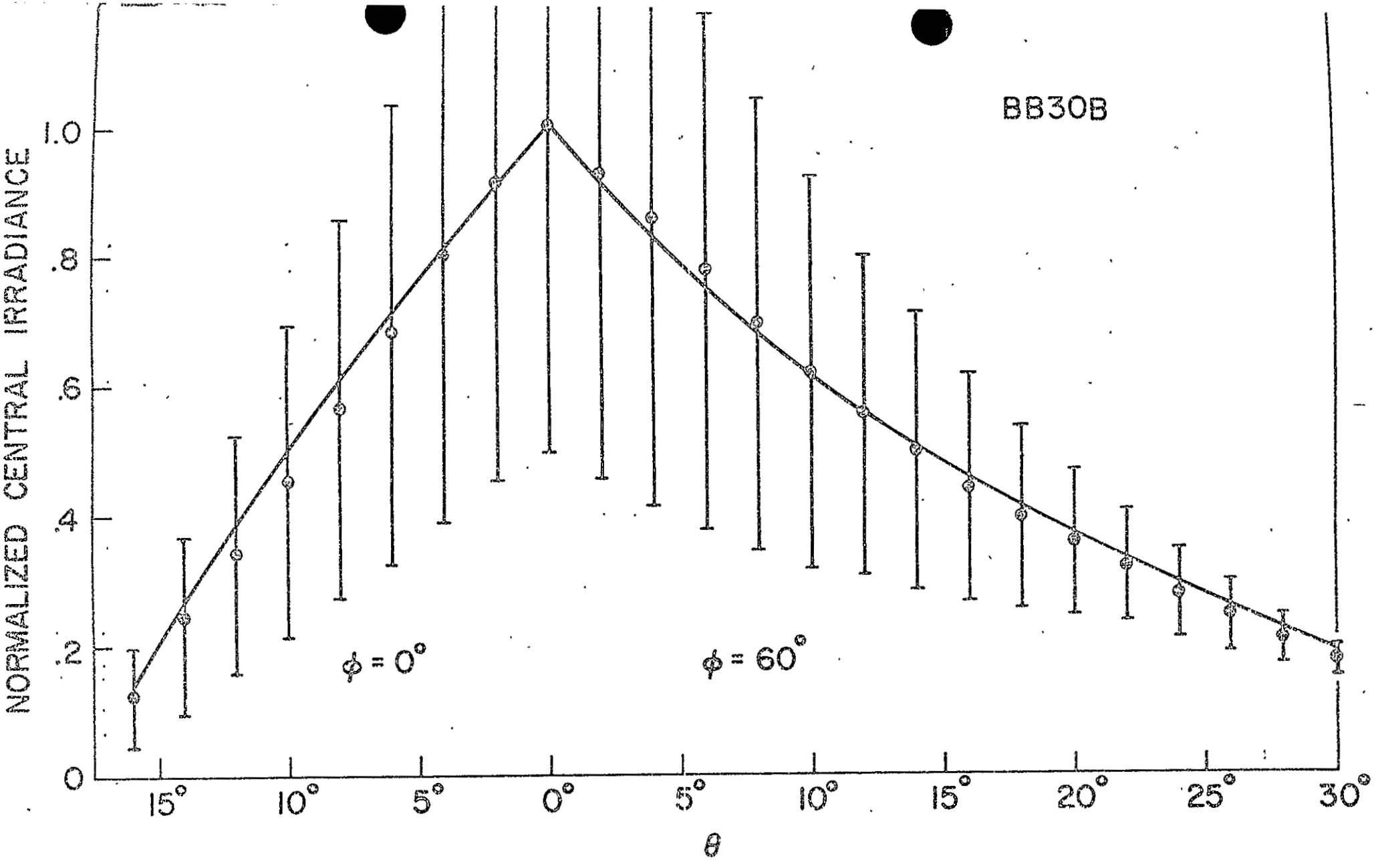

Fig. 5

The normalized central irradiance of diffraction pattern measured as a function of the angle of incidence θ for ϕ = 0° and 60° on BB30B.

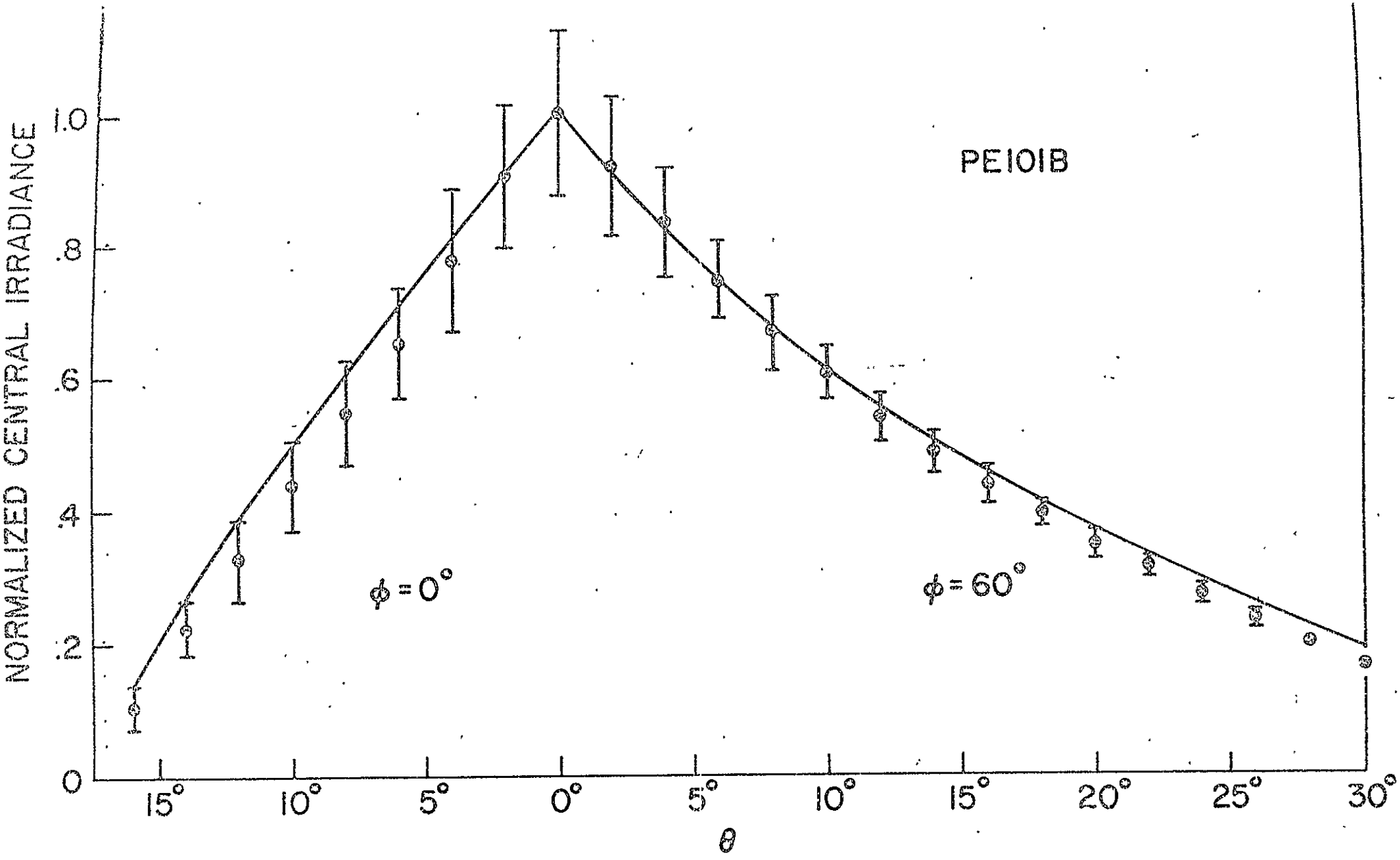

Fig. 6

The normalized central irradiance of diffraction pattern measured as a function of the angle of incidence θ for $\phi = 0°$ and $60°$ on PE101B.

APPENDIX 7

Effects of Small Angular Errors in Retroreflectors on the Far Field Diffraction Pattern

R. F. Chang

EFFECTS OF SMALL ANGULAR ERRORS IN RETROREFLECTORS ON THE FAR FIELD DIFFRACTION PATTERN

R. F. Chang

TECHNICAL REPORT NO. 71-041

October 1970

This research was supported by

NASA Grant NAS 9-7809

UNIVERSITY OF MARYLAND

Department of Physics and Astronomy

College Park, Maryland

ABSTRACT

We have examined the effects of small errors in a retroreflector on the diffraction pattern with emphasis on erroneous back angles.

The central irradiance of the diffraction pattern depends upon the orientation of polarization relative to the retroreflectors for a linearly polarized incident monochromatic light wave. This effect is most prominent in an uncoated retroreflector. A variation of about ±70% from the mean central irradiance may occur if the error is about 1 second of arc in one of the back angles in a solid uncoated quartz retroreflector whose front face is 38mm in diameter.

The unexpected side-lobes in the diffraction pattern of a metalized retroreflector are also shown to be attributable to the errors in the back angles.

The effects of other types of error are also discussed.

Index Headings: Diffraction, Retroreflectors.

I. Introduction

Because of the retrodirective nature, the applications of retroreflectors can be found in a wide range of field from optical interferometry [1,2] to highway marking. Especially in recent years, in conjunction with lasers, retroreflectors are used in ranging of the distance to far away points. The recent Apollo 11 Laser Ranging Retroreflector experiment [3,4,5,6] measures earth-moon distances with high precision.

The thorough understanding of the far field diffraction pattern of a retroreflector becomes highly essential for applications in long-distance ranging experiments. We have previously analyzed effects of the complicated polarization properties of geometrically perfect retroreflectors[7] on the far field diffraction pattern[8]. However, in practice, geometrically perfect retroreflectors are not easy to obtain at the present time, and in some applications deliberately introduced error is desired. Therefore, the understanding of the effects from various types of error becomes also important in system design.

In this report, we attempt to deal with the most common type of error, which is the deviation from 90° of the angles between two reflecting surfaces. The geometry of this type of error has been reported some years ago[9,10]. We will now extend the examination of the effects of small angular errors of about one second of arc to the far field diffraction pattern. In addition to the effects of erroneous angles, we would also examine the effects of all types of error in retroreflectors.

Although our approach can be applied to more general conditions, we will consider mainly a solid retroreflector with a circular front face. The incident light is assumed to be a linearly polarized monochromatic plane wave which enters the reflector along the direction parallel to the axis of symmetry. We will discuss in details the case of a single erroneous angle as an illustration.

We will start discussing in Section II the diffraction integral which takes into account the additional phase factors resulting from various errors. In Section III, we will consider the special case when the retroreflector is coated with metal on the back surfaces and present a qualitative comparison between the analysis and a photograph of diffraction pattern of an aluminized retroreflector. In Section IV, we will present discussions of the results with emphasis on the comparison between the experimental data and analysis. A summary and comment is in section V.

II. Diffraction Integral for Central Irradiance

The front view of a retroreflector is divided into six equal subapertures. Each subaperture represents an unique sequence of back surfaces by which a ray is reflected as it travels through the reflector. In the case of a geometrically perfect retroreflector, the reflected light is parallel to the axis of symmetry when the incident light is parallel to the axis of symmetry except the incident light and the reflected light are in opposite directions.

Let us now consider the case of only one erroneous angle in a retroreflector. If we assume that the angle between the surfaces II and III (see Fig. 1) is $90°+\theta$ where θ is the small error in the angle along OA. Then it has been shown[9] that the reflected light emerging from the subapertures 1, 2, and 3 will deviate upward from the axial direction by an angle of $1.63N\theta$, where N is the index of refraction of the glass, whereas the light emerging from the subapertures 4, 5, and 6 will deviate downward by the same amount.

Therefore, there is a systematic phase lag along the vertical axis (q axis) in the wave front in the aperture plane which is taken just outside the front face of the retroreflector. The phase factor can be represented by $e^{ik\alpha|q|}$ where k is the wave number and $\alpha = 1.63N\theta$.

Because of the complicated polarization properties of retroreflectors, the emerging light from different subapertures is in different states.

The errors in the angles under consideration are on the order of 10^{-5} radians which is negligible as far as the polarization effects on the

state of emerging light is concerned. Therefore, the normalized complex amplitudes derived for geometrically perfect retroreflectors are still valid. It has been shown that when the incident light is linearly polarized the normalized complex amplitudes are[11],

$$\gamma_1^p = \gamma_4^p = \xi - \sqrt{1/2}\,\eta \cos(2\phi) - \sqrt{3/2}\,\eta \sin(2\phi), \tag{1.a}$$

$$\gamma_2^p = \gamma_5^p = \xi + \sqrt{2}\,\eta \cos(2\phi), \tag{1.b}$$

$$\gamma_3^p = \gamma_6^p = \xi - \sqrt{1/2}\,\eta \cos(2\phi) + \sqrt{3/2}\,\eta \sin(2\phi), \tag{1.c}$$

$$\gamma_1^s = -i\zeta - \sqrt{1/2}\,\eta \sin(2\phi) + \sqrt{3/2}\,\eta \cos(2\phi), \tag{1.d}$$

$$\gamma_2^s = i\zeta + \sqrt{2}\,\eta \sin(2\phi), \tag{1.e}$$

$$\gamma_3^s = -i\zeta - \sqrt{1/2}\,\eta \sin(2\phi) - \sqrt{3/2}\,\eta \cos(2\phi), \tag{1.f}$$

$$\gamma_4^s = i\zeta - \sqrt{1/2}\,\eta \sin(2\phi) + \sqrt{3/2}\,\eta \cos(2\phi), \tag{1.g}$$

$$\gamma_5^s = -i\zeta + \sqrt{2}\,\eta \sin(2\phi), \tag{1.h}$$

$$\gamma_6^s = i\zeta - \sqrt{1/2}\,\eta \sin(2\phi) - \sqrt{3/2}\,\eta \cos(2\phi), \tag{1.i}$$

where the superscript p (or s) denotes component having the same (or cross) polarization with respect to the polarization of incident light, and the polarization angle ϕ is the angle between the direction of the polarization of incident light and the projection of OA on the front face in Fig. 1. The coefficients ξ, η and ζ are[8]

$$\xi = (r_s - r_p)[3(r_s + r_p)^2 - 2(r_s - r_p)^2]\ /16, \qquad (2.a)$$

$$\eta = \sqrt{2}\ (r_s + r_p)^3/16, \qquad (2.b)$$

$$\zeta = -\,i\ \sqrt{3}\ (r_s + r_p)^2\ (r_s - r_p)/16, \qquad (2.c)$$

where r_s and r_p are the conventional complex coefficients of reflectance of the back surfaces.

The diffraction integral, which is normalized to unity at the origin in the diffraction field for a circular aperture of radius a, can be written for polarization p component in polar corrdinates as[12]

$$U_p(x,\psi) = \frac{1}{\pi} \int_0^1 \rho\, d\rho \sum_{j=1}^{6} \int_{(j-1)\pi/3}^{j\pi/3} \gamma_j^p\ e^{iy\rho|\sin\theta|} e^{-ix\rho\cos(\theta-\psi)}\, d\theta, \qquad (3)$$

where $x = kaw$, $y = ka\alpha$, w is the sine of the angular radius and ψ is the angular coordinate. The diffraction integral for cross polarization is the same as Eq. (3) except the index p is replaced by s.

Although Eq. (3) can be evaluated to yield an analytical expression of the diffraction pattern, we do not intend to do so. Experimental observations indicated that within the range of angular errors under consideration the pattern remains basically the same. The significant effect was observed in the sensitivity of the central irradiance on the polarization angle, ϕ, of incident light in contrary to the conclusion for a geometrically perfect retroreflector[8] that the central irradiance was not a function of ϕ.

The analytical expression of central irradiance of the diffraction pattern can be obtained from Eq. (3) for x = 0, and we have

$$U_p(0) = \frac{2}{\pi} \int_0^1 \rho d\rho \int_{(j-1)\pi/3}^{j\pi/3} \sum_{j=1}^{3} \gamma_j^p \, e^{iy\rho\sin\theta} \, d\theta, \tag{4}$$

since $\gamma_{j+3}^p = \gamma_j^p$ for j = 1, 2, and 3.

In order to evaluate Eq. (4), we can expand the exponential function in terms of Bessel functions,[13]

$$e^{iz \sin \theta} = J_0(z) + 2 \sum_{n=1}^{\infty} J_{2n}(z)\cos 2n\theta + i2 \sum_{n=0}^{\infty} J_{2n+1}(z)\sin(2n+1)\theta, \tag{5}$$

and then expand each Bessel function into a power series,

$$J_n(z) = \sum_{m=0}^{\infty} \frac{(-)^m (z/2)^{2m+n}}{m! \; (m+n)!} \tag{6}$$

After integrating Eq. (4), we obtain

$$U_p(0) = \xi[2J_1(y)/y + iA(y)] - \eta[B(y) + iC(y)] \cos(2\phi), \tag{7}$$

$$\text{where } A(y) = \frac{12\sqrt{2}}{\pi} \sum_{n=1}^{\infty} \sin(2n\pi/3) \sum_{m=0}^{\infty} \frac{(-)^m (y/2)^{2m+2n}}{m!\,(m+2n)!\,(2m+2n+2)\,(2n)}, \tag{8.a}$$

$$B(y) = \frac{4\sqrt{2}}{\pi} \sum_{n=0}^{\infty} [1 - 3\cos(2n+1)\pi/3] \sum_{m=0}^{\infty} \frac{(-)^m (y/2)^{2m+2n+1}}{m!\,(m+2n+1)!\,(2m+2n+3)\,(2n+1)}, \tag{8.b}$$

$$C(y) = \frac{8}{\pi} \sum_{n=0}^{\infty} \sum_{m=0}^{\infty} \frac{(-)^m (y/2)^{2m+2n+1}}{m!\,(m+2n+1)!\,(2m+2n+3)\,(2n+1)}. \tag{8.c}$$

The s component (cross polarization) can be obtained similarly,

$$U_s(0) = -\eta\,[B(y) + iC(y)]\sin(2\phi). \tag{9}$$

The total irradiance at the origin is then the sum of the individual irradiance of each polarization component and we have

$$I_0(\phi) = |\xi|^2 D_0(y) + |\eta|^2 D_1(y) - [(\xi^*\eta + \xi\eta^*)D_2(y) - i(\xi^*\eta - \xi\eta^*)D_3(y)]\cos(2\phi) \tag{10}$$

where $$D_0(y) = [2J_1(y)/y]^2 + A^2(y)\,, \tag{11.a}$$

$$D_1(y) = B^2(y) + C^2(y)\,, \tag{11.b}$$

$$D_2(y) = [2J_1(y)/y]B(y) + A(y)C(y)\,, \tag{11.c}$$

$$D_3(y) = A(y)B(y) - [2J_1(y)/y]C(y)\,. \tag{11.d}$$

The functions A(y), B(y), C(y) as well as $2J_1(y)/y$ are plotted in Fig. 2 and the functions $D_0(y)$, $D_1(y)$, $D_2(y)$ and $D_3(y)$ are plotted in Fig. 3 to illustrate how these functions behave.

For the case of three erroneous angles, it has been shown that the reflected light breaks up into six different directions in general. Because of the symmetry in the process of reflection, rays from opposite subapertures deviate from the axial direction also in opposite directions with the same amount [9,10]. Therefore the diffraction integral for the central irradiance is, for the p component,

$$U_p(0) = \frac{2}{\pi}\sum_{j=1}^{3}\gamma_j^p \int_0^1 \rho\,d\rho \int_{(j-1)\pi/3}^{j\pi/3} e^{ika\alpha_j\sin(\theta+\delta_j)}\,d\theta, \tag{12}$$

where δ_j is the angle between the direction of deviation and the q axis, and α_j is the angle of deviation for j-th subaperture.

There are too many parameters in Eq. (12) to yield a compact expression; yet the final form is still a linear combination of γ_j^p and it can be written as

$$U_p(0) = \xi C_1 + \eta C_2 \cos(2\phi) + \eta C_3 \sin(2\phi), \tag{13}$$

where C_1, C_2 and C_3 are complex functions of α_j and δ_j. Similarly, for s component, we have

$$U_s(0) = \eta C_2 \sin(2\phi) - \eta C_3 \cos(2\phi) . \tag{14}$$

Then the total irradiance is

$$I_0(\phi) = H_1 + H_2 \cos[2(\phi-\Delta)] \tag{15}$$

where $H_1 = |\xi|^2|C_1|^2 + |\eta|^2(|C_2|^2 + |C_3|^2)$,

$$H_2 = [(\xi^*\eta C_1^* C_2 + \xi\eta^* C_1 C_2^*)^2 + (\xi^*\eta C_1^* C_3 + \xi\eta^* C_1 C_3^*)^2]^{1/2},$$

and

$$\Delta = 1/2 \tan^{-1}[(\xi^*\eta C_1^* C_3 + \xi\eta^* C_1 C_3)/(\xi^*\eta C_1^* C_2 + \xi\eta^* C_1 C_2^*)].$$

Except an extra residual phase angle Δ, Eq. (15) has the same basic form as Eq. (10).

In general, other than errors in the angles, there are different types of error such as inhomogeneity in the material, departures from flatness of surfaces, variations in the index of refraction caused by thermal gradients, and so on. We can describe the resulting wave-front

distortion with an extra phase factor that is a function of position in the aperture plane. Under the conditions that the flaws do not affect the normalized complex amplitudes in Eq. (1) appreciably, we can generalize Eq. (12) and obtain

$$U_p(0) = \frac{2}{\pi} \sum_{j=1}^{3} \gamma_j^p \int_0^1 \rho d\rho \int_{(j-1)\pi/3}^{j\pi/3} e^{if(\rho,\theta)} d\theta, \tag{16}$$

where $f(\rho,\theta)$ is the phase error in the aperture plane.

The central irradiance resulted from Eq. (16) has the same form as Eq. (15) and its sinusoidal dependence on the polarization angle still remains true. The constants C_1, C_2 and C_3 can be evaluated if $f(\rho,\theta)$ is either known analytically or numerically.

III. Diffraction Integral for Metalized Retroreflectors

As mentioned in a previous report[8], the coefficients $|\eta|$ and $|\zeta|$ are much less than $|\xi|$ for the case of silvered or aluminized retroreflectors. Therefore, we can neglect η and ζ in Eq. (1) and the diffraction integral in Eq. (3) becomes

$$U(x,\psi) = \frac{\xi}{\pi}\int_0^1 \rho d\rho \left[\int_0^{\pi} e^{iy\rho \sin\theta} e^{-ix\rho\cos(\theta-\psi)} d\theta + \int_{\pi}^{2\pi} e^{-iy\rho\sin\theta} e^{-ix\rho\cos(\theta-\psi)} d\theta\right]. \quad (17)$$

By changing the variable and expanding exponential functions into Bessel functions and then expanding each Bessel function into power series as before we can evaluate Eq. (17) and obtain[14]

$$U(x,\psi) = \xi\{ J_1(x_1)/x_1 + J_1(x_2)/x_2 + i[E(x_1,\psi_1) - E(x_2,\psi_2)]\} \quad (18)$$

where $x_1 = (x^2 + 2xy\sin\psi + y^2)^{1/2}$,

$x_2 = (x^2 - 2xy\sin\psi + y^2)^{1/2}$,

$\psi_1 = \tan^{-1}\left(\dfrac{x\sin\psi + y}{x\cos\psi}\right)$,

$\psi_2 = \tan^{-1}\left(\dfrac{x\sin\psi - y}{x\cos\psi}\right)$, and

$$E(x,\psi) = \frac{4}{\pi}\sum_{n=0}^{\infty}(-)^n \sin(2n+1)\psi \sum_{m=0}^{\infty}\frac{(-)^m (x/2)^{2m+2n+1}}{m!(m+2n+1)!(2m+2n+3)(2n+1)}.$$

Eq. (18) can be readily evaluated for various error parameters y. As an example, a contour plot of Eq. (18) is presented in Fig. 4 for y=1.

We also present, in Fig. 5, a photograph of diffraction pattern from an aluminized retroreflector which is made of fused silica. The circular front face of the reflector is 3.8 cm in diameter. There is a strong agreement between the plot and the photograph.

IV. Discussion

Let us first review Eq. (11) in Section II and examine the dependence of functions D_0, D_1, D_2, and D_3 on the error parameter y. For a small y, the leading term in D_0, D_1 and D_2 is quardratic in y whereas it is linear in D_3. Therefore, in the case of an uncoated retroreflector where $|\xi| \simeq |\eta|$ the effect of polarization angle on the central irradiance becomes very significant. As an example, we have written Eq. (10) in the form

$$I_0 = |\xi|^2 (I_1 + I_2 \cos 2\phi) \tag{19}$$

and plotted I_1 and I_2 as functions of y in Fig. 6. The index of refraction is taken to be 1.4571. It is also worth mentioning that for uncoated retroreflectors $\xi^*\eta + \xi\eta^* \equiv 0$, and I_2 is consequently D_3 with an appropriate coefficient. Furthermore, D_0, D_1 and D_2 are even functions of y whereas D_3 is an odd function of y, the reversal of the sign of the error in the angle would result in the reversal of the sign of I_2; therefore by observing the sign of I_2 one can also determine the sign of error. The error parameter itself can be extracted from experimental measurements by taking the ratio of the variational amplitude and the mean and comparing that with I_2/I_1 which is plotted as a function of y in Fig. 7.

The result from an experimental measurement on the central irradiance as a function of polarization angle ϕ is presented in Fig. 8. The circular dots are the experimental data whose standard deviation is about the size of the dot. The best fit analytical expression, shown as the solid curve, is

$$I_0 = 1. - 0.68 \cos[2(\phi+5.28^\circ)] \tag{20}$$

The retroreflector is made of fused silica and its circular front face is 3.8 cm in diameter. The actual error parameters of the reflector are unknown because the errors under consideration are too small to be resolved with presently available technique. Approximating the error to be a single angular error, the comparison between 0.68 in Eq. (20) and the curve in Fig. 7 indicates that the error parameter is about 2.2 which corresponds to about one second of arc of error in one of the back angles.

For the case of a metalized retroreflector, the effect of polarization angle on the central irradiance is greatly reduced because $|\eta| << |\xi|$. But on the other hand, the deviation of the total diffraction pattern from Airy pattern becomes obvious as indicated by the contour of Fig. 4 for y=1. A photograph of the diffraction pattern of an aluminized retroreflector is shown in Fig. 5. The error parameter of the retroreflector is also unknown for the same reason as mentioned before, but the resemblance seems to indicate a possibility that the error in the reflector is predominantly in one of the angles.

Additionally, the best fit analytical expression of the experimental measurement of the same retroreflector before aluminization is

$$I_0 = 1 + .39 \cos 2(\phi - 7.7^\circ). \tag{21}$$

Intuitively one feels that the small residual phase angle also seems to indicate the consistency with the diffraction pattern analysis.

For a general case as described in Eq. (16), when $f(\rho,\theta)$ is very small so that we can expand the exponential function into a power series to second order, then the constants C_1, C_2 and C_3 in Eq. (15) can be expressed as functions of means and mean squares of $f(\rho,\theta)$ in the aperture plane and we have

$$C_1 = (1 - \langle f^2\rangle/2\ ) + i\langle f\rangle\ , \tag{22.a}$$

$$C_2 = \sqrt{(1/2)}[\ (\langle f^2\rangle - \langle f^2\rangle_2)/2 - i(\langle f\rangle - \langle f\rangle_2)]\ , \tag{22.b}$$

$$C_3 = \sqrt{(1/6)}[\ (\langle f^2\rangle_1 - \langle f^2\rangle_3)/2 - i\ (\langle f\rangle_1 - \langle f\rangle_3)]\ , \tag{22.c}$$

where $\langle\ \rangle$ denotes the average over the whole aperture and $\langle\ \rangle_j$ denotes the average over the j-th subaperture. Notice that $|C_1|^2$ is equal to unity less the variance of $f(\rho,\theta)$ in the aperture plane just as expected of a single aperture diffraction.

When H_1 and H_2 in Eq. (15) are expressed in terms of the means and the mean squares of $f(\rho,\theta)$, the leading terms of the phase error in H_1 are quadratic (mean squares and squares of mean) in $f(\rho,\theta)$, whereas they are linear (means) in H_2. The results are consistent with Eq. (10) that is the result of an error in one of the angles.

Also note that the dependence of the central irradiance on the polarization angle ϕ vanishes when the phase error is not a function of θ, and Eq. (16) reduces to the same expression derived for a single aperture

$$I_0 = |\xi|^2 \left| \int_0^1 e^{if(\rho)}\ d(\rho^2) \right|^2 . \tag{23}$$

V. Summary and Comment

We have examined in detail the effects of one angular error in a retroreflector on the far field diffraction pattern. The central irradiance of the diffraction pattern has been shown to have cosine dependence on twice the polarization angle in addition to a constant term for a given angular error. The cosine dependence is also true for the more general case where all possible errors are taken into account. The variational effect in central irradiance is most significant for uncoated retroreflectors and negligible for aluminized or silvered ones.

The diffraction pattern of an aluminized retroreflector is basically an Airy pattern except there are two additional side-lobes located on the opposite side of the central disc for the case of only one erroneous back angle.

Finally, for those who are interested in the design of a reflector array for long-distance ranging, we might comment that the total return signal should not depend greatly on the orientation of the polarization of the incident light when there are a large number of retroreflectors in the array. Because each retroreflector maximizes its central irradiance at a polarization orientation different from that of another retroreflector, there is a tendency that the additional sinusoidal term to the mean in Eq. (15) will cancel out each other. Therefore the performance of an array is mainly determined by the mean performance of the individual retroreflector in the array.

Footnotes

1. E. R. Peck, J. Opt. Soc. Am. 38, 1015 (1948).

2. P. Rabinowitz, S. F. Jacobs, T. Shultz and G. Gould, J. Opt. Soc. Am. 52, 452 (1962).

3. C. O. Alley, R. F. Chang, D. G. Currie, J. V. Mullendore, S. K. Poultney, J. D. Rayner, E. C. Silverberg, C. A. Steggerda, H. H. Plotkin, W. Williams, B. Warner, H. Richardson, and B. W. Bopp, Science 167, 368 (1970).

4. C. O. Alley, R. F. Chang, D. G. Currie, S. K. Poultney, P. L. Bender, R. H. Dicke, D. T. Wilkinson, J. E. Faller, W. M. Kaula, G. J. F. MacDonald, J. D. Mulholland, H. H. Plotkin, W. Carrion, and E. J. Wampler, Science 167, 458 (1970).

5. C. O. Alley, P. L. Bender, R. F. Chang, D. G. Currie, R. H. Dicke, J. E. Faller, W. M. Kaula, G. J. F. MacDonald, J. D. Mulholland, H. H. Plotkin, S. K. Poultney, D. T. Wilkinson, Irvin Winer, Walter Carrion, Tom Johnson, Paul Spadin, Lloyd Robinson, E. Joseph Wampler, Donald Wieber, E. C. Silverberg, C. A. Steggerda, J. V. Mullendore, J. D. Rayner, W. Williams, Brian Warner, Harvey Richardson, and B. W. Bopp, Apollo 11 Preliminary Science Report, SP-214, 163 (1969).

6. J. E. Faller, Irving Winer, Walter Carrion, Thomas S. Johnson, Paul Spadin, Lloyd Robinson, E. J. Wampler, and Donald Wieber, Science 166, 99 (1969)

7. E. R. Peck, J. Opt. Soc. Am. 52, 253 (1962).

8. R. F. Chang, D. G. Currie, C. O. Alley, and M. E. Pittman, to be published in J. Opt. Soc. Am. April (1971); University of Maryland, Department of Physics and Astronomy Technical Report 70-104 (1970).

9. P. R. Yoder, Jr., J. Opt. Soc. Am. 48, 496 (1958).

10. N. E. Rityn, Sov. J. Opt. Tech. 1, 198 (1968).

11. These equations were derived in Ref. 8 except the reference line for the incident polarization here is different from that of Ref. 8.

12. M. Born and E. Wolf, Principles of Optics, Second Revised Edition, p. 395 (MacMillan Company, New York, 1964).

13. Abramowitz and Stegun, Handbook of Mathematical Functions, (Dover, New York, 1965).

14. This is essentially superimposing two diffraction patterns of half-circles; see A. I. Mahan, C. V. Bitterli and S. M. Cannon, J. Opt. Soc. Am. 54, 721 (1964).

Figure Captions

Fig. 1 The front view of a retroreflector with a circular front face. The polarization angle ϕ is the angle between the projection of OA and the direction of polarization of the incident light.

Fig. 2 Functions A(y), B(y), C(y) and $2J_1(y)/y$.

Fig. 3 Functions $D_0(y)$, $D_1(y)$, $D_2(y)$ and $D_3(y)$.

Fig. 4 Contour lines of the diffraction pattern of a metalized retroreflector with one erroneous back angle. The error parameter is taken to be 1.

Fig. 5 Photograph of the diffraction pattern of an aluminized retroreflector.

Fig. 6 The analytical expression of the mean, I_1, and the variational amplitude I_2 of the central irradiance of the diffraction pattern of an uncoated solid retroreflector with single erroneous angle are plotted as functions of error parameter y for $\alpha>0$. The index of refraction of the retroreflector is assumed to be 1.4571.

Fig. 7 The ratio I_2/I_1 is plotted as a function of y for $\alpha>0$.

Fig. 8 Comparison between the best fit curve and the experimental data of central irradiance as a function of polarization angle ϕ. The best fit expression is $I_0 = 1.0 - 0.68 \cos 2(\phi + 5.28°)$.

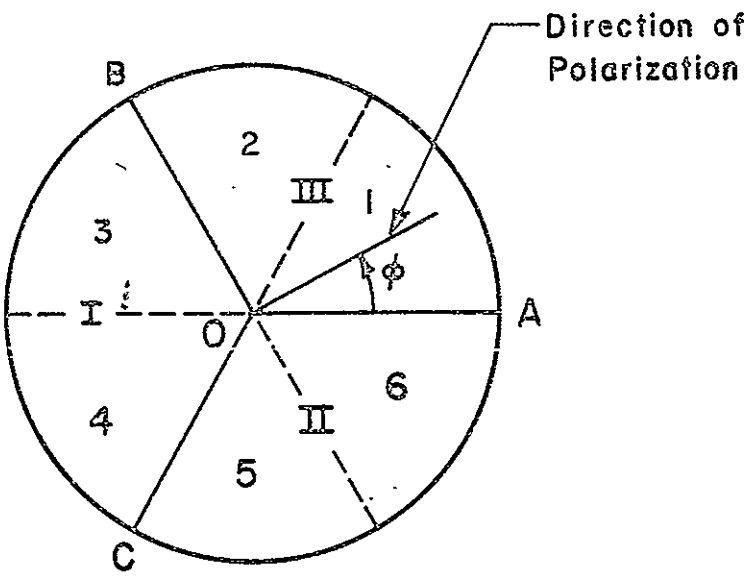

Fig. 1

The front view of a retroreflector with a circular front face. The polarization angle ϕ is the angle between the projection of OA and the direction of polarization of the incident light.

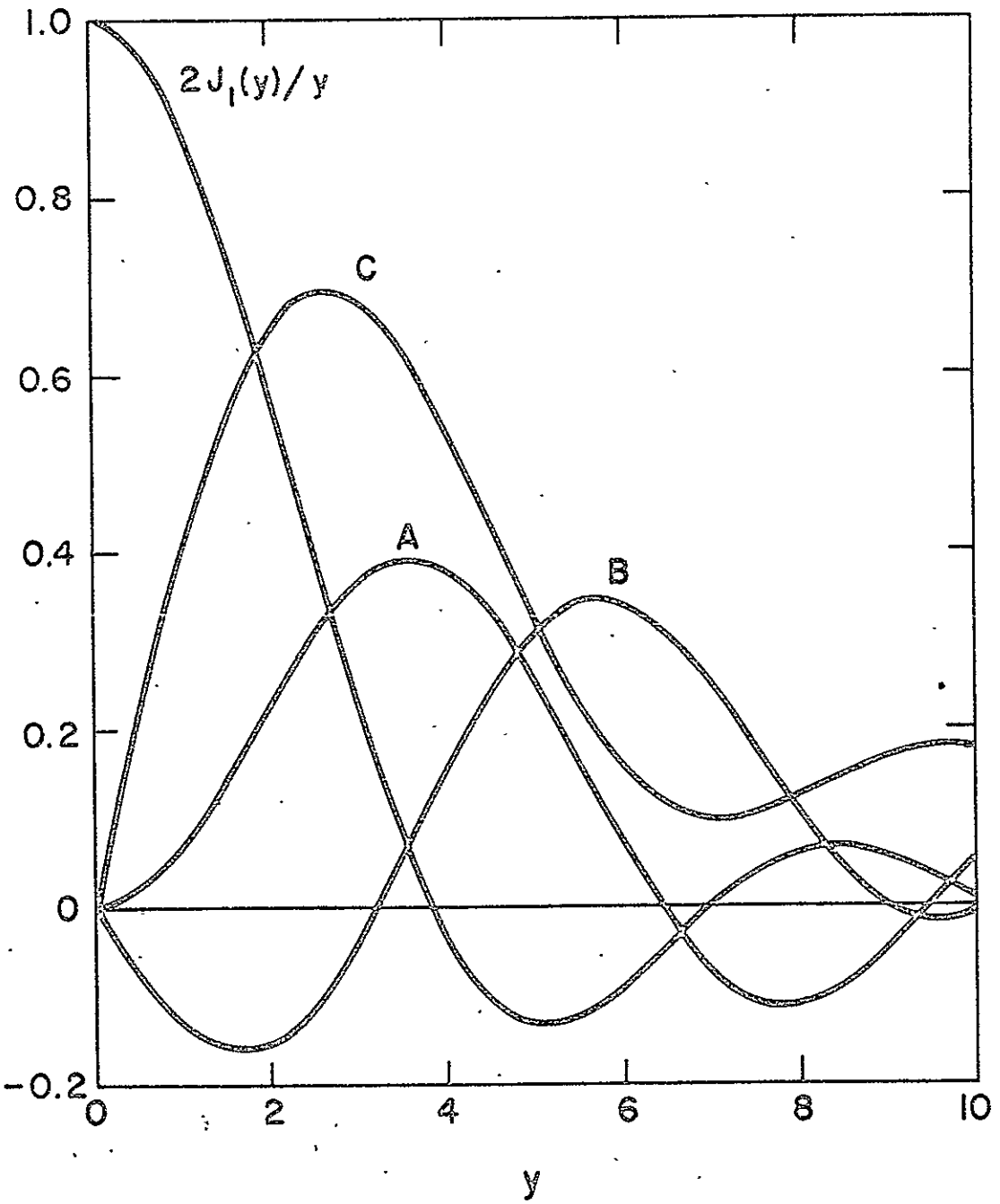

Fig. 2

Functions A(y), B(y), C(y) and $2J_1(y)/y$.

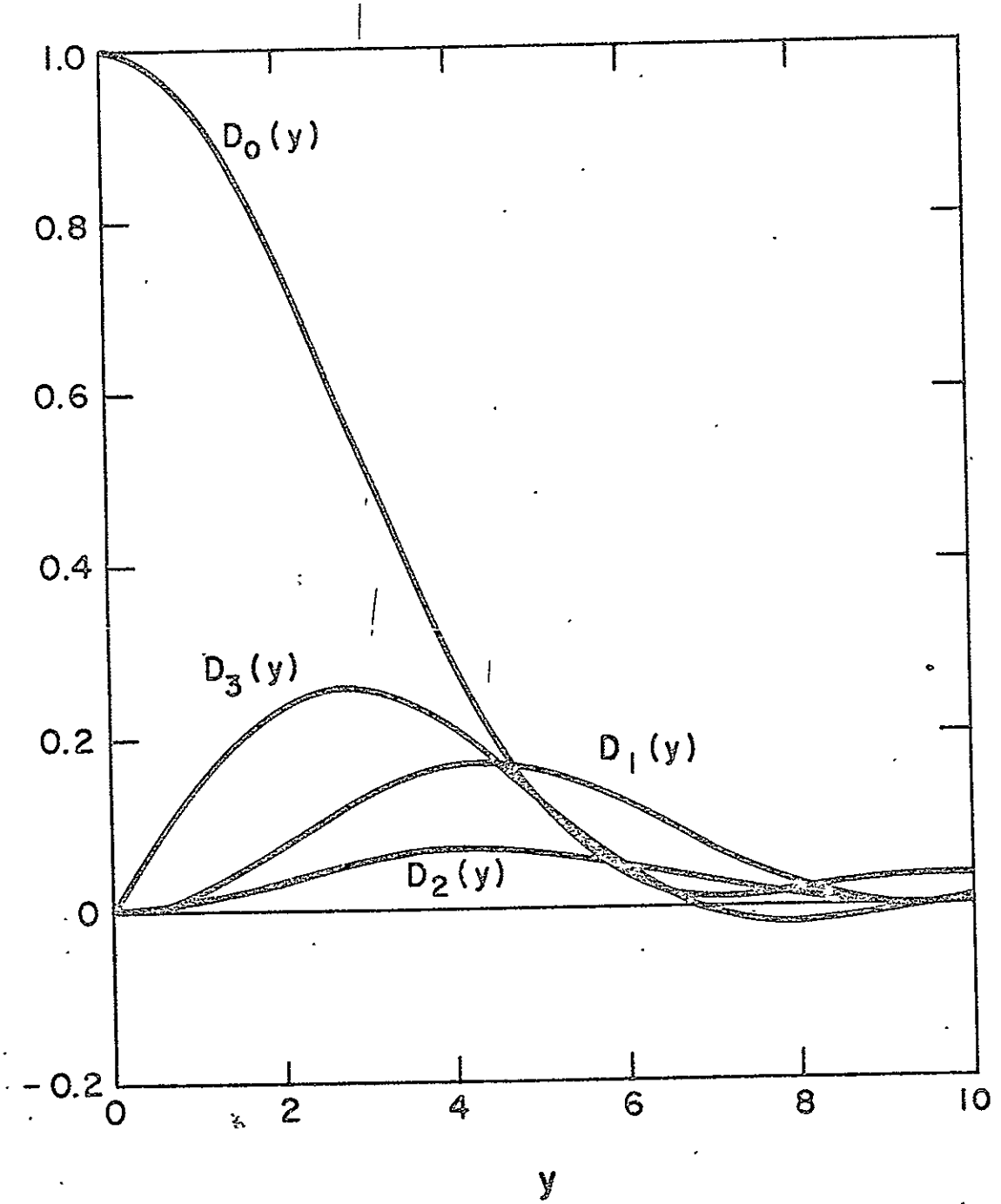

Fig. 3

Functions $D_0(y)$, $D_1(y)$, $D_2(y)$ and $D_3(y)$.

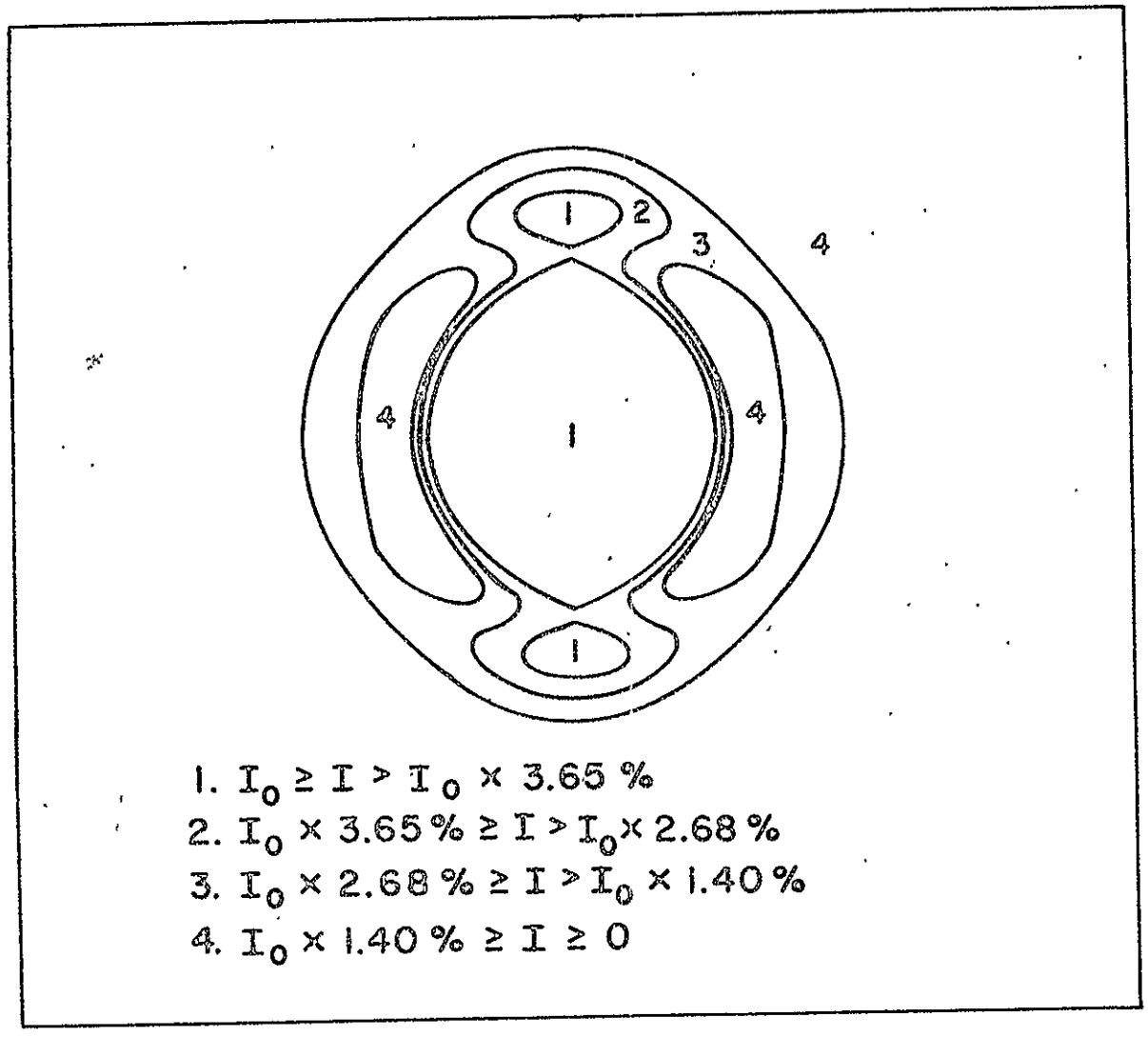

Fig. 4

Contour lines of the diffraction pattern of a metalized retro-reflector with one erroneous back angle. The error parameter is taken to be 1.

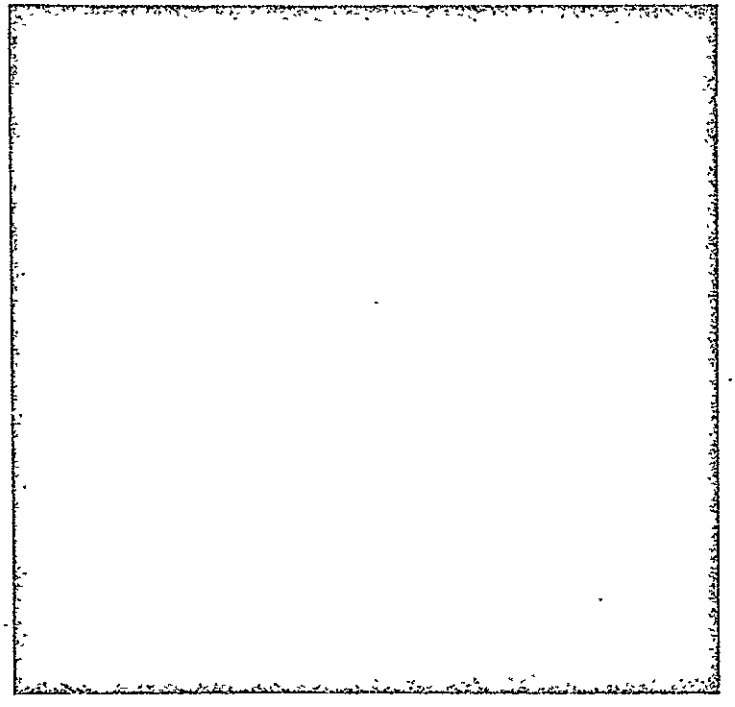

Fig. 5

Photograph of the diffraction pattern of an aluminized retroreflector.

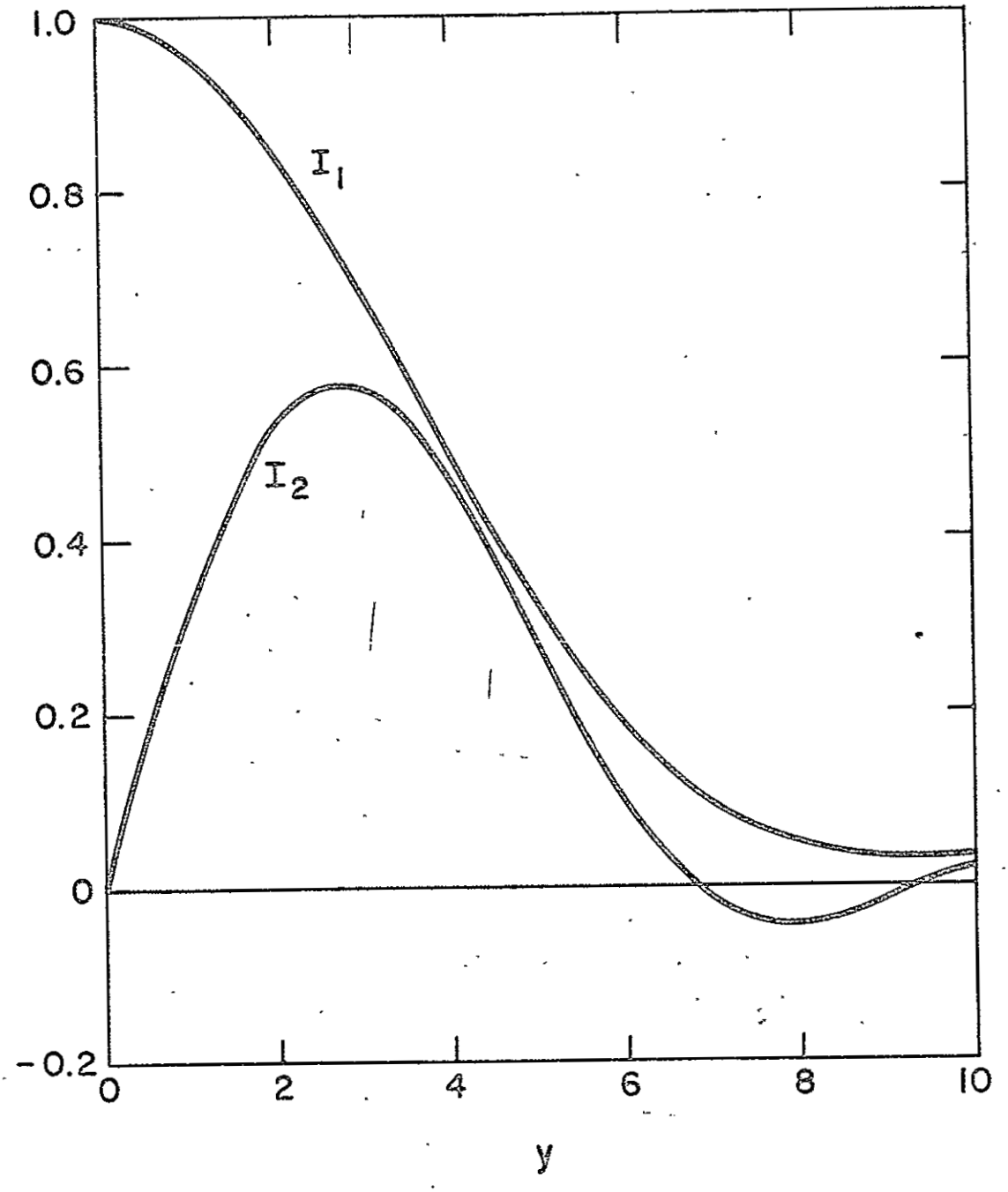

Fig. 6

The analytical expression of the mean, I_1, and the variational amplitude I_2 of the central irradiance of the diffraction pattern of an uncoated solid retroreflector with single erroneous angle are plotted as functions of error parameter y for $\alpha>0$. The index of refraction of the retroreflector is assumed to be 1.4571.

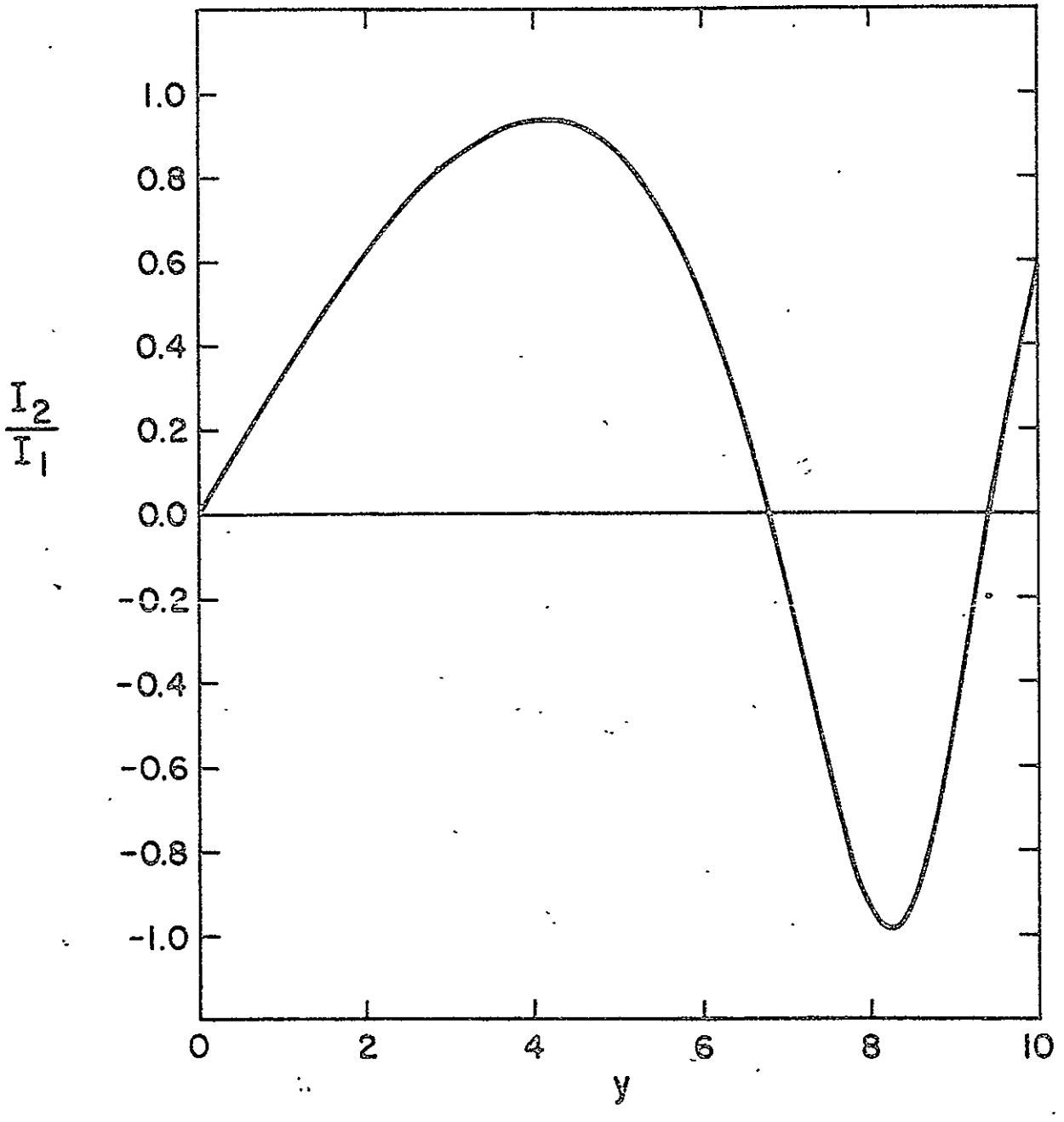

Fig. 7

The ratio I_2/I_1 is plotted as a function of y for $\alpha>0$.

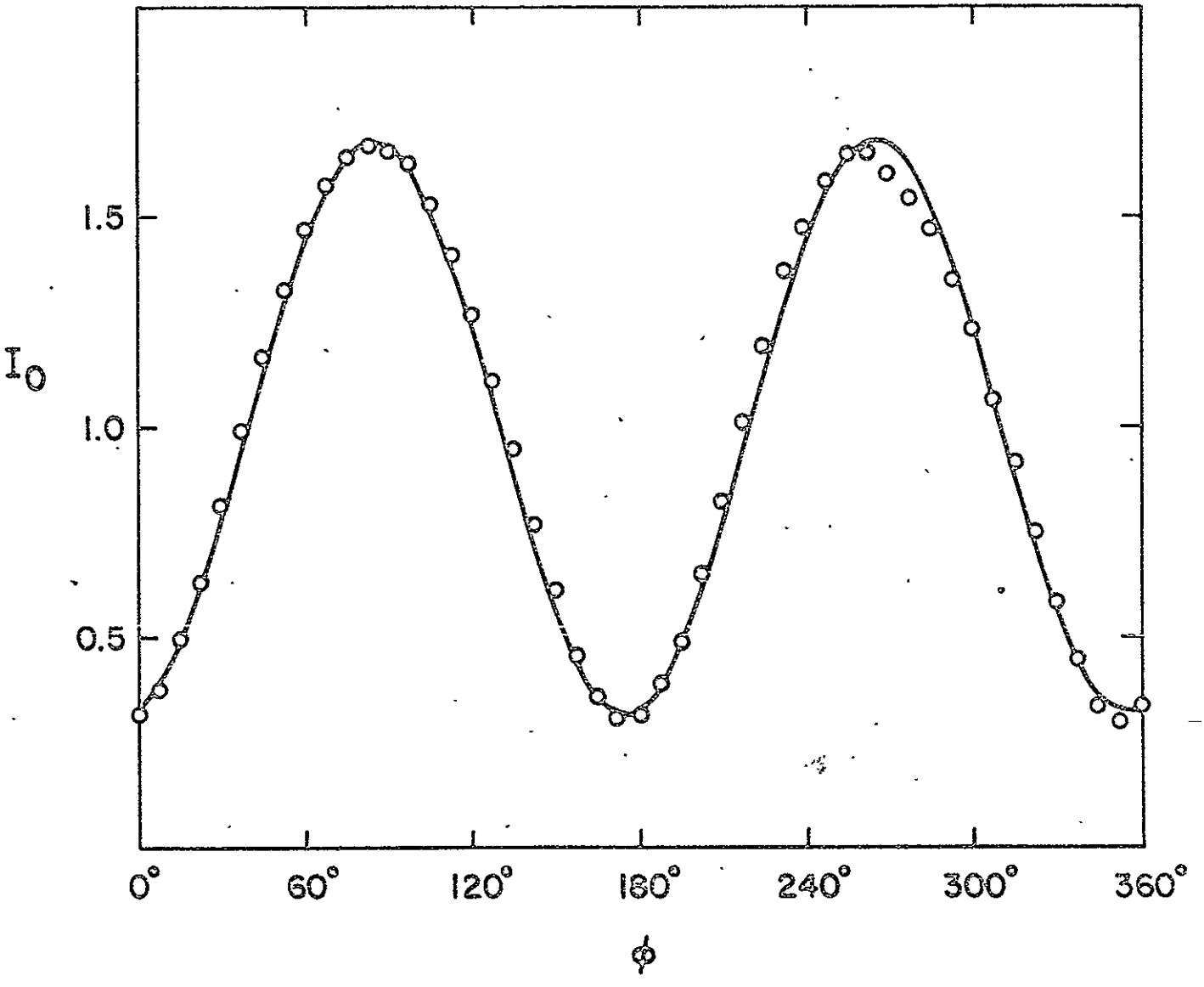

Fig. 8

Comparison between the best fit curve and the experimental data of central irradiance as a function of polarization angle ϕ. The best fit espression is $I_0 = 1.0 - 0.68 \cos 2(\phi + 5.28°)$.

APPENDIX 8

Analysis of Thermal Control Designs for Retro-Reflector Array

ANALYSIS OF THERMAL CONTROL DESIGNS FOR RETRO-REFLECTOR ARRAY

Final Report

Prepared for

UNIVERSITY OF MARYLAND
DEPARTMENT OF PHYSICS AND ASTRONOMY
COLLEGE PARK, MARYLAND

Purchase Order No. 210900

C-70472

December 1968

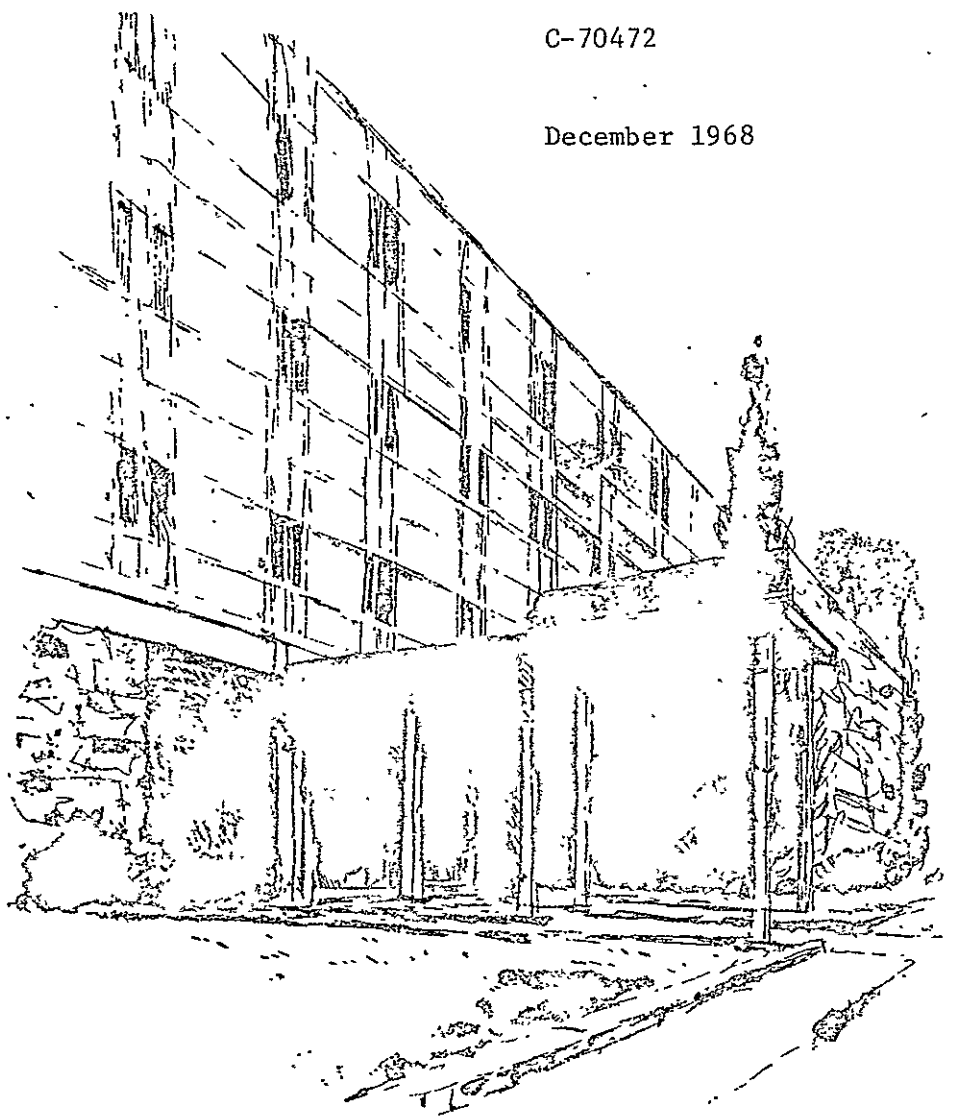

Arthur D. Little, Inc.

TABLE OF CONTENTS

SUMMARY

A. PURPOSE AND SCOPE

The purpose of this study was to define the thermal performance of various array thermal control systems as a necessary first step in the development of an array design for the Laser Ranging Retro-Reflector (LRRR) Experiment. Initially, the design requirements were based on the LRRR Experiment being part of the Mainline ALSEP. However, in the latter stages of the work (modification No. 2 to our contract) emphasis was given to those tasks having applicability to the EASEP Program, as well as the Mainline ALSEP.

The work discussed in this report includes thermal analysis and associated tasks relative to the array thermal control system. The thermal analysis tasks included development of a computer model and using it to determine retro-reflector temperature distributions for louver and surface radiator thermal control configurations. Various design parameters were then investigated for both configurations for a range of sun angles. In conjunction with the thermal analysis, preliminary ray-tracing work was started to assess the effects of temperature gradients on optical performance. Design studies were conducted to establish feasible control configurations for analysis, to explore techniques of panel structural design, and to evaluate surface coatings.

B. BACKGROUND

Arthur D. Little, Inc. (ADL) has had a long association with the investigator group and Bendix Aerospace Systems Division on the Laser Ranging Retro-Reflector Experiment, dating back to early 1967. Two contracts have been funded through the University of Maryland in addition to a very substantial effort funded by ADL.

Under contract to the University of Maryland during the Spring of 1967 we conducted preliminiminary thermal analysis and mechanical design of the retro-reflector array for the Mainline ALSEP Program. Our final report entitled, "Thermal Analysis and Preliminary Mechanical Design of Retro-Reflector Array" (August 1967), contained predictions of retro-reflector temperature gradients and included a preliminary design concept incorporating both thermal control and structural protection.

From mid-1967 to mid-1968, under our own funding, we participated in an investigation of retro-reflector vendors, and liaison with the investigator group. In this period we also submitted several proposals to the Bendix Aerospace Systems Division for the Mainline ALSEP:

- August 1967 - for the design, development and fabrication of arrays for the LRRR. (This proposal presented our plan for the overall program and included preliminary design drawings of a baseline array configuration meeting space limitations for a selected ALSEP location);
- January 1968 - for the design definition (Phase I) of the arrays for the LRRR Program;
- March 1968 - a budgetary cost proposal for a matching Phase II Program;
- April 1968 - a budgetary cost proposal for a reduced scope program. (Major reductions in scope and cost were achieved by eliminating all responsibility for the selection, specification, and procurement of flight quality retro-reflectors. In addition, solar-optical testing was eliminated from the basic program and proposed as an option.)

In June of 1968 we were awarded the contract through the University of Maryland to define the thermal performance of various array thermal control systems for the LRRR. This work, primarily thermal analysis, was consistent with the scope and funding of certain initial tasks described in our April 1968 proposal to Bendix Aerospace Systems Division. Early in October 1968, we received modification No. 2 to our contract which enabled us to continue our work in thermal analysis, computation of optical performance, and design support. In accomplishing modification No. 2, we gave priority to those tasks having applicability to the EASEP Program, as well as the Mainline ALSEP. This work was performed on an accelerated schedule, and except for report preparation, was essentially completed in October.

In mid-October 1968, in anticipation of a contract from the Bendix Aerospace Systems Division, we began an intensive effort to design, develop, and test a retro-reflector array for the EASEP Program. Phase A of this program, engineering design, terminates with a critical design review scheduled for early January 1969.

C. RESULTS

1. Thermal Analysis

Analytical studies were performed to determine the temperature gradients in a retro-reflector array located on the lunar surface. Computer thermal models were used to predict the temperature distributions as a function of time for two design configurations. One utilized a surface radiator of selected thermal properties to lower the structural temperatures and gradients within the retro-reflector during the lunar day. The other utilized a louver (egg-crate) array to minimize the temperature gradients during the lunar day.

The details of the thermal analysis work are presented in Technical Memoranda Nos. 1, 2, and 4 of this report. A brief summary of the major results is presented below.

Using a thermal model representing the retro-reflector, the structure enclosing the retro-reflector, and a surface radiator, a number of parametric computer studies were completed to obtain temperature distributions as functions of time. The maximum vertical temperature difference (ΔT) between the apex of the retro-reflector and the center of the front (exposed) surface was computed for a range of solar absorptance-to-emittance ratios (α/ε) and surface areas for the radiator configuration. The most effective surface radiator configuration examined utilizes a radiator surface with a low solar absorptance-to-emittance ratio ($\alpha = 0.06$, $\varepsilon = 0.85$). With a radiator area of approximately 4.7 sq cm per reflector element (40% of the surface area of the retro-reflector) and an array with multilayer insulation used to radiatively decouple the cylindrical structure from the lunar surface, the maximum vertical ΔT in the retro-reflector (measured from the apex to the center of the top surface) was calculated to be 1.4°K. The maximum ΔT occurs in the range of sun angles from 20° to 30° (measured from the normal to the front surface of the retro-reflector) and is a function of the mounting conductance between the retro-reflector and structure. The performance of this surface radiator configuration, with zero mount conductance, is shown by the "best radiator" curve in Figure 1.

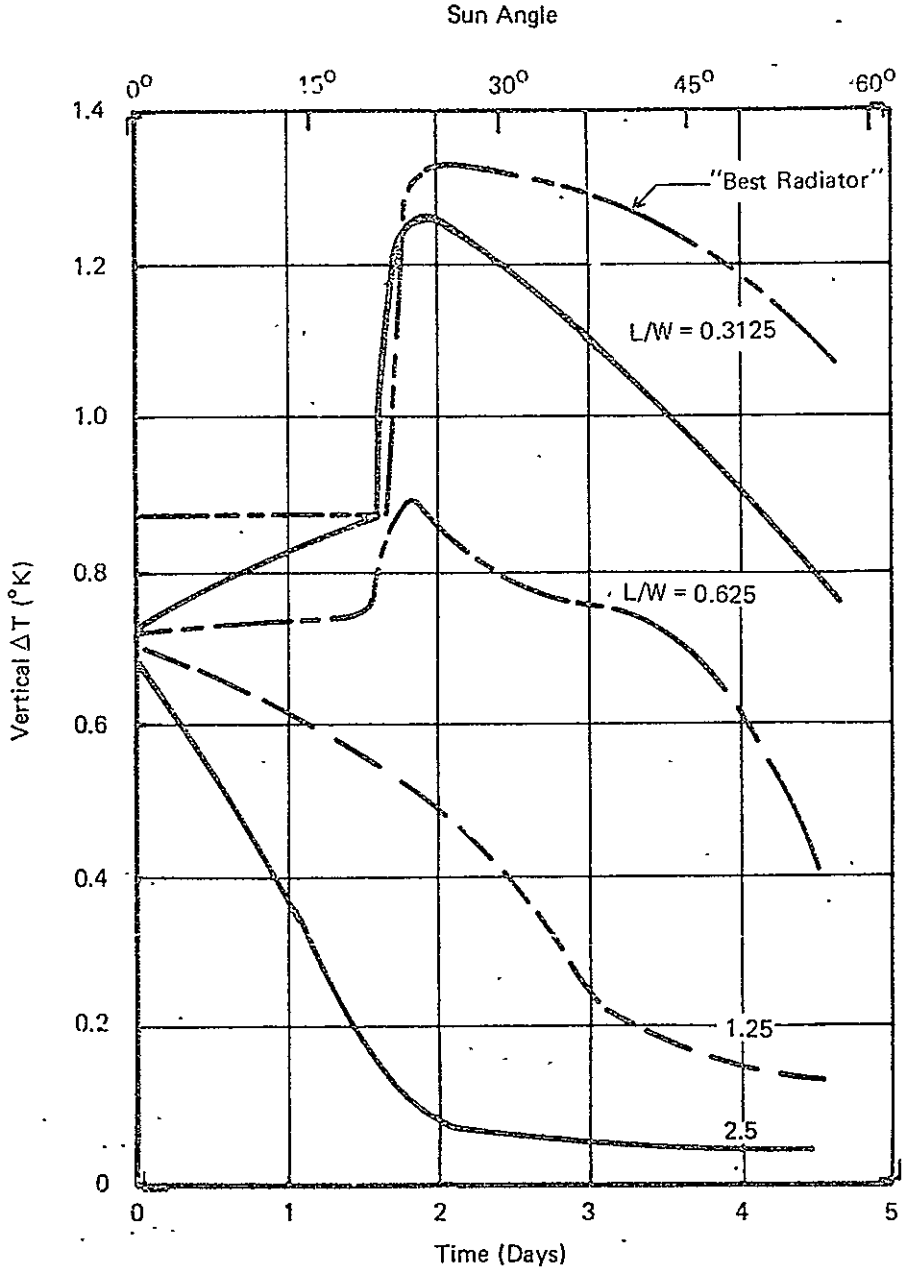

FIGURE 11 INFLUENCE OF LOUVER HEIGHT ON VERTICAL ΔT

$\epsilon = \alpha_s = 1, \quad C_L = \infty, \quad C_R = 0$

During the lunar night and at sunrise and sunset, the calculated temperature differences in the retro-reflector were less than 0.25°K for the surface radiator configuration. The maximum and minimum mean temperatures of the retro-reflector were predicted to be 207°K and 46°K, respectively.

For the louver configuration, the computer studies showed that the retro-reflector is most nearly isothermal when louver cells of large height-width ratios of high emittance are used. The maximum temperature gradients in the retro-reflector occur with the sun nearly overhead for large height-width ratios (>1.25) and at sun angles of approximately 16° from the normal (when the retro-reflector undergoes "breakthrough" or loss of reflectance) for smaller height-width ratios of the louver. Figure 1 shows the thermal performance, expressed as vertical temperature difference, for "black" louvers with height-width ratios ranging from 0.3125 to 2.5. The results are based on zero mount conductance. As was the case for the surface radiator, the thermal conductance between the structure and retro-reflector at the mounting points was found to significantly influence the temperature gradients in the retro-reflector.

2. Computation of Optical Performance

A major portion of this task was concerned with estimating the effects of thermal gradients on optical performance. Technical Memorandum No. 3 in this report describes the analytical ray-tracing procedure which was developed and applied to a vertical temperature gradient in the retro-reflector. The major result, shown in Figure 2, presents relative central irradiance as a function of vertical temperature gradient. It is tempting to combine the results of Figures 1 and 2 to obtain relative central irradiance for various configurations as a function of time. However, it should be realized that products of such a combination can only result in a very gross performance estimate, not only because the Figure 1 temperature results do not include certain real effects such as finite mount conductance, but also because radial as well as vertical gradients will influence optical performance.

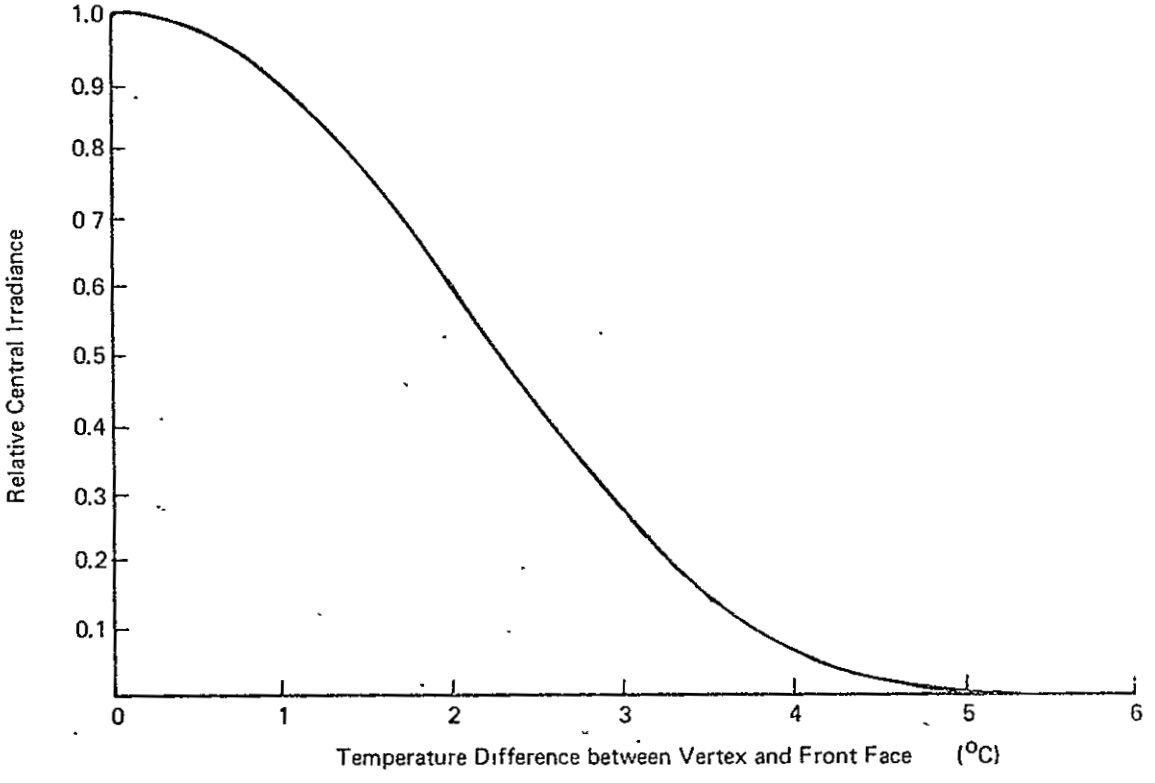

FIGURE 2 RELATIVE CENTRAL IRRADIANCE AS A FUNCTION OF TEMPERATURE DIFFERENCE (LINEAR GRADIENT)

A second part of the task was concerned with determining the effects of retro-reflector face shape, louver obscuration, and optical performance. This work is discussed in Technical Memorandum No. 6. The results indicate that no clear-cut performance advantage is obtained with ratios of superscribed to inscribed circle greater than 1.0. Therefore, a round or hexagonal face is preferable to a triangular face. Obscuration of off-axis laser beams by louvers was found to be a significant effect; for instance, at an off-axis angle of 10°, a height-width ratio of 0.5 results in an obscuration loss of about 40%.

3. Design

The preliminary design of a brazed panel structure for the Mainline ALSEP Program was accomplished and a mock-up constructed to demonstrate fabrication feasibility and to measure panel stiffness. Although the fabrication technique was involved, it appeared to yield a satisfactory structure of near optimum strength per unit weight. This design is described in more detail in Technical Memorandum No. 5.

In the latter part of this program, the design effort was focused on work which would be applicable to EASEP, as well as Mainline ALSEP. Some of the results obtained were as follows:

- For louver height ratios in the general range of .3 to .5, and if weight is not a paramount consideration, it is feasible to machine the array panel from a solid block of aluminum.
- A clear chromic or sulphuric acid anodize appears to be an appropriate "high emittance" surface coating for 6061-T6 aluminum.

D. CONCLUSIONS AND RECOMMENDATIONS

1. The louver thermal control configuration appears to be the best design for obtaining minimum optical distortion throughout the lunar cycle consistent with practical surface coatings.

2. Large louver height-to-width ratios favor thermal control, but at the expense of obscuration in off-axis operation. The optimum louver height should be obtained by balancing thermal performance against laser obscuration. In performing this optimization, a ray-tracing program could be used to determine the overall effect of the actual temperature distributions on optical performance.

3. To obtain the optimum thermal performance for a given louver height, the array design should incorporate the following:

- Minimum conductance across the mounts between the retro-reflectors and array,
- Maximum thermal conductance between the elements of the array structure in front of and behind the retro-reflectors,
- A minimum emittance surface (i.e., polished aluminum) on the canister behind the retro-reflector,
- A high emittance surface (i.e., clear anodize) on the louver (or cavity) walls on the front of the retro-reflector,
- A low emittance, low solar absorptance surface, (i.e., polished aluminum) on the top of the array,
- If the array is positioned above another surface, such as the pallet, and conductively coupled to this surface, the surfaces of the bottom of the array and the top of the mounting pallet should have low emittance and low solar absorptance.

TECHNICAL MEMORANDUM #1

Temperature Gradients Within A Single Retro-Reflector Arising From Solar Heating - Preliminary Results

prepared for

University of Maryland
College Park
Maryland 20742

by

Richard L. Merriam

Arthur D. Little, Inc.
20 Acorn Park
Cambridge, Massachusetts 02140

July 22, 1968

C-70472

TABLE OF CONTENTS

I. SUMMARY AND CONCLUSIONS

A preliminary analytical study was made to determine the temperature gradients caused by solar heating in several geometric configurations representative of the actual retro-reflector geometry. The configurations studied were: 1) a parallel plane slab, 2) a conical segment of a sphere, 3) a right cone, and 4) a pyramid. In all cases, the altitudes (or vertical heights) were chosen to be equal (2.54 cm) and all faces--with the exception of the face normal to the incident solar flux--were taken to be adiabatic. The face normal to the incident flux was assumed to radiate to a 0°K sink. Thermophysical properties characteristic of fused silica were used in the calculations.

With the assumptions of a uniform volumetric heating and the solar flux incident normally on the reflector, the predicted temperature differences across the slab, spherical segment, and pyramid were roughly 3/4°K. For the same conditions, the temperature difference predicted for a cone was approximately 3/5°K; calculations performed for a slab with a non-uniform distribution of volumetric heating yielded a temperature difference slightly larger than 1/2°K. The exact numerical results are summarized in Table 1.

TABLE 1

Temperature Difference Across Reflector Caused by Solar Heating

Geometry	$(\Delta T)_{uniform}$	$\frac{(\Delta T)_{non\text{-}uniform}}{(\Delta T)_{uniform}}$
Slab	0.733	0.766
Segment of sphere	0.733	-
Right cone	0.578	-
Pyramid	0.733	-

Several important conclusions can be drawn from the results obtained:

- Calculations performed assuming a uniform heating will be conservative. However, the assumption of a uniform

volumetric heating leads to a predicted temperature difference only slightly larger than obtained with the actual distribution of heating taken into account.

A simplified model such as a slab can be used to estimate the thermal performance of the more complex retro-reflector configuration. In addition, exact analytical solutions can be obtained for comparison with results from a numerical solution. This procedure will be adopted to determine the number of subdivisions required for accurate computations using a finite-difference technique.

II. INTRODUCTION

Detailed examinations of the temperature gradients caused by a volumetric heating have been performed for several simplified geometries. A description of these geometries and the appropriate analytical expressions for the temperature distribution will be given in the following section.

In order to highlight the importance of volumetric heating, the boundaries of the configurations representing the single retro-reflector were taken to be adiabatic with the exception of the surface normal to the incident solar energy. (It is expected that these faces will be nearly adiabatic in the actual physical situation.) The face normal to the incident radiation radiates energy to free space. The further assumption was made that the solar radiation suffered complete internal reflection at the back face of the reflector and that the total path length within the quartz is the same for any arbitrary ray of incident radiation.

III. ANALYTICAL MODELS FOR HEAT TRANSFER

In a previous report[1] some preliminary estimates were made of the temperature gradients arising within a single retro-reflector from solar

---

1. "Thermal Analysis and Preliminary Mechanical Design of Retro-Reflector Array," Arthur D. Little, Inc., 1967.

heating. Values for the total absorptance versus path length of Englehard "Suprasil" quartz for incident 5800°K blackbody radiation were illustrated in Figure 16 of that report. For a reflector of altitude h = 2.54 cm, the total absorptance was reported to be $\alpha^*(2h) = 0.047$. With a solar flux F incident on a surface area A_S, the energy radiated to space in steady state is simply

$$\varepsilon_S A_S \sigma T_S^4 = \alpha^*(2h) A_S F \tag{1}$$

where ε_S is the surface emittance and T_S is the surface temperature; the quantity σ is the Stefan-Boltzmann constant. The value assumed for F was the solar constant[1]; values used for the surface emittance and thermal conductivity were characteristic of fused silica[2,3]:

$$F = 0.14 \text{ watts/cm}^2$$
$$\varepsilon_S = 0.85$$
$$k = 0.0114 \text{ watts/cm-°K}$$

Before discussing the individual heat transfer configurations, we will consider the volumetric heat generation terms. If κ_λ represents the spectral absorption coefficient within the quartz and F_λ is the spectral incident solar flux, the heat generation term has the following form:

$$q'''(x) = \int_0^\infty \kappa_\lambda F_\lambda \left[e^{-\kappa_\lambda x} + e^{-\kappa_\lambda (2h-x)} \right] d\lambda \tag{2}$$

Note that the second term within the integral accounts for the complete internal reflection of the radiant energy at the back face x = h.

Defining

$$\alpha^*(x) = 1 - \int_0^\infty \left(\frac{F_\lambda}{F}\right) e^{-\kappa_\lambda x} d\lambda \tag{3a}$$

where

$$F = \int_0^\infty F_\lambda d\lambda \tag{3b}$$

---

2. R. A. Breuch, G. A. Bell, N. J. Douglas, "Temperature Control Coatings for Cryogenic Temperature Substrates," Air Force Materials Laboratory, Report AFML-TR-66-10, Part II, 1967.

3. Thermophysical Properties Research Center, Purdue University, Lafayette, Indiana, 1966.

we find that

$$\int_0^{\xi} q'''(\eta)\, d\eta = F\{\alpha^*(\xi) + \alpha^*(2h) - \alpha^*(2h - \xi)\} \qquad (4)$$

In the formulation which follows, we will need to evaluate integrals of the form $\int_0^{x}\left[\int_0^{\xi} q'''(\eta)\, d\eta\right] d\xi$. In order to compute these integrals, the function $\alpha^*(\xi)$ shown in Figure 16 of Reference (1) was fitted by a third-order polynomial:

$$\alpha^*(\xi) = 0.0274\,\xi - 0.0072\,\xi^2 + 0.0007\,\xi^3 \qquad (5)$$

1. Volumetric Heating in a Slab

The physical situation and the coordinate system for a slab are illustrated in Figure 1.

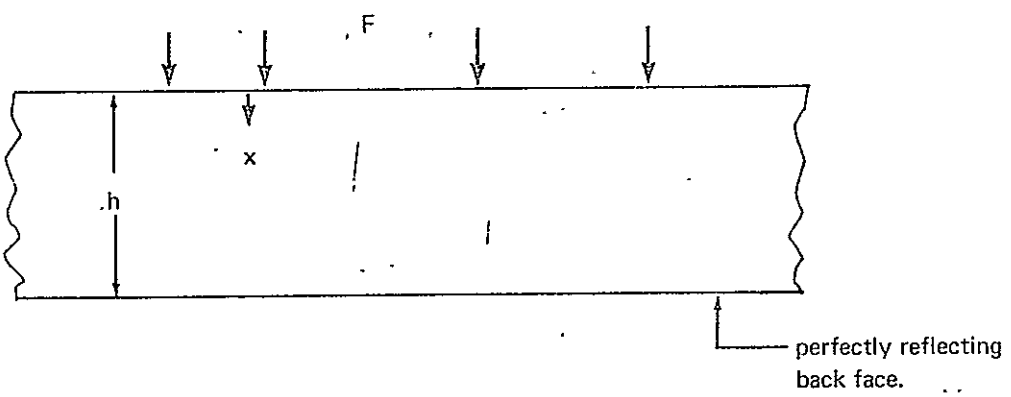

FIGURE 1 PHYSICAL SITUATION – SLAB

The governing equations are

$$0 = k\frac{d^2T}{dx^2} + q'''(x) \quad ,$$

$$k\frac{dT}{dx}\Big|_{x=h} = 0$$

and

$$-k\frac{dT}{dx}\Big|_{x=0} + \varepsilon\sigma T^4(o) = 0 \ .$$

Solving these equations, we obtain

$$T(x) = T(o) + \frac{F}{k}\int_o^x \left[\alpha^*(2h - \xi) - \alpha^*(\xi)\right] d\xi \qquad (6)$$

where

$$\varepsilon\sigma T^4(o) = \int_o^h q'''(\xi)\, d\xi \qquad (7)$$

Therefore, for the general case of non-uniform heating,

$$\Delta T_{NU} = T(h) - T(o) = \frac{F}{k}\int_o^h \left[\alpha^*(2h - \xi) - \alpha^*(\xi)\right] d\xi \qquad (8)$$

In the case of uniform volumetric heating

$$\int_o^x \int_o^\xi q'''(\eta)\, d\eta d\xi = \frac{1}{2}\alpha^*(2h)\, F \frac{x^2}{h},$$

and we obtain

$$\Delta T_U = \frac{1}{2}\frac{h}{k}\alpha^*(2h)\, F \qquad (9)$$

The ratio of these two temperature differences is simply

$$\frac{\Delta T_{NU}}{\Delta T_U} = \frac{2\int_o^h \left[\alpha^*(2h - \xi) - \alpha^*(\xi)\right] d\xi}{h\,\alpha^*(2h)} \qquad (10)$$

2. Volumetric Heating of a Conical Segment of a Sphere

Consider a sphere with a uniform volumetric heat generation rate and which radiates freely to space. We may obtain the temperature distribution in the conical segment illustrated in Figure 2 by computing the temperature distribution within the sphere itself.

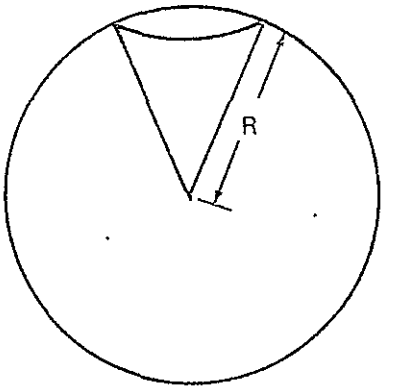

FIGURE 2 PHYSICAL SITUATION – SEGMENT OF SPHERE

The governing equations for this geometry are

$$0 = \frac{k}{r^2}\frac{d}{dr}\left(r^2 \frac{dT}{dr}\right) + q''' = 0$$

$$\frac{4}{3}\pi R^3 q''' = 4\pi R^2 \varepsilon\sigma T^4(R)$$

and

$$-k \left.\frac{dT}{dr}\right|_{r=R} = \varepsilon\sigma T^4(R)$$

Solving these equations, we obtain

$$\Delta T = T(o) - T(R) = \frac{1}{2}\frac{R}{k}\alpha^* F \qquad (11)$$

If $\alpha^* = \alpha^*(2R)$ and R = h, we obtain the same result that we found for a slab.

3. Volumetric Heating of a Cone

No exact solutions are known for the temperature distribution in a cone. The method used here is the so-called Method of Zones.

This method is based on the use of an assumed functional form for the temperature distribution in a zone. Mean surface temperatures and a mean zone temperature are determined in terms of the constants appearing in the expression for the temperature distribution. Integrated surface heat fluxes are then found in terms of the same constants and are written in terms of the mean surface and mean zone temperatures.

The conical geometry analyzed in this section is illustrated in Figure 3. The radius ρ is taken to be 1.9 cm.

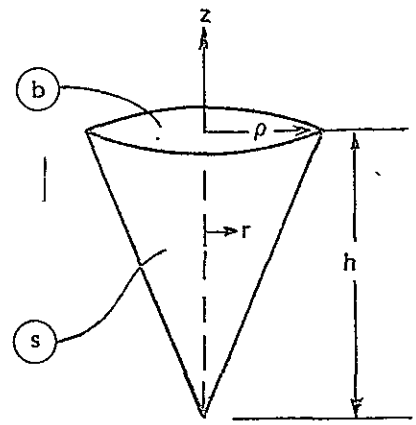

FIGURE 3 PHYSICAL SITUATION – RIGHT CONE

The temperature distribution for the cone is taken to be

$$T\ (r,z) = \alpha_o + \alpha_1 r^2 z + \alpha_2 z^2$$

where α_o, α_1 and α_2 are constants to be determined from expressions for the mean surface temperatures, T_s and T_b, and the mean zone temperature, T_m. Using this functional form for the temperature distribution, the integrated surface fluxes in the direction of the outward drawn normals are

$$Q_b = \frac{10}{17} \left(\frac{\pi\rho^2}{h}\right) k\ (T_m + 6T_s - 7T_b)$$

and

$$Q_s = \frac{20}{17} \pi h k\ (5T_m - 4T_s - T_b)$$

$$+ \frac{10}{51} \frac{\pi\rho^2}{h} k\ (15\ T_b - 8T_s - 7T_m)$$

In the present case,

$$Q_s = 0$$

$$Q_b = (\pi\rho^2)\ \alpha^*(2h)\ F$$

With these boundary conditions, the temperature difference across the cone reduces to

$$\Delta\hat{T} = T(0,0) - T(0,h) = 0.394 \frac{h}{k} \alpha^{*}(2h)F \qquad (12)$$

4. Volumetric Heating of a Pyramid

An approximate expression for the temperature drop across a pyramid was also obtained using the Method of Zones. The physical configuration and coordinate systems are shown in Figure 4.

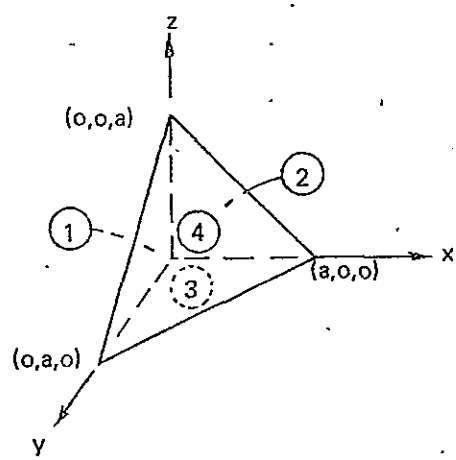

FIGURE 4 PHYSICAL SITUATION – PYRAMID

The functional form of the temperature distribution within a pyramid was taken to be

$$T(x,y,z) = \alpha_o + \alpha_1 x + \alpha_2 y + \alpha_3 z + \alpha_4 (x^2 + y^2 + z^2)$$

Again solving for mean surface temperatures and the mean zone temperature, the integrated surface heat fluxes become

$$Q_1 = ka \frac{1}{6} (20\ T_m + 4T_4 - 14T_1 - 5T_2 - 5T_3)$$

$$Q_2 = ka \frac{1}{6} (20\ T_m + 4T_4 - 5T_1 - 14T_2 - 5T_3)$$

$$Q_3 = ka \frac{1}{6} (20\ T_m + 4T_4 - 5T_1 - 5T_2 - 14T_3)$$

and

$$Q_4 = ka \frac{1}{3} (10\ T_m + 2T_1 + 2T_2 + 2T_3 - 16T_4)$$

Since the surface area of the slanted face is $\frac{\sqrt{3}}{2} a^2$ and the altitude of the pyramid is $h = a/\sqrt{3}$, the heat transfer boundary conditions are

$$Q_1 = 0$$

$$Q_2 = 0$$

$$Q_3 = 0$$

$$Q_4 = \frac{\sqrt{3}}{2} a^2 \; F \; \alpha^*(2h)$$

and the temperature drop across the pyramid becomes

$$\Delta T = T(0,0,0) - T(a/3,\ a/3,\ a/3) = \frac{1}{2} \frac{h}{k} \alpha^*(2h) \; F \quad . \qquad (13)$$

TECHNICAL MEMORANDUM #2

Preliminary Thermal Analysis of Surface Radiator Configuration

prepared for

University of Maryland
College Park
Maryland 20742

Contract 21099

by

Daniel Nathanson

Arthur D. Little, Inc.
20 Acorn Park
Cambridge, Massachusetts 02140

October 1, 1968

C-70472

TABLE OF CONTENTS

Arthur D. Little, Inc.

LIST OF FIGURES

LIST OF TABLES

I. SUMMARY AND CONCLUSIONS

Using a thermal model representing the retro-reflector, the structure enclosing the retro-reflector and a surface radiator, a number of parametric computer studies were completed to obtain the temperature distributions as a function of time. The maximum temperature difference (ΔT) between the apex of the retro-reflector and the center of the front (exposed) surface was computed for a range of solar absorptance-to-emittance ratios (α/ε) for the surface radiator. Parametric studies were completed to examine the effects of the following variables on the ΔT in the retro-reflector; a) radiator area, b) surface properties of the structure enclosing the retro-reflector, c) the effectiveness of "super" insulation between the structure and the lunar surface, d) sun-angle limits for total internal reflection, e) the absorption coefficient for volumetric heating in the retro-reflector, and f) the orientation of the array, with respect to the lunar surface.

The most effective surface radiator configuration examined to date utilizes a radiator surface with a low solar absorptance-to-emittance ratio ($\alpha = .06$, $\varepsilon = .85$). With a radiator area of approximately 4.7 cm^2 (40% of the surface area of the retro-reflector) and an array with multilayer insulation used to radiatively decouple the cylindrical structure from the lunar surface, the maximum ΔT in the retro-reflector (measured from the apex to the center of the top surface) was calculated to be 1.4°K. The maximum ΔT occurs in the range of sun angle of from 20° to 30° (measured from the normal to the front surface of the retro-reflector). For this case, at angles greater than 20°, the solar energy is assumed to pass through the retro-reflector without internal reflection, and is partially absorbed in the cavity formed by the structure surrounding the retro-reflector. Because of the "greenhouse" effect that occurs, a portion of the solar flux absorbed in the cavity must be reradiated by the retro-reflector thereby increasing the ΔT. For a retro-reflector aligned so that total internal reflection occurs for sun angles between +20 and -45 degrees, the maximum ΔT during the period of total internal reflection within the retro-reflector is approximately 0.9°K. The maximum ΔT, during total internal reflection occurs when the sun is directly overhead.

During the lunar night and at sunrise and sunset, the gradients in the retro-reflector are less than 1/4°K. Over the entire lunar period of approximately 29.5 days, the fraction of the time during which the temperature difference in the retro-reflector exceeds 1°K is 17%. The maximum and minimum mean temperatures of the retro-reflector are 207 and 46°K, respectively.

At the suggestion of the principal investigators, a calculation was made for the above surface radiator configuration considering the retro-reflector to be properly oriented in a modified containing structure (instead of a cylindrical container) such that the effective solar absorptance of the container was 0.1 and independent of sun angle. This modification reduced the maximum temperature difference in the retro-reflector by 0.2K; the fraction of the lunar period where the vertical temperature difference in the retro-reflector exceeded 1K was reduced from 17% to 5%.

As a result of the calculations completed with the computer model of the retro-reflector and surface radiator, we have found that temperature differences in the retro-reflector can be minimized by:

a) Using the largest possible surface radiator with the lowest possible solar absorptance-to-emittance ratio.

b) Thermally de-coupling the retro-reflector from the supporting structure by use of a low-emittance surface (e.g., polished aluminum) on the interior of the structure and a low thermal conductance mounting arrangement.

c) Thermally de-coupling the structure from the lunar surface by use of multilayer insulation.

In addition, we found that the ΔT was relatively insensitive to the orientation of the array with respect to the lunar surface and to small variations in the effective path length or uncertainties in the total solar absorptance of the retro-reflector.

The ΔT's in the retro-reflector versus sun angle were computed for both quasi-steady and transient conditions. The results showed that computations for the ΔT based on the quasi-steady model gave accurate results when the ΔT was relatively large, i.e., during the lunar day. At low sun angles, when the ΔT in the retro-reflector was relatively small, there were differences in the ΔT's and the average temperatures of the retro-reflector predicted for the two models. Since the fraction of the total lunar period where the two models were not in agreement was small and the ΔT in the retro-reflector was also small during the corresponding period, we conclude that a quasi-steady model of the retro-reflector can be effectively utilized in parametric studies on the surface radiator configuration.

A high reflectance coating (e.g., vapor-deposited aluminum) on the back surfaces of the retro-reflector does not appear promising from the standpoint of reducing temperature differences in the retro-reflector. With a coating having a solar absorptance of 0.06, the ΔT's in the retro-reflector were computed to exceed 6°K.

II. INTRODUCTION

During a meeting with the principal investigators on June 20, 1968, it was agreed that an early study of the retro-reflector array with a surface radiator configuration would provide useful design information. Therefore, a simplified computer thermal model describing the retro-reflector, the structure enclosing the retro-reflector and a surface radiator was formulated prior to the completion of a detailed, multi-zone thermal model of the retro-reflector.

A description of the thermal model of the surface radiator configuration and the computed temperature differences in the retro-reflector for various parametric studies are presented in this memorandum.

III. THERMAL MATHEMATICAL MODEL

A schematic drawing of the computer thermal model of the surface radiator and a definition of the variables are shown in Figure 1. The retro-reflector is a regular tetrahedron with the front surface exposed to space; the other three mutually perpendicular sides (equilateral triangles) communicate with the structure enclosing the retro-reflector via radiation.

The heat flow in the retro-reflector and the boundary conditions are described by five simultaneous heat-balance equations formulated using the Method of Zones[1]. This formulation is sufficient to compute the temperatures at five locations in the retro-reflector and the temperature difference between the apex of and the center of the front (exposed) surface.

---

1. R. Merriam, Technical Memorandum No. 1, "Preliminary Thermal Analysis of Retro-reflector," July 1968.

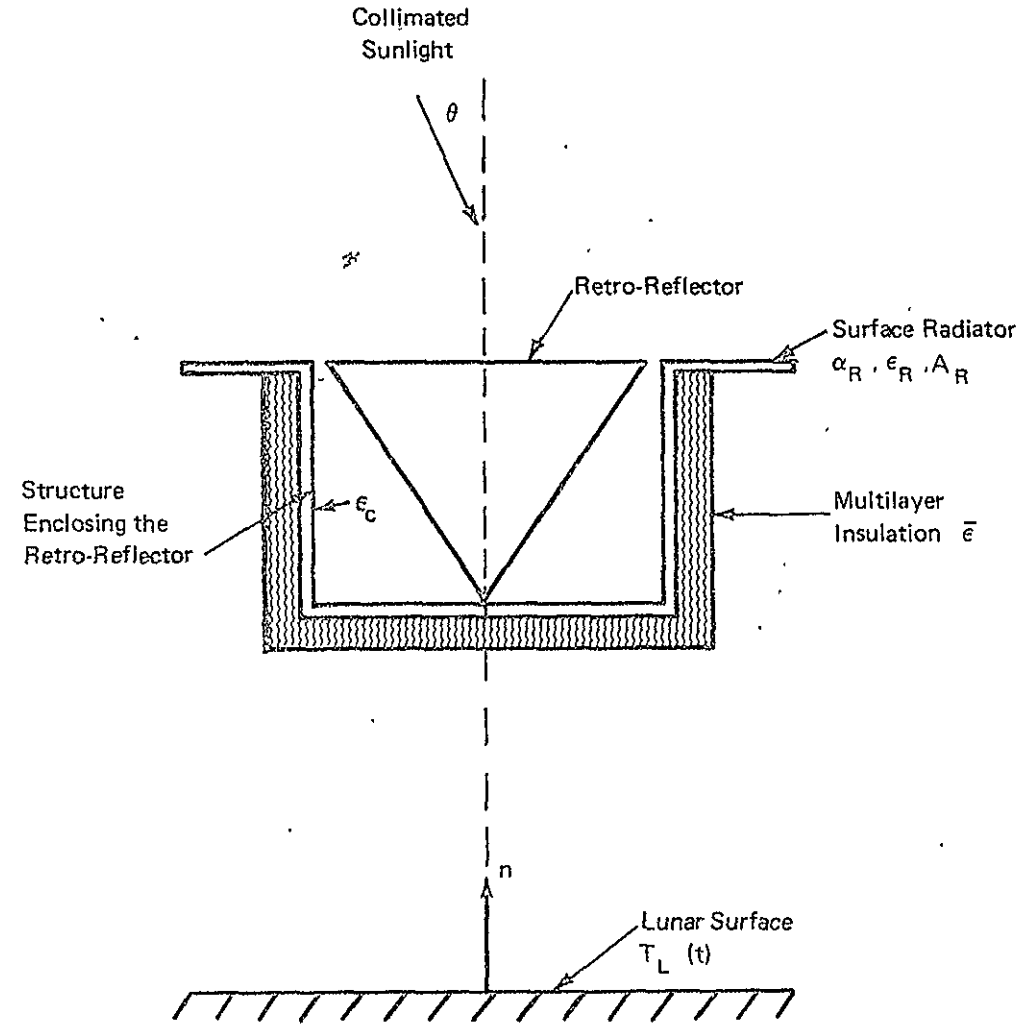

Definition of Variables

A_R = area of surface radiator (cm^2)

α_R = solar absorptance of surface radiator

ϵ_R = total hemispherical emittance of surface radiator

ϵ_C = total hemispherical emittance of internal surface of the structure enclosing the retro-reflector

$\bar{\epsilon}$ = effective emittance of the multilayer insulation (MLI) defined as follows:

$$\bar{\epsilon} = \frac{(q/A)}{\sigma T^4}$$

where (q/A) is the heat flux through the MLI and T is the outer surface temperature of the MLI.

α^* = total absorption coefficient for volumetric heating in the retro-reflector

θ = sun angle, measured from the normal to the lunar surface (deg.)

ΔT = temperature difference between apex and center of the front surface of the retro-reflector (°K)

FIGURE 1 SCHEMATIC REPRESENTATION OF THE THERMAL MODEL OF THE SURFACE RADIATOR CONFIGURATION

The model representation of the structure enclosing the retro-reflector was based on a preliminary design drawing of the "Reflector Mount Detail," Arthur D. Little, Inc., Drawing No. D-SK-71868-1 (July 18, 1968). The retro-reflector is enclosed by a cylindrical structure, 1 1/2 inches in diameter and approximately 1 inch in depth, with specularly reflecting surfaces having a solar absorptance of 0.1. Since this structure forms a cavity for incident collimated sunlight (which is assumed to pass through the retro-reflector when it is not totally internally reflecting), the effective solar absorptance of the opening of the cavity changes with sun angle.

Figure 2 illustrates the effective solar absorptance and the absorbed solar power of the cavity formed by the structure versus sun angle. The sun angle in Figure 2 measured from the normal to the center-line of the cavity, assuming that the array is positioned at the equator.

In this formulation it was assumed that the aluminum structure of high thermal conductance was isothermal and that the radiator was well thermally coupled to the structure. Thus, the structure and radiator were represented as one isothermal zone which was internally coupled to the three back surfaces of the retro-reflector by radiation and externally coupled to the lunar surface via multilayer insulation. In addition, it is subject to the time-variant power comprised of the absorption in the cavity formed by the structure, for sun angles where solar energy passes through the retro-reflector without internal reflector, and the absorption of solar energy on the surface radiator.

The solar absorptance and emittance of the lunar surface were taken as unity. The periodic variation of the temperature of the lunar surface versus sun angle which was used in our studies, for a period of approximately 29.5 days, is described in Table I.

There were two areas which could not be meaningfully investigated with the thermal model described above: 1) the effect of conductive couplings via mounting points between the structure and the retro-reflector and 2) the transfer function relating a small axial temperature difference in the structure surrounding the retro-reflector to the ΔT in the retro-reflector. These considerations can, however, be effectively described

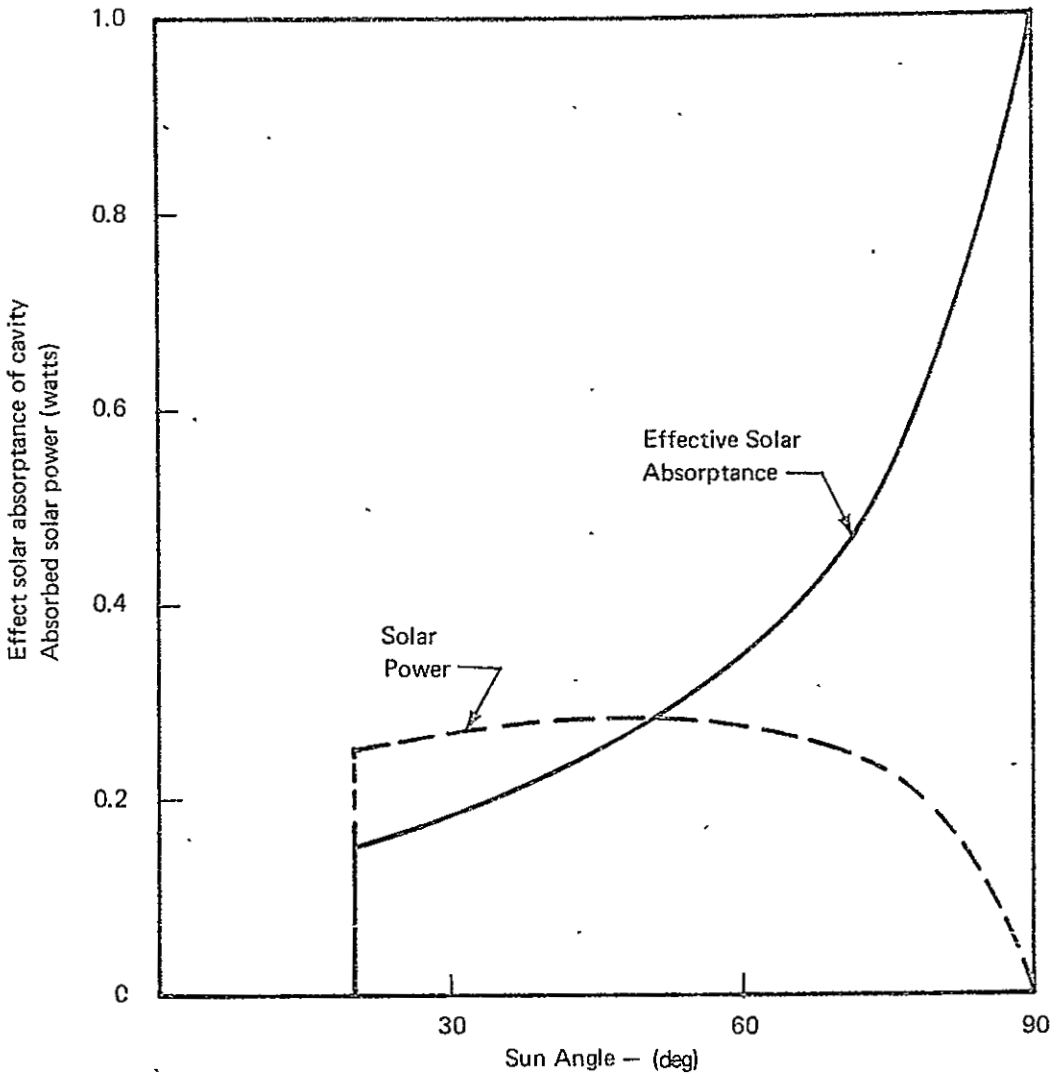

FIGURE 2 EFFECTIVE SOLAR ABSORPTANCE AND ABSORBED SOLAR POWER OF STRUCTURE ENCLOSING THE RETRO-REFLECTOR

TABLE I

TEMPERATURE OF THE LUNAR SURFACE VERSUS SUN ANGLE*

Sun Angle (deg)	Temperature (°K)
0	394
15	389
30	375
45	372
60	333
75	289
90	200
105	133
120	117
135	111
150	105
165	103
180	97
195	97
210	94
225	92
240	89
255	89
270	89
285	200
300	306
315	356
330	375
345	394

* LEM Design Criteria and Environments, LED-520-1F, 15 May 1966.

using a more detailed, subdivided thermal model of the retro-reflector. Calculations of their effects on the ΔT in the retro-reflector are described in Section V of this memorandum.

IV. VERTICAL TEMPERATURE DIFFERENCES IN RETRO-REFLECTOR

The temperatures at five locations in the retro-reflector, the temperature of the structure and radiator, and the temperature difference between the apex of the retro-reflector and the center of the front (exposed) surface were computed as a function of sun angle measured from the normal to the lunar surface. Parametric computer studies were made to examine the effects of solar absorptance-to-emittance ratio of the surface radiator area, surface properties of the structure enclosing the retro-reflector, the effectiveness of "super" insulation between the structure and the lunar surface, sun angle limits for total internal reflection, the total absorption coefficient for volumetric heating in the retro-reflector and the orientation of the array on the ΔT in the retro-reflector. Unless otherwise noted, the array is positioned at the equator and the plane of the array is parallel to the lunar surface.

A. Quasi-steady and Transient Models

The ΔT in the retro-reflector versus sun angle was computed for both quasi-steady and transient conditions. The results demonstrated that the computations for the ΔT and the mean temperature of the retro-reflector, using the quasi-steady model, gave accurate results during the portion of the lunar period when the ΔT was relatively large.

As an example, consider a radiator configuration where the solar absorptance and emittance of the radiator are unity, the radiator area is 10% of the surface area of the retro-reflector (1.2 cm^2) and the effective emittance of the insulation on the structure is 0.01. The internal surfaces of the structure, which are radiatively coupled to the retro-reflector, have an emittance of 0.03.

In Figure 3 the temperature difference between the apex and the center of the front surface of the retro-reflector and the mean temperature of the retro-reflector are plotted versus time for one-quarter of the lunar period, measured from a sun angle of zero. The array is aligned so

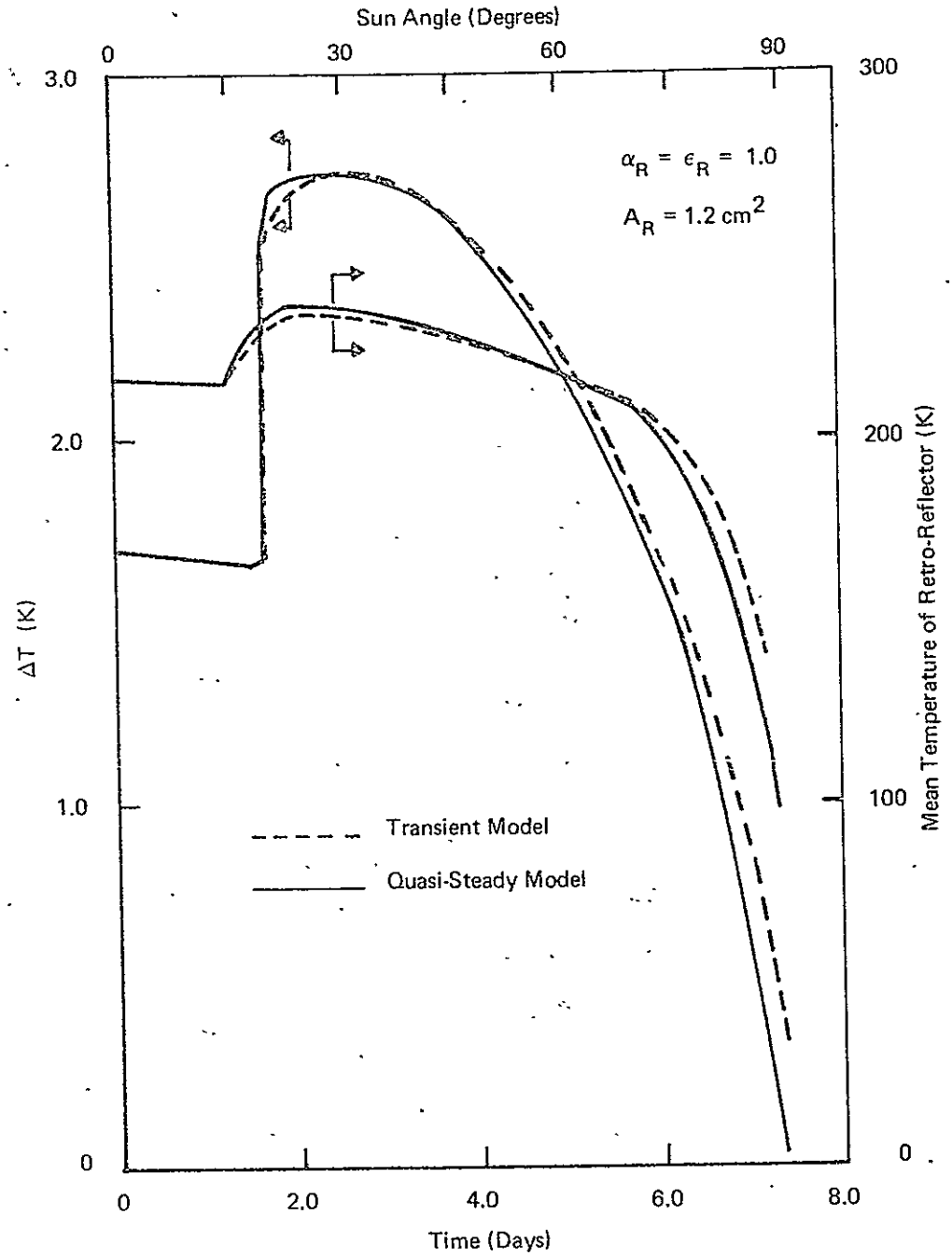

FIGURE 3. COMPARISON OF QUASI-STEADY AND TRANSIENT THERMAL MODELS

that for this portion of the total lunar period total internal reflection occurs for the range of sun angles between 0 and 20°. The maximum ΔT for both models are essentially identical and occur in the range of sun angles of 20 to 30°

The results in Figure 3 for this configuration show that the computations of ΔT based on the quasi-steady model give accurate results when the ΔT is relatively large, i.e., during the lunar day. Near sunset, when the ΔT and the temperature in the retro-reflector are relatively low, there are differences in the ΔT's and the mean temperatures of the retro-reflector predicted for the two models. Since the fraction of the total lunar period where the two models are not in agreement is small, and the ΔT in the retro-reflector is also small during the corresponding period, a quasi-steady model of the retro-reflector can be effectively utilized in parametric studies.

B. Effect of Solar Absorptance, Emittance and Area of Surface Radiator

Early studies were concerned with determining desirable surface properties for a surface radiator and the relationship between the radiator area and the ΔT's in the retro-reflector. Two configurations, which represented extremes of surface properties obtainable with existing technology, were analyzed--one with a high solar absorptance-to-emittance ratio ($\alpha_R = \cong 1.0$, $\varepsilon_R \cong 1$), the other with a low solar absorptance-to-emittance ratio ($\alpha_R = 0.06$, $\varepsilon_R = 0.85$). A configuration with a surface radiator having a solar absorptance of 0.32 and an emittance of 0.76 was also analyzed. These optical properties correspond to those measured for a 0°C surface with a 0.4 mil thick Alzak (Alcoa Anodizing Process) coating after exposure in a vacuum-ultraviolet environment for 700 equivalent space sun hours (approximately 1/10 year).* It should be noted that the initial values of solar absorption and emittance were 0.16 and 0.78 respectively and that the solar absorptance was still increasing at 700 ESSH. In these calculations the effective emittance of the insulation on the structure was 0.01, the

*Weaver, J. H., AFML-TR-67-421, "Effects of UV Environment on Optical Properties of Bright Anodized Aluminum" (May 1968).

emittance of the internal surfaces of the structure was 0.03, and the total absorption coefficients for volumetric heating in the retro-reflector was 0.047 for sun angles between +90° and -90°.

The configurations are compared in Figure 4, where the maximum ΔT in the retro-reflector is plotted versus radiator area. The retro-reflector was aligned so that total internal reflection occurred for sun angles between +20 and -45 degrees. Plots of ΔT versus sun angle or time are shown in Figure 5 for the three configurations when the radiator area was approximately 10% of the surface area of the retro-reflector (1.2 cm^2). The maximum ΔT's resulted in the range of sun angles from 20° to 30°. At these angles the solar energy is assumed to pass through the retro-reflector without internal reflection, and is partially absorbed in the cavity formed by the structure surrounding the retro-reflector. Because of the "greenhouse" effect that occurs, a portion of the solar flux absorbed in the cavity must be reradiated by the retro-reflector, thereby increasing the ΔT.

In Figure 6, the maximum ΔT during total internal reflection (which occurs when the sun is directly overhead) is plotted versus radiator area. In previous analytical studies of a retro-reflector with adiabatic back surfaces and the front surface exposed to normally incident sunlight and uniform volumetric heating, the ΔT in the retro-reflector was computed to be approximately 3/4°K.* It is interesting to note that for the low α/ε radiator configuration the maximum ΔT during total internal reflection is less than 1/4°K higher than this value. However, for the high α/ε radiator configuration the ΔT's during total internal reflection exceed this value by more than 1°K.

The temperature differences in the retro-reflector are less than 1/4°K at sunrise and sunset and during the lunar night. The mean temperature of the retro-reflector was in the range of a maximum of 200 to 235°K during the lunar day to a minimum of 46°K during the lunar night.

---

* R. Merriam, Technical Memorandum No. 1, "Preliminary Thermal Analysis of a Retro-Reflector," July 1968.

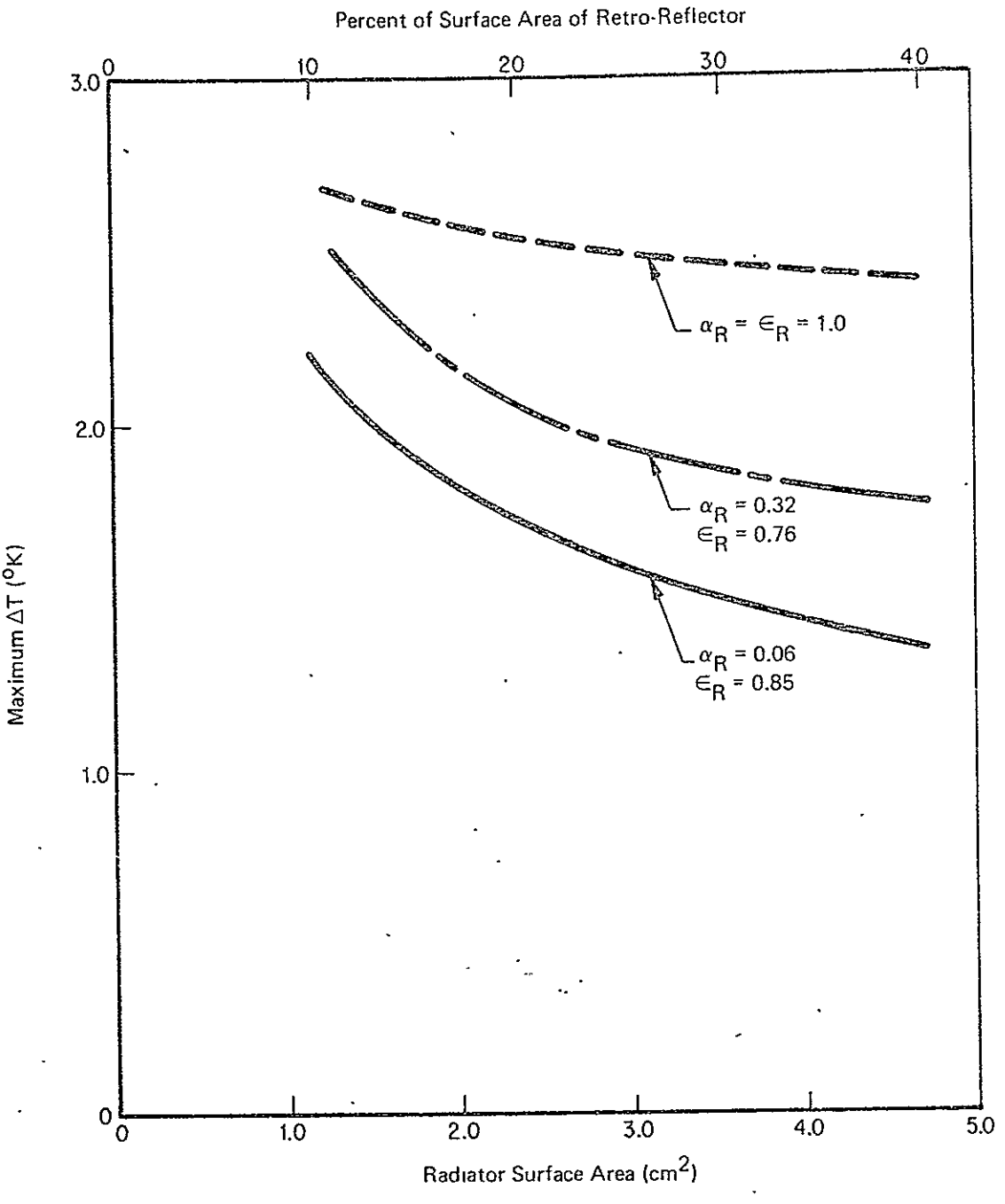

FIGURE 4 MAXIMUM ΔT IN THE RETRO-REFLECTOR FOR THREE SURFACE RADIATOR CONFIGURATIONS

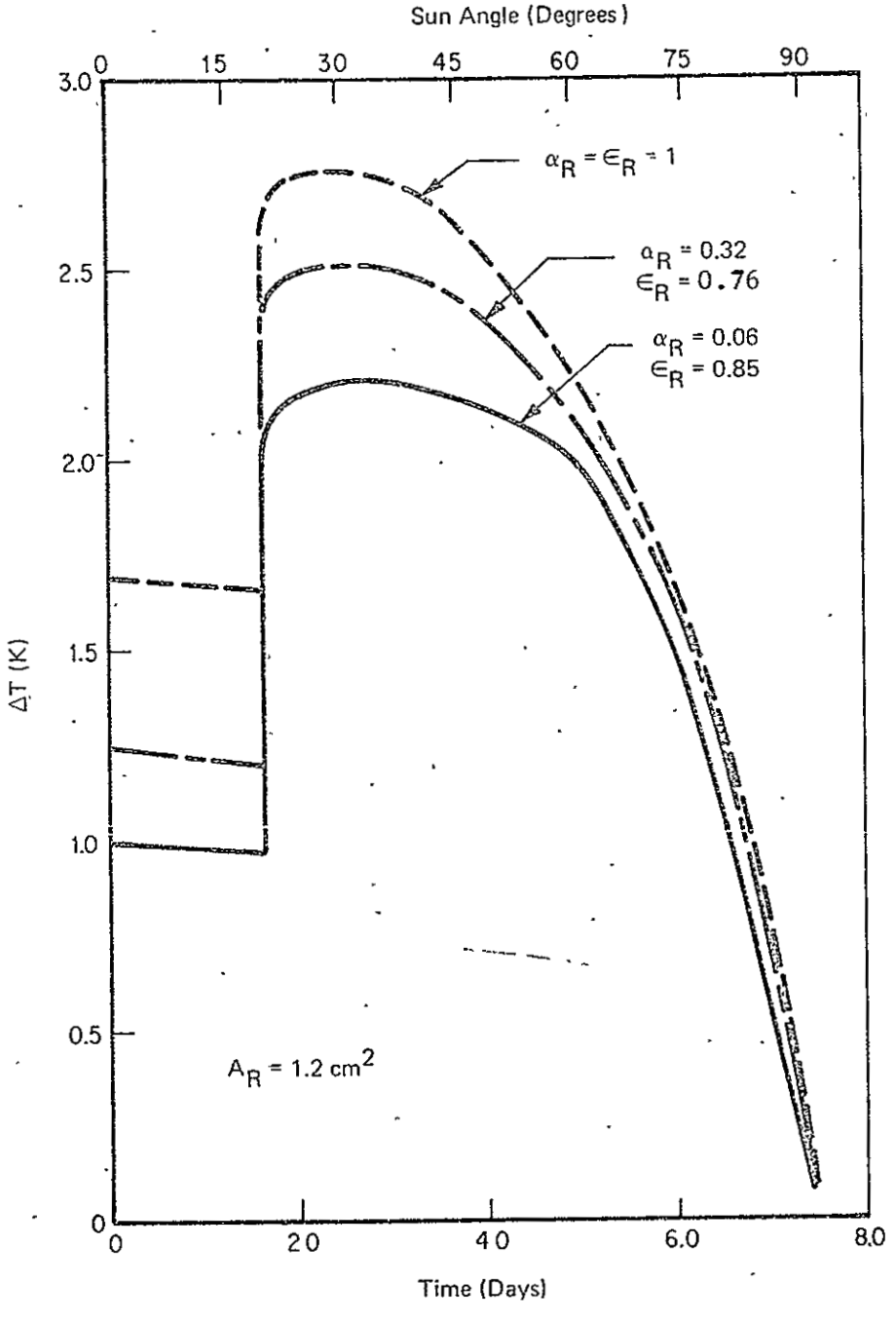

FIGURE 5 ΔT IN THE RETRO-REFLECTOR DURING THE LUNAR PERIOD

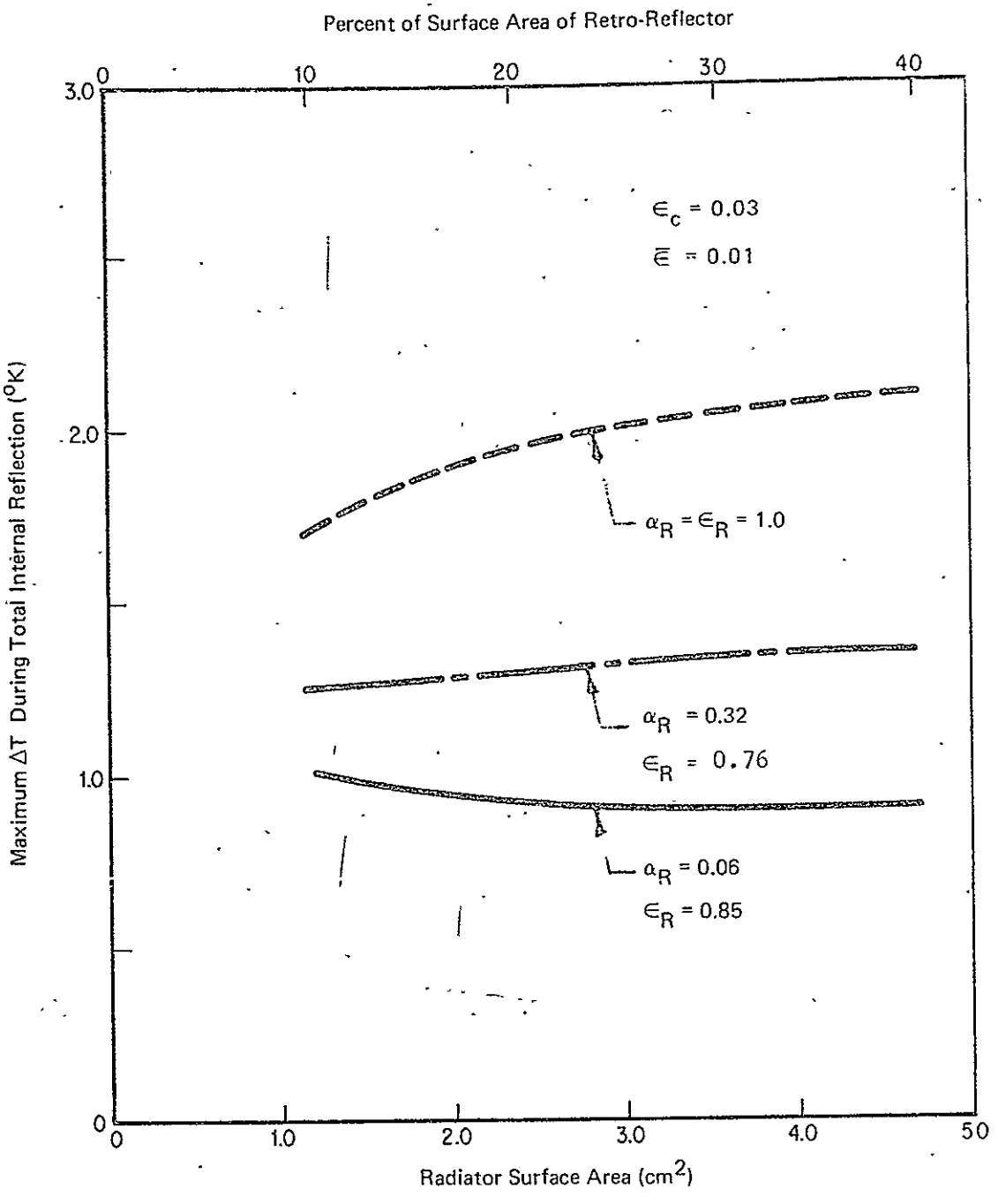

FIGURE 6 MAXIMUM ΔT DURING TOTAL INTERNAL REFLECTION – THREE SURFACE RADIATOR CONFIGURATIONS

From this study, it is evident that the low solar absorptance-to-emittance surface radiator configuration is more promising from the thermal standpoints of the maximum ΔT in the retro-reflector, the size of the radiator required to reduce the ΔT, and the fraction of the lunar period that the ΔT is large. For example, the following tabulation compares the three surface radiator configurations on the basis of the fraction of the total lunar period that the vertical ΔT exceeds 1°K (which is nearly equal to the ΔT computed for a retro-reflector having adiabatic back surfaces and exposure to normally incident sunlight.

Surface Radiator Configuration		Fraction of Lunar Period where ΔT Exceeds 1°K (%)	
α_R	ε_R	$A_R = 1.2$ cm^2	$A_R = 4.7$ cm^2
0.06	0.85	27	17
0.32	0.76	45	39
1.0	1.0	45	41

However, as indicated by the plots shown in Figure 5, if the above comparison was made on the basis of a lower ΔT or a substantially high ΔT (2°K), there would not be a significant difference between the three configurations.

C. Parametric Computer Studies

Thus far the results presented were for calculations which included the following assumptions:

- The total absorption coefficient for volumetric heating in the retro-reflector (α^*) equaled 0.047 for sun angles of -90 to +90 degrees.
- The total hemispherical emittance of the surfaces surrounding the retro-reflector (ε_C) was 0.03.
- The effective emittance of the insulation on the external surface of the structure ($\bar{\varepsilon}$) was 0.01.
- The plane of the array was parallel to the lunar surface and located at the equator.

Using the low solar absorptance-to-emittance surface radiator as a reference ($\alpha_R = 0.06$, $\varepsilon_R = 0.85$), parametric computer runs were made to determine the effects of α^*, ε_C, $\bar{\varepsilon}$ and the orientation of the array on the ΔT's in the retro-reflector. The purpose of these studies was to obtain a measure of the influence of uncertainties in the thermal properties used in calculations on the computed ΔT in the retro-reflector and to determine features which were desirable for the design of the array from the thermal standpoint.

For the reference problem, in addition to the assumptions listed above, the radiator area was 4.7 cm^2 and the retro-reflector was totally internally reflecting when the angle between the solar vector and the normal to the front surface was between +20 and -45°.

In each of the parametric computer runs only one parameter was varied to determine its influence on the ΔT's in the retro-reflector. A description of the variation in each study follows:

a) The effective emittance of the multilayer insulation was increased from 0.01 to unity.**

b) The emittance of the surfaces enclosing the retro-reflector was increased from 0.03 to 0.06.

** This represents an extreme case which is equivalent to having an uninsulated structure with an emittance of unity on the external surfaces of the structure.

c) The total absorption coefficient for volumetric heating in the retro-reflector was arbitrarily increased from 0.047 to 0.094 for the time when the retro-reflector is not totally internally reflecting.

d) The orientation of the array with respect to the lunar surface was changed. Instead of the plane of the array being parallel to the lunar surface, the array was inclined so that there was a 45° angle between the normal to the front surface of the retro-reflector and the normal to the lunar surface. A sketch of this orientation is shown in Figure 7.

The results of the four parametric computer runs are summarized in Table II and are compared to the reference configuration.

Studies (a) and (b) deal with design parameters of the retro-reflector array. In case (a), where there is no insulation between the structure and the lunar surface, the maximum ΔT (an increase of 0.7°K) occurs when the sun is directly overhead. The ΔT decreases monotonically with sun angle until sunset, and over the entire period the ΔT exceeds 1°K for 37% of the time.

Due to the large amount of heat which can be transferred to the structure via radiation from the lunar surface, it is desirable from the thermal standpoint to insulate the structure and radiatively de-couple it from the lunar surface. For example during the time when there was no total internal reflection in the retro-reflector, the heat flux transferred from the lunar surface to the structure was 5 to 10 times greater than the sum of heat flux absorbed by the radiator and the heat flux absorbed by the cavity due to sunlight passing through the retro-reflector. When there was insulation on the structure, the ability to dissipate heat was reduced, but the reduction in the total heat flux absorbed by the structure was sufficient to reduce the amount of heat reradiated by the retro-reflector and the ΔT's in the retro-reflector.

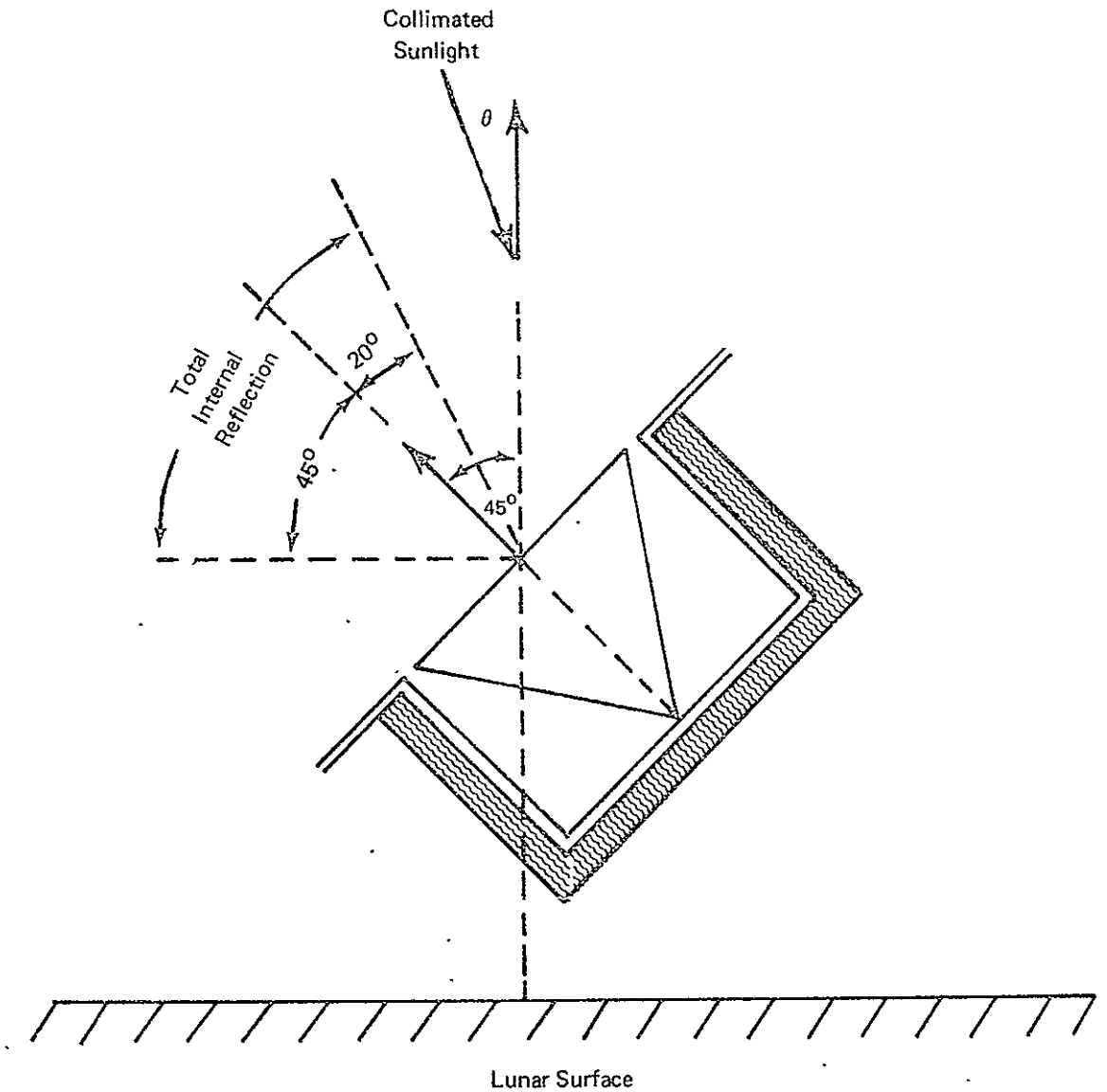

FIGURE 7 ORIENTATION OF RETRO-REFLECTOR ARRAY IN PARAMETRIC STUDY d.

TABLE II

RESULTS OF PARAMETRIC STUDIES

	ΔT_{max} (°K)	ΔT_{max} during total internal reflection (°K)	Fraction of lunar period where ΔT exceeds 1°K (%) - %	Mean temperature of retro-reflector (°K)	
				max	min
Reference configuration	1.4	0.9	17	207	46
Parametric Variation					
a) An increase in the effective emittance of multilayer insulation from 0.01 to unity.	2.1	2.1	37	224	52
b) An increase in the emittance of the surfaces enclosing the retro-reflector from 0.03 to 0.06.	1.8	1.0	24	216	46
c) An increase in the adsorption coefficient for volumetric heating in the retro-reflector from 0.047 to 0.094 for the time when the retro-reflector is not totally internally reflecting.	2.0	0.9	23	235	46
d) A change in the orientation of the array. The angle between the normal to the front surface of the retro-reflector and the normal to the lunar surface was changed from 0 to 45°.	1.3	0.9	17	268	61

The results for case (b) indicate that the emittance of the internal surfaces of the structure is an important parameter and that changes in emittance can cause noticeable changes in the ΔT's in the reflector. Therefore, in using a low-solar-absorptance structure to enclose the retro-reflector, it is desirable to use materials with low-emittance surfaces.

The results for case (c) show that doubling the total absorption coefficient has approximately the same effect as doubling the emittance of the internal surfaces of the structure.

A calculation was also made accounting for a variation in the total absorption coefficient for volumetric heating in the retro-reflector with sun angle during the time of total internal reflection. The change in the total absorption coefficient with sun angle was described by the following equation:

$$\frac{\alpha^*(\theta)}{\alpha^*(\theta=0)} = 0.574 + 0.085 \left[\frac{2hn_2}{(n_2^2 - \sin^2\theta)^{1/2}} \right]$$

where h is the altitude of the retro-reflector

n_2 is the index of refraction of fused silica

θ is the sun angle measured from the normal to the front surface of the retro-reflector

and $\left[\frac{2hn_2}{(n_2^2 - \sin^2\theta)^{1/2}} \right]$ is the variation of the path length of an absorbed ray with sun angle

Thus, the absorption coefficient varies from 0.047 at $\theta = 0$ to 0.050 at $\theta = 45°$.

The effect of this variation on the ΔT in the retro-reflector was quite small. The maximum increase in the ΔT was less than 0.04°K.

Finally, in case (d) where the array was titled and infrared radiation from the lunar surface was absorbed on the front surface of the

retro-reflector and on the surface radiator, there was a slight reduction (approximately 0.1°K) in the computed value of the maximum ΔT. A calculation was also made neglecting the infrared energy to the radiator, and it was found that the maximum ΔT decreased by 0.2°K. This would indicate that the absorption of radiant energy on the front surface tends to reduce to back-to-front ΔT in the retro-reflector. The reductions in the maximum ΔT, although relatively small, are partially offset by the additional radiant energy absorbed by the radiator, transferred to the retro-reflector via the structure and reradiated by the retro-reflector. Based on this study, the orientation of the array with respect to the lunar surfaces does not seem particularly significant.

D. ΔT in a Retro-reflector with a High-reflectance, Metallized Back Surface

The ΔT's in a retro-reflector were calculated considering the three, mutually perpendicular, back surfaces of the retro-reflector to have a high reflectance coating (e.g., vapor-deposited aluminum). The solar absorptance of the coating was taken as 0.06, and the total hemispherical emittance was assumed to be 0.03. The emittance of the surfaces of the structure surrounding the retro-reflector was 0.03, and the effective emittance of the multilayer insulation was 0.01. This configuration did not include a surface radiator.

The uniform volumetric heating in the retro-reflector was computed considering a total coefficient of 0.047. The absorption coefficient for solar energy absorbed on the metallized back surfaces (α_*), referenced to the area of the front surface of the retro-reflector, was determined from the following equation:

$$\alpha_* = 1 - (1-\alpha)^3$$

where α is the solar absorptance of the metal coating.

The computation of α_* is based upon each ray of incident sunlight making three bounces when the sun angles are between +90° and -90°. The power absorbed on the back surfaces is significant from a thermal standpoint since its magnitude is more than three times greater than the power for volumetric heating in the retro-reflector, and the power is localized on the back surfaces, as opposed to being uniformly distributed.

For this configuration, the maximum ΔT was computed to be 6.6°K and occurred when the sun was directly overhead. Also, the ΔT in the retro-reflector exceeded 2°K for 41% of the total lunar period.

From a thermal standpoint, the use of a metallized coating on the back surfaces of the retro-reflector does not appear promising. In comparison to the surface radiator configurations studied, the metallized coating results in larger ΔT's during total internal reflection as well as the time when there is no total internal reflection.

E. Effect of Structure Configuration

The previous calculations for the surface radiator configurations were based on a cylindrical structure or cavity enclosing the retro-reflector. The surfaces of this structure reflected specularly, and their solar absorptance was 0.1. As shown previously in Figure 2, the effective solar absorptance of this cylindrical cavity (based on the aperture area of the cavity) was greater than 0.1 and increased with sun angle.

At the suggestion of the principal investigators during a meeting on August 9, the vertical ΔT's in the retro-reflector were calculated assuming that the surrounding structure was adjacent to and matched the geometry of the back faces of the retro-reflector, i.e., equalateral triangles. It was agreed that a reasonable approximation would be to set the effective solar absorptance at 0.1 and independent of sun angle, for sun angles greater than those where total internal reflection occurs.

The results of this calculation are shown in Figure 8 for a surface radiator configuration with a radiating area of 4.7 cm^2 (40% of the area of the retro-reflector), a solar absorptance of 0.06, and an emittance of 0.85. Also shown in Figure 8 for comparison are the computed vertical ΔT's in the retro-reflector considering the same surface radiator configuration and a cylindrical structure enclosing the retro-reflector. The structure with the constant effective solar absorptance ($\bar{\alpha} = 0.1$) reduces the maximum vertical ΔT in the retro-reflector by approximately 0.2K. It also reduces the fraction of the total lunar period where the ΔT exceeds 1°K from 17% to 5%.

V. CALCULATIONS WITH MULTI-ZONE THERMAL MODEL

As described in Section III, in the computer model of the retro-reflector and surface radiator configuration, the retro-reflector was represented as a single-zone pyramid with temperatures calculated at five locations. This arrangement was used to facilitate parametric design analyses and obtain results for the surface radiator configuration early in the program. Comparisons between results obtained with the single-zone model of the retro-reflector and a more detailed subdivided model

(developed for the study of the louver array) have indicated good agreement; however, the subdivided model was required and used for two studies which investigated the influence of "local" effects on the ΔT in the retro-reflector. One study was made to examine the effect of conductive coupling via the mounting points between the structure and the retro-reflector (mounting conductance). The other was made to determine the influence of axial temperature differences in the structure on the ΔT in the reflector. A low α/ε surface radiator configuration was used for both studies (e.g., a solar absorptance of 0.06, an emittance of 0.85 and a radiating area of 2.85 cm^2, approximately 25% of the surface area of the retro-reflector).

A. Effect of Mounting Conductance

Present design concepts consider each retro-reflector to be structurally mounted to its containing structure by two preloaded mounting rings. For example, a preliminary design drawing* of the "Reflector Mount Detail" shows the retro-reflector structurally supported by two zigzag stainless steel mounting rings which are in continuous contact with the structure and restrain the retro-reflector at three peripheral tabs near the front surface.

The structure-to-reflector mounting conductance depends upon the geometry and material of the mounting rings and the preload forces necessary to provide support for shock and vibration. In the following study the mounting conductance was varied parametrically over a probable range of values expected for this type of support design in order to determine thermal design guidelines.

As shown previously, when solar energy is assumed to pass through the retro-reflector without internal reflection at sun angles between +20 and -45 degrees, the maximum vertical ΔT's in the retro-reflector occur in the range of sun angles between 20 and 30 degrees. In Figure 9 the vertical ΔT (difference in temperature between apex and center of top surface and the radial ΔT (difference in temperature between mounting tab and center of top surface) are plotted versus mounting conductance at a sun angle of 30°. For this low α/ε radiator

* Arthur D. Little, Inc., Drawing No. D-SK-71868-1 (July 18, 1968).

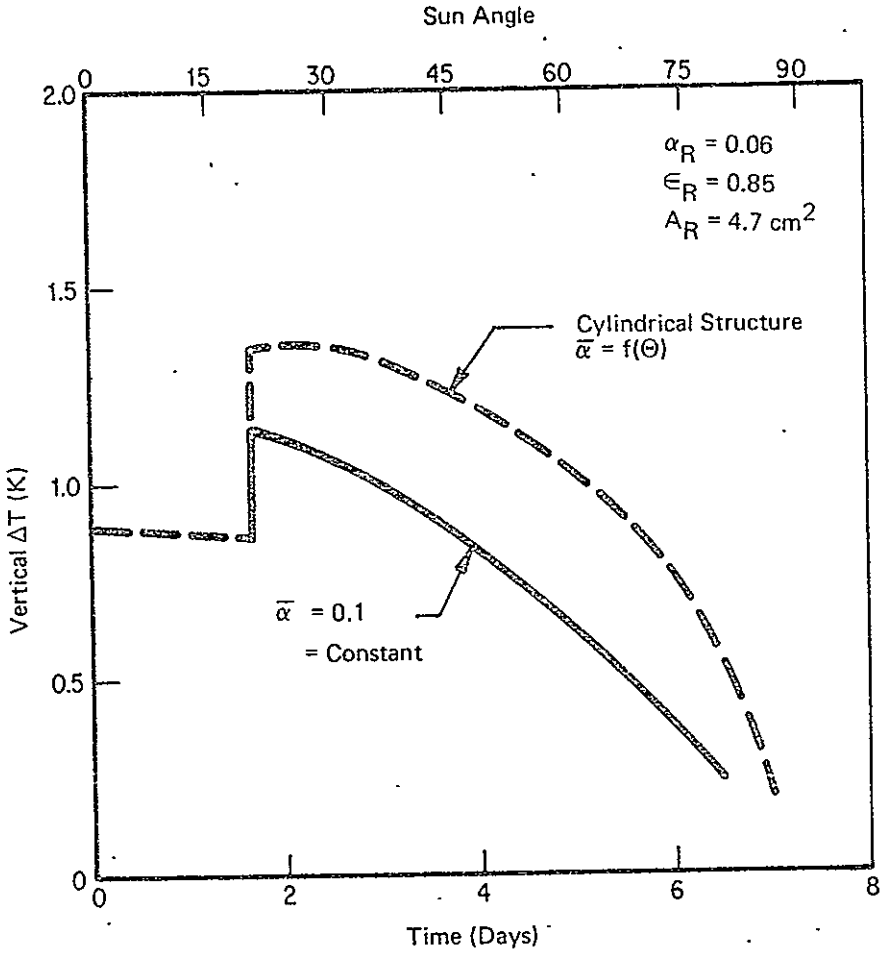

FIGURE 8 COMPARISON OF CYLINDRICAL STRUCTURE AND STRUCTURE WITH A CONSTANT EFFECTIVE SOLAR ABSORPTANCE

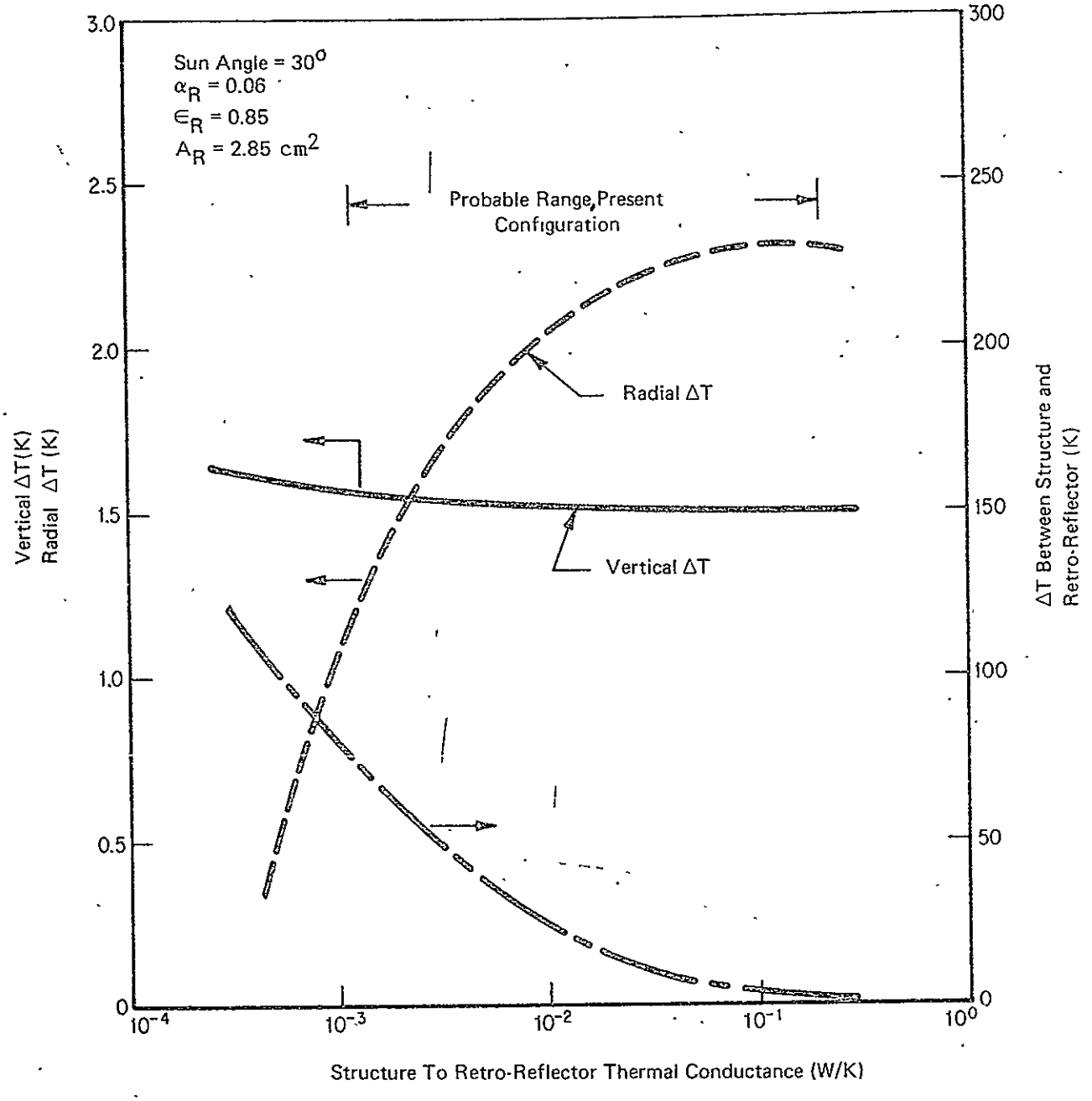

FIGURE 9 EFFECT OF MOUNTING CONDUCTANCE ON THE ΔT IN THE RETRO-REFLECTOR

configuration, the maximum ΔT with zero mounting conductance was approximately 1.6°K. Also, at a sun angle of 30°, where the maximum occurred, the mean temperature of the retro-reflector was 216K and the temperature of the structure was 354K. As shown in Figure 9, the computed vertical ΔT in the retro-reflector was 1.6K at a conduction of 10^{-4} W/K, decreased as the conductance increased and assymptotically approached a value of 1.5K at large conductances (approximately 0.2 W/K). On the other hand, the radial ΔT increased with increasing mounting conductance, was greater than the vertical ΔT for conductances larger than 10^{-3} W/K, and reached a maximum of approximately 2.2K.

Also shown in Figure 9 is the temperature difference between the structure and the retro-reflector. The structure is warmer than the retro-reflector, and there is always a net heat flow from the structure to the retro-reflector. As the mounting conductances increase, the structure-to-reflector ΔT decreases and the net radiative flux to the reflector, which is distributed over the back surface, also decreases. However, the conductive heat flow to the retro-reflector, which is localized near the top surface, can be radiatively dissipated to space and becomes a driving force for radial ΔT's (i.e., radiating fin effect). At large conductances the temperatures of the retro-reflector and structure were nearly equal at a value of 254K.

These results indicate that a low mounting conductance ($< 10^{-3}$ W/°K) is desirable. The vertical ΔT is relatively insensitive to changes in mounting conductance; however, as the conductance becomes large, the mounting tabs become the warmest regions in the reflector and the difference in temperature between the mounting tab and the center of the top surface becomes the dominant ΔT.

B. Effect of Axial Temperature Gradients in the Structure

In the parametric studies of the surface radiator configurations it was assumed that the aluminum structure of high thermal conductance (surrounding the retro-reflector) was isothermal. Calculations using detailed computer models and analytical models have shown that this assumption is valid and that vertical temperature gradients in the structure do not substantially increase the vertical ΔT in the retro-reflector.

For the low α/ε surface radiator configuration described above, a calculation was made at an orbital time when the vertical ΔT in the retro-reflector was maximum (i.e., at a sun angle of approximately 30°). A multi-zone computer thermal model was used to compute the vertical ΔT in the retro-reflector as a function of specified vertical ΔT's in the structure (measured from back to front).

An analytical calculation was also made for an analogous, but more simplified, thermal model. The one-dimensional temperature distribution was calculated for the problem of a straight fin of triangular profile. The front surface of the fin (base of triangle) was exposed to outer space; the two sides of the triangle were radiatively coupled to a surrounding structure with a linear temperature gradient; and it was assumed that the width of the fin was large in comparison to the altitude of the triangle. Since the temperature differences in the retro-reflector are small (1 to 2K), the differential equation can be linearized by letting:

$$\theta(x) = T(x) - \bar{T}$$

where $T(x)$ is the axial temperature in the fin, and $\bar{T}$ is the mean temperature,

and $$T(x)^4 \doteq \bar{T}^4 + 4\,\bar{T}^3\,\theta(x)$$

In this problem the mean temperature levels of the surrounding structure and the fin were specified at 354K and 210K, respectively. (These values were based on the computer solution of this surface radiator configuration when the sun angle was 30 degrees.)

The calculated effects of the axial temperature gradients in the structure obtained with the computer and analytical models showed good agreement. Figure 10 summarizes the results and shows the computed increase in the vertical ΔT in the retro-reflector due to a vertical ΔT in the structure.

The specified values of the vertical ΔT's in the structure ranged from 0 to 8K and were conservatively estimated by assuming that the maximum total heat input to the structure was conducted along the sides of the cylindrical structure and was radiatively dissipated to space via the surface radiator. Thus, the ΔT was estimated according to the following simple equation:

$$\Delta T = \frac{q_T}{K\pi Dt/\ell}$$

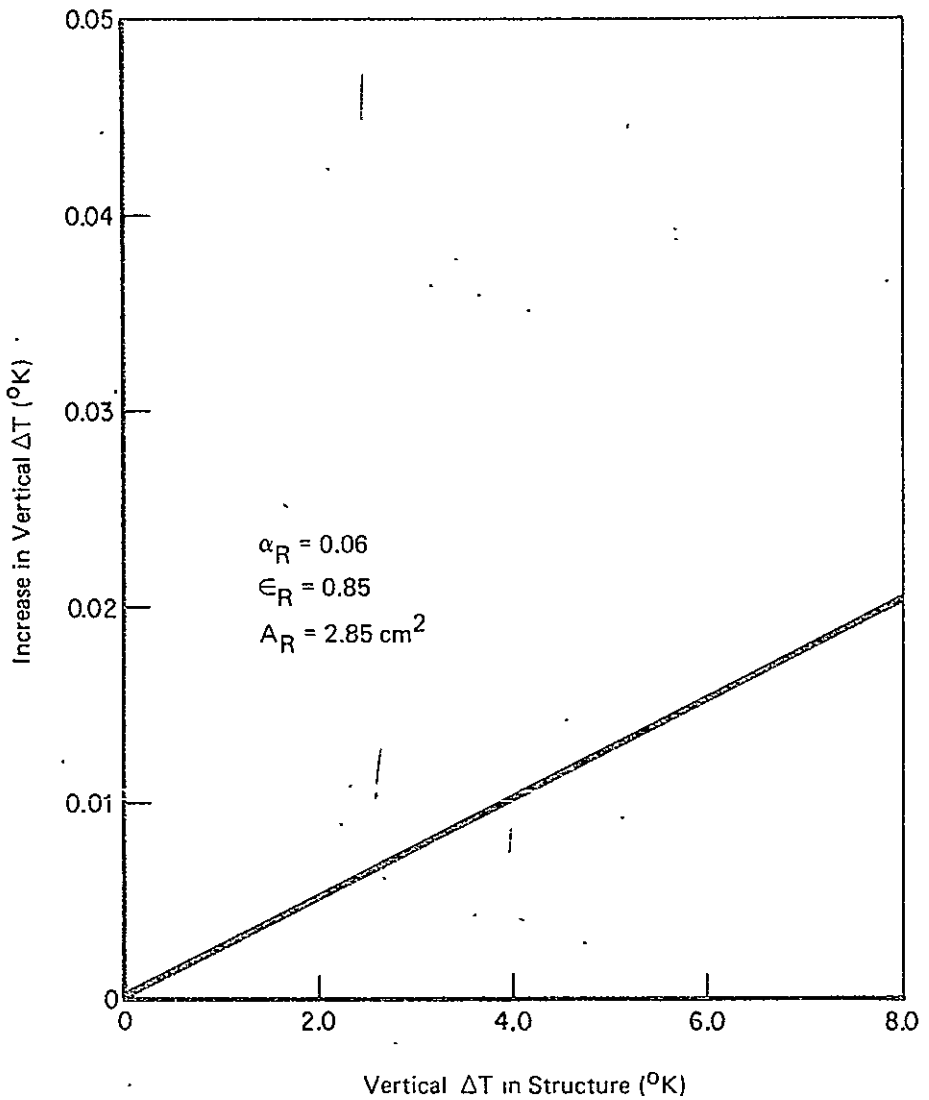

FIGURE 10 EFFECT OF VERTICAL TEMPERATURE GRADIENTS IN THE STRUCTURE

where q_T is the maximum total heat input to the structure during the lunar period (comprised of solar absorption on the surface radiator, solar absorption on the interior of the structure, and IR power absorbed from radiation interchange with the lunar surface), and κ, D, t, and ℓ are the thermal conductivity, diameter, wall thickness, and length of the structure, respectively. The maximum ΔT in the structure for practical configurations, where the structure is radiatively de-coupled from the lunar surface, was 1.5K. The ΔT in the structure was approximately 8°K when the structure was well thermally coupled to the lunar surface (i.e., no "super" insulation between the structure and the lunar surface).

For the above range of ΔT's in the structure, the increase in the vertical ΔT in the retro-reflector was less than 0.05K (less than 3% of the vertical ΔT computed when an isothermal structure was assumed).

TECHNICAL MEMORANDUM #3

Optical Distortion Caused by a Vertical Temperature Gradient in a Retro-Reflector

prepared for

University of Maryland
College Park
Maryland 20742

Contract 21099

by

A. G. Emslie and P. F. Strong
Arthur D. Little, Inc.
Acorn Park
Cambridge, Massachusetts 02140

August 30, 1968

C-70472

TABLE OF CONTENTS

LIST OF FIGURES

I. SUMMARY

In this report we calculate the distortion in the wavefront emergent from a solid totally internally reflecting retroreflector caused by linear and quadratic temperature distributions with vertical gradients. From these wavefront calculations we determine the fractional change in the central irradiance of the Fraunhofer diffraction pattern. Polarization effects are neglected and light is assumed to be incident normally.

The results of these calculations for linear and quadratic temperature distributions are summarized in Figure 4 at the end of this memorandum, which shows the fractional change in central irradiance (W/W_o) that results from temperature differences (δT) ranging from 0 to 6°C.

II. METHOD

Figure 1 shows a typical ray incident normally on the front face of the retroreflector at the point A. The ray is reflected successively by the three inclined planes at the points B, C, D and emerges at the point E. Relative to axes x'y'z' along the edges of the reflector, as shown, the direction cosines l', m', n' of the path segments are as follows:

Path Segment	l'	m'	n'
AB	$-1/\sqrt{3}$	$-1/\sqrt{3}$	$-1/\sqrt{3}$
BC	$1/\sqrt{3}$	$-1/\sqrt{3}$	$-1/\sqrt{3}$
CD	$1/\sqrt{3}$	$1/\sqrt{3}$	$-1/\sqrt{3}$
DE	$1/\sqrt{3}$	$1/\sqrt{3}$	$1/\sqrt{3}$

It will be noted that at each reflection the direction cosine corresponding to the axis normal to the reflecting plane is reversed in sign in accord with Snell's law of reflection.

A more convenient set of axes are those shown as Ox, Oy, Oz in Fig. 1. Relative to the original axes (x', y', z'), Oz has the direction cosines ($1/\sqrt{3}$, $1/\sqrt{3}$, $1/\sqrt{3}$). Therefore, the cosine of the angle γ that

each ray segment makes with Oz is as follows:

Segment	cosγ
AB	- 1
BC	- 1/3
CD	1/3
DE	1

The coordinates $(x_0y_0z_0)$, $(x_1y_1z_1)$, $(x_2y_2z_2)$, $(x_3y_3z_3)$, $(x_4y_4z_4)$ of the points A, B, C, D, E can be expressed without difficulty in terms of x_0, y_0 and the vertical height h of the retroreflector with the help of the above values of cosγ and the diagram of the projections of the path segments on the front face, shown in Fig. 2. The projection of segment BC is perpendicular to the edge ab of the front face while the projection of segment CD is perpendicular to the edge ac. The projections are bisected at the points p, q. The results of the calculations are:

Point	Coordinates
A	$(x_0y_0z_0) = (x_0 , y_0 , h)$
B	$(x_1y_1z_1) = (x_0 , y_0 , \frac{\sqrt{6}}{2} x_0 + \frac{\sqrt{2}}{2} y_0)$
C	$(x_2y_2z_2) = (- x_0, y_0 - \frac{2}{\sqrt{3}} x_0, \frac{1}{\sqrt{6}} x_0 + \frac{1}{\sqrt{2}} y_0)$
D	$(x_3y_3z_3) = (- x_0, - y_0 , \sqrt{2}\, y_0)$
E	$(x_4y_4z_4) = (- x_0, - y_0 , h)$

As a check one can calculate the lengths of the path segments, which are:

Segment	Length
AB	$h - \frac{\sqrt{6}}{2} x_0 - \frac{\sqrt{2}}{2} y_0$
BC	$\sqrt{6}\, x_0$
CD	$\frac{3\sqrt{2}}{2} y_0 - \frac{\sqrt{6}}{2} x_0$
DE	$h - \sqrt{2}\, y_0$

The path lengths add up to 2h as they should.

We are now in a position to calculate the phase shift ϕ caused by the temperature gradient as a function of the coordinates (x_0, y_0) of the entering ray by means of the formula

$$\phi = \frac{2\pi}{\lambda} \int_{\text{path}} \delta n \, ds$$

$$= \frac{2\pi}{\lambda} \frac{dn}{dT} \int_{\text{path}} \delta T \, ds$$

$$= \frac{2\pi}{\lambda} \frac{dn}{dT} \int_{\text{path}} \delta T \, \frac{dz}{\cos\gamma}$$

where λ is the wavelength of the light, δn is the change in refractive index at any point along the path of the ray, ds is an element of length of the path, dn/dT is the temperature coefficient of refractive index, δT is the temperature increment at a point on the path, and γ, as before, is the inclination of the path to Oz.

Linear Temperature Distribution

A linear temperature distribution with vertical gradient can be represented by the formula

$$T = T_o - \Delta T \frac{z}{h}$$

where T_o is the temperature at the vertex of the retroreflector and ΔT is the temperature difference between the vertex and the front face. Therefore

$$\delta T = - \Delta T \frac{z}{h}$$

and

$$\phi = - \frac{2\pi}{\lambda} \frac{dn}{dT} \frac{\Delta T}{h} \int_{path} \frac{z dz}{\cos\gamma}$$

On integrating over each segment of path and substituting the appropriate values of γ, as given above, we obtain:

$$\phi = - \frac{2\pi}{\lambda} \frac{dn}{dT} \frac{\Delta T}{h} \cdot \frac{1}{2} \left[\frac{z_1^2 - z_0^2}{-1} + \frac{z_2^2 - z_1^2}{-1/3} + \frac{z_3^2 - z_2^2}{1/3} + \frac{z_4^2 - z_3^2}{1} \right]$$

After inserting the values of $z_0 \ldots z_4$, given above, we find

$$\phi = -\frac{2\pi}{\lambda}\frac{dn}{dT}\frac{\Delta T}{h}\left(h^2 + x_0^2 + y_0^2\right)$$

$$= -\frac{2\pi}{\lambda}\frac{dn}{dT}\frac{\Delta T}{h}\left(h^2 + r^2\right) \qquad (1)$$

where r is a radial coordinate on the front face. Therefore, the emerging wavefront is a paraboloid of revolution.

Quadratic Temperature Distribution

For the quadratic temperature distribution

$$T = T_o - \Delta T \left(\frac{z}{h}\right)^2$$

we find, in exactly the same way, that

$$\phi = -\frac{2\pi}{\lambda}\frac{dn}{dT}\frac{\Delta T}{h^2} \cdot \frac{1}{3}\left[\frac{z_1^3 - z_0^3}{-1} + \frac{z_2^3 - z_1^3}{-1/3} + \frac{z_3^3 - z_2^3}{1/3} + \frac{z_4^3 - z_3^3}{1}\right]$$

On substituting for $z_0 \ldots z_4$ we get

$$\phi = -\frac{2\pi}{\lambda}\frac{dn}{dT}\frac{\Delta T}{h^2} \cdot \left[\frac{2}{3}h^3 + \frac{4\sqrt{6}}{9}x_0^3 + \sqrt{2}\,x_0^2 y_0 + \sqrt{2}\,y_0^3\right]$$

where $(x_0 y_0)$ must lie in the shaded area shown in Fig. 3 in order that all incident rays are reflected in the same sequence from the three side faces of the retroreflector. On rotating the axes counterclockwise through 60°, so that the new x-axis lies symmetrically in the shaded area, the expression becomes

$$\phi = \frac{2\pi}{\lambda} \frac{dn}{dT} \frac{\Delta T}{h^2} \left[\frac{2}{3} h^3 + \frac{5\sqrt{6}}{9} x^3 + \sqrt{6}\, xy^2 \right]$$

Since this expression is symmetrical with respect to the x-axis, we see that the emerging wavefront consists of a six-fold scalloped surface. However, the relative amplitude of the scalloping is quite small. On transforming to polar coordinates r,θ we find:

$$\phi = -\frac{2\pi}{\lambda} \frac{dn}{dT} \frac{\Delta T}{h^2} \left[\frac{2}{3} h^3 + \sqrt{6}\, r^3 \left(\frac{5}{9} \cos^3\theta + \cos\theta \sin^2\theta \right) \right]$$

where $-30° \leq \theta \leq 30°$. Over this range of θ the factor $(5/9)\cos^3\theta + \cos\theta \sin^2\theta$ varies by only ±2% about a mean value of 0.566. Therefore to a good approximation we have

$$\phi = -\frac{2\pi}{\lambda} \frac{dn}{dT} \frac{\Delta T}{h^2} \left[\frac{2}{3} h^3 + 0.566\sqrt{6}\, r^3 \right] \qquad (2)$$

Relative Central Irradiance

The relative central irradiance of the Fraunhofer diffraction pattern of the retroreflector is

$$\frac{W}{W_o} = \frac{1}{A^2}\left|\int e^{i\phi}\, dA\right|^2 \tag{3}$$

where W is the irradiance at the center of the diffraction pattern, W_o is the irradiance for an isothermal reflector, A is the area of the front face of the reflector, and ϕ is the phase at a point on the front face.

In the case of the linear temperature distribution, with δ given by (1), the integral in (3) can be evaluated in closed form to give:

$$\frac{W}{W_o} = \frac{\sin^2\left(\frac{KR^2}{2}\right)}{\left(\frac{KR^2}{2}\right)^2} \tag{4}$$

where R is the radius of the front face of the retroreflector and

$$K = \frac{2\pi}{\lambda}\,\frac{dn}{dT}\,\frac{\Delta T}{h}$$

For the quadratic temperature distribution Eq. (3) takes the form

$$\frac{W}{W_o} = \frac{1}{(\pi R^2)^2}\left[\left(\int_0^R (\cos kr^3)\, 2\pi r dr\right)^2 + \left(\int_0^R (\sin kr^3)\, 2\pi r dr\right)^2\right] \qquad (5)$$

where

$$k = 0.566\sqrt{6} \cdot \frac{2\pi}{\lambda}\frac{dn}{dT}\frac{\Delta T}{h^2}$$

The integrals in this equation must be evaluated by numerical integration.

III. RESULTS

Figure 4 shows how W/W_o depends on ΔT for both linear and quadratic temperature distributions. The curves were computed for the following data:

$h = 2.69$ cm

$R = 1.905$ cm

$\lambda = 6.943 \times 10^{-5}$ cm

$dn/dT = 1.0 \times 10^{-5}\ (°C)^{-1}$

The graphs show that, for a given ΔT, there is not much difference between the effects of linear and quadratic temperature distributions. W/W_o falls to zero in both cases when ΔT is about 5.5°C. This zero value of the central irradiance corresponds to two complete Fresnel zones filling the aperture of the retroreflector.

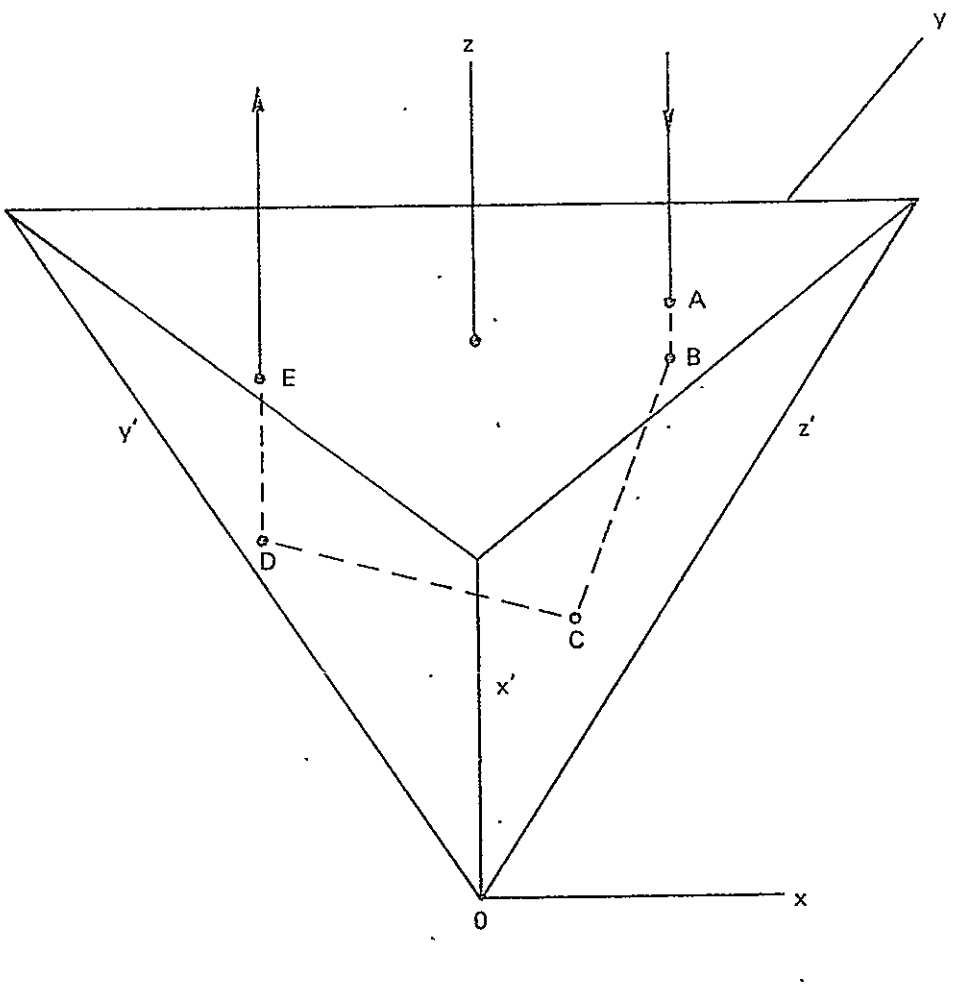

FIGURE 1 PATH SEGMENTS OF A TYPICAL NORMALLY INCIDENT RAY

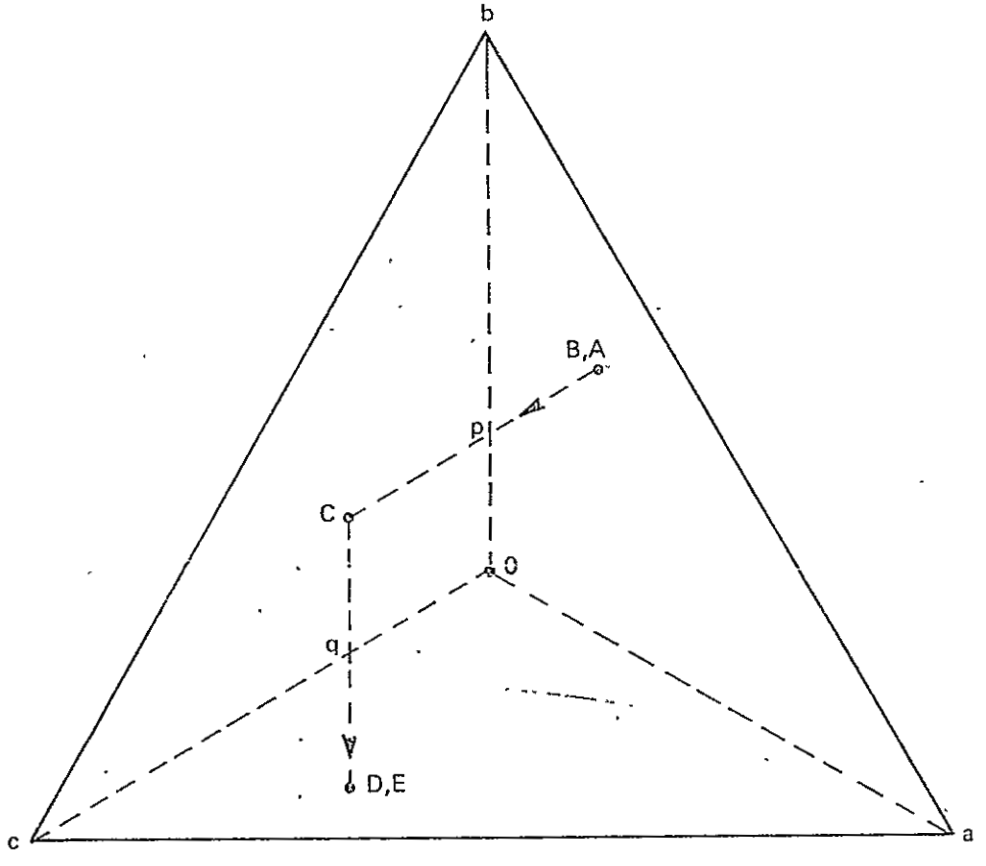

FIGURE 2 PROJECTIONS OF RAY PATH SEGMENTS ON THE RETRO-REFLECTOR FRONT FACE

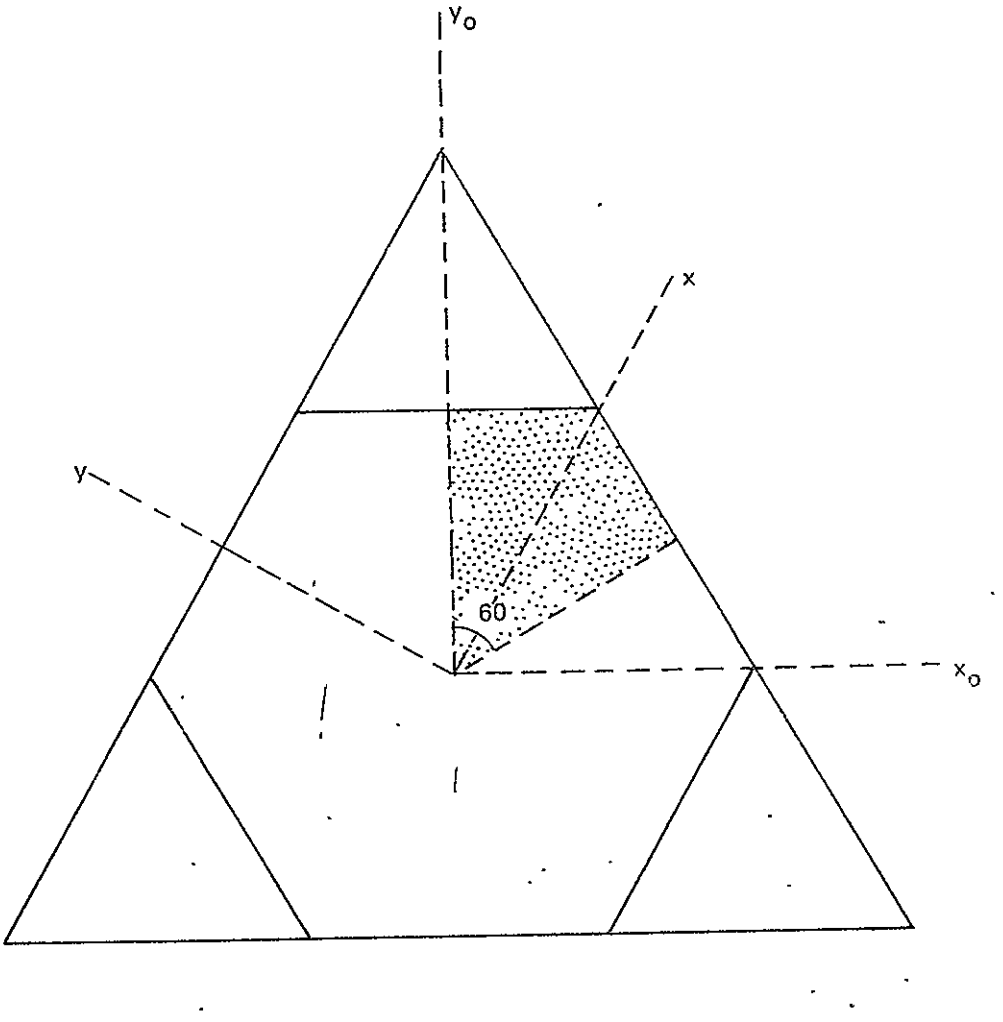

FIGURE 3 ROTATION OF AXES

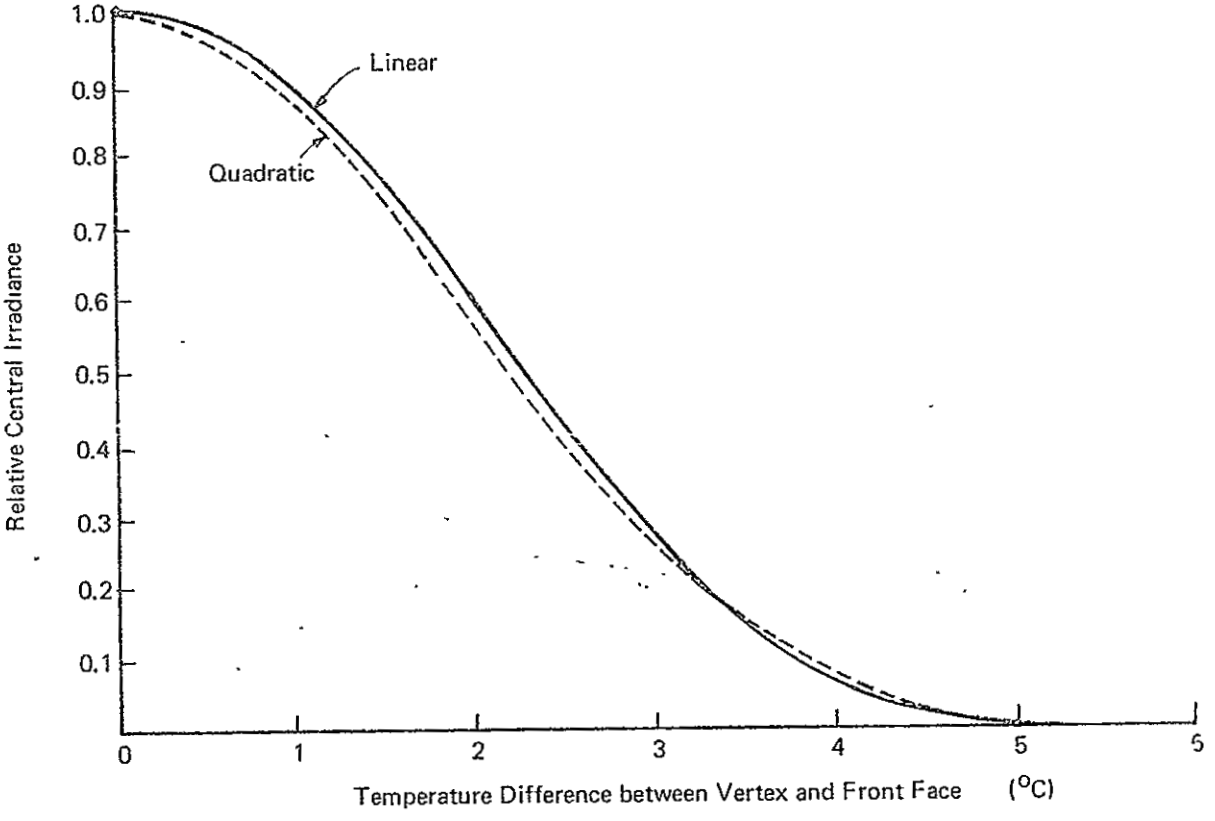

FIGURE 4 RELATIVE CENTRAL IRRADIANCE AS A FUNCTION OF TEMPERATURE DIFFERENCE

TECHNICAL MEMORANDUM #4

Thermal Analysis of Louver Configuration

prepared for

University of Maryland
College Park
Maryland 20742

by

Richard L. Merriam

Arthur D. Little, Inc.
20 Acorn Park
Cambridge, Massachusetts 02140

September 27, 1968

C-70472

TABLE OF CONTENTS

LIST OF FIGURES

LIST OF TABLES

I. SUMMARY AND CONCLUSIONS

An analytical study has been performed to investigate the thermal performance of a retro-reflector with various louver configurations. Some parameters considered were the louver cell height-to-width ratio, louver surface properties, the thermal conductance between the louver and cannister and the conductance across the mounting tabs.

The retro-reflector was modeled by a regular tetrahedron subdivided into five zones. Conduction and heat generation within the reflector, as well as radiant energy exchange between the retro-reflector and the louver-cannister surroundings, were taken into account. The louvers were considered conducting and an effective conductance between the louver array and the cannister was determined. All calculations of thermal performance were based on a uniform volumetric heating assumption since a detailed analysis showed that the actual heating distribution within the quartz reflector is nearly uniform. Most of the calculations were performed assuming quasi-steady heat transfer.

The results showed that the retro-reflector is most nearly isothermal where high-emittance louver cells of large length-to-width ratios are used. Of the three louver materials considered - as-received aluminum, anodized aluminum (ALZAK) and "black" aluminum - the poorest performance was obtained with the as-received aluminum louvers. Even in this case, however, the maximum vertical ΔT^* was less than 1°K. The predicted temperature gradients associated with the use of black or ALZAK louvers were considerably smaller. There appeared to be little difference in the results predicted for these last two louver materials.

Predicted temperature gradients were found to be sensitive to the mounting conductance - particularly with the as-received aluminum. With a large mounting conductance, large distortions of the temperature distribution within the retro-reflector could result because of the

---

* Defined as the temperature at the retro-reflector apex *minus* the temperature at the center of the upper surface.

radial flow of heat into or out of the cannister. This distortion could be diminished by decreasing the mounting conductance and using high-emittance louvèrs.

Quasi-steady heat transfer analyses for black louvers indicated satisfactory performance for louver cell height-to-width ratios as small as 0.625. No studies were performed using smaller values of this ratio. It was found that the maximum vertical ΔT was less than 0.9°K for this configuration.

A transient analysis was also performed for a black louver configuration. The thermal response predicted was substantially the same as that predicted assuming quasi-steady heat transfer.

From the results it is concluded that the optimum thermal performance is obtained when highly conducting louvers of high emittance are used, and when the thermal conductance across the mounting tabs is kept to a minimum. With these restrictions, the use of louvers as short as $L/W = 0.625$ will insure temperature differences across the quartz reflector of less than 1°K.

II. THERMAL MODEL

A. General Description of Physical Configuration

A schematic drawing of the computer model of a retro-reflector with a louver cell array is shown in Figure 1. The retro-reflector, which is connected to the cannister by three mounting tabs, is treated as a regular tetrahedron of altitude equal to 1.06 inches.

The retro-reflector is in thermal communication with the cannister and louver array by radiant energy transfer in the infrared. In addition, heat may be conducted to the reflector through the mounting tabs. A solar flux, which is collimated at an angle θ from the normal to the lunar surface, is incident on the louver array and over certain sun angles is directly incident on the quartz reflector. The cannister receives solar energy which is not retro-reflected and absorbs infrared radiation from the lunar surface.

Through the processes of emission of radiant energy at the surfaces and internal heating due to absorption of solar energy, a non-uniform temperature distribution is established within the quartz reflector. The details of the various energy transfer mechanisms which lead to these temperature gradients are discussed in the sections which follow.

B. Model of Retro-Reflector

The heat flow within the interior and the heat fluxes at the surfaces of the retro-reflector were determined using the Method of Zones discussed in Ref. [1]. Briefly, a functional form for the temperature distribution within a volume element or "zone" is assumed, and a mean zone temperature and average surface temperatures are determined. Integrated surface heat fluxes are then found in terms of the constants appearing in the expression for the temperature distribution. A series of simultaneous equations results which can then be solved for the mean zone and average surface temperatures. For a complete description of

---

1. R. Merriam, Technical Memorandum #1, "Preliminary Thermal Analysis of a Retro-Reflector," July 1968.

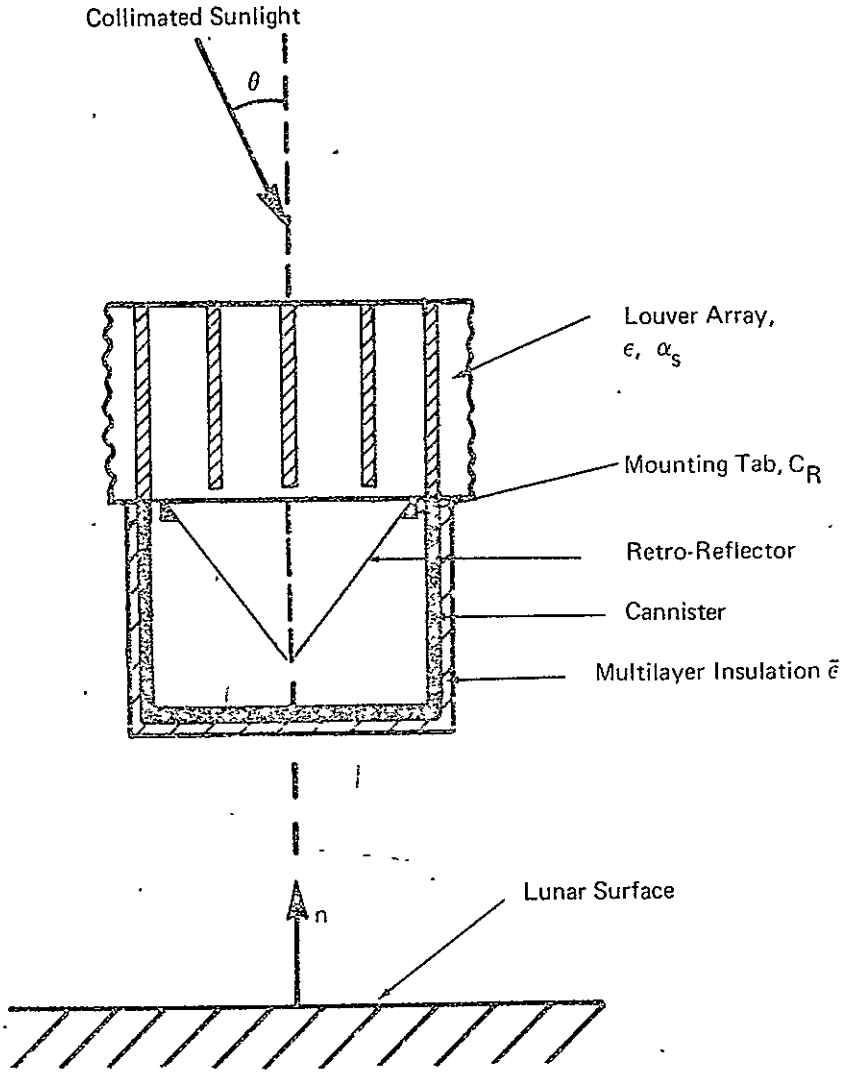

FIGURE 1 SCHEMATIC REPRESENTATION OF THERMAL MODEL

the Method of Zones, the reader is directed to Ref. [2].

Most of the thermal studies were performed with the five-zone model illustrated in Figure 2. Use of the five-zone model, rather than the single-zone model discussed in Ref. [1], allowed for a more detailed description of the conduction process within the reflector. In particular, a multi-zone model was necessary to accurately account for the local conductive transfer across the mounting tabs.

All calculations were performed with the assumption of a uniform volumetric heating rate corresponding to a total absorptance of 0.047 within the quartz. An earlier report [1] indicated that for a simple slab the assumption of a uniform solar heating could result in a predicted temperature gradient higher than would be obtained with the actual heating distribution taken into account. However, an analysis performed for a tetrahedron showed that the heating rate in a retro-reflector is nearly uniform. The difference between the uniform and the actual heating rates did not justify further calculations. The details of this analysis are presented in APPENDIX I.

C. Louver Configuration

A top view of the modeled louver array configuration is shown in Figure 3. The retro-reflectors are represented as circles in the figure. Since the panels form a nearly square network, the louver was considered to consist of an infinite array of unit cells. A typical unit cell is illustrated in Figure 4.

The heat transfer mechanisms within a unit cell include: (1) conduction within the cell array; (2) radiant energy interchange between the various cell panels, and between the cell panels and the retro-reflector; and (3) the absorption and reflection of incident solar energy. For the purpose of analysis, the typical unit cell is shown divided into eight individual panels. Surface "i" illustrated in Figure 4 represents one of the four elements on the retro-reflector upper surface.

The conduction mode of transfer within the louver cell was calculated using the Method of Zones. Temperatures were computed for each

---

2. P. F. Strong and A. G. Emslie, "The Method of Zones for the Calculation of Temperature Distribution," ASME 65-WA/HT-47.

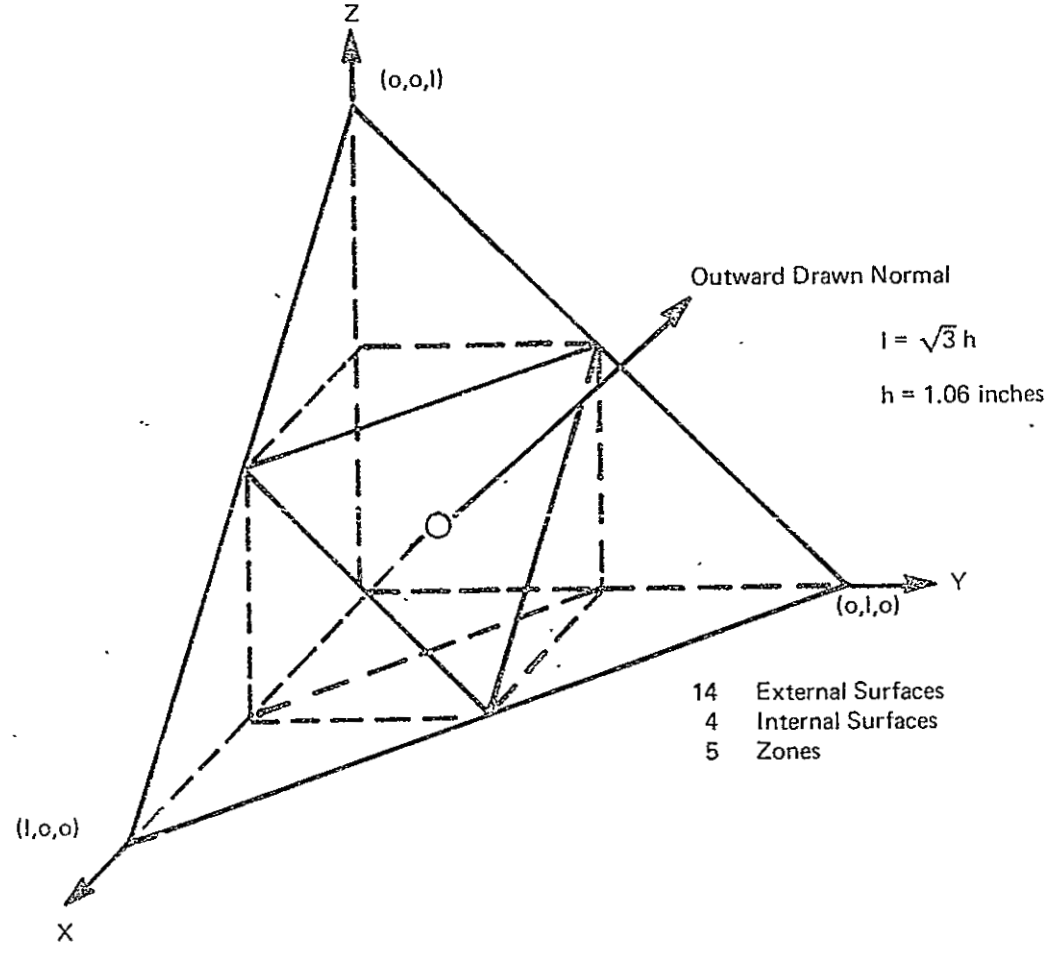

FIGURE 2 FIVE ZONE MODEL OF RETRO-REFLECTOR

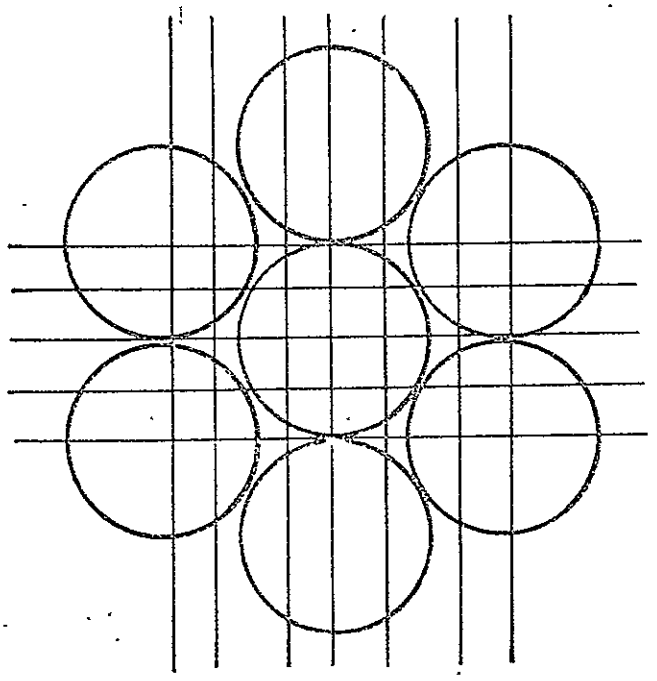

FIGURE 3 TOP VIEW OF LOUVER ARRAY

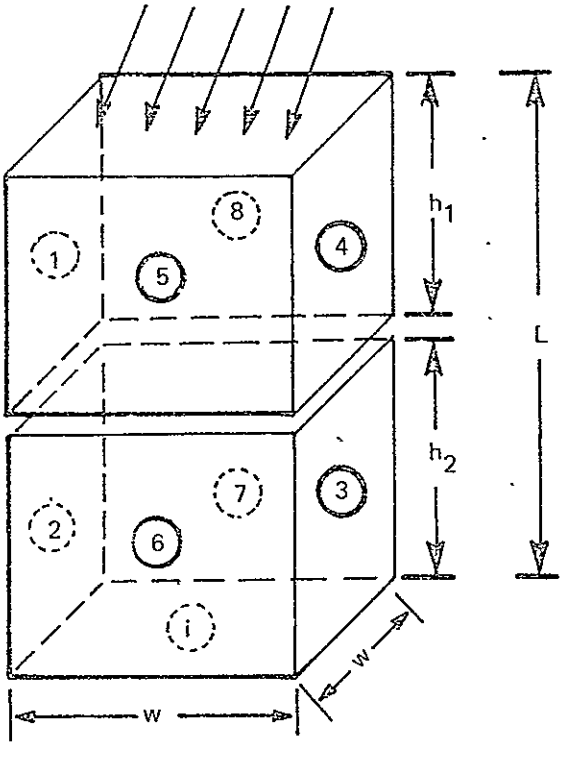

FIGURE 4 TYPICAL LOUVER CELL

of the zones 1 through 8 and at the edges joining each of the zones. In addition, temperatures were computed at the bottom edges of the cell where the louver array is coupled to the cannister. The model used to predict the extent of this coupling is developed in APPENDIX II.

The infrared radiation transfer between elements of a cell and the retro-reflector was computed in terms of the "view areas" (equivalent to the Hottel script - F factor) between the various elements. For example, if the view area between elements i and j is denoted by the quantity $A_i \mathcal{F}_{i-j}$, then the net radiative interchange between these two surfaces is simply

$$Q_{i \rightleftarrows j} = A_i \mathcal{F}_{i-j} (\sigma T_i^4 - \sigma T_j^4) \quad .$$

For given louver cell dimensions w, h_1 and h_2 and surface properties ε and α_s, the view areas were computed using a utility program available at ADL. The surface emittance of the quartz reflector was taken to be 0.85[3]

Calculations of the net solar energy absorbed by each element were somewhat more complicated. The accounting procedure included not only the solar energy absorbed and reflected by the louver panels but also that portion of the solar flux which passed through the retro-reflector and was partially absorbed by the cannister.

The cannister was treated as a cavity when performing the solar power absorption calculations. Solar energy could enter the cavity in two possible ways. When the louver cell length-to-width ratio was less than 2.5 and the sun angle was greater than 20°, incident solar energy could pass directly through the retro-reflector. In this case the cavity was treated as having specular walls, as described in Ref. [4]. The

---

3. R. A. Breuch, G. A. Bell and N. J. Douglas, "Temperature Control Coatings for Cryogenic Temperature Substrata," Air Force Materials Laboratory, Report AFML-TR-66-10, Part II, 1967.

4. D. Nathanson, Technical Memorandum #2, "Preliminary Thermal Analysis of Surface Radiator Configuration," August 6, 1968.

effective solar absorptance and absorbed solar power for various sun angles is illustrated in Figure 2 of Ref. [4]. Solar energy could also pass through the reflector into the cannister after reflection off a louver panel. In this case, the cannister was treated as a cavity with diffusely incident radiant energy. For a cavity having surfaces with a solar absorptance of 0.1 and having the dimensions of the cannister, the absorptance is approximately 0.2.[5]

The solar powers absorbed by the louver panels and zone "i" of Figure 4 (representing the cavity in these calculations) were computed using a utility program available at ADL. Solar energy retro-reflected by the quartz reflector and impinging on a louver panel was taken into account. Net absorbed powers were computed for sun angles between 0 and 90 degrees and were used in the heat transfer calculations.

D. Heat Transfer to Cannister

The total energy input to the cannister consists of: solar energy, infrared transfer from the retro-reflector, infrared transfer from the lunar surface, conductive transfer with the louver, and the conductive transfer with the retro-reflector across the mounting tabs. For computational simplicity, the cannister was considered to be isothermal. The correspondence between any temperature gradients within the cannister and temperature gradients within the retro-reflector has been shown to be very weak.[6]

Solar heating of the cannister has been treated in the preceding section. Infrared radiant transfer between the cannister and quartz reflector was computed in the same manner as the radiant transfer between the louver and reflector - that is, in terms of the view areas. The emittance of the inside surface of the cannister was taken to be 0.03 in these calculations.

---

5. S. H. Lin, "Radiant Interchange in Cavities and Passages with Specularly and Diffusely Reflecting Surfaces," Ph.D. thesis, University of Minnesota, 1964.

6. Arthur D. Little, Inc., Monthly Progress Report #3, prepared for University of Maryland, August 1968.

Radiant energy transfer between the moon and cannister was computed as described in Ref. [4]. The cannister was considered to be well insulated by MLI with an effective emittance $\bar{\varepsilon} = 0.01$.

The largest uncertainty concerned the conductive coupling between the cannister and the retro-reflector via the mounting tabs. Since it is virtually impossible to be able to state with certainty the value of this conductance prior to a detailed design of the retainer, a parametric study was performed. A range of conductance values from 0 to 0.1 watt/°K was studied.

III. RESULTS

Parametric computer studies were performed to determine the influence on retro-reflector temperature gradients of louver height, louver emittance and solar absorptance, thermal conductance between the louver and cannister and conductance across the mounting tabs. Because of the large computer time required to obtain the temperature distributions within the reflector and within a unit louver cell, most of the results were obtained for quasi-steady transfer and over only a small fraction of the lunar day. One transient study was performed for a black louver configuration where the calculations extended over several lunar days.

Results are presented for several important temperatures and temperature differences. The term "vertical ΔT" is used to describe the temperature difference across the reflector along a line vertical to the upper face and passing through the apex; i.e., the apex temperature minus the temperature at the center of the upper face. The use of this term is not intended to imply that the temperature on the upper face is everywhere the same. The term "radial ΔT" signifies the temperature difference between the center of the top face and the mounting tab.

A. Influence of Louver Radiation Properties on Thermal Performance

Values for the vertical ΔT across the retro-reflector vs. time (solar angle) are illustrated in Figure 5 for three sets of louver surface properties. The (quasi-steady) calculations assume a louver cell height (L) to width (W) ratio of 2.5, a louver-cannister conductance of 0.25 watt/°K and zero mounting conductance. Shown for comparison are the corresponding results obtained for the so-called "best" surface radiator configuration (with an OSR coating and a forty percent radiating area based on the retro-reflector upper face area).* The properties chosen are typical of as-received aluminum ($\varepsilon = 0.13$, $\alpha_s = 0.25$), and ALZAK ($\varepsilon = 0.78$, $\alpha_s = 0.32$). The limiting case of purely "black" louvers is also considered ($\varepsilon = \alpha_s = 1$).

---

* See Technical Memorandum No. 2.

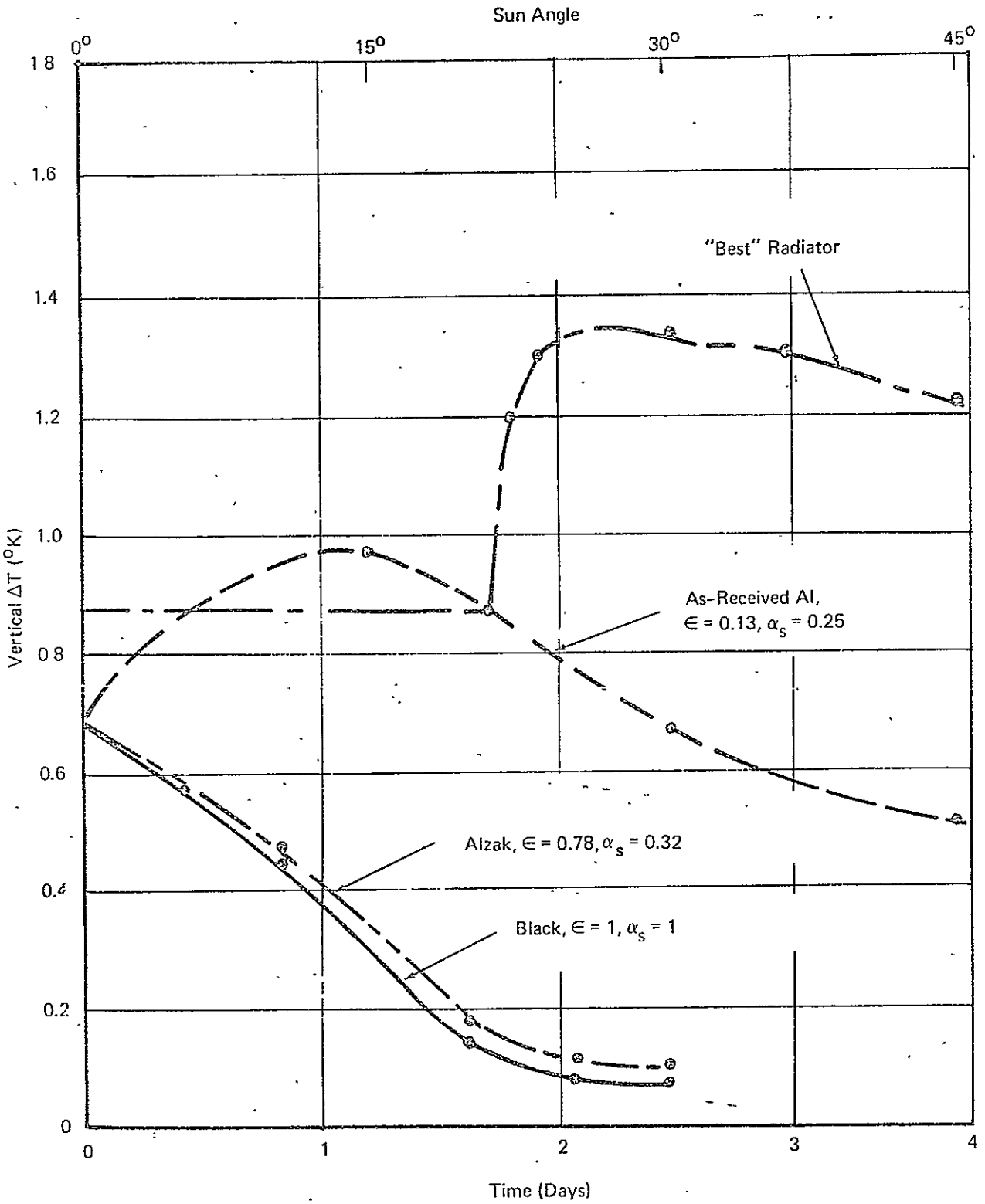

FIGURE 5 INFLUENCE OF LOUVER SURFACE PROPERTIES ON VERTICAL ΔT;

L/W = 2.5, C_L = 0.25, C_R = 0.

From a purely thermal standpoint, all three louver configurations are superior to the "best" surface radiator. The presence of a louver array reduces the reflector view area to space and provides a more uniform thermal environment for the retro-reflector. As expected, the best performance is obtained with the louvers with the highest surface emittance. For these louvers the maximum vertical ΔT occurs when the sun is directly overhead and is due primarily to the volumetric heating within the retro-reflector. On the other hand, the maximum vertical ΔT occurs near a 15° sun angle with the "as-received" aluminum louver configuration. In this case, as with the ALZAK louvers, a large fraction of the incident solar energy is reflected off the louver panels and is eventually absorbed by the cannister. The energy absorbed by the cannister is a maximum near the 15° sun angle. Since the as-received aluminum surface emittance is small, little heat is conducted to the louver and radiated to the retro-reflector upper surface. Rather, the energy is trapped within the cannister and is radiated to the back surfaces of the reflector.*

The results illustrated in Figure 5 show little difference between the black and anodized aluminum (ALZAK) louver configuration. Of the two surface properties, the absorptance and emittance, the surface emittance has the greater influence on the thermal performance. When the absorptance is high, much of the incident solar radiation is absorbed on the louver. When the absorptance is low, much of the incident energy is reflected off the louvers, absorbed by the cannister, and conducted to the louver array. In either case, the relatively hot louvers radiate energy to the retro-reflector thereby diminishing the so-called greenhouse effect. It is expected that with shorter louvers, or low-emittance louvers, the influence of the solar absorptance on the vertical ΔT would be more pronounced.

B. Influence of Louver and Mounting Conductance on Thermal Performance

The dependence of the vertical ΔT on the louver-cannister conductance, C_L, and the mounting conductance, C_R, is illustrated in

---

* This process is called the "greenhouse effect" in Ref. [4].

Figure 6. Comparisons are made assuming an as-received aluminum louver array with a cell height-to-width ratio of 2.5.

The results show that the vertical temperature gradient decreases with increasing conductance between the louver and cannister and increases with increasing mounting conductance. The reason for the influence of louver-cannister conductance, C_L, is clear. As this conductance increases, the thermal environment becomes more uniform. Heat which might otherwise have been radiated from the cannister to the retro-reflector back surfaces is now conducted to the louver array where it can be radiated to the reflector front surface.

The behavior of the vertical ΔT with mounting conductance is more complex and will be explained with reference to Table 1. Listed in Table 1 are the retro-reflector temperatures at the apex, tab and center of the top face. Shown also are values for the cannister temperature.

It is seen that the mounting tab temperature always lies between the cannister temperature and the other retro-reflector temperatures. That is, the tab is either the coldest or the warmest location on the reflector. This means that heat either flows to the tab from everywhere within the reflector, or flows away from the tab in all directions into the retro-reflector. When the cannister is warmer than the reflector (for sun angles somewhat greater than zero), heat flows into the reflector. Since the top surface can easily radiate much of this additional heat to space and the bottom surfaces cannot dissipate this heat (the greenhouse effect), a net flow of heat into the reflector results in an increase in the "vertical" ΔT. At normal sun incidence (0°), the cannister is cooler than the reflector and heat flows from the quartz resulting in a lower vertical ΔT.

It is expected that sizeable temperature gradients across the retro-reflector in the horizontal direction would result from the conductive heat flow from the cannister. A measure of this distortion of the temperature distribution is the "radial" ΔT defined as temperature difference between the center of the top face, T_{TOP}, and the tab, T_{TAB}.

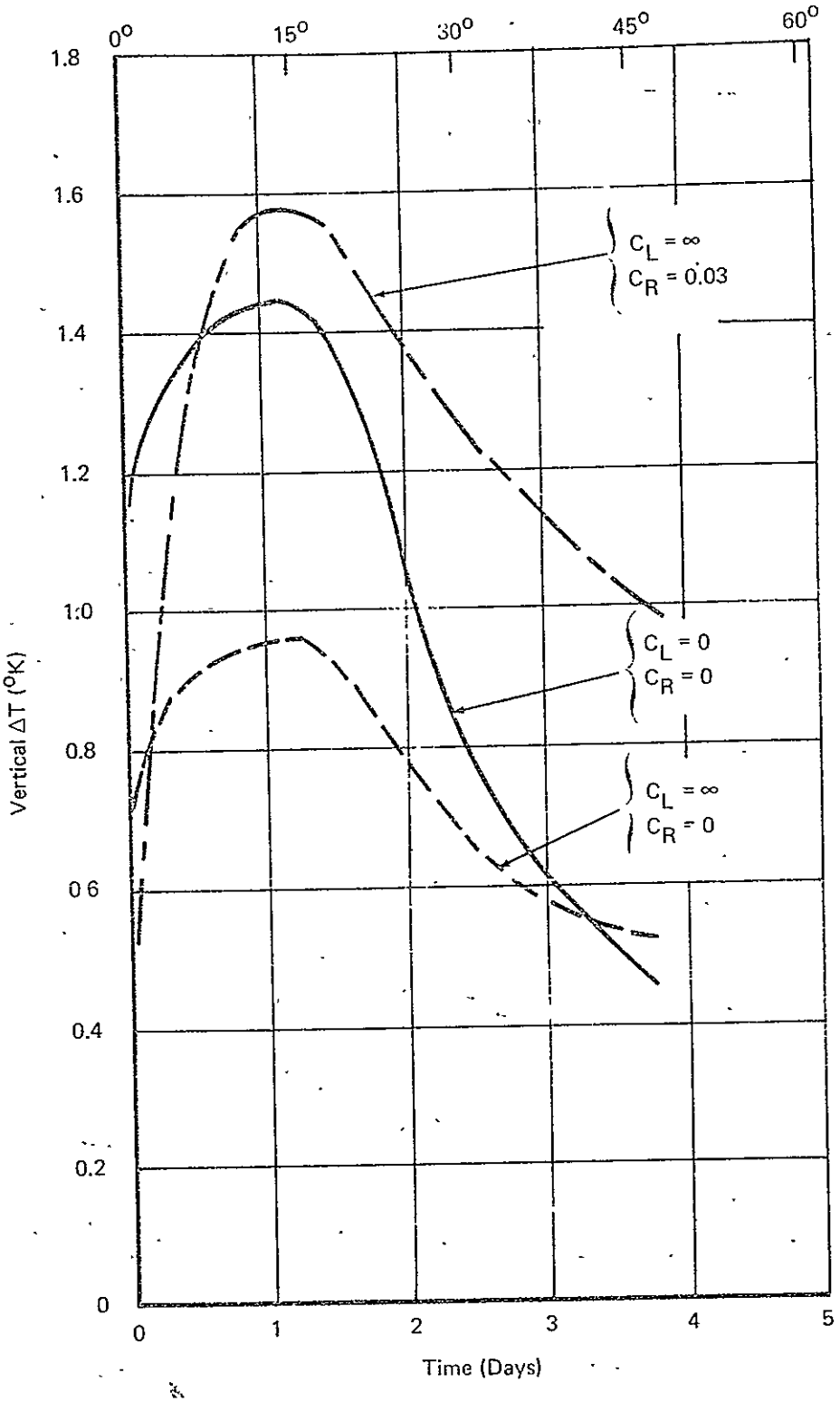

FIGURE 6 INFLUENCE OF CONDUCTANCE ON VERTICAL ΔT;

$\epsilon = 0.13$, $\alpha_s = 0.25$, L/W = 2 5

TABLE 1

SELECTED LOCAL TEMPERATURES WITH
AS-RECEIVED ALUMINUM LOUVER ARRAY,
$C_L = \infty$, $C_R = 0.03$

θ	T_{APEX}	T_{TOP}	T_{TAB}	$T_{CANNISTER}$
0	200.9	200.4	199.1	196.3
15	405.7	404.1	407.6	418.8
30	391.4	390.2	393.6	404.4
45	368.8	367.8	370.6	379.6

"Vertical" $\Delta T = T_{APEX} - T_{TOP}$

"Radial" $\Delta T = T_{TOP} - T_{TAB}$

Values of this quantity versus sun angle are shown in Figure 7 for the cases of zero and 0.03 watts/°K mounting conductance. Shown also is the temperature difference between the cannister and the retro-reflector apex. The louver-cannister conductance of 0.25 watt/°K was determined as described in Appendix II.

When the quartz is not conductively coupled to the cannister ($C_R = 0$), the radial ΔT is less than 0.5°K for all sun angles. However, a large distortion of the temperature distribution occurs with a mounting conductance of 0.03. As the temperature difference between the cannister and quartz increases, the magnitude of the radial ΔT also increases. Comparison with Figure 6 reveals that the radial temperature difference can be 2-3 times larger in magnitude than the vertical ΔT.

As discussed previously, the choice of a mounting conductance value is somewhat arbitrary since it can only be determined when the retainer design is complete. Results of a parametric study of the influence of mounting conductance are shown in Figure 8. Here, values for the two characteristic temperature differences are plotted assuming a sun angle of 15° and the use of as-received aluminum louvers. The choice of a 15° sun angle was made because the ΔT's are maximum at this point.

The magnitudes of both the vertical and radial ΔT's increase as the mounting conductance increases. The reason for this behavior has already been explained. Clearly, the results indicate the desirability of obtaining the smallest possible mounting conductance in practice.

An equivalent set of results obtained for the ALZAK louver configuration is illustrated in Figure 9. The vertical ΔT is the maximum value obtained over all sun angles. Radial ΔT's are given for sun angles of 0° and 5°. A zero-degree sun angle is really a singular case since the assumption implies that the louvers receive no sunlight. In this limiting case, the radial ΔT is a maximum. Since the louvers will be expected to receive some solar energy near lunar noon, the 5° sun angle case is felt to represent a more reasonable limiting case.

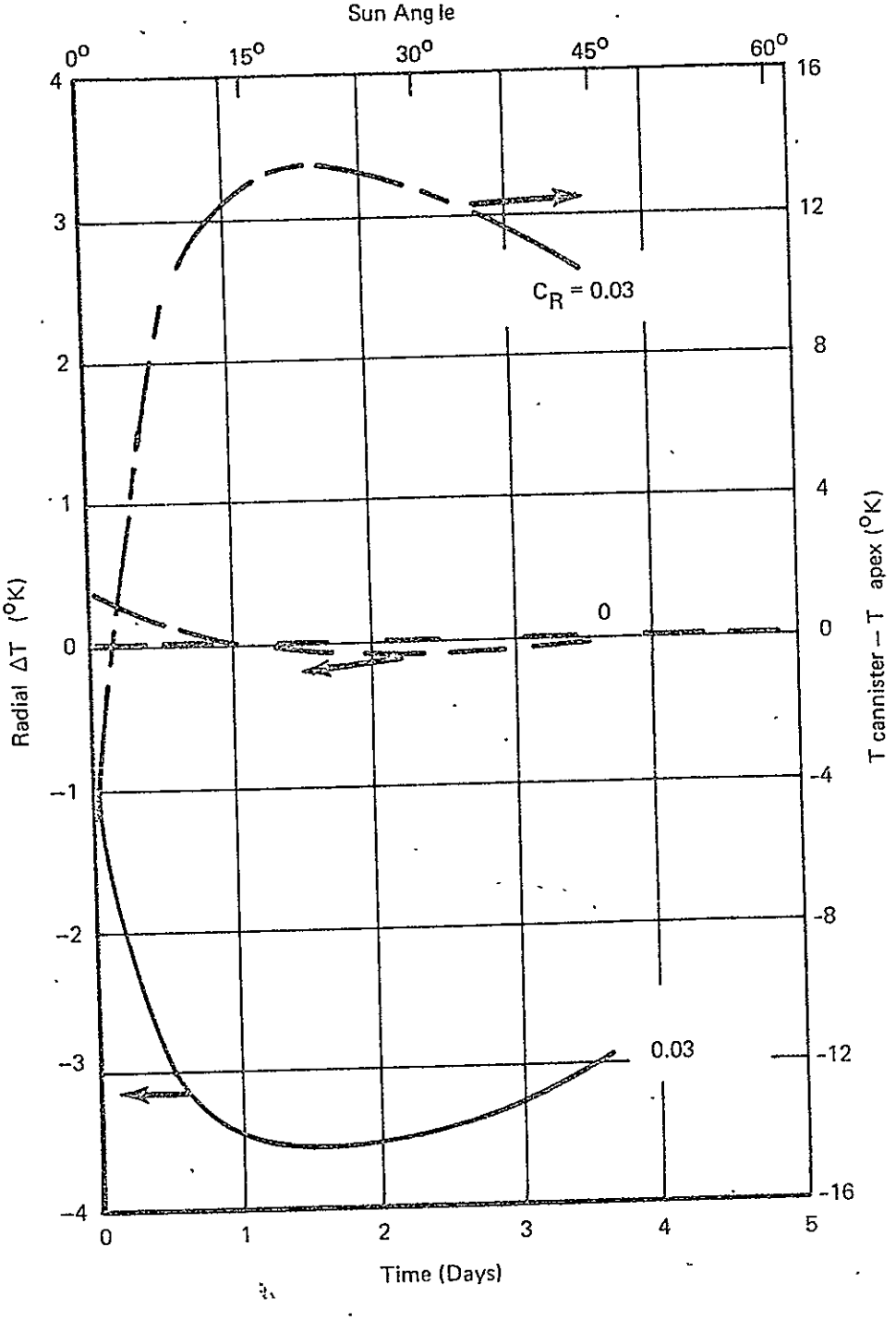

FIGURE 7 INFLUENCE OF CONDUCTANCE ON RADIAL ΔT;

ϵ = 0.13, α_s = 0.25, L/W = 2.5, C_L = 0.25

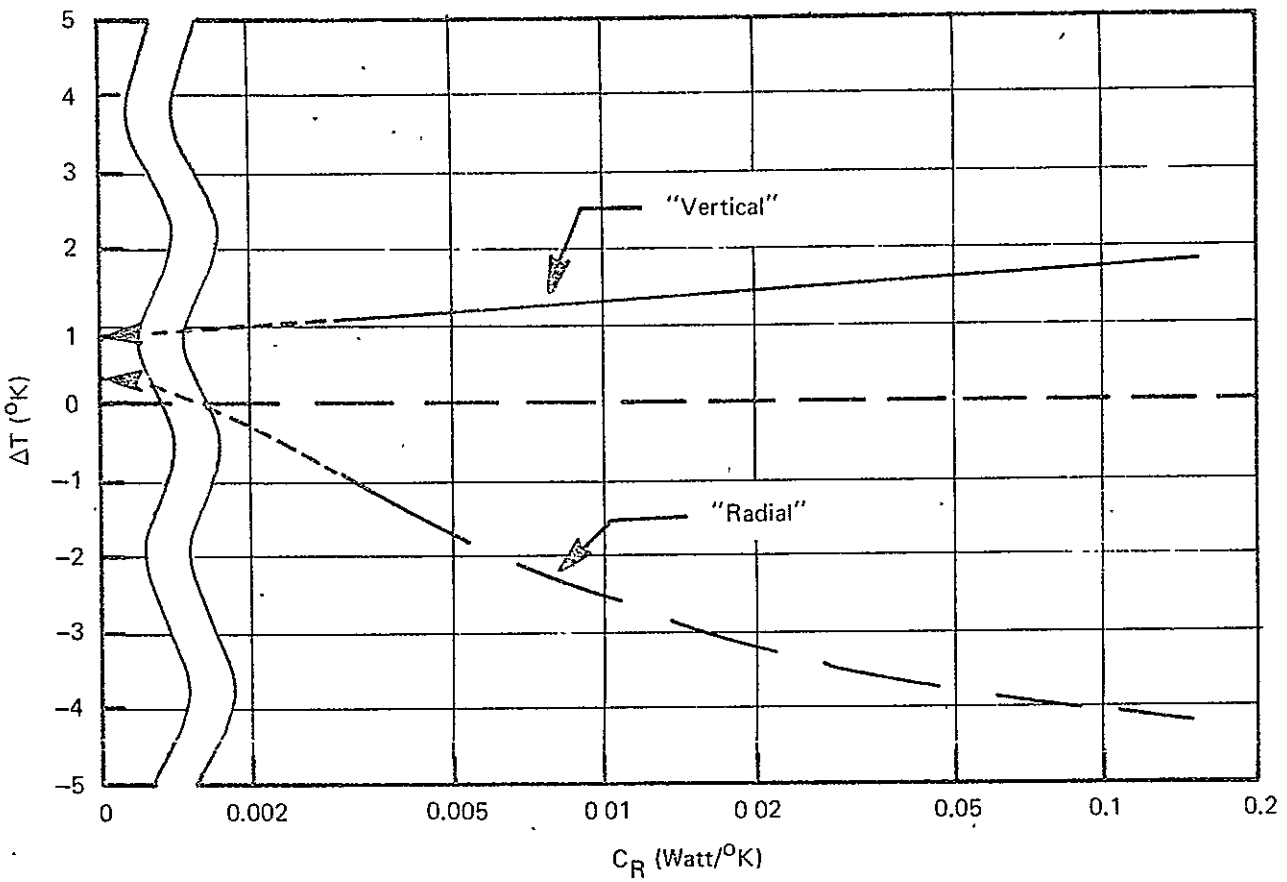

FIGURE 8 TEMPERATURE DIFFERENCES IN REFLECTOR WITH AS-RECEIVED ALUMINUM LOUVER;

ϵ = 0.13, α_s = 0 25, L/W = 2.5 C_L = 0.25, θ = 15°

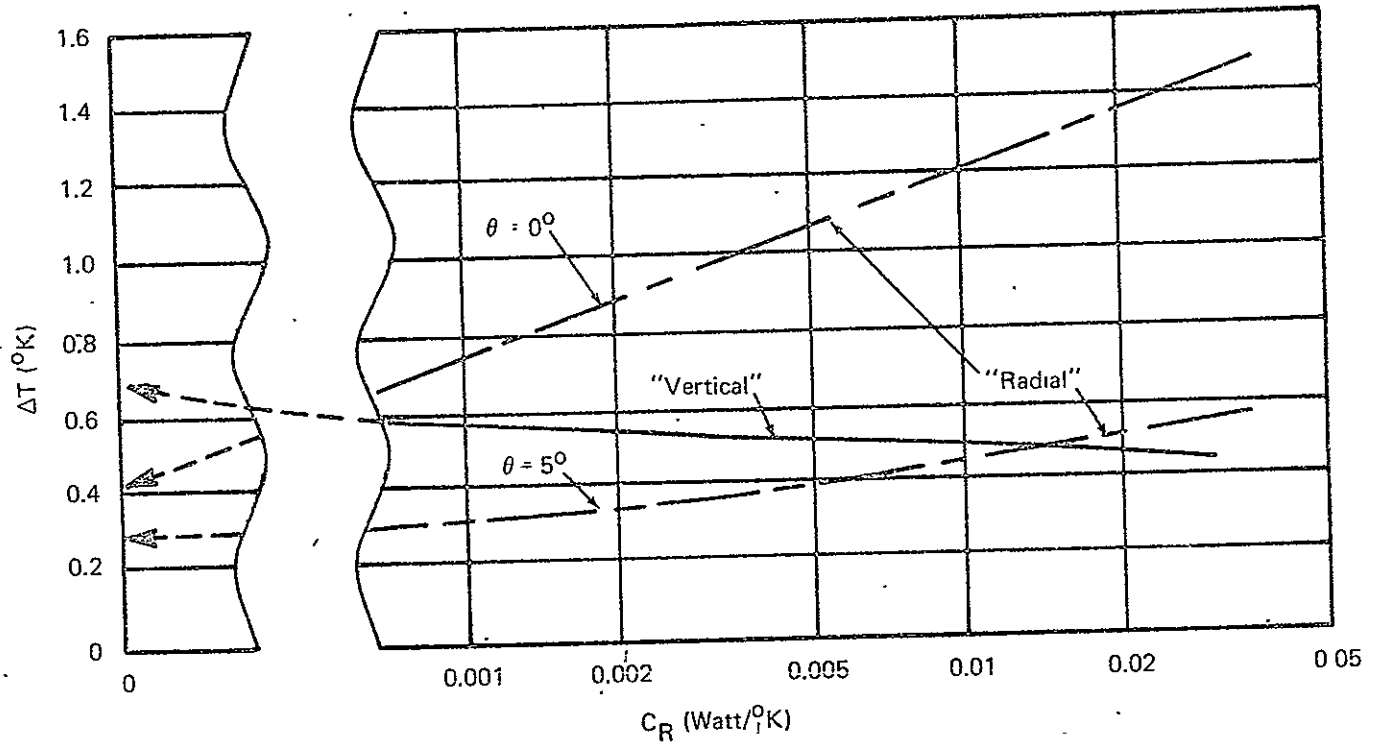

FIGURE 9 TEMPERATURE DIFFERENCES IN REFLECTOR WITH ALZAK LOUVER;

ϵ = 0 78, α_s = 0.32 L/W = 2.5, C_L = 0.25

Comparison of Figures 8 and 9 reveals that the thermal problems associated with mounting conductance are much less severe with the ALZAK louver configuration than with the as-received aluminum structure. It is noted that the maximum vertical ΔT decreases with increasing mounting conductance. This occurs because the cannister is always cooler than the retro-reflector at the sun angles where the vertical ΔT is a maximum.

C. Influence of Louver Height on Thermal Performance

The results presented to this point have all been obtained for a louver cell height-to-width ratio of 2.5. This ratio was chosen so that sunlight impinging directly on the quartz would be retro-reflected. A large penalty is paid in the direct loss of laser energy due to this shading, however. We have therefore examined the thermal performance attendant with the use of shorter louvers. For computational simplicity, the louvers have been considered to be black.

With shorter louvers the additional heating of the cannister by sunlight not retro-reflected must be taken into account. This has been done in the manner described in Section II - C. The calculations have been based on the assumption of quasi-steady heat transfer.

Figure 10 illustrates the vertical ΔT's across the retro-reflector as a function of sun angle (time) for several louver heights. Shown for comparison are the results obtained with the so-called "best" surface radiation configuration.*

Clearly, the thermal performance is best for the louver configuration with the largest height-to-width ratio. However, even for an L/W of 0.625, the vertical ΔT's are always less than 0.9°K and are smaller than could be obtained with even a very good surface radiator. From a thermal standpoint, a black louver as short as L/W = 0.625 appears to be a very attractive configuration.

D. Transient Studies

Within this section we will discuss the influence of thermal mass on the retro-reflector thermal performance. It is important to

---

* See Technical Memorandum #2.

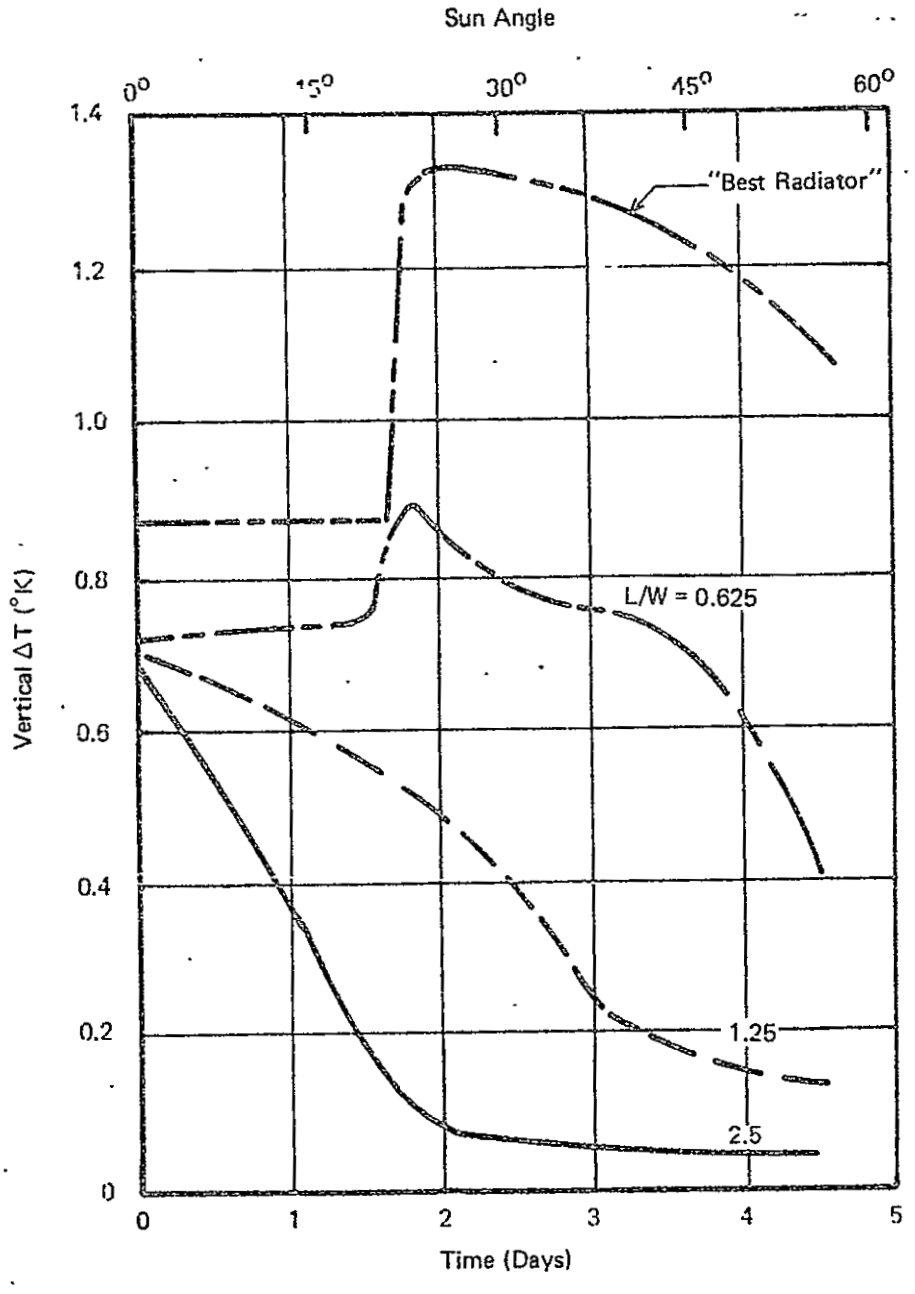

FIGURE 10 INFLUENCE OF LOUVER HEIGHT ON VERTICAL ΔT

$\epsilon = \alpha_s = 1, \quad C_L = \infty, \quad C_R = 0$

remember that both the quartz and the louver-cannister have thermal mass and both must be included in the transient calculations.

In general, the presence of thermal mass tends to smooth out the temperature response of a system to perturbing influences. The extent of this smoothing (or damping) is dependent on the nature of the perturbing influence. In the present case, it can be shown that the response time of the retro-reflector is much longer when the perturbing force is infrared radiant transfer than when it is associated with volumetric heating.

Figure 11 provides a comparison between the transient and quasi-steady predictions of retro-reflector thermal response. The "zone temperatures" are representative of the retro-reflector and cannister. Since these two zone temperatures are for the most part within 10°K of each other, the only zone temperatures illustrated are those corresponding to the retro-reflector.

The general trends predicted by the two analyses are seen to be the same. However, at lunar noon (sun angle of 0°) the vertical ΔT predicted by the transient analysis is approximately 0.15°K higher than that predicted by the quasi-steady analysis. As discussed earlier, the 0° sun angle case is really a singular case since the louvers are assumed to receive no solar energy. Where the heat transfer is quasi-steady, the cannister temperature drops considerably at this sun angle, thereby diminishing the greenhouse effect. The presence of the louver-cannister and retro-reflector thermal masses prevents this rapid decrease in temperature and maintains the vertical ΔT at a higher value.

The other prominent feature in Figure 11 is the transient response of the vertical temperature gradient between sun angles of 10 and 15 degrees. This behavior can be explained in terms of the response times of the retro-reflector for volumetric heating and infrared radiant transfer. As the sun angle increases from the normal, the power input to the reflector drops rapidly. At the same time, the cannister temperature begins to rise slowly at first and then more rapidly near a 7 1/2° sun angle. Since the response time for volumetric heating is shorter than

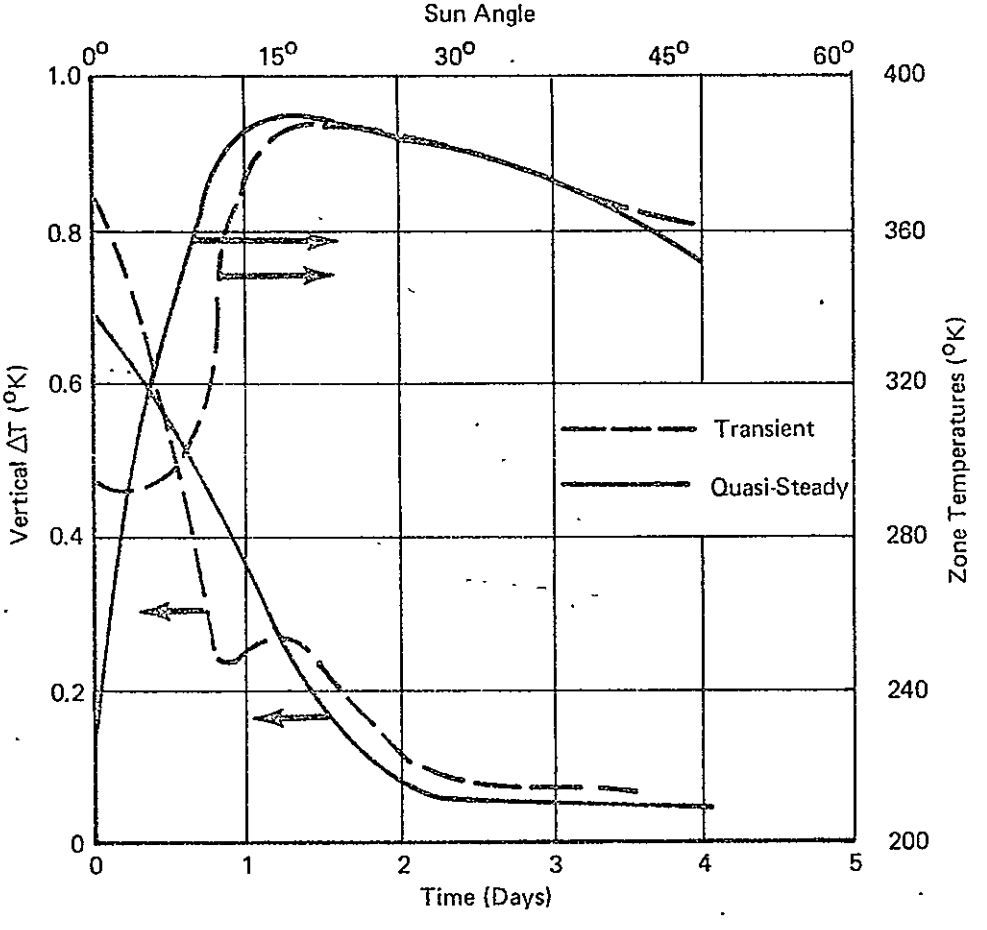

FIGURE 11 COMPARISON OF TRANSIENT AND QUASI-STEADY RESULTS FOR BLACK LOUVER;

$L/W = 2.5, \quad C_L = \infty, \quad C_R = 0.$

that for infrared radiant heating, the temperature gradient in the retro-reflector drops rapidly at first until a 10° sun angle is reached. At this point the heating by the cannister (greenhouse effect) becomes dominant, and the temperature gradient rises slightly. It should be noted that between a 5° and 10° sun angle the cannister temperature is significantly higher in the quasi-steady case than in the transient case. Because the greenhouse effect is therefore dominant at lower sun angles, the rapid initial decrease in the vertical ΔT is not predicted by the quasi-steady analysis.

The transient response of the reflector over an entire lunar day is shown in Figure 12. In general, the vertical ΔT is high where volumetric heating occurs, and low elsewhere.

The detailed behavior of the vertical ΔT is quite complex but can, again, be explained in terms of the response time and the various perturbing influences. The two prominent features that appear in this figure are the rise in vertical ΔT between a 45° and a 90° sun angle, and the negative peak in the ΔT shortly after a 270° sun angle (lunar dawn).

Shortly after a sun angle of 30°, the solar heating of the louvers begins to decrease rapidly. As a result, the louver temperature begins to drop rapidly with a resultant decrease in the infrared heating of the reflector. As the quartz cools, the upper surface cools more rapidly since it can dissipate its energy more easily than can the back surfaces. Therefore, as the quartz rapidly loses its energy, the vertical ΔT increases slightly. After the rapid cooling period is over (100° sun angle), the temperature gradients drops again.

Shortly after lunar dawn, the louver temperature begins to rise rapidly as a result of solar heating. Since the louver panels are black, they radiate much of this energy to the retro-reflector. On the other hand, the cannister is highly polished on the inside and is a poor emitter of energy. Nearly all of the energy radiated to the quartz reflector is at the upper surface so that its temperature is higher than the back faces of the reflector. After the quartz (and cannister) temperature reaches 350°K, the greenhouse effect begins to dominate and the temperature gradient is reversed.

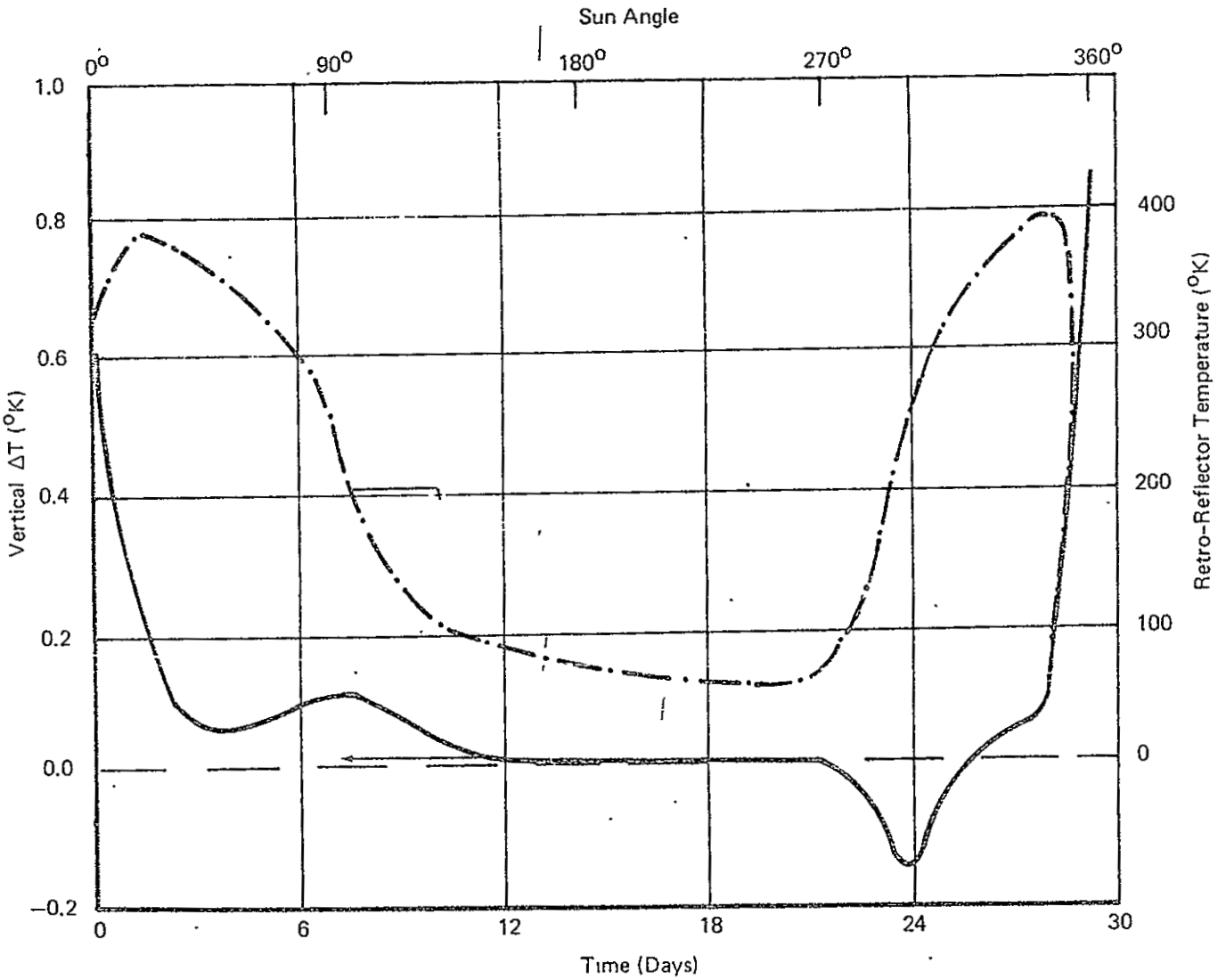

FIGURE 12 TRANSIENT THERMAL PERFORMANCE WITH BLACK LOUVER CONFIGURATION;

$L/W = 2.5, \quad C_L = \infty, \quad C_R = 0.$

Clearly, the transient thermal behavior of a retro-reflector with a louver array is very complex. This behavior and the explanations offered above should not detract from the most important result of these calculations. That important result is that the temperature gradients within the reflector remain small throughout a full lunar day. A corollay result is that the performance may be adequately predicted assuming quasi-steady heat transfer.

APPENDIX I

Volumetric Heating in a Retro-Reflector

An exact calculation of the actual rate of volumetric heating requires a detailed ray tracing within the retro-reflector to determine the path lengths of rays passing through any given point. Rather than perform these calculations at every point within the reflector, we have considered local heating at or near the centroids of the five zones into which the retro-reflector is divided. The assumption is made that the heating rates at these locations are characteristic of the respective zones. Hence, the rate within each zone is simply the product of the zone volume and the heating rate at the centroid.

At an arbitrary point (x,y,z) within the interior of an absorbing medium, the heat generation rate is dependent on the energy incident at the location and the absorption coefficient over the spectral range of the radiant energy. If N collimated beams of solar energy pass through a location, the local heating rate is

$$q'''(x,y,z) = \int_0^\infty \left\{ F_\lambda K_\lambda \sum_{i=1}^{N} e^{-K_\lambda \eta_i} \right\} d\lambda \qquad \text{(I-1)}$$

where $F_\lambda \equiv$ spectral value of incident solar flux

$K_\lambda \equiv$ spectral value of absorption coefficient

$\eta_i \equiv$ total path length of beam i within medium before reaching location (x,y,z)

The heat generation rate can also be written as

$$q'''(x,y,z) = \sum_{i=1}^{N} F \frac{d}{d\eta_i} \alpha^*(\eta_i) \qquad \text{(I-2)}$$

where $\alpha^*(\xi)$ is the total solar absorptance defined in Ref. [1] as

$$\alpha^*(\xi) = 1 - \int_0^\infty \left(\frac{F_\lambda}{F}\right) e^{-K_\lambda \xi} d\lambda \qquad \text{(I-3a)}$$

and

$$F = \int_0^\infty F_\lambda \, d\lambda \qquad \text{(I-3b)}$$

From [1] the derivative of the quantity α^* may be approximated by the expression

$$\frac{d}{d\eta}\,\alpha^*(\eta) = 0.0274 - 0.0144\eta + 0.0021\eta^2. \qquad \text{(I-4)}$$

Hence, the problem is reduced to determining the path length η_i of the rays passing through each point.

For computational simplicity, rays were traced only for the case of normal incidence (i.e., for the sun directly overhead). The actual evaluations of the path lengths of all the beams passing through the centroids were performed in the same fashion as described in Ref. [7] and will not be repeated here.

In general, deep within the interior of the tetrahedron (see Figure 2) there is a total of eight beams of solar energy passing through each point. These consist of a beam passing directly through the given point before reaching a reflecting back surface, three beams passing through the same point after one reflection off each of the back surfaces of the retro-reflector, and the reciprocal rays. A reciprocal ray is a beam of energy entering the reflector at the same location and in the opposite direction of beams leaving the reflector.

Near the top surface of the reflector there may be fewer than eight rays passing through a point. In particular, near the corners of the tetrahedron where retro-reflection no longer occurs there may be as few as one beam passing through a given location. On the other hand, these beams will be more energetic than those deep within the reflector.

The net result of these effects is that the zonal heating rates based on the local heat generation of the centroids are nearly the same as those corresponding to a uniform volumetric heating. The heat generation rates within each zone can be expressed as a fraction of the heat generation rate within the entire reflector:

---

7. A. G. Emslie and P. F. Strong, Technical Memorandum #3, "Optical Distortion Caused by a Vertical Temperature Gradient in a Retro-Reflector," August 30, 1968.

$$\frac{q_{ZONE}}{q_{TOTAL}} = f_{ZONE}$$

A table of the quantities f obtained for the two cases of uniform and non-uniform volumetric heating is presented below.

TABLE 2

Fraction of Total Heating in Each Zone

	f	
Zone	Uniform	Non-Uniform
19	0.3750	0.3634
20	0.2500	0.2649
21	0.1250	0.1239
22	0.1250	0.1239
23	0.1250	0.1239

APPENDIX II

Thermal Conductance between the Louver and Cannister

From Figure 3 it is clear that not all of the louver cells will be physically connected to a cannister surrounding the retro-reflector. The thermal model is, however, based on the assumption that each louver cell is virtually indistinguishable from any other cell within the array. This necessitates the use of some equivalent thermal conductance to connect our "typical" louver cell to the cannister.

The model of a typical array of cells associated with any one retro-reflector is illustrated in Figure II-1. The number of cells in the array is based on the surface area of the upper face of the tetrahedron model of the reflector, and the width of a typical cell. The effective thermal conductance is taken to be that between points 1 and 2 on Figure II-1, where the outer boundary containing point 2 is considered isothermal.

The value for the conductance can be determined from the solution of the electrical analogue problem shown in Figure II-2 where

$$R = \frac{W}{kL\delta} ,$$

The quantities W and L are the width and height of a louver cell, and δ is a louver panel thickness. The numerical values assigned to these quantities are

$W = 0.44$ inches

$L = 1.10$ inches

$\delta = 0.010$ inches

$k = 1.5$ watt/cm-°K

Based on these values and the model described above, the equivalent conductance was found to be 0.25 watt/°K.

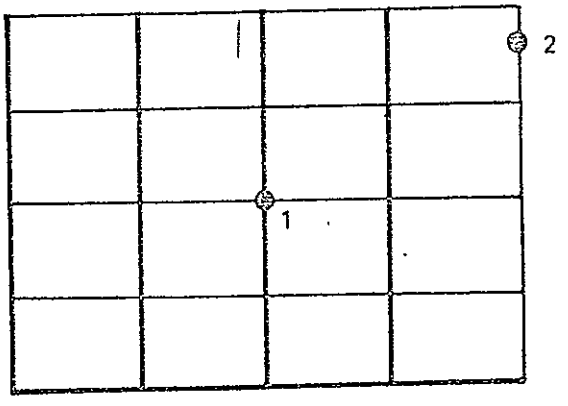

FIGURE II–1 SECTION OF CELL ARRAY ASSOCIATED WITH SINGLE RETRO-REFLECTOR

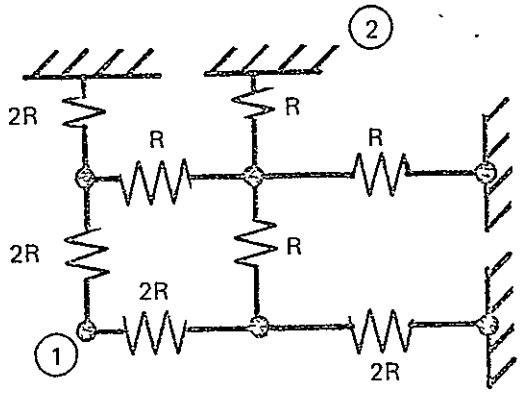

FIGURE II–2 ELECTRICAL ANALOGUE PROBLEM

TECHNICAL MEMORANDUM #5

Mechanical Design of Retro-reflector Array for Mainline ALSEP Program

prepared for

University of Maryland
College Park
Maryland 20742

by

John E. McCullough

Arthur D. Little, Inc.
20 Acorn Park
Cambridge, Massachusetts 02140

October 10, 1968

C-70472

TABLE OF CONTENTS

This memorandum summarizes the work completed to date on the mechanical design of a Laser Ranging Retro-Reflector Array for the Mainline ALSEP Program. This work consisted of 1) providing model designs for thermal analysis, 2) evaluating structural and fabrication feasibility of various array mechanical design schemes, and 3) establishing a promising mechanical design in conjunction with thermal analysis results.

1. Thermal Model Designs

The preliminary mechanical design of a louvered retro-reflector mount was produced to serve as a model for thermal analysis. This design is very similar to the reflector mount detail evolved in the past, i.e., it is based upon the use of "circular" reflectors held in thin wall tubes by spring mounting rings which are clamped by a cup retainer. Louvers, meshed egg crate fashion, are secured to the front end of the mounting tubes. This latest design uses a right circular retainer cup instead of the conical cup used previously. In addition, the louvers were made 0.020 inch thick (the same thickness as the mounting tubes) instead of the previous 0.010 inch. These changes were made for convenience of mathematical analysis and test model fabrication.

A "surface radiator" reflector mount concept was also evolved which consisted of a thin wall mounting tube and retainer identical to that just described except there are no louvers in front of the reflector face. Surface radiator elements would be, probably, mechanically clamped to the front face of the array in the interstices between mounting tubes.

No preliminary mechanical design was made for the surface radiator concept since it was not required for thermal analysis.

2. Evaluation of Structural and Fabrication Feasibility of Array Models

Because of limited funds the evaluation of several different array models for structural and fabrication feasibility was not possible. Also at this time there is no definition of array panel configuration, weight, reflector capacity, volume, or mechanical environment (shock and vibration levels at array mounting points), and, therefore, the possible array mechanical design problem solutions are too numerous to deal with individually. However, these possible design solutions can be arranged in a spectrum with surface radiator designs at one end and louvered structures at the other. In effect, the design concepts would be located within the spectrum according to louver height; the surface radiator concept representing louvers of zero height.

From purely an array panel fabrication point of view, the louvered structures are more complicated than the surface radiator concepts because many more pieces of metal must be fabricated, assembled, and brazed together. Also, the louvered structures, being more complex, are more difficult to analyze from a mechanical stiffness point of view. For these reasons it was decided to fabricate a fully louvered array panel structural mock-up, since, if this proved feasible, all other array concepts would be feasible to construct since they are simpler. Mechanical stiffness measurements could then be made on this mock-up which would be far more accurate than a paper analysis result because of the uncertainty of assumptions about joint stiffness.

A louver array panel mock-up was constructed using 44 2.33 inch long lengths of standard 0.020 inch wall, 1.75 inch diameter 6061 aluminum tubing packed side by side (see Figure No. 1). An "egg crate" structure consisting of interwoven 0.020 inch thick 6061 aluminum strips 1.10 inch wide was inset flush with the front face of the tube complex. This whole structure was then dip brazed in a jig to maintain flatness. The successful

brazing of this assembly demonstrated the feasibility of this construction method. Therefore, we have concluded that it is feasible and practical to construct louvered array panels in sizes 8 in. x 18 in. of interleaved thin wall aluminum tubes and strips.

a. Panel Stiffness Evaluation

The panel mock-up is not identical to the final array in that it does not have cup retainers to stiffen the back of the mounting tubes, however, a preliminary stiffness can be measured. The stiffness of the brazed louver panel was evaluated by measuring the spring constant of the panel when loaded along a lateral mid plane while supported at its ends. This spring constant was found to be 5,000 lbf/in. Using the formula:[1]

$$y = \frac{1}{48} \frac{W\ell^3}{EI}$$

knowing $\frac{W}{y}$, ℓ and E, I can be evaluated. This value of I is 2.865×10^{-2} in^4.

Interestingly enough, this value for I is equivalent to the total I for all the longitudinal louver strips in the array panel. This means that only the longitudinal louver strips contribute to the panel stiffness as defined here and that the mounting tubes packed side by side do not contribute.

Using this value for I and knowing the weight of the glass retro-reflectors, the first lateral natural frequency of the panel can be computed from:[2]

$$f_n = \frac{9.87}{2\pi} \sqrt{\frac{EI}{\mu_1 \ell^4}} \quad \frac{\text{cycles}}{\text{sec.}}$$

$$f_1 = 122.0 \ \frac{\text{cycles}}{\text{sec.}}$$

This value is much too low for ALSEP pallet mounted hardware and should be increased by a factor of 2.0 for safety.

The addition of cup retainers on the back of the mounting tubes will increase the moment of inertia of the section by a factor of 4.0, roughly, and therefore double the natural frequency.

In summary, the louver array design concept presented herein is feasible to fabricate, and, when equipped with appropriate retaining cups to stiffen the mounting tubes, should be sufficiently stiff to survive the ALSEP pallet mechanical environment. Similar panel design concepts using shorter louvers or no louvers at all (surface radiator designs) will be feasible to make using brazed assembly techniques since they are of simpler construction. These variations in the panel design, however, must incorporate the moment of inertia present in the louvered mock-up in order to withstand the probable mechanical environment.

b. Retro-reflector Mounting Considerations

The retro-reflector mounting rings were analyzed with the following results, which are based upon the assumption of a retro-reflector having a circular cross section at the mounting plane:

- The retro-reflector should be held in such a way that no tensile forces are induced in the reflector. Any tensile stresses multiplied by stress concentration factors could cause fracture of the retro-reflector during its 10 year life. Therefore, the reflector must be equipped with external, or protruding, mounting tabs.
- To minimize rocking of the mounted reflector during lateral shock and vibration, the mounting tabs should be located symmetrically to a plane parallel to the front face of the reflector which contains the center of gravity.

- The protruding mounting tabs of the retro-reflector should be clamped between two opposed truncated toroidal rings which have a spring constant k along their radial length. Under these conditions, the spring constant of the whole mount assembly will be:

$$K_{\text{transverse to reflector axis}} = 2k \cos^2\alpha \, (2\cos^2\beta + 1)$$

$$K_{\text{parallel to the reflector axis}} = 6 \, k \sin^2\alpha$$

where:

α = the angle between the sides of the truncated cone and its base.

β = one-half the angle between the protruding mounting tabs--constant at 60° in this analysis.

To obtain a uniform spring constant in the two orthogonal directions, $\alpha = 35.3°$. The natural frequency of the mount assembly can be adjusted by varying k. Generally, the mount natural frequency should be as large as possible so that the mount does not amplify the shock and vibration of array panel.

3. Establishing a Promising Mechanical Array Design

The results of preliminary thermal and mechanical analyses of retro-reflector array design schemes indicate that the following would be the most promising design concept: the array panel should be basically a louvered structure. The actual louver height and height/separation ratio are not determinant, however, without further and more

comprehensive analysis. It is quite likely that louver height/separation ratio will be less than the 2.5 figure used in the fabrication mock-up. The louver structure should consist of thin aluminum strips interwoven, egg crate fashion, and incorporated with thin wall tubes which house the reflectors. The whole assembly would be dip brazed.

The retro-reflectors should be clamped between truncated toroidal clamping rings which, in turn, are held in the panel tubes by a retaining cup. The reflectors should be equipped with protruding mounting tabs located on a circular cross section containing the center of gravity. The retaining cups should be right cylindrical or, possibly, conform to the shape of the back of the reflector, but in all cases should be polished on those surfaces facing the reflector.

The back of the array panel should be covered with multilayer insulation.

Nomenclature

y = lateral deflection, in.

W = lateral load, lbf

ℓ = span length, in.

E = modulus of elasticity, lbf/in^2

I = moment of inertia, in^4

f_n = natural frequency, cycles/sec.

μ_l = mass per unit length, $\frac{lbf\text{-}sec^2}{in^2}$

References

1. Formulas for Stress and Strain, R.J. Roark, McGraw-Hill Book Co., New York, 4th edition.

2. Mechanical Vibrations, J.P. DenHartog, McGraw-Hill Book Co., New York, 2nd edition.

TECHNICAL MEMORANDUM #6

The Influence of Retro-Reflector Shape and Cavity (Louver) Height on Optical Performance

prepared for

University of Maryland
College Park
Maryland 20742

Contract 21099

by

D. F. Comstock
Arthur D. Little, Inc.
Acorn Park
Cambridge, Massachusetts 02140

November 25, 1968

C-70472

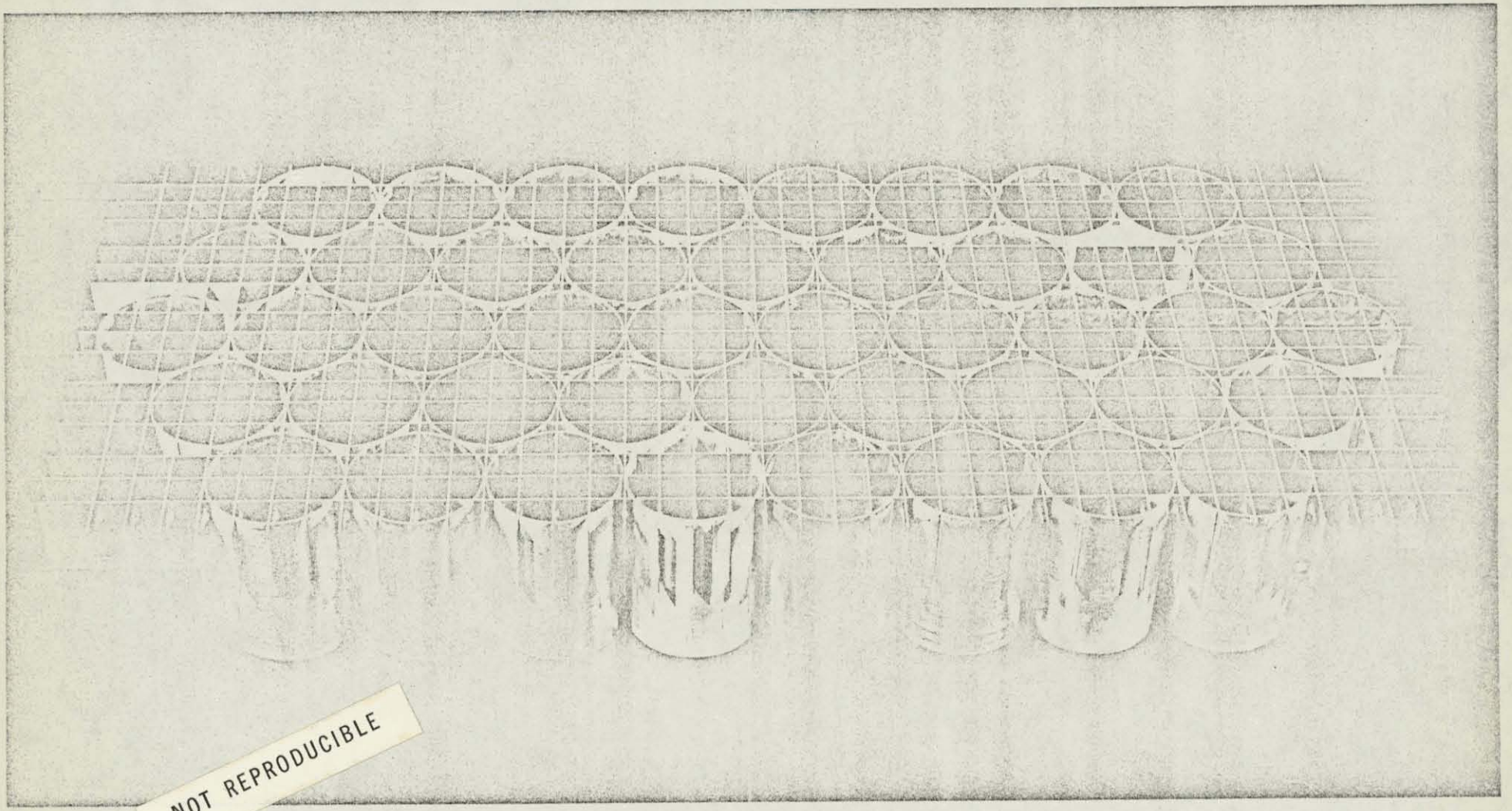

FIGURE 1 LOUVER ARRAY PANEL MOCK-UP
(MAINLINE ALSEP DESIGN)

TABLE OF CONTENTS

LIST OF FIGURES

LIST OF TABLES

I. SUMMARY

The purpose of this work was to determine the optical performance of each retro-reflector and the array as a function of off-normal laser beam entry angle affected by two particular factors:

- The shape of the face of each retro-reflector, and
- Shadowing related to the height of the thermal control cavity surrounding each retro-reflector.

The results of the analysis of each of these factors (shape and shadowing) are presented in Tables 1 and 2 and Figures 4 and 5. They show the relative measures of central irradiance for isothermal retro-reflectors in which the shape is varied from inscribed circle to nearly triangular and the thermal control cavity (louver) height is varied from a length-over-width ratio of 0 to 0.6. In general, both the retro-reflector shape and cavity shadowing are important and have comparable magnitude for the ranges considered. The inscribed circle retro-reflector appears to be the most favorable shape.

II. RESULTS

A. Retro-Reflector Shape

The retro-reflector face shapes considered were constrained by mechanical design considerations to a triangular shape on which is superimposed a circle, the tab base circle, outside of which all silica (the triangular tips) has been removed. The geometry of the retro-reflector face is shown in Figure 1. The shapes considered vary from a fully inscribed tab base circle ($R_2/R_1 = 1.0$) to a nearly triangular shape ($R_2/R_1 = 1.6$). For a particular shape in this range, a laser beam incident at some zenith angle between 0 and 15 degrees from the normal will experience obscuration of edge rays resulting in reduction of the optical return (central irradiance) of the retro-reflector and reduction of the total central irradiance of the array. A typical pattern of area of unobscured rays emerging from the retro-reflector face is shown in Figure 2.

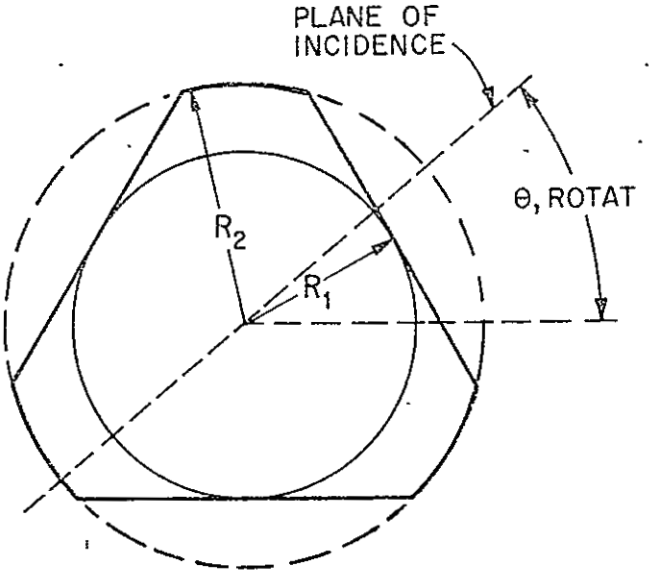

FIGURE 1 SHAPE OF RETRO-REFLECTOR FRONT FACE

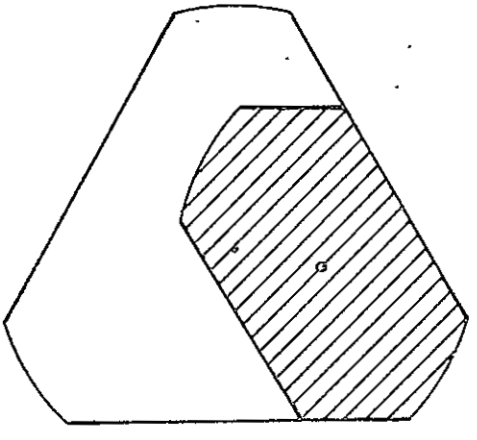

FIGURE 2 OPTICALLY UNOBSCURED AREA
NO CAVITY (LOUVER)

The results of the shape calculation, including definitions of terms, is shown in the computer printout in Tables 1a, 1b, and 1c and Figures 3a, 3b, and 3c. The term N*OPA2 is the product of the number of retro-reflectors that can be fitted into the array on a rectangular grid (N is determined on the basis of other design weight and bulk constraints) times the square of the optically unobscured area in arbitrary units (square inches). This product (N*OPA2) is a proportional measure of the central irradiance for the whole array for isothermal retro-reflectors having no thermal control cavities or optical obstructions other than the retro-reflectors themselves. The value of N*OPA2 in Table 1 represents the relative performance at any chosen off-normal zenith angle. However, bearing in mind the real nonisothermal use, the larger retro-reflector is not necessarily the most favorable. The conclusion can be drawn from Table 1 that the most favorable shape is a ratio of 1.0, i.e., a tab base circle which is the fully inscribed circle.

B. Cavity (Louver) Shadowing

The configuration of the thermal control cavities was constrained by other design considerations to a vertical cylindrical cavity concentric with and just slightly larger than the tab base circle. Accordingly, the question was, what is the effect of cavity height on the optical return of a retro-reflector?

At the time in the project when the shadowing was analyzed, the decision had already been made to specify a fully inscribed circle shape for the retro-reflector front face. Therefore, in computing the shadowing effects of the cavity, only a fully inscribed circle (ratio = 1.0) retro-reflector was considered. The geometry of the retro-reflector and thermal control cavity (louver) is shown in Figure 4.

When the zenith angle of the incident laser beam is other than normal, some edge rays are optically obscured (shadowed) by the cavity in addition to those obscured by the retro-reflector itself, resulting in further reduction of the central irradiance from each retro-reflector and from the whole array. The pattern of optically unobscured ray area on the face of the retro-reflector is quite similar to that of Figure 2.

TABLE 1a

LASER BEAM OFF-ANGLE OBSCURATION EFFECTS DUE TO RETRO-REFLECTOR GEOMETRY
(ROTAT = 0.0)

LASER BEAM OFF ANGLE OBSCURATION EFFECTS DUE TO RR GEOMETRY

CASE 70472 OPTICAL PERFORMANCE NOV 1 1968 , SHAPE

GEOMETRY,TAB BASE CIRCLE IMPOSED ON TRIANGULAR RR FRONT FACE

MATERIAL,FUSED SILICA REFRACTIVE INDEX 1.4555

DEFINITIONS
RATIO=RATIO OF TAB BASE CIRCLE DIAM TO INSCRIBED CIRCLE DIAM
RATAC=RATIO RR FACE AREA TO TAB BASE CIRCLE AREA
OFFAN=ZENITH ANGLE INC LASER BEAM RE NORMAL RR FRONT FACE,DEG
ROTAT=AZIMUTH ANGLE INC LASER BEAM RE EDGE RR FRONT FACE,DEG
OFFAC=RATIO OPTICALLY UNOBSCURED TO GEOM RR FRONT FACE AREA
D =DIAMETER TAB BASE CIRCLE , INCH
OPA =OPTICALLY UNOBSCURED AREA , OPA=PI*(D/2)SQ*RATAC*OFFAC
OPA2 =OPA SQUARED
N =TOTAL NUMBER OF RR IN ARRAY FROM OTHER DESIGN DATA
N*OPA2 IS PROPORT TO RELATIVE CENTRAL IRRADIANCE WHOLE ARRAY

RR	RATIO	RATAC	K	OFFAN	ROTAT	OFFAC	D=1.5 N=100. OPA	N*OPA2	D=1.6 N= 90. OPA	N*OPA2	D=1.7 N= 81. OPA	N*OPA2	D=1.8 N= 72. OPA	N*OPA2	D=1.9 N= 64. OPA	N*OPA2
1	1.10	0.994	1	0.0	0.0	1.000	1.757	308.9	1.999	359.9	2.257	412.9	2.531	461.3	2.820	509.0
1	1.10	0.994	2	5.0	0.0	0.891	1.566	245.4	1.782	285.9	2.012	327.9	2.255	366.3	2.513	404.3
1	1.10	0.994	3	10.0	0.0	0.784	1.379	190.3	1.569	221.7	1.771	254.3	1.986	284.1	2.213	313.5
1	1.10	0.994	4	15.0	0.0	0.681	1.198	143.5	1.363	167.2	1.538	191.8	1.725	214.3	1.922	236.5
2	1.11	0.982	1	0.0	0.0	1.000	1.594	264.2	1.814	296.2	2.048	339.7	2.296	379.5	2.558	418.8
2	1.11	0.982	2	5.0	0.0	0.936	1.493	223.0	1.699	259.8	1.918	298.0	2.150	332.9	2.396	367.4
2	1.11	0.982	3	10.0	0.0	0.837	1.335	178.3	1.519	207.7	1.715	238.2	1.922	266.2	2.142	293.7
2	1.11	0.982	4	15.0	0.0	0.739	1.179	139.1	1.342	162.1	1.515	185.9	1.698	207.7	1.892	229.2
3	1.12	0.765	1	0.0	0.0	1.000	1.352	182.9	1.538	213.1	1.737	244.4	1.947	273.1	2.170	301.3
3	1.12	0.765	2	5.0	0.0	0.987	1.335	178.4	1.520	207.9	1.715	238.4	1.923	266.4	2.143	296.0
3	1.12	0.765	3	10.0	0.0	0.904	1.223	149.7	1.392	174.4	1.571	200.0	1.762	223.5	1.963	246.6
3	1.12	0.765	4	15.0	0.0	0.805	1.088	118.5	1.238	138.1	1.398	158.4	1.567	177.0	1.747	195.3
4	1.13	0.652	1	0.0	0.0	1.000	1.152	132.8	1.311	154.7	1.480	177.4	1.659	198.2	1.849	218.8
4	1.13	0.652	2	5.0	0.0	0.993	1.144	131.0	1.302	152.7	1.470	175.1	1.648	195.7	1.837	215.9
4	1.13	0.652	3	10.0	0.0	0.963	1.110	123.2	1.262	143.5	1.425	164.6	1.598	183.9	1.780	202.9
4	1.13	0.652	4	15.0	0.0	0.863	0.995	99.0	1.132	115.3	1.278	132.3	1.433	147.8	1.596	163.1
5	1.14	0.562	1	0.0	0.0	1.000	0.993	98.7	1.130	115.0	1.276	131.9	1.430	147.4	1.594	162.6
5	1.14	0.562	2	5.0	0.0	0.993	0.987	97.4	1.123	113.5	1.268	130.2	1.421	145.5	1.583	160.5
5	1.14	0.562	3	10.0	0.0	0.971	0.965	93.1	1.097	108.4	1.239	124.4	1.389	139.0	1.548	153.4
5	1.14	0.562	4	15.0	0.0	0.911	0.905	81.9	1.030	95.5	1.163	109.5	1.303	122.4	1.457	135.0
6	1.15	0.489	1	0.0	0.0	1.000	0.865	74.9	0.984	87.3	1.111	100.1	1.246	111.8	1.388	123.4
6	1.15	0.489	2	5.0	0.0	0.993	0.860	73.9	0.978	86.1	1.104	98.8	1.238	110.4	1.379	121.8
6	1.15	0.489	3	10.0	0.0	0.971	0.840	70.6	0.956	82.3	1.079	94.4	1.210	105.5	1.348	116.4
6	1.15	0.489	4	15.0	0.0	0.935	0.809	65.5	0.920	76.3	1.039	87.5	1.165	97.8	1.298	107.9
7	1.16	0.430	1	0.0	0.0	1.000	0.760	57.8	0.865	67.4	0.977	77.3	1.095	86.4	1.220	95.3
7	1.16	0.430	2	5.0	0.0	0.993	0.755	57.1	0.860	66.5	0.970	76.3	1.088	85.2	1.212	94.1
7	1.16	0.430	3	10.0	0.0	0.971	0.738	54.5	0.840	63.5	0.948	72.9	1.063	81.4	1.185	91.3
7	1.16	0.430	4	15.0	0.0	0.935	0.711	50.6	0.809	58.9	0.913	67.6	1.024	75.5	1.141	83.3

TABLE 1b

LASER BEAM OFF-ANGLE OBSCURATION EFFECTS DUE TO RETRO-REFLECTOR GEOMETRY
(ROTAT = 90.0)

LASER BEAM OFF ANGLE OBSCURATION EFFECTS DUE TO RR GEOMETRY

CASE 70472 OPTICAL PERFORMANCE NOV 1 1968 , SHAPE

GEOMETRY=TAB BASE CIRCLE INPOSED ON TRIANGULAR RR FRONT FACE

MATERIAL=FUSED SILICA REFRACTIVE INDEX 1.4555

DEFINITIONS
RATIO=RATIO OF TAB BASE CIRCLE DIAM TO INSCRIBED CIRCLE DIAM
RATAC=RATIO RR FACE AREA TO TAB BASE CIRCLE AREA
OFFAN=ZENITH ANGLE INC LASER BEAM RE NORMAL RR FRONT FACE,DEG
ROTAT=AZIMUTH ANGLE INC LASER BEAM RE EDGE RR FRONT FACE,DEG
OFFAC=RATIO OPTICALLY UNOBSCURED TO GEOM RR FRONT FACE AREA
D =DIAMETER TAB BASE CIRCLE , INCH
OPA =OPTICALLY UNOBSCURED AREA , OPA=PI*(D/2)SQ*RATAC*OFFAC
OPA2 =OPA SQUARED
N =TOTAL NUMBER OF RR IN ARRAY FROM OTHER DESIGN DATA
N*OPA2 IS PROPORT TO RELATIVE CENTRAL IRRADIANCE WHOLE ARRAY

RR	RATIO	RATAC	K	OFFAN	ROTAT	OFFAC	D=1.5 N=100. OPA	N*OPA2	D=1.6 N= 90. OPA	N*OPA2	D=1.7 N= 81. OPA	N*OPA2	D=1.8 N= 72. OPA	N*OPA2	D=1.9 N= 64. OPA	N*OPA2
1	1.00	0.994	1	0.0	90.0	1.000	1.757	308.9	1.999	359.9	2.257	412.9	2.531	461.3	2.820	509.0
1	1.00	0.994	2	5.0	90.0	0.896	1.576	248.5	1.793	289.5	2.024	332.0	2.270	371.0	2.529	409.4
1	1.00	0.994	3	10.0	90.0	0.787	1.383	191.4	1.574	223.0	1.777	255.8	1.992	285.8	2.220	315.4
1	1.00	0.994	4	15.0	90.0	0.677	1.191	141.8	1.355	165.2	1.529	189.5	1.715	211.8	1.911	233.7
2	1.01	0.992	1	0.0	90.0	1.000	1.594	254.2	1.814	296.2	2.048	339.7	2.296	379.5	2.558	418.8
2	1.01	0.992	2	5.0	90.0	0.925	1.475	217.8	1.679	253.8	1.895	291.1	2.125	325.2	2.368	358.9
2	1.01	0.992	3	10.0	90.0	0.818	1.305	170.3	1.484	198.4	1.676	227.6	1.879	254.3	2.094	280.6
2	1.01	0.992	4	15.0	90.0	0.714	1.138	129.7	1.295	151.1	1.462	173.3	1.640	193.6	1.827	213.7
3	1.02	0.765	1	0.0	90.0	1.000	1.352	182.9	1.538	213.1	1.737	244.4	1.947	273.1	2.170	301.3
3	1.02	0.765	2	5.0	90.0	0.980	1.326	175.8	1.508	204.9	1.703	235.0	1.909	262.5	2.127	289.7
3	1.02	0.765	3	10.0	90.0	0.881	1.192	142.1	1.356	165.6	1.531	189.9	1.717	212.2	1.913	234.2
3	1.02	0.765	4	15.0	90.0	0.777	1.051	110.6	1.196	128.8	1.350	147.8	1.514	165.1	1.687	182.2
4	1.03	0.652	1	0.0	90.0	1.000	1.152	132.8	1.311	154.7	1.480	177.4	1.659	198.2	1.849	218.8
4	1.03	0.652	2	5.0	90.0	0.988	1.139	129.7	1.296	151.1	1.463	173.4	1.640	193.7	1.827	213.7
4	1.03	0.652	3	10.0	90.0	0.939	1.082	117.1	1.231	136.5	1.390	156.6	1.558	174.9	1.736	193.0
4	1.03	0.652	4	15.0	90.0	0.835	0.962	92.6	1.095	107.9	1.236	123.8	1.386	138.3	1.544	152.7
5	1.04	0.562	1	0.0	90.0	1.000	0.993	98.7	1.130	115.0	1.276	131.9	1.430	147.4	1.594	162.6
5	1.04	0.562	2	5.0	90.0	0.988	0.982	96.4	1.117	112.4	1.261	128.9	1.414	144.0	1.575	158.9
5	1.04	0.562	3	10.0	90.0	0.962	0.956	91.4	1.088	106.5	1.228	122.2	1.377	136.5	1.534	150.6
5	1.04	0.562	4	15.0	90.0	0.885	0.879	77.3	1.000	90.1	1.129	103.3	1.266	115.5	1.411	127.4
6	1.05	0.489	1	0.0	90.0	1.000	0.865	74.9	0.984	87.3	1.111	100.1	1.246	111.8	1.388	123.4
6	1.05	0.489	2	5.0	90.0	0.988	0.855	73.2	0.973	85.2	1.099	97.8	1.232	109.3	1.372	120.6
6	1.05	0.489	3	10.0	90.0	0.962	0.833	69.4	0.947	80.8	1.070	92.7	1.199	103.6	1.336	114.3
6	1.05	0.489	4	15.0	90.0	0.924	0.799	63.9	0.910	74.5	1.027	85.5	1.151	95.5	1.283	105.4
7	1.06	0.430	1	0.0	90.0	1.000	0.760	57.8	0.865	67.4	0.977	77.3	1.095	86.4	1.220	95.3
7	1.06	0.430	2	5.0	90.0	0.988	0.752	56.5	0.855	65.8	0.965	75.5	1.082	84.4	1.206	93.1
7	1.06	0.430	3	10.0	90.0	0.962	0.732	53.6	0.833	62.4	0.940	71.6	1.054	80.0	1.174	88.3
7	1.06	0.430	4	15.0	90.0	0.932	0.709	50.3	0.807	58.6	0.911	67.3	1.021	75.2	1.138	82.9

TABLE 1c

LASER BEAM OFF-ANGLE OBSCURATION EFFECTS DUE TO RETRO-REFLECTOR GEOMETRY
(ROTAT = 270.0)

LASER BEAM OFF ANGLE OBSCURATION EFFECTS DUE TO RR GEOMETRY

CASE 70472 OPTICAL PERFORMANCE NOV 1 1968 , SHAPE

GEOMETRY=TAB BASE CIRCLE IMPOSED ON TRIANGULAR RR FRONT FACE

MATERIAL=FUSED SILICA REFRACTIVE INDEX 1.4585

DEFINITIONS
RATIO=RATIO OF TAB BASE CIRCLE DIAM TO INSCRIBED CIRCLE DIAM
RATAC=RATIO RR FACE AREA TO TAB BASE CIRCLE AREA
OFFAN=ZENITH ANGLE INC LASER BEAM RE NORMAL RR FRONT FACE,DEG
ROTAT=AZIMUTH ANGLE INC LASER BEAM RE EDGE RR FRONT FACE,DEG
OFFAC=RATIO OPTICALLY UNOBSCURED TO GEOM RR FRONT FACE AREA
D =DIAMETER TAB BASE CIRCLE , INCH
OPA =OPTICALLY UNOBSCURED AREA , OPA=PI*(D/2)SQ*RATAC*OFFAC
OPA2 =OPA SQUARED
N =TOTAL NUMBER OF RR IN ARRAY FROM OTHER DESIGN DATA
N*OPA2 IS PROPORT TO RELATIVE CENTRAL IRRADIANCE WHOLE ARRAY

RR	RATIO	RATAC	K	OFFAN	ROTAT	OFFAC	D=1.5 N=100. OPA	N*OPA2	D=1.6 N= 90. OPA	N*OPA2	D=1.7 N= 81. OPA	N*OPA2	D=1.8 N= 72. OPA	N*OPA2	D=1.9 N= 64. OPA	N*OPA2
1	1.00	0.994	1	0.0	270.0	1.000	1.757	308.9	1.999	359.9	2.257	412.9	2.531	461.3	2.820	509.0
1	1.00	0.994	2	5.0	270.0	0.896	1.576	248.5	1.793	289.5	2.024	332.0	2.270	371.0	2.529	409.4
1	1.00	0.994	3	10.0	270.0	0.707	1.383	191.4	1.574	223.0	1.777	255.8	1.992	285.8	2.220	315.4
1	1.00	0.994	4	15.0	270.0	0.677	1.191	141.8	1.355	165.2	1.529	189.5	1.715	211.8	1.911	233.7
2	1.01	0.902	1	0.0	270.0	1.000	1.594	254.2	1.814	296.2	2.048	339.7	2.296	379.5	2.558	418.8
2	1.01	0.902	2	5.0	270.0	0.951	1.517	230.3	1.726	268.4	1.949	307.8	2.185	343.9	2.435	379.5
2	1.01	0.902	3	10.0	270.0	0.851	1.357	184.2	1.544	214.6	1.743	246.2	1.954	275.1	2.177	303.5
2	1.01	0.902	4	15.0	270.0	0.738	1.177	138.6	1.339	161.4	1.512	185.2	1.695	206.9	1.888	228.3
3	1.02	0.765	1	0.0	270.0	1.000	1.352	182.9	1.538	213.1	1.737	244.4	1.947	273.1	2.170	301.3
3	1.02	0.765	2	5.0	270.0	0.981	1.328	176.3	1.511	205.5	1.705	235.7	1.912	263.3	2.130	290.6
3	1.02	0.765	3	10.0	270.0	0.952	1.288	165.9	1.465	193.3	1.654	221.7	1.854	247.7	2.066	273.3
3	1.02	0.765	4	15.0	270.0	0.836	1.131	128.1	1.287	149.2	1.453	171.1	1.629	191.2	1.815	211.0
4	1.03	0.652	1	0.0	270.0	1.000	1.152	132.8	1.311	154.7	1.480	177.4	1.659	198.2	1.849	218.8
4	1.03	0.652	2	5.0	270.0	0.981	1.131	128.0	1.287	149.2	1.453	171.1	1.629	191.1	1.815	210.9
4	1.03	0.652	3	10.0	270.0	0.966	1.114	124.1	1.267	144.6	1.431	165.8	1.604	185.3	1.787	204.5
4	1.03	0.652	4	15.0	270.0	0.913	1.052	110.7	1.197	129.0	1.352	148.0	1.515	165.4	1.688	182.5
5	1.04	0.562	1	0.0	270.0	1.000	0.993	98.7	1.130	115.0	1.276	131.9	1.430	147.4	1.594	162.6
5	1.04	0.562	2	5.0	270.0	0.981	0.975	95.2	1.110	110.9	1.253	127.2	1.405	142.1	1.565	156.8
5	1.04	0.562	3	10.0	270.0	0.966	0.960	92.2	1.093	107.5	1.233	123.3	1.383	137.7	1.541	152.0
5	1.04	0.562	4	15.0	270.0	0.916	0.910	82.8	1.035	96.5	1.169	110.7	1.311	123.7	1.460	136.5
6	1.05	0.489	1	0.0	270.0	1.000	0.865	74.9	0.984	87.3	1.111	100.1	1.246	111.8	1.388	123.4
6	1.05	0.489	2	5.0	270.0	0.981	0.850	72.2	0.967	84.1	1.091	96.5	1.223	107.8	1.363	119.0
6	1.05	0.489	3	10.0	270.0	0.966	0.836	70.0	0.952	81.5	1.074	93.5	1.205	104.5	1.342	115.3
6	1.05	0.489	4	15.0	270.0	0.916	0.793	62.9	0.902	73.2	1.018	84.0	1.142	93.9	1.272	103.6
7	1.06	0.430	1	0.0	270.0	1.000	0.760	57.8	0.865	67.4	0.977	77.3	1.095	86.4	1.220	95.3
7	1.06	0.430	2	5.0	270.0	0.981	0.747	55.8	0.850	65.0	0.959	74.5	1.075	82.3	1.198	91.9
7	1.06	0.430	3	10.0	270.0	0.966	0.735	54.1	0.836	63.0	0.944	72.2	1.059	80.7	1.180	89.1
7	1.06	0.430	4	15.0	270.0	0.916	0.697	48.5	0.793	56.6	0.895	64.9	1.003	72.5	1.118	80.0

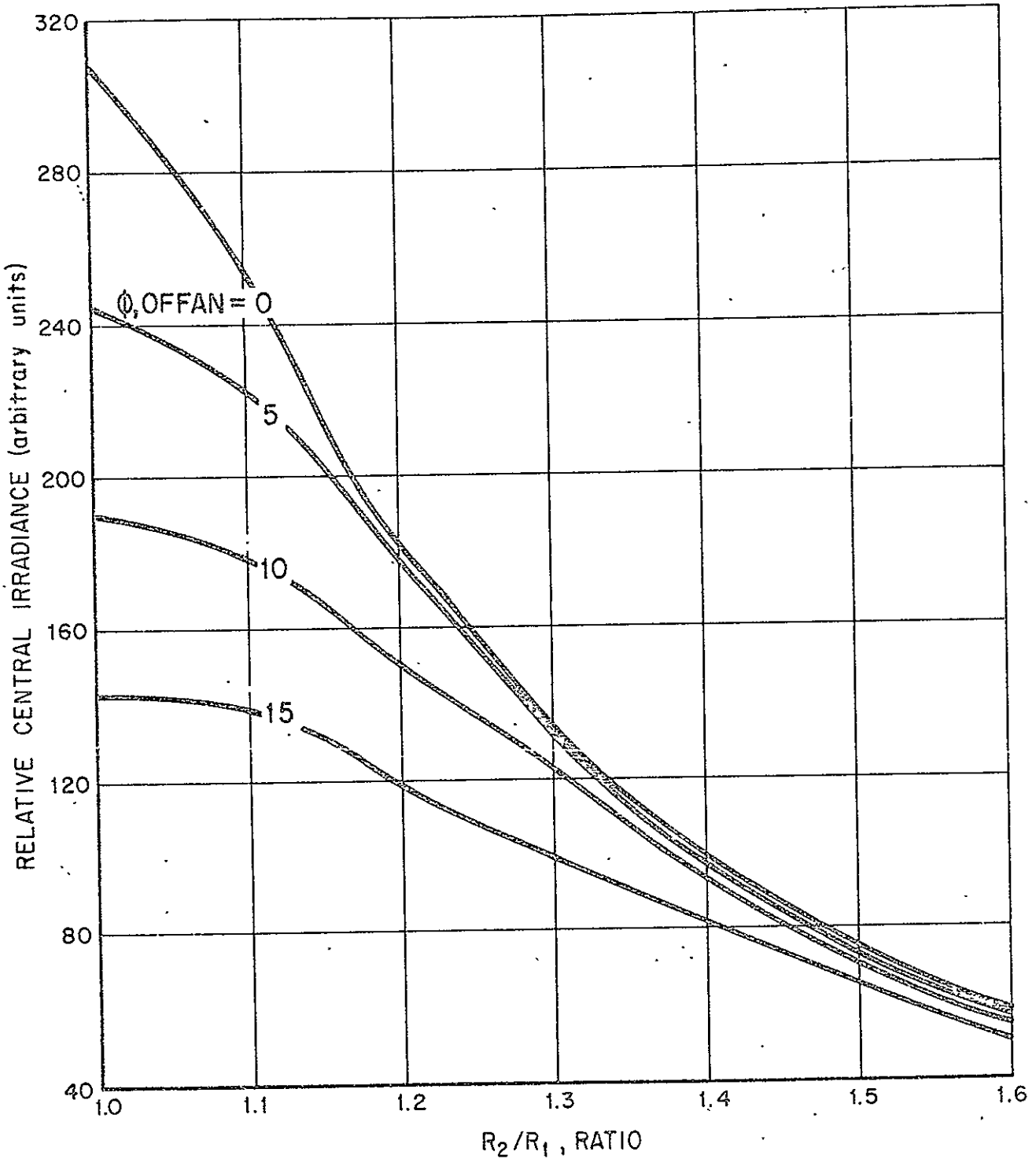

FIGURE 3a RELATIVE CENTRAL IRRADIANCE FROM ARRAY VERSUS RETRO-REFLECTOR SHAPE, R_2/R_1 (ROTAT = 0.0)

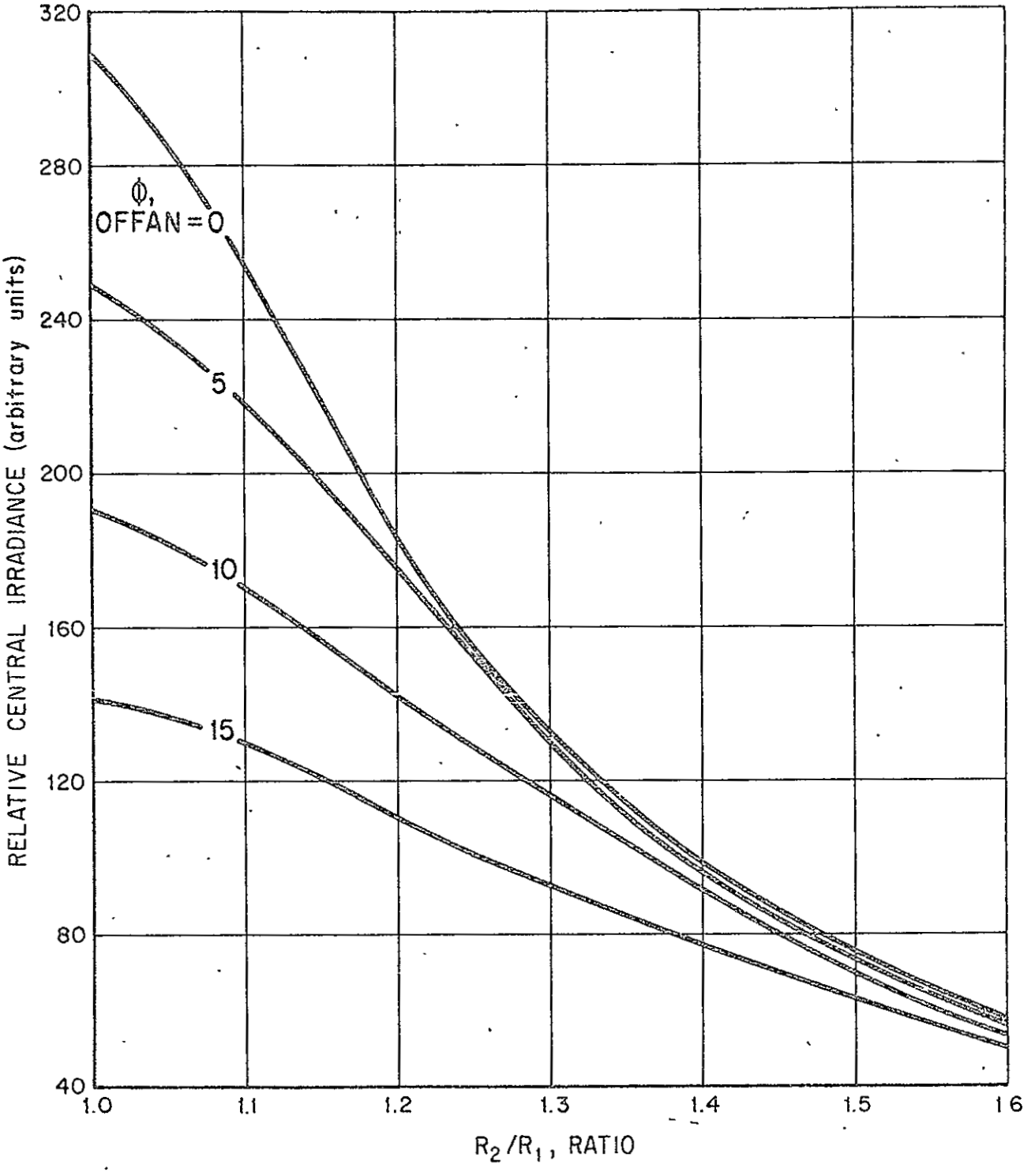

FIGURE 3b RELATIVE CENTRAL IRRADIANCE FROM ARRAY VERSUS RETRO-REFLECTOR SHAPE, R_2/R_1 (ROTAT = 90.0)

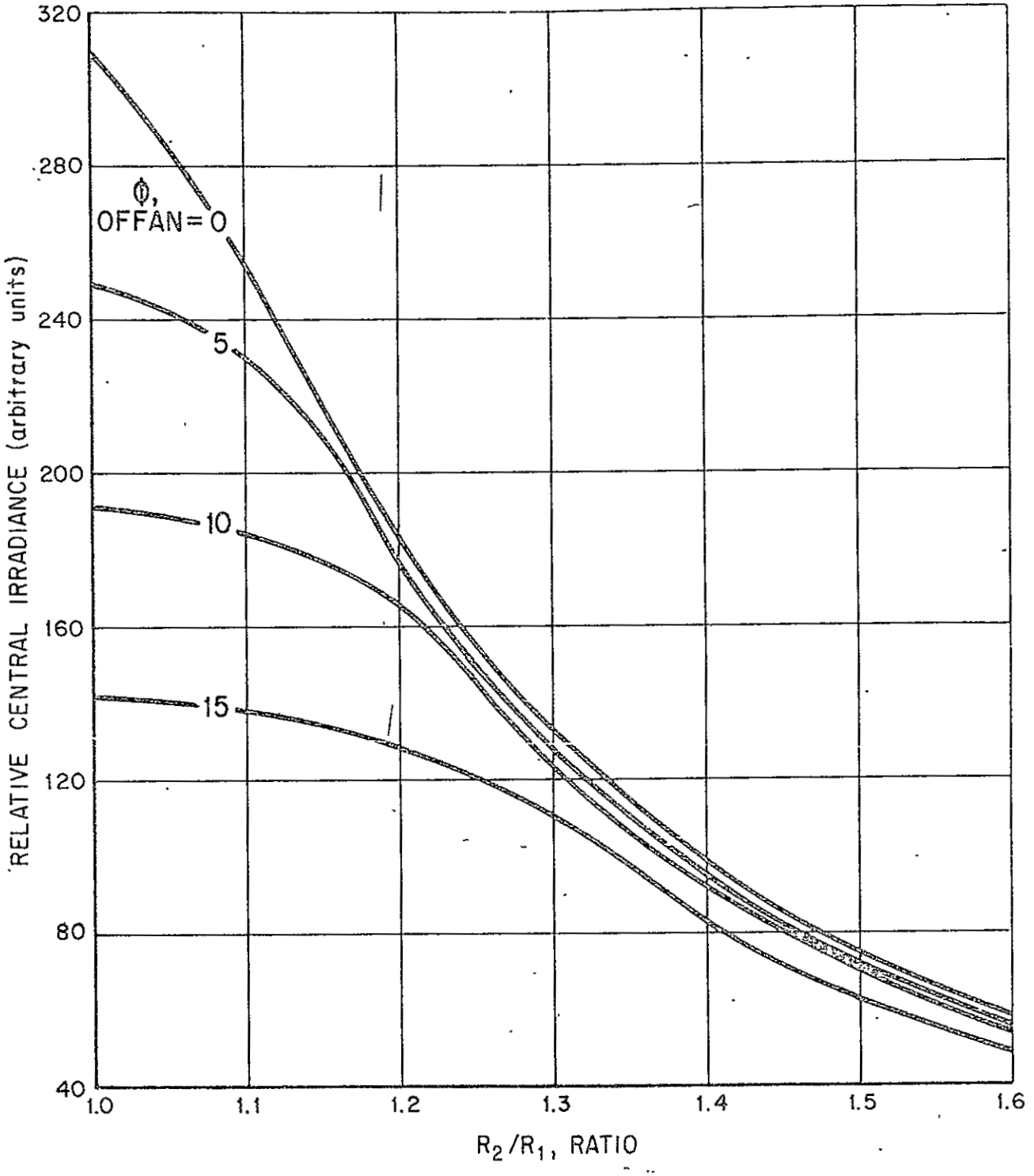

FIGURE 3c RELATIVE CENTRAL IRRADIANCE FROM ARRAY VERSUS RETRO-REFLECTOR SHAPE, R_2/R_1 (ROTAT = 270.0)

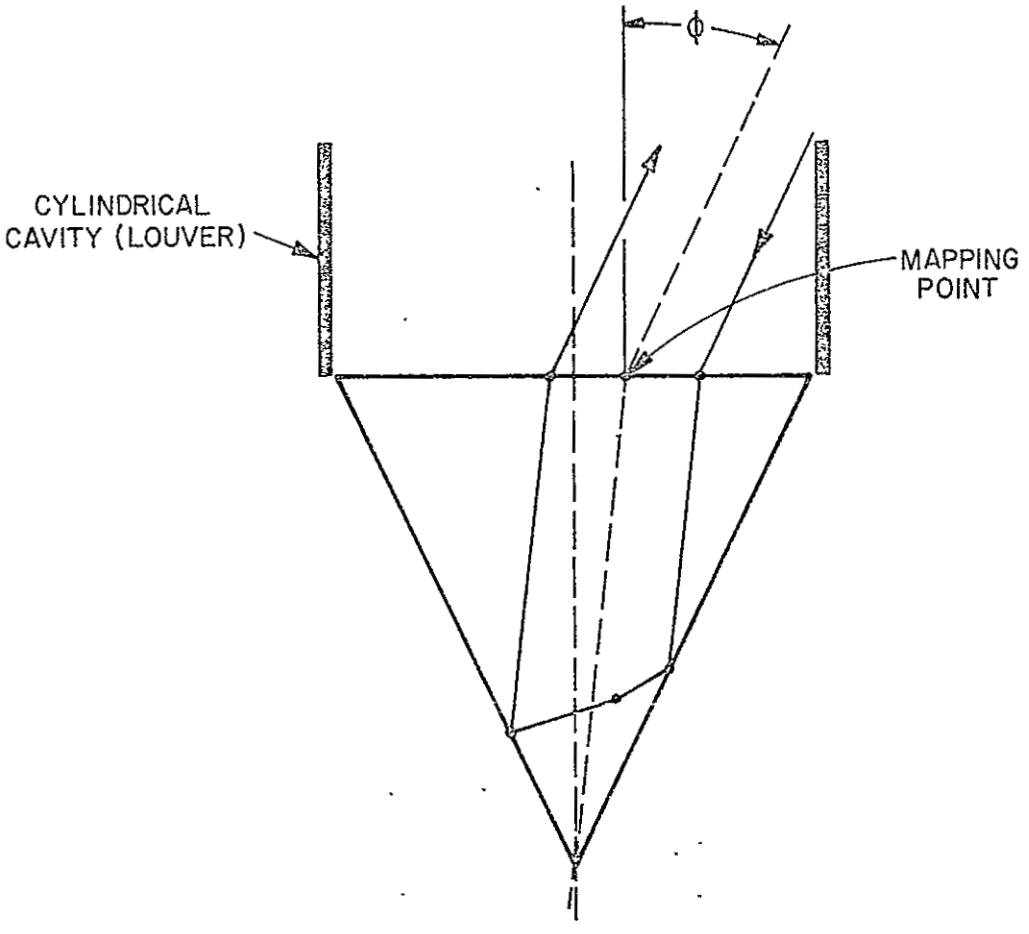

FIGURE 4 GEOMETRY OF RETRO-REFLECTOR AND THERMAL CONTROL CAVITY

The results of the cavity shadowing computation, including definitions of terms, are shown in Table 2. The cavity height is expressed in terms of the ratio (RLOW) of the length of the cavity above the retro-reflector face to the inside diameter of the cavity. RLOW ranges from 0 to 0.6. The term OFFC2 is the square of the optically unobscured area in units normalized to the value for a normally incident laser beam. This term (OFFC2) is proportional to the central irradiance for an isothermal retro-reflector of inscribed circle shape mounted in a vertical cylindrical thermal control cavity with a length-to-diameter ratio RLOW.

The results of Table 2 are plotted in Figure 5. The results suggest that the off-normal effects of the retro-reflector itself are significant even for a zero height cavity.

III. METHOD

A. Retro-Reflector Shape--No Cavity

The optical performance of a retro-reflector as indicated in Table 1 is computed by a computer program that generates a sequence of test rays on an x, y grid over the face of the retro-reflector and applies the following conditions for each ray:

(1) Is the ray inside the triangular face as defined by the equation of the three lines comprising the triangle sides?

AND

(2) Is the ray inside the tab base circle as defined by the equation for this circle?

AND

(3) Is the ray inside the cross radially mapped image of the triangle (1)?

AND

(4) Is the ray inside the cross radially mapped image of the tab base circle (2)?

TABLE 2

LASER BEAM OFF-ANGLE SHADOW EFFECTS DUE TO RETRO-REFLECTOR AND CAVITY

LASER BEAM OFF ANGLE SHADOW EFFECTS DUE TO RR AND CAVITY

CASE 70472 CRITICAL PERFORMANCE NOV 25 1968

DEFINITIONS
RLOW =RATIO LENGTH/WIDTH(DIAM) OF CAVITY(LOUVER)
OFFAN=ZENITH ANGLE OF INCIDENT LASER BEAM,DEGREES
ROTAT=AZIMUTH ANGLE INC BEAM,DEG,RE EDGE OF TRIANGL FACE
OFFAC=RATIO OPTICALLY ACTIVE TO GEOMETRIC FRONT FACE AREA
OFFC2=OFFAC SQUARED,RELATIVE CENTRAL IRRADIANCE
SHAPE RR INSCRIBED CIRCLE RATIO=1.0 ,CAVITY CONCENT CIRCLE

L	RLOW	K	OFFAN	ROTAT	OFFAC	OFFC2
1	0.0	1	0.0	0.0	1.000	1.000
1	0.0	2	5.0	0.0	0.891	0.794
1	0.0	3	10.0	0.0	0.784	0.615
1	0.0	4	15.0	0.0	0.681	0.464
1	0.0	5	20.0	0.0	0.574	0.329
2	0.1	1	0.0	0.0	1.000	1.000
2	0.1	2	5.0	0.0	0.888	0.788
2	0.1	3	10.0	0.0	0.764	0.583
2	0.1	4	15.0	0.0	0.635	0.403
2	0.1	5	20.0	0.0	0.507	0.257
3	0.2	1	0.0	0.0	1.000	1.000
3	0.2	2	5.0	0.0	0.870	0.757
3	0.2	3	10.0	0.0	0.722	0.521
3	0.2	4	15.0	0.0	0.568	0.322
3	0.2	5	20.0	0.0	0.420	0.177
4	0.3	1	0.0	0.0	1.000	1.000
4	0.3	2	5.0	0.0	0.848	0.720
4	0.3	3	10.0	0.0	0.672	0.452
4	0.3	4	15.0	0.0	0.499	0.249
4	0.3	5	20.0	0.0	0.337	0.113
5	0.4	1	0.0	0.0	1.000	1.000
5	0.4	2	5.0	0.0	0.827	0.684
5	0.4	3	10.0	0.0	0.627	0.393
5	0.4	4	15.0	0.0	0.436	0.190
5	0.4	5	20.0	0.0	0.261	0.068
6	0.5	1	0.0	0.0	1.000	1.000
6	0.5	2	5.0	0.0	0.804	0.647
6	0.5	3	10.0	0.0	0.588	0.345
6	0.5	4	15.0	0.0	0.378	0.143
6	0.5	5	20.0	0.0	0.188	0.035
7	0.6	1	0.0	0.0	1.000	1.000
7	0.6	2	5.0	0.0	0.781	0.610
7	0.6	3	10.0	0.0	0.538	0.289
7	0.6	4	15.0	0.0	0.319	0.101
7	0.6	5	20.0	0.0	0.126	0.015

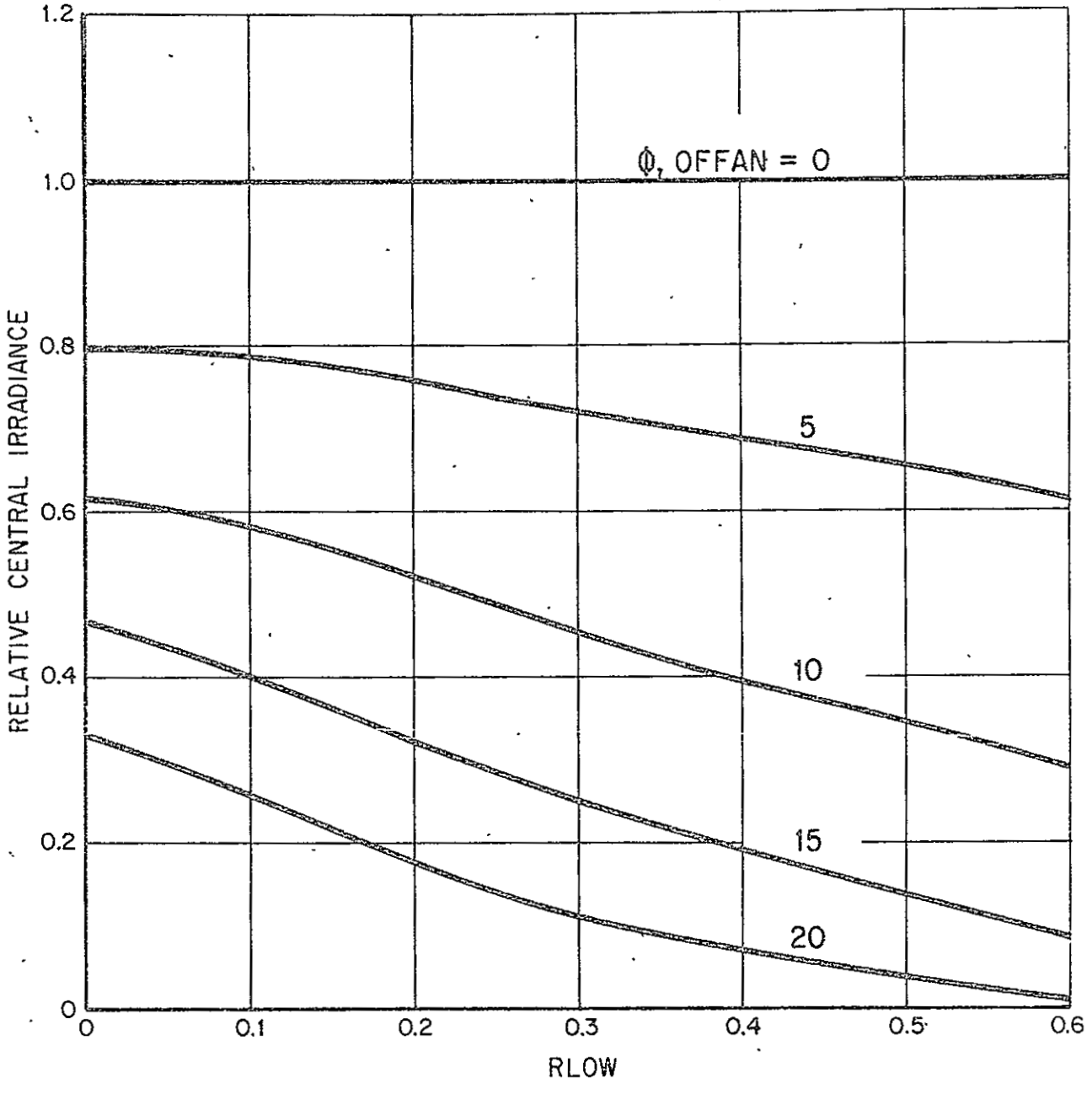

FIGURE 5 RELATIVE CENTRAL IRRADIANCE FROM RETRO-REFLECTOR VERSUS CAVITY (LOUVER) HEIGHT OVER DIAMETER RATIO, RLOW

B. Mapping

The basis for determining which rays are optically unobscured is the mapping point. For a laser beam incident at some off-normal zenith angle, there is a point on the retro-reflector face (the mapping point) about which any exiting ray can be cross-radially mapped (equidistant from the mapping point and 180° away) from the corresponding entrant ray. The mapping point is displaced from the center of the retro-reflector face and is in the plane of incidence. The geometry is indicated in Figure 6.

The procedure for determining the optically unobscured area is first, a ray is tested to be in or out of the triangle and to be in or out of the tab base circle, then the mapped position of the ray is tested in the same way.*

The rationale of the location of the mapping point on the retro-reflector face was established experimentally using a precise optical laboratory model.** The mapping point was found (as might have been expected) to correspond to the entering position on the retro-reflector face of the refracted ray that also passes through the apex of the retro-reflector. Therefore, by Snell's law and the geometry of the retro-reflector, the distance between the center point on the face of the retro-reflector and the mapping point is

$$C = H\tan\left[\arcsin\left(\frac{\sin\phi}{n}\right)\right]$$

and the x and y components of the position of the mapping point relative to the center point of the retro-reflector face are:

$$a = C\cos\theta$$

$$b = C\sin\theta$$

---

* The center of the retro-reflector face is (x=0, y=0).

**The laboratory model consisted of a hollow acrylic retro-reflector with a ruled grid on its front face and filled with mineral oil containing a trace of white paint to make a light beam visible. A zirconium arc lamp (with a narrow, 2-millimeter diameter parallel beam), a collimator, and the oiled-filled retro-reflector were mounted in a milling machine. This set-up provided indexed x, y, and z cross adjustments by which the location of rays and entrance and exit points on the retro-reflector could be studied.

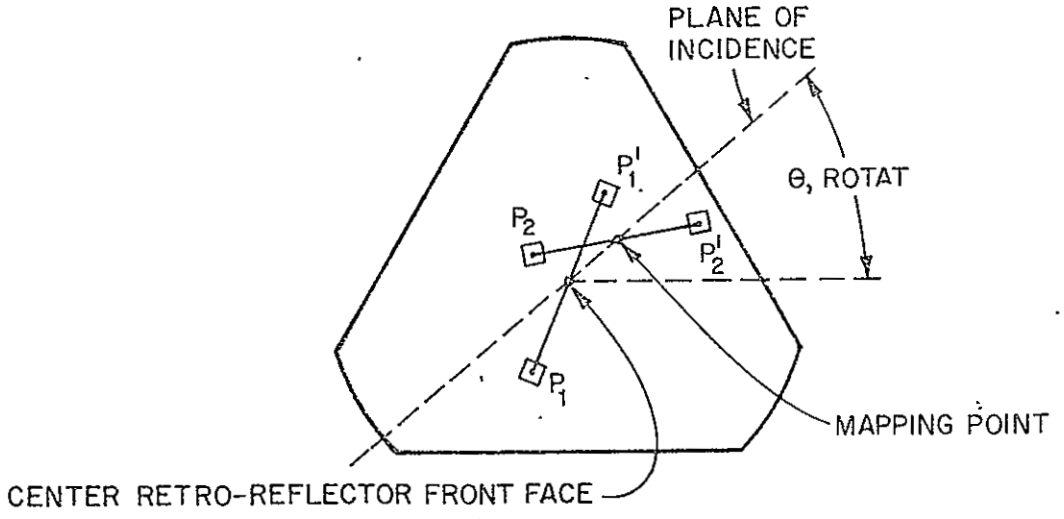

FIGURE 6 GEOMETRY OF MAPPING POINT

where:

n is the optical index of refraction, 1.4555 for silica,

C is the distance between the mapping point and the center of the front face of the retro-reflector,

H is the apex to front face distance of the retro-reflector,

ϕ is the zenith angle of the incident (laser) beam,

θ is the azimuth angle of the incident (laser) beam relative to one side of the front face triangle,

a is the x component of c, and

b is the y component of c.

C. Cavity Shadowing

The computation of the effect of cavity shadowing as printed out in Table 2 is carried out by imposing two conditions in addition to 1, 2, 3, and 4 stated in Section A above:

AND

(5) Does the ray under examination lie at a point on the retro-reflector face which is unshadowed by the cavity for the given (laser) beam zenith and azimuth angles?

AND

(6) Does the cross-radially mapped ray meet condition (5)?

The area defined by all rays on the retro-reflector face that meet conditions 1, 2, 3, 4, 5, and 6 is optically unobscured and defines the light that will emerge from the retro-reflector given an inscribed circle front face shape, a cavity (louver) of height to diameter ratio of RLOW, and a laser beam incident at given zenith (OFFAN) and azimuth (ROTAT) angles. For the particular inscribed circle shape concentric cylindrical cavity considered, the optical return is independent of azimuth and therefore the listed azimuth (ROTAT = 0.0) is representative of any azimuth angle.

APPENDIX 9

Solar Optical Tests of a Retro-Reflector in Simulated Lunar Environment

SOLAR OPTICAL TESTS

OF A RETRO-REFLECTOR

IN SIMULATED LUNAR ENVIRONMENT

FINAL REPORT

November 1970

Prepared for

UNIVERSITY OF MARYLAND
DEPARTMENT OF PHYSICS AND ASTRONOMY
College Park, Maryland

Under
Purchase Order No. 240495

By

ARTHUR D. LITTLE, INC.
Cambridge, Massachusetts

C-72071

(7)

TABLE OF CONTENTS

LIST OF FIGURES

LIST OF TABLES

FOREWORD

A solar optical test program for a retro-reflector in simulated lunar environment was conducted by Arthur D. Little (ADL), Inc., for the Department of Physics and Astronomy, University of Maryland, in support of the Manned Spacecraft Center, National Aeronautics and Space Administration (Contract NAS9-7809).

The authors acknowledge the assistance and cooperation of Carroll O. Alley, the Project Monitor, Ren Fang Chang, Douglas Currie and Harry Krimelmeyer of the University of Maryland, and James E. Faller of Wesleyan University. The principal ADL personnel contributing to the program included James C. Burke, Program Director; Daniel F. Comstock and Peter C. Von Thuna, optical instrumentation and measurements; Frank E. Ruccia, thermal facility; Richard L. Merriam, analytical predictions; David L. Richardson, solar simulation and test program; and John E. McCullough and Major M. White, test model design.

I. SUMMARY

A. PURPOSE

The solar optical test program was conducted by Arthur D. Little, Inc., to substantiate the analytical methods used to predict the optical performance of the retro-reflectors mounted in an array on the lunar surface. Increasing the confidence level and accuracy of the analysis used to predict the optical signal return from an array of retro-reflectors on the moon at various sun conditions would aid in the analysis of data being returned currently from such arrays and serve as the basis for design optimization of future arrays.

B. SCOPE AND DESCRIPTION OF EXPERIMENT

A test facility was constructed which permitted thermal and optical measurements of a single retro-reflector exposed to the simulated lunar environment of vacuum, solar heat, and low-temperature radiation. The test retro-reflector was mounted in a canister incorporating the physical dimensions, mounting hardware, and thermal boundary conditions typical of an array of retro-reflectors on the lunar surface. Solar simulation was accomplished by means of a collimated beam of light emanating from a xenon lamp mounted over the test chamber. A mirror arrangement in the test chamber permitted changing the angle of incidence of the sun. The optical test apparatus, which was mounted on a bench outside of the test chamber, consisted of a laser collimator with an internal beam-splitter, optics to focus the diffraction pattern, a photomultiplier tube and apertures for measuring the central and total irradiance in the diffraction pattern, associated readout equipment, and a camera for photographing the diffraction pattern.

Testing was conducted during two time periods three months apart. In the initial tests, accomplished in June 1970, the test facility, including solar simulator and retro-reflector model, were operated successfully. However, measurements of the central irradiance varied widely with an uncertainty in excess of $\pm 40\%$. This disparity precluded

meaningful comparison of the data with analytical results. After modifications and improvements were made to the optical instrumentation, the tests were repeated in September 1970. In this test program, two separate series of tests were made, each covering a range of solar angles. In the first series of tests, the laser beam operated in its normally polarized condition. In the second series of tests, a laser-beam polarizer (provided by the University of Maryland) was incorporated. It permitted rotation of the angle of polarization of the laser beam with respect to the retro-reflector.

C. RESULTS

A summary of measured and predicted canister temperatures and relative central irradiance values are presented in Table 1. The canister temperatures were predicted on the basis of a detailed thermal model, using the measured thermal physical properties of the retro-reflector, canister, and retainer ring, and the measured values of incident thermal flux. The conductance values between elements of the retro-reflector canister assembly were assumed to be those measured for the Apollo 11 array.

TABLE 1

SUMMARY OF CANISTER TEMPERATURES AND RELATIVE CENTRAL IRRADIANCE VALUES

Condition	Canister Temperature (°K)		Relative Central Irradiance		
				Measured	
	Analysis	Measured	Analysis	Normal Polarization	Min-Max Polarization
Room Temperature	-	294	1.0	1.0	1.0
-10 degrees	323	373	.92	.87	.94
-30 degrees	406	391	.33	.26	.67
-60 degrees	326	349	.46	.24	.99
Lunar Night	-	144	1.0	.80	no measurements

The relative central irradiance value of the retro-reflector was computed from the predicted local temperature distribution within the retro-reflector, using an optical ray trace program to determine the phase distribution of the laser energy leaving the retro-reflector. These phase distributions were then used to predict the central irradiance of the reflected energy.

The measured relative central irradiance values are presented, first, for the laser beam operating in its normally polarized condition and, second, with the polarization rotator installed. In the latter case, the experimentally reported central irradiance values are the average of the maximum irradiance (corrected for polarization effects in the measurement optics) and minimum irradiance obtained as the plane of polarization was rotated. The uncertainty in the central irradiance measurements is low. The probable error in the relative central irradiance for all measurements is less than $\pm 6\%$.

The measured temperatures of the canister fall within 3 to 10% of those predicted analytically. A comparison of the measured relative central irradiance value for normal polarization indicates good agreement with the analysis at all but the -60-degree solar angle. However, in light of the large polarization effect found during the second series of measurements, there is some doubt as to the validity of the normal polarization measurements. Experimental relative central irradiances based on the average between the maximum and minimum polarization return signal show the same general trend with increasing sun angle as do both the normal polarization results and the analysis. However, the maximum-minimum polarization results indicate much higher relative central irradiances than do either the normal polarization results or the analysis.

D. CONCLUSIONS

Based on the results of the solar optical tests, we reached the following conclusions:

1. The optical performance of a retro-reflector in a lunar environment agrees, in most important aspects, with the analytical methods

previously used in the thermal design of flight arrays.

(a) During lunar night when heat fluxes, temperatures, and temperature gradients are small, the relative central irradiance predicted by analysis and confirmed by measurements is close to unity.

(b) During near normal sun incidence (i.e., -10 degrees) when the incident solar energy is retro-reflected, relative central irradiance is again near unity for results obtained by analysis and from measurements.

(c) When the sun angle exceeds the critical angle (-16 degrees) for retro-reflection, degradation in optical performance is most severe and improves as the sun angle approaches -90 degrees. In this region the trend of the analytical results and experimental data (at -30 and -60 degrees) was the same. However, we did not achieve consistently good agreement between the analysis and measured results.

2. Since the analysis in its present form does not include polarization effects, and since the return signal from a thermally perturbed retro-reflector is extremely sensitive to the angle of polarization, it is difficult to interpret differences in relative central irradiance between the analysis and experimental measurements at different polarization conditions.

3. The difference between analytical and experimental canister temperatures, while generally about 10% or less, is greater than would be anticipated from the known tolerances on input data such as mount conductance, material properties, and solar beam intensities. The resolution of these differences would require additional detailed thermal measurements.

The experimental results of this program demonstrate the correspondence between analysis and experiment and verify the general applicability of our analytical techniques. The underlying analysis for the optical performance and thermal control of the retro-reflectors in the lunar array has been verified with successful signal returns from the arrays deployed on the lunar surface during the Apollo 11 and Apollo 14 missions.

II. INTRODUCTION

The Laser Ranging Retro-Reflector (LRRR) experiment, as well as its basic design, was conceived by an investigative group of scientists from several institutions headed by C. O. Alley of the University of Maryland. The LRRR experiment was originally suggested in a letter to the Journal of Geophysical Research[1] in 1965. A complete discussion of the technique for the experiment, including design considerations for the LRRR array, was presented by the University of Maryland in a proposal submitted to NASA in December 1965. Under a NASA grant, retro-reflectors were successfully tested[2] by the University of Maryland with the assistance of the Perkin-Elmer Corporation. Using the facilities of NASA's Goddard Spaceflight Center, investigators tested the optical performance of the retro-reflector in a simulated lunar environment during the Summer of 1966. The placement of a retro-reflector package on the moon as an official Apollo experiment was approved by NASA in 1967, and the decision to include it on Apollo 11 as part of the Early Apollo Scientific Experiment Package (EASEP) was made by NASA in January 1969.

The first retro-reflector package, a 100-unit array, was placed on the lunar surface on July 20, 1969, as a part of the Apollo 11 mission, and it has been operating successfully ever since.[3-6] A second retro-reflector array, also 100 units, was placed on the moon as part of the Apollo 14 mission. Construction of a third package, a 300-unit retro-reflector array, planned for Apollo 15 mission in July, is currently underway.

ADL's association with the LRRR experiment dates back to early 1967. Under contract to the University of Maryland during the Spring of 1967, we conducted preliminary thermal analyses and mechanical design of the LRRR array for the Apollo Lunar Scientific Experiment Package (ALSEP) program. Our final report, which contained predictions of retro-reflector temperature gradients, included a preliminary design concept incorporating both thermal control and structural protection.

From mid-1967 to mid-1968, we participated in an investigation of retro-reflector vendors, and acted as liaison with the investigative group. In June 1968, we were awarded a contract by the University of Maryland to define the thermal performance of various thermal control designs of LRRR arrays. Upon completion of this work, we accomplished the design and fabrication of LRRR arrays for the Apollo 11 and Apollo 14 missions under contract to the Bendix Aerospace Systems Division. Currently, we are engaged in the assembly and test of the retro-reflector array for Apollo 15, also in conjunction with Bendix.

Because of schedule limitations, we established thermal design of this retro-reflector array and predicted optical returns from the array in a lunar thermal environment solely by analysis with no test verification other than those initial tests conducted by the University of Maryland in the Summer of 1966. These early tests, while demonstrating the basic feasibility of the retro-reflector concept, did not provide quantitative data necessary for designing the final array configuration. The decision to rely, to a large extent, on the analytical thermal design has since been vindicated by the successful performance of the Apollo 11 and 14 mission arrays.

The solar/optical test program, which is the subject of this report, was conducted to refine the predicted optical performance of the present array hardware, improve the accuracy of data reduction, provide a basis for future array design optimization, and aid in assessing possible degradation in the return signal at some much later time. The test program was begun in December 1969.

III. EXPERIMENTAL FACILITY

A. EXPERIMENTAL APPROACH

The objective of the solar optical test program was to verify that a thermal/optical analysis could be used to predict the optical return of a retro-reflector in a lunar environment. Therefore, the experimental equipment was designed to provide optical measurements of the return of retro-reflector when exposed to thermal environment similar to that which might be experienced by an array on the lunar surface.

In experiments of this type, an exact simulation of the actual operating conditions would be impractical, because it would require using a full array with support and aiming mechanism placed on a reasonably large expanse of simulated lunar soil in a vacuum chamber which had both a solar beam and simulated space background temperatures. To produce all of these conditions simultaneously would be prohibitively expensive and, to a large extent, is quite unnecessary. A far more reasonable approach would be to devise an experiment which simulated the most important boundary conditions, and then use this experiment to verify the analytical method when applied to these experimental conditions. Therefore, we designed a facility capable of testing a single retro-reflector in a simulated array segment.

A single retro-reflector in an array segment allowed use of a reasonably sized solar beam, and was consistent with previous analytical studies which have indicated that transverse temperature gradients in the array and variations in performance from retro-reflector to retro-reflector were extremely small. The array segment was insulated on the sides and back to eliminate external heat transfer other than that associated with the front face of the retro-reflector and array segment. In the actual array, the sidewise, or transverse, heat transfer was negligible. However, heat transfer through the back of the array may be significant. In actual operation, the heat leak from the back may be either positive, negative, or essentially zero, depending on the particulars of site and

the specific design of the support hardware. By electing to eliminate back heat transfer, we conducted tests under a real condition which was as valid as any other for comparing the analytical data with experimental results. The use of a liquid nitrogen temperature background (77°K rather than that of outer space, a few degrees Kelvin) simplified the experiment greatly, because, in either case, the radiation from the test chamber walls to the model or from space to the array was negligible.

The solar simulator, a xenon lamp, used in the experiment, also provided inaccurate simulation since its spectral content did not actually match that of the sun. However, this did not compromise the objective of verifying the analysis since, when the analysis was applied to the experimental situation, we used the actual solar radiation properties of materials when exposed to the xenon beam.

B. TEST CHAMBER

The ADL vacuum test chamber used in this test has an internal working space approximately 2 feet in diameter and 4 feet long, and was modified by the addition of appropriate windows, penetrations, and LN_2 shrouds. The chamber also has a vacuum system capable of producing a vacuum of less than 10^{-6} torr, and is supported by pneumatic mounts to minimize mechanical inputs to the optical system.

The test chamber and its relationship to the solar simulator and optical instrumentation are shown in Figure 1. A 4-inch diameter stainless-steel tube, which penetrates one end of the chamber, is used as an optical rail on which are mounted both the retro-reflector test model within the chamber and the optical instrumentation table outside the chamber. The beam from the laser collimator enters and leaves the chamber through a BK-7 window which is flat and parallel to 1/20λ. The solar simulator is located on top of the test chamber. The solar beam enters the chamber through a 0.75-inch thick Infrasil window. Within the chamber the solar beam can be rotated in the horizontal plane by a mirror system which provides sun angles from +30 to -70 degrees with respect to the retro-reflector axis. (As the retro-reflector is installed, with its pointing axis and one true edge in a horizontal plane, total internal

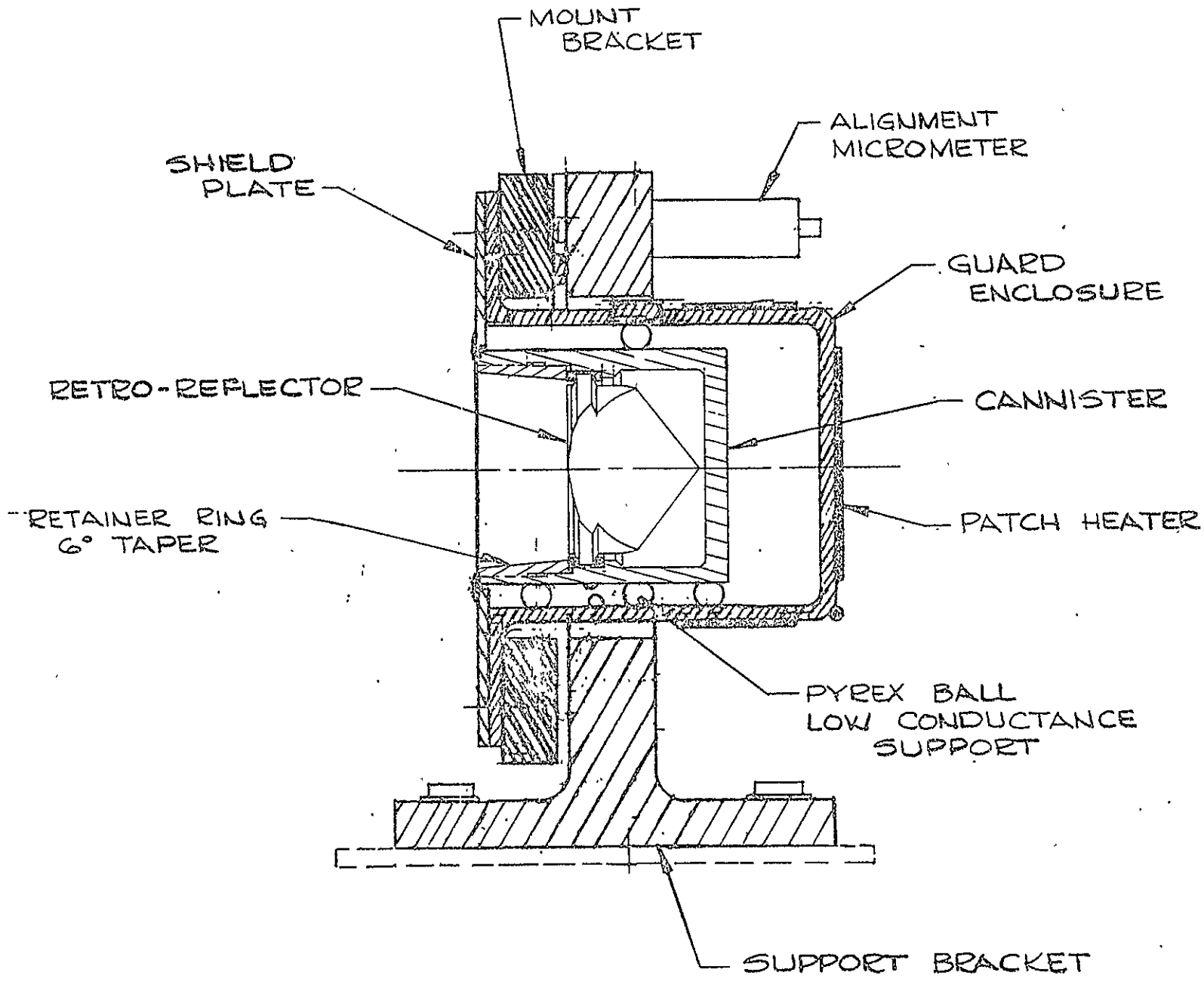

FIGURE 1 TEST MODEL ASSEMBLY

reflection exists between sun angles of approximately -60 to +90 degrees.)

A liquid nitrogen-cooled shroud encloses the retro-reflector test model and rotating mirrors. This shroud has a semicircular cross-section matching the upper half of the test chamber and is about 20-inches long. Cutouts are provided in the shroud for the solar beam, the optical path, and the test model support.

C. TEST MODEL

The test model consists of the test retro-reflector mounted in a simulated array segment (canister) with the associated thermal isolation, positioning, and support equipment. Figure 2, which presents a sectional view of the test model, illustrates these features. As Figure 2 shows, the test retro-reflector is mounted within an aluminum canister which incorporates both the internal geometry of the array cavity and a representative portion of the array front surface. The retro-reflector is retained in the canister with Apollo 14 flight-type support rings and retainer ring (6-degree taper).

The canister is connected to the copper guard enclosure with low-conductance supports made from 0.25 inch diameter Pyrex balls. The copper guard enclosure is heated with electrical patch heaters applied to its back and side surfaces. Temperatures are measured with chromel-constantan thermocouples located at two axial positions on the copper guard enclosure, and one location on both the canister and the retainer ring. A differential thermocouple (chromel-constantan) measures the temperature difference between the canister and the copper guard enclosure. In practice we have been able to control the temperature difference between the canister and the copper guard enclosure to less than 0.5°K. This resulted in a heat flow between the guard enclosure and the canister of less than 2 percent of the solar energy absorbed on the front face of the canister.

The guard enclosure has a shield plate which surrounds the front surface of the canister and prevents solar energy from impinging on its sides. The guard enclosure is attached to a mount bracket which, in turn, is attached to the support bracket by means of a micrometer/spring system by which accurate alignment of the retro-reflector with respect to

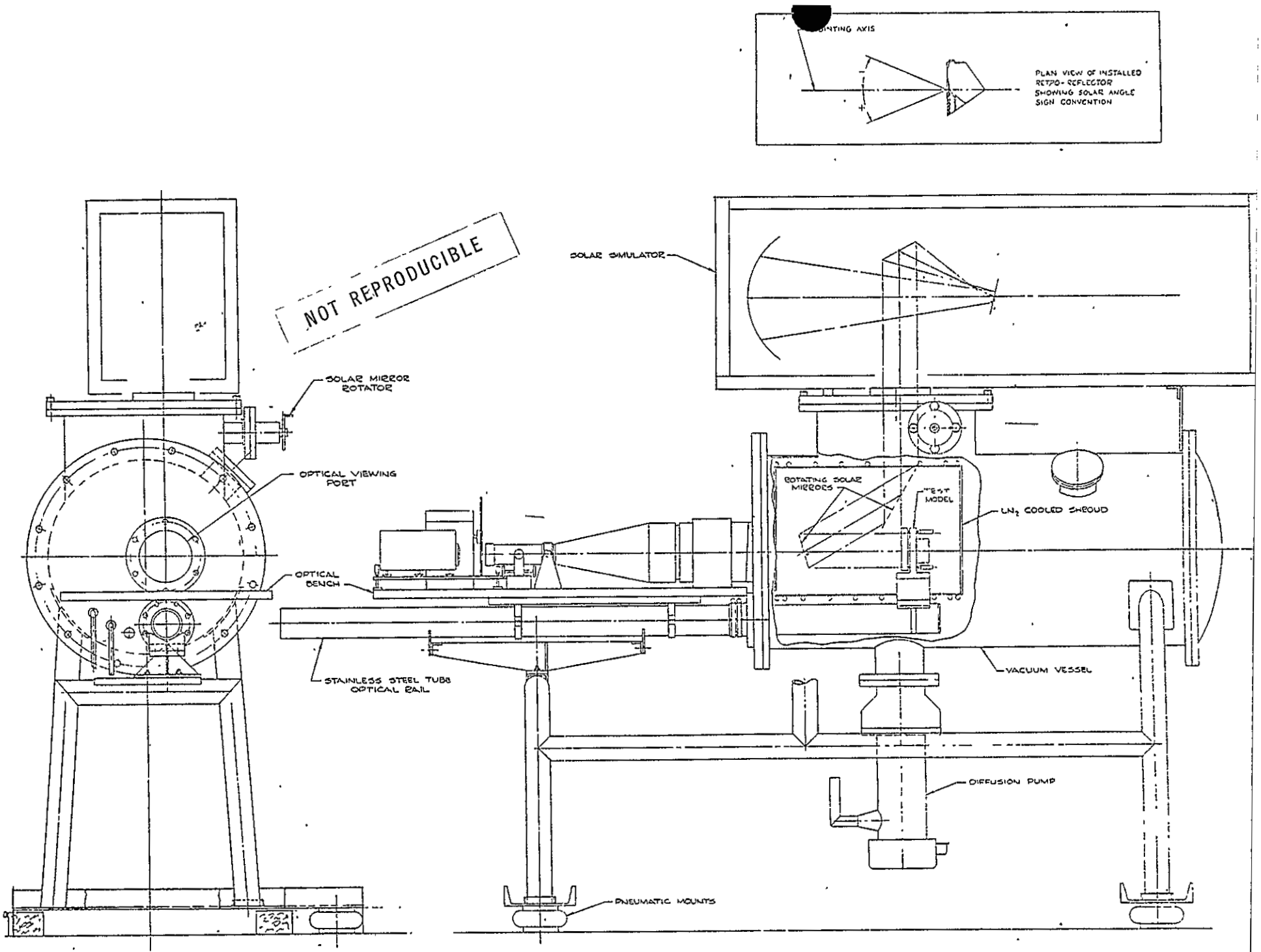

FIGURE 2 TEST MODEL SECTION

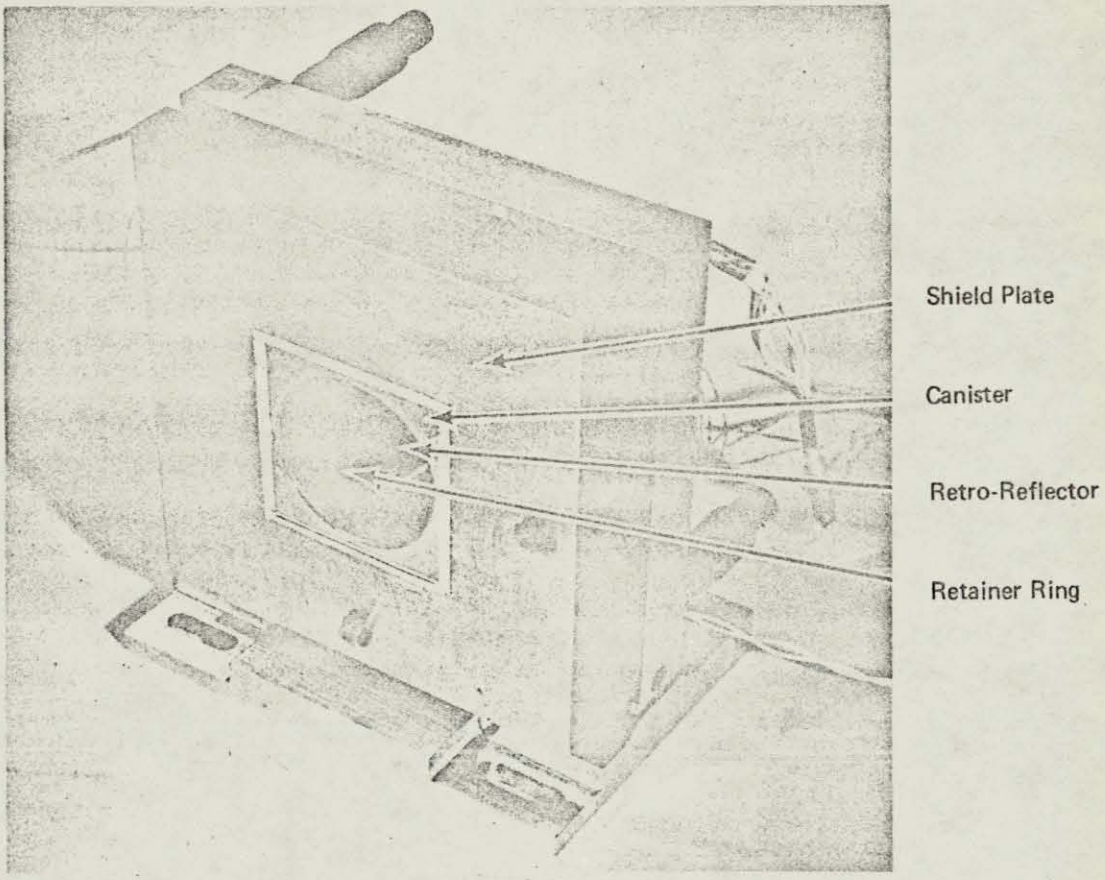

FIGURE 3 TEST MODEL

the laser beam can be effected. The support bracket is attached to the optical rail through a low conductance pad.

Figure 3 shows the test model from the front or solar-beam side. It shows how the front face of the canister is framed by the shield plate and how the gap between the canister and the shield plate is covered with a thin ribbon of aluminized Mylar tape. The thermocouple on the retainer ring, the alignment micrometers, and the leads to the various thermocouples and heaters are also shown in Figure 3.

D. FACILITY INSTRUMENTATION

1. Temperature Measurements

Copper-constantan thermocouples were used to take temperature measurements at various locations on the liquid-nitrogen shroud of the chamber, and chromel constantan thermocouples were used in the test model. The location, type, and size of the thermocouples used are presented in Table 2. All thermocouples had one junction in an ice reference.

TABLE 2

THERMOCOUPLE DATA

Location	No.	Type	Size (in. dia.)
Shroud			
End	(2)	Copper-Constantan	0.005
Side	(2)	Copper-Constantan	0.005
LN_2 in	(1)	Copper-Constantan	0.005
LN_2 out	(1)	Copper-Constantan	0.005
Test Model			
Canister	(1)	Chromel-Constantan	0.006
Guard heater	(2)	Chromel-Constantan	0.006
Differential canister-guard	(1)	Chromel-Constantan	0.006
Retainer ring	(1)	Chromel-Constantan	0.002

2. Solar-Beam Monitor

Throughout the test, the output of the solar simulation system was continuously monitored by means of a water-cooled pyrehliometer* to detect changes attributable to lamp or mirror degradation. The instrument has linear characteristics with a sensitivity of 0.0264 W/cm^2-mV. A small front-surface mirror placed in the fringe of the solar beam just ahead of the Infrasil window was used to deflect a small sampling of the solar beam onto the pyrheliometer.

*Hy-Cal Engineering Co., Model No. P-8400-B-01-120

IV. SOLAR SIMULATION

A. DESIGN

The solar simulator used in this test program is shown in Figure 1. The simulator uses a 2.5-kW Osram xenon lamp as its source of radiant power. This lamp is located at the first focus of an 18-inch diameter ellipsoidal front-surface mirror. The beam is next reflected from a flat front-surface mirror upward to a 4.25-inch diameter front-surface, aluminized spherical mirror of 9-inch focal length which collimates the beam. This mirror directs the beam downward through a 0.75-inch thick Infrasil window (provided by the University of Maryland) into the chamber, from whence it passes centrally through a large bull gear which carries both of the flat, in-chamber mirrors used to direct the solar beam onto the test model at various solar angles. One turn of the pinion gear which drives the bull gear produces a 1-degree rotation of the sun angle.

Two optical apertures are used to limit both the amount of stray light entering the chamber and the diameter of the beam incident on the test model. One aperture is located above the chamber Infrasil window and the other is located in the chamber, immediately upstream of the first in-chamber mirror. With these apertures, the half-angle divergence of the solar beam was 3.9 degrees.

B. CALIBRATION

1. Background

The basic philosophy behind the solar optical tests was to measure the effect of a simulated solar beam on a retro-reflector rather than to try to simulate the sun itself (an almost impossible task). The procedure, therefore, was to design and build a solar simulator which would minimize the losses in long-wavelength radiation (through the use of front-surface optics and an Infrasil chamber window), and to measure the absorptance of the retro-reflector and all components of its mounting resulting from the "as-produced" solar beam. By this technique, absorptance to

the energy present in the line spectra of the xenon lamp could be measured. To complete this simulation, the total energy incident on the retroreflector model had to be 1.0 solar constant (0.14 W/cm^2).

2. Technique

The solar intensity at the front of the test model was measured with an Eppley eight-junction, circular thermopile with bismuth-silver elements. The sensing element in this instrument is 0.219 inch in diameter and is coated with 3M Black Velvet. This coating gave it a flat spectral absorptance in the wavelength of interest in this program. A 0.5-mm thick quartz window covered the receiving element. With this window, the sensitivity of the thermopile was measured at 0.00897 W/cm^2-mV.

Solar-intensity measurements were made in the test chamber with the sensing element of the thermopile being traversed in the plane of the front surface of the test model. Traversing was achieved with a two-axis milling table adapted for this application. An alignment target was used throughout this program to locate the center of the front surface of the test model. A cathetometer focused on the optical alignment target was used as a reference for adjusting the zero position of the thermopile when the thermopile replaced the target.

The intensity level of the solar beam was adjusted with the thermopile in the X = 0, Y = 0 position with the solar beam at normal incidence. In the calibration procedure, the xenon lamp was allowed to reach equilibrium temperature at least 10 minutes prior to setting the thermal intensity level at 1 solar constant. Throughout both the calibration test and the solar test program, the lamp current was maintained at the level measured during the initial calibration. The dc solid-state power supply for the xenon lamp was stable, and the lamp current required virtually no adjustment throughout the complete test program.

Calibrations of the solar intensity over the front surface ($\pm$1 inch in both directions from the center of the test model) were made at sun angles (measured from the normal) of normal incidence (solar noon) of -16, -30, and -60 degrees. At these angles of incidence, the sensing

element of the radiometer was maintained perpendicular to the solar beam by wedge blocks. The tilted radiometer was then traversed in the plane of the front surface of the test model. Thus, the intensity measured was the intensity incident on the model at the angle of interest.

3. Results

Calibration measurements were made both before and after the second series of tests. Flux intensities were measured at discrete locations throughout the 2- by 2-inch area and thermal flux patterns were plotted. The flux intensity maps both before and after tests had essentially the same shape. Representative flux intensity patterns for normal and 60-degree incidence angles before testing are shown in Figures 4 and 5. The outline of the 2- by 2-inch central area of the test model and the 1.5-inch diameter area of the retro-reflector are shown as dotted lines.

We characterized the solar beam by the flux intensity level in the 1.5-inch diameter central area and those in the remaining area covering the front surface of the model. In our analysis of the thermal behavior of the test model, the flux intensity value for the central 1.5-inch diameter area was 0.140 W/cm^2 and 0.115 W/cm^2 for the remainder of the 2- by 2-inch area. Figures 4 and 5 show that the solar intensity did not vary appreciably from 1 solar constant throughout the 1.5-inch diameter central area, but that the intensity level dropped off somewhat for the remainder of the 2- by 2-inch front surface of the model.

At the end of the retest program, the solar intensity in the central 1.5-inch diameter area of the test model had decreased to an average value (all solar angles) of 0.13 W/cm^2, a 7.1% decrease from the pre-test average value of 0.14 W/cm^2. We estimate that this decrease in solar flux could result in a decrease of about 2% in the temperature of the canister. Since the xenon lamp current and the solar-beam monitor both remained constant during the test program, there was no degradation in either the lamp or external transfer optics. The chamber window was also unaffected. However, the two mirrors in the test chamber had a noticeable haze resulting from an accumulation of oil which had back-streamed from

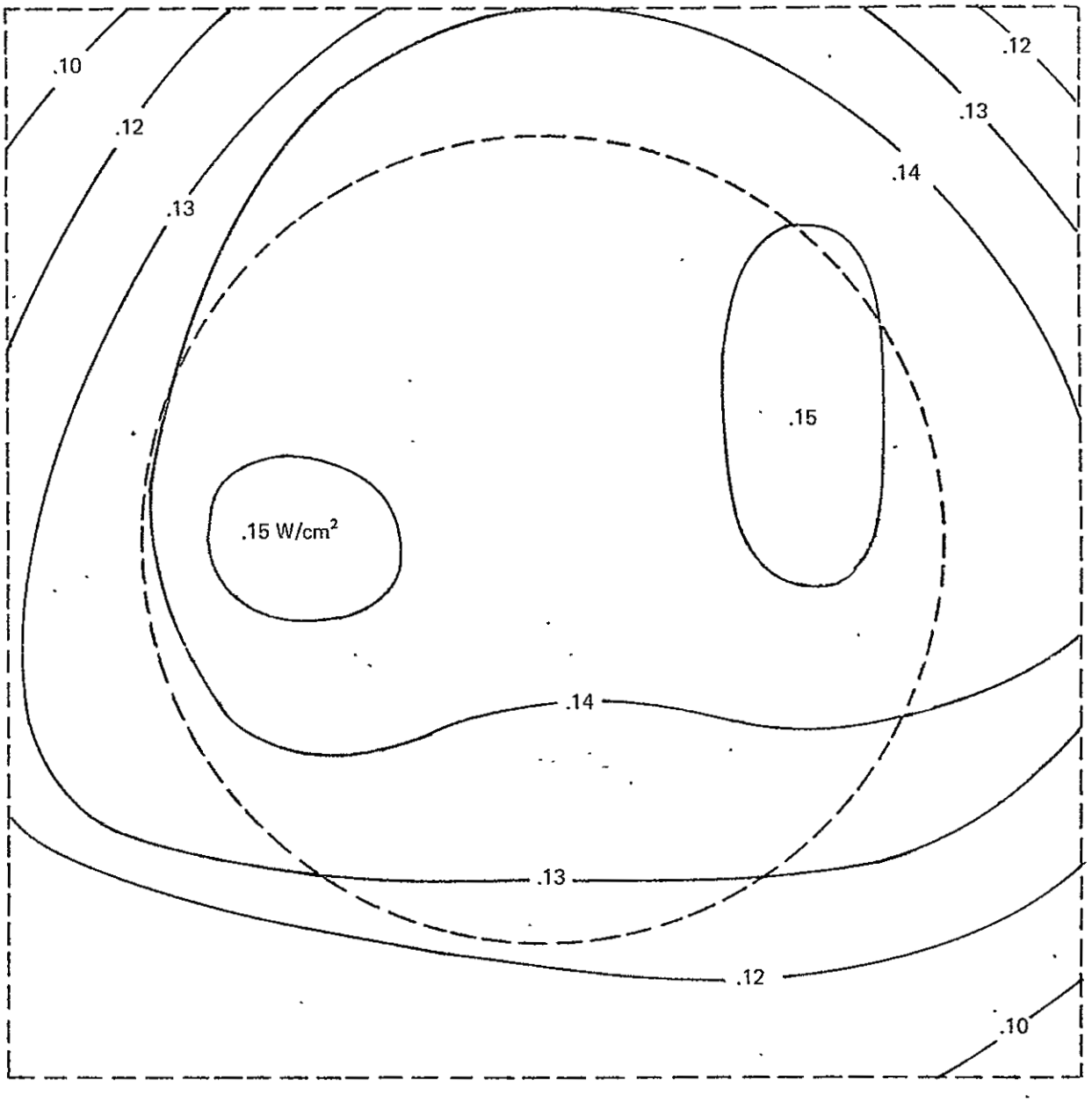

FIGURE 4 FLUX INTENSITY DISTRIBUTION – NORMAL INCIDENCE

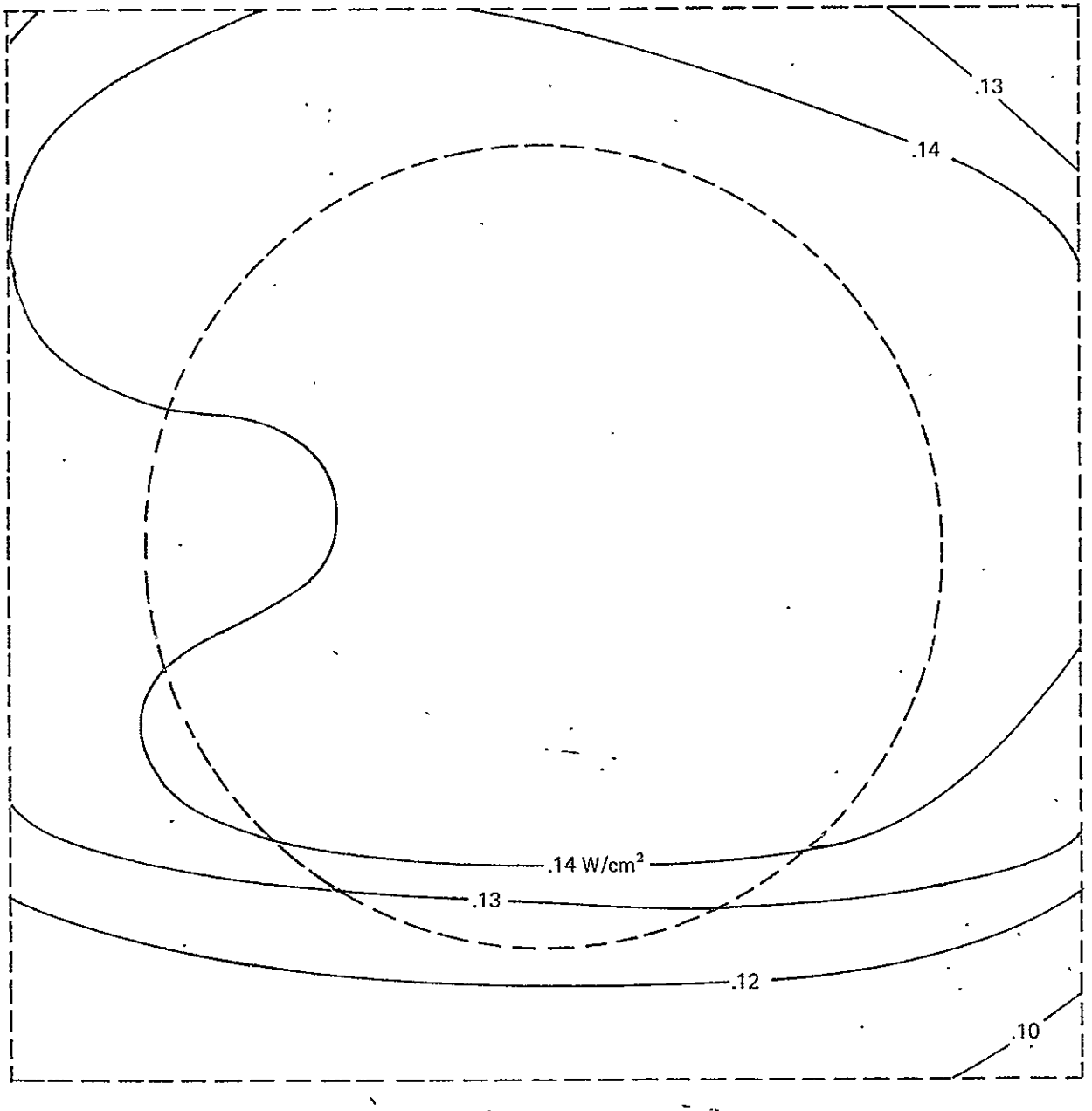

FIGURE 5 FLUX INTENSITY DISTRIBUTION – 60° INCIDENCE

the diffusion pump. This appears to have been the major contributor to the solar degradation.

C. PROPERTY MEASUREMENTS

In the analytical program, the solar absorptance values in the array represent an important input in the model used to predict the optical performance of the materials in an array on the lunar surface. Likewise, when applying this analysis to predict retro-reflector performance during the solar optical tests, it is important to know the absorptance of the materials of the test model to the simulated solar energy (a xenon lamp).

1. Absorptance Measurements

The absorptance of the retro-reflector, the anodized retainer ring, and the structural aluminum of the retro-reflector array was measured by exposing samples of the material to the xenon lamp beam, while the test chamber was maintained at a constant temperature by liquid nitrogen. The samples were suspended (one at a time) by low-conductance, stainless-steel wires as shown schematically in Figure 6. With the chamber evacuated to a pressure of less than 10^{-6} torr, heat from the test sample is transferred principally by radiation. At equilibrium-temperature conditions, the relationship between solar absorptance and the temperature of the retro-reflector and the aluminum samples is given by the following equations:

Retro-Reflector in Equilibrium:

$$\alpha_s = \frac{\varepsilon A_t}{q_s A_f} \sigma \left[T_R^4 - T_{amb}^4 \right] \qquad (1)$$

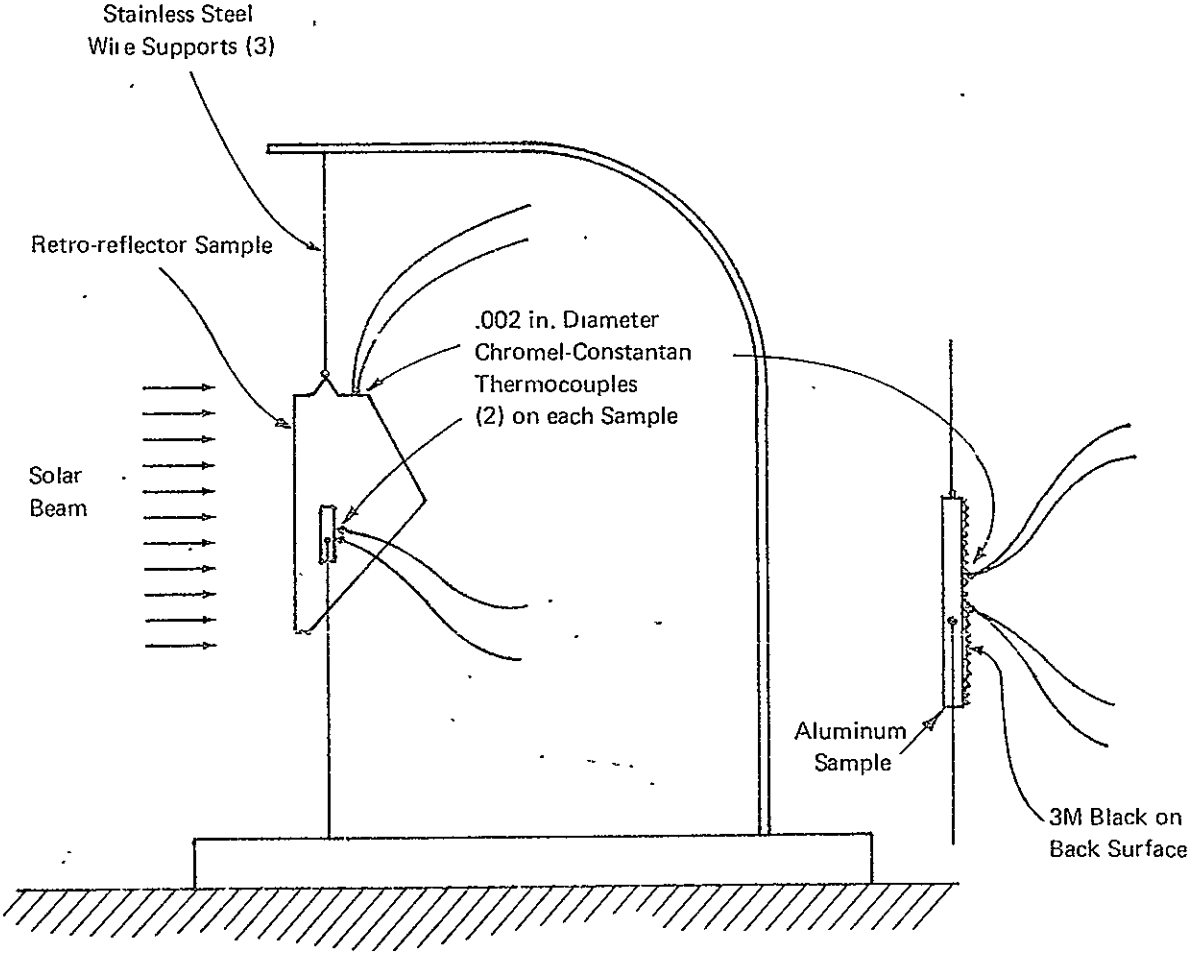

FIGURE 6 SAMPLE HOLDER FOR SOLAR ABSORPTANCE MEASUREMENTS

Aluminum Samples in Equilibrium:

$$\alpha_s = \frac{\left[A_f\varepsilon_f + A_f\varepsilon_R + A_s\varepsilon_f\right]}{q_s A_f} \sigma \left[T^4 - T_{amb}^4\right] \qquad (2)$$

where

α_s = solar absorptance

ε = emittance of quartz

A_t = total area of retro-reflector (37.6 cm^2)

A_f = front area (13.5 cm^2)

A_s = side area of aluminum samples (0.333 A_f)

T_R = retro-reflector temperature (°K)

T_{amb} = ambient temperature (°K)

q_s = solar intensity (W/cm^2)

ε_R = emittance of blackened rear surface of aluminum

ε_f = emittance of front surface of aluminum

The samples to be tested included a flight-quality quartz retro-reflector 1.5 inches in diameter, a 6061-T6 aluminum plate 1.5 inches in diameter with a 32-micro-inch finish, and a 1100 anodized aluminum plate in accordance with Specification QA-1-0511-E1-16 which is used in the laser retro-reflector array for Apollo 11. Because of their low emittance values, we painted the back surface of both of the aluminum samples with 3M Black Velvet paint to ensure that we had a high-emittance surface, and also to ensure that errors in measurement of the reported values of the emittance of both 6061-T6 and 1100 anodized aluminum were minimized.

2. Results

Table 3 presents a summary of the results of the solar absorptance measurements, as well as values for the long-wavelength emittance. The emittance values for aluminum are based on measurements made by ADL during

design of the Apollo 11 LRRR and the emittance values for quartz are taken from data published by the Thermophysical Properties Research Center at Purdue University in 1966.

TABLE 3

THERMAL PROPERTIES OF LRRR MATERIALS

Sample Description	Emittance, ε	Solar Absorptance, α (W/cm^2)
Flight-quality quartz retro-reflector	0.85	0.069
6061-T6 aluminum (32-μin. finish)	0.023	0.19
1100 aluminum anodized in accordance with specification QA-1-0511-E1-16	0.78	0.34

V. OPTICAL INSTRUMENTATION

A. SYSTEM ARRANGEMENT

The optical test apparatus consisted of the following components which are listed in the sequence in which the light wave progresses (see Figure 7) through the instrumentation:

Laser	Microscope objective
Chopper	Fixed flat mirror
Collimator	Movable flat mirror
Isolation box	Photomultiplier
BK-7 window	Removable camera
Test model	External calibration fixtures.

Figure 8 shows the major components of the optical instrumentation and the associated electronics.

B. OPTICAL COMPONENTS

1. Laser

A helium-neon gas laser* designed to provide intense, uniphase, frequency-stable visible radiation at a wavelength of 6328 angstroms, was used in this experiment. The temporal coherence of the output radiation is achieved by the use of a stabilized optical resonator designed so that only a single mode (transverse and longitudinal) can operate. The plasma tube contains isotopically pure helium-3 and neon-20. The tube and optical are mounted on an Invar resonator structure having bimetallic temperature compensation. The dielectric resonator mirrors are mounted at the ends of the Invar resonator structure; one is fixed and the other is mounted on a piezoelectric element which is voltage-controlled for mirror spacing, which, in turn, controls the laser frequency. The resonator and plasma tube are housed in a temperature-controlled oven for thermal stability.

An exciter,** which houses the high-voltage power supply for the plasma tube excitation, the proportional temperature-control circuit, a test

*Spectra-Physics, Inc., Model 119

**Spectra-Physics, Inc., Model 259B

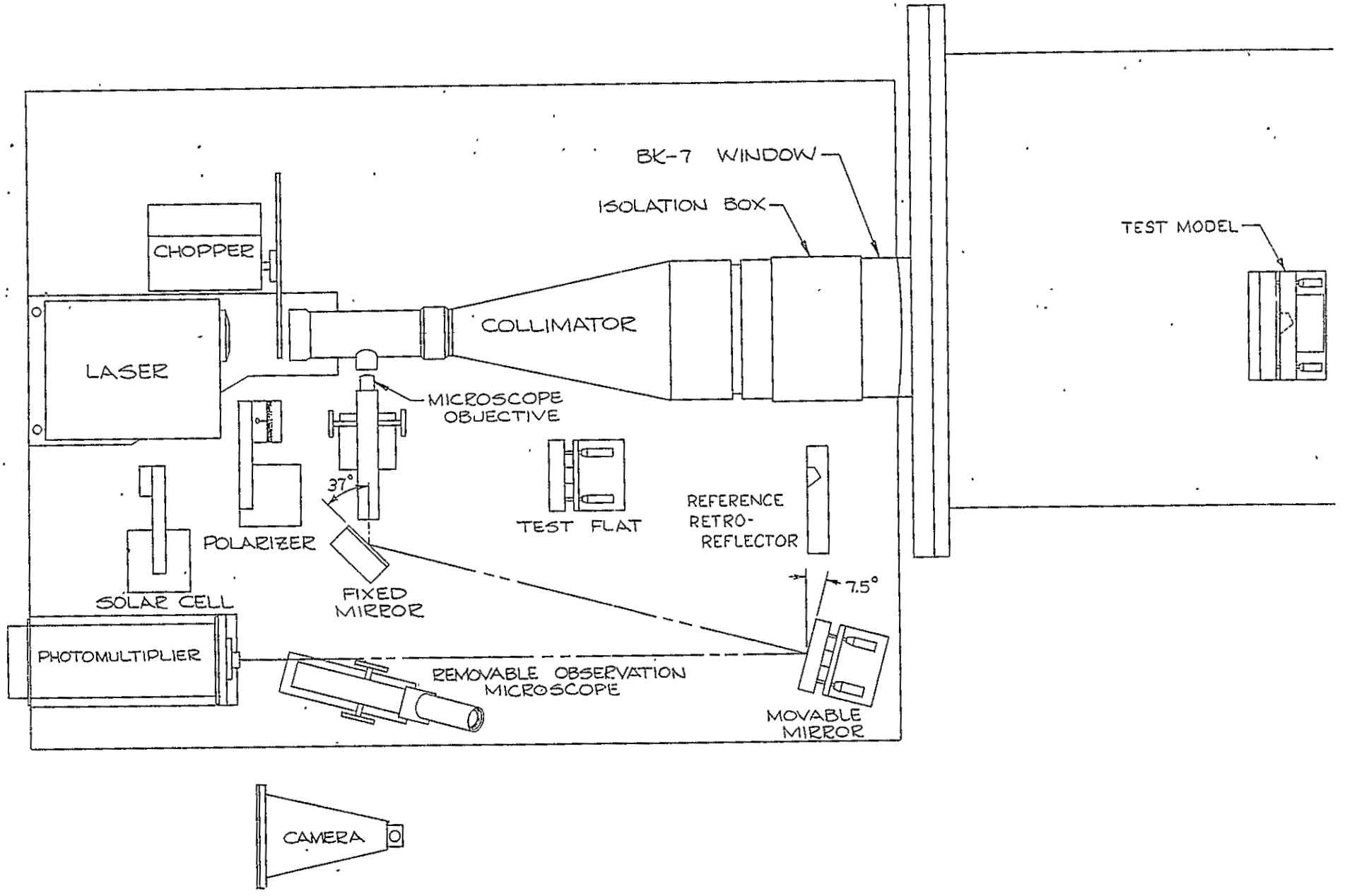

FIGURE 7 SCHEMATIC OF OPTICAL INSTRUMENTATION

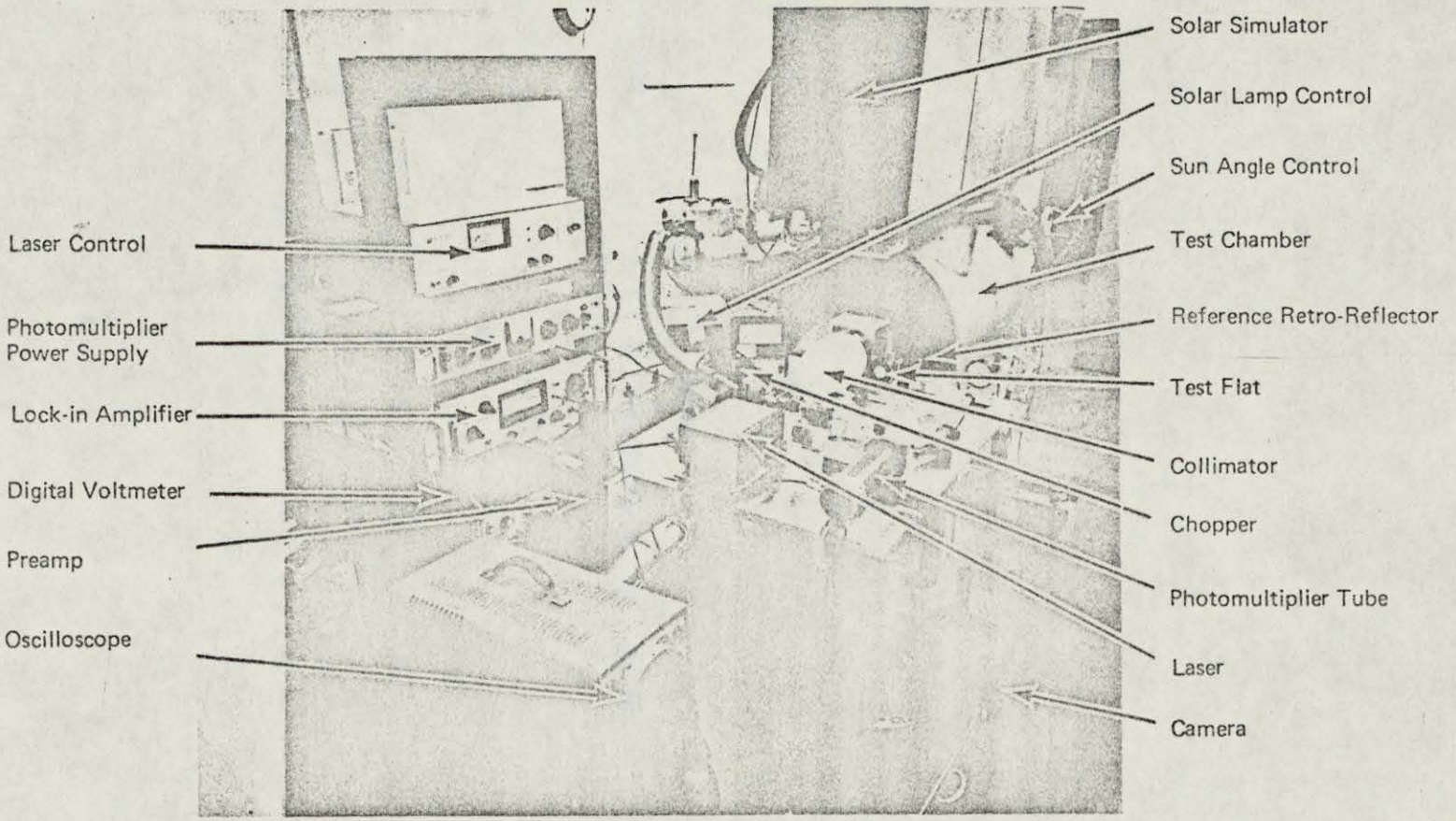

FIGURE 8 OPTICAL INSTRUMENTATION

meter circuit, and a module for manual control of mirror spacing, is used with the laser. The output power of the laser is greater than 100 microwatts.

2. Laser Collimator

The laser collimator* was modified so it could be used as a Fizeau interferometer for viewing interference fringes. (The collimator was never used in the Fizeau interferometer mode.) The beam-splitter in the unit has an aluminum-coated hypotenuse to provide a laser beam transmittance of 5 to 10% at a wavelength equal to 6328 angstroms. The entrance pupil of the collimator contains a lens which focuses the laser light on a 6-micron pinhole, which serves to filter the laser beam spatially. From the pinhole, the beam expands to fill the 5-inch collimator lens 50 cm away from the pinhole. This lens changes the spherical wave to a plane wave for illumination of the retro-reflector.

3. BK-7 Window

The parallel laser beam passes through a 2-inch thick BK-7 vacuum-chamber window.** This thickness was necessary to preclude the window deflecting under vacuum with the consequent degradation effects on the lens. It was also ground flat to less than 1/20 wavelength distortion.

4. Magnification Optics

The collimated beam in the chamber falls on the retro-reflector model which is centrally located in the beam. The return beam passes through the BK-7 window into the 5-inch lens and is focused down to a diffraction pattern 50 cm. The return beam is diverted from the axis of the collimator by the 45-degree beam-splitter located 45 cm from the lens, and the retro-reflector diffraction pattern is generated in a plane approximately 5 cm outside of the collimator housing. The objective lens of a "10-power" infinity-corrected microscope is focused on this plane to form a magnified image of the diffraction pattern. Further magnification and control of the diffraction pattern is achieved by folding the light

*A modified Tropel model 280-125.

**Provided by the University of Maryland.

path with two flat mirrors. The first mirror, located at the exit of the microscope, is fixed to the optical platform, and the second mirror is mounted on a two-axis precision micrometer stand. With this movable mount, the diffraction pattern can be aligned on the aperture of the photomultiplier

5. Photomultiplier Detector

The intensity of the diffraction pattern is measured quantitatively with a photomultiplier tube (RCA Type 6217, which has a response characteristic of Type S-10). An interference filter with a 30-angstrom bandwidth is placed in front of the photomultiplier tube and a 0.250-inch diameter aperture is located ahead of this filter. A removable pinhole aperture (185-μin. diameter) can be fitted into the larger aperture. The pinhole aperture at the magnification of our optical system corresponds to 0.116 of the Airy disc in a 1.5-inch diameter retro-reflector.

The photomultiplier tube is powered by a John Fluke Manufacturing Co. Model 412A high-voltage dc power supply. Output from the photomultiplier is amplified in a Brower Laboratory Model 261 preamplifier. Final amplification is with a Brower Laboratory Model 131 lock-in voltmeter. Output from the amplifier was displayed with a Hickok Model DP-100 dc digital voltmeter. Additionally, the signal waveform was monitored on a Hewlett-Packard Model 122A oscilloscope. The laser beam is chopped with a Brower Laboratory Model 312 light beam chopper. This chopper has a 50-50 duty cycle at 39 Hz. Signals of that frequency only are amplified selectively and phase-sensitively demodulated by this system to discriminate against other sources of spurious signals such as room light and the xenon lamp.

6. Camera and Photograph

Photographs of the diffraction patterns were obtained with a removable camera equipped with a Polaroid-type 545 film holder. This camera, which is equipped with a shutter and has no lens, was placed in the light beam immediately upstream of the photomultiplier tube and aligned visually before each photograph. Polaroid-type 55 positive-negative film was used

for all photographs, and the exposure time was 1/15 of a second when the chopper was in operation and 1/30 of a second when no chopper was used. The positive film record of the diffraction pattern was entered in the laboratory notebook as a permanent record. Each of the negative films was identified and is available for photographic enlargements.

7. External Calibration Fixtures

In the course of the test procedure, three external calibration fixtures were used. A solar cell was used for measuring the laser output and for adjusting the laser for optimum output. Output from the solar cell was measured with a Hewlett-Packard Model 412A dc vacuum tube milliammeter.

A 1.5-inch diameter 1/20 wavelength optically flat mirror was used in each series of measurements for system calibration and check. This flat was placed between the field lens of the collimator and the BK-7 window. Schlieren effects were minimized by enclosing the flat within an isolation box which was built around the area between the collimator and the BK-7 window.

A reference retro-reflector was used for aligning the laser with respect to the 6-micron diameter pinhole and for determining where the central irradiance pattern should be located on the test retro-reflector in the chamber when that test retro-reflector was thermally perturbed and no central irradiance pattern was visible.

VI. SOLAR OPTICAL TESTS

A. OVERVIEW OF THE TEST PROGRAM

Upon completion of the alignment procedure for the collimator, output optics, and intensity measuring equipment, the test model was placed in the test chamber, and the chamber was secured and evacuated. A flight-quality retro-reflector (PE 148B) with an RMS wave front deviation of $\lambda/24.6$ was used in the test model. It was made by Perkin-Elmer, but had been reworked by them for this program to achieve a $\lambda/33$ front-face surface finish.

The test program began with measurement of the return diffraction pattern of the test retro-reflector taken at room temperature. Next, the chamber was cooled and the solar simulator was turned on. Equilibrium temperatures were achieved at sun angles of -10, -30, -60 and -16 degrees. Upon completion of these tests, the solar simulator was turned off and lunar night conditions were simulated.

The basic test program, which included measurements taken at solar angles of -10, -30, and -60 degrees and lunar night conditions, was initially accomplished in June and early July of 1970. In this initial series of tests the test facility, including solar simulator and retro-reflector mounting equipment, operated successfully. However, due to certain problems in the set-up and operation of the optical instrumentation, the experimental measurements of relative central irradiance obtained in the June test program had an uncertainty of about $\pm 40\%$ which, of course, precluded any meaningful comparison with analytical results. After a number of diagnostic checks and various modifications and improvements to the optical instrumentation, the test program was rerun in September and October 1970. The retest program consisted of two series of tests. After the first series of tests was completed (sun angles of -10, -16, -30, and -60 degrees, and lunar night), the data accumulated to this point were briefly reviewed with R. F. Chang from the University of Maryland, with the result that a second test series was planned. A laser

beam polarizer was obtained and polarization measurements were initiated to determine the effect of laser beam polarization on the relative central irradiance of the test retro-reflector. The remainder of the second test series included polarization measurements as well as the usual optical tests at sun angles of -10, -30, and -60 degrees. The chamber was then allowed to warm slowly to room temperature while maintaining vacuum. Room temperature measurements were again made (with polarization also). This completed testing with the test retro-reflector. Additional diagnostic tests were made with the reference flat and with the reference retro-reflector to determine the effect of laser beam polarization. Test results are included in Section C below.

B. TEST PROCEDURES

1. Optical Tests

As the test program proceeded, we rapidly converged on the following measurement sequence:

- Place the solar cell at the laser output and adjust the $\Delta\lambda$ control on the laser for optimum laser output;
- Place the reference retro-reflector (sometimes called the reference cube) in the isolation box at the collimator objective lens;
- Adjust the position of the laser with respect to the 6-micron pin hole of the collimator; this was done by measuring with the photomultiplier tube the total energy (TRC) in the reference retro-reflector and setting it at a peak value.
- Remove the reference retro-reflector from the isolation box and measure the total energy (TTC) in the return pattern from the test retro-reflector;
- Place the reference flat in the isolation box, align the diffraction pattern with the photomultiplier tube, and measure the total energy (TF) in the return pattern from the test flat;

- Place the pin hole aperture in the photomultiplier, align the diffraction pattern on this pin hole with movable mirror, and measure the central irradiance (CF) of the test flat;
- Replace the flat with the reference retro-reflector and measure the TRC again.
- Measure the central irradiance (CRC) of the reference retro-reflector by peaking the location of the diffraction pattern with the movable mirror;
- Remove the reference retro-reflector and measure the central irradiance (CTC) of the test retro-reflector in the chamber;
- Place the polarizer between the laser and the collimator and measure the CTC for both maximum and minimum polarization angles.
- Obtain photograph of the diffraction pattern for maximum and minimum polarization angle and for no polarizer.

During these test procedures, measurements were alternately made with the solar cell to determine the laser output. The above procedure was generally followed for each test sequence (with the exception of the polarization measurements made in earlier tests). At least three complete sets of measurements were made at each equilibrium temperature condition. In most instances, many determinations of the central irradiance of the test retro-reflector (CTC) were made in each test set.

2. Procedure for Thermal Tests

Upon completion of the optical tests at room temperature, we initiated the first thermal perturbation by cooling the chamber shroud with liquid nitrogen and turning on the solar simulator. The test procedure requires keeping the solar intensity constant by monitoring the xenon lamp current and the solar beam. No difficulty was experienced in maintaining the lamp at a constant current.

To minimize the heat transfer between the canister which contains the test retro-reflector and the external environment, the copper guard enclosure around the canister was maintained at the same temperature as the canister by manually controlling the electrical heaters on the copper heater box. The success of this procedure was dependent upon the skill of the test operator and, although it required constant attention, it was not difficult to maintain a near-zero temperature differential between these two elements.

The retro-reflector canister assembly had a long time constant (estimated to be about 4 hours) and the time required to achieve equilibrium at various sun angles was about 12 hours. For the nighttime condition when radiative coupling is particularly weak, complete equilibrium was never achieved (i.e., the retro-reflector never reached the chamber wall temperature even after 65 hours). Likewise, when achieving final room-temperature conditions after all testing was complete, we allowed four days before making our final daytime optical measurements. With the exception of the lunar nighttime condition, we arbitrarily assumed that the equilibrium conditions were achieved when the canister temperature varied less than 0.2 degree/hr. In the case of the lunar nighttime, the temperature of the canister was dropping less than 0.5 degree/hr when equilibrium measurements were being made.

C. TEST RESULTS

1. Thermal Tests

The equilibrium temperatures of the canister and the retro-reflector retainer ring are summarized in Table 4. These data of Table 4 are the first measurements (Series 1) in the latest series of tests and for the second series of tests (Series 2)--after lunar nighttime conditions. In comparing the equilibrium temperatures of the Series 1 tests with the Series 2 tests for -10 and -60 degrees, we see that the equilibrium temperature of the canister decreased slightly. We suspect that this decrease resulted from a decrease in the solar intensity at the test model which occurred progressively during the latter phases of the second series

TABLE 4

SUMMARY OF THERMAL AND OPTICAL TESTS

Test Condition	Test Sequence	Series	No. of Measurements	Temperature		"Initial" Test Temperature (°K)	Mean Value of Central Irradiance I (CTC/TF)	Probable Error E_I	I/I_o	Probable Error E_{I/I_o}	Analysis	
				Canister (°K)	Retainer (°K)						I/I_o	Canister Temp
Room Temp.	1	1	4	≈300		295	.00656		-			
"	10	2	26	294	294		.00617		-			
"		1&2	30	-	-		.00623	4.9×10^{-5}	1.0	.011	1.0	300
θ = -10	5	1	9	384	340	376	.00401					
-10	8	2	17	373	343		.00618					
-10		1&2	26	-	-		.00543	15	0.87	.025	.92	323
-16	2	1	3	390	362	-	.00387	4.7	0.62	.009	-	329*
-30	3	1	1	392	365	401	.00183					
-30	7	2	27	391	366		.00165					
-30		1&2	28	-	-		.00165	1.0	0.26	.003	.33	406
-60	4	1	13	359	333	368	.00144					
-60	9	2	18	349	330		.00149					
-60		1&2	31	-	-		.00147	.67	0.24	.002	.46	326
Lunar Night	6	1	15	144	144	155	.00501	2.8	0.80	.008	1.0	-

* θ = -13°

of tests. This suspicion was further confirmed by the measured decrease in the solar intensity of the beam at the end of the test program (see discussion under Section IV-B-3, Results of Calibration).

In addition, Table 4 includes the canister equilibrium temperatures measured during the "initial" test program (during the period June 30 through July 11, 1970).

2. Optical Tests

The optical measurements data made with the test retro-reflector, the reference retro-reflector, and the optical flat were reduced according to the following procedures:

- All data were corrected for minute-to-minute variations in the laser output (approximately $\pm 3\%$ maximum) by dividing all measurements by the laser output (as measured by the solar cell).
- All data were corrected for possible long-period drifts in the photomultiplier and amplifier system by dividing all measurements by the measured total energy from the test flat (TF). Of particular interest to the program are values of central irradiance of the test retro-reflector corrected for possible photomultiplier drift (CTC/TF). Sufficient values of CTC/TF were obtained at each equilibrium-temperature operating condition to perform statistical analyses for each set of data. We calculated the arithmetic mean and the probable error of the arithmetic mean for the CTC/TF for each set of data.

Table 4 also includes a summary of the mean value and the probable error of the mean value for the central irradiance of the test retro-reflector for various operating conditions (CTC/TF).

Of particular interest to this program is the ratio of the central irradiance when thermally perturbed to the central irradiance in the unperturbed (room temperature) condition expressed as follows:

$$\frac{I}{I_o} = \frac{\left(\frac{CTC}{TF}\right)}{\left(\frac{CTC}{TF}\right)_{\text{room temperature}}}$$

The relative central irradiance ratio and its probable error are also summarized in Table 4.

3. Diffraction Patterns--Normal Laser Polarization

The diffraction pattern from the reference test flat is shown in Figure 9. At the conclusion of each equilibrium test condition, representative photographs were made of the diffraction pattern from the test retro-reflector. Photographs of the test retro-reflector diffraction pattern with normal laser polarization are shown in Figure 10 for room temperature, lunar night, and for solar angles of -10, -30, and -60 degrees. The central pattern of the diffraction pattern for solar angles of -30 and -60 degrees is too weak to be seen in a photograph, which indicates that there is a low central irradiance. This is indeed what was found when measurements were made of central irradiance for these two solar beam angles.

4. Polarization Measurements

Near the end of the program, a laser polarizer was obtained and polarization measurements were made at solar angles of -10, -30, and -60 degrees at room temperature. In addition, diagnostic polarization measurements were made on the reference flat. The results of these polarization measurements are summarized in Table 5. The data of Table 5 include a measurement of the central irradiance with the beam polarizer rotated for maximum signal (I_{max}) and for minimum signal (I_{min}), the corresponding beam polarization angle (θ) referenced to the vertical, the mean value (I_{mean}) between maximum and minimum central irradiance (corrected for polarization effects within the optical measurement system), the relative mean central irradiance (I/I_o), and the probable errors of measured and derived values (E).

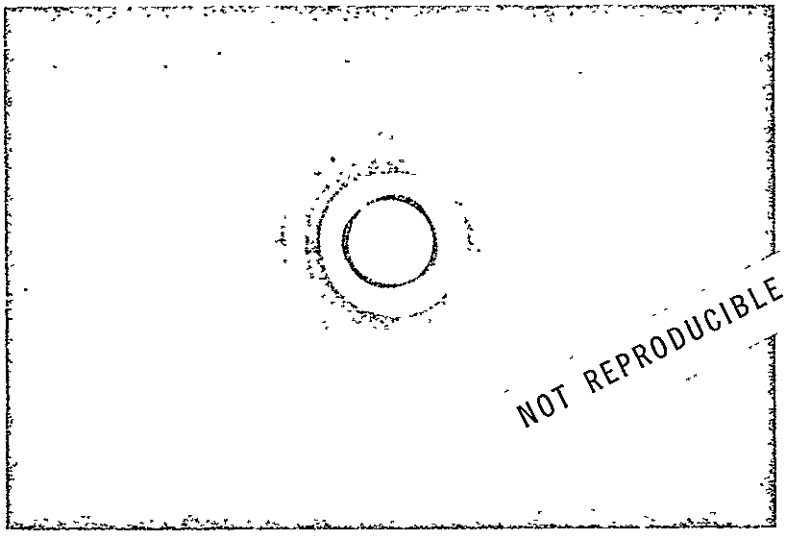

FIGURE 9 DIFFRACTION PATTERN FOR THE REFERENCE FLAT

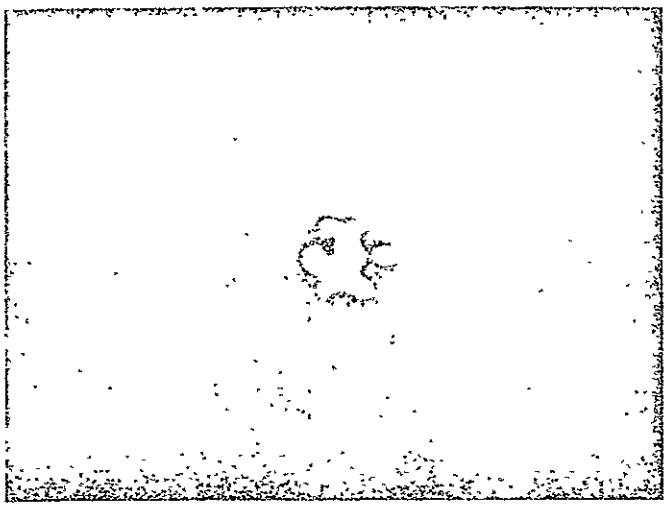

Room Temperature

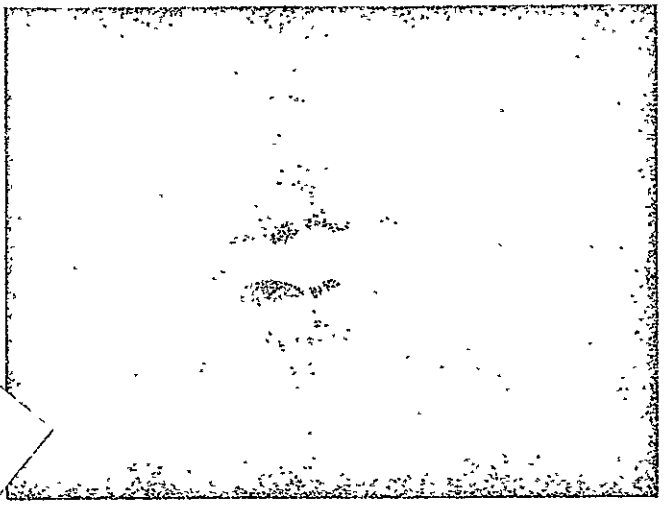

Lunar Night

θ = -10 Degrees

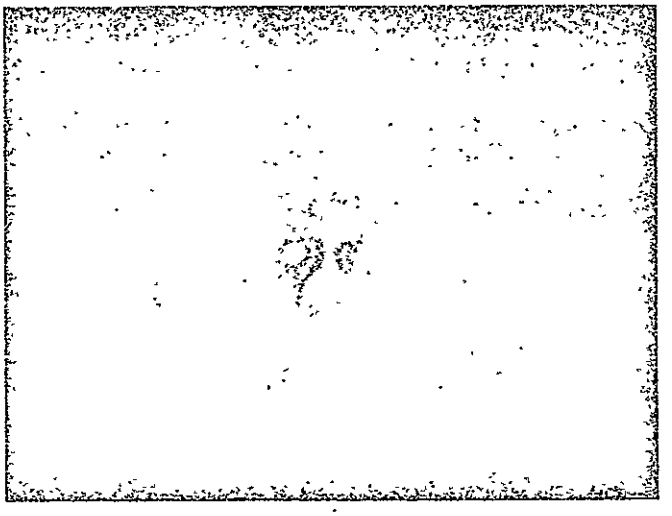

θ = -30 Degrees

θ = -60 Degrees

FIGURE 10 DIFFRACTION PATTERNS FOR NORMAL LASER POLARIZATION

TABLE 5

SUMMARY OF POLARIZATION DATA--TEST SERIES 2

Condition	No. of Measure-ments	I_{max}	Probable Error $E_{(I_{max})}$	θ_{max}	I_{min}	Probable Error $E_{(I_{min})}$	θ_{min}	I_{mean}	$\frac{(I)_{mean}}{(I_o)_{mean}}$	Probable Error $E_{(I/I_o)}$
Room Temperature	12	.0210	3.5×10^{-4}	70	.00412	1.0×10^{-4}	160	0.00715	1.0	.05
θ = -10	6	.0177	1.7	46	.00487	1.9	136	0.00673	.94	.05
- 30	2	.0173	0.3	40	.00116	0.07	130	0.00478	.67	.04
- 60	6	.0267	3.2	55	.00133	0.28	145	0.00714	.99	.06
Reference Flat	6	.0891	30.	58	.0433	16	148	-	-	-

For Retro-Reflector $I_{max, min} = \dfrac{(CTC)_{\text{polarized at } \theta}}{(TF)_{\text{normal polarization}}}$

For Reference Flat $I_{max, min} = \dfrac{(CF)_{\text{polarized at } \theta}}{(TF)_{\text{normal polarization}}}$

$$I_{mean} = \frac{1}{2}\left[\frac{(I_{max})_{\text{Retro-Reflector}}}{\left(\frac{I_{max}}{I_{min}}\right)_{\text{Flat Polarized}}} + (I_{min})_{\text{Retro-Reflector}}\right]$$

The diffraction patterns for both maximum and minimum angles were photographed with and without a polarizer. Representative photographs of the test retro-reflector for room temperature are shown in Figure 11. With no polarizer, the central irradiance in the pattern is weak. For maximum polarization angles the central irradiance in the photograph is much more intense, and for the minimum polarization angle the pattern is less intense than with no polarization.

Representative photographs for the test retro-reflector when thermall perturbed (sun angle -30 degrees) are shown in Figure 12. When the polarization of the laser beam was adjusted for maximum central irradiance, the central pattern became intense as the photograph shows. When the polarization of the laser beam was adjusted for minimum central irradiance, the central pattern became too weak to be seen in the photograph.

At the conclusion of the thermal/optical testing, we performed diagnostic measurements on the optical flat. Values of central irradiance with the polarizer rotated for maximum and minimum polarization were measured for the reference flat. These values are summarized in Table 5. The ratio of central irradiance for maximum and minimum polarization for the flat is 2.06. We believe that this polarization effect is not generated at the reference flat, but is generated by deflecting the diffraction pattern from the collimator beam-splitter and the two external mirrors in the optical train.

5. Significance of Polarization Measurements

A large sinusoidal dependence of the polarization angle had been anticipated, particularly when a retro-reflector was thermally perturbed.[7] As indicated by the analysis, the sinusoidal dependence on the polarization angle is mainly first order in the thermal perturbation. The central irradiance maximizes at different polarization angles for different retro-reflectors. Thus, for an array with a large number of retro-reflectors, the overall optical return is properly represented by the average of the maximum and minimum returns corresponding to the maximum and minimum polarization values.

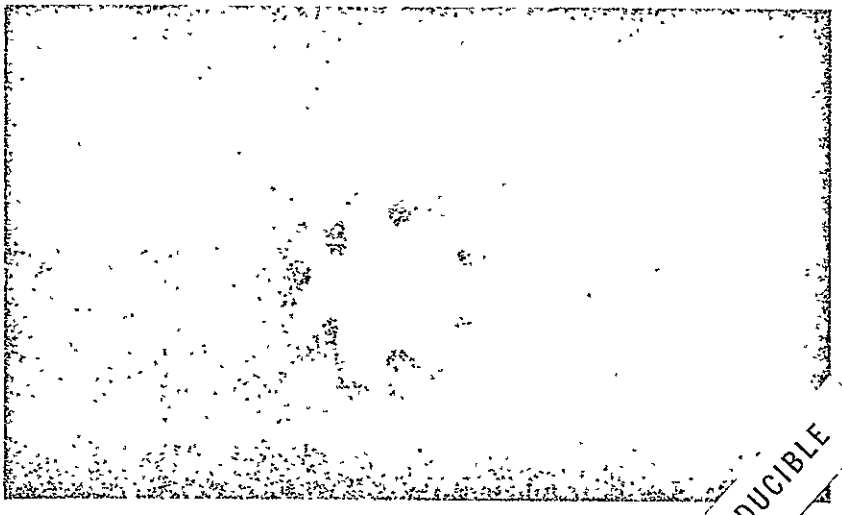

Maximum Polarization Angle

NOT REPRODUCIBLE

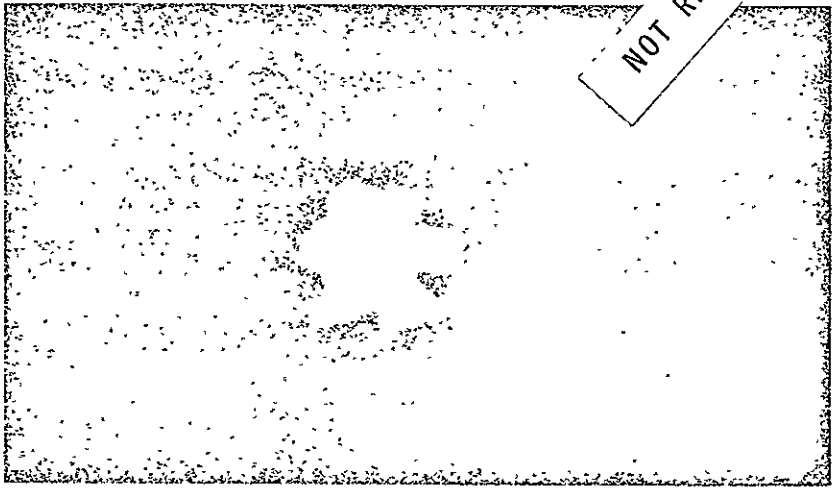

Minimum Polarization Angle

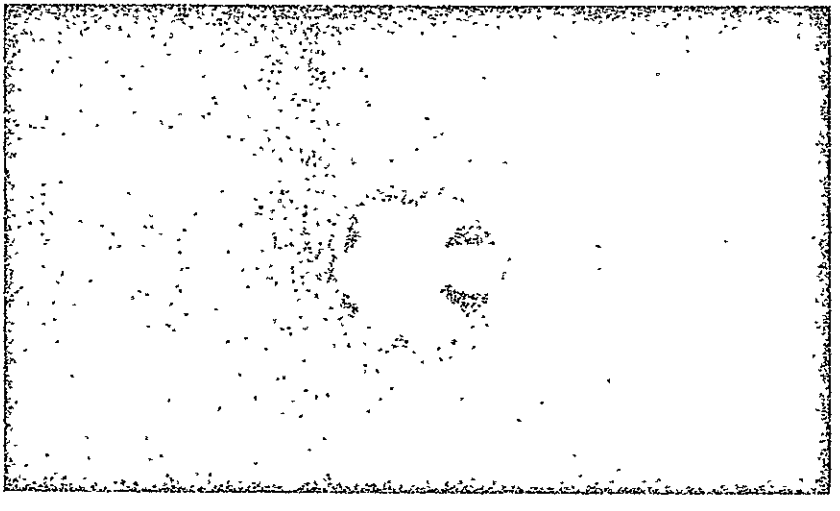

Normal Laser Polarization

FIGURE 11 DIFFRACTION PATTERNS FOR THE RETRO-REFLECTOR AT ROOM TEMPERATURE CONDITIONS

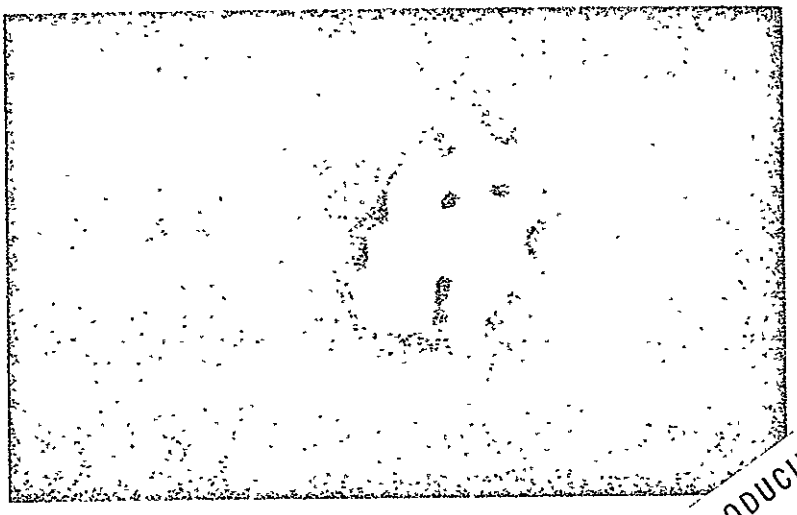

Maximum Polarization Angle

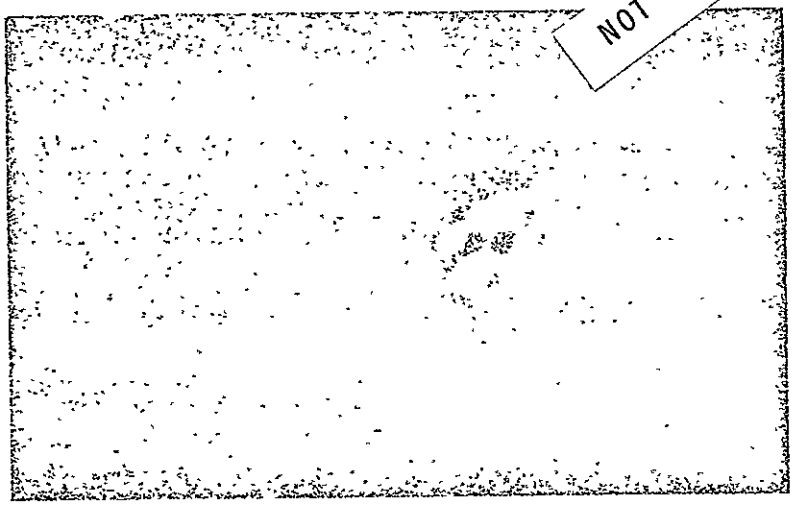

Minimum Polarization Angle

Normal Laser Polarization

FIGURE 12 DIFFRACTION PATTERNS FOR THE RETRO-REFLECTOR WHEN THERMALLY PERTURBED ($\theta = -30^{o}$)

D. COMPARISON WITH ANALYTICAL DATA

The thermal/optical analysis performed for the test configuration is similar to that used for the thermal design of the Apollo 11 and Apollo 14 flight arrays. Simulated solar heat inputs to the structure, retainer ring, and various zones of the retro-reflector were determined from the incident flux, the shadow pattern cast by the aperture of the retainer ring on the retro-reflector front surface, and the reflecting properties of the various surfaces. Solar energy directly incident on the retro-reflector face was considered to undergo total internal reflection if the angle of the incidence were less than 16 degrees. At larger angles, the energy was considered partially transmitted through the back surface where it could be partially absorbed by the aluminum cavity. Distribution of absorbed energy from diffusely reflected energy was determined using a radiation network.

Prior to installing the test assembly, the intensity of simulated solar energy incident over the area occupied by the front surface of the test assembly was measured using a thermopile. From these measurements the average solar intensity values used in the analysis were 0.140 W/cm^2 over the area of the retainer ring aperture and 0.115 W/cm^2 over the remaining surface area of the aluminum structure.

Surface absorptance values for the simulated solar flux were determined experimentally in the June test series and are summarized in Table 3. Mount conductance and retainer ring-structure conductance values used were those established experimentally during the development program for the Apollo 11 retro-reflector array. The present retainer ring configuration has a 6-degree taper which is different from that used in Apollo 11 array. Thus, the conductance values used in the present analysis might be expected to be slightly different. Additionally, the fused silica retro-reflector rests on its side in the present test arrangement whereas the retro-reflector rested with its weight equally distributed over the three tabs in the Apollo 11 experimental studies on the conductance of the mounts.

Predictions were made of the local temperature distributions within the retro-reflector for each of the test conditions covered in the present series of experiments. These temperature distributions were used as input to an optical ray-trace program to predict the phase distribution of the laser energy leaving the retro-reflector. The computed phase distributions were then used to predict the resultant far-field diffraction pattern, including the central irradiance of the reflected energy. The method of optical analysis is discussed in more detail in References 8 and 9.

Table 6 presents a comparison between predicted and measured temperatures for the canister and retainer ring for test Series 1 and 2. Table 6 also presents predicted values of retro-reflector temperature. For the -10 and -60 degree sun angle condition the measured temperatures of canister and ring are appreciably higher than the predicted values whereas at -30 degrees, the agreement is quite good. Following the June solar optical experiments,[10] in which canister, but not retaining ring, temperature was measured, it was postulated that the high values of canister temperature measured could be partially accounted for by a low conductance between the canister and the retainer-ring. This low conductance would be manifested by a large temperature difference between the ring and the aluminum structure. Measurements of retainer-ring temperature in the two tests (Series 1 and 2) conducted in September, revealed that temperature differences between ring and canister were, in fact, higher than predicted at -10 and -60 degrees. However, at -30 degrees the measured temperature differences are less than predicted. Therefore, the data do not consistently indicate a low mount conductance.

The exact value of the ring-cavity conductance cannot be determined from the present test data. However, it is interesting to note that the conductance value showed evidence of increasing with time during the tests. From Table 6, the temperature difference between the cavity and ring was consistently smaller in the second series (tests 7 to 9) than in the first series (tests 3 to 5).

TABLE 6

COMPARISON BETWEEN ANALYTICALLY PREDICTED AND EXPERIMENTALLY MEASURED TEMPERATURES (°K)

		ANALYSIS				EXPERIMENT		
Sun Angle	Test #	Canister	Ring	(Canister Ring)	Retro-Reflector	Canister	Ring	(Canist Ring)
Test Series 1								
-10	5	323	297	26	297	384	340	44
-30	3	406	354	52	348	392	365	27
-60	4	326	313	13	300	359	333	26
Test Series 2								
-10	8	323	297	26	297	373	343	30
-30	7	406	354	52	348	391	366	25
-60	9	326	313	13	300	349	330	19

The experimental data were analyzed in several ways to establish the reason for the differences between measured and predicted canister temperatures. These data analyses were aimed at determining values of conductance and total absorbed energy which, when utilized in the analysis, were consistent with the measured temperatures. In general, it was found that with reasonable conductance values the measured temperatures could be predicted for the -30 degree sun angle case, but that the results obtained for the -10 and -60 degree could be explained only on the basis of larger absorbed energy than predicted. In particular, for the -10 degree incidence angle, the large absorbed energy suggested that a significant portion (about 50%) of the incident solar energy was transmitted through the retro-reflector to be partially absorbed by the canister. Since a -10 degree incidence angle is well below the limit established for retro-reflection of incident energy, it was expected that less solar energy would be absorbed by the test assembly at this angle. To resolve the source of the large absorption of incident solar energy, further experimental studies would be required. These would include measurement of the retro-reflector temperature and measurement of internal thermal flux in the canister of the test assembly.

A comparison between predicted values of relative central irradiance and measured normally polarized values is shown in Table 4. In general, the agreement is quite good.

The trend of the measured central irradiance with incident solar angle follows that predicted by the analysis. At near normal angles of incidence where the solar energy is not expected to be transmitted to the absorbing canister and where the temperature gradients within the retro-reflector are expected to be small, the optical return is highest. On the other hand, at larger sun angles where significant portions of the incident solar energy are transmitted through the test retro-reflector and where retro-reflector thermal gradients are expected to be high, the predicted and measured relative central irradiance values are relatively low.

The difference between analytically predicted and measured relative central irradiance is less than 30% except for the -60 degree sun angle case, where the measured relative central irradiance is about half that analytically predicted. The agreement is rather surprising, since the analysis, in its present form, does not incorporate polarization effects.

Table 5 presents relative central irradiance data obtained with the polarization rotator installed. In this case the relative central irradiances are based on the arithmetic averages of the maximum and minimum intensities obtained as the polarizer is rotated. These results give consistently higher values than the normal polarization measurements and the analysis. At sun angles of -30 degrees and -60 degrees, the minimum-maximum polarization relative central irradiances are about twice those analytically predicted.

VII REFERENCES

1. Alley, C.O., Bender, P.L., et al., J. Geophys. Research, 70, 1965, p. 2267.

2. University of Maryland, Confirmation of Predicted Performance of Solid Fused Silica Optical Corner Reflectors in a Simulated Lunar Environment, NASA Grant NGR 21-002-109, Oct. 10, 1966.

3. Anon., Apollo 11 Preliminary Science Report, National Aeronautics and Space Administration, NASA SP-214, Oct. 31, 1969, p. 163.

4. Alley, C.O., Chang, R.F., et al., Science, 167, 1970, p. 368.

5. Alley, C.O., Chang, R.F., et al., Science, 167, 1970, p. 458.

6. Faller, J.E., Winer, I., et al., Science, 166, 1969, p. 99.

7. Chang, R.F., Effects of Small Angular Errors in Retroreflectors on the Far Field Diffraction Pattern, University of Maryland, Dept. of Physics and Astronomy, Technical Report No. 71-041, Oct. 1970.

8. Arthur D. Little, Inc., Cambridge, Mass., Anon., Analysis of Thermal Control Designs for Retro-Reflector Array, Final Report to University of Maryland, December 1968.

9. Arthur D. Little, Inc., Cambridge, Mass., Anon., Laser Ranging Retro-Reflector Array for the Early Apollo Scientific Experiment Package, Final Report to Bendix Corporation, June 30, 1969.

10. Arthur D. Little, Inc., Cambridge, Mass., Anon., Solar/Optical Test Program, Preliminary Test Report to University of Maryland, August 1970.

APPENDIX 10

Apollo 11 - Preliminary Science Report, October 1969

NASA SP-214

APOLLO 11

Preliminary Science Report

Scientific and Technical Information Division
OFFICE OF TECHNOLOGY UTILIZATION 1969
NATIONAL AERONAUTICS AND SPACE ADMINISTRATION
Washington, D.C

Contents

7. Laser Ranging Retroreflector

C. O. Alley, P. L. Bender, R. F. Chang, D. G. Currie, R. H. Dicke, J. E. Faller, W. M. Kaula, G. J. F. MacDonald, J. D. Mulholland, H. H. Plotkin, S. K. Poultney, D. T. Wilkinson, Irvin Winer, Walter Carrion, Tom Johnson, Paul Spadin, Lloyd Robinson, E. Joseph Wampler, Donald Wieber, E. Silverberg, C. Steggerda, J. Mullendore, J. Rayner, W. Williams, Brian Warner, Harvey Richardson, and B. Bopp

Concept of the Experiment

The compact array of high-precision optical retroreflectors (cube corners) deployed on the Moon is intended to serve as a reference point in measuring precise ranges betwen the array and points on the Earth by using the technique of short-pulse laser ranging. The atmospheric fluctuations in the index of refraction prevent a laser beam from being smaller than approximately 1 mile in diameter at the Moon. The curvature of the lunar surface results in one side of the short pulse being reflected before the other side, producing a reflected pulse measured in microseconds, even if the incident pulse is measured in nanoseconds. The retroreflector array eliminates this spreading because of the small size of the array. (The maximum spreading of a pulse because of optical libration tipping of the array will be approximately ± 0.125 nsec.) In addition, the retroreflective property causes a much larger amount of light to be directed back to the telescope from the array than is reflected from the entire surface area illuminated by the laser beam.

The basic uncertainty in measuring the approximately 2.5-sec round-trip travel time is associated with the performance of photomultipliers at the single photoelectron level. This uncertainty is estimated to be approximately 1 nsec. When the entire system is calibrated and the effects of the atmospheric delay are calculated from local temperature, pressure, and humidity measurements and subtracted from the travel time, where the uncertainty in this correction is estimated to be less than 0.5 nsec, an overall uncertainty of ± 15 cm in one-way range seems achievable.

With the ± 15-cm uncertainty, monitoring the changes in point-to-point distances from Earth to the lunar reflector (by daily observations for many years) will produce new information on the dynamics of the Earth-Moon system. The present uncertainty of three parts in 10^7 in the knowledge of the velocity of light will not affect the scientific aims of the experiment, since it is the practice to measure astronomical distances in light travel time. Primary scientific objectives include the study of gravitation and relativity (secular variation in the gravitational constant), the physics of the Earth (fluctuation in rotation rate, motion of the pole, large-scale crustal motions), and the physics of the Moon (physical librations, center-of-mass motion, size and shape). Some of these objectives are discussed in references 7–1 to 7–4. Estimates made by P. L. Bender of improvements expected in some of these categories are shown in tables 7–I to 7–III.

Properties of the Laser Ranging Retroreflector

Although the Laser Ranging Retroreflector (LRRR) is simple in concept, the detailed design of a device that would satisfy the stated scientific aims has received much attention. The primary design problem has been to avoid systematic gaps in ranging data expected to result from the extreme variation in thermal conditions on the Moon (from full Sun illumination to lunar night). A preliminary design based on discussions among various members of the investigator group and optical engineers was put

TABLE 7–I. *Lunar orbital data parameters*

Quantity	*Present accuracy (approximate)*	*1.5-m range uncertainty*		*0.15-m range uncertainty*[a]	
		Accuracy	*Time, yr*	*Accuracy*	*Time, yr*
Mean distance	500 m	250 m	1	75 m	0.5
				25 m	1
Eccentricity	1×10^{-7}	4×10^{-8}	1	1.5×10^{-8}	.5
				4×10^{-9}	1
Angular position of Moon with respect to perigee	2×10^{-6}	4×10^{-7}	1	1.5×10^{-7}	.5
Angular position of Moon with respect to Sun	5×10^{-7}	4×10^{-7}	1	1.5×10^{-7}	.5
				4×10^{-8}	1
Time necessary to check predictions of Brans-Dicke scalar-tensor gravitational theory, yr	—	25	25	8	8

[a] Three observing stations are assumed for periods longer than 0.5 yr.

TABLE 7–II. *Lunar libration and relation of Laser Ranging Retroreflector (LRRR) to center of mass*

Quantity	*Present accuracy (approximate)*	*1.5-m range uncertainty*		*0.15-m range uncertainty*[a]	
		Accuracy	*Time, yr*	*Accuracy*	*Time, yr*
Libration parameters:					
$\beta = (C\text{-}A)/B$	1×10^{-5}	3×10^{-7}	4	3×10^{-7}	0.5
				3×10^{-8}	4
$\gamma = (B\text{-}A)/C$	5×10^{-5}	2×10^{-6}	1.5	1.5×10^{-6}	.5
Coordinates of LRRR with respect to center of mass:				2×10^{-7}	1.5
X_1	500 m	250 m	1	75 m	.5
				25 m	1
X_2	200 m	70 m	1	40 m	.5
				7 m	1
X_3	-200 m	50 m	3	50 m	.5
				5 m	3

[a] Three observing stations are assumed for periods longer than 0.5 yr.

TABLE 7–III. *Geophysical data determinable from LRRR*

Quantity	*Present accuracy (estimated)*	*1.5-m range uncertainty*	*0.15-m range uncertainty*
Rotation period of Earth, sec	5×10^{-3}	10×10^{-3}	1×10^{-3}
Distance of station from axis of rotation, m	10	3	0.3
Distance of station from equatorial plane,[a] m	20	6 to 20[b]	0.6 to 2[b]
Motion of the pole,[a] m	1 to 2	1.5	0.15
East-west continental drift rate observable in 5 yr,[a] cm/yr	30 to 60	30	3
Time for observing predicted 10-cm/yr drift of Hawaii toward Japan,[a] yr	15 to 30	15	1.5

[a] Three or more observing stations are required.
[b] Depending upon the latitude of the station.

forth by J. E. Faller in a proposal to NASA (ref. 7–5).

The first financial support provided by NASA was used to test the proposed design, which consisted of small solid-corner reflectors made of homogeneous fused silica. The test and evaluation facilities at the NASA Goddard Space Flight Center were used to simulate the lunar environment. These tests verified that a metal coating could not be used on the reflectors and showed that the

failure of total internal reflection at off-axis angles posed serious problems in mounting the reflectors to maintain small temperature gradients during larger off-axis Sun angles (ref. 7–6).

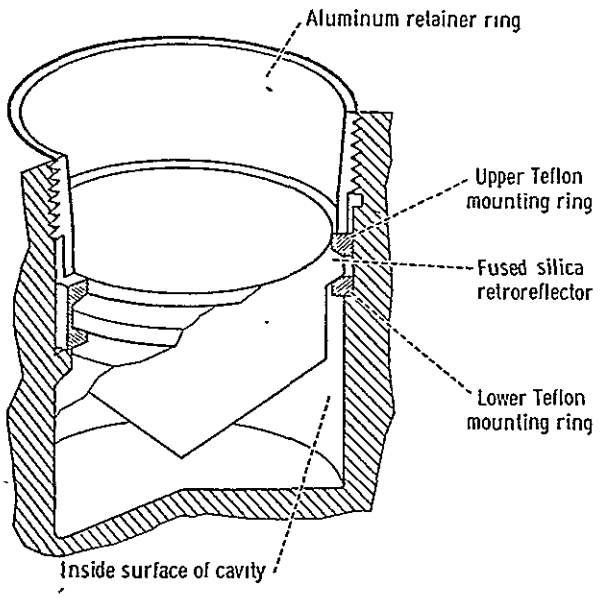

FIGURE 7-1. — Corner reflector mounting.

The tests verified the predicted performance during lunar night and during direct Sun illumination within the total internal reflection region of angles.

The efforts of thermal and mechanical design engineers in close association with members of the investigator group solved the problems and led to the design shown in figure 7–1. The corner reflectors are lightly mounted on tapered tabs between Teflon rings, and are recessed by one-half their diameter into cylindrical cavities in a solid aluminum block. The predicted optical performance, based on thermal analyses under changing lunar conditions, is shown in figure 7–2.

The need for careful pointing of the LRRR toward the center of the Earth libration pattern is shown by figure 7–3, which displays the off-axis response of the recessed corner reflectors. (The curve is the result of averaging over azimuthal orientation and polarization dependence.) The motion of the Earth in the lunar sky because of the optical librations of the Moon is shown in figure 7–4 for the period July to October 1969.

The alinement in the east-west direction

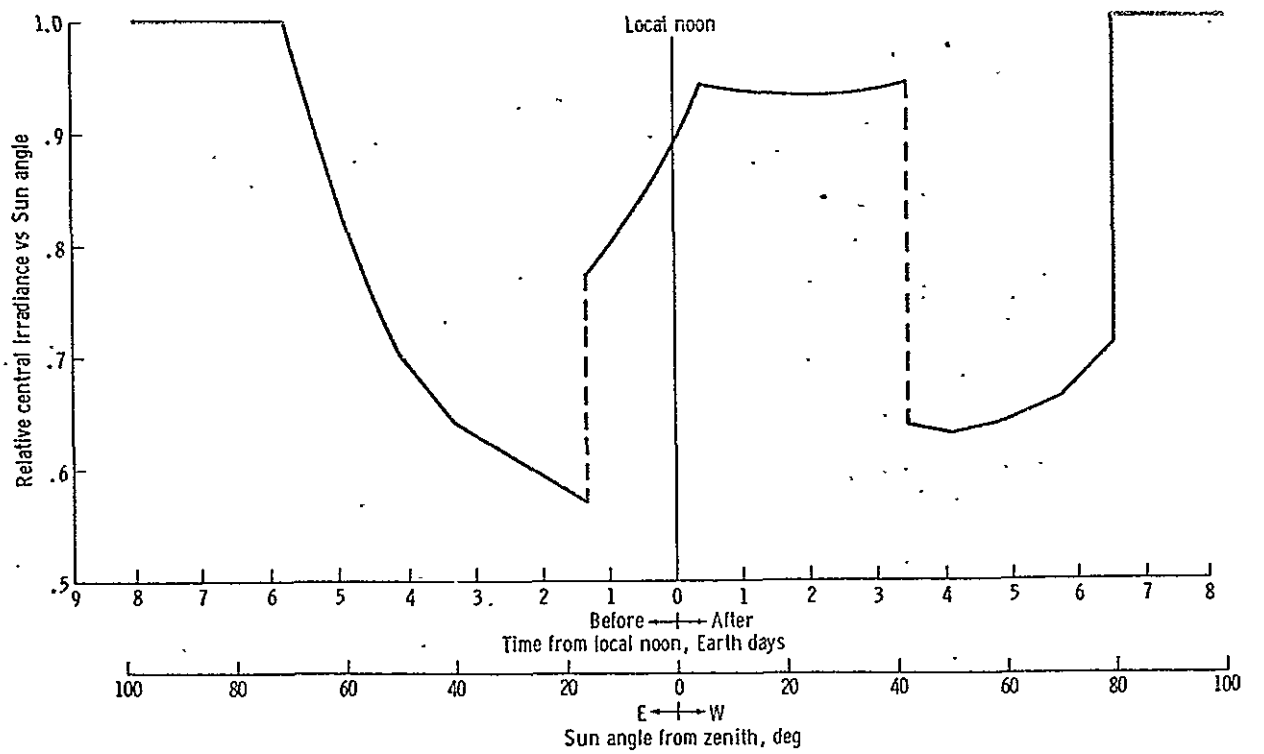

FIGURE 7-2. — Predicted optical performance as a function of Sun angle, from thermal analysis.

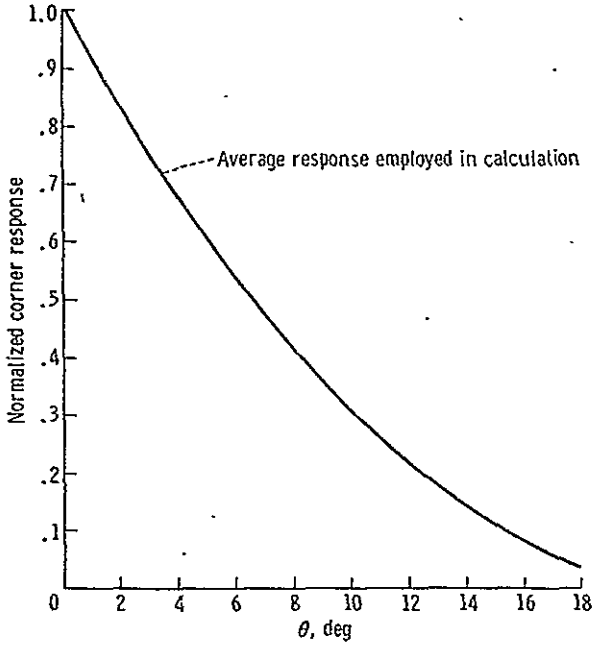

FIGURE 7-3. — Average off-axis performance of recessed circular corner reflectors.

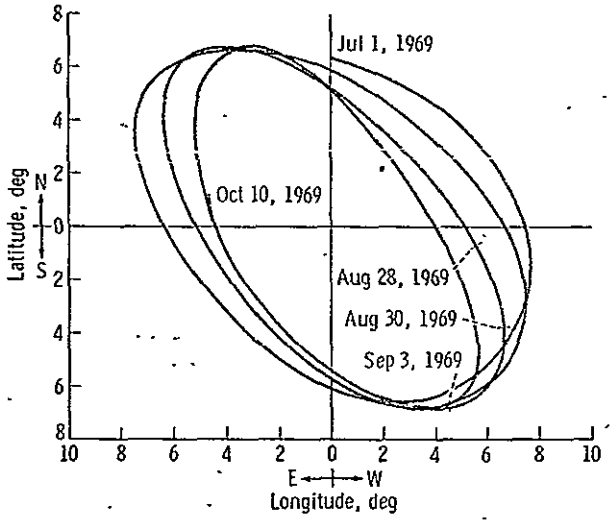

FIGURE 7-4. — Optical librations for the period July to October 1969.

achieved by Astronaut Neil A. Armstrong was within the width of a division on the compass mark. The leveling was within 0.5°, with the bubble oriented toward the southwest. When combined with the worst possible mechanical tolerances of construction, the east-west alinement is ±0.7°, and the overall pointing is within 1° of the center of the libration pattern. This excellent pointing means that the return will not fall to extremely low values during the extremes of the libration cycle. With the previous information included, the relative expected response from July 20 to September 9, 1969, is shown in figure 7–5. Figure 7–5 is an upper bound for the performance expected.

The flight hardware is shown in figure 7–6. The gnomon, the alinement marks, and the bubble level are clearly shown. In figure 7–7, the LRRR is shown deployed on the Moon.

In tests, each corner reflector which was selected for the flight array exhibited an on-axis diffraction performance greater than 90 percent of that possible for a corner reflector having no geometrical or homogeneity defects. The on-axis, nondistorted performance is conveniently characterized by a differential scattering cross section.

$$\left.\frac{d\sigma}{d\Omega}\right|_{180^\circ} = 5\times10^{11} \text{ cm}^2/\text{steradian}$$

which yields the number by which the photon flux density (photons per square centimeter) incident on the reflector array must be multiplied to give the number of photons per steradian intercepted by the telescope receiver. The cross section includes the effect of velocity aberration and is evaluated for a wavelength of 6943 Å.

Observations of returns on August 1 and 3, 1969 (immediately before lunar sunset), and on

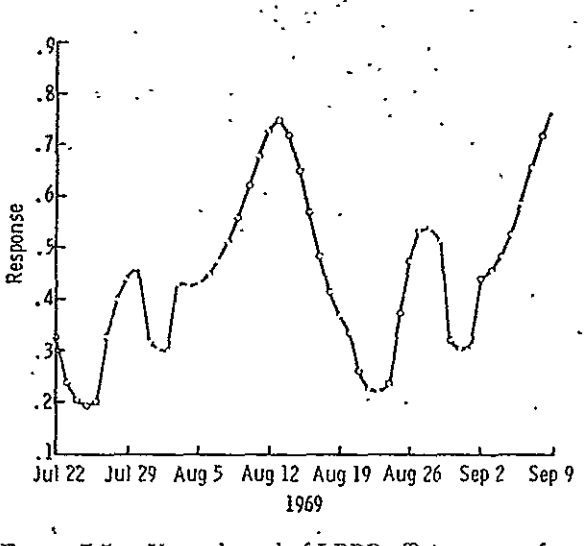

FIGURE 7-5. — Upper bound of LRRR efficiency as a function of time.

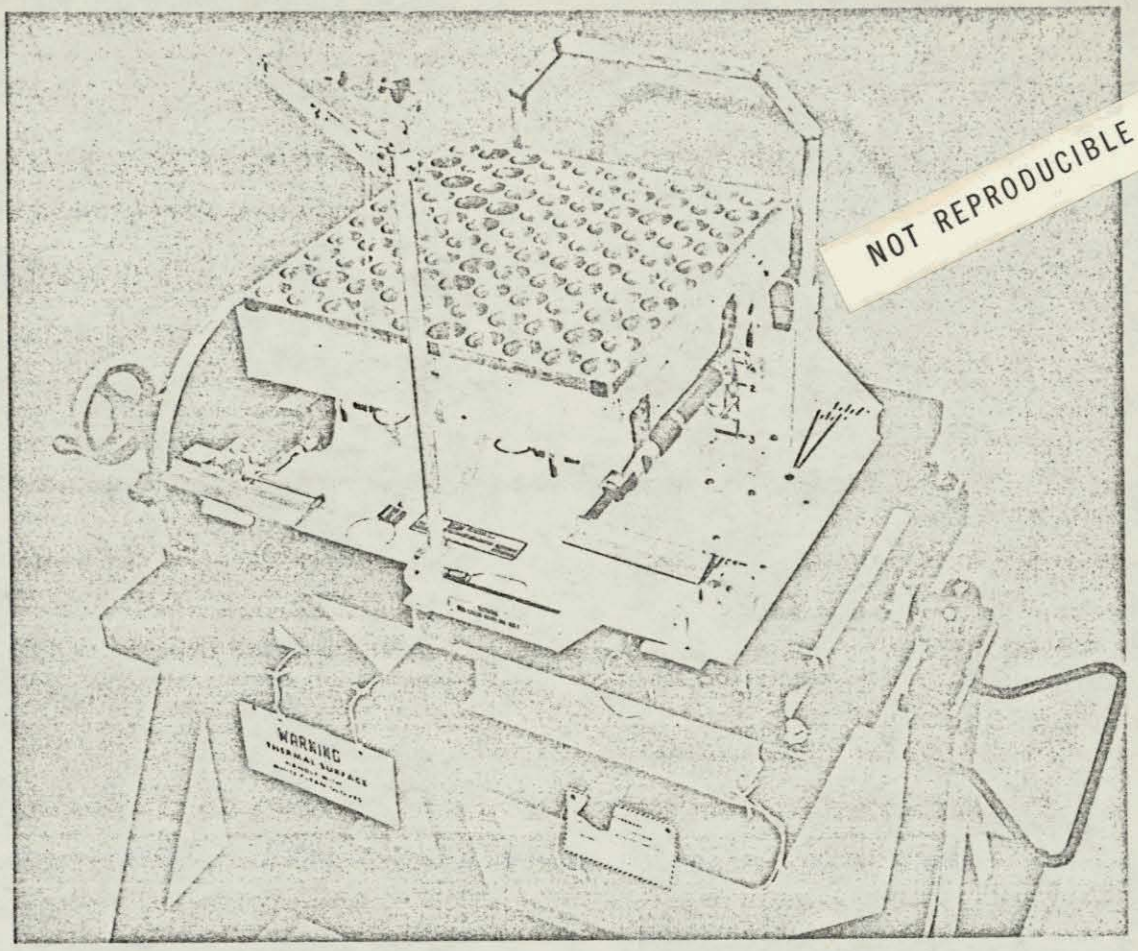

FIGURE 7-6. – The LRRR before stowage in the scientific equipment bay.

August 20, 1969 (immediately after lunar sunrise), show that the mounting (designed to minimize temperature gradients at these large Sun angles) has been successful. Observations of returns on September 3 and 4, 1969 (during lunar night), confirm the expectation that the reflector would perform at very low temperatures and that the differential thermal contractions of the mount and corners do not produce large strains. The survival of the reflectors throughout a lunar night has been demonstrated. Performance degradation, if any, caused by the presence of debris during lunar module (LM) ascent does not appear to be severe.

Ground Station Design

A single telescope can be used both as a transmitter and a receiver because the large diffraction pattern resulting from the 3.8-cm-diameter corner reflectors (the central spot has a diameter on the Earth of approximately 10 miles) allows for a velocity aberration displacement of approximately 1 mile without significant loss of signal. This was one of the major considerations in the design of the LRRR array discussed previously. The 2.5-sec light travel time between transmitting and receiving readily allows the mechanical insertion of a mirror that directs the returning photons collected by the telescope into a photomultiplier detector.

The present beam divergence of short-pulse, high-energy ruby lasers requires the use of a large aperture to recollimate the beam so that the beam is narrowed to match the divergence allowed by the atmospheric fluctuations of the

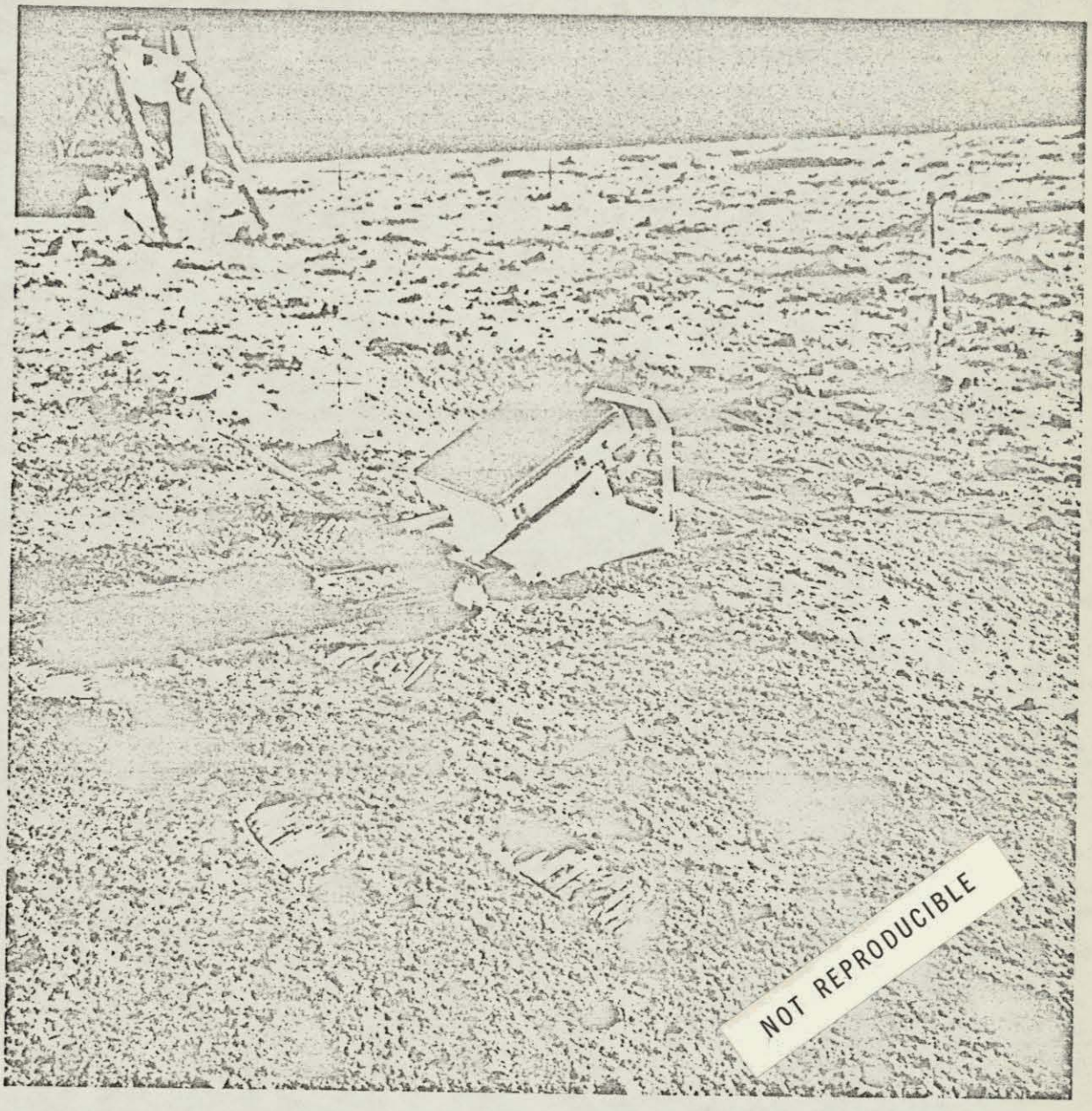

FIGURE 7-7. – The LRRR deployed on the Moon.

index of refraction – typically several seconds of arc. Astronomers refer to this effect as "seeing." The degree of atmospheric turbulence at an observatory at a given time thus determines the size of the laser beam on the lunar surface, producing a spread of approximately 2 km per sec of arc divergence.

Techniques for pointing such narrow beams to a specific location on the Moon were developed during the successful Surveyor 7 laser-beam-pointing tests (ref. 7–7). An argon-ion laser beam was brought to a focus in the telescope focal plane at the Moon-image spot that was chosen for illumination. When the laser beam filled the exit pupil of the telescope and matched the *f*-number, the collimated beam was projected to the selected location on the Moon and detected by the television camera on the Surveyor

7. For the Apollo laser ranging experiment, the beam is matched into the telescope by using a diverging lens, because it is not possible to focus high-power ruby laser beams in air without causing electrical breakdown. The direction of the projected beam is monitored by intercepting a small portion of the beam with corner reflectors mounted on the secondary mirror-support structure. These reflectors return the intercepted light in such a manner that the light is brought to focus, superimposed on the image of the Moon, at the spot to which the beam is being sent. A beam splitter coated with a highly damage-resistant, multilayer dielectric coating reflects the laser beam into the telescope and transmits the image of the Moon and the laser light intercepted by the telescope corner reflectors into the guiding system (ref. 7–8).

A view of the region of the Moon around Tranquility Base is shown in figure 7–8, which was taken through the guiding eyepiece of the McDonald Observatory 107-in. telescope. The reticle marks used to guide from craters are clearly shown, along with the intercepted laser light. In final alinement, the small circle is made to coincide with both Tranquility Base and the center of the laser spot. The large size of the laser spot is caused by imperfections in the telescope corner reflectors, not by beam divergence. The diameter of the reticle circle is approximately 3.6 seconds of arc. Many craters are not resolved because of poor seeing conditions at the time the photograph was made.

FIGURE 7-8. – View through guiding eyepiece of the McDonald Observatory 107-in. telescope during process of alinement.

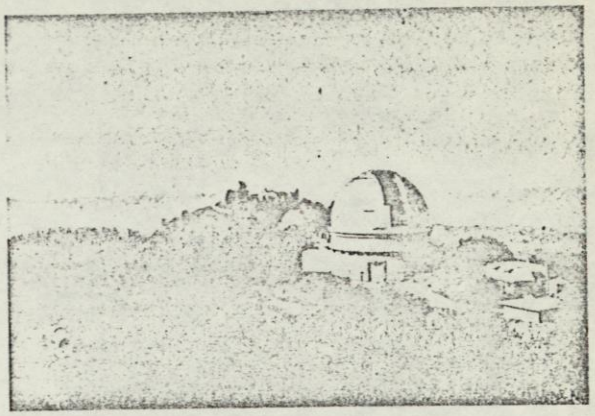

FIGURE 7-9. – Lick Observatory, University of California, at Mount Hamilton, California.

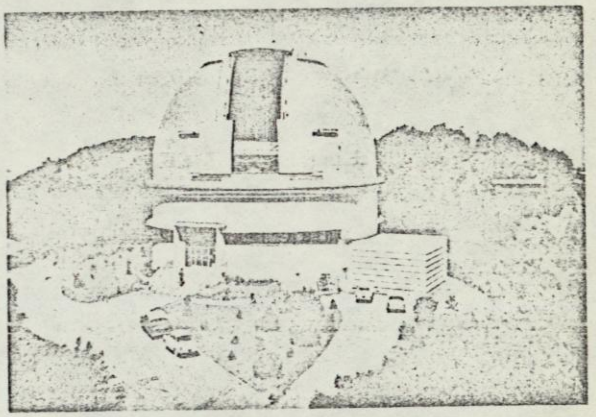

FIGURE 7-10. – Lick Observatory 120-in. telescope dome.

Figures 7–9 to 7–14 are views of the Lick Observatory, University of California, at Mount Hamilton, California; the Lick Observatory 120-in. telescope, the second largest in the world; the McDonald Observatory, University of Texas, at Mount Locke, Tex.; and the McDonald Observatory 107-in. telescope, the third largest in the world. Lasers were mounted in a stationary position at a coudé focus of each instrument.

The Lick Observatory participated in the acquisition phase of the experiment to increase

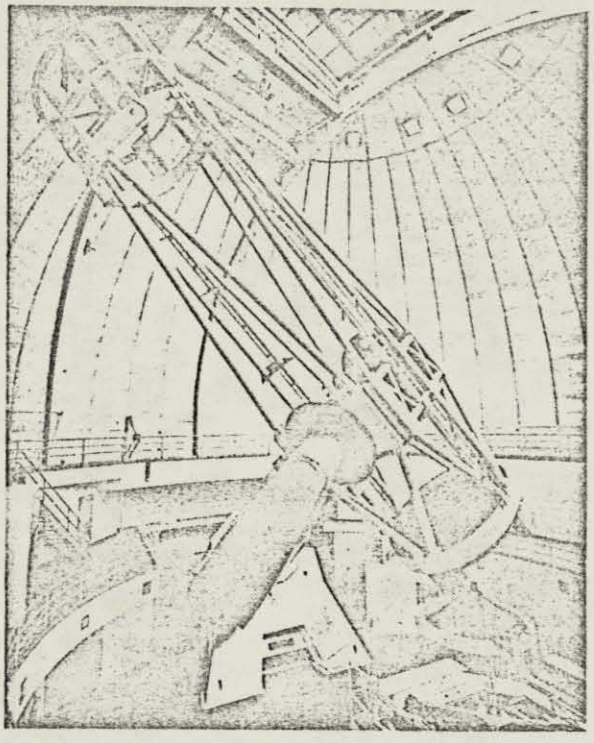

FIGURE 7-11. — Lick Observatory 120-in. telescope.

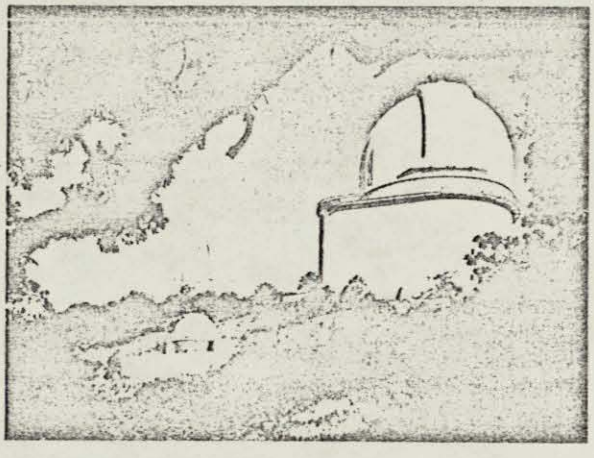

FIGURE 7-12. — McDonald Observatory, University of Texas, at Mount Locke, Tex.

the probability of getting early returns because the weather and seeing there are generally excellent in the summer. Returns at the Lick Observatory, which is no longer in operation, were observed on August 1 and 3, 1969. The McDonald Observatory is equipped to make daily range measurements, weather permitting, for years. Returns were observed on August 20, September 3, September 4, and September 22, 1969, at the McDonald Observatory.

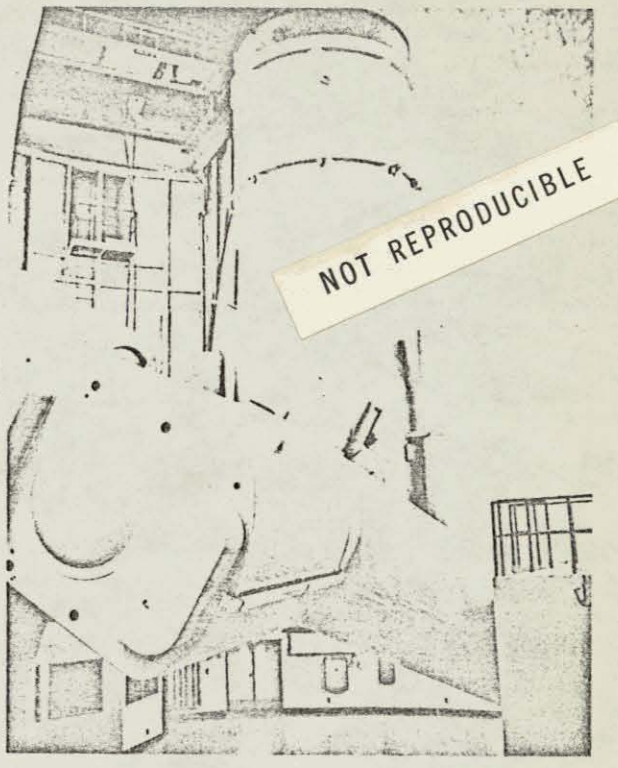

FIGURE 7-13. — McDonald Observatory 107-in. telescope.

Observations at the Lick Observatory

System A

The ranging system at the Lick Observatory consisted of a giant-pulse, high-powered ruby laser (operated at the coudé focus) which was optically coupled through the 120-in. telescope and could be fired at 30-sec intervals. The angular diameter of the outgoing beam was approximately 2 seconds of arc and made a spot of light on the Moon approximately 2 miles in diameter. The return signal was detected by a photomultiplier that was mounted at the coudé focus behind a 10-second-of-arc field stop and a narrow (0.7 Å) filter, which were used to reduce the background illumination from the sunlit Moon. A time-delay generator (TDG), initiated by the firing of the laser, was used to activate the acquiring electronics approximately 2.5 sec (the Earth-Moon round-trip time for light) later. The

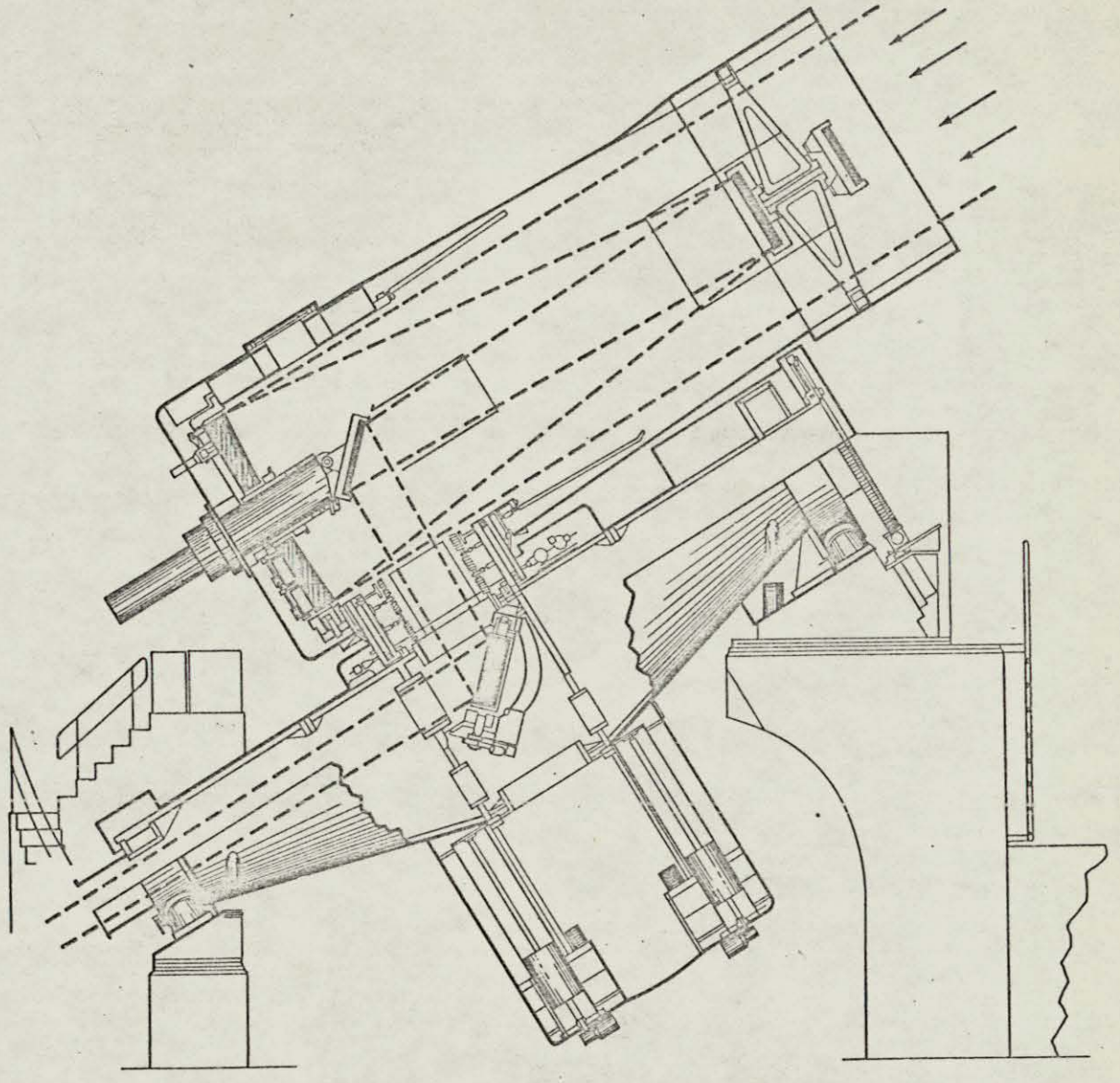

FIGURE 7-14. – Optical path in the McDonald Observatory 107-in. telescope.

delay generator was set for each shot by using the LE 16 ephemeris. (See the section of this report entitled "The Lunar Ephemeris: Predictions and Preliminary Results.")

Following the pulse produced by the TDG, the output pulses from the photomultiplier were channeled sequentially into 12 binary scalers. Each scaler channel had a dwell time that was adjustable from 0.25 to 4 μsec (ref. 7–8). The routing of the pulses to the scalers was such that a pulse arriving within 0.1 μsec of the end of a channel would also add a count to the following channel. The scalers then contained a quantized summary of the detector output for a short time interval centered on the expected arrival time of the reflected signal. After each scaler cycling following a laser firing, a small online computer read the contents and reset the scalers. The computer stored the accumulated count for each of the scalers and provided a printed output and a cathode-ray-tube display of the data.

Scattered sunlight from the lunar surface produced a random background that slowly filled the 12 time channels. Because the return from

the retroreflector occurred with a predetermined delay, the channel that corresponded in time to the arrival of the signal accumulated data at a faster rate than the other 12 channels. Figure 7–15 illustrates this point by showing the way in which the data actually accumulated during run 18. Following acquisition on the night of August 1, 1969, 169 shots were fired. Range gate errors occurred on 27 shots, and 22 shots were fired with the telescope pointed away from the reflector. For the remaining 120 shots, approximately 100 above-background counts were received. These results represent a return expectation in excess of 80 percent and show that all parts of the experiment operated satisfactorily. Assuming a Poisson distribution of the recorded photoelectrons, the returns correspond to an average of 1.6 detectable photoelectrons per shot. This number is a lower limit to the true average because interference effects and guiding errors probably reduced the number of returns that were recorded. The strength of this signal and the lack of "spill" into adjacent channels clearly show that the signal did not come from the "natural" lunar surface, from which the return would be distributed over approximately 8 μsec. The timing of the trigger from the TDG relative to Mulholland's ephemeris was changed three times, and the channel widths were decreased from 2 to 1 μsec and then to 0.5 μsec. After each change, the signal appeared in the appropriate channel. The data from runs 10 to 21, the interval from the first acquisition to the close of operation, are shown in table 7–IV. Nine runs containing 162 shots were made before acquisition.

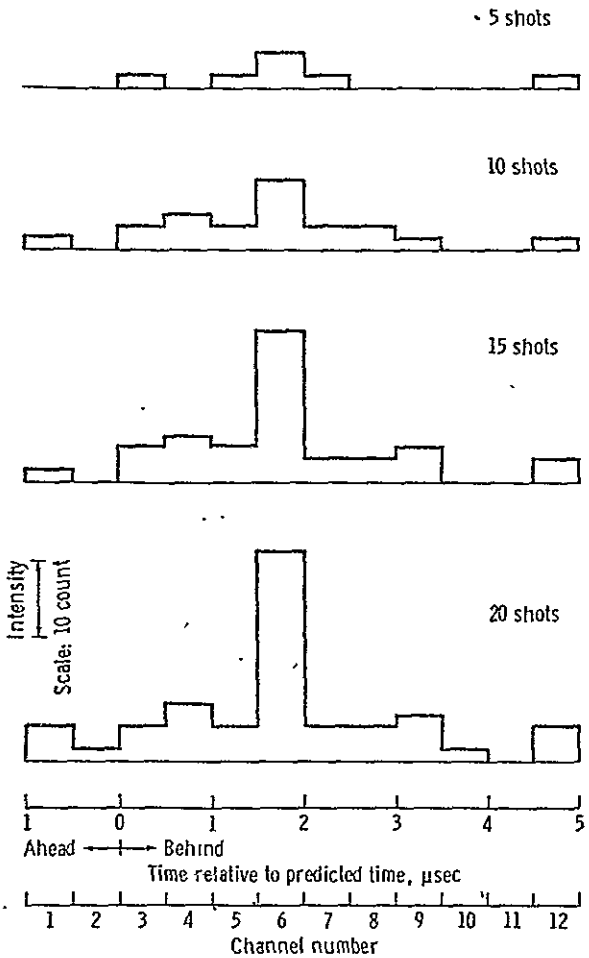

FIGURE 7-15. – Histogram showing the growth of the retroreflected signal in channel 6.

Figure 7–16 shows a plot of the data taken from table 7–IV. Runs 12 and 14 have not been plotted in figure 7–16 because errors in setting the TDG invalidated the timing. During run 19, the telescope was not pointed at the reflector, and no returns were seen. Because of a fortuitous splitting of the return between two channels on two runs, an effective timing precision of 0.1 μsec was achieved. This precision is equivalent to a range error of approximately 15 m. In figure 7–16 an apparent drift in the time the returns were detected, relative to Mulholland's predictions, is shown. The drift was caused by the 120-in. telescope being located approximately 524 m east of the locations given for the Lick Observatory in the American Ephemeris and Nautical Almanac. A curve showing this correction to the original ephemeris is given in figure 7–16. Translation of this curve along the ordinate is allowable, and the amount of time gives the difference between the observed range and the predicted range. When the correct coordinates are used, the observations agree with the predicted curve.

System B

The primary function of acquisition system B at the Lick Observatory was to locate the deployed LRRR in range and position. System B was not intended to satisfy the long-term objectives of the lunar ranging experiment; however,

TABLE 7–IV. *Log of observation data showing acquisition*

Run	Total counts												No. of shots	u.t. for middle of run, hr.min	Channel width, μsec	Time of first channel[a] μsec
	Channel															
	1	2	3	4	5	6	7	8	9	10	11	12				
10	12	8	16	18	12	14	10	17	13	[b]27	12	12	20	10:21	2.0	−20
11	12	12	12	11	11	6	13	11	14	[b]26	10	14	14	10:32	2.0	−20
12	(c)	(c)	(c)	(c)	(c)	(c)	(c)	(c)	(c)	(c)	(c)	(c)	16	—	2.0	−10
13	13	8	8	12	7	[b]18	11	5	6	7	8	12	13	11:04	2.0	−10
14	(c)	(c)	(c)	(c)	(c)	(c)	(c)	(c)	(c)	(c)	(c)	(c)	6	—	1.0	−10
[d]15	4	3	3	5	4	[b]17	6	8	10	5	6	8	18	11:23	1.0	−5
16	1	1	2	2	[b]6	3	3	1	2	1	3	2	10	11:36	.5	−1
17	6	3	4	2	[b]11	[b]9	2	7	2	4	2	5	16	11:45	.5	−1
18	3	1	3	5	3	[b]19	3	3	4	1	0	4	22	12:03	.5	−1
[e]19	3	3	3	10	4	3	5	2	5	5	8	5	22	12:19	.5	−1
[f]20	2	1	1	0	3	4	[b]6	2	4	2	2	4	10	12:23	.5	−1
21	5	2	2	3	2	1	[b]12	[b]11	3	4	5	2	22	12:45	.5	−1

[a] With respect to ephemeris predictions.
[b] Channel in which return was expected.
[c] Range-gate errors invalidated data.
[d] Data from three shots with erroneous range gates deleted from tabulation.
[e] Telescope pointed 16 km south of reflector.
[f] Thin clouds noted near Moon.

System B was designed to be a sensitive, moderately precise, semiautomatic, high-repetition rate system using existing off-the-shelf equipment wherever possible.

System B was composed of several essentially independent subsystems. These subsystems were the laser-transmitter/power-supply assembly, the receiver-detector ranging system, the range gate generator and data control and recorder system, and the time standard system.

The laser transmitter uses oscillator and amplifier heads employing a conventional rotating-prism, bleachable-absorber, "Q-switch" mechanism. The oscillator and amplifier heads are identical and use 110-mm-long, 15-mm-diameter Brewster-Brewster rubies. An existing laser system that was modified for this program was capable of operation at 10 J at 3-sec intervals with a pulse width of 60 to 80 nsec.

For operation at the Lick Observatory, modification of the laser system required the incorporation of all normal transmit-receive ranging functions and of a boresight capability onto the laser case. An optical-mechanical assembly (fig. 7–17) was designed to be attached to the laser case. The exiting laser beam passed through a beam splitter, which was oriented at Brewster's angle for minimum reflection of horizontally polarized light. The small fraction of light scattered or reflected from the beam splitter was detected by an FW 114A biplanar photodiode. The output of the photodiode was used for the range measurement initiation pulse and for monitoring the operation of the laser. The beam splitter was also used to couple a vertically polarized helium-neon laser beam along the same axis as the ruby beam. A helium-neon laser was mounted parallel to the ruby laser, and the resultant beam was expanded by a small autocollimator and then reflected by a mirror mounted parallel to the beam splitter. The reflected beam was then rereflected by the beam splitter along the laser axis. The laser produced an elliptical cross-section beam that was corrected and expanded to 50 mm in diameter by the Brewster entrance prism telescope. The 50-mm exit beam was reflected at right angles onto a 50-mm-aperture F39 lens that was positioned at the appropriate place with respect to the coudé focus of the 120-in. telescope optical system.

The returning energy follows essentially the same path as the transmitted energy. A flip mirror, actuated by a small solenoid, reflects the returning signal after the signal is passed through the correcting telescope to a field-limiting lens and aperture. The aperture in the field-limiting

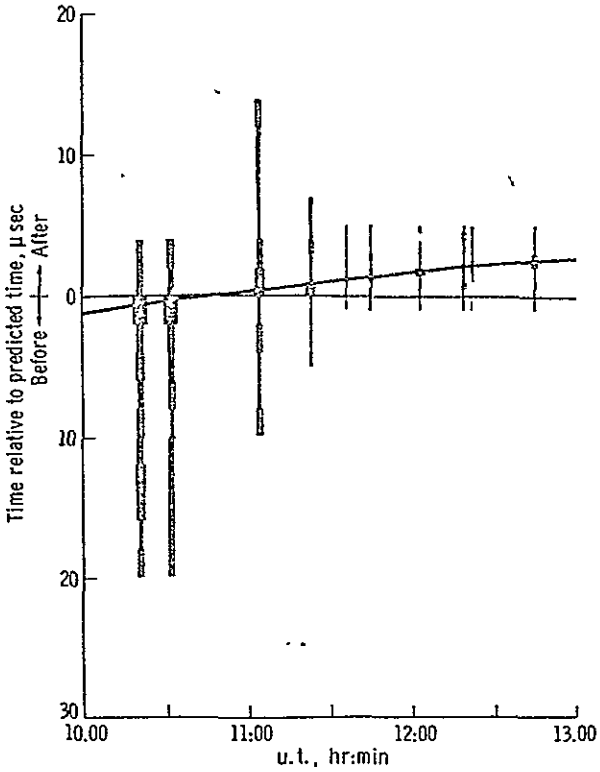

FIGURE 7-16. – Three-dimensional figure showing the time of the run (abscissa), the range window during which the equipment was open for receiving data (ordinate), and the number of counts in each channel (width of the bar). It is clear that in each run in which returns were expected they were seen in the correct channel. During run 19 (third from right-hand end), the telescope was pointed away from the reflector, and no returns were seen.

system is sized for a 10-second-of-arc field of view in space. Light passing through the aperture is collimated and passed through a 2.7-Å bandpass filter. The light is divided into two equal beams by a dividing prism; then, the beams of light enter the enhancement prism on each of the two photomultipliers.

Two detectors (operating in coincidence) and a range gate were used to eliminate as much extraneous background noise as possible. Type 56 TVP photomultipliers used enhancement prisms to allow multiple reflection of the entrance light from the photocathode. The output of each photomultiplier tube was discriminated and shaped with an EGG T105/N dual discriminator. Because theoretical considerations indicate that only a few photoelectrons occur for each transmitted pulse, the discriminator was used to stretch each detected pulse by the length of the transmitted pulse. A coincidence overlap equal to the transmitted pulse duration was necessary because, lacking discrimination, a photoelectron from each photomultiplier tube could be related to any time within the transmitted pulse duration. The outputs of the discriminators were AND'ed in the EGG C102B/N coincidence module.

The actual range measurement (fig. 7–18) was made with a 1-nsec time-interval counter. The time-interval counter was started by the photodiode output each time the laser transmitter operated. The discriminators and the stop channel of the time-interval unit were disabled by the range gate until the expected time of arrival of the reflected laser pulse. If both photomultiplier tubes detected a photoelectron within the coincidence resolving time of the EGG C102B/N, the output would stop the time-interval unit.

The photodiode signal was used in two other measurements. First, the signal was used to stop a 100-μsec-resolution time-interval unit that was started by the "ontime" timing signal from the real-time clock. This measurement determined the time, to the nearest 100 μsec, of the range measurement. The pulse was also converted, monitoring the overall performance of the laser during the operation.

System B was controlled and operated by a special digital logic assembly. This device (fig. 7–19) generated laser fire signals and the range gate window, sampled all measurement devices for information, and recorded the information. One of the most important aspects of the operation is the generation of the range gate window, based on knowledge of where the retroreflectors should be. Furthermore, because this information may not be as accurate as required, it is necessary to change the information essentially in real time. The range gate window was generated with an externally, as well as manually, programed delay pulse generator. The programed input for the delay pulse generator was obtained from a lunar prediction drive tape containing the expected round-trip time interval to the lunar surface for every 3 sec of time. A digital comparison between the command time on the tape and real time was made to maintain the tape in

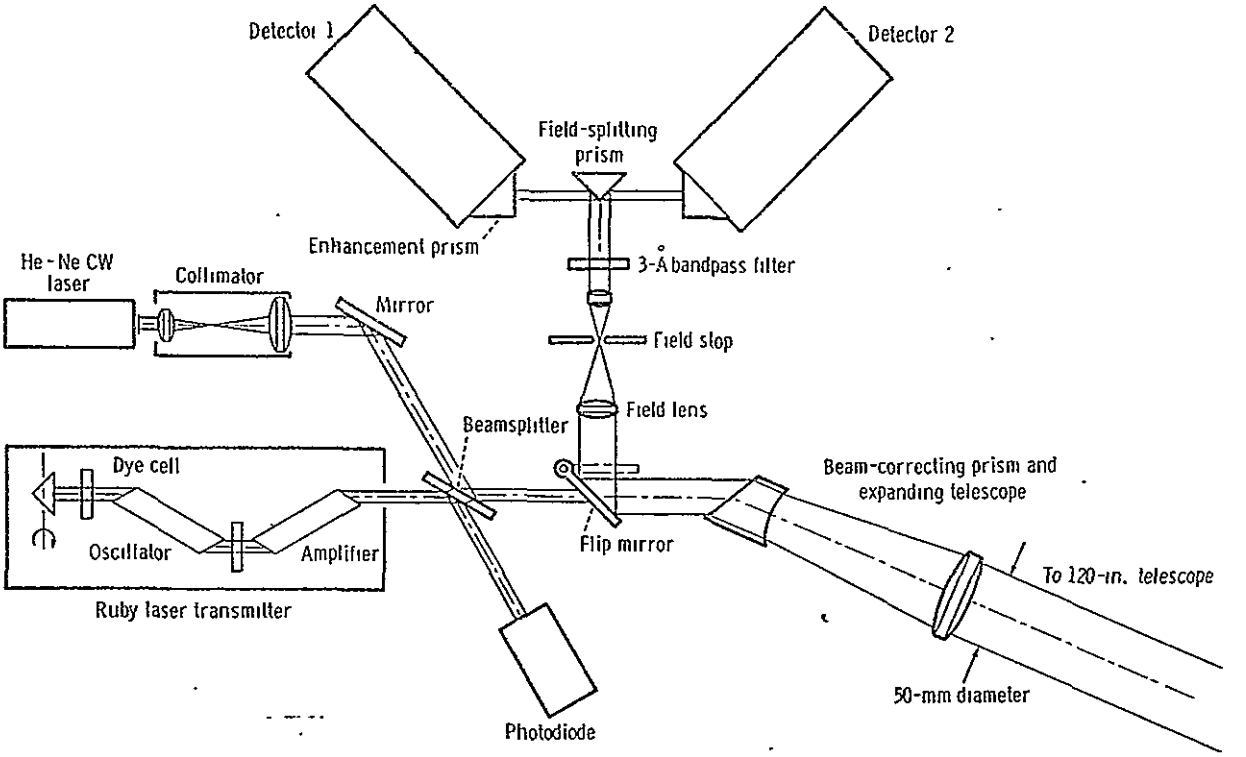

FIGURE 7-17. — Optical schematic of system B at Lick Observatory.

synchronization with real time. The range information on the tape was then stored and transferred to the delay pulse generator prior to each laser firing. The laser firing started the delay pulse generator; and after the predicted delay, a pulse initiated the range-gate-window pulse generator. The range-gate-window length was variable and was used to enable the detector discriminators and the range time-interval unit at the time a return signal was expected.

The measured data were recorded with a multiplexing data gate and standard line printer. The control section generated print commands for each series of measurements at the correct time during the 3-sec cycle period. The control section obtained timing signals from the time standard rack (fig. 7-20). Real time was maintained to an accuracy of ± 10 μsec during the operation, by comparing signals from the Loran C chain with the real-time clock using the Loran C synchronization generator.

The system was operated for a period of 1 hr and 45 min on the morning of August 3, 1969, during which the laser was fired 1230 times. The total number of apparent measured ranges during this period was 98. The low number of returns relative to the number of transmitted pulses is related to a slight (2 sec of arc) misalinement in the detector optical system and to the failure of the delay pulse generator to operate in the externally programed mode. Furthermore, because returns were not immediately recognized, an angle search was made over a longer time period.

The measured range time could have three possible sources: a return from the retroreflector, a return from the lunar surface, or random noise coincidence from reflected sunlight and background. Statistically, 35 to 50 noise coincidences and approximately 30 lunar surface ranges would be expected in 1200 firings. Because the numbers agree, within acceptable limits, with the total number measured, it is not obvious that returns from the retroreflectors were measured. However, any returns from the retroreflectors should fall within the precision of the system or within 100 nsec with respect to the true range to the package.

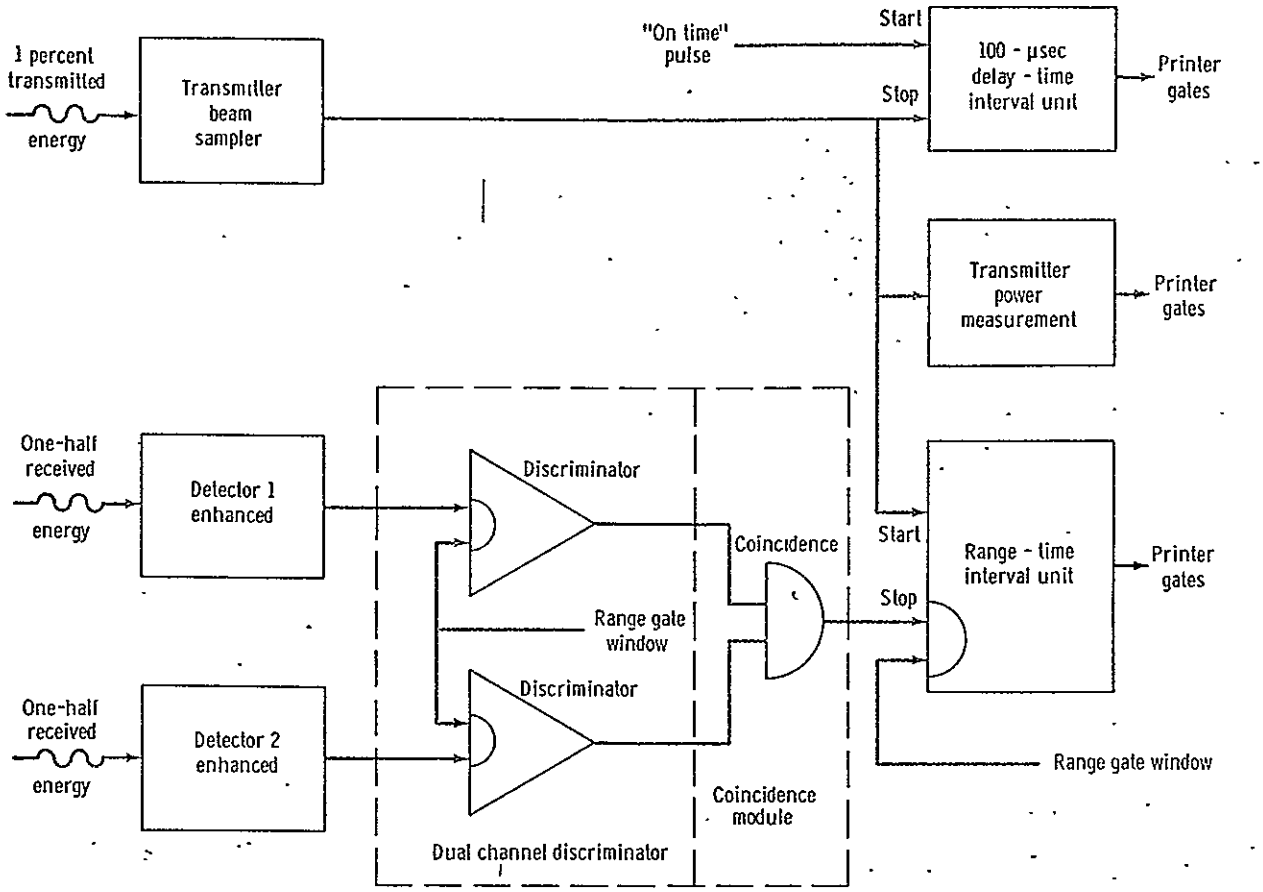

FIGURE 7-18. — Receiver and ranging section.

The observed range time measurements were compared arithmetically with the predicted range time and then linearly corrected because of a known parallax error. The parallax error occurred because a different site was used for the range predictions. The linear correction was performed by taking the initial range residuals and fitting (in a least squares sense) a first-order polynomial to the residuals. Then, only those residuals occurring within a certain range of the polynomial were used to redefine the polynomial. This technique was used successively three times to generate a polynomial about which 11 of the measured ranges had a root mean square of 45 nsec. Furthermore, because of the parallax error, the coefficients of the polynomial agree with the expected deviations from the predicted range.

The range residuals corrected to this linear equation were used to construct a histogram (fig. 7-21) with 100-nsec intervals from −5 to +5 μsec. The data lying outside of the ±5 μsec were not displayed because no interval contained more than one point and because no significant bunching was observed. The histogram clearly shows a central peak that cannot be supported by any statistical interpretation other than one assuming returns from the retroreflector.

Observations at the McDonald Observatory

The laser in use presently is a custom-built two-stage pockels-cell switched ruby system. Typical operating conditions were as follows:

(1) Energy: 7 J
(2) Pulse width: 20 nsec
(3) Beam divergence: 2.4 mrad (measured at full energy points)
(4) Repetition rate: once every 6 sec
(5) Wavelength: 6943.0 ± 0.2 Å at 70° F
(6) Amplifier rod diameter: 0.75 in.

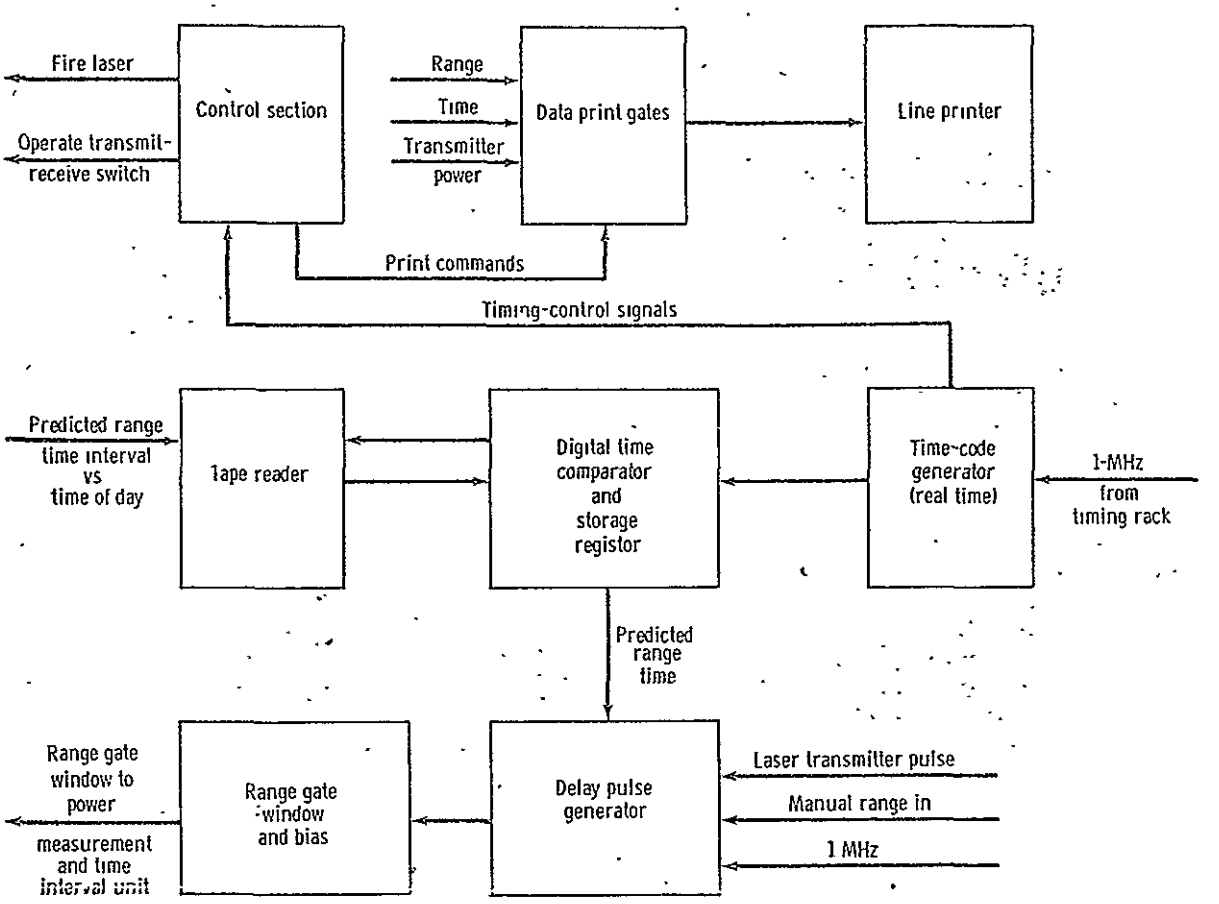

FIGURE 7-19. — Range gate generator and data control.

The detector package contained a photomultiplier that had a measured quantum efficiency of 5 percent at 6943 angstroms and a dark current of 80 000 counts per second. When cooled by dry ice (as during ranging operations), the dark current was 10 000 counts per second. Spectral filters with widths of 3 and 0.7 Å were available. Both filters were temperature controlled. Pinholes restricting the field of view of the telescope to 6″ or 9″ were commonly used. An air-driven protective shutter was closed during the time of laser firing, opening for approximately 1 sec around the time for receiving returns. The net efficiency of the whole receiver, ratio of photoelectrons produced to photons entering the telescope aperture (with a 3-Å filter), including telescope optics, was measured to be 0.5 percent, using starlight from Vega.

The block diagram of the timing electronics used during the acquisition period is shown in figure 7-22. The electronics consist of a multistop time-to-pulse-height converter (MSTPHC) for coarse range search covering an interval of 30 μsec with 0.5-μsec bins (ref. 7-8) in addition to the core circuits forming part of the intended subnanosecond timing system. The initial and final vernier circuits of this system were not in use. The range prediction provided by J. D. Mulholland was recorded on magnetic tape at 6-sec intervals. The online computer read the range prediction, set the range gate TDG, and fired the laser within 1 μsec of the integral 6-sec epoch. The TDG activated the MSTPHC, triggered a slow-sweep oscilloscope (the display being recorded on photographic film) and a fast-sweep oscilloscope (recorded on Polaroid), and activated a 10-μsec gate into the time-interval meter (TIM). The computer read the number of counts in the TIM and calculated the difference between this reading and the range prediction, printing out

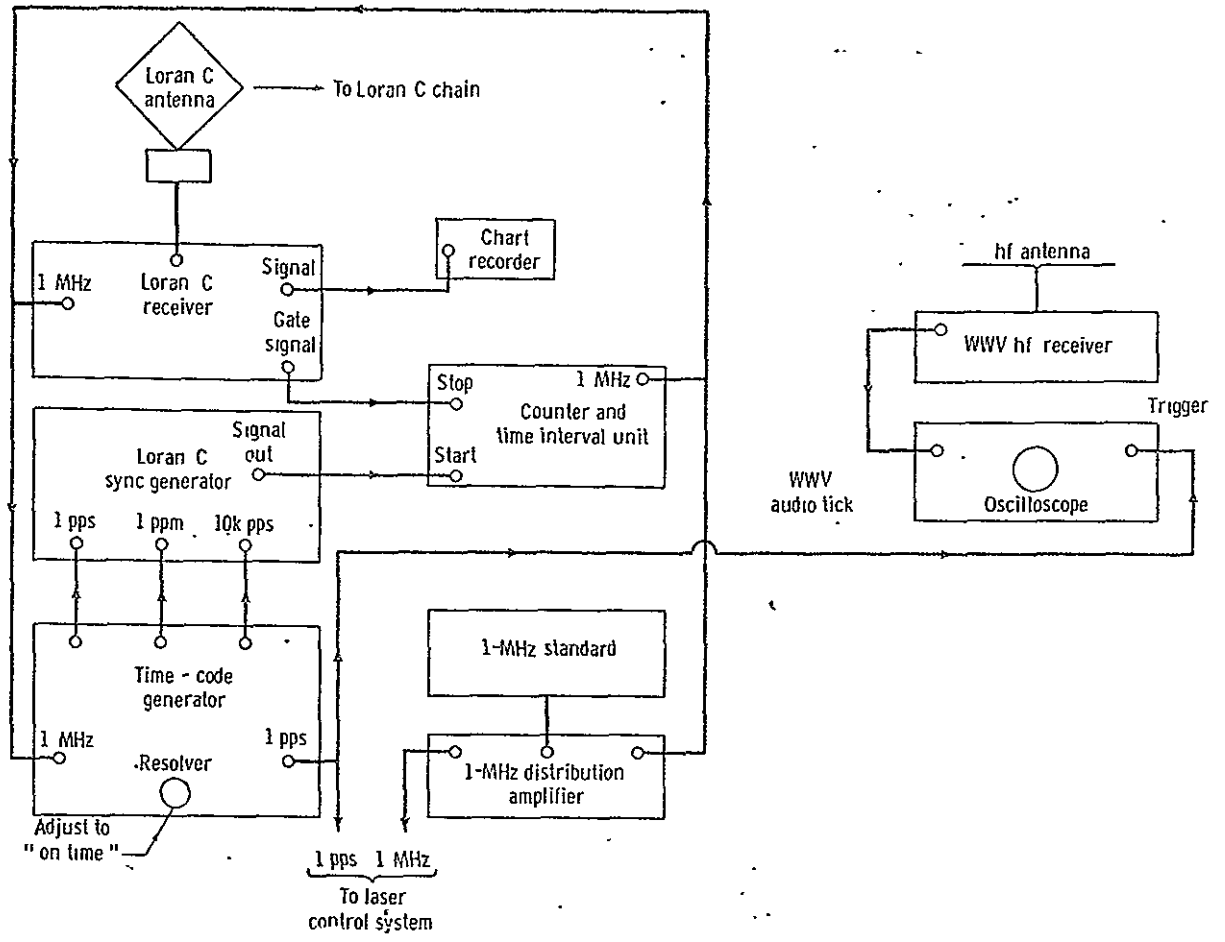

FIGURE 7-20. — Block diagram, time standard system for system B at Lick Observatory.

this difference on the teletypewriter to the nearest nanosecond. The MSTPHC range accuracy depended on the TDG, whereas the TIM range accuracy is entirely independent of the TDG.

The first high-confidence-level return was recorded by the MSTPHC for a 50-shot run at approximately 2:50 Greenwich mean time (G.m.t.) on August 20, 1969 (fig. 7–23). A part of the corresponding TIM printouts is displayed as a histogram in figure 7–24. Here, the origin of the time axis is at the predicted range. The lower histogram shows a portion of the printouts for a 50-shot run taken a few minutes later in which a 5-μsec internal delay was introduced. (This delay has been subtracted in the drawing.) Noise scans in which the laser was fired into a calorimeter displayed no buildup. Four other scans recording signals were made in the 50 min before the Moon sank too low in the sky. Operation earlier in the night had been prevented by cloud cover.

The randomness of the difference between the TIM printout and the ephemeris prediction enabled a statistical reduction of the data even without the vernier circuits designed to interpolate between the 50-nsec digital intervals. The result is a measured round-trip travel time in excess of the Mulholland prediction by 127±15 nsec of time at 3:00 G.m.t., August 20, 1969, from the intersection of the declination and polar axes of the 107-in. telescope. The uncertainty corresponds to ±2.5 m in one-way distance.

Return signals were again recorded on September 3 and 4, 1969, with equivalent uncertainty. Round-trip travel times were also shown in excess of the prediction by 497±15 nsec on September 3, 1969, at 11:10 G.m.t. and by

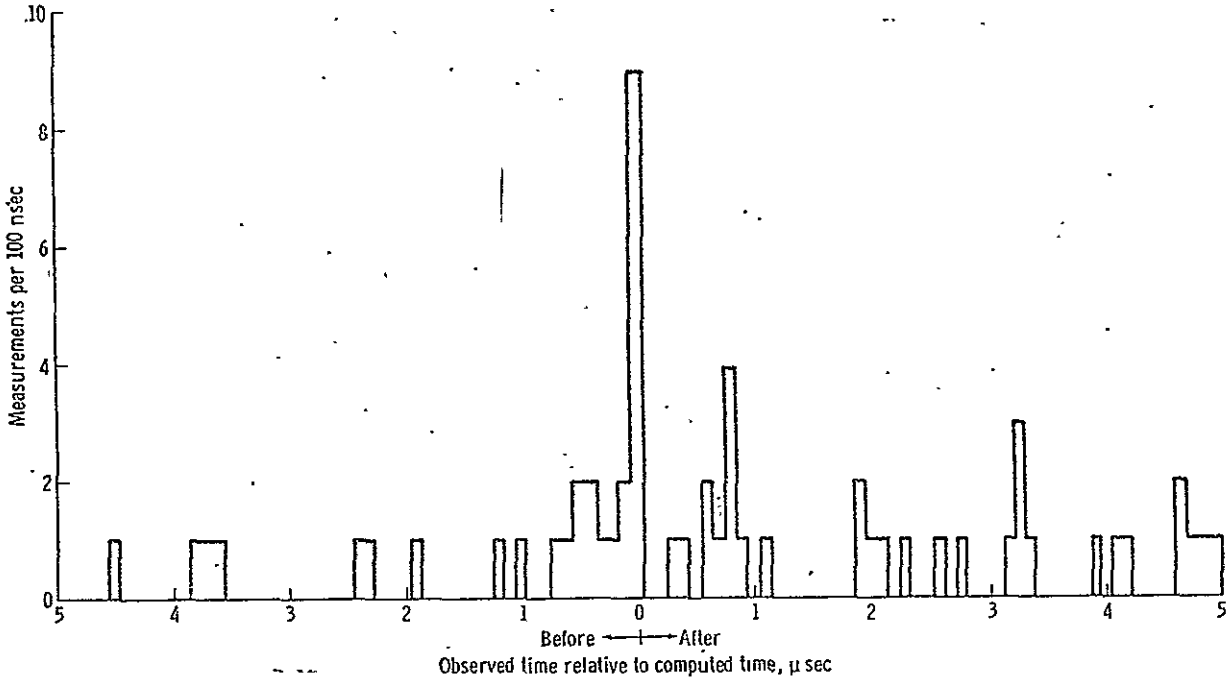

FIGURE 7-21. — Range residuals from system B at Lick Observatory.

797±24 nsec on September 4, 1969, at 10:10 G.m.t. During these observations, Tranquility Base was in darkness, and the computer-controlled drive of the telescope was used successfully to offset from visible craters and track the reflector.

The Lunar Ephemeris: Predictions and Preliminary Results

The fundamental input to the calculation of predictions for the LRRR is the lunar ephemeris, which gives the geocentric position and velocity of the lunar center of mass. An ephemeris is being used that was developed at the Jet Propulsion Laboratory (JPL) and is designated LE 16. This ephemeris is believed to be far superior in the range coordinate to any other extant ephemeris. The available observational evidence is meager but supports this belief. The modeling of the topocentric effects relating to the motions of the observatory and the reflector about the centers of mass of the respective bodies is complete and is similar to that used in JPL spacecraft tracking programs. Universal time (u.t.) 1 is modeled and extrapolated by polynomials fit to the instantaneous determinations by the U.S. Naval Observatory Time Service. The Koziel-Mitielski model is currently being used for the lunar librations.

Coordinates of the telescope and the reflector package are input variables to the prediction program. Reflector coordinates presently used are those derived at the NASA Manned Spacecraft Center from spacecraft tracking of the lunar module, since this dynamic determination is essentially the inverse of the predictive problem and is, thus, more compatible than the selenographic determinations.

It was anticipated that the topographic modeling would be the primary error source in the earliest phase of ranging operations. This belief was based upon the indications from command and service module (CSM) tracking of Apollo 8 and Apollo 10, both of which indicated LE 16 ephemeris errors of 40 to 50 m (0.3 μsec), and is based on the knowledge that various estimates of the selenocentric distances of surface locations disagreed by perhaps 2 km for a specific region. The decision to use the dynamic determinations of the location simplified the real-time processes but did not relieve the radial distance uncertainty until laser acquisition was an accom-

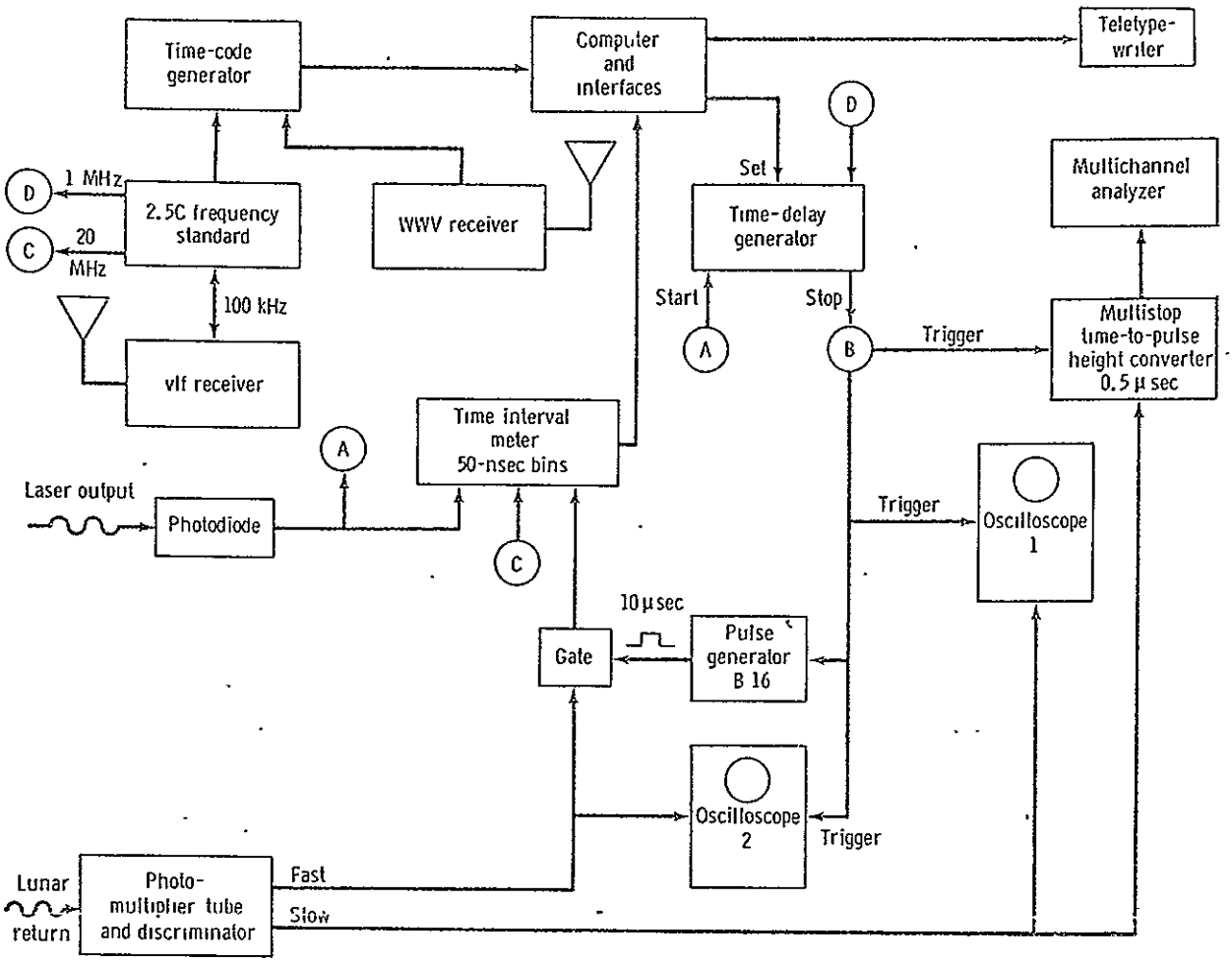

FIGURE 7-22. — Block diagram of McDonald Observatory acquisition and early measurement phase electronics.

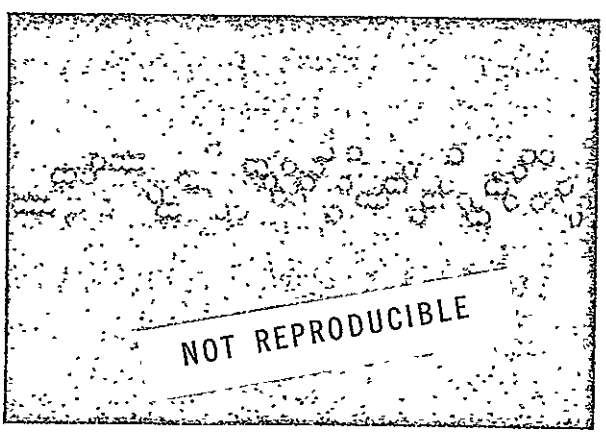

FIGURE 7-23. — MSTPHC display of McDonald Observatory acquisition.

plished fact. As the current "best estimate" of the landing site shifted, predicted ranges were affected by approximately 4 km (28 μsec). Site coordinates for Tranquility Base provided by the NASA Manned Spacecraft Center on July 22, 1969, are currently being used.

Tracking information is available on both the CSM and the lunar module during lunar surface operations. The CSM data indicate an ephemeris error not greater than 50 m. Computations of predictions for comparison with the LM ranging data, using the coordinates mentioned previously, show residuals of approximately 2 km, with a drift of 0.3 km in 15 min. The explanation of this anomaly is not yet known, but it seems to be associated with the tracking station location.

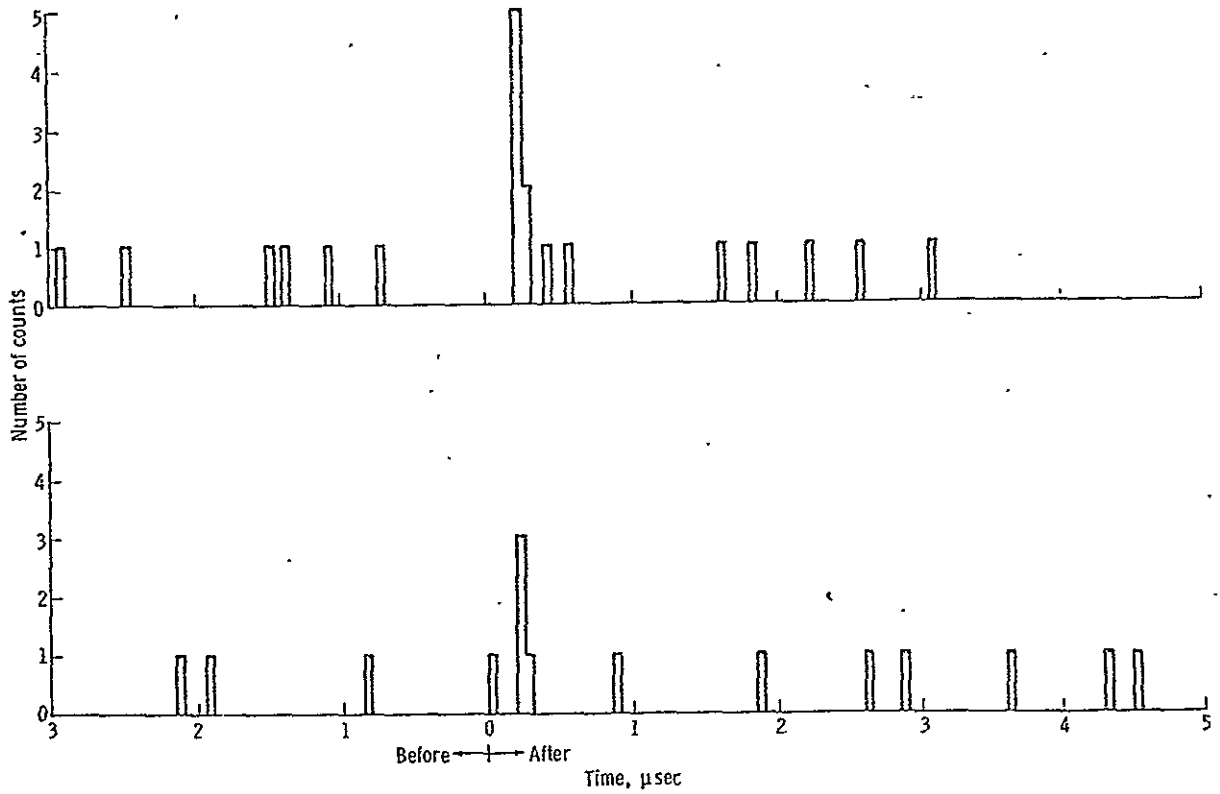

FIGURE 7-24. — Histogram of single-stop TIM readings on two successive 50-shot runs on August 20, 1969, at the McDonald Observatory.

Initial acquisition of the LRRR was accomplished with predictions based on the coordinates of the Lick Observatory, as published in the American Ephemeris and Nautical Almanac. The Lick Observatory 120-in. telescope used in the experiment is actually a distance of approximately 1800 ft from that location, causing drift in the observation residuals. The result of introducing the proper telescope coordinates into the computations is shown in figure 7–25. The residuals relative to the new telescope coordinates appear to be given within 1 μsec. Figure 7–25 is provisional and subject to later refinement. Within the limitations of figure 7–25, these data are consistent with the subsequent observations at McDonald Observatory.

Although it is premature to discuss the data from the standpoint of any meaningful application, one aspect invites speculation and preliminary inference. The three indirect pseudo-observations (range biases on CSM tracking data)

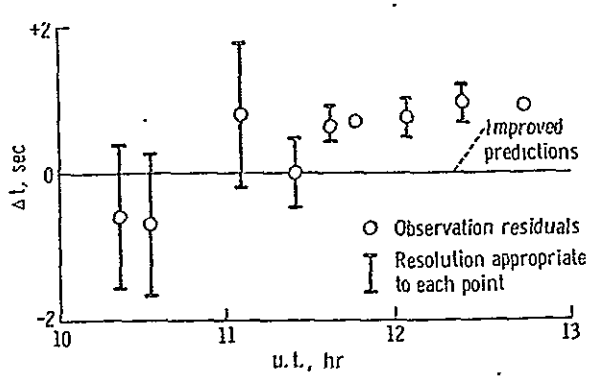

FIGURE 7-25. — Result of using adjusted telescope coordinates for the Lick Observatory. The data are shown for August 1, 1969.

and the first few laser acquisitions yield positive observation residuals. If no observation selection effect is involved, this may be an indication that the ephemeris scaling factor and hence the lunar mean distance requires an adjustment in the seventh place. Such a result would not be

surprising because the uncertainty in the scaling factor is five parts in 10^7 (ref. 7–10), based on the results of Mariner spacecraft tracking.

References

7-1. ALLEY, C. O.; BENDER, P. L.; DICKE, R. H.; FALLER, J. E.; FRANKEN, P. H.; PLOTKIN, H. H.; and WILKINSON, D. T.: Optical Radar Using a Corner Reflector on the Moon. J. Geophys. Res., vol. 70, May 1965, p. 2267.

7-2. ALLEY, C. O.; and BENDER, P. L.: Information Obtainable from Laser Range Measurements to a Lunar Corner Reflector. Symposium No. 32 of the International Astronomical Union on Continental Drift, Secular Motion of the Pole, and Rotation of the Earth, W. Markowitz and B. Guinot, eds., D. Reidel Publishing Co. (Dordrecht, Holland), 1968.

7-3. ALLEY, C. O.; BENDER, P. L.; CURRIE, D. G.; DICKE, R. H.; and FALLER, J. E.: Some Implications for Physics and Geophysics of Laser Range Measurements from Earth to a Lunar Retro-Reflector. Proceedings of NATO Advanced Study Institute on the Application of Modern Physics to the Earth and Planetary Interiors, S. K. Runcorn, ed., John Wiley & Sons (London), 1969.

7-4. MACDONALD, G. J. F.: Implications for Geophysics of the Precise Measurement of the Earth's Rotation. Science, 1967, pp. 157 and 204-205.

7-5. ALLEY, C. O.; ET AL.: Laser Ranging to Optical Retro-Reflectors on the Moon. Univ. of Maryland proposal to NASA, Dec. 13, 1965 (Rev. Feb. 11, 1966); Appendix VII – Design and Testing of Lunar Retro-Reflecting Systems by J. E. Faller.

7-6. ALLEY, C. O.; CHANG, R. F.; CURRIE, D. G.; FALLER, J. E.; ET AL.: Confirmation of Predicted Performance of Solid Fused Silica Optical Corner Reflectors in Simulated Lunar Environment. Univ. of Maryland Progress Report to NASA, Oct. 10, 1966.

7-7. ALLEY, C. O.; and CURRIE, D. G.: Laser Beam Pointing Tests. Surveyor Project Final Report, Part 2, Science Results. Jet Propulsion Laboratory NASA Tech. Rept. 32-1265, June 15, 1968.

7-8. SILVERBERG, E. C.: An Inexpensive Multichannel Scaler With Channel Widths of Less than One Microsecond. Rev. of Sci. Inst., Oct. 1969.

7-9. CURRIE, D. G.: Some Comments on Laser Ranging Retro-Reflector Ground Stations. Univ. of Maryland Tech. Rept. 956, Sept. 4, 1968.

7-10. MELBOURNE, W. G.; MULHOLLAND, J. D.; ET AL.: Constants and Related Information for Astrodynamic Calculations, 1968. Jet Propulsion Laboratory Tech. Rept. 32-1306, July 15, 1968.

ACKNOWLEDGMENTS

Responsibility for the design and conduct of the experiment has rested with the following groups: Principal Investigator, C. O. Alley (University of Maryland); Co-Investigators, P. L. Bender (National Bureau of Standards), R. H. Dicke (Princeton University), J. E. Faller (Wesleyan University), W. M. Kaula (University of California at Los Angeles), G. J. F. MacDonald (University of California at Santa Barbara), J. D. Mulholland (JPL), H. H. Plotkin (NASA Goddard Space Flight Center), and D. T. Wilkinson (Princeton University); Participating Scientists, W. Carrion (NASA Goddard Space Flight Center), R. F. Chang (University of Maryland), D. G. Currie (University of Maryland), and S. K. Poultney (University of Maryland).

The following people are responsible for the section of this report entitled "Observations at the Lick Observatory": James Faller and Irwin Winer (Wesleyan University); Walter Carrion, Tom Johnson, and Paul Spadin (NASA Goddard Space Flight Center); and Lloyd Robinson, E. Joseph Wampler, and Donald Wieber (Lick Observatory, University of California). These authors of the "Observations at the Lick Observatory" section wish to acknowledge the efforts of Norman Anderson (Berkeley Space Science Laboratory); Harold Adams, Raymond Greeby, Neal Jern, Terrance Ricketts, and William Stine (Lick Observatory); Barry Tumrose, Steve Moody, Tom Giuffrida, Dick Plumb, and Tuck Stebbins (Wesleyan University); and James MacFarlane, Bill Schaefer, Richard Chabot, James Hitt, and Robert Anderson (NASA Goddard Space Flight Center). Support from funds to the Lick Observatory by NASA grant NAS5-10752 and National Science Foundation grant GP 6310, from funds to Wesleyan by NASA Headquarters grant NGR–07–006–005, and from in-house funds used by Goddard personnel is acknowledged.

The people who are responsible for the section of this report entitled "Observations at the McDonald Observatory" include D. G. Currie, S. K. Poultney, C. O. Alley, E. Silverberg, C. Steggerda, J. Mullendore, and J. Rayner (University of Maryland); H. H. Plotkin and W. Williams (NASA Goddard Space Flight Center); and Brian Warner, Harvey Richardson, and B. Bopp (McDonald Observatory). The authors of this section wish to acknowledge the efforts of Harlan Smith, Charles Jenkins, Johnny Floyd, Dave Dittmar, Mike McCants, and Don Wells (McDonald Observatory); Faust Meraldi, Norris Baldwin, Charles Whitted, and Harry Kriemelmeyer (University of Maryland); and Jim Poland, Peter Minott, Cal Rossey, Jim Fitzgerald, Walter Carrion, Mike Fitzmaurice, and Herb Richard (NASA Goddard Space Flight Center.

Support for the activities at the McDonald Observatory from NASA Grant NGR 21–002–109 to the University of Maryland and from in-house funds at the Goddard Space Flight Center is acknowledged.

J. D. Mulholland (JPL) is responsible for the section entitled "The Lunar Ephemeris."

APPENDIX 11

Laser Ranging Retro-Reflector:
Continuing Measurements and Expected Results

C. O. Alley, et al

Science, Vol. 167, p 458, Jan. 1970

Reprinted from
30 January 1970, Volume 167, pp. 458-460

SCIENCE

Apollo 11 Lunar Science Conference

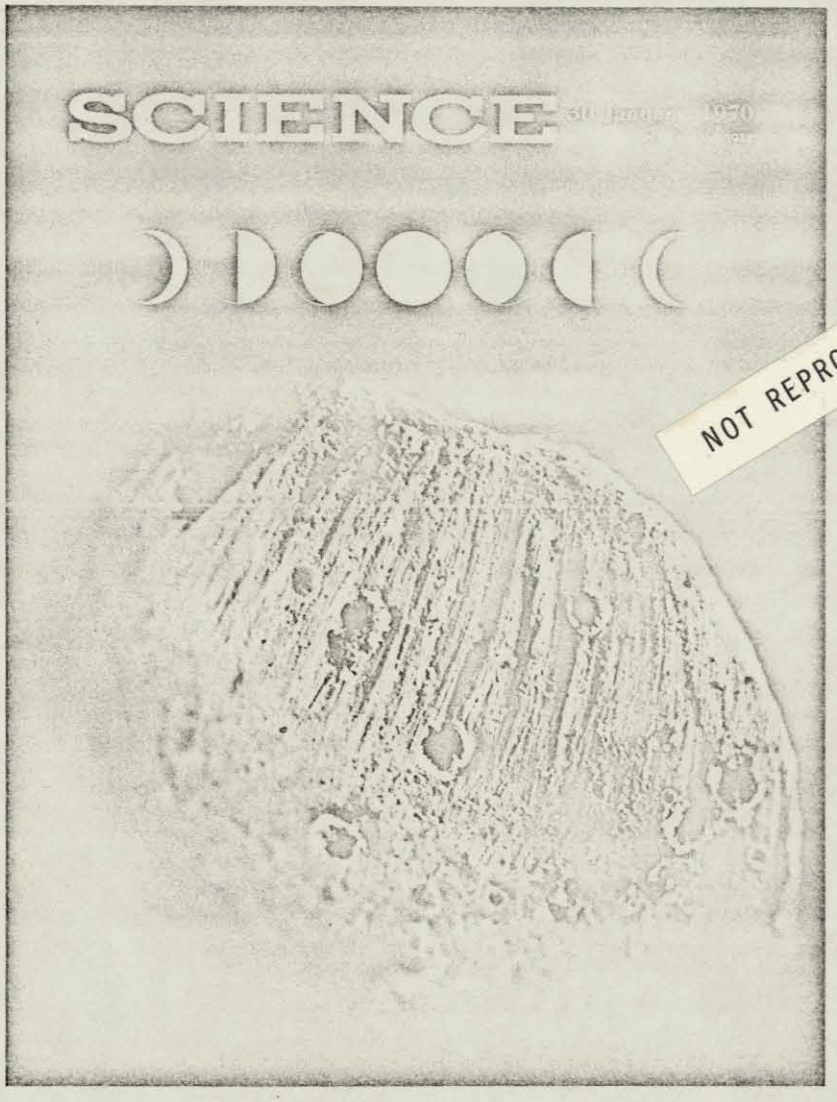

Laser Ranging Retro-Reflector: Continuing Measurements and Expected Results

C. O. Alley, R. F. Chang, D. G. Currie, S. K. Poultney, P. L. Bender, R. H. Dicke, D. T. Wilkinson, J. E. Faller, W. M. Kaula, G. J. F. MacDonald, J. D. Mulholland, H. H. Plotkin, W. Carrion and E. J. Wampler

Laser Ranging Retro-Reflector:
Continuing Measurements and Expected Results

Abstract *After successful acquisition in August of reflected ruby laser pulses from the Apollo 11 laser ranging retro-reflector (LRRR) with the telescopes at the Lick and McDonald observatories, repeated measurements of the round-trip travel time of light have been made from the McDonald Observatory in September with an equivalent range precision of ±2.5 meters. These acquisition period observations demonstrated the performance of the LRRR through lunar night and during sunlit conditions on the moon. Instrumentation activated at the McDonald Observatory in October has yielded a precision of ±0.3 meter, and improvement to ± 0.15 meter is expected shortly. Continued monitoring of the changes in the earth-moon distance as measured by the round-trip travel time of light from suitably distributed earth stations is expected to contribute to our knowledge of the earth-moon system.*

The performance (*1*) of the Apollo 11 laser ranging retro-reflector (LRRR) left on the moon, as well as that of the instrumentation at the ground observatories, has been in accord with the original expectations (*2–5*). The scientific objectives are such that lengthy analysis of a long-continuing series of frequent measurements is required before results are available. The experiment had its origin in discussions among members of the experimental gravitational research group at Princeton University (*6*). Because of the many areas of science and technology involved in the experiment, a group (*7*) was organized to carry it out.

The compact array of high-precision optical retro-reflectors (cube corners) deployed on the moon (*1, 8*) is intended to serve as a reference point in measuring precise ranges between the array and points on the earth by using the technique of short-pulse laser ranging The atmospheric fluctuations in the index of refraction diverge a laser beam and prevent the spot on the moon from being smaller than approximately 1.6 km in diameter The curvature of the lunar surface results in part of the short pulse being reflected before the rest, producing a reflected pulse measured in microseconds, even if the incident pulse is measured in nanoseconds. The retro-reflector array eliminates this spreading because of the small size of the array. (The maximum spreading of a pulse because of optical libration tipping of the array will be approximately ± 0.125 nsec.) In addition, the retro-reflective property causes a much larger amount of light to be directed back to the telescope from the array than is reflected from the entire surface area illuminated by the laser beam.

The basic uncertainty in measuring the approximately 2.5-sec round-trip travel time is associated with the performance of photomultipliers at the single photoelectron level. This uncertainty is estimated to be approximately 1 nsec. When the entire system is calibrated and the effects of the atmospheric delay are calculated from local temperature, pressure, and humidity measurements and subtracted from the travel time, where the uncertainty in this correction is estimated to be less than 0.5 nsec, an overall uncertainty of ± 15 cm in one-way range seems achievable.

The present uncertainty of three parts in 10^7 in the knowledge of the velocity of light will not affect the scientific aims of the experiment, since it is the practice to measure astronomical distances in light travel time. Primary scientific objectives include the study of gravitation and relativity (secular variation in the gravitational constant), the physics of the earth (fluctuation in rotation rate, motion of the pole, large-scale crustal motions), and the physics of the moon (physical librations, center-of-mass motion, size, and shape) (*2–5*). Estimates of improvements expected in some of these categories are shown in Tables 1 to 3. The estimated uncertainty for each quantity is intended to be an upper limit

Reflected signals from the LRRR were acquired 1 August (and 3 August, with a different laser system) with the 120-inch telescope of the Lick Observatory (*9*) at Mt Hamilton, California, and 20 August with the 107-inch tele-

Table 1. Lunar orbital data parameters

Quantity	Present uncertainty (approximate)	0.15-m Range accuracy*	
		Uncertainty	Time (yr)
Mean distance	500 m	25 m	1
Eccentricity	1×10^{-7}	4×10^{-9}	1
Angular position of Moon			
With respect to perigee	2×10^{-6} rad	4×10^{-8} rad	1
With respect to Sun	5×10^{-7} rad	4×10^{-8} rad	1
Time necessary to check predictions of Brans-Dicke scalar-tensor gravitational theory			8

* Three observing stations

Table 2. Lunar libration and relation of LRRR to center of mass.

Quantity	Present uncertainty (approximate)	0.15-m Range accuracy*	
		Uncertainty	Time (yr)
Libration parameters†			
$\beta = (C-A)/B$†	1×10^{-5}	3×10^{-8}	4
$\gamma = (B-A)/C$	5×10^{-5}	2×10^{-7}	1.5
Coordinates of LRRR with respect to center of mass‡			
X_1	500 m	25 m	1
X_2	200 m	7 m	1
X_3	200 m	5 m	3

* Three observing stations are assumed. † A is the moment of inertia about the principal axis toward the earth, B is the moment about the principal axis tangent to the orbit, and C is the moment about the moon's rotation axis. Knowledge of the parameters β and γ is important in determining the mass distribution within the moon ‡ X_1, X_2, and X_3 are measured along the principal axes about which the moments A, B and C are defined

Table 3 Geophysical data determinable from LRRR.

Quantity	Present uncertainty (estimated)	0.15-m Range accuracy
Rotation period of earth (sec)	5×10^{-7}	1×10^{-7}
Distance of station from axis of rotation (m)	10	0.3
Distance of station from equatorial plane (m)*	20	0.6 to 2†
Motion of the pole (m)*	1 to 2	0.15
East-west continental drift rate observable in 5 years (cm/yr)*	30 to 60	3
Time for observing predicted drift of 10 cm/yr of Hawaii toward Japan (years)	15 to 30	1.5

* Three or more observing stations are required † Depending upon the latitude of the station

Table 4. Measurements at the McDonald Observatory of round-trip travel time during acquisition. The residuals represent the difference between the observed time of travel and that predicted on the basis of the JPL LE16 ephemeris

Day	U.T	Residual round-trip travel time (nsec)
20 August	03 00	96 ± 15
3 September	11:10	490 ± 15
4 September	10:10	795 ± 24
22 September	04:00	−1430 ± 15
17 October	01:44	−798 ± 15*
18 October	01:17	−978 ± 15*
1 November	11:40	−2034 ± 15*
16 December	01:45	−1232 ± 15*

* The present accuracy is ±15 nsec in the knowledge of the electronic time delays. Upon completion of the current calibration, the accuracy will be determined by the present overall resolution, less than ±2 nsec, limited by the laser pulse length and photomultiplier jitter

scope of the McDonald Observatory (*10*) at Mt. Locke, Texas. These observations showed that the LRRR did not suffer any major degradation, if any at all, from debris generated during lift-off of the lunar module. The signals are consistent with the return expected from the LRRR design, within the uncertainties of atmospheric "seeing," telescope transmission, and other optical losses. Continued acquisition period measurements at McDonald in September (*10*), taken with the initial observations, have demonstrated the successful performance of the LRRR at several sun illumination angles, as well as during and after a lunar night, confirming the prediction of thermal design analyses.

A first "geodetic result" from the acquisition observations at Lick (*9*) was the discovery, from the drift of the residual round-trip travel time with respect to the JPL lunar ephemeris 16 (LE16) predictions, that the coordinates for the 120-inch telescope are not those given for Mt. Hamilton (Lick Observatory) in the *American Ephemeris and Nautical Almanac* (*9a*). The Lick Observatory participated in the acquisition phase of the experiment to increase the probability of getting early returns. The weather and seeing are generally excellent there in the summer. Laser ranging activities ceased at Lick in August.

In October a custom-built four-stage ruby laser, made by Korad, was installed at the McDonald Observatory. This laser was built to specifications developed for long-term precision measurements in the lunar ranging experiment. The pulse length is produced by a time-varying reflectivity mode of operation and can be as short as 2.8 nsec, although a more typical value is 4 nsec. It transmits 5 joules with a beam divergence (full width) of 1.4 mradian at a repetition rate capability of one shot every 3 seconds. At the same time, vernier timing circuits (*11–13*) shown schematically in Fig. 1 were activated. This instrumentation allows a resolution uncertainty of ±2 nsec on each measured return. The accuracy depends on thorough calibration of all electronic delays. This will be completed soon to the 1-nsec level. The measurements made in October, November, and December, and which are shown in Table 4, still have a calibration uncertainty in accuracy of ±15 nsec. These later measurements are subject to reduction of the accuracy uncertainty upon completion of the final calibration.

As more experience is gained in the use of the new 107-inch McDonald telescope, the goal is three measurement periods daily. Each period would last about 15 minutes, enabling several hundred laser shots to be fired; the periods would be scheduled near the time of meridian crossing, several hours before, and several hours after.

From these measurements, one can obtain the minimum range and its epoch of occurrence. Harmonic analysis of this range time series will permit the determination of the quantities listed in Tables 1 through 3.

In order to satisfy all the scientific aims of the experiment, it is hoped that more U.S. and foreign ground stations can be established to carry out regular precision ranging to the LRRR. The deployment of several more LRRR's on the moon would allow a more detailed study of the lunar physical librations, independent of any model. One of these should be designed to give a larger return than the Apollo 11 LRRR, so as to allow participation in the ranging program by smaller telescopes.

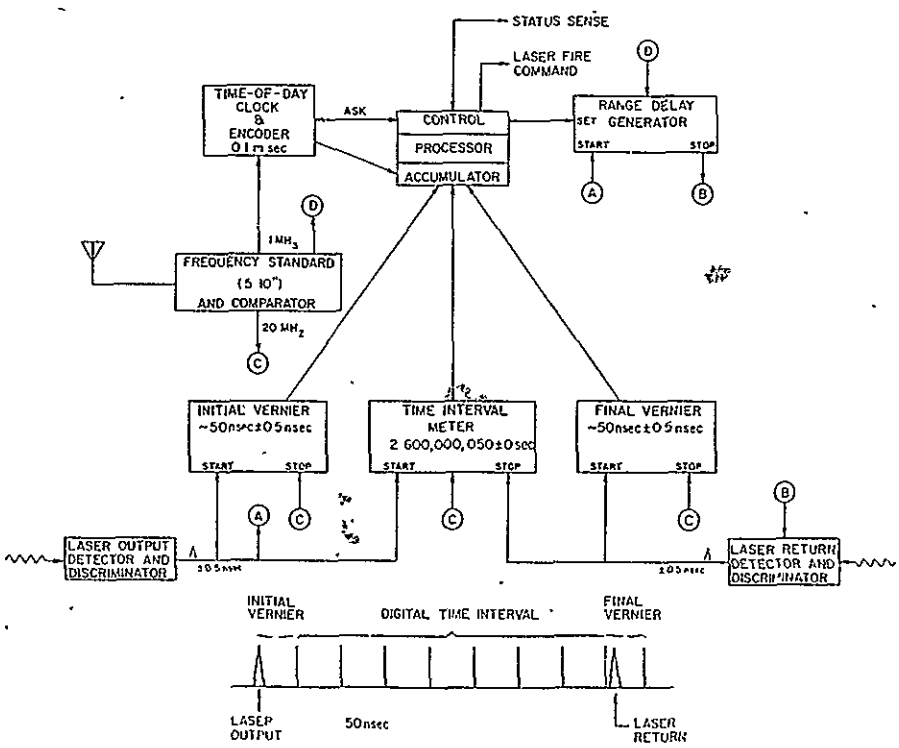

Fig. 1. Representation of the nanosecond-resolution time-interval measurement system now in use at the McDonald Observatory. Special circuits eliminate any ±1 count uncertainty in the 20-Mhz, digitally measured interval. The vernier components are time to pulse height converters.

C. O. ALLEY, R. F. CHANG
D. G. CURRIE, S. K. POULTNEY
Department of Physics and Astronomy, University of Maryland, College Park
P. L. BENDER
Joint Institute for Laboratory Astrophysics, National Bureau of Standards and *University of Colorado, Boulder 80302*
R. H. DICKE, D. T. WILKINSON
Palmer Physical Laboratory, Princeton University, Princeton, New Jersey 08540
J. E. FALLER
Department of Physics, Wesleyan University, Middletown, Connecticut
W. M. KAULA
Institute of Geophysics and Planetary Physics, University of California, Los Angeles 90024
G. J. F MACDONALD
University of California, Santa Barbara
J. D. MULHOLLAND
Jet Propulsion Laboratory, California Institute of Technology, Pasadena 91103
H. H. PLOTKIN, W. CARRION
Goddard Space Flight Center, Greenbelt, Maryland 20771
E. J. WAMPLER
Lick Observatory, University of California, Santa Cruz 95060

References and Notes

1. C. O. Alley *et al*, "Laser ranging retro-reflector" in *Apollo 11 Preliminary Science Report* (NASA Special Publication SP-214, 1969).
2. C. O. Alley, P. L Bender, R. H. Dicke, J. E. Faller, P. A. Franken, H. H. Plotkin, D. T. Wilkinson, *J. Geophys Res.* 70, 2267 (1965)
3. C. O Alley and P L. Bender, in *Symposium No. 32 of the International Astronomical Union on Continental Drift, Secular Motion of the Pole, and Rotation of the Earth*, W. Markowitz and B. Guinot, Eds. (Reidel, Holland, 1968).
4. C. O. Alley, P. L. Bender, D G. Currie, R. H. Dicke, J. E. Faller, *Proceedings of the N.A.T.O. Advanced Study Institute on the Application of Modern Physics to the Earth and Planetary Interiors*, S. K. Runcorn, Ed. (Wiley, London, 1969).
5. G. J. F. MacDonald, *Science* 157, 204 (1967).
6. W. F. Hoffman, R. Krotkov, R. H. Dicke, *Inst. Radio Eng. IRE Trans. Military Electron.* 4, 28 (1960) The authors served as a committee for the whole group. C. O Alley, J Brault, D. Brill, R. H. Dicke, J. Faller, W. F. Hoffman, L Jordan, R. Krotkov, S Liebes, R. Moore, J. Peebles, J. Stoner, and K. Turner.
7. Formal responsibility has rested with the following group principal investigator, C. O. Alley (University of Maryland); co-investigators· P L Bender (National Bureau of Standards), R H. Dicke (Princeton University), J. E Faller (Wesleyan University), W. M. Kaula (University of California at Los Angeles), G. J. F. MacDonald (University of California at Santa Barbara), J. D. Mulholland (Jet Propulsion Laboratory), H. H. Plotkin (NASA Goddard Space Flight Center), and D. T. Wilkinson (Princeton University); participating scientists: W. Carrion (NASA Goddard Space Flight Center), R F. Chang (University of Maryland), D. G Currie (University of Maryland) and S K. Poultney (University of Maryland).
8. Responsibility for the detailed design of the LRRR to perform continuously in the lunar environment has been carried primarily by J. E. Faller, D. G. Currie, R. F. Chang, and C O Alley, supported by the following engineering companies: Arthur D Little, Inc. (P. Glaser, J. Burke, F. Gabron, and D. Comstock); Perkin-Elmer Corporation (J. Atwood, P. Forman, G. Watt, D. Corbett, and S. Lauffer); and the Bendix Aerospace Corporation (C. Weatherred, R. Hill, J. Brueger, R. Wolford, and K. Moore); and by project engineer H. Kriemelmeyer (University of Maryland).
9. J. E Faller *et al*, "Observations of the First Returns from a Laser Beam Directed at the Lunar Retro-Reflector Array," *Science* 166, 99 (1969).

9a U S. Government Printing Office, Washington, D.C. (1969).

10 C. O. Alley, R F. Chang, D. G. Currie, J. Mullendore, S K Poultney, J D Rayner, E. C Silverberg, C. A. Steggerda, H. H. Plotkin, W Williams, B. Warner, H. Richardson, B. Bopp, *Science* 167, 368 (1970).

11. S. K. Poultney, *The Concept of the Time Interval Measurement and Control Circuitry for the Lunar Ranging Experiment. a History* (University of Maryland Department. of Physics and Astronomy Technical Report No 70–068, December 1969)
12 C. A. Steggerda, *A Description of the Time Interval Measurement and Laser Control Circuitry for the Lunar Ranging Experiment* (University of Maryland Department of Physics and Astronomy Technical Report No. 70–049, November 1969).
13. J. D. Rayner, *A Description of the Control Program for the Lunar Ranging Experiment* (University of Maryland Department of Physics and Astronomy Technical Report No. 70–064, November 1969)

6 January 1970

APPENDIX 12

Second Apollo Lunar Science Conference - January 11 - 14, 1971

Lunar Laser Ranging Experiment: Current Results and Future Plans

Second Apollo Lunar Science Conference

January 11 - 14, 1971

Lunar Laser Ranging Experiment: Current Results and Future Plans

C. O. Alley[1], P. L. Bender[2], D. G. Currie[1], R. H. Dicke[3], J. E. Faller[4], W. M. Kaula[5], G. J. F. MacDonald[6], J. D. Mulholland[7], H. H. Plotkin[8], E. C. Silverberg[9], and D. T. Wilkinson[3]

Summary

Several hundred range determinations have been made of the point to point distance between the McDonald Observatory in West Texas and the Laser Ranging Retro-Reflector left at the Tranquillity Base by the Apollo 11 astronauts. Measurements are being made routinely on a regular and frequent schedule averaging about twelve to fifteen measurement periods per month. The precision of the measurement of the time of flight is about one nanosecond with an accuracy of about two nanoseconds (equivalent to thirty centimeters in the one-way distance).

The accompanying plot of raw time of flight residuals with respect to the JPL LE16 lunar ephemeris as a function of epoch of laser firing shows the results of a good run of fifty shots. The basic uncertainty per shot is $\pm$ 2 nanoseconds due to the laser pulse width of 4 nanoseconds. A jitter of about $\pm$ 1 nanosecond is inherent in the photomultiplier tube in current use. The statistics of such a run support a precision of $\pm$ 1 nanosecond. The accuracy quoted above is the current level of calibration. The drift in the residuals during this run is due to the use of incorrect geocentric coordinates for the McDonald Observatory.

The accompanying histogram displays the background noise for the same run of fifty shots. The accompanying line drawing shows the optical arrangement at the observatory. A brief description of the aims and techniques of the experiment is contained in Science, Vol. 167, pp. 458-460, 1970.

Significant adjustments to the eccentricity of the moon's orbit and to either its mean distance or to one reflector coordinate appear to be indicated by the preliminary analysis of the data through June 1970. Analysis of the twenty-four hour period terms in the range residuals indicates rough agreement with the presently available geocentric coordinates for the McDonald Observatory. Full application of the laser ranging technique for the establishment of geocentric coordinates requires the measurement of the polar motion which will only be possible when several more stations are operating with comparable precision in well distributed earth locations.

Ground instrumentation has been prepared by groups in France, the USSR, and Japan, and the possibility of participation is being discussed with scientists in a number of other countries. The Air Force Cambridge Research Laboratory in the United States has developed instrumentation and the Smithsonian Institution is engaged in such development.

The French-made Laser Ranging Retro-Reflector placed on the moon by the Soviet Luna 17 in the western part of Mare Imbrium emphasizes the international aspect of the lunar ranging program. A second U.S. LR^3 will be carried to the Fra Mauro region by Apollo 14 and a third U.S. reflector having three times the number of corner reflectors as the Apollo 11 and 14 LR^3's is planned for the Apollo 15 landing in the area near Hadley Rille. These additional reflector sites on the moon will allow the direct measurement by laser ranging of all the rotational motions associated with the physical librations. The larger LR^3 will also allow a larger number of observatories to participate in the lunar laser ranging program.

Recent developments in lasers, timing techniques, and in the knowledge of atmospheric corrections indicate that an accuracy of better than three centimeters can be achieved in lunar laser ranging.

1 University of Maryland, Department of Physics and Astronomy, College Park, Maryland

2 Joint Institute for Laboratory Astrophysics, National Bureau of Standards and University of Colorado, Boulder, Colorado

3 Joseph Henry Laboratories, Princeton University, Princeton, New Jersey

4 Wesleyan University, Department of Physics, Middletwon, Connecticut

5 University of California, Institute of Geophysics and Planetary Physics, Los Angeles, California

6 Council on Environmental Quality, Washington, D.C.

7 Jet Propulsion Laboratory, California Institute of Technology, Pasadena California

8 Optical Systems Branch, Goddard Space Flight Center, Greenbelt, Maryland

9 University of Texas, McDonald Observatory, Fort Davis, Texas

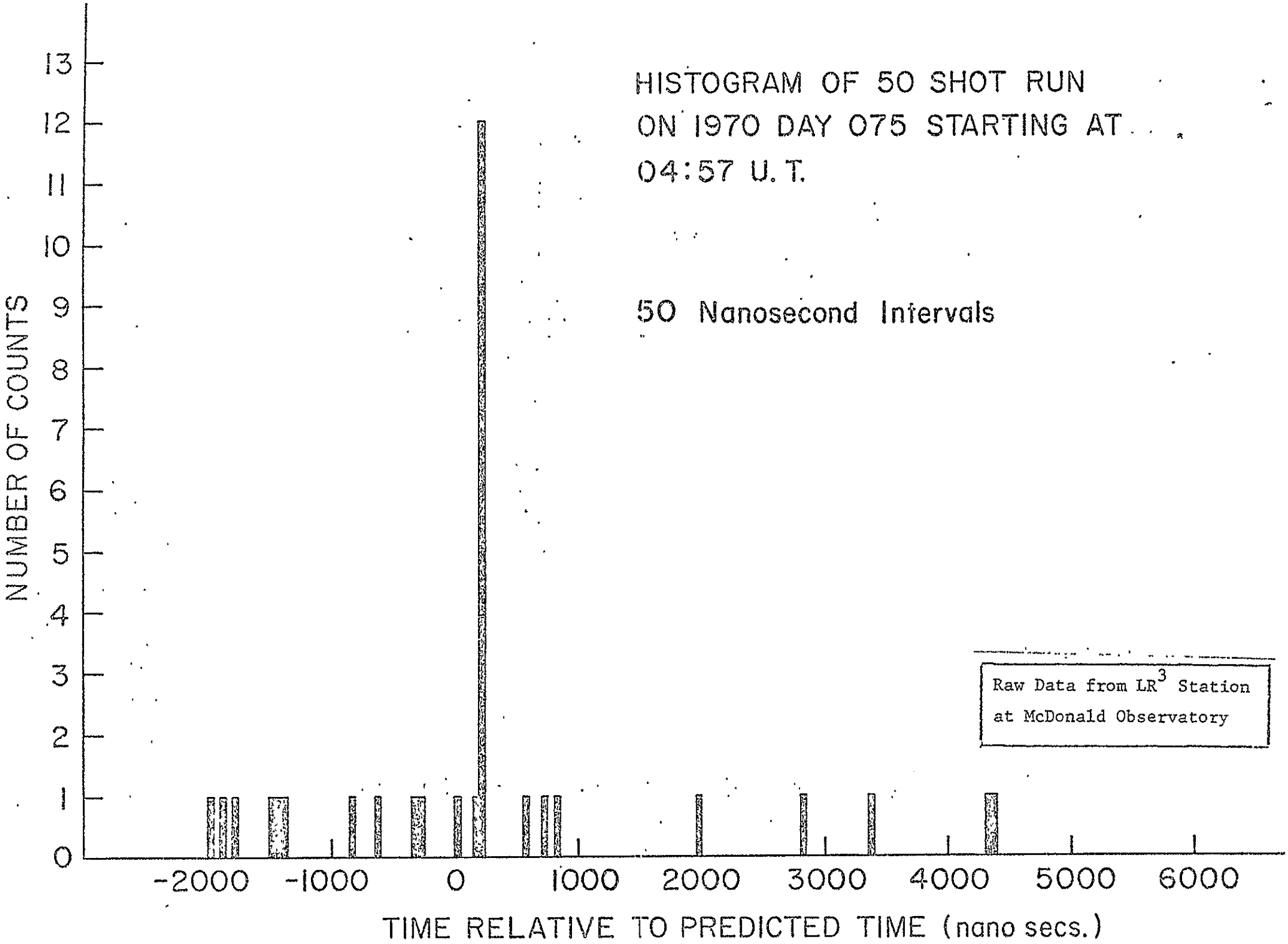
HISTOGRAM OF 50 SHOT RUN
ON 1970 DAY 075 STARTING AT
04:57 U.T.
50 Nanosecond Intervals
Raw Data from LR3 Station
at McDonald Observatory
NUMBER OF COUNTS
0
1
2
3
4
5
6
7
8
9
10
11
12
13
-2000
-1000
0
1000
2000
3000
4000
5000
6000
TIME RELATIVE TO PREDICTED TIME (nano secs.)

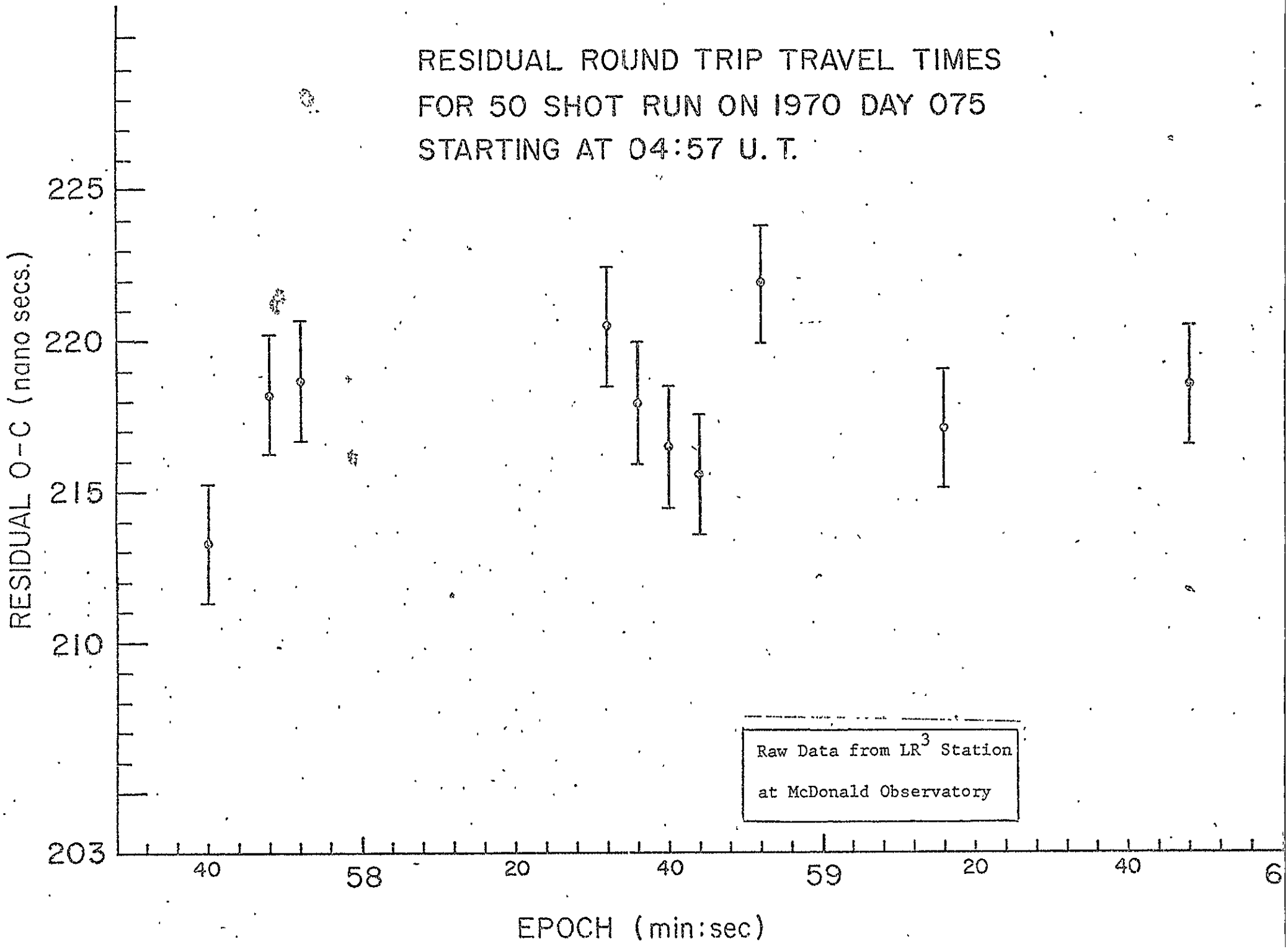
RESIDUAL ROUND TRIP TRAVEL TIMES
FOR 50 SHOT RUN ON 1970 DAY 075
STARTING AT 04:57 U.T.
RESIDUAL O-C (nano secs.)
225
220
215
210
203
40
58
20
40
59
20
40
6
EPOCH (min:sec)
Raw Data from LR3 Station
at McDonald Observatory

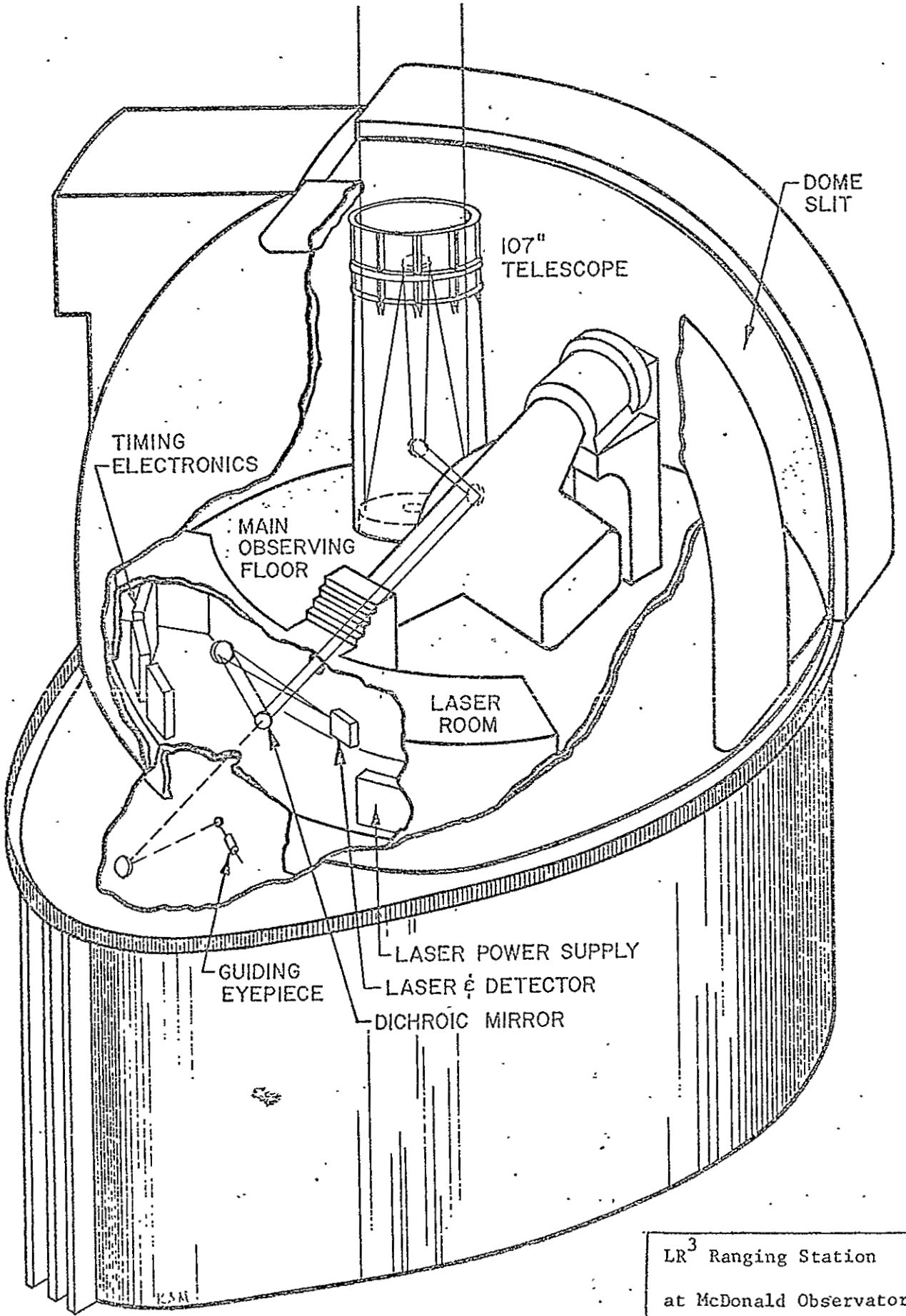

LR^3 Ranging Station

at McDonald Observatory

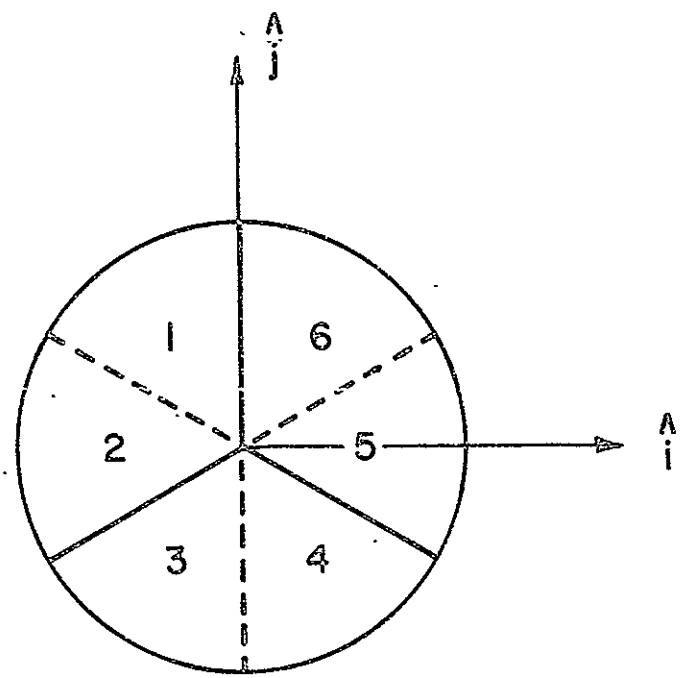

Figure 1

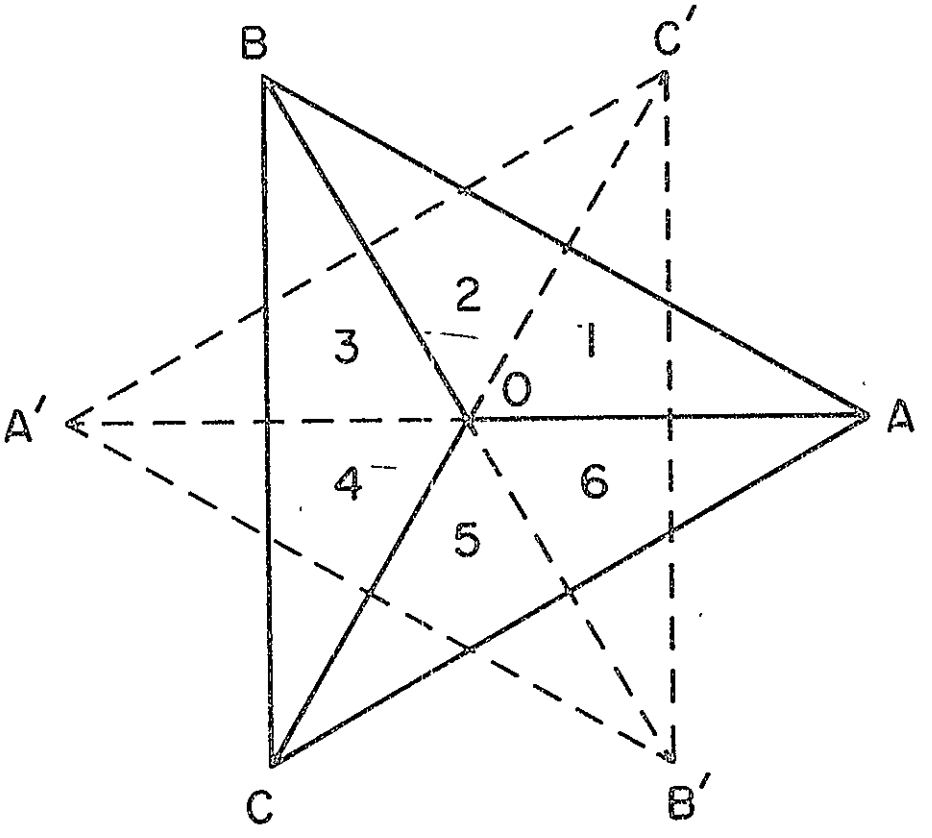

Fig. 3

The effective aperture and the subapertures of a retroreflector for normal incidence of light.

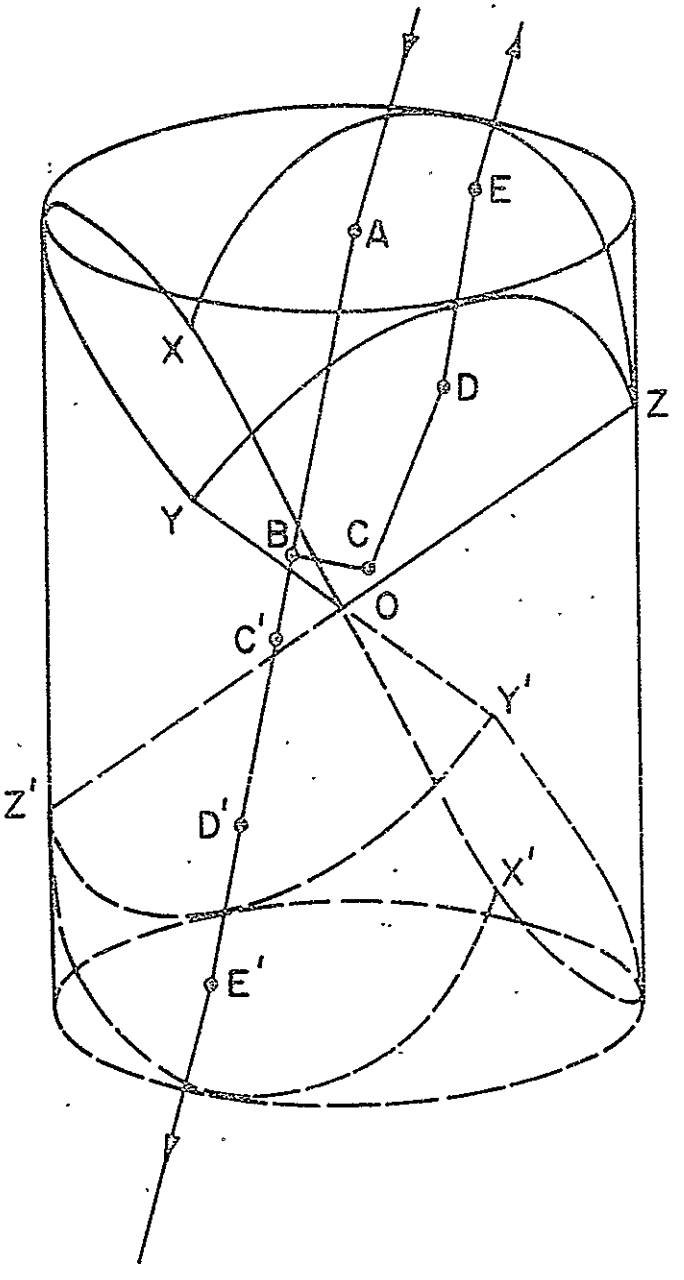

Fig. 5

Three-dimensional illustration of ray-trace in a retroreflector.

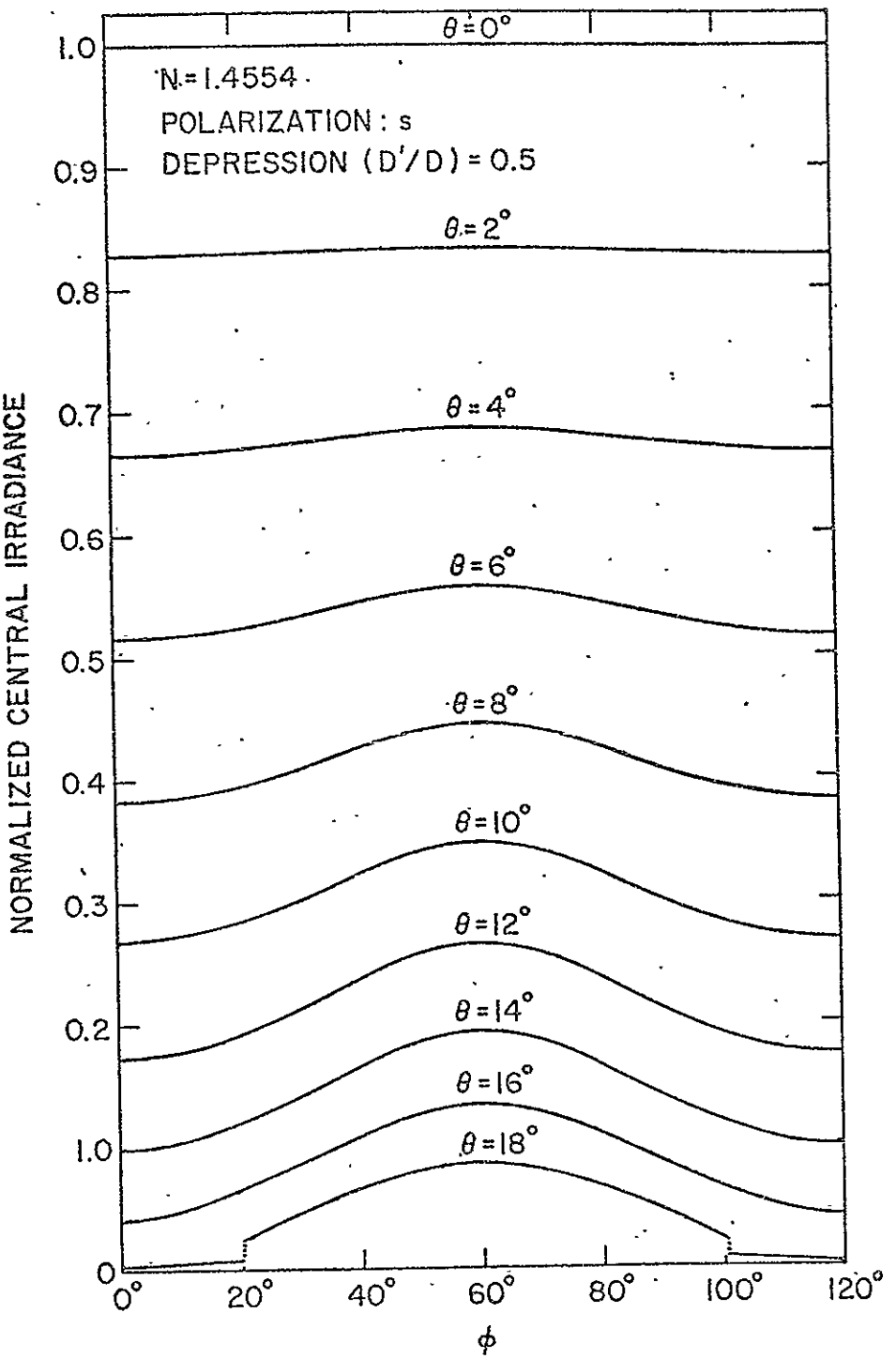

Fig. 16

The same as Figure 15 except the polarization of light is in s- direction.

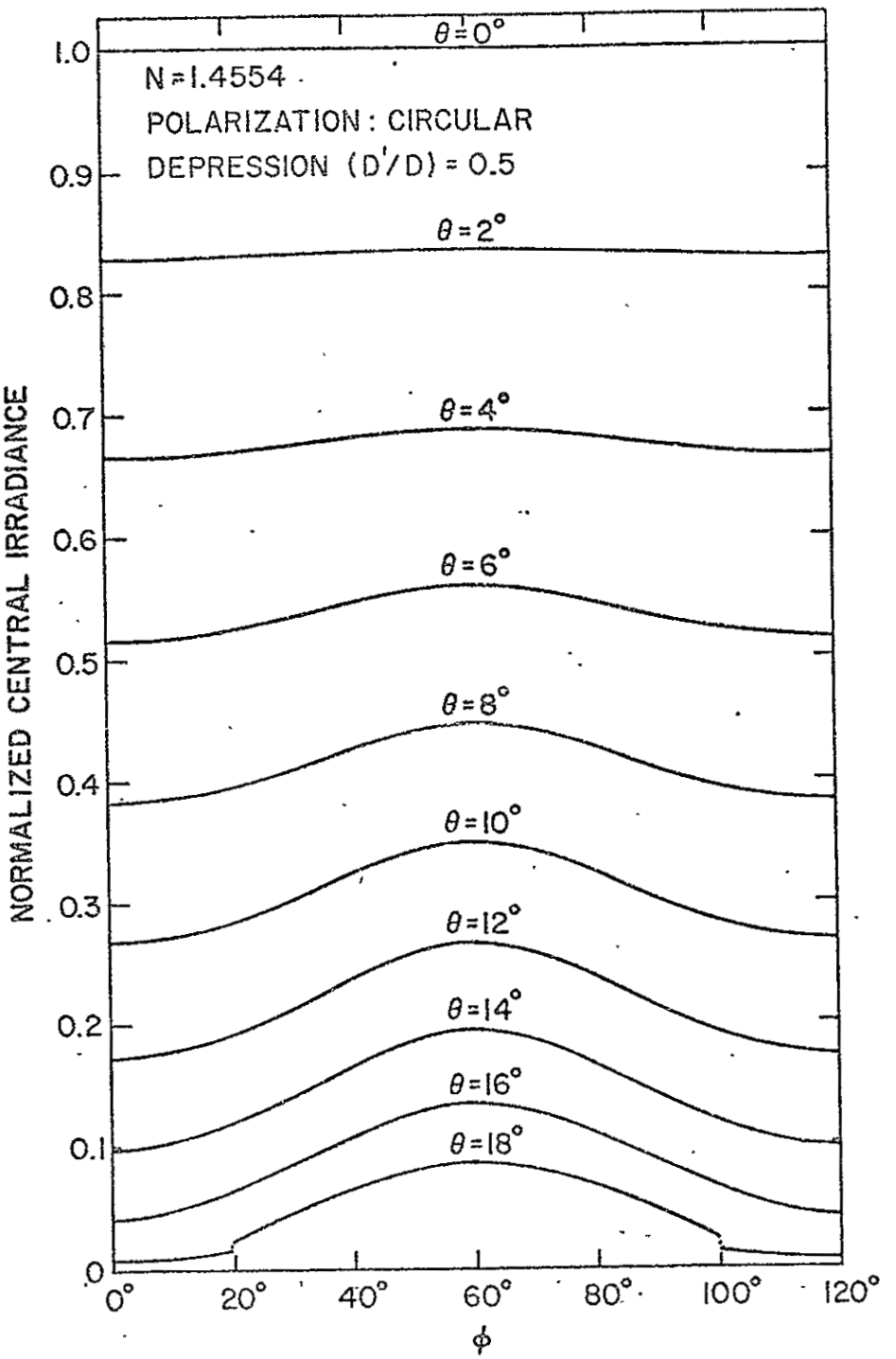

Fig. 17

The same as Figure 15 except the polarization of light is circular.

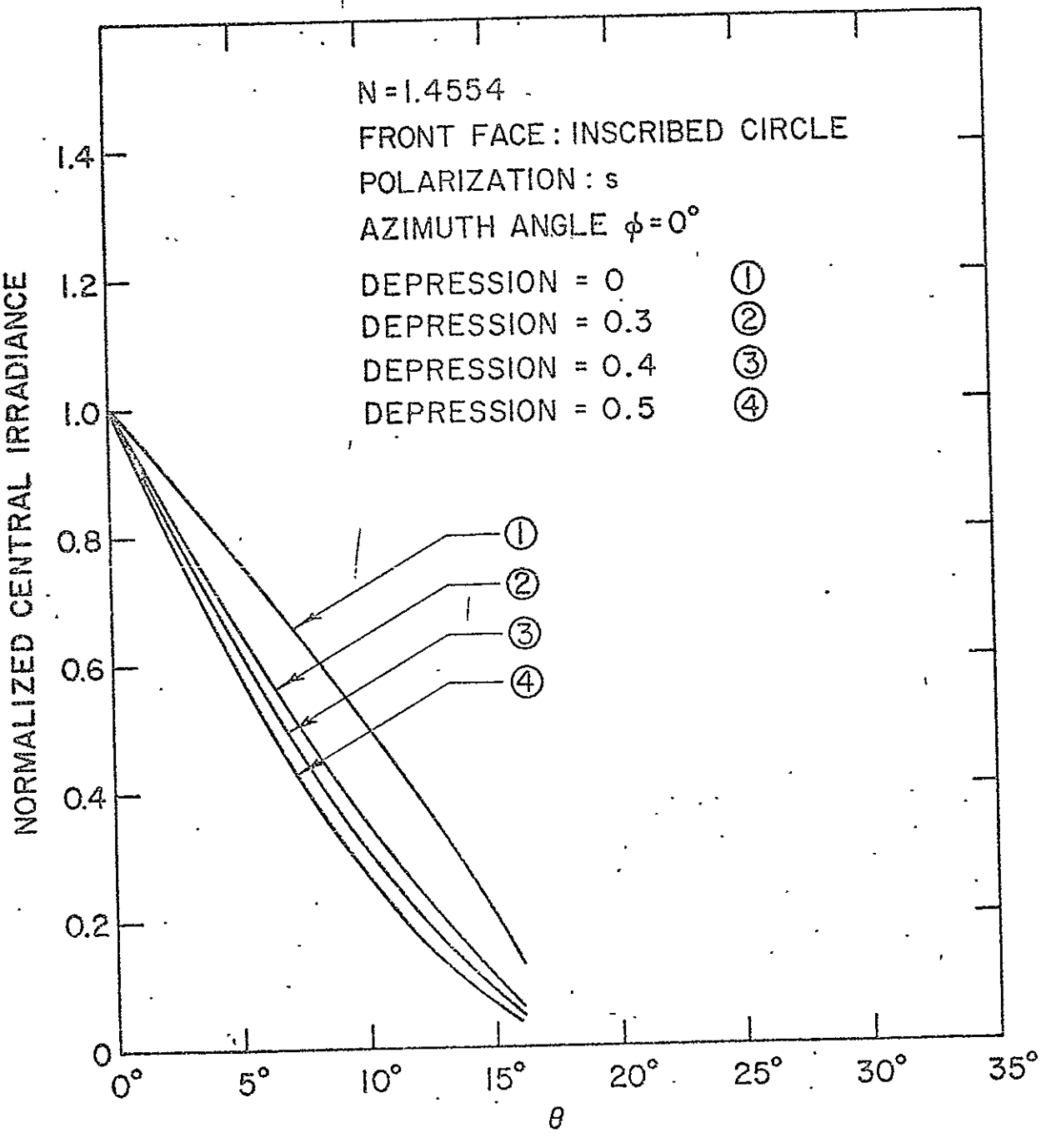

Fig. 18

Normalized central irradiance is plotted versus θ for φ = 0°. The depth of the depression is expressed in the unit of the diameter of the front face.

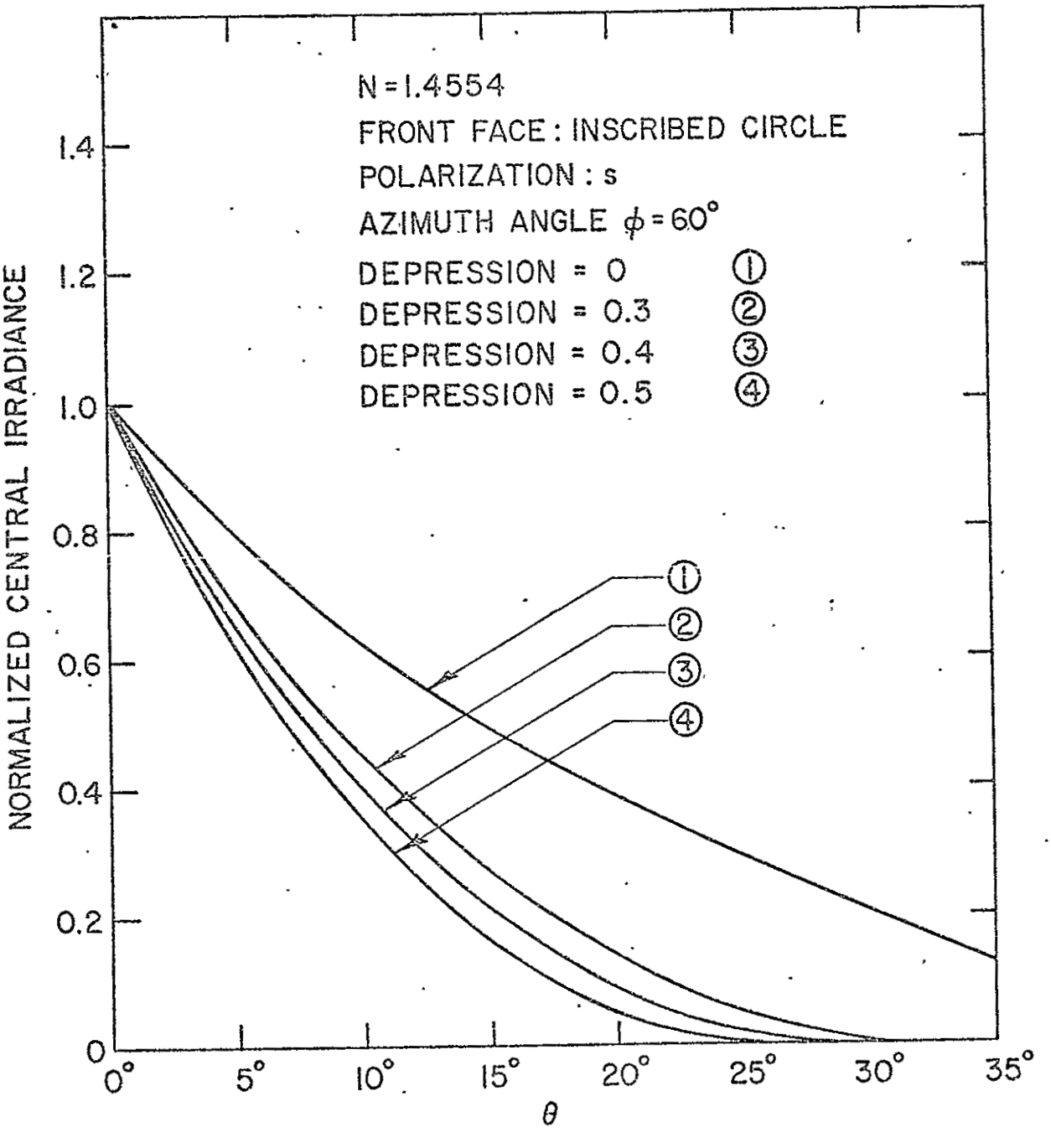

Fig. 19

The same as Figure 18 except ϕ = 60°.

ABSTRACT

A limit on the angle of incidence is imposed on a solid retroreflector with uncoated back surfaces because of the possible failure of total reflection. An expression is derived for the critical angle of incidence as a function of the index of refraction and the azimuth angle. The critical angle is the angle at which the total reflection initially fails.

The index of refraction must be greater than $\sqrt{3/2} = 1.23$ if we intend to utilize the total reflection in a retroreflector. On the other extreme, if the index of refraction is greater than $\sqrt{(3 + \sqrt{3})} = 2.18$ the retroreflector will retain its reflecting property at all angles of incidence.

In the range $\sqrt{3/2} \leq N \leq \sqrt{2}$, the expression under the radical sign in Eq.(8) is always non-negative therefore sin θ_c is always real, which is a fact supported by the geometrical analysis that the cones intersect each other.

A geometrical inspection on the cones of failure reveals that sin θ_c is a monotonic function of ϕ with its smallest value at $\phi = 0°$ and its largest at $\phi = 60°$. Now we shall prove that θ_c is always less than θ_L in the range $\sqrt{3/2} < N < \sqrt{2}$; the failure of total reflection occurs before the effective aperture vanishes and the limit on the angle of incidence is θ_c alone.

The largest θ_c is given by Eq.(8) as

$$\sin \theta_c \ (\phi = 60°) = \sqrt{2/3} \ (\sqrt{N^2-1} - \sqrt{2-N^2}). \tag{10}$$

Comparing Eq.(10) with Eq.(9), we obtain

$$r \equiv \sin \theta_c(\phi=60°) \ / \ \sin \theta_L = \frac{\sqrt{2}}{N} \ (\sqrt{N^2-1} - \sqrt{2-N^2}). \tag{11}$$

Since Eq.(11) indicates that $r = 1$ when $N = \sqrt{2}$ and $dr/dN > 0$, it is certainly true that $r < 1$ if $N < \sqrt{2}$. Consequently, $\theta_c < \theta_L$ for $\sqrt{3/2} < N < \sqrt{2}$ and $\theta_L = \theta_c$ at $\phi = 60°$ when $N = \sqrt{2}$.

The earlier geometrical analysis indicated that there should be a certain range in ϕ where no failure of total reflection can occur. The mathematical manifestation of the situation in Eq.(8) is that sin θ_c becomes complex because the expression under the radical sign becomes negative when $60° > \phi \geq \phi_o$ where $\phi_o = \sin^{-1}(\sqrt{3/2}/N)$.

Comparing sin θ_L with sin θ_c at $\phi = \phi_o$ for the case of $N > \sqrt{2}$, we find that θ_L is less than θ_c at $\phi = \phi_o$. The implication is that the angle θ_L becomes the limit even before ϕ reaches ϕ_o. The exact angle ϕ at which

$\theta_L = \theta_c$ can be evaluated by equating Eq.(8) to Eq.(9) and solving for ϕ.

If $N > \sqrt{3}$, Eq. (9) indicates that the effective aperture does not vanish; therefore the limit on the angle of incidence is imposed by the ultimate limit of 90° or θ_c.

The condition that a retroreflector retains its reflecting properties at all times is $N \geq \sqrt{3+\sqrt{3}}$. The condition is obtained from Eq.(8) by setting ϕ to 0° and $\sin \theta_c = 1$.

The critical angle θ_c combined with θ_L as the overall limit on the angle of incidence is plotted as a function of ϕ for various N in Figure 3. The region below the curve is the region in which a retroreflector retains its reflecting properties.

IV. CONCLUSIONS.

We have obtained the critical angle of incidence as a function of N and ϕ. The critical angle increases monotonically for increasing ϕ and N. The minimum value necessary for the index of refraction is $\sqrt{3/2}$ if a retroreflector with uncoated back surfaces is to retain its reflecting properties. The internal total reflection fails at all times when $N < \sqrt{3/2}$.

We also found that there was a range of ϕ where the internal reflection does not fail if $N > \sqrt{2}$; the limit on the angle of incidence is then the vanishing of the effective aperture. A retroreflector can be used even for the 90° angle of incidence for a certain range of ϕ if $N > \sqrt{3}$ and for all ϕ if $N > \sqrt{3+\sqrt{3}}$.

REFERENCES

1. N. E. Rityne, Soviet Journal of Optical Technology 1, 198 (1968).
2. C. O. Alley, P. L. Bender, R. F. Chang, D. G. Currie, R. H. Dicke, J. E. Faller, W. M. Kaula, G. J. F. MacDonald, J. D. Mulholland, H. H. Plotkin, S. K. Poultney, D. T. Wilkinson, I. Winer, W. Carrion, T. Johnson, P. Spadin, L. Robinson, E. J. Wampler, D. Wieber, E. C. Silverberg, C. A. Steggerda, J. V. Mullendore, J. D. Rayner, W. Williams, B. Warner, H. Richardson, and B. W. Bopp, "Laser Ranging Retro-Reflector," Apollo 11 Preliminary Science Report (NASA Special Publication SP-214, 1969).
3. C. O. Alley, R. F. Chang, D. G. Currie, J. V. Mullendore, S. K. Poultney, J. D. Ranyer, E. C. Silverberg, C. A. Steggerda, H. H. Plotkin, W. Williams, B. Warner, H. Richardson, B. W. Bopp, Science 167, 368 (1970).
4. C. O. Alley, R. F. Chang, D. G. Currie, S. K. Poultney, P. L. Bender, R. H. Dicke, D. T. Wilkinson, J. E. Faller, W. M. Kaula, G. J. F. MacDonald, J. D. Mulholland, H. H. Plotkin, W. Carrion, and E. J. Wampler, Science 167, 458 (1970).
5. J. E. Faller, I. Winer, W. Carrion, T. S. Johnson, P. Spadin, L. Robinson, E. J. Wampler, and D. Wieber, Science 166, 99 (1969).
6. R. F. Chang, University of Maryland, Department of Physics and Astronomy, Technical Report No. 70-129, 1970.

FIGURES

1 (a). A geometrical representation of a retroreflector.

(b). Cross-section of a retroreflector illustrating the failure of total reflection at some angle of incidence.

(c). Illustration showing the disappearance of the effective aperture.

2. The cones of failure for various values of the index of refraction.

3. The limit on the angle of incidence plotted as a function of azimuth angle for different values of the index of refraction.

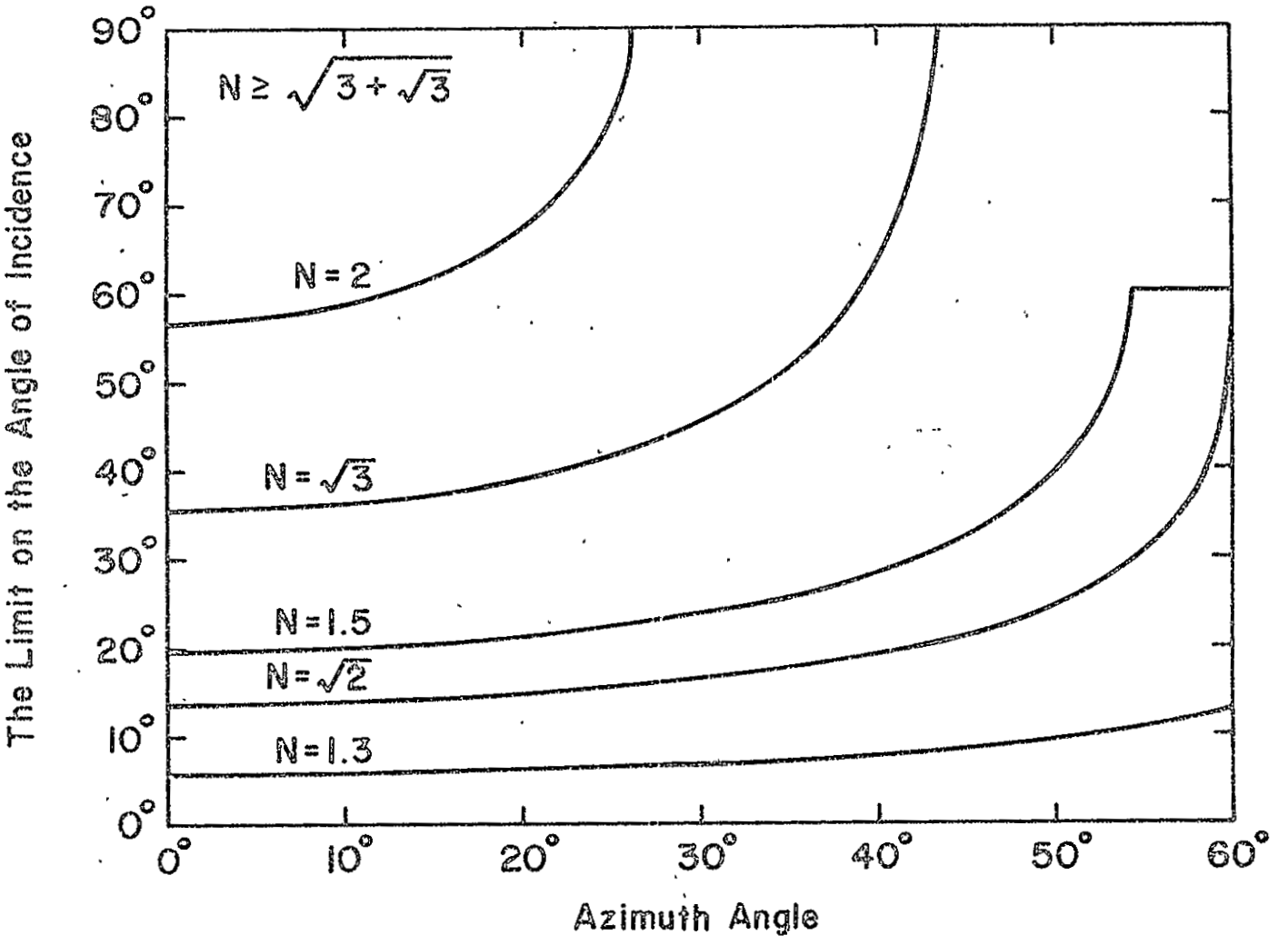

Fig. 3

The limit on the angle of incidence plotted as a function of azimuth angle for different values of the index of refraction.

ABSTRACT

Three aluminized 1-1/2" retroreflectors have been tested in the laboratory for their optical quality. The diffraction patterns from the retroreflectors are presented in comparison with the Airy pattern from a flat mirror. These retroreflectors are now in current use in the 107" telescope for the purpose of pointing the telescope precisely at the laser ranging retroreflector array on the moon.